C 55.612/3:971-72

COLLECTED REPRINTS: 1971- 1972 ATMOSPHERIC PHYSICS AND CHEMISTRY LABORATORY

A UNITED STATES
DEPARTMENT OF
COMMERCE
PUBLICATION

U.S. DEPARTMENT OF COMMERCE
NATIONAL OCEANIC AND ATMOSPHERIC ADMINISTRATION
Environmental Research Laboratories

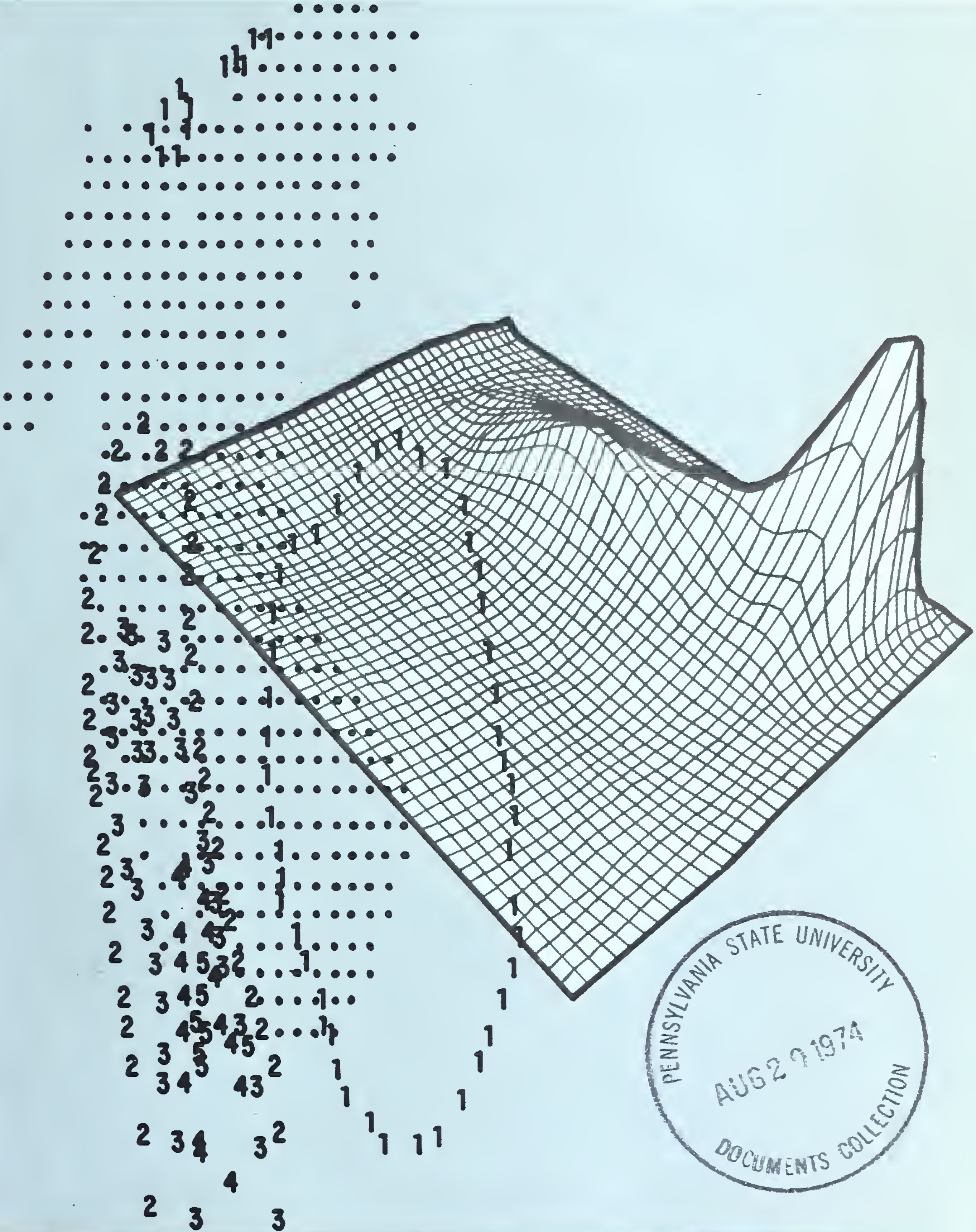

BOULDER,COLO.
JULY 1973

PENNSYLVANIA STATE UNIVERSITY
AUG 29 1974
DOCUMENTS COLLECTION

Digitized by the Internet Archive
in 2012 with funding from
LYRASIS Members and Sloan Foundation

http://archive.org/details/collectedreprin00atmo

U.S. DEPARTMENT OF COMMERCE
Frederick B. Dent, Secretary

NATIONAL OCEANIC AND ATMOSPHERIC ADMINISTRATION
Robert M. White, Administrator
ENVIRONMENTAL RESEARCH LABORATORIES
Wilmot N. Hess, Director

COLLECTED REPRINTS: 1971 - 1972
ATMOSPHERIC PHYSICS AND CHEMISTRY LABORATORY

BOULDER,COLO.
July 1973

For sale by the Superintendent of Documents, U. S. Government Printing Office, Washington, D. C. 20402

U. S. Depository Copy

FOREWORD

Weather modification is progressing rapidly from the purely empirical operational experiment towards a science based on physical principles. This is progress. Few, however, realize that such progress and evolution cost a price: The price is that many problems in basic research related to weather modification which formerly could be pushed aside on the basis of empiricism no longer can be pushed aside and behind the glamorous and glittering goal--they have to be solved. This collection contains publications and reports many of which deal with the problems arising behind the scenes of the laboratory mission. To the reader who expects revelations and new vistas in the field of weather modification they may not always seem to be "relevant," but they are, like stones in a mosaic.

Helmut K. Weickmann

COVER FIGURE

A numerical model predicts a Lake Michigan Snow storm over Chicago. The heights of the storm clouds over the lake and surrounding land area are depicted by the computer in both a contoured and a perspective mode. D. Valentine composed the picture from the output of a computer model by E. L. Magaziner.

TABLE OF CONTENTS

Page

A. FOREWORD

B. INTENTIONAL WEATHER MODIFICATION

Allee, P. A., B. T. Patten, and E. W. Barrett 1

The Dynamic Calibration of an Airborne Ice Nuclei Generator, Journal de Recherches Atmosphériques *VI*, Nos. 1,2,3, pp. 29-39, Dessens Memorial, Jan.-Sept. 1972.

Eadie, W. J., U. Katz, and C. W. Rogers 12

Investigations of Lake-Effect Snowstorms, Cornell Aeronautical Laboratory, Inc., Cornell Univ. CAL Rept. No. VC-3034-M-1, Final Rept. NOAA Contract E22-59-71(N), 50 pp., Nov. 1971.

Grote, H. H. 61

Computer Subroutine for Presenting Meteorological Flight Data on the Printer (CURVPT), NOAA Tech. Rept. ERL 199-APCL 17, 24 pp., Mar. 1971 *(Abstract only)*.

Grote, H. H. 63

Plotter Subroutine for Meteorological Flight Path, NOAA Tech. Rept. ERL 139-APCL 9, 42 pp., Dec. 1969 *(Abstract only)*.

Grote, H. H. 65

Plotter Subroutine for Meteorological Straight Line Flight Data (Slender), (Revised), NOAA Tech. Rept. ERL 140-APCL 10, 55 pp., Mar. 1971 *(Abstract only)*.

Hallett, J. D., H. D. Orville, D. Sartor, and H. K. Weickmann 67

Cloud Physics, EOS *52*, No. 6, IUGG 341-IUGG 351, June 1971.

Hoppel, W. A., and B. B. Phillips 78

The Electrical Shielding Layer Around Charged Clouds and its Role in Thunderstorm Electricity, Journal Atmospheric Sciences *28*, No. 7, 1258-1271, Oct. 1971.

Jiusto, J. E. 91

Crystal Development and Glaciation of a Supercooled Cloud, State University of New York, Albany, N. Y., Grant E22-13-69(G) and E22-49-70(G), Journal de Recherches Atmosphériques *V*, No. 2, 69-85, 1971.

TABLE OF CONTENTS (Cont'd)

Page

Kasemir, H. W. 108

Basic Theory and Pilot Experiments to the Problem of Triggering Lightning Discharges by Rockets, NOAA Tech. Memo. ERL APCL-12, April 1971 *(Abstract only)*.

Kasemir, H. W. 111

Calibration of Atmospheric Electric Field Meters and the Determination of Form Factors at Kennedy Space Center, NOAA Tech. Memo. ERL APCL-11, 92 pp., April 1971 *(Abstract only)*.

Kasemir, H. W. 115

The Cylindrical Field Mill, Meteorologische Rundschau *25*, No. 2, 33-38, Feb. 1972.

Kasemir, H. W., and F. J. Holitza 121

Description and Instruction Manual for the Cylindrical Field Mill System, NOAA Tech. Memo. ERL APCL-14, 23 pp., Feb. 1972 *(Abstract only)*.

Magaziner, E. L. 124

Statistical Evidence of Electrical Modification of Thunderstorms by Artificially Triggered Lightning, Third Conference on Weather Modification, June 26-29, 1972, Rapid City, South Dakota, 239-240.

Phillips, B. B., H. H. Grote, P. M. Kuhn, and H. K. Weickmann 126

NOAA Objectives and Results within NHRE, Third Conference on Weather Modification, June 26-29, 1972, Rapid City, South Dakota, 254-259.

Ruhnke, L. H. 132

Atmospheric Electric Cloud Modelling, Meteorologische Rundschau *25*, No. 2, 38-41, Feb. 1972.

Ruhnke, L. H. 136

Atmospheric Electricity Problems at Kennedy Space Center, Proc. Eighth Space Congress, April 19-23, 1971.

TABLE OF CONTENTS (Cont'd)

Page

Ruhnke, L. H. 138

Determining Distance to Lightning Strokes from a Single Station, NOAA Tech. Rept. ERL 195-APCL 16, 29 pp, Jan. 1971 *(Abstract only)*.

Ruhnke, L. H. 141

A Rocketborne Instrument to Measure Electric Field Inside Electrified Clouds, NOAA Tech. Rept. ERL 206-APCL 20, 31 pp., May 1971 *(Abstract only)*.

Uhlenhopp, P. B. 143

Variable DC Offset Using a Current Source, EDN/EEE *16*, No. 16, p. 46, Aug. 1971.

Weickmann, H. K. 144

Design, Execution, and Results of a Mesoscale Snowstorm Modification Project, NOAA Tech. Memo ERL APCL-15, 56 pp., May 1972 *(Abstract only)*.

Weickmann, H. K. 147

Man-Made Weather Patterns in the Great Lakes Basin, Weatherwise *26*, No. 6, 260-267, Dec. 1972.

Weickmann, H. K. 156

Snow Crystal Forms and Their Relationship to Snowstorms, Journal de Recherches Atmosphériques *VI*, Nos. 1,2,3, Dessens Memorial, 603-615, Jan.-Sept. 1972.

Weickmann, H. K., B. B. Phillips, P. M. Kuhn, and W. J. Eadie 169

Progress of the Great Lakes Weather Modification Program, Third Conference on Weather Modification, June 26-29, 1972, Rapid City, South Dakota, 287-291.

Barrett, E. W. 174

Depletion of Short-Wave Irradiance at the Ground by Particles Suspended in the Atmosphere, Solar Energy *13*, 323-337, 1971.

Page

C. INADVERTANT WEATHER MODIFICATION

Barrett, E. W., and H. K. Weickmann 189

Background and Methodology of Benchmark Stations, American Meteorol. Society Meeting, San Diego, California, 70-73, Mar. 1972.

Chin, J. F. S., H. T. Ellis, B. G. Mendonca, R. F. Pueschel, and H. J. Simpson 193

Geophysical Monitoring at Mauna Loa Observatory, NOAA Tech. Memo. ERL APCL-13, July 1971 *(Abstract only)*.

Ellis, H. T., and R. F. Pueschel 196

Solar Radiation: Absence of Air Pollution Trends at Mauna Loa, Science *172*, 845-846, May 1971.

Kasemir, H. W. 199

Atmospheric Electric Measurements in the Arctic and Antarctic Archives for Meteorologie *100*, No. 8, 70-80, 1972.

Komhyr, W. D., and T. B. Harris 210

Development of an ECC Ozonesonde, NOAA Tech Rept. ERL 200-APCL 18, 59 pp., Feb. 1971 *(Abstract only)*.

Komhyr, W. D., E. W. Barrett, G. Glocum, and H. K. Weickmann 214

Atmospheric Total Ozone Increase during the 1960's, Nature *232*, No. 5310, 390-391, Aug. 1971.

Kuhn, P. M., and L. P. Stearns 220

Radiative Transfer Observations and Calculations during BOMEX, NOAA Tech. Rept. ERL 203-APCL 19, 173 pp., April 1971 *(Abstract only)*.

Kuhn, P. M., and L. P. Stearns 222

Radiosonde Humidity Retrieval by Simultaneous Radiation Measurement, Journal Applied Meteorology *66*, No. 11, 130-135, Feb. 1972.

TABLE OF CONTENTS (Cont'd)

Page

Kuhn, P. M., M. S. Lojko, and E. V. Petersen 228

Water Vapor: Stratospheric Injection by Thunderstorms, Science *174*, 1319-1321, Dec. 1971.

Pueschel, R. F., and B. G. Mendonca 232

Sources of Atmospheric Particulate Matter on Hawaii, Tellus *24*, No. 2, 139-149, 1972.

Ruhnke, L. H. 243

Fog Droplet Sizes at the Panama Canal, NOAA Tech. Rept. ERL 209-APCL 22, 20 pp., May 1971 *(Abstract only)*.

Simpson, H. J. 245

Aerosol Cations at Mauna Loa Observatory, Journal Geophysical Research *77*, No. 27, 5266-5277, Sept. 1972.

Van Valin, C. C. 257

Effects on the Stratosphere of SST Operation, NOAA Tech. Rept. ERL 208-APCL 21, 44 pp., May 1971 *(Abstract only)*.

Van Valin, C. C., and P. A. Allee 260

Water Cloud Stabilization with Chlorinated Silanes, Journal Atmospheric Sciences *26*, No. 6, 1076-1078, Sept. 1971.

Weickmann, H. K. 263

Inadvertant Weather Modification, 14th Interagency Conference on Weather Modification, Skyland, Virginia, Oct. 1972.

Weickmann, H. K., and C. C. Van Valin 276

The Sources and Sinks of Water Vapor in the Upper Atmosphere, Preprint volume of the Internatl. Conference on Aerospace and Aeronautical Meteorology, May 22-26, Washington, D. C., 186-191, June 1972.

Reprinted with permission from Journal de Recherches Atmosphériques *VI*, Nos. 1,2,3, Dessens Memorial, Jan-Sept 1972.

THE DYNAMIC CALIBRATION OF AN AIRBORNE ICE NUCLEI GENERATOR

by

Paul A. ALLEE (1), Bradley T. PATTEN (2)
and Earl W. BARRETT (1)

RÉSUMÉ

Les générateurs aéroportés de noyaux glaçogènes sont généralement calibrés au sol : on introduit une partie de la fumée émise dans une chambre contenant un nuage d'eau surfondue maintenu à une température connue et on compte le nombre de cristaux de glace produits. On peut critiquer l'applicabilité d'une telle calibration en ce sens que les conditions réelles en vol, telles que la température de l'air, la pression, la vitesse de l'avion et la façon d'opérer ne sont pas simulées lors de la calibration. Il était souhaitable de vérifier le rendement du générateur dans des conditions de vol pour augmenter la confiance dans ces calibrations au sol. On décrit deux techniques de mesure du rendement en vol d'un générateur aéroporté de noyaux glaçogènes.

Dans une première méthode, l'avion, volant en air clair, laisse un panache de noyaux glaçogènes, puis revient couper le panache à angle droit. On mesure les concentrations en noyaux glaçogènes et en noyaux d'Aitken et on calcule le débit du générateur de noyaux glaçogènes en admettant que la distribution des concentrations en noyaux le long de la ligne de vol coupant l'axe du panache est gaussienne.

Dans la seconde méthode, le générateur aéroporté ensemence un stratus surfondu et le panache ensemencé qui se développe est photographié à partir d'un autre avion volant au-dessus du nuage. Des considérations théoriques et des mesures de la concentration en cristaux de glace sous une partie ensemencée de stratus indiquent que les concentrations en cristaux inférieurs à 100/l déterminent l'extension latérale d'un panache ensemencé. On mesure le volume ensemencé maximal du stratus et, admettant qu'à un noyau glaçogène corresponde un cristal, on calcule le nombre total de noyaux glacogènes pour deux types de solution d'iodure d'argent. De la même manière, on a mesuré l'efficacité de la neige carbonique en tant qu'agent d'ensemencement en noyaux de glace.

ABSTRACT

Airborne ice nuclei generators are usually calibrated on the ground by introducing a portion of the generated smoke into a chamber containing a supercooled

---

(1) Atmospheric Physics and Chemistry Laboratory, Boulder, Colorado, U.S.A.

(2) Research Flight Facility, Miami, Florida, U.S.A.
Environmental Research Laboratories, National Oceanic and Atmospheric Administration.

water cloud maintained at a known temperature and counting the number of ice crystals thus produced. The applicability of such a calibration is subject to the criticism that actual in-flight conditions, such as air temperature, pressure, aircraft velocity, and operational attitude, are not simulated during calibration. It was desirable to make confirmatory measurements of generator output under flight conditions since agreement between such measurements and ground based calibrations would increase confidence in the latter. Two techniques to measure the in-flight output of an airborne ice nuclei generator are described.

In one method the aircraft flew in clear air, generated an ice nuclei plume, then made a turn to intersect the plume at a right angle. Measurements of the ice nuclei and Aitken nuclei concentrations were made, and assuming the distribution of nuclei concentrations along the flight path intersecting the axis of the plume to be Gaussian, the output of the ice nuclei generator was computed.

In the second method the airborne generator was used to seed a supercooled stratus cloud and the seeded plume which developed was photographed from another aircraft above the cloud. Theoretical considerations and measurements of the ice crystal concentration under a seeded portion of the stratus cloud indicated that crystal concentrations less than one hundred per liter limit lateral spreading of a seeded plume. The maximum seeded volume of the stratus cloud was measured, and allowing one ice nucleus per crystal the total number of ice nuclei was computed to determine the output of the airborne ice nuclei generator for two types of silver iodide solution utilized. In the same manner the efficiency of dry ice used as an ice nuclei seeding agent was measured.

INTRODUCTION.

Airborne ice nuclei generators are usually calibrated on the ground by introducing a portion of the generated smoke into a chamber containing a supercooled water cloud maintained at a known temperature and counting the number of ice crystals produced. The applicability of such a calibration is always subject to the criticism that actual in-flight conditions, such as air temperature, pressure, aircraft velocity, and operational attitude, are not simulated during these calibrations. It was desirable to make confirmatory measurements of the output of a generator under actual flight conditions since agreement between such measurements and ground based calibrations would increase confidence in the latter. This paper describes two techniques used to measure the in-flight output of an airborne ice nuclei generator.

The generator chosen for these experiments was the Patten Mark Series Generator, developed by Bradley T. Patten of the Research Flight Facility of the National Oceanic and Atmospheric Administration (NOAA), U. S. Department of Commerce (Patten [1], [2] and Patten et al. [3]). This particular generator has been used by the Atmospheric Physics and Chemistry Laboratory of NOAA for seeding supercooled stratocumulus clouds in the vicinity of Lake Erie during the Great Lakes Snow Redistribution Project (McFadden and Friedman [4]).

FIRST DYNAMIC CALIBRATION PROCEDURE.

In these experiments, the generator was operated while the aircraft flew on a straight and level track for a two-minute period in clear, clean air, the airplane then made a 270 degree procedural turn to the right followed by a straight leg which intersected the seeded plume at a right angle. Figure 1 shows a diagram of the flight path. During the

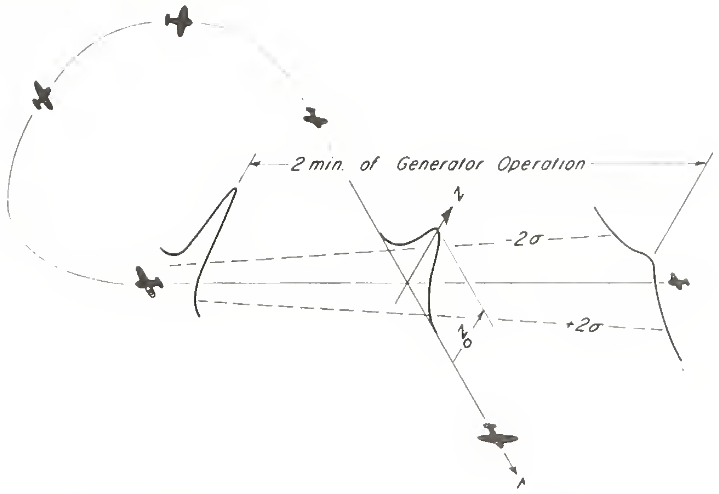

Fig. 1. — Flight path of the airplane used to sample the plume of particles from the ice nuclei generator-N, N_0, r and σ are some of the parameters in the Gaussian expression that describes the distribution of the particles within the plume.

cross-plume leg, concentrations of Aitken and ice nuclei were measured by an Environment One Condensation Nuclei Monitor and an NCAR acoustic ice nucleus counter, respectively. Elapsed time between starting of the generator and passage through the plume was about 3 ½ minutes. The experiments were conducted at about 9,700 ft pressure altitude where the background counts of natural nuclei concentrations were below the detection thresholds of the counting instruments. Significant counts were positive evidence of penetration of the plume.

The ice nucleus and Aitken particle counts obtained on the cross-plume flight paths were used, together with the theory given below, to compute the rate of nucleus production by the generator.

Theory.

The plume of silver-iodide (and other) particles emitted by the generator undergoes spreading as a result of eddy diffusion. This spreading rate is quite rapid during the first minute or so after release because of the large eddy energy generated by the aircraft, but decreases thereafter to a rate which corresponds to the natural eddy diffusivity of the free atmosphere at flight level. We therefore assume that, after the initial large perturbation has decayed, the concentration of particles is given to a fair degree of approximation by a Gaussian function of radial distance from the plume axis. This is equivalent to the assumption of local isotropy of turbulence in all directions orthogonal to the plume axis. On the basis of this assumption, the distribution of ice-nucleus counts obtained on a pass which is perpendicular to, and intersects the axis of, the plume should be a Gaussian function of time (at constant airspeed). Furthermore, as will be shown, this distribution of counts determines the total number of nuclei per unit length of plume, and hence the output of the generator per unit time.

Unfortunately, the response time of the ice-nucleus counter is too long to permit resolution of the actual distribution during a pass through the plume. However, experiments have shown that the counter is a quite accurate integrator, i.e., the total count obtained on a pass through a plume is proportional to the area under the actual spatial distribution curve. The total count thus gives the integral of the assumed Gaussian function, but does not permit unique calculation of the two parameters of the function, namely, the peak concentration and the standard deviation σ. However, the more rapid resolution time of the Aitken counter (1 sec) does resolve some details of the curve shape. Since the diffusion process should not cause any preferential fractionation of ice nuclei relative to inert particles, it follows that the value of σ obtained from the Aitken measurements is also correct for the ice-nucleus distribution.

Having these independent measurements of the spread and the integral of the Gaussian distribution of ice nuclei, it is a simple matter to compute the number N of ice nuclei per meter of plume length. Let N_1 be the total number of ice-nucleus counts obtained on a pass, and A be the effective capture area of the intake probe of the counter. Then, quite generally, for any distribution n(r) of particle concentration (number/m^3) as a function of radial distance r (meters) from the plume axis, we have

$$N_1 = A \int_{-\infty}^{\infty} n(r)\, dr \tag{1}$$

by virtue of the integrating property of the ice-nucleus counter. Letting N_0 be the concentration of ice nuclei at the peak of the plume axis, we have

$$N_1 = A N_0 \int_{-\infty}^{\infty} \exp(-r^2/2\sigma^2)\, dr \tag{2}$$

which yields, on integration

$$N_0 = N_1/(2\pi)^{1/2}\ \sigma\ A \tag{3}$$

Now, since the two-dimensional distribution of ice nuclei is simply the axisymmetric surface generated by rotating the Gaussian function $N_0 \exp(-r^2/2\sigma^2)$ about its axis ($r = 0$), the total number of particles per meter of plume is given by

$$N = N_0 \int_0^{\infty} \int_0^{2\pi} \exp(-r^2/2\sigma^2)\, r\, d\theta\, dr \tag{4}$$

Again, the integral may be evaluated in closed form as

$$N = 2\pi N_0 \sigma^2 \tag{5}$$

Elimination of N_0 between eqs. (3) and (5) gives the desired result

$$N = (2\pi)^{1/2}\ \sigma\ N_1/A \tag{6}$$

in terms of the known quantities N_1, σ, and A.

Since N is the number of particles emitted per unit length of flight path, the product of N by the airspeed v of the plane gives the total number of active ice nuclei emitted per unit time. Also, since the AgI concentration in the generator charge and the rate of burning of the charge are known, the product Nv can be converted immediately to the ratio of nuclei produced per gram of AgI.

The accuracy of the calculation depends on : (a) the accuracy of the ice-nucleus counter as an integrator ; (b) the *relative* accuracy of the Aitken or total-particle counter during a pass through the plume ; c) the degree to which the assumption of laterallyisotropic turbulence is met in practice ; and (d) the exactness with which the sampling pass intersects the true plume axis. The last of these is one of the largest sources of error ; it may be minimized by making several passes through the plume at slightly different altitudes until the true maximum is found. It is clear from the geometry that, if a pass is made at height h above or below the true plume axis, the distribution actually seen is given by the intersection of the two curves $n = N_0 \exp [- (x^2 + y^2)/2 \sigma^2]$ and $y = \pm h$, which is

$$n = N_0 \exp (- h^2/2 \sigma^2) \exp (- x^2/2 \sigma^2) \tag{7}$$

in which x is the distance along the sampling flight path. Thus, a pass above or below the plume axis gives a correct measure of σ, but a value of N_0 (and hence ultimately a value of N) which is too low by a factor of $\exp (- h^2/2 \sigma^2)$.

Results.

Nine experiments were carried out as described above. The measurements showed that the vertical extent of the plume (to the point where it was indistinguishable from the background) was from + 20 to — 450 ft relative to the aircraft altitude at time of release. The level of maximum count was at — 200 ft. Such a lowering is to be expected because of the downwash from the aircraft.

Because of the narrowness of the plume, it was not possible to obtain a very precise figure for the standard deviation σ. Usually, only one reading above background was obtained on a pass. The width of the plume was therefore less than the distance covered by the aircraft in 2 sec, or 206 m. Taking the effective plume width to be 4 σ, one obtains an approximate upper bound for σ of about 50 m. It is evident that a total-particle counter with much faster response time is needed to improve the accuracy of determination of σ in future work.

Using this value of σ and the ice-nucleus counts obtained on the pass at —200 ft yields an ice-nucleus production rate of 3.0×10^{15} nuclei (active at —20 °C) per gram of AgI dispersed. As may be seen in Figure 8, this value lies near the spread of data points obtained in ground calibrations of the same generator at the testing facility of Colorado State University, Fort Collins, Colorado.

Conclusions.

The results given above demonstrate the feasibility of in-flight calibrations of ice-nucleus generators. The vertical and horizontal dimensions of the plume were found to be of the same general order of magnitude, thus lending some support to the assumption of isotropic diffusion. The major limitation to accuracy in the experiments as conducted was the inability of the Aitken counter to give enough data points per pass to define the plume profile satisfactorily ; an isokinetic-flow counter using optical sensing will be required to remove this limitation in future work.

SECOND DYNAMIC CALIBRATION PROCEDURE.

Two DC-6 aircraft were used in this experiment. One DC-6 (39 C) was equipped with a dry ice dispenser and AgI generators for seeding and with a formvar ice crystal sampler. In addition, IR radiometers measured cloud temperatures for any release of the heat of fusion, the liquid water content was measured by the Johnson Williams meter, two nuclei counters measured the concentration of Aitken and freezing nuclei, and two pyrheliometers measured changes in albedo such as may occur from seeding. A second DC-6 (40 C) flew well above the cloud deck. Its mission was to direct the lower aircraft after seeding to traverse the seeding pattern for analysis, to follow the development of the seeding pattern, and to observe the halo phenomena which are related to the habit of crystal forms.

The decision to conduct an experiment was made on the basis of the availability of extended persistent supercooled stratus decks in the temperature range —5 to —15 °C. The DC-6 (39 C) then flew a predetermined flight path within the stratus cloud releasing the seeding agents. Several seeding agents were tested side by side by flying parallel lines through the cloud deck. Each line was about ten miles long and separated by five miles. It was planned that the seeding aircraft would release the following chemicals, not necessarily in this order :

Line A : Aircraft only without artificial seeding generator.

Line B : Seeding with dry ice at a rate of approximately 7 kg per mile.

Line C : Seeding with the Patten generator, burning a 2 percent solution of AgI + NaI ; 7 g AgI /mile.

Line D : Seeding with the Patten generator, burning a 2 percent solution of AgI + NH_4I ; 7 g AgI /mile.

Theory.

Figures 2 to 7 show some aspects of the seeding patterns as seen from the observation aircraft after seeding. The track first develops as (Fig. 2) a distinct glaciated line within the cloud top. The seeded line then spreads out rather homogeneously perpendicular to the original flight path as long as there exists an abundance of ice crystals. If this homogeneous spreading is due to an isotropic eddy diffusion process throughout the cloud layer, then the rate of lateral spreading will be comparable to the vertical motion in the cloud deck. In the cases under investigation this lateral spreading ranged from less than 1 m /sec to more than 2 m /sec. These velocities are comparable to vertical velocities which have been measured by Doppler radar in similar clouds in this Great Lakes region. The diffusion process transports the ice crystals generated by the seeding into new cloud areas which glaciate and snow-out as long as the crystal concentration is sufficiently high. Sometimes (Fig. 7) a sharp and steep cloud edge develops indicating the efficient ice crystal fallout of the water clouds after seeding. Based upon Jiusto's work [5], [6], on overseeding conditions of clouds with 1 m /sec updrafts, one can estimate that 100 crystals /liter are necessary to accomplish this for liquid contents comparable to the cloud decks shown in the figures. (Measurement with a Johnson Williams and a Levine liquid water content meter varied widely from .1 to 1 g /m^3). It takes less than 10 minutes to convert such a cloud into an ice-cloud through diffusion of the water content onto the ice crystals. Flying underneath the seeded region on 21 February 1971, and sampling the crystals with a foil sampler also indicated a maximum concentration of 100 particles per liter. It can now be postulated that a crystal concentration of 100 / liter is the minimum which will still advance the artificial ice cloud into the water cloud ; therefore, this threshold number can be used to estimate the efficiency of the generator. It is assumed that a concentration of 100 crystals /liter throughout the entire converted area is the limiting condition when spreading of the line will stop.

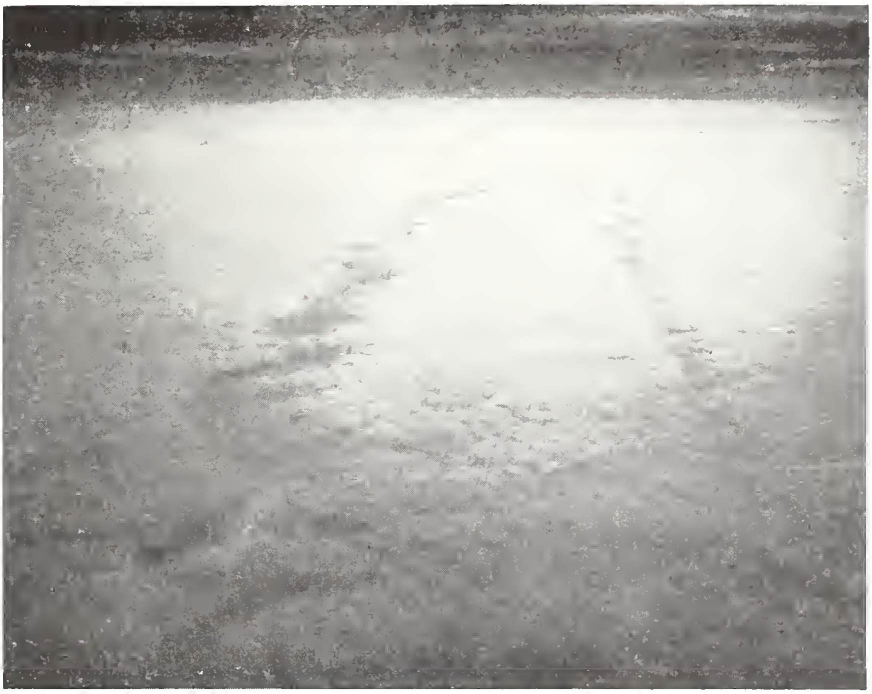

FIG. 2. — 21 February 1971, 1040 EST, Legs # 1 and 2, U shaped, AgI + NH_4I, 2 percent solution, rate 5 g AgI/km.

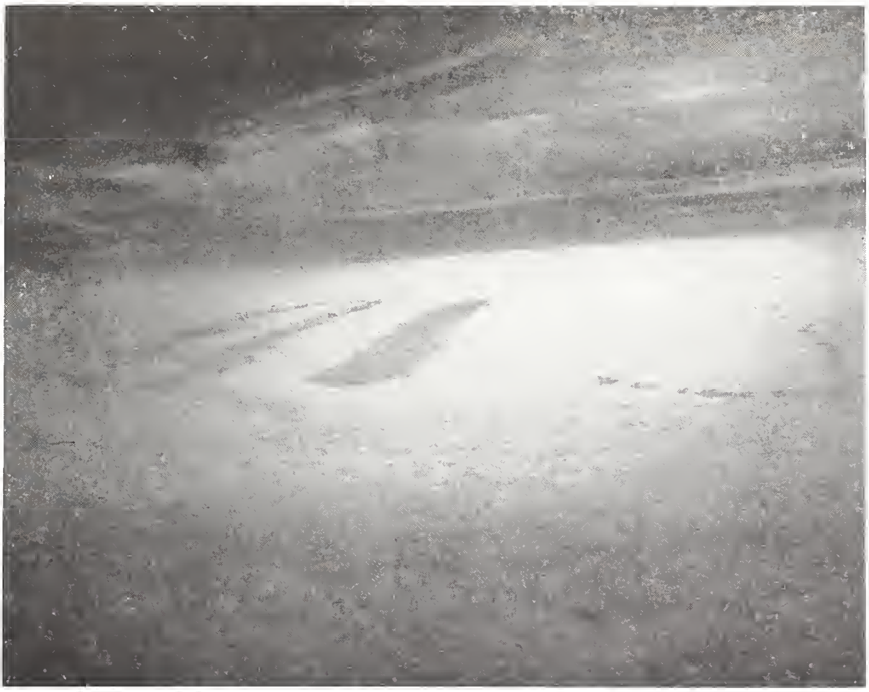

FIG. 3. — 21 February 1971, 1053 EST.
Leg #1} U shaped AgI + NH_4I, 2 percent solution
Leg #2} seeding, rate 5 g AgI/km.
Leg #3 Dry ice seeding, rate 2850 g/km.
Leg #4 Invisible, aircraft without artificial seeding.
Leg #5 J pattern AgI + NaI, 2 percent solution, rate 5 g AgI/km.

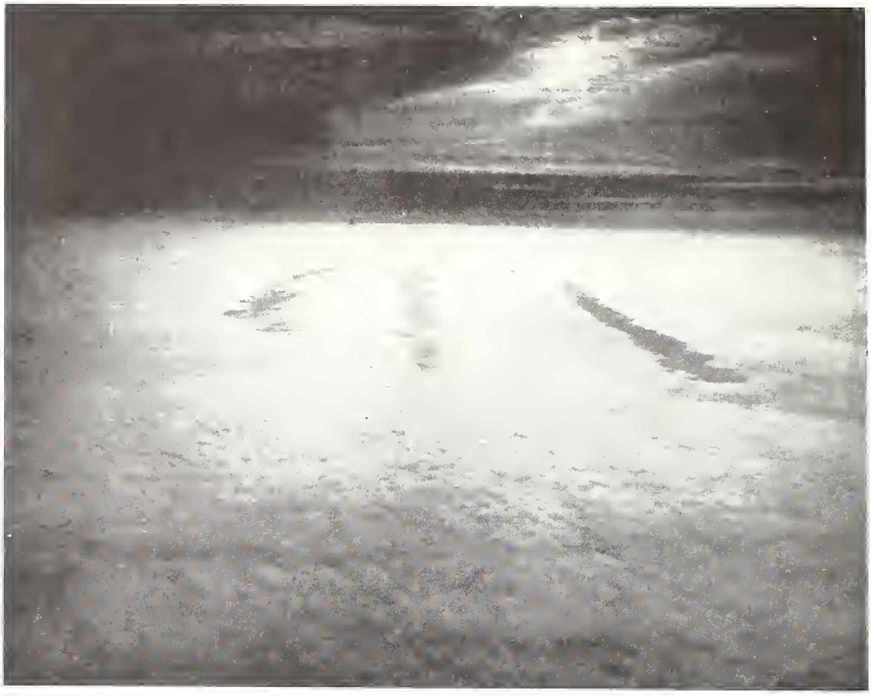

FIG. 4. — 21 February 1971, 1045 EST,
Leg #1 U shaped AgI + NH_4I, 2 percent solution,
Leg #2 rate 5 g AgI /km.
Leg #3 Dry ice, rate 2850 g /km.

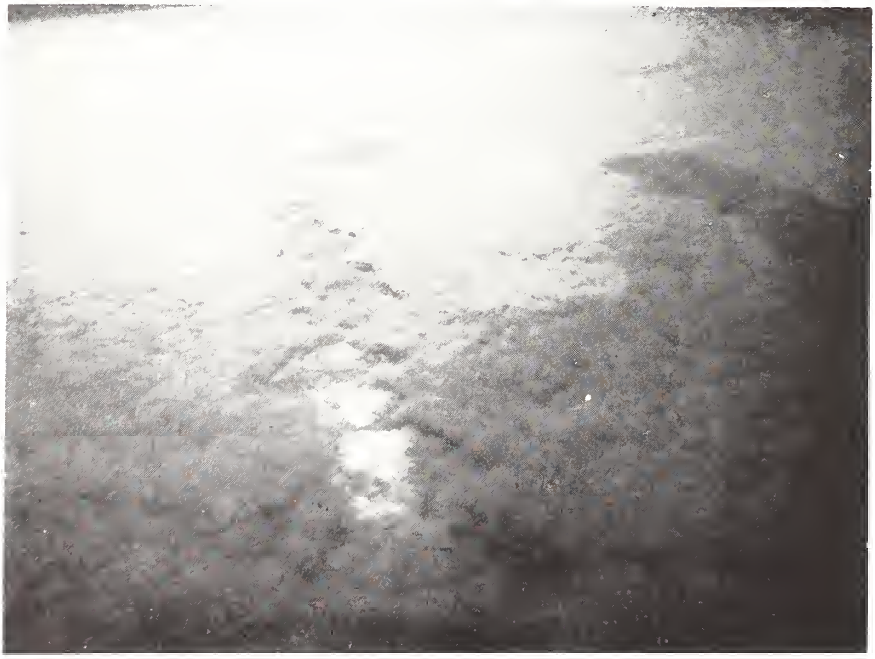

FIG. 5. — 21 February 1971, 1100 EST.
Leg #5 AgI + NaI, 2 percent solution, rate 5 g AgI /km.
Leg #6 Dry ice seeding, rate 2850 g /km.

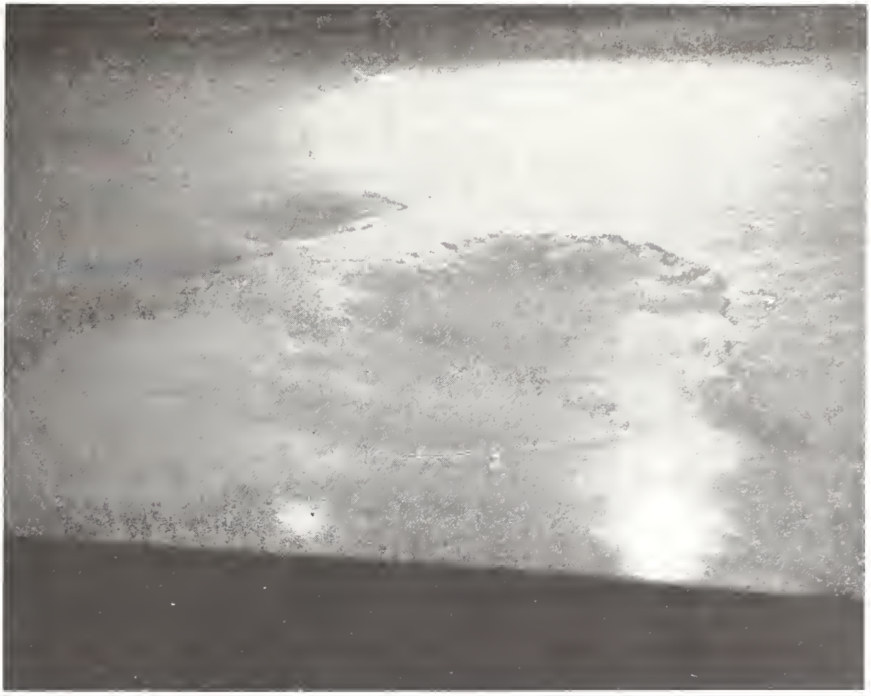

FIG. 6. — 21 February 1971, 1115 EST.
Leg #5 AgI + NaI, 2 percent acetone solution, rate 5 g AgI/km.
Leg #6 Dry ice seeding, rate 2850 g/km.

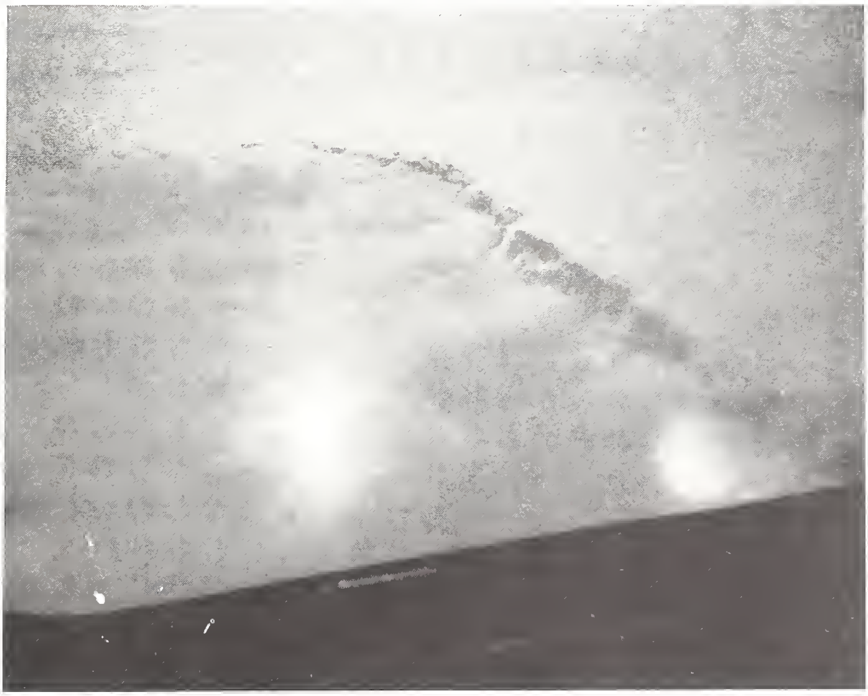

FIG. 7. — 21 February 1971, 1113 EST.
Leg #3 Dry ice seeding area.

Flight Procedures and Observations.

Only two flights had cloud conditions suitable to make subsequent calculations of the efficiency of the ice nuclei generator.

21 *February* 1971.
Take off : 0945 EST, landing : 1435 EST.
Mission : Seeding mission in homogeneous cloud deck, base at 4500 feet, —6 °C, tops at 7000 feet, —7.5 °C, wind at tops 300°, 16 kts.
Six legs were treated as follows and are shown on Figures 2 through 7 :
Leg # 1 and # 2 : $AgI + NH_4I$, 2 percent in acetone solution, 5 g AgI /km.
Leg # 3 : Dry ice, seeding rate 2850 g /km.
Leg # 4 : No seeding, control.
Leg # 5 : AgI + NaI, 2 percent in acetone solution, 5 g AgI /km.
Leg # 6 : Dry ice, seeding rate 2850 g /km.
In 30 minutes after seeding the AgI + NaI leg had spread to about .6 km, the $AgI + NH_4I$ to about 1 km, and the dry ice to about 2 km.

24 *February* 1971.
Take off : 1105 EST, landing : 1625 EST.
Seedings took place over western Lake Ontario, cloud deck varying but with average base at 5000 feet, —8.5 °C, and tops 7000 feet, —10.8 °C.
Leg # 1 : $AgI + NH_4I$, 2 percent in acetone solution, rate 5 g AgI /km.
Leg # 2 : Dry ice seeding rate 2400 g /km.
Leg # 3 : AgI + NaI, 2 percent in acetone solution, rate 5 g AgI /km.
Seeding was accomplished 800 feet below cloud tops. In 30 minutes after seeding the cloud deck dissipated in the seeded area and the AgI + NaI leg had spread to about 1 km, $AgI + NH_4I$ to about 2 km, the dry ice to about 3 to 3½ km ; the cloud deck was still dissipating 2 hours after seeding began. Data were also obtained on formvar and foil hydrometer samplers.

Radar echoes were observed on the Buffalo WSR-57 radar of the National Weather Service and reported over national teletype network.

Results.

On the assumption that a crystal concentration of 100 /liter is the minimum concentration which will advance an artificial ice cloud into a water cloud, this threshold number was used to estimate the efficiency of the generator. The results are :

21 Februrary 1971 : Temperature range —6 to —7.5 °C.
Dry ice : 7.0×10^{10} crystals per gram of dry ice.
AgI + NaI in 2 percent solution : 9.6×10^{12} crystals per gram of AgI.
$AgI + NH_4I$ in 2 percent solution : 1.6×10^{13} crystals per gram of AgI.

24 February 1971 : Temperature range —8.5 to —10.8 °C.
Dry ice : 7.5×10^{10} crystals per gram of dry ice.
AgI + NaI in 2 percent solution : 1.2×10^{13} crystals per gram of AgI.
$AgI + NH_4I$ in 2 percent solution : 2.4×10^{13} crystals per gram of AgI.
The number of crystals generated per gram of AgI are plotted on Figures 8 and 9, as appropriate.

CONCLUSION.

While the concentrations computed for dry ice compare satisfactorily with concentrations established in the literature, the AgI concentrations are in general lower than those derived from the cold chamber calibrations of the RFF burner (Figs 8, 9), particularly if the values with 0.5 g water content per cubic meter are compared. One can only say that the dynamic calibrations confirm the cold chamber data. It is noteworthy that the $AgI + NH_4I$ solution in the field test performs better by a factor of 2 than the $AgI + NaI$ solution.

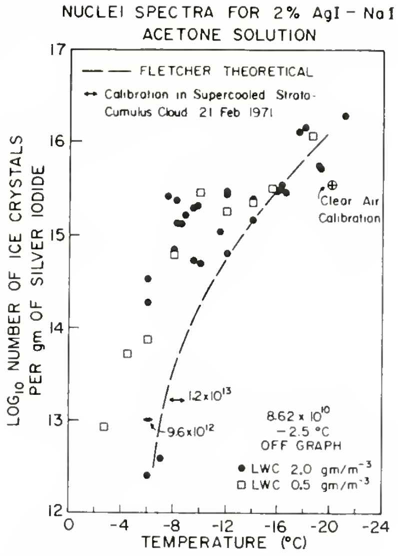

FIG. 8. — Nuclei spectra for 2 percent $AgI + NaI$ acetone solution. Dynamic calibration, 21 February 1971.

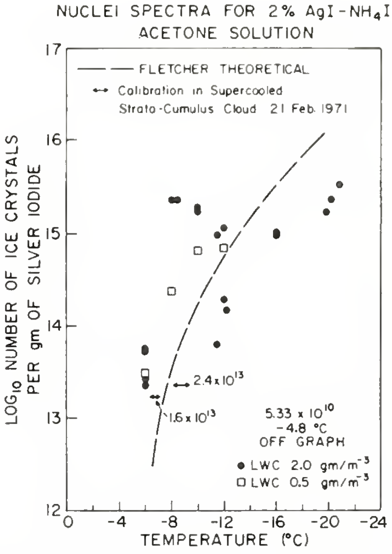

FIG. 9. — Nuclei spectra for 2 percent $AgI + NH_4I$ acetone solution. Dynamic calibration, 21 February 1971.

ACKNOWLEDGMENT.

The authors wish to acknowledge that the details of the second dynamic calibration procedure were furnished by Dr. H. K. Weickmann, Director of the Atmospheric Physics and Chemistry Laboratory, NOAA, Boulder, Colorado.

REFERENCES

[1] PATTEN B.T. — Preliminary report on the Patten Mark Series Generators. On file at RFF, NOAA, Miami, Florida.

[2] PATTEN B.T. — Information and data sheet for Patten Mark Series Generators. On file at RFF, NOAA, Miami, Florida.

[3] PATTEN B.T., MCFADDEN J.D. and FRIEDMAN H.A. (1971). — NOAA Research Flight Facility

capabilities for weather modification research. Part III. Airborne cloud seeding systems developed and utilized by the Research Flight Facility. Proc. Int. Conf. on Weather Modification, Canberra, Australia, p. 358.

[4] MCFADDEN J.D. and FRIEDMAN H.A. (1971). — NOAA Research Flight Facility capabilities for weather modification research. Part I. The Research Flight Facility's involvement in weather research programs. Proc. Int. Conf. on Weather Modification, Canberra, Australia, p. 361.

[5] JIUSTO J.E. and HOLROYD E.W. (1970). — Great Lakes snowstorms — Part 1 : Cloud physics aspects. ASRC, State Univ. of New York at Albany, ESSA Grant No. E22-49-70, 142 p.

[6] JIUSTO J.E. (1971). — Crystal development and glaciation of a supercooled cloud. J. *Rech. Atmos.*, V, nº 2, pp. 69-85.

CORNELL AERONAUTICAL LABORATORY, INC.
Buffalo, New York 14221

INVESTIGATIONS OF LAKE-EFFECT SNOWSTORMS

Final Report

Contract No. E22-59-71(N)

CAL Report No. VC-3034-M-1

29 November 1971

Prepared by: William J. Eadie
William J. Eadie
Principal Investigator

Approved by:
Roland J. Pilié, Asst. Head
Exploration Systems Department

Ulrich Katz
Ulrich Katz

C. William Rogers
C. William Rogers

Prepared for:

U. S. Department of Commerce
National Oceanic and Atmospheric Administration
Boulder, Colorado 80302

TABLE OF CONTENTS

Section | Page

LIST OF FIGURES iii

ACKNOWLEDGEMENTS v

ABSTRACT vi

I. INTRODUCTION 1

II. OBSERVATIONAL STUDIES OF LAKE-EFFECT SNOW 3

  A. Terminal Velocity Measurements of Snow Crystals 3

    1. Description of Sampler 5
    2. Field Testing of the Sampler 8
    3. Evaluation of Samples 8
    4. Conclusions 12

  B. Surface Snow Crystal Observations 17

    1. The Storm of 23 November 1970 17
    2. The Storm of 7 January 1971 19
    3. The Storm of 28 January 1971 21
    4. Conclusions 24

  C. Test of Automatic Snow Gauges 26

III. MESOSCALE MODELING OF LAKE-EFFECT SNOWSTORMS 31

  A. Development of a Lake Erie-Lake Ontario Model 32

  B. Numerical Experiments with the Lake Erie-Lake Ontario Model 33

  C. Recommendations for Future Studies 42

REFERENCES 43

LIST OF FIGURES

Figure No.		Page
1	Map of Experimental Area	4
2	Snow Sampler in Operating Configuration	6
3	Interior View of Snow Sampler	6
4	Paired Snow Crystal Photographs from 7 January 1971	9
5	Paired Snow Crystal Photographs from 7 January 1971	10
6	Paired Snow Crystal Photographs from 7 January 1971	11
7	Snow Crystals Measurements Obtained on 27 December 1970	13
8	Snow Crystal Measurements Obtained on 5 January 1971 (All Snow Pellets)	14
9	Snow Crystal Measurements Obtained on 7 January 1971	15
10	Snow Crystal Measurements Obtained on 16 January 1971	16
11	Precipitation Echo Contours (dB Attenuation) from WSR-57 Radar at Buffalo Weather Station at 1142Z on 23 November 1970	18
12	Precipitation Echo Contours (dB Attenuation) from the WSR-57 Radar of the Buffalo Weather Station at 1740Z on 7 January 1971	20
13	Precipitation Echo Contours (dB Attenuation) from WSR-57 Radar at Buffalo Weather Station at 2041Z on 28 January 1971	23
14	Size Distributions of Snow Crystals Obtained from a Lake Effect Band off Lake Ontario in the Vicinity of Lockport and Medina, New York on 28 January 1971	25
15	Comparison of Snow Gauge Measurements Obtained at Ashford Experimental Site during a Lake-Effect Snowstorm on 7 January 1971	28

Figure No.		Page
16	Comparison of Snow Gauge Measurements Obtained at Ashford Experimental Site During Wet Snow and Rain on 26 January 1971	29
17	Precipitation Echo Contours (db Attenuation) from the WSR-57 Radar of the Buffalo Weather Bureau at 2243Z on 15 November 1969	34
18	Deformation of Inversion Surface (m) Predicted for 15-16 November 1969 Storm (Initial Height = 1000 m)	39
19	Distribution of Precipitation Rate (mm hr^{-1} of Melt Water) Predicted for 15-16 November 1969 Storm	40

ACKNOWLEDGEMENTS

Several CAL personnel, in addition to the authors, made important contributions to the work presented in this report. Mr. George A. Zigrossi, Mr. Roy R. Lapp, and Mr. Alfred Wright installed and maintained the snow gauge network. The snow gauge records were analyzed by Mr. Eugene J. Mack. Mr. Warren C. Kocmond and Mr. Mack carried out snow crystal observations in lake-effect snowstorms.

We are indebted to Dr. Helmut K. Weickmann and Mr. Byron B. Phillips of NOAA for several valuable discussions and suggestions on both the field observations and the numerical modeling research. Finally, it is important to again acknowledge the excellent support and cooperation provided by the staff of the National Weather Service station at Buffalo.

ABSTRACT

The results of observational and mesoscale modeling studies of lake-effect snowstorms are presented.

Field observations were carried out in the Western New York area during the winter of 1970-1971. A portable snow sampling system to measure the fall velocities of snow crystals and to record the size and shape of the crystals was developed and successfully tested. Data are presented for small snow pellets, plane dendrites, spatial dendrites, aggregates, and a variety of unclassifiable snow forms. Additional surface snow crystal observations were obtained in lake-effect snowstorms produced by Lake Erie and Lake Ontario. A test of a small network of automatic snow gauges showed generally satisfactory correlations among the measurements of the individual gauges in light to moderate snowfall, but revealed some inadequacies in heating.

The single-layer Lavoie model for the steady state mesoscale circulations produced by the flow of cold air over Lake Erie was generalized to treat the joint Lake Erie-Lake Ontario system. The results of numerical experiments with moist modifications of the two-lake model are discussed. An example is given of a numerical experiment, based on a Lake Erie storm, in which narrow intense bands were predicted from both Lake Erie and Lake Ontario. Calculated water budget values for the predicted storm bands are discussed. Recommendations for future mesoscale modeling studies are presented.

I. INTRODUCTION

The Cornell Aeronautical Laboratory has conducted research on lake-effect snowstorms under sponsorship of the Atmospheric Physics and Chemistry Laboratory of NOAA (formerly of ESSA) since 1965. The objectives of these studies have been the understanding of the dynamics and cloud physics of lake-effect snowstorms, and the determination of the feasibility of their artificial modification. During the winters of 1968-1969 and 1969-1970, CAL participated in NOAA weather modification experiments on lake-effect cloud systems produced by Lake Erie. These experiments were initiated to test two lake snow modification hypotheses: (a) that the snowfall from intense lake-effect storms can be redistributed over a larger area by overseeding with ice nuclei, thereby reducing the heavy natural snowfall near the lakeshore, and (b) that seeding can stimulate significant precipitation from lake-effect cloud systems not naturally producing heavy snow. In addition, the cloud physics and dynamics of lake-effect snowstorms were investigated using a single-layer numerical model of the steady state mesoscale circulations produced by the flow of cold air over Lake Erie.

Results from the weather modification experiments have been presented in CAL final reports (Eadie, 1970; Eadie et al., 1971) and in reports of the other participating organizations (Layton, 1969; Warburton and Owens, 1969; Lavoie et al., 1970; Jiusto and Holroyd, 1970). On numerous occasions, significant amounts of precipitation were induced from fairly thick stratocumulus clouds by seeding with 1-10 ice nuclei per liter of cloud air. The experiments also demonstrated that overseeding could be accomplished for short periods in lake-effect snow bands of moderate intensity. The direct results were great increases in the number of elementary snow crystals and the reduction or elimination of riming. However, the weather situations encountered in the experimental area during the winters of 1968-1969 and 1969-1970 were not conducive to definitive tests of the overseeding hypothesis. It remained to be demonstrated that overseeding could be achieved in practice in intense lake-effect snowstorms, or more important, that overseeding would, in fact, result in significant redistribution of snowfall from these storms.

Funding limitations prevented a continuation of weather modification experiments on lake-effect snowstorms during the past winter. Under a contract from NOAA covering the period from 23 November 1970 to 22 September 1971, CAL carried out observational and theoretical studies intended to provide an improved basis for future weather modification experiments, and to expand mesoscale modeling capabilities. This report presents a description of the work performed and the results achieved.

A portable instrument to measure the fall velocities of snow crystals and to record the size and shape of the crystals was constructed and successfully tested during the past winter. Additional surface snow crystal observations were obtained in several lake-effect snowstorms. A test of a small network of automatic snow gauges to establish their usefulness in measuring precipitation rates in lake-effect snowstorms showed generally satisfactory correlations between the measurements of the individual gauges in light to moderate snowfall, but revealed some inadequacies in heating. These observational studies on lake-effect snow are described in Chapter II of this report.

In earlier lake-effect studies at CAL (McVehil et al., 1967, 1968), a single-layer numerical model developed by Lavoie (Davis et al., 1968) was applied to investigate the mesoscale circulations produced in cold air flowing across Lake Erie. Subsequent research with moist modifications of the Lavoie model both at CAL (Eadie et al., 1971) and Pennsylvania State University (Lavoie et al., 1970) resulted in the prediction of precipitation distributions from lake-effect snowstorms. Under the present contract, the Lake Erie model was successfully generalized to treat the joint Lake Erie-Lake Ontario system, and numerical experiments were carried out with moist modifications of the two-lake model. Chapter III contains a discussion of this mesoscale modeling research and recommendations for future modeling studies.

II. OBSERVATIONAL STUDIES OF LAKE-EFFECT SNOW

The objectives of the limited field observation program carried out during the early winter of 1970-1971 were: (1) to obtain measurements of snow crystal fall velocities; (2) to make supporting measurements of snow crystal type and size; and (3) to test a small network of automatic snow gauges to establish their usefulness in measuring precipitation rates in lake-effect snowstorms. These studies were undertaken to develop an improved basis for the design of future weather modification experiments. They were performed in the Western New York area, shown in Figure 1.

A. Terminal Velocity Measurements of Snow Crystals

The basic concept in the overseeding experiments on lake-effect snowstorms is to replace natural rimed snow crystal types with slower falling unrimed crystals. For the design as well as the verification of modification experiments, it is, therefore, essential to know the terminal velocities of the relevant snow types.

Since Nakaya (1954) and more recently several others (Magono and Nakamura, 1965; Jayaweera and Cottis, 1969; Brown, 1970; Jiusto and Holroyd, 1970) established correlations between fall velocity and size for various shapes of snow crystals, it would seem that snowfall records in the form of replicas or photomicrographs would suffice to establish the corresponding terminal velocities. However, for several reasons this is possible only to a limited degree. In very many cases, replicas or micrographs are not clear enough to positively identify the group to which snow crystals belong. In particular, the many irregular shapes, fragments and aggregates which are frequently observed in lake-effect snowstorms are hard to place in the published size-velocity diagrams. Furthermore, aggregates often disintegrate upon landing and give the impression of several individually fallen particles. Finally, the fall velocities reported in the literature, both experimental and theoretical, are not without discrepancies.

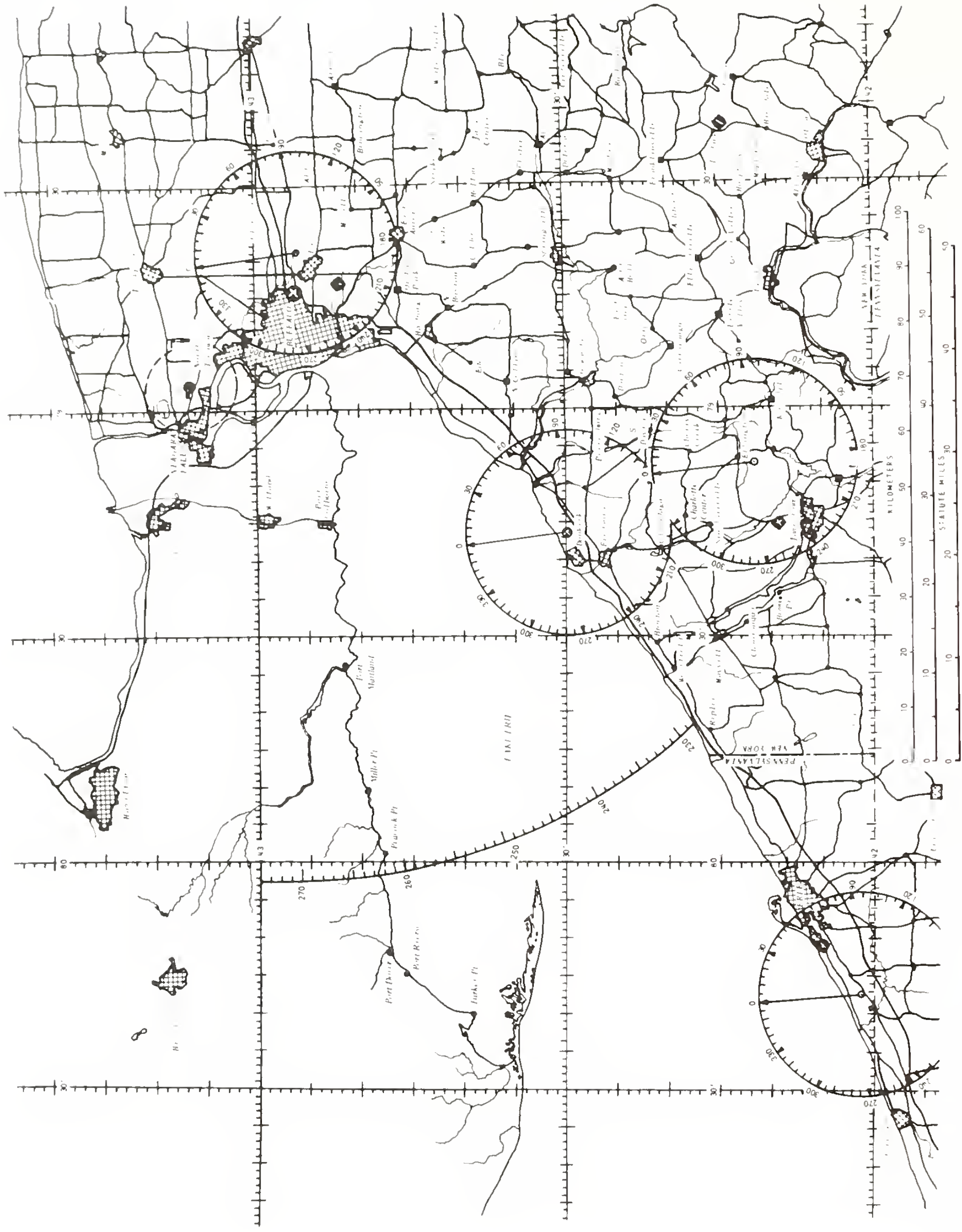

Figure 1 MAP OF EXPERIMENTAL AREA

With so many potential sources of error, it seems obvious that the direct measurement of the fall velocity can provide more reliable data for evaluation of future modification experiments than can be obtained through use of published size-type-velocity relationships.

In order to determine the feasibility of such a direct terminal velocity measurement in the field, a portable snow sampling system was developed and tested during the past winter.

1. Description of Sampler

The primary design criterion for the snow sampler was the ability to provide reliable fall velocity measurements in a manner that resulted in a permanent record of particle geometry and speed. Also required were portability, ruggedness, and the ability to set up and operate the sampler with only one person.

The instrument is designed so that the snow falls through a horizontal light beam of a stroboscope and produces multiple image photographs on a single frame of a 35 mm camera. Once calibrated, the fall speed is determined directly from the photograph. In principle, the shape and size of the snow crystals are also recorded photographically.

Early experience showed that the images of airborne crystals often tended to be rather faint or present only a view which did not reveal the shape sufficiently. For this reason, it was necessary to equip the system with an additional method of recording the snow crystal geometry. Since in prior years close-up photography of snow crystals after landing on a black velvet surface proved to be a good way to determine crystal shapes, this method was adopted in preference to replication which tends to be rather "messy". Another advantage of this decision will become evident in later discussion.

After preliminary tests, the system was assembled in the configuration depicted in Figures 2 and 3. Figure 2 shows the apparatus in operational condition.

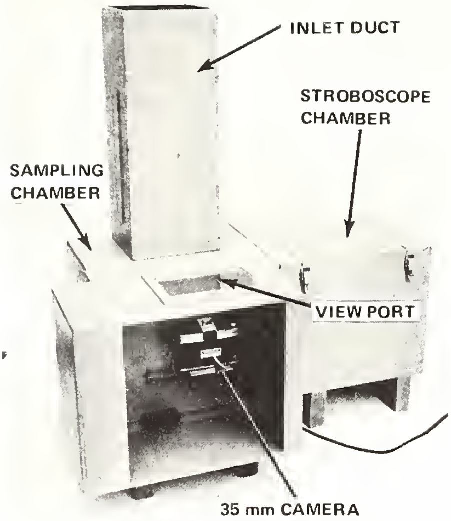

Figure 2 SNOW SAMPLER IN OPERATING CONFIGURATION

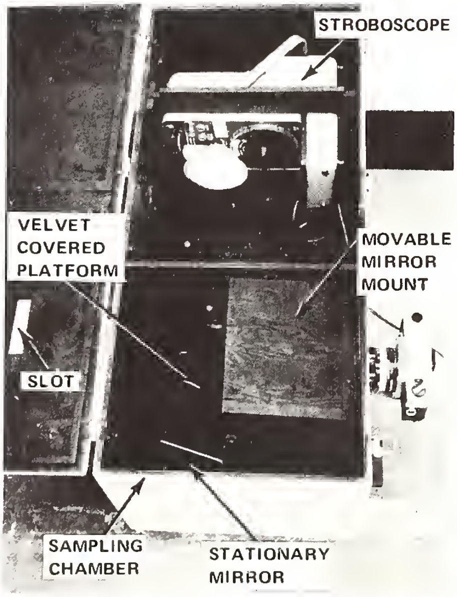

Figure 3 INTERIOR VIEW OF SNOW SAMPLER

A vertical duct on top of the box provides calm air so the snow entering it will gradually assume a vertical fall direction. A small portion of this snow enters the left-hand side of the box through a 2 cm x 8 cm slot in the top. A few centimeters below the slot the snow crystals enter the light beam of the stroboscope located in the right-hand side of the box. A 35 mm camera is mounted on the outside of the box to record the images of crystals falling through the beam. To limit the number of particles on one picture, a lid is kept on the intake duct except for a few seconds during which time the camera shutter is kept open.

The snowflakes land on a black velvet-covered platform inside the box below the light beam. This platform, which is attached to a mirror by a very simple linkage, is then pulled toward the camera. The linkage causes the mirror to move into correct position to permit the camera to view the crystals from above and a photograph is taken. The strobe light reflected from a stationary mirror provides the illumination. After each sampling, the velvet platform is removed through a small door (visible on Figure 2) and brushed clean.

It is essential that the air inside the box is calm, i.e., that there are no up- or downdrafts. This was accomplished by carefully avoiding any other opening besides the sampling slot. In addition, the stroboscope which generates considerable heat during operation was completely separated from the snow receiving part of the box. A condenser lens (f = 26 cm) serves as a window in the separating wall and intensifies the stroboscope beam. Figure 3 shows the inside of the sampling box with the features just described.

The beam dimensions are 8 cm high and 5 cm wide. The latter dimension is more than the depth of focus of the camera; however, it is better to see the crystal blurred than not at all because a larger number of crystals on the velvet than in-flight make the correlation between the picture pairs more difficult. Operation of the stroboscope at 70 Hz yields the best results.

2. Field Testing of the Sampler

Most of the sampling was done as field test for the sampler rather than to acquire data on lake-effect snow. Also, many samples were obtained while the apparatus was not yet in its final version as described above.

Under the adverse conditions of a snowstorm, the simplicity of the instrument and small number of manipulations required for operation proved to be very valuable; by and large, the sampler performed satisfactorily. The most serious problem encountered was the wind. We learned that deceleration of snowflakes into a vertical fall should not occur abruptly; otherwise, heavy fragmentation is unavoidable because of the eddies in the transition zone. The lee of a car, for instance, proved to be a poor sampling location because of excessive turbulence. Similarly, a one-foot trap door in the roof of a hangar-type building produced only a shower of fragments even at moderate wind speeds. Acceptable conditions were found in clearings of woods or downwind from large buildings.

A problem inherent to all samplers with an inlet hole is the fragmentation due to a particle hitting the edge. In our case, fragmentation can be recognized from the resulting dense shower of small particles and can be eliminated from evaluation. In circumstances where the temperature is very close to $0^{\circ}C$ and premature melting of the sample must be avoided, a few pieces of dry ice inside the box solves the problem in this instrument.

3. Evaluation of Samples

Snow samples for terminal velocity measurements were taken on 25 and 27 December 1970 and on 5, 6, 7, and 16 January 1971. On the average, 10 to 15 pairs of photographs were taken per day. Figures 4, 5, and 6 are examples of data from an intense lake-effect storm on 7 January 1971. The pictures clearly indicate that it is important to have only few snow crystals per sample in order to be able to correlate the two images. To evaluate the data, each picture pair was searched for those crystals which could be found on both pictures. The crystal habit, dimensions, and fall velocity were then determined from two pictures.

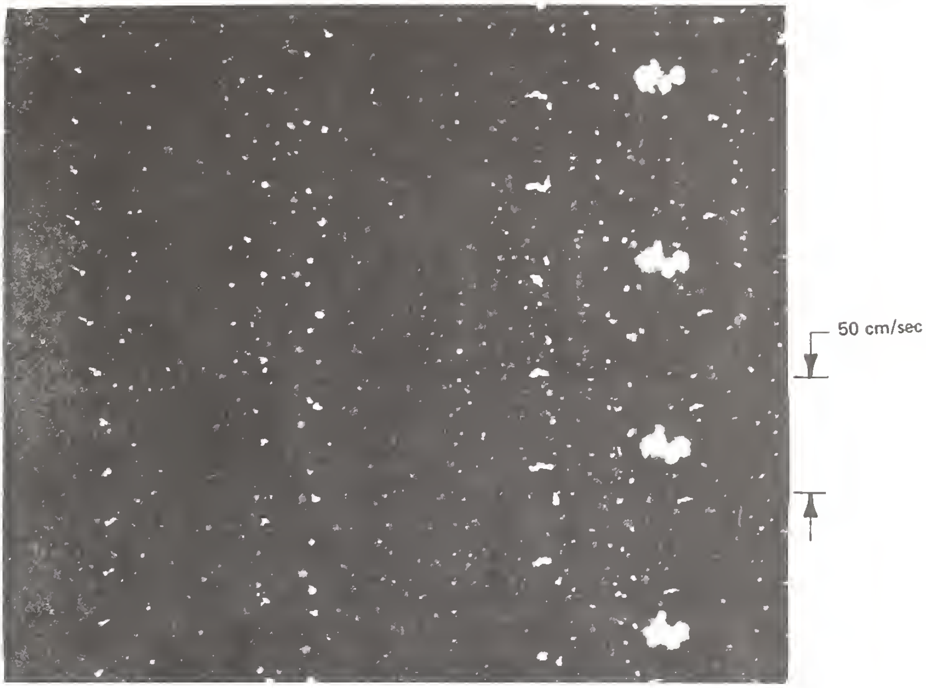

STROBOSCOPIC PHOTOGRAPH OF FALLING CRYSTALS

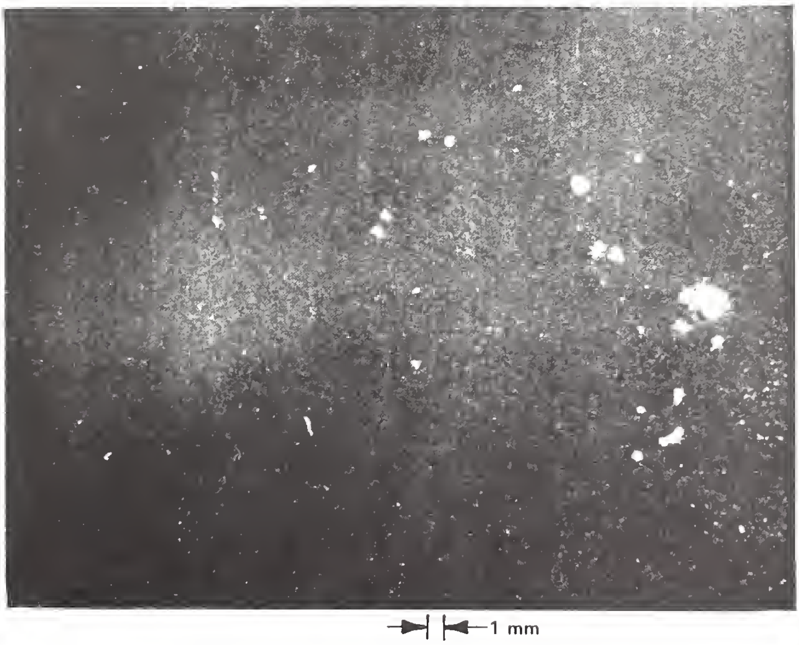

PHOTOGRAPH FROM ABOVE OF CRYSTALS AT REST

Figure 4 PAIRED SNOW CRYSTAL PHOTOGRAPHS FROM 7 JANUARY 1971

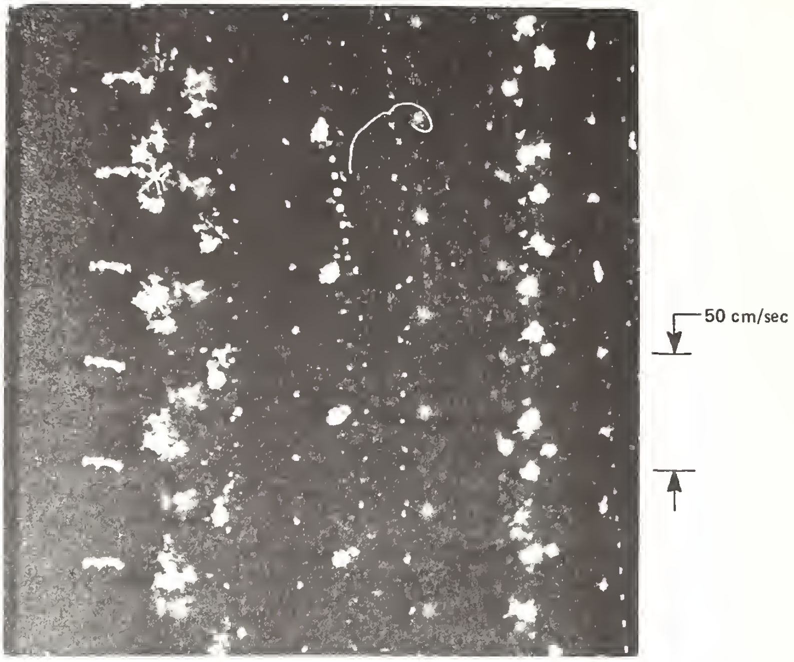

STROBOSCOPE PHOTOGRAPH OF FALLING CRYSTALS

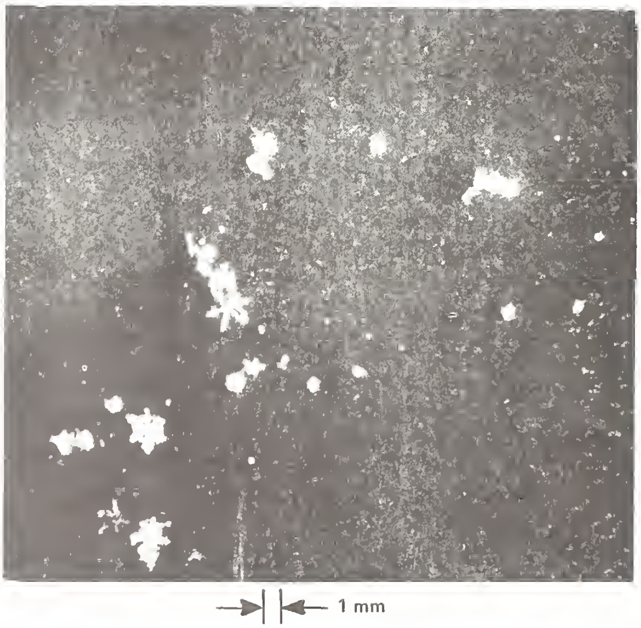

PHOTOGRAPH FROM ABOVE OF CRYSTALS AT REST

Figure 5 PAIRED SNOW CRYSTAL PHOTOGRAPHS FROM 7 JANUARY 1971

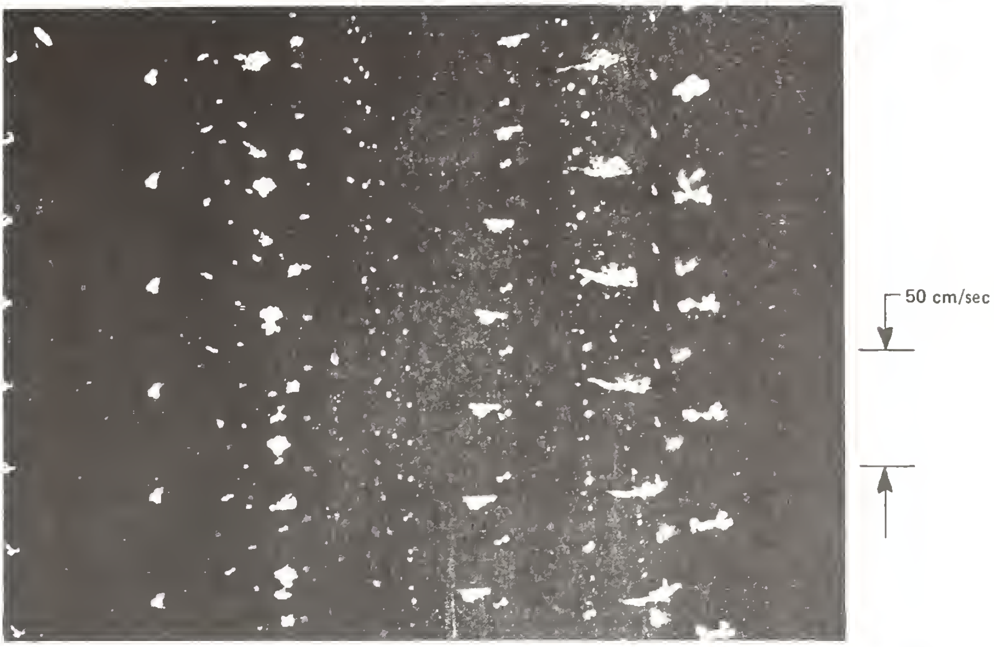

STROBOSCOPE PHOTOGRAPH OF FALLING CRYSTALS

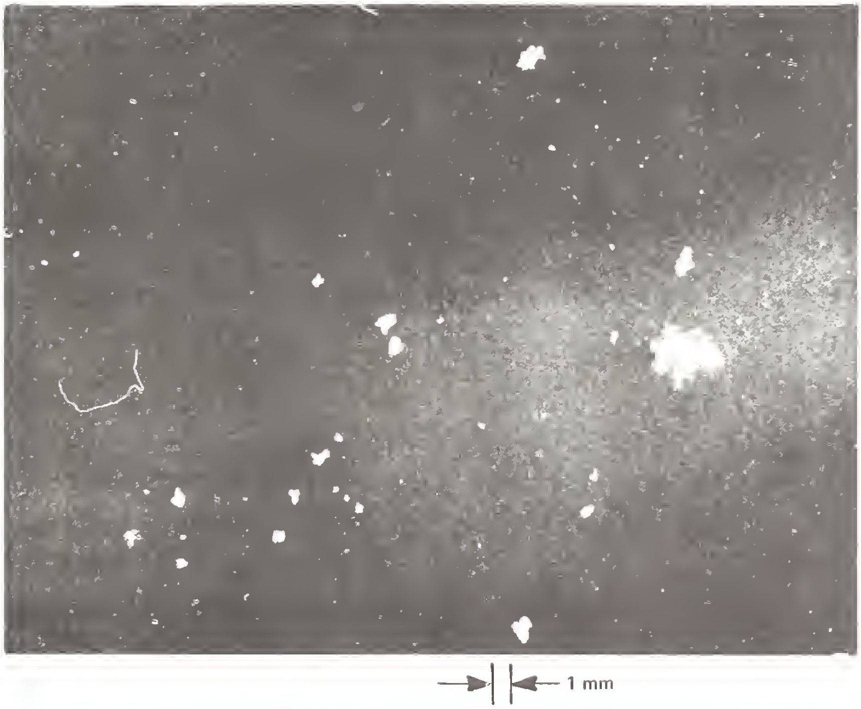

PHOTOGRAPH FROM ABOVE OF CRYSTALS AT REST

Figure 6 PAIRED SNOW CRYSTAL PHOTOGRAPHS FROM 7 JANUARY 1971

Figures 7, 8, 9, and 10 show the data plotted on a velocity versus size diagram for the days of 27 December, and 5, 7, and 16 January, respectively. A horizontal bar describes the dimensions of a crystal; for example, a plate 4 mm long and 2 mm wide is shown as a bar from 2 to 4 mm. In cases where the two major dimensions of a crystal are nearly equal, the crystal is indicated by a dot. Thicknesses cannot be measured on our photographs and are neglected here. About 30% of the particles can be clearly classified, either as plane dendrite (d), spatial dendrite (s), aggregate (a), or snow pellets. A remarkably large number of crystals were of unrecognizable or unclassifiable shape and are therefore unlabeled. For the purpose of comparison, the values found by Nakaya (1965) are indicated in light gray lines on each diagram.

For the day of 27 December (Figure 7) with light, fluffy flakes composed of plane and spatial dendrites with no visible riming, it is surprising to find fall velocities for plane dendrites so much higher than those of Nakaya. However, Brown (1970) found values similar to ours, especially for larger sizes.

Data from several short snow pellet showers on 5 January are shown in Figure 8. No snow crystal types other than the .5 to 1.5 mm pellets were found. The measured fall velocities very nicely complement the curve of Nakaya for graupel.

On the days of 7 January and 16 January, visual snow observations indicated aggregates of plane and spatial dendrites, partly with rimed centers. Our photographic samples show a similar picture; however, a large number of relatively small particles with undefinable shape were present. In some cases, their appearance suggests fragmentation.

4. Conclusions

The simple instrumentation described above is very useful for gathering the information on snow crystal fall velocities needed for evaluation of future lake-effect storm modification experiments.

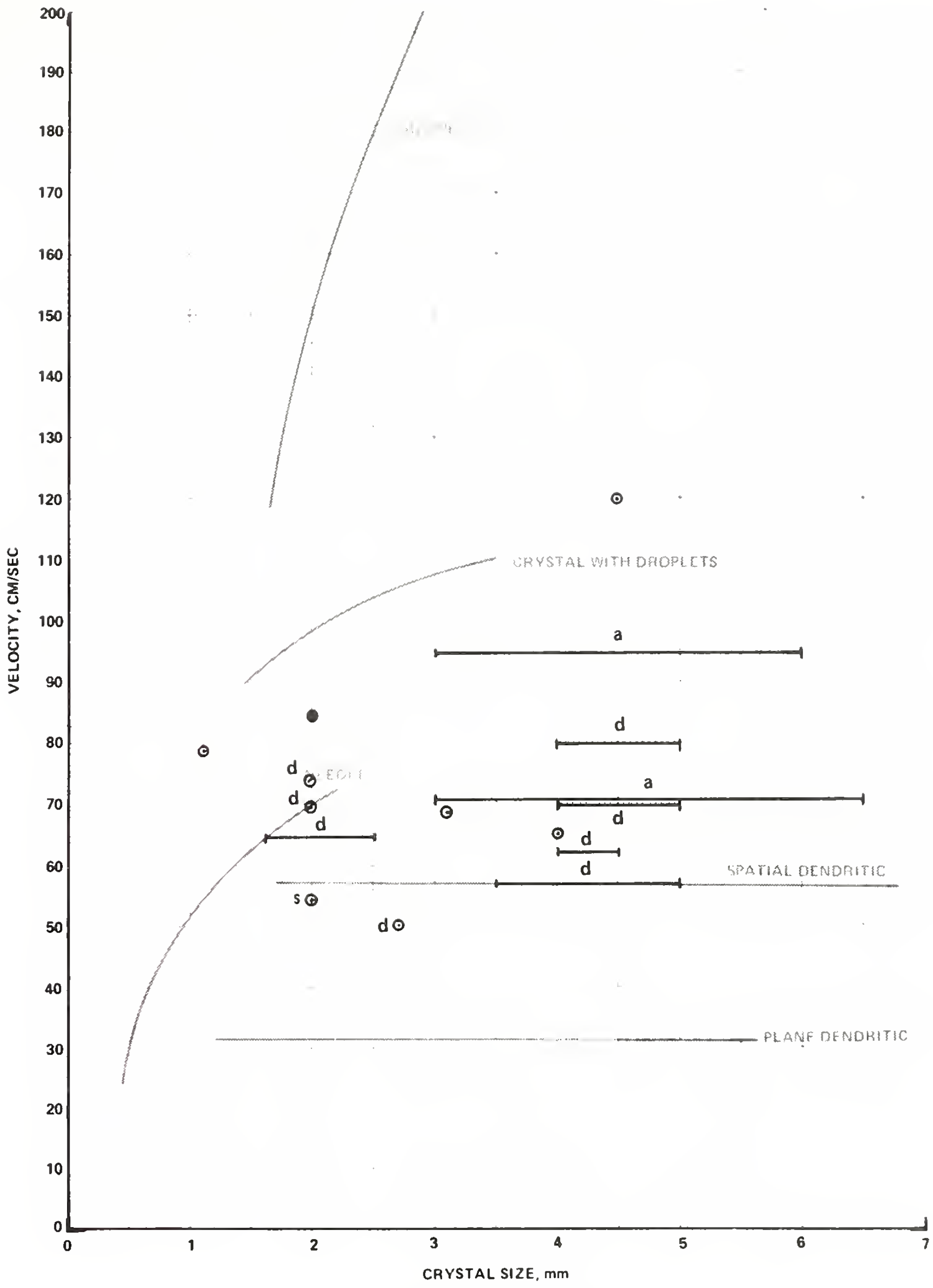

Figure 7 SNOW CRYSTALS MEASUREMENTS OBTAINED ON 27 DECEMBER 1970

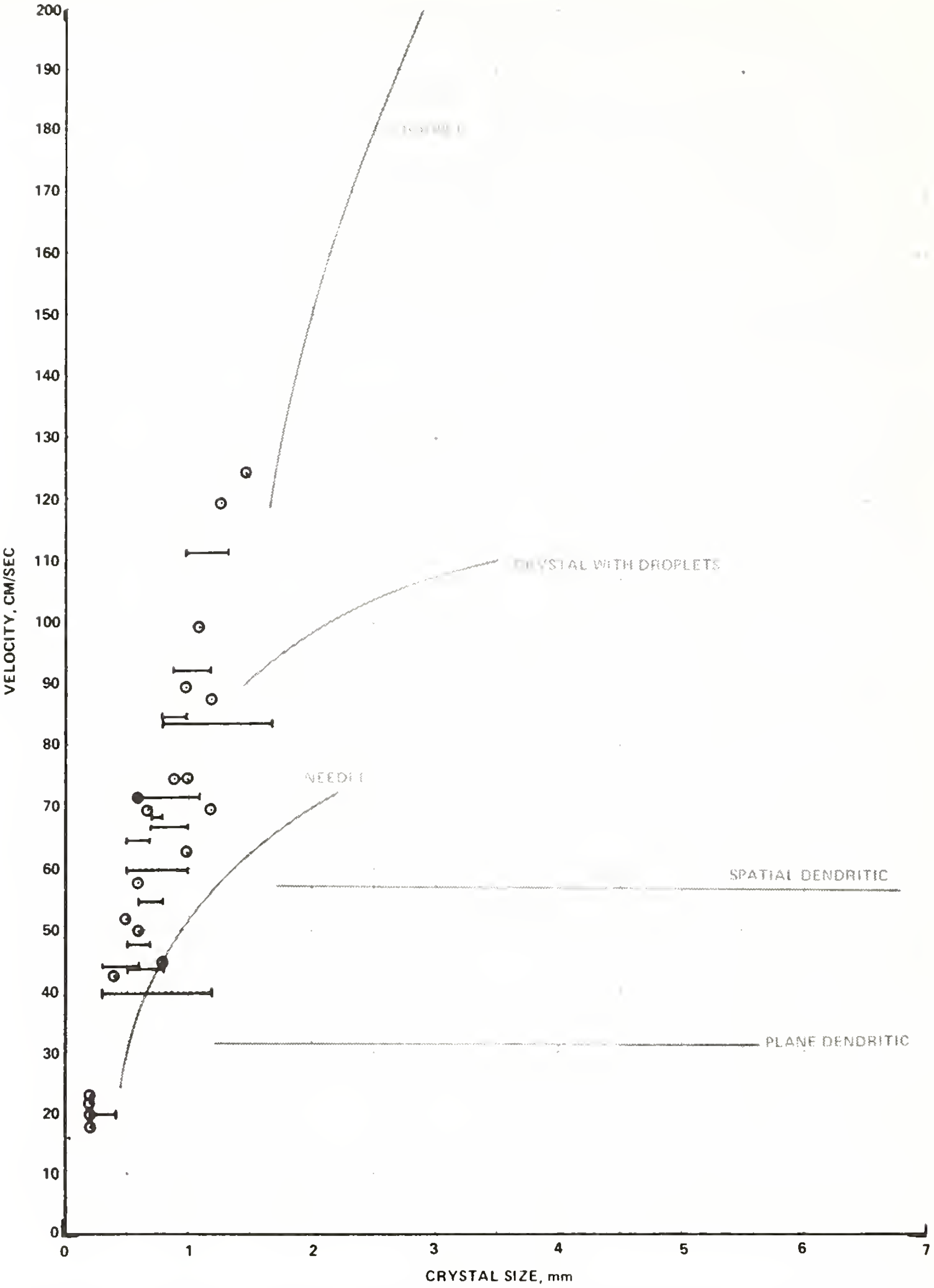

Figure 8 SNOW CRYSTAL MEASUREMENTS OBTAINED ON 5 JANUARY 1971 (ALL SNOW PELLETS)

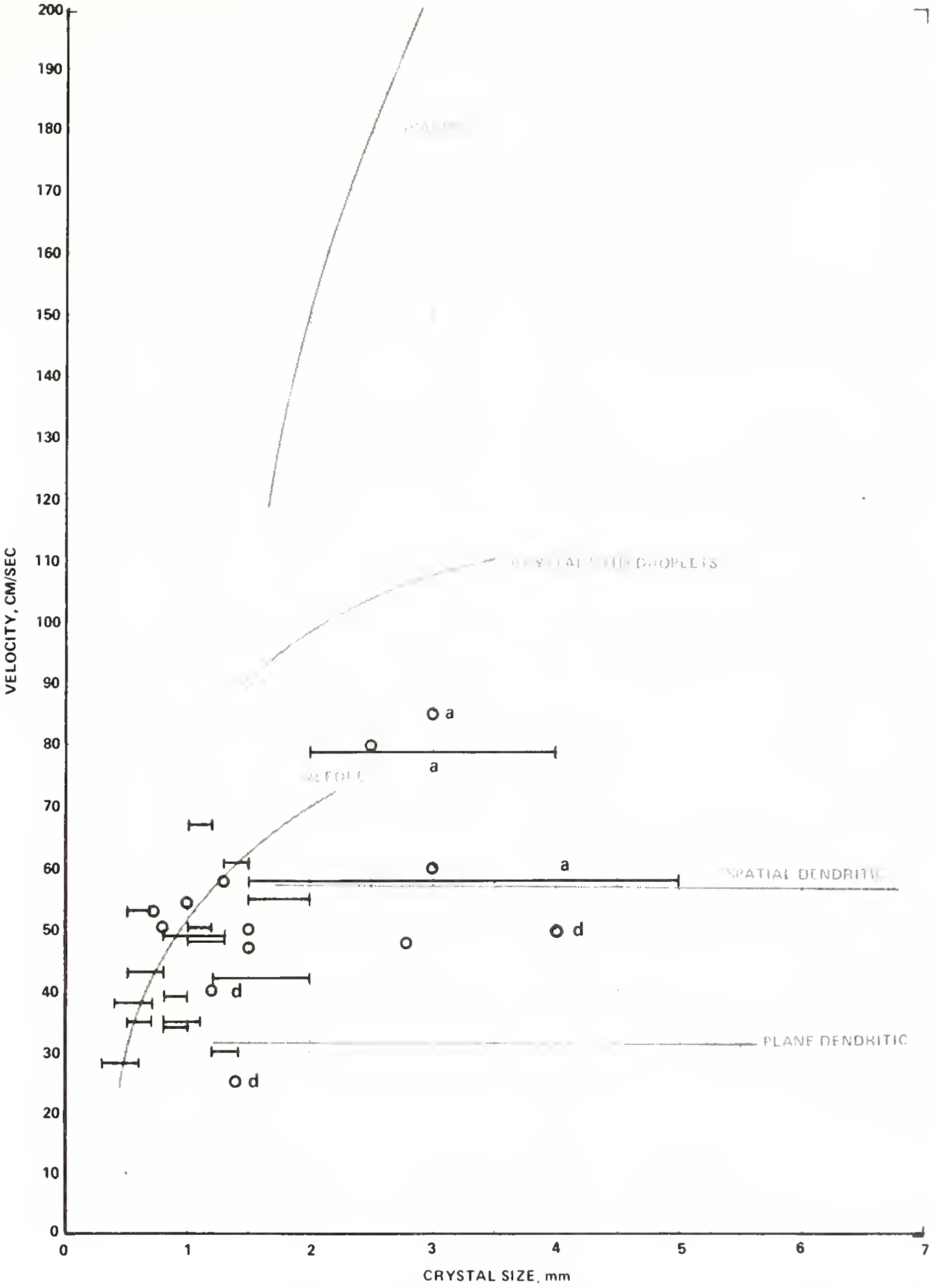

Figure 9 SNOW CRYSTAL MEASUREMENTS OBTAINED ON 7 JANUARY 1971

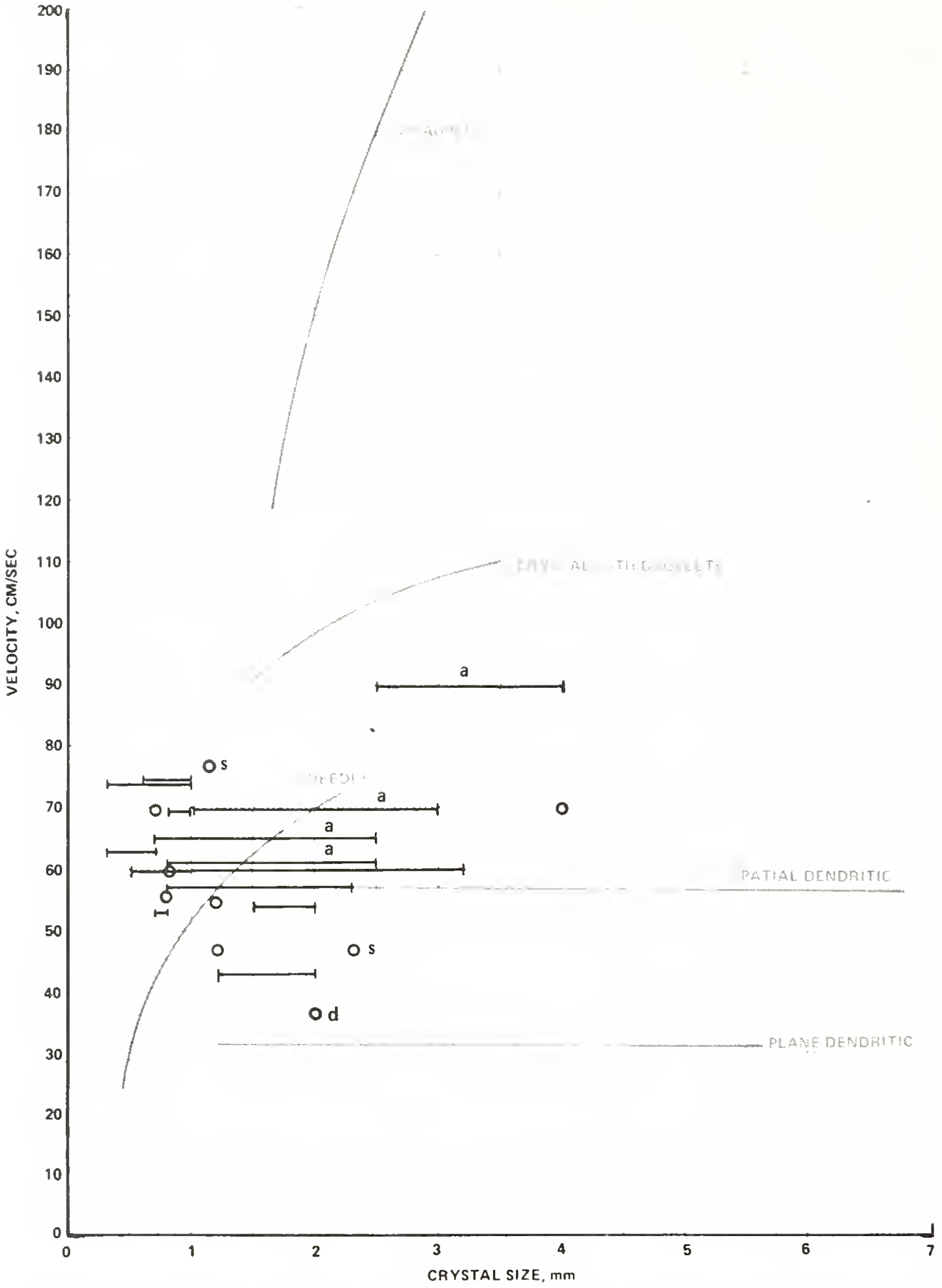

Figure 10 SNOW CRYSTAL MEASUREMENTS OBTAINED ON 16 JANUARY 1971

It is evident, however, that the resolution of the photographic method is insufficient to yield the geometric data that is desirable for basic crystal studies. Replication would certainly help in this case, but we think that an even more important parameter, namely, the mass of the crystals, ought to be included in some of the further research with the sampler. It seems that the method already used for this purpose by Nakaya is applicable here. Instead of discarding the sample after photographing, it can be transferred to a microscope stage for photomicrography and subsequent melting for recording of the size of the resulting drop. While this procedure is very tedious, the information gained is so comprehensive that it is certainly worth the effort for a few hundred crystals. A preliminary test of this procedure was carried out during one of the last snowfalls of the season, and it was found that the present equipment could easily be adapted to this mode of operation.

B. Surface Snow Crystal Observations

1. The Storm of 23 November 1970

Limited, but important, snow crystal observations were obtained on 23 November 1970 in an intense lake-effect snowstorm produced by Lake Erie. This classic early season storm, which occurred with west-southwest winds after a frontal passage, deposited as much as 18 to 24 inches of heavily rimed snow in a band 10 to 20 miles wide and extending east-northeast from Dunkirk to Batavia, New York. Precipitation echo contours from the storm as measured by the Buffalo WSR-57 radar at 0642 EST on the 23rd are shown in Figure 11. It is important to note the characteristic sharp northern edge of the storm band revealed in the radar return. Since the synoptic situation and satellite pictures for the storm have been discussed by Ferguson (1971) and Parmenter (1971), that material will not be repeated here.

The maximum radar tops for the storm as measured by the Buffalo WSR-57 radar were around 14,000 feet, and the storm showed considerable lightning activity. The Buffalo sounding at 1200Z on the 23rd showed a moist adiabatic lapse rate to 10,000 feet and a stable stratification above. The -20°C level was around 8,000 feet. The storm could be particularly

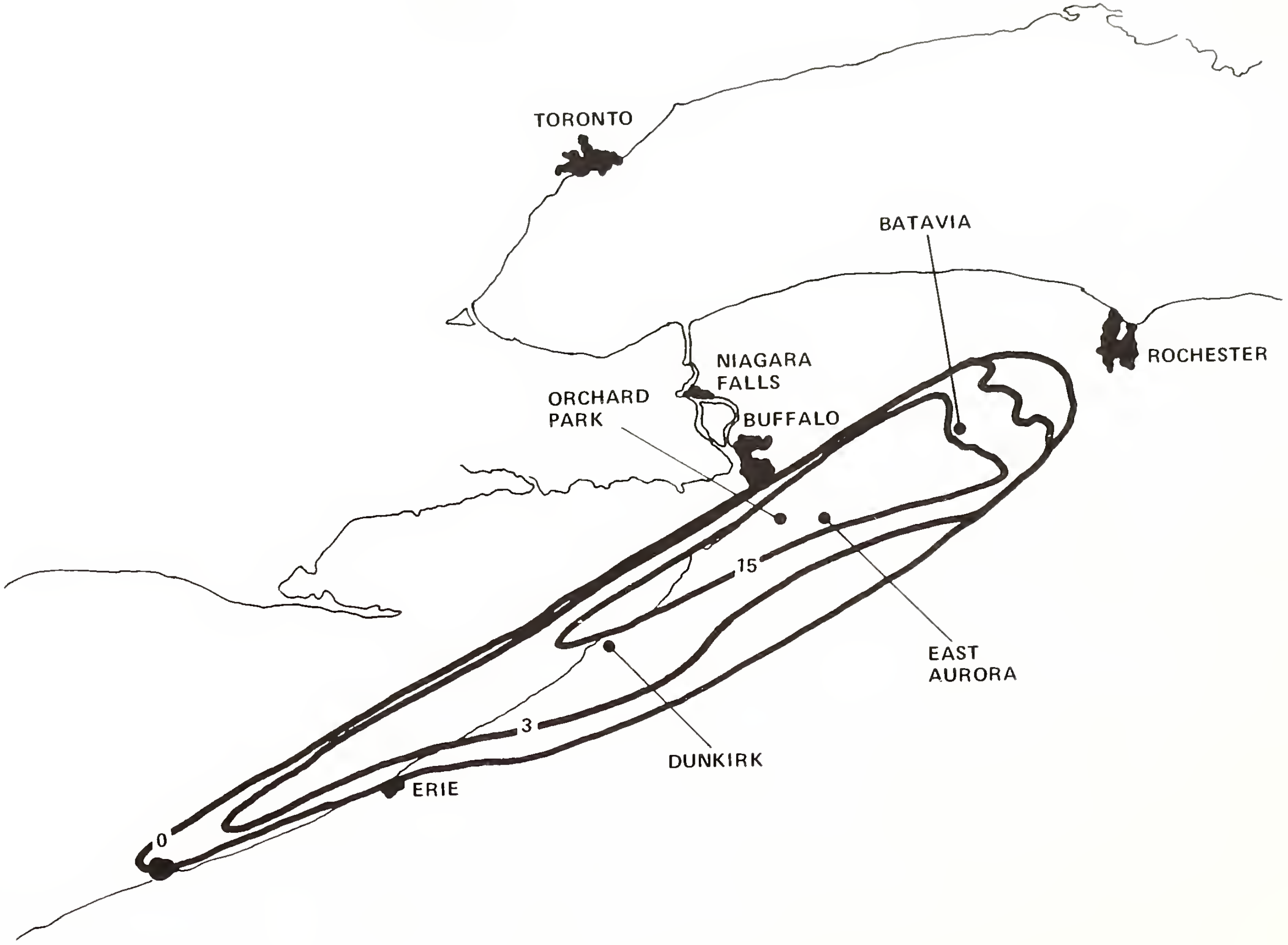

Figure 11 PRECIPITATION ECHO CONTOURS (dB ATTENUATION) FROM WSR-57 RADAR AT BUFFALO WEATHER STATION AT 1142Z ON 23 NOVEMBER 1970

difficult to simulate using the Lavoie model as the upwind soundings also indicate a stable stratification above a well-mixed lower layer but without the characteristic capping inversion. This situation may have contributed to the relatively large vertical development of the storm.

Precipitation records from Colden, New York on the southern side of initial snow band from the storm show a total accumulation of 18 inches of snow between 1800 EST on the 22nd and 1800 EST on the 23rd. Approximately 1.2 inches of melted precipitation were recorded during the same period, yielding a snow depth to melt water ratio of 15.

Surface snow crystal observations were obtained at East Aurora and Orchard Park, New York in heavy snow from the center of the storm band. These locations received 22 to 24 inches of snow from the storm between approximately 0000 and 1800 EST on the 23rd, at which time the band was shifting southward under the influence of westerly winds. The predominant type of snow at both locations was small snow pellets or grains of 1 to 2 mm diameter, occurring individually and in heavily rimed aggregates approximately one centimeter in diameter. Although heavy riming obscured almost all crystal structure, occasional stellars and tiny plates (< 1 mm) were observed. This type of snow persisted with only minor variations during the daylight hours of the 23rd. The surface temperatures during this period were -6 to -7°C. No large graupel, which has proven to be a common type of snow in early season lake-effect storms, was observed at either location.

2. The Storm of 7 January 1971

On 6 and 7 January 1971, an outbreak of cold polar air accompanied by westerly winds resulted in substantial snowfall in the Lake Erie snowbelt areas south of Buffalo, New York. By 1000 EST on the 7th, a shallow but intense lake-effect band had developed, extending inland from Erie, Pennsylvania. Precipitation echo contours from the band as measured by the Buffalo WSR-57 radar at 1240 EST are shown in Figure 12. Surface snow crystal observations were obtained between 1230 and 1530 EST in heavy snow at the site of the snow gauge network near Springville, New York. At 1530 EST, the band weakened and moved south under the influence of a wind shift to the west-northwest.

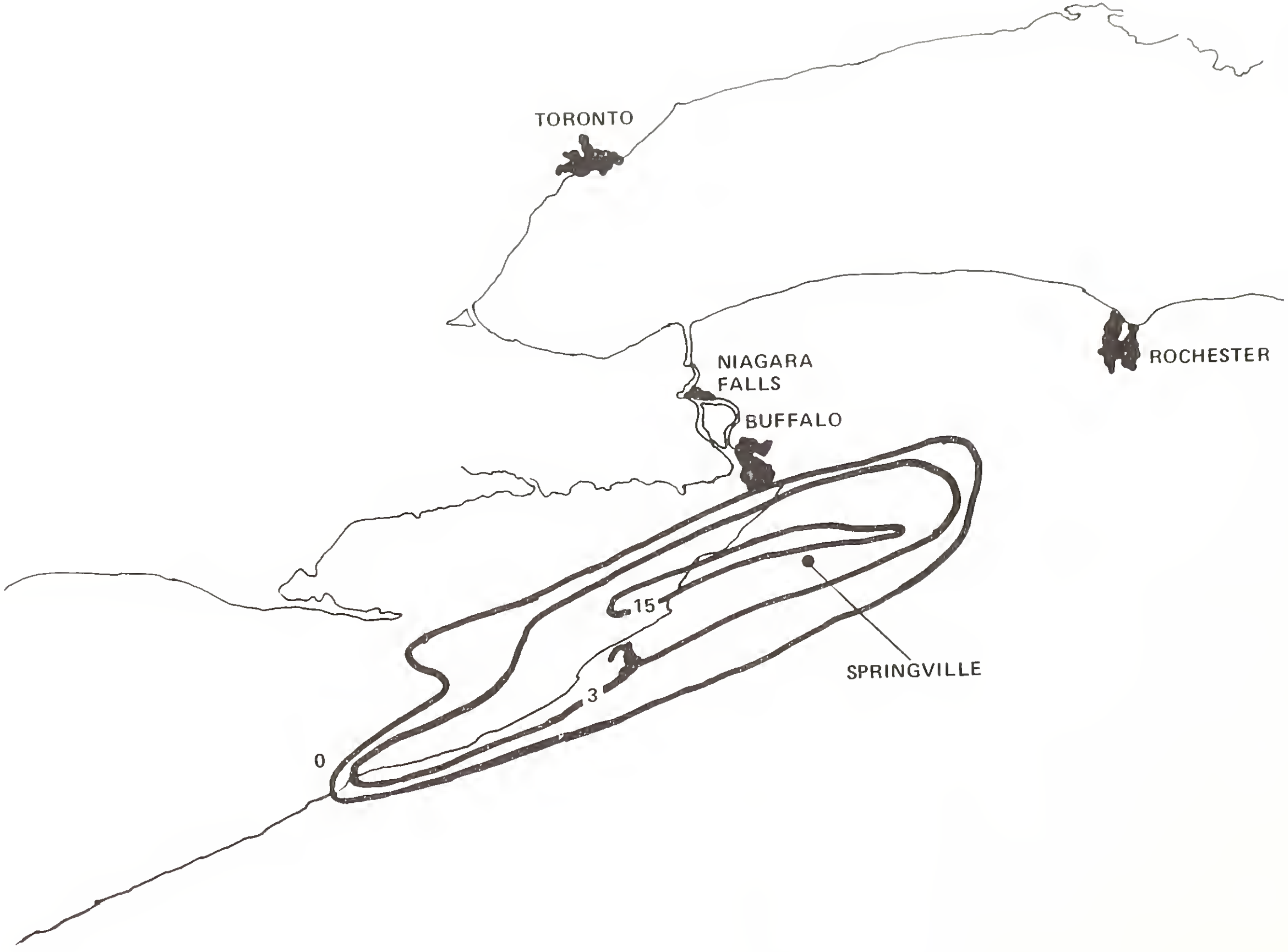

Figure 12 PRECIPITATION ECHO CONTOURS (dB ATTENUATION) FROM THE WSR-57 RADAR OF THE BUFFALO WEATHER STATION AT 1740Z ON 7 JANUARY 1971

The Buffalo sounding at 1200Z on the 7th showed a moist adiabatic lapse rate to 4,000 feet, a cloud layer between 4,000 and 6,000 feet, and a substantial inversion above 6,000 feet. The surface temperature was -11°C, and -20°C was reached at 4,000 feet. The maximum radar tops from the storm band as measured by the Buffalo WSR-57 radar were at 6,000 to 7,000 feet.

The predominant type of snow observed at Springville was in the form of aggregates of about one centimeter diameter, which contained 20-50 unrimed stellars and spatial dendrites (some with rimed centers) in the 1-3 mm diameter range. Some tiny unrimed plates approximately 0.5 to 1 mm in diameter were also observed. These observations are in agreement with the limited vertical development and low temperatures of the cloud band. Apparently, sufficient natural ice crystals were produced in this case to glaciate portions of the cloud band and develop the unrimed snow crystal forms which were observed at the surface.

Measurements of snow crystal fall velocities at Springville were presented in the preceding section (Figures 3, 4, 5, and 9). The snow gauge network near Springville recorded approximately 0.20 inches of melt water between 0200 EST and 1600 EST on the 7th (see Figure 15). During the same period, an accumulation of approximately 18 inches of snow was measured, yielding an extremely high snow depth to melt water ratio on the order of 100, in general agreement (see Jiusto et al., 1970) with the forms of snow observed.

3. The Storm of 28 January 1971

During most of the day, the southern shore of Lake Ontario, from Rochester, New York westward, experienced a lake-effect storm. The area is no stranger to these storms, as they frequently occur off the lake in the form of multiple bands. The storm of 28 January was a single band located along the coast and was unusual in that for much of the period the intense portion was located over the land. Single bands frequently occur at the eastern ends of Lake Erie and Lake Ontario where the downwind end of the intense portion can be sampled over land. The 28 January storm provided a potential for field measurements in the upwind end of an intense region since it occurred in a region readily accessible to CAL field observations.

Early in the morning, the storm's cloud band was observed visually; and a check with the Buffalo WSR-57 radar showed that part of the band was located over the shoreline. Most of the previous data on snow crystal types have been gathered at the eastern ends of lakes, either in single intense bands with long overwater trajectories or weak multiple bands with short overwater trajectories. The situation of 28 January 1971 provided an opportunity for observations from a single intense band with a short overwater trajectory.

The western Lake Ontario region experienced strong westerly winds and cold temperatures during the day. Hamilton, Ontario, located at the western tip of the lake, reported westerly winds averaging 25 knots and gusting to 35 knots most of the day. Surface temperatures averaged about $-12^{\circ}C$. The Buffalo sounding at 0700 EST showed a moist adiabatic lapse rate up to 10,000 feet, with an accompanying strong westerly flow through the layer. The $-20^{\circ}C$ level was around 4,500 feet.

According to Buffalo WSR-57 radar observations, the Lake Ontario band became predominant in the morning, weakened around noon, and then intensified again during the afternoon. The maximum radar tops varied accordingly from 9,000 to 10,000 feet in the morning, down to 4,000 feet around noon time, and up to 10,000 to 15,000 feet in late afternoon. Precipitation echo contours from the most intense afternoon phase of the Lake Ontario storm band at 1541 EST are shown in Figure 13. A well-defined lake-effect band had developed off Lake Erie as well by this time.

Using Krylon replication, snow crystal measurements were obtained in various regions of the Lake Ontario storm band as the intensity of the band changed during the period from 1100 to 1500 EST. Data were obtained from the southern edge of an intense band, from the northern edge, and center of the same band as it weakened, and near the center of a new intense band as it developed.

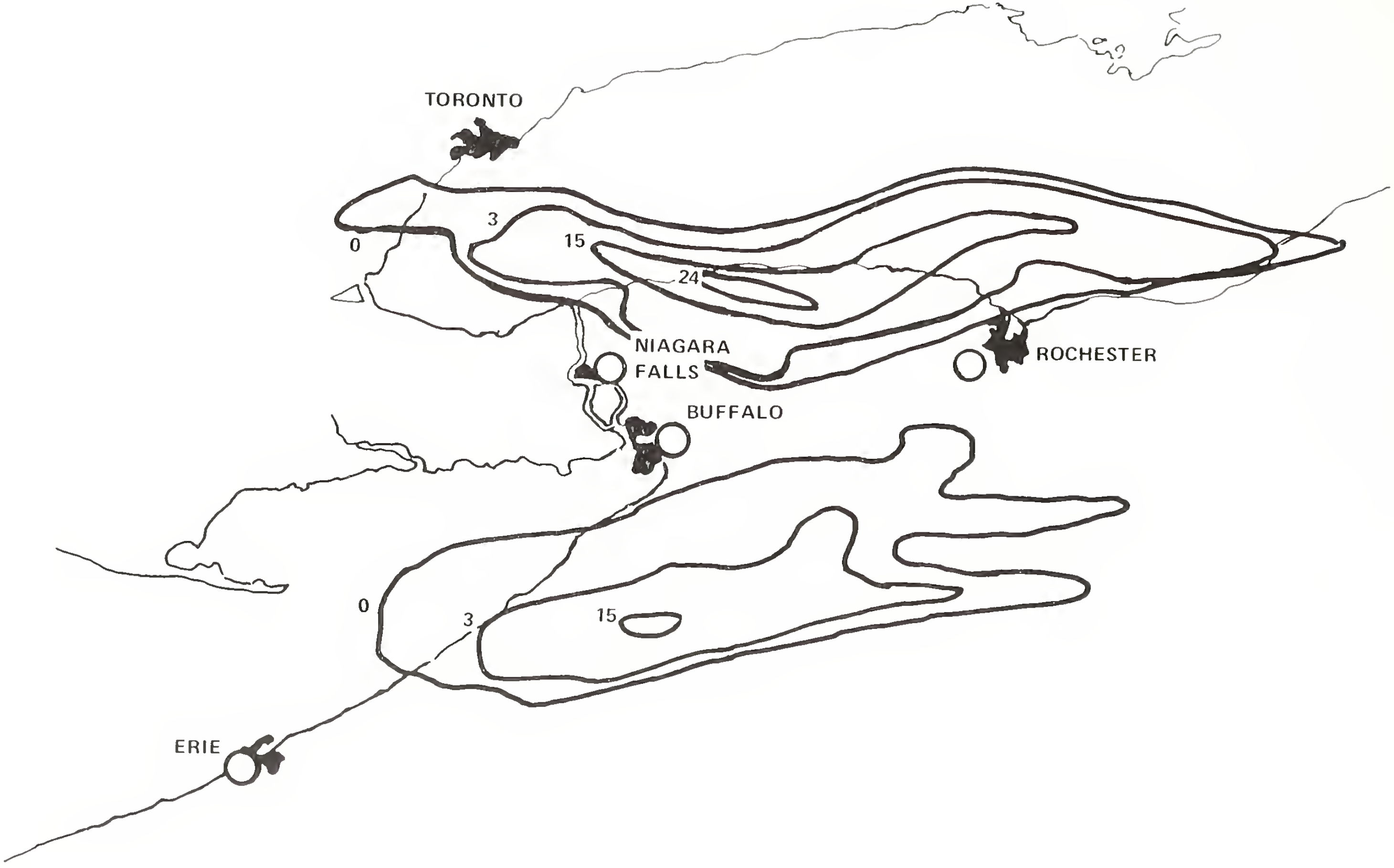

Figure 13 PRECIPITATION ECHO CONTOURS (dB ATTENUATION) FROM WSR-57 RADAR AT BUFFALO WEATHER STATION AT 2041Z ON 28 JANUARY 1971

The principal type of snow observed at all locations was aggregates ranging in size from 2 mm up to 1 cm and containing many tiny crystals. Unrimed stellars and plates were the predominant well-defined crystal types found in the snow crystal replicas. High winds, however, resulted in many fractured and undefinable crystals. Size distributions of snow crystals obtained by sizing well-defined crystal types in the replicas are shown in Figure 14. At the centers of the snow bands, mean crystal diameters were 0.5 to 0.6 mm and approximately one-half of the crystals were stellars. At the edges of the bands, smaller crystals (0.2 to 0.4 mm) were found. These edges samples also contained more plates than stellars, and a few columns.

As in the case of the 7 January 1971 storm discussed previously, sufficient natural ice nuclei must have been activated at the cold cloud temperatures to glaciate portions of the cloud band and produce the tiny unrimed snow crystals which appeared in aggregates at the surface.

4. Conclusions

These surface snow crystal observations during the past year, although fragmentary, provide yet another piece of information about this most complex and varied phenomena, lake-effect snowstorms. It is important to contrast the late season storms of 7 and 28 January 1971 with the early season storm of 23 November 1970. The evidence of abundant natural glaciation in the late season storms suggests that it may not be fruitful to extend the period of future overseeding experiments on lake-effect snowstorms into January in hopes of increasing the number of suitable experimental situations. The presence of heavy riming in the 23 November 1970 storm, on the other hand, would have made this intense storm a suitable situation for a large-scale overseeding experiment.

It should be noted, however, that practically no information exists on the fall velocities of principal natural precipitation types observed in the 23 November storm, aggregates of approximately one centimeter diameter made up 1 to 2 mm snow pellets or grains. Clearly additional measurements of snow crystal fall velocities in both natural and seeded lake-effect snowstorms using the portable snow sampler discussed in Section A would be valuable in the planning of overseeding experiments and measurement of seeding effects.

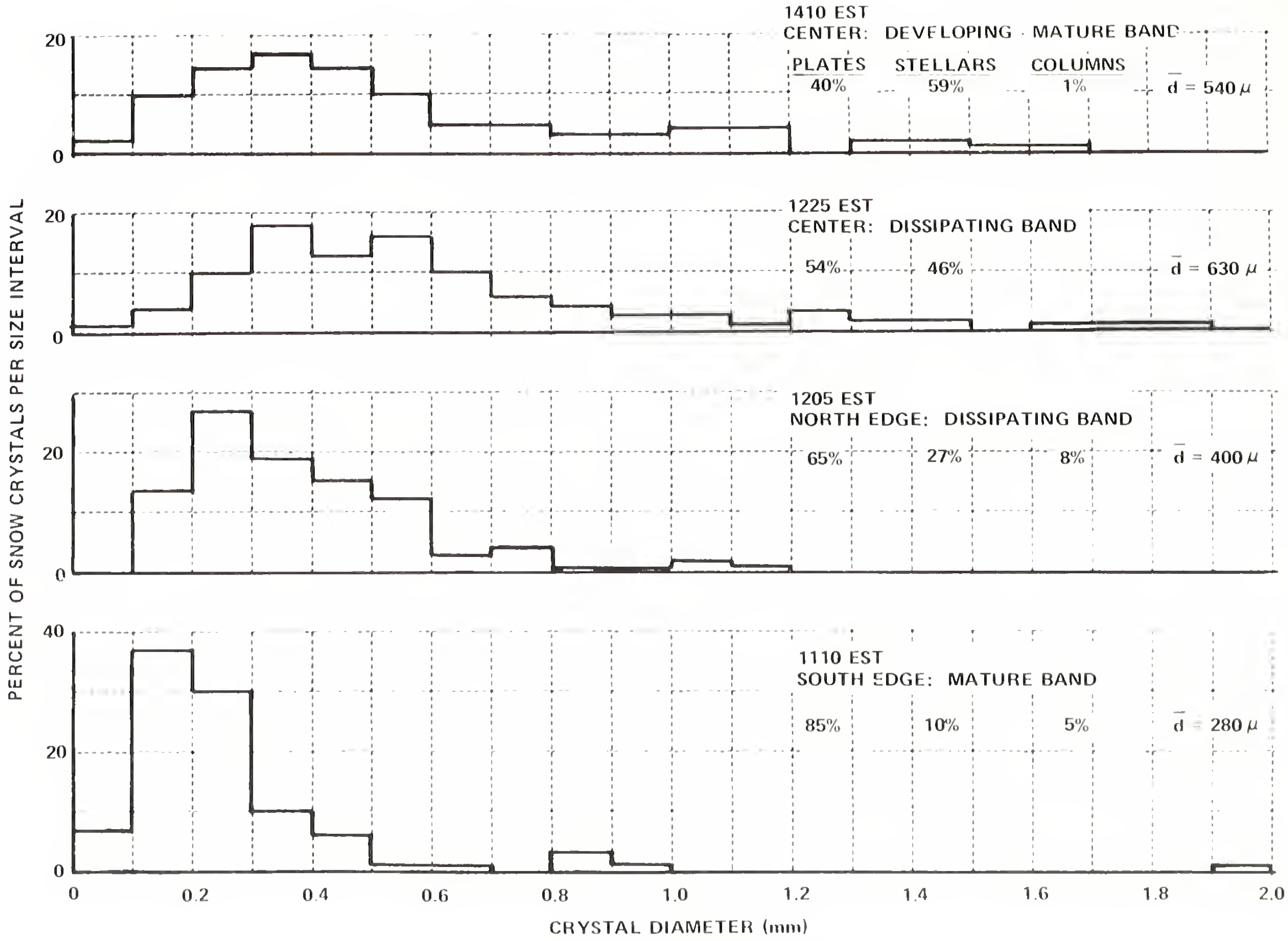

Figure 14 SIZE DISTRIBUTIONS OF SNOW CRYSTALS OBTAINED FROM A LAKE EFFECT BAND OFF LAKE ONTARIO IN THE VICINITY OF LOCKPORT AND MEDINA, N.Y. ON 28 JANUARY 1971

C. Test of Automatic Snow Gauges

During the past winter, CAL performed a test of a small network of heated tipping-bucket snow gauges to determine their usefulness in measuring precipitation rates in lake-effect snowstorms. The test was undertaken to provide NOAA with information on the feasibility of operating a large (50-60 gauges) network of snow gauges in the Western New York area to measure changes in precipitation rates during future overseeding experiments on intense lake-effect snowstorms.

Previous snow gauge measurements in the Lake Erie snowbelt area were carried out by the State University of New York at Albany (Jiusto and Holroyd, 1970) during the winter of 1968-1969. By comparison with the measurements of cooperative weather observers, it was found that the MRI electrically heated gauges recorded about two-thirds of the total precipitation and were inadequately heated at temperatures below $-4^{\circ}C$. A small (10 gauges) network of electrically-heated snow gauges was operated by NOAA during the 1969-1970 weather modification experiments to measure the effects of seeding on snowfall distributions. It is believed that the failure of the network to provide data of significant value can be attributed to the relative sparseness of network, and the great variations in time and space of the snowfall from the poorly organized lake-effect snow bands experienced in the experimental area near Dunkirk, New York.

Between 21 December 1970 and 29 January 1971, eight snow gauges provided by NOAA were operated at CAL's Ashford Experimental Site, near Springville, New York in the Lake Erie snowbelt area. The gauges were located on level ground near Cattaraugus Creek, away from any large natural or man-made obstacles. The gauges were placed approximately in a circle about a single central gauge. The minimum distance between any two gauges was 24 feet and the maximum distance was 53 feet.

The snow gauges were tipping-bucket rain gauges, which had been modified by NOAA for snow measurement by addition of insulating material and a single 100 watt light bulb for heating. The gauges were operated without wind screens during the test period. They recorded melted precipitation in units of 0.01 of an inch. The Rustrak recorders were operated at a two-inch per hour chart speed which provided approximately 15 days of continuous operation. Downtime, primarily for recorder repair and maintenance, averaged about 20%, so that at a given time only six or seven of the eight snow gauges were in good working order.

Since the principal reason for possible employment of a snow gauge network in future weather modification experiments would be to measure changes in precipitation rates, rather than to measure absolute precipitation amounts, the objective of the snow gauge test was to establish the degree of correlation among the precipitation rate measurements of the individual gauges at a common site during lake-effect snow conditions. Unfortunately, the snow gauge network was established late in the lake-effect season, after the occurrence of the intense 23 November 1970 storm. No lake-effect or general snowstorms yielding a large amount of melted precipitation occurred at Springville during the test period.

Measurements from the 7 January 1971 lake-effect storm, which was characterized by an 18-inch accumulation of snow yielding only about 0.20 inches of melt water, are presented in Figure 13. The surface temperature during this period was approximately $-10^{\circ}C$ and winds near the surface were approximately 20 to 30 knots. Visual observation of the snow gauges during this storm revealed some bridging of partially melted snow in the intake funnels of the gauges, an indication of inadequate heating. It is recommended that a second 100 watt light bulb should be incorporated in these snow gauges to provide greater and more uniform heating of the intake funnel. In view of this deficiency and the low amount of total precipitation measured, the agreement among the measurements of the individual gauges shown in Figure 15 is fairly encouraging. The standard deviation of the total precipitation measured during the storm was approximately 10% of the mean or 0.02 inches.

The highest precipitation rates measured during the test period were in wet snow and rain on 26 January 1971 and are shown in Figure 16. It is not surprising that the standard deviation of the total precipitation measured during this period was approximately 3% of the mean or 0.01 inch. For the

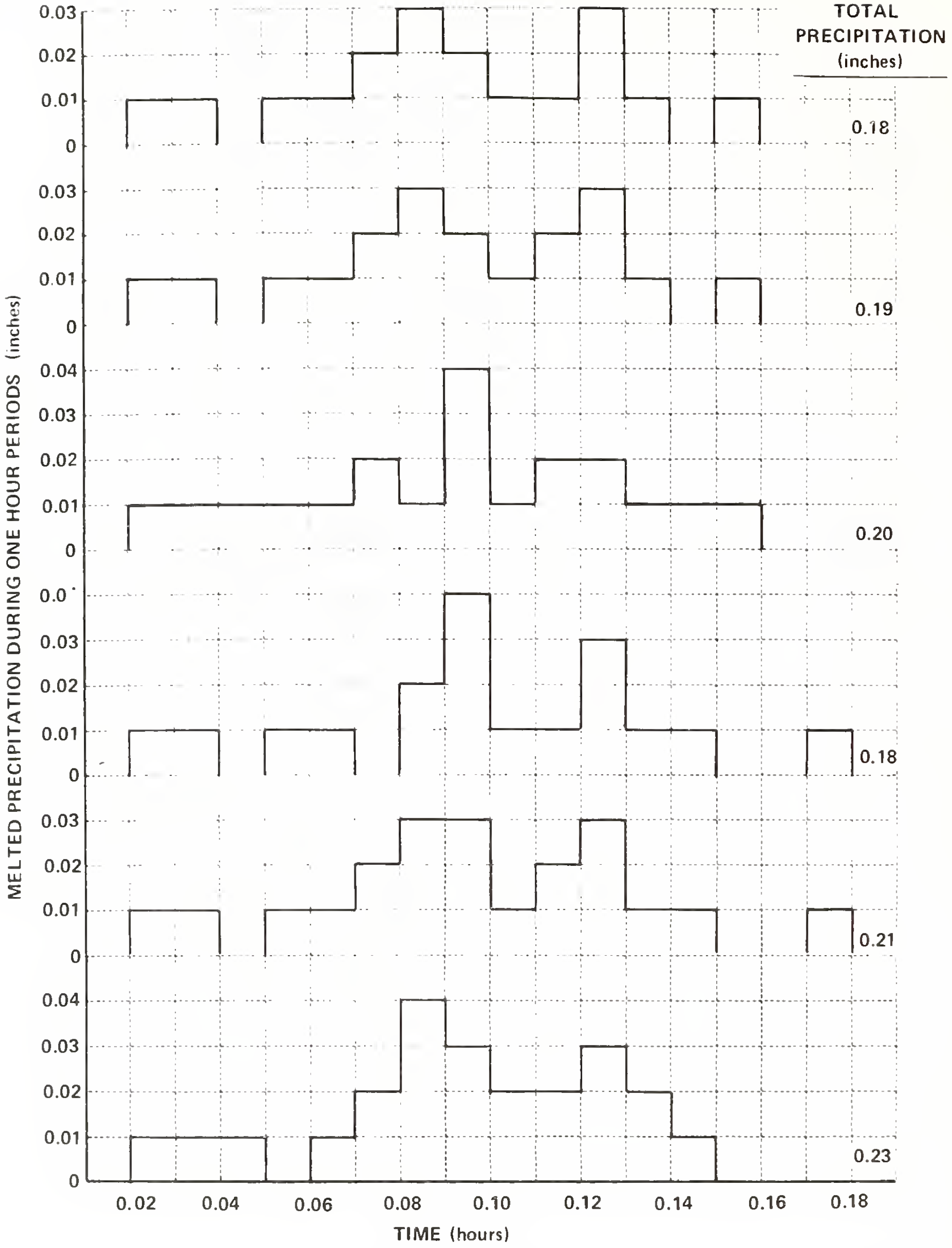

Figure 15 COMPARISON OF SNOW GAUGE MEASUREMENTS OBTAINED AT ASHFORD EXPERIMENTAL SITE DURING A LAKE–EFFECT SNOWSTORM ON 7 JANUARY 1971

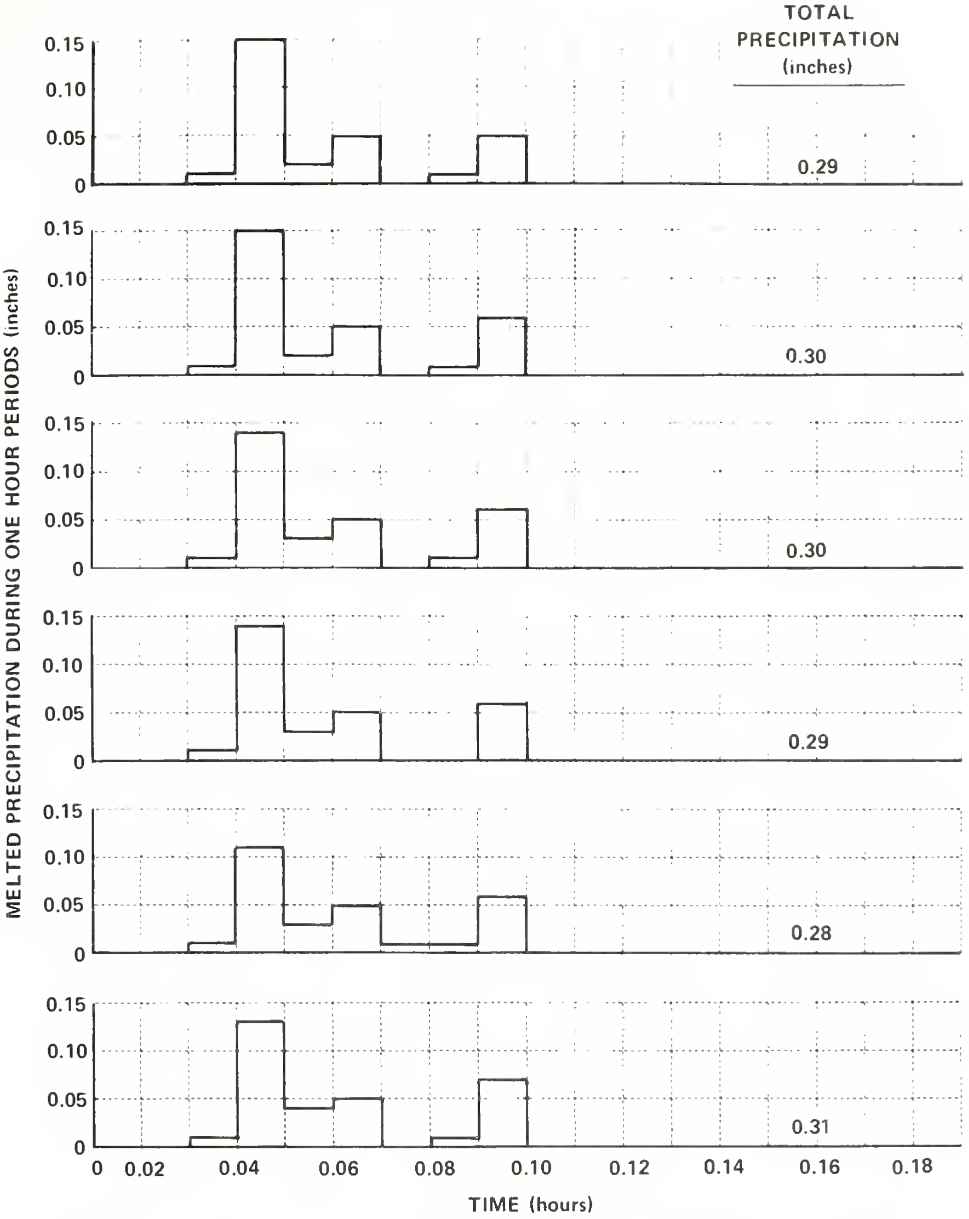

Figure 16 COMPARISON OF SNOW GAUGE MEASUREMENTS OBTAINED AT ASHFORD EXPERIMENTAL SITE DURING WET SNOW AND RAIN ON 26 JANUARY 1971

period between 0400 and 0500 EST, the mean precipitation rate of approximately 0.14 inch per hour would be typical of the precipitation rate from an intense lake-effect storm, which yields one to two inches per hour of heavily rimed snow. The standard deviation of the measured precipitation rate between 0400 and 0500 EST was 0.015 inch per hour or approximately 10% of the mean.

Considerably greater deviations would have been expected in heavy snow, particularly under high wind conditions. Hence, it is likely that an overseeding experiment on an intense lake-effect snowstorm involving a one-hour seeding pulse would have to produce alterations in precipitation rates well in excess of 10% to be detected by even a very dense snow gauge network. Contemplation of the hour-by-hour variations in the measured precipitation rates, shown in Figure 15, emphasizes the desirability of conducting overseeding experiments on well-organized, intense lake-effect storms producing steady snowfall, if the principal tool for the measurement of seeding effects is a snow gauge network.

Perhaps representative of a good experimental situation are the NOAA hourly precipitation values measured between 1400 EST and 2200 EST at Colden, New York during the intense lake-effect snowstorm of 23 November 1970 (see Section B). The mean precipitation rate during that period was about 0.10 inch of melt water per hour and the standard deviation of the hourly values was 0.025 inch per hour or 25% of the mean.

In conclusion, the incorporation of a large (50-60 gauge) network of automatic snow gauges into future NOAA weather modification experiments on lake-effect snowstorms is recommended provided that (1) steps can be taken to assure adequate heating of all gauges in low temperature, high wind situations, and (2) it is recognized that overseeding experiments should be restricted to well-organized, intense storms to maximize the probability of detecting seeding effects from the background of relatively large time and space variations in the natural snowfall.

III. MESOSCALE MODELING OF LAKE-EFFECT SNOWSTORMS

Lavoie (Davis et al., 1968) developed a single-layer numerical model of the atmosphere to study the effects of heating, gradients in surface friction, and orography on the two-dimensional horizontal flow over Lake Erie in wintertime lake-effect situations. The Lavoie model is based on the observation that lake-effect snowstorms are generally confined to a rather shallow layer of the atmosphere, usually less than 3 km deep, which is well-mixed by strong winds and surface heating. The model describes the horizontal flow field in a single well-mixed layer of the atmosphere extending from the top of the constant-flux layer to an assumed capping inversion and/or stable upper layer. While the model provides no detailed information on vertical structure, it can represent mesoscale effects arising from the actual configuration of lake boundaries and varying wind directions relative to the lake. On the basis of the original results obtained by Lavoie and additional numerical experiments carried out at CAL (McVehil et al., 1967, 1968), the Lavoie model can provide fairly realistic descriptions of the mesoscale circulation features produced by the flow of cold air over Lake Erie.

More recent research with the Lavoie model both at CAL (Eadie et al., 1971) and Pennsylvania State University (Lavoie et al., 1970) has resulted in the addition of a moisture equation to the model, incorporation of the dynamic influences of latent heat release, and predictions of natural snowfall distributions from lake-effect snowstorms. The moist modification of the Lavoie model developed at CAL incorporated a diagnostic relationship for the prediction of precipitation rate distributions based upon a parameterization of the ice nucleation process and a physical modeling of snowfall production by riming growth. An alternative approach in which snowfall rate was parameterized in terms of predicted vertical velocity and cloud depth was applied with considerable success by Lavoie et al. (1970).

During the past year, the Lake Erie model was successfully generalized to treat the joint Lake Erie-Lake Ontario system, and numerical experiments were carried out with a moist modification of the two-lake model. A discussion of this mesoscale modeling research and some recommendations for future modeling studies are presented in this chapter.

A. Development of a Lake Erie-Lake Ontario Model

Lake Erie generally freezes over by mid-January, effectively terminating lake-effect activity until spring when the ice begins to melt. Since Lake Ontario remains unfrozen, a longer period of suitable lake-effect weather for future NOAA modification experiments might be achieved by working with short-trajectory storms off the west end of Lake Ontario after the Lake Erie lake-effect season is over. To provide for such a possibility and to permit the mesoscale modeling of Lake Ontario storms in general, the CAL moist version of the Lavoie model was modified to simulate the mesoscale influences of the joint Lake Erie-Lake Ontario system. The more general two-lake model was developed, rather than an additional one-lake model for Lake Ontario because the influences of Lake Erie and Lake Ontario are not clearly separable under many wind conditions.

The two-lake model has a 60 x 40 point rectangular grid system covering the Lake Erie-Lake Ontario area. In order to avoid a large increase in computational requirements accompanying the increase in the area covered by the model, the horizontal grid spacing is increased 33% over that employed in the Lake Erie model. The grid spacing in the 45 x 25 point interior grid spanning the two lakes and immediately adjacent land areas is 16 km in the direction parallel to the long axes of the lakes (approximately WSW-ENE) and 8 km in the direction perpendicular to the long axes of the lakes (approximately NNW-SSE). It was felt that this increased spacing would still delineate the boundaries of the two lakes, including the Niagara Peninsula, with sufficient precision to represent the important mesoscale influences of the lakes.

As in the Lake Erie model, outside the interior grid system, the grid spacing is increased exponentially to minimize the propagation of any deleterious effects from the boundaries of the grid system into the region of interest during the period of integration. Orographic effects were not included in the two-lake model.

The two-lake model was tested by carrying out a numerical experiment based upon a set of initial and boundary conditions which had previously been utilized in an experiment with the Lake Erie model. Since the initial wind direction was westerly, the disturbances produced by Lake Erie and Lake Ontario were for the most part separable. The steady state solutions computed from the two-lake model show disturbance patterns produced by Lake Erie which were quite similar to those obtained from the Lake Erie model. Quantitatively, the values predicted by the two models for the deformation of the inversion surface produced by Lake Erie differed by as much as 30 to 40% with more typical differences on the order of ±15%. It is believed that these differences resulted primarily from upwind influences of Lake Ontario on the Lake Erie disturbance, although the effects of the increased grid spacing upon the resolution of Lake Erie and the integration of the finite difference equations undoubtedly contributed.

Using moist modifications of the two-lake model, numerical experiments were carried out on the intense 15 November 1969 lake-effect snowstorm, which had been previously simulated with considerable success using the Lake Erie model (Eadie et al., 1971). The results are described in the following section.

B. Numerical Experiments with the Lake Erie-Lake Ontario Model

A series of numerical experiments were carried out with the joint Lake Erie-Lake Ontario model based upon a lake-effect storm which occurred on 15 and 16 November 1969 and deposited 12 to 15 inches of snow just north of Buffalo, New York over Grand Island, Tonawanda, and Niagara Falls. Figure 17 shows typical precipitation echo contours for the storm as measured by the Buffalo WSR-57 radar at 2243Z on the 15th. The maximum radar tops measured for the storm ranged from 8,000 to 9,000 feet. The Buffalo sounding at 0000Z on the 16th shows a capping inversion at 11,000 to 12,000 feet. The -20°C level was at approximately 9,000 feet.

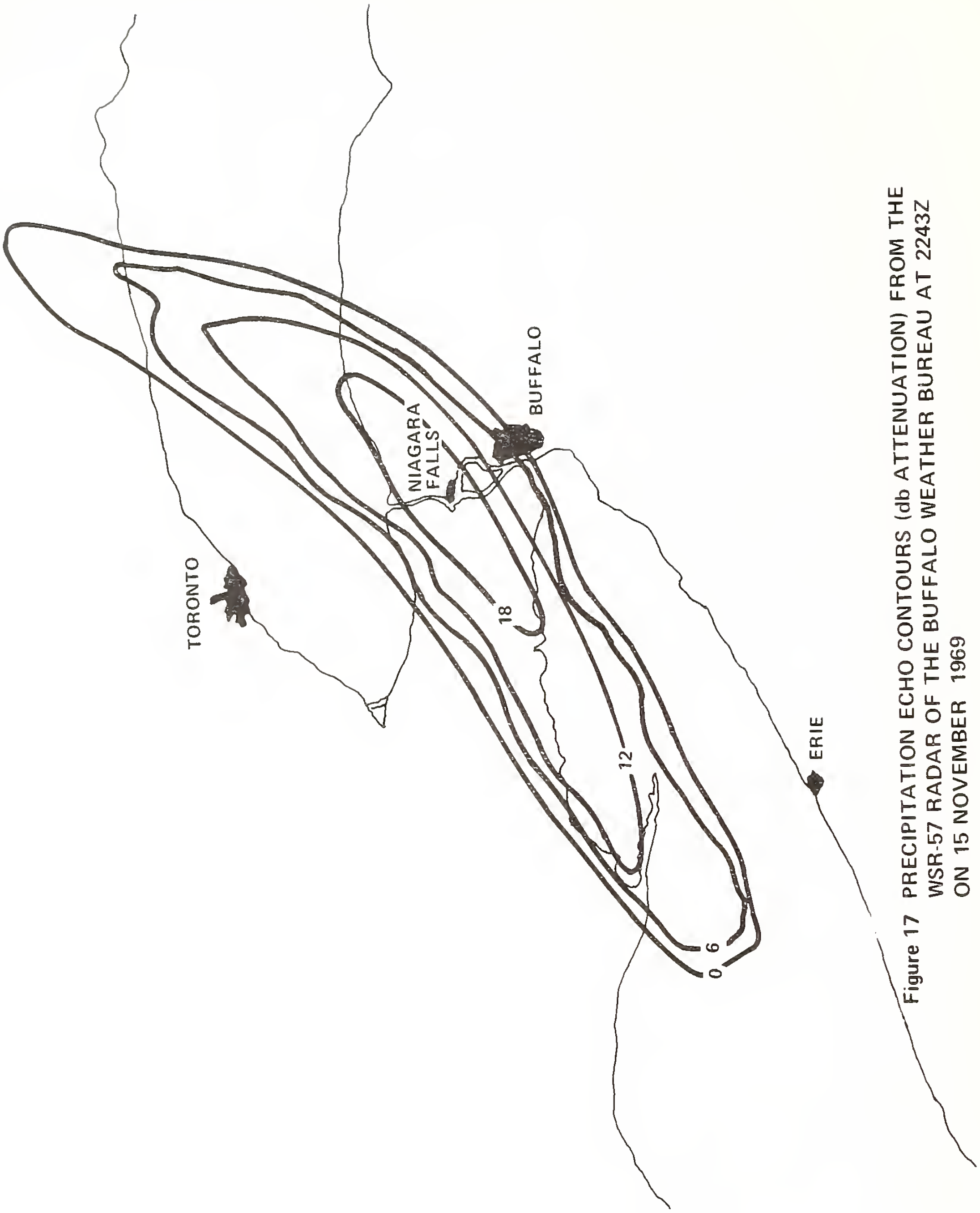

Figure 17 PRECIPITATION ECHO CONTOURS (db ATTENUATION) FROM THE WSR-57 RADAR OF THE BUFFALO WEATHER BUREAU AT 2243Z ON 15 NOVEMBER 1969

This storm had been extensively studied at CAL (Eadie et al., 1971) using several versions of the Lake Erie model. It was shown that including the dynamic effects of the release of latent heat of condensation could cause a 50% increase in the maximum vertical development of the predicted disturbance. A precipitation distribution was computed from the model which was in good agreement with observational data on the heavy snow zone from the storm. It was concluded, however, that the total precipitation from the storm may have been significantly underestimated by the model when compared with estimates by Jiusto et al. (1970) of total precipitation from a number of lake-effect storms.

The 1200Z sounding at Dayton, Ohio on the 15th had been selected as being most representative of undisturbed conditions upwind of Lake Erie. It showed a southwesterly flow through a well-mixed lower layer, capped by a 4 to 5°C inversion at 1 to 1.5 kilometers. Above the inversion was a stable layer with approximately a 2°C per kilometer increase in potential temperature.

These same upwind initial conditions were employed in a number of numerical experiments with the two-lake model. Except where noted, these experiments were carried out using the moist modifications to the Lavoie model described by Eadie et al. (1971). With the basic southwesterly flow generally parallel to the long axis of both Lake Erie and Lake Ontario, about 12 hours of meteorological time (corresponding to approximately 20 minutes of computer time on an IBM 360/65 digital computer) were required for the computed solutions to evolve from the uniform initial conditions to approximately steady state conditions. Within the framework of the Lavoie model, these steady state conditions represent the mesoscale response to the perturbing influences of the two lakes on an assumed uniform synoptic-scale flow.

The initial numerical experiments with the two-lake model based on the 15 and 16 November 1969 storm revealed several interesting features. The basic southwesterly flow in this case resulted in the eventual advection of considerable heat, which was originally transferred to the atmosphere in its passage over Lake Erie or released by condensation in the Lake Erie disturbance, into the Lake Ontario disturbance. The addition of this heat to that originating from Lake Ontario resulted in significantly greater increases in potential temperature in the Lake Ontario disturbance than in the Lake Erie disturbance. Trajectory analysis indicates that the initial southwesterly wind direction tended to maximize this effect.

One of the principal problem areas in research with the Lavoie model has been the parameterization of the influences of an overlying stable atmosphere on the horizontal flow in a well-mixed lower layer. The density stratification above the well-mixed layer affects the perturbation pressure gradients in the horizontal momentum equations of the model. The problem is to include this effect on the flow in the lower layer without simultaneously predicting the flow in the stable upper atmosphere. It can be said that there is no unique solution to this problem in a mathematical sense; rather, proposed solutions must be judged on the physical realism of the predictions produced by the model. For a more detailed discussion of this problem and a proposed improvement over the original Lavoie model, the reader is referred to Lavoie et al. (1970).

Returning to the numerical experiments with the two-lake model, it was found that for a variety of parameterizations of the influences of the stable upper layer, the Lake Ontario disturbance eventually became considerably stronger than the Lake Erie disturbance. As a result of greater potential temperature increases in the Lake Ontario disturbance, any upper layer parameterization which served to keep the development of the Lake Ontario disturbance within any reasonable bounds eventually produced a weaker disturbance over Lake Erie.

This state of affairs is at variance with the observational data for 15 to 16 November 1969 which show little evidence for a strong Lake Ontario storm in addition to the already documented intense lake-effect storm produced by Lake Erie. It is believed that this is an example of the restrictive nature of requirements in the Lavoie model for horizontal homogeneity of initial conditions and constant upwind boundary conditions. It is well-known that the time and space variations in the synoptic flow can be of crucial importance in determining the inhibition or intensification of lake-effect storms (McVehil et al., 1968; Jiusto et al., 1970).

In order to provide an example of results from the two-lake model based on the 15 and 16 November 1969 storm, a numerical experiment which yielded strong disturbances from both Lake Erie and Lake Ontario will be discussed. Following Lavoie et al. (1970), the effective potential temperature of the upper layer was chosen to be

$$\theta_u = \theta_h + \frac{\Gamma}{4} \Delta H^* \tag{1}$$

where θ_h = 273°K is the potential temperature above the inversion surface, Γ = 2°K per kilometer is the average rate of increase in potential temperature with height in the stable upper layer, and ΔH^* is the instantaneous maximum upward deformation of inversion surface from its initial uniform value. The initial potential temperature θ in the well-mixed layer of the model was assumed to be 268°K, giving an initial capping inversion of 5°K. However, when heating of the well-mixed layer produced a potential temperature $\theta \geq 273°K$, θ_h in Eq. (1) was replaced by θ, yielding

$$\theta_u = \theta + \frac{\Gamma}{4} \Delta H^* \tag{2}$$

This procedure yields bounded solutions for any degree of heating and had the effect of permitting the Lake Erie disturbance to intensify.

In order to investigate the effects of greater condensation on the precipitation predictions generated by the model, the parameterization of condensation in the moist modification of the Lavoie model developed at CAL (Eadie et al., 1971) was changed in this experiment to

$$\begin{aligned} \mathrm{COND} &= r W_H \quad , W_H > 0 \\ &= 0 \quad , W_H \leq 0 \end{aligned} \tag{3}$$

where $COND$ is the condensation rate in a unit column of the layer, r is the average mixing ratio for the layer, and $W_H = -H \nabla \cdot V$ is the vertical velocity at the inversion surface H. This in effect assumes that all of the water vapor convergence in the layer as a result of convergence in the horizontal velocity field is converted into liquid water.

Finally, the empirical expression

$$n = .216 e^{-.216T} \tag{4}$$

for the number of ice nuclei per liter active at temperature T in °C was substituted in the diagnostic expression for precipitation production by riming growth of snowfall in an attempt to account for ice crystal multiplication at warmer temperatures (Lavoie et al., 1970).

The steady state solution computed in the numerical experiment for inversion height deformation ΔH is shown in Figure 18. It is important to note the extremely strong narrow band disturbances produced by both lakes. Although the upwind location of the Lake Erie disturbance is in good agreement with the radar echoes shown in Figure 17, the extension of the Lake Erie disturbance over Lake Ontario is apparently limited by the presence of the strong disturbance field generated by Lake Ontario. The maximum inversion height of four kilometers or over 13,000 feet predicted for the Lake Erie band is compatible with the radar and radiosonde observations at Buffalo during the storm.

The distributions of the computed precipitation rate in mm of melt water per hour are shown in Figure 19. Jiusto et al. (1970) suggest a snow to melt water ratio between 6 and 15 for rimed crystals. Adopting a mean ratio of 10, precipitation rate of 2.5 mm per hour corresponds to a snowfall rate of one inch per hour. The predicted precipitation rate distributions from both bands are, therefore, generally representative both in size and intensity of snowfall from intense lake-effect bands. It is obvious, however, that the precipitation from the Lake Erie band was released too far upstream to be in good agreement with snowfall and radar observations from the actual storm. Horizontal advection of snow in falling to the surface is neglected in the present

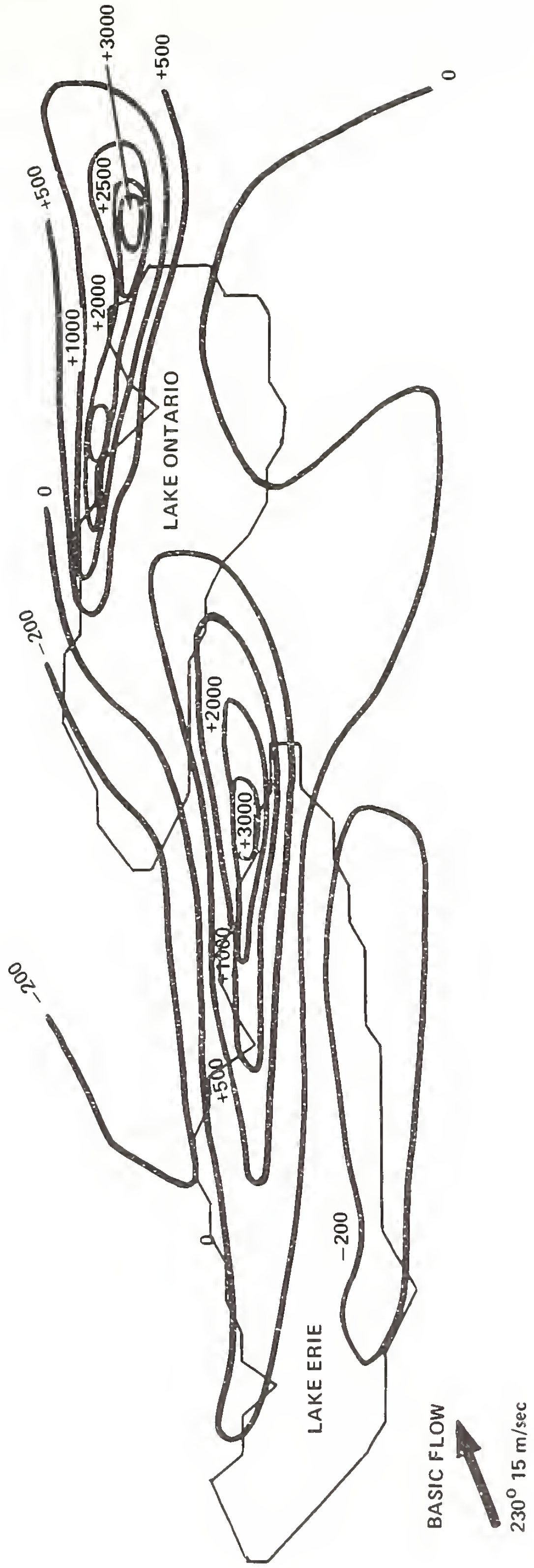

Figure 18 DEFORMATION OF INVERSION SURFACE (m) PREDICTED FOR 15-16 NOVEMBER 1969 STORM (INITIAL HEIGHT = 1000 m)

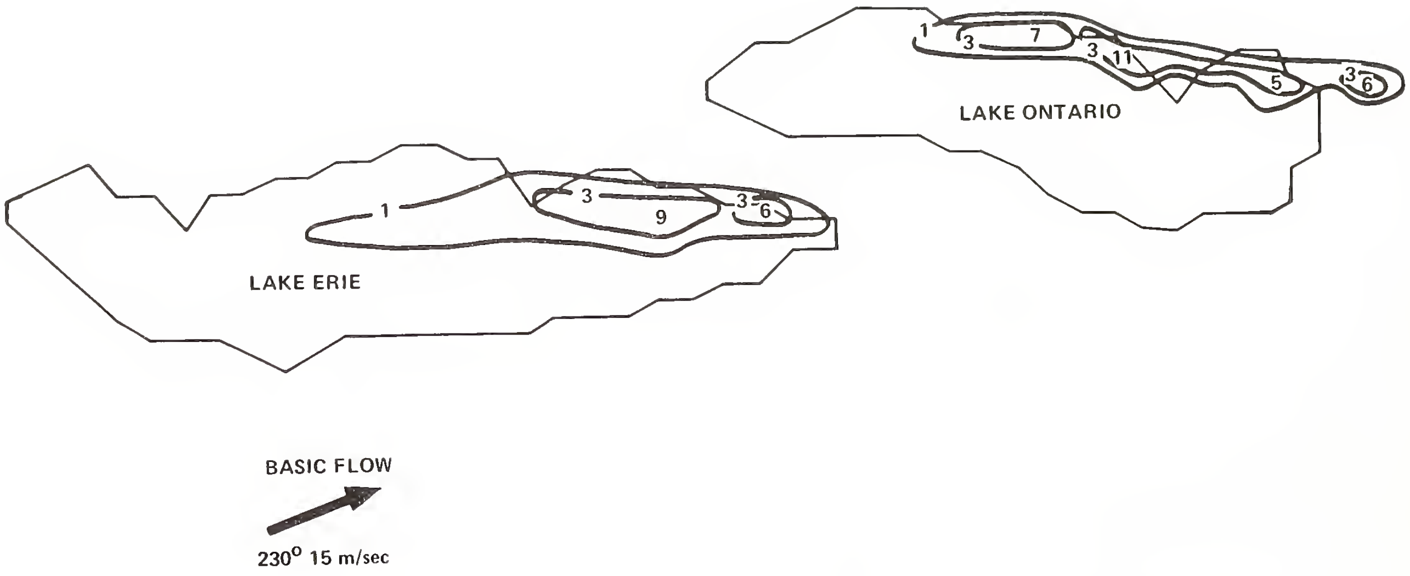

Figure 19 DISTRIBUTION OF PRECIPITATION RATE (mm hr^{-1} OF MELT WATER) PREDICTED FOR 15-16 NOVEMBER 1969 STORM

model. If a 45 kilometer advection distance were introduced, based on snow crystals falling 3 km from a generation level to the surface at an average fall speed of one meter per second in a horizontal wind of 15 meters per second, it would bring the predicted precipitation distribution from the Lake Erie band into reasonable agreement with observations.

Based upon the steady state solutions obtained in the numerical experiment, several water budget figures were calculated by integrating over the appropriate variables. Principally because of increased condensation in the present experiment, these water budget figures differ significantly from those computed from a simulation of the 15-16 November 1969 storm with the Lake Erie model. The figures for the two-lake model are given below:

Total rate of evaporation from Lake = 5.2×10^{9} g $\sec^{-1}$
Total rate of evaporation from Lake Ontario = $\underline{4.1 \times 10^{9}}$ g $\sec^{-1}$
Total = 9.3×10^{9} g $\sec^{-1}$

Total condensation rate = 1.6×10^{10} g $\sec^{-1}$
Total precipitation rate = 1.2×10^{10} g $\sec^{-1}$

The condensation and precipitation rate values were obtained by integrating over the entire grid system and thus represent the combined contributions of both the Lake Erie and Lake Ontario bands.

It should be noted that the total condensation rate and the total precipitation rate now exceed the total evaporation rate, indicating that intense lake-effect storms may precipitate more water out of the atmosphere than is made available by evaporation leaving the downstream flow with a diminished water vapor content. The precipitation efficiency of the two intense bands or the ratio of precipitation rate to condensation rate was 75%, an extremely high value. The total precipitation rate gives an estimated total precipitation in 12 to 24 hours of 1 to 2×10^{12} lb, in good agreement with the estimates of Jiusto et al. (1970) based upon observational data for a number of lake-effect snowstorms produced by Lake Erie and Lake Ontario.

C. Recommendations for Future Studies

The number of lake-effect storms studied with the Lavoie model and its various modifications has been quite small. To make any reasonable evaluation of the potential usefulness of the single-layer mesoscale modeling framework for the prediction of snowfall distributions in future Great Lakes weather modification experiments, it will be necessary to significantly expand the number of case studies. Particularly with the increased area covered by the two-lake model, it will be important to establish limitations imposed by the requirements for horizontal homogeneity of initial conditions and constant upwind boundary conditions in the present model.

A preliminary analysis during the past year indicated that physically realistic modeling of snow crystal development by diffusional and riming growth as a function of ice nucleus concentration and liquid water content cannot be accomplished within the vertically averaged, single-layer modeling framework of the Lavoie model. However, consideration should be given to incorporating the horizontal advection of snow crystals in falling to the surface into the model, based upon some a priori assumptions about snow crystal morphology. In this manner, improved precipitation distributions may be generated for natural lake-effect snowstorms, and some crude representation of the effects of seeding may be incorporated into the model.

In addition, some further research on the parameterization of condensation in the CAL moist modification of the model is recommended, since the condensation exerts a strong influence on the predicted vertical development and distribution of precipitation.

IV. REFERENCES

Brown, S. R., 1970: Terminal Velocities of Ice Crystals. Paper No. 170, Department of Atmospheric Science, Colorado State University, Fort Collins, Colorado, 52 pp.

Davis, L. G., R. L. Lavoie, J. I. Kelly, and C. L. Hosler, 1968: Lake Effect Studies. Final Report on Contract No. E22-80-67(N), Department of Meteorology, Pennsylvania State University.

Eadie, W. J., 1970: The Experimental Modification of Lake-Effect Weather. Final Report on Contract No. E22-7-69(N), CAL Report No. VC-2898-P-1, Cornell Aeronautical Laboratory, Inc., Buffalo, New York.

Eadie, W. J., R. J. Pilié, and W. C. Kocmond, 1971: Modification and Modeling of Lake-Effect Weather. Final Report on Contract No. E22-39-70(N), CAL Report No. VC-2898-P-2, Cornell Aeronautical Laboratory, Inc., Buffalo, New York.

Ferguson, E. W., 1971: Picture of the Month - Satellite View of a Lake-Effect Snowstorm. Mon. Wea. Rev., 99, 247-248.

Jayaweera, K. O. L. F., and R. E. Cottis, 1969: Fall Velocities of Plate-like and Columnar Ice Crystals. Quart. J R. Meteor. Soc., 95, 703-709.

Jiusto, J. E., and E. W. Holroyd, 1970: Great Lakes Snowstorms, Part 1. Cloud Physics Aspects. Report on Grant No. E22-49-70, Atmospheric Sciences Research Center, State University of New York at Albany.

Jiusto, J. E., D. A. Paine, and M. L. Kaplan, 1970: Great Lakes Snowstorms, Part 2. Synoptic and Climatological Aspects. Report on Grant No. E22-49-70, Atmospheric Sciences Research Center, State University of New York at Albany.

Lavoie, R. L., W. R. Cotton, and J. B. Hovermale, 1970: Investigations of Lake Effect Storms. Final Report on Contract No. E22-103-68(N), Department of Meteorology, Pennsylvania State University.

Layton, R. G., 1969: *Lake Effect Snow: A Study of Snow Crystals in Great Lakes Snowstorms.* Final Report on Subcontract No. 24-6002-A, State University College of New York at Fredonia, New York.

Magono, C., and T. Nakamura, 1965: Aerodynamic Studies of Falling Snowflakes. *J. Meteor. Soc. Japan, Ser. 2*, *43*, 139-147.

McVehil, G. E., J. E. Jiusto, R. A. Brown, and R. L. Peace, Jr., 1967: *Project Lake Effect - A Study of Lake-Effect Snowstorms.* Final Report on Contract No. E22-49-67(N), CAL Report No. VC-2355-P-2, Cornell Aeronautical Laboratory, Inc., Buffalo, New York.

McVehil, G. E., C. W. C. Rogers, and W. J. Eadie, 1968: *The Structure and Dynamics of Lake-Effect Snowstorms.* Final Report on Contract No. E22-89-68(N), CAL Report No. VC-2559-P-1, Cornell Aeronautical Laboratory, Inc., Buffalo, New York.

Nakaya, U., 1954: *Snow Crystals: Natural and Artificial.* Cambridge, Mass., Harvard University Press.

Parmenter, F. C., 1971: From Above: A Lake-Effect Snowstorm. *Weatherwise*, *24*, 39.

Warburton, J. A., and M. S. Owens, 1969: *Silver Analysis in Lake-Effect Studies - Lake Erie Experiments, 1968.* Final Report on Contract No. E22-9-69(N), Desert Research Institute, University of Nevada, Reno, Nevada.

U.S. DEPARTMENT OF COMMERCE
Maurice H. Stans, Secretary

NATIONAL OCEANIC AND ATMOSPHERIC ADMINISTRATION
Robert M. White, Acting Administrator
ENVIRONMENTAL RESEARCH LABORATORIES
Wilmot N. Hess, Director

NOAA TECHNICAL REPORT ERL 199-APCL 17

Computer Subroutine for Presenting Meteorological Flight Data on the Printer (CURVPT)

HEINZ H. GROTE

ATMOSPHERIC PHYSICS AND CHEMISTRY LABORATORY
BOULDER, COLORADO
March 1971

TABLE OF CONTENTS

Page
ABSTRACT 1
1. INTRODUCTION 1
2. INPUTS 2
3. FURTHER DETAIL ON THE SUBROUTINE 4
APPENDIX A. TEST CP PRINTOUT 12
APPENDIX B. CURVPT PRINTOUT 14

COMPUTER SUBROUTINE FOR PRESENTING METEOROLOGICAL FLIGHT DATA ON THE PRINTER

(CURVPT)

Heinz H. Grote

This paper describes a subroutine CURVPT that provides a plot on the peripheral printer of up to six parameters with curve separation and automatic scaling. It was developed for automatic presentation of meteorological flight data by the computer but can be used universally.

U. S. DEPARTMENT OF COMMERCE
Maurice H. Stans, Secretary

ENVIRONMENTAL SCIENCE SERVICES ADMINISTRATION
Robert M. White, Administrator
RESEARCH LABORATORIES
Wilmot N. Hess, Director

ESSA TECHNICAL REPORT ERL 139-APCL 9

Plotter Subroutine for Meteorological Flight Path (PATH)

HEINZ H. GROTE

ATOMOSPHERIC PHYSICS AND CHEMISTRY LABORATORY
BOULDER, COLORADO
December 1969

TABLE OF CONTENTS

Page

1. INTRODUCTION 1

2. VARIABLES 4

3. PROGRAM TESTPATH 8

4. FURTHER DETAILS ON SUBROUTINE PATH 9

5. ACKNOWLEDGMENT 11

6. REFERENCES 12

APPENDIX A. PATH Lettering 13

APPENDIX B. Time Scale for PATH Lettering 14

APPENDIX C. TESTPATH Printout 15

APPENDIX D. PATH Printout 16

PLOTTER SUBROUTINE FOR METEOROLOGICAL FLIGHT PATH (PATH)

Heinz H. Grote

This paper describes a subroutine PATH that works in connection with the plotter subroutine CRTPLT to provide a two-dimensional plot of a meteorological flight path with wind vectors, time notations, and a legend.

U.S. DEPARTMENT OF COMMERCE
Maurice H. Stans, Secretary

NATIONAL OCEANIC AND ATMOSPHERIC ADMINISTRATION
Robert M. White, Administrator
ENVIRONMENTAL RESEARCH LABORATORIES
Wilmot N. Hess, Director

NOAA TECHNICAL REPORT ERL 140-APCL 10

Plotter Subroutine for Meteorological Straight Line Flight Data (SLENDER) (Revised)

HEINZ H. GROTE

BOULDER, COLO.
March 1971

TABLE OF CONTENTS

1. INTRODUCTION 1

2. TILTING GEOMETRY 6

3. INPUT VALUES 12

4. GENERAL STRUCTURE 19

4.1 Timing 20
4.2 Flight path approximation 21
4.3 Scaling 24
4.4 Plotting of flight path 24
4.5 Plotting of wind vectors 25
4.6 Plotting of coordinate grid 25
4.7 Scaling and plotting of meteorological parameters 28

5. ACKNOWLEDGMENT 32

6. REFERENCES 32

APPENDIX A PROGRAM TESTSLEN 33

APPENDIX B SUBROUTINE SLENDER 37

PLOTTER SUBROUTINE FOR METEOROLOGICAL STRAIGHT LINE FLIGHT DATA (SLENDER)

Heinz H. Grote

This paper describes a subroutine SLENDER that works in connection with the plotting subroutine CRTPLT to provide a two-dimensional plot of a relatively straight flight path and four analog traces of selected meteorological parameters lined up with the flight path.

Reprinted from
E⊕S
Vol. 52, No. 6, June 1971
Copyright 1971 by American Geophysical Union

Cloud Physics

J. Hallett, H. D. Orville, D. Sartor,
and H. K. Weickmann

Nuclei and Nucleation

Problems of the origin and physical characteristics of ice crystal and cloud drop nuclei continue to receive considerable attention. There is good evidence that sea salt particles play only a minor role in the world supply of cloud drop nuclei, although they do provide the largest nuclei that are of importance in the initiation of coalescence rain. The mode of action of ice nuclei is still inadequately understood, there is increasing disillusionment with the concept that any direct correspondence of ice nuclei measurements and ice crystals in clouds should exist. Possible mechanisms for ice crystal production other than by solid particle nucleation have been investigated. Increasing interest has developed on the role of pollution products in both drop and crystal nucleation.

Two papers indicate that the cloud physicist has not been sufficiently rigorous in applying thermodynamic principles. *Abraham* [1968] pointed out that Helmholtz free energy (not Gibbs free energy) should be used for consideration of phase nucleation phenomena with equal temperature-pressure conditions. *Abraham and Pound* [1968] and *Reiss et al.* [1968] raise problems about whether the concept of free energy applied to an embryo should include rotational degrees of freedom. *Long* [1969] re-emphasized that the curves for free energy of an embryo as a function of radius as discussed by earlier authors are incorrect, insofar as they apply equilibrium thermodynamics to a definitely non-equilibrium situation, the equilibrium condition occurring only at the critical radius for a given departure from plane-surface equilibrium. (Volmer was well aware of this fact.) A derivation of the Kelvin equation on a rigorous basis is given.

Condensation Nuclei

New instrumentation for measurement of both Aitken nuclei and cloud nuclei has been developed, with regard to defects in earlier instruments. *Kassner et al* [1968*a*, *b*] describe operation of an expansion chamber necessary to give realistic counts of Aitken nuclei; they take into account that, at very large concentrations, competition between neighboring drops may prevent growth and detection of the smaller sizes. The calibration of generally available nuclei counters is inadequate and can only be made by continuous dilution of the sample until competition between drops is unimportant [*Kassner et al.*, 1969].

Radke and Hobbs [1969*b*] automated a diffusion chamber developed earlier by Twomey to give counts at 2-min intervals. Field use led to observations of the interaction of nuclei with drops as the drops pass through the cloud-forming process [*Radke and Hobbs*, 1969*a*]. Criticism of the diffusion chamber technique [*Fitzgerald*, 1970*b*; *Saxena et al.*, 1970] showed that deep chambers required a much longer time for equilibrium than had generally been used, and that, if turbulence occurred as the sample was admitted, an accurate estimation of maximum supersaturation could not be obtained. More important, under operating conditions with inlet air temperature equal to the bottom plate temperature, the supersaturation may exceed the equilibrium value by a factor of 3. *Twomey and Warner* [1967], counting nuclei with a thermal diffusion chamber, found a good correlation between cloud nuclei measured in a thermal diffusion chamber and cloud drops measured by a cloud sampler.

J. Hallett is with the Desert Research Institute, University of Nevada, Reno 89507. H. D. Orville is with the South Dakota School of Mines and Technology, Rapid City 57701. D. Sartor is with the National Center for Atmospheric Research, Boulder, Colorado 80302. H. K. Weickmann is with the National Oceanographic and Atmospheric Administration, Environmental Research Laboratories, Boulder Colorado 80302.

Jiusto and Kocmond [1968] used a thermal diffusion chamber to show that silver iodide and wax aerosol acted as drop nuclei at an estimated supersaturation as low as 0.3 to 0.5%, which was unexpected on theoretical grounds.

There has been considerable interest in the role of artificial cloud nuclei to be used for seeding warm fog. *Jiusto et al.* [1968] seeded a laboratory cloud with NaCl particles and produced improvements in visibility that indicated the utility of the technique in the field. *Low* [1969] examined the hygroscopic properties of electrolyte aerosols, taking into account the effect on surface tension, activity, and solution density, and concluded that chloride salts were useful seeding materials.

From theoretical studies *Kornfeld* [1970*a*] and *Silverman and Kunkel* [1970] deduced criteria for the seeding rate of warm fog to produce given improvements of visibility; a comparison of the properties of various hygroscopic substances showed that urea and ammonium nitrate were the most suitable for field use. An alternative approach was examined by *Warner and Warne* [1970], who investigated theoretically the effect on fog formation of a surface film in retarding drop growth. They concluded that the fog formation could be delayed by more than 10 min but that, when it did finally form, smaller more numerous particles would be activated and the visibility would be worse than would have occured naturally.

Inadvertent weather modification by production of condensation nuclei has been demonstrated in several situations. *Conover* [1969] has produced further observational evidence that nuclei produced by a ship's exhaust form cloud lines hundreds of miles long and 25 miles wide. *Twomey and Warner* [1967] and *Warner* [1968] suggest that nuclei produced by cane fires lead to a reduction of precipitation, whereas *Hobbs et al.* [1970] suggest that nuclei from paper plants produced at a rate of 10^{19}/sec lead to an increase of precipitation.

The origin of cloud nuclei is still under debate. *Garrett* [1968] showed experimentally that bubbles bursting in sea water with an organic surface film produced at least 3 times more large nuclei. *Blanchard* [1968] found that natural sea salt nuclei contained varying amounts of surface active material. He subsequently showed that coastal surf may be a sufficient source of cloud nuclei. The technique of heating an aerosol before measuring its cloud drop nucleating ability has shown in field and laboratory that many cloud nuclei are volatile at temperatures between 250° and 300°C. This result shows that the nuclei are not NaCl and suggests an origin other than the ocean [*Twomey*, 1968, 1969; *Dinger et al.* 1970]. These particles are probably sulfate, resulting from oxidation of atmospheric SO_2 or H_2S. These findings conflict with those of *Blanchard* [1969], who finds that coastal surf may be a sufficient source of cloud nuclei. Measurements of nuclei concentration on a world-wide scale [*Twomey and Wojciechowski*, 1969] indicate a uniform source of nuclei not correlated to an oceanographic production and show that at higher levels in the troposphere pollution sources are unimportant in the nuclei balance.

Ice Crystal Nuclei

The way in which AgI nucleates ice crystals has been studied more extensively but problems still remain. *Corrin et al.* [1967] showed that the nucleating activity of AgI particles decreased with increase of sample purity; *Layton and Lavign* [1969] confirmed that the cycling of single crystals leads to a significant reduction of activity. *Edwards and Evans* [1968], on the other hand, in a test of particles in freezing water drops, found that there was not a reduction of activity after melting and recooling; they also found that their AgI particles had a significantly lower effectiveness when nucleating from the vapor at water saturation than when enclosed in drops. *Steele and Davis* [1969] found that an AgI aerosol introduced with a precooled cloud become increasingly more effective as the liquid water content was increased from 0.5 to 2.5 gm^{-3}. *Gokhale and Goold* [1968] and *Odencrantz* [1969] found that AgI particles were significantly more effective in freezing when contact nucleation occurred, that is, AgI particles were carried into a drop surface by Brownian motion. *Weickmann et al.* [1970] bring experimental evidence from special crystal forms developed in a fog chamber after seeding with various types of AgI in the temperature range −10 to −20°C that AgI acts only as a contact nucleus and not as a sublimation nucleus. Theoretical studies [*Fletcher*, 1969] of the effect on nucleation of a distribution of active sites (idealized as conical pits) were consistent with experimental observations and provided further evidence that a knowledge of the detailed surface topography of a nucleating substance is important in understanding its nucleating behavior. *Knollenberg* [1969*a*, *b*] has interpreted his earlier results of ice seeding with urea in terms of an endothermic reaction on dissolution. Urea in suspension nucleates supercooled water at about −15°C; it nucleates at temperatures up to +4°C when introduced as a dry powder. Other substances having a negative heat of solution have been found to behave in a similar way. *Parungo and Lodge* [1967*a*] found a relation between nucleation temperature of some amino acids and their heats of solution. *Parungo and Lodge* [1967*b*], from laboratory studies of the freezing of supercooled drops, concluded that dissolved nonpolar gases caused nucleation some 15° higher than pure water; *Kuhns* [1968], from somewhat different laboratory studies, found that the effect was not greater than 1°C. *Bigg and Giutronich* [1967] examined the nucleating ability of meteoritic material dispersed in a manner more closely resembling the upper atmosphere interactions than earlier workers used. Bigg and Giutronich found a sufficiently high level of activity to suggest that meteoritic material may make a significant contribution to the tropospheric ice nuclei count. New techniques for investigating the presence and activity of nuclei in the atmosphere have been developed. *Allee et al.* [1969] deposited nuclei according to size in a Goetz spectrometer and activated

IUGG 342

the particles in a supersaturated environment. *Parungo and Rhea* [1970*b*] developed an idea from *Knight* [1969] for detection of AgI particles on individual snow crystals. Replicas are immersed in a solution of AgI that is supersaturated by heating, which causes AgI crystals to grow only on AgI nuclei remaining from the original snow crystal. Work has continued on the ice nucleating characteristics of AgI particles produced by a variety of field devices. The influence of a water soluble component such as KI or NaI was investigated theoretically by *Fletcher* [1968]. He concluded that small AgI particles are less active as ice nuclei because they tend to dissolve in the form of a complex. *B. L. Davis* [1969] used an X-ray technique to show that the dry particles consisted of distinct hydrates; thus he confirmed the results of earlier workers. *Davis and Steele* [1968] investigated in considerable detail the effect of burner conditions on the nucleation ability and concluded that there was a maximum rate of AgI input beyond which the number of nuclei failed to increase. *Blair and Davis* [1969] found that an aerosol aged under dry conditions subsequently gave more crystals than an aerosol aged under moist conditions

The origin of ice crystals in clouds in the atmosphere has been a foremost problem in cloud physics and is still far from resolved. Aircraft observations have shown that on occasion concentration of ice crystals in clouds with a minimum temperature of -5° is high and, moreover, is considerably higher (10^3) than values inferred from ice nucleus counts. [*Mossop et al.*, 1968; *MacCready and Baughman*, 1968. *Koenig*, 1968*a*, *b*, *c*; *Sax*, 1969]. *Mossop* [1970], *Hobbs* [1969], and *Auer et al.* [1969] measured ice crystals and nuclei in the neighborhood of the cloud and concluded that, although at temperatures below -25° ice crystal and nuclei concentrations were comparable, at higher temperatures ice crystals were present in concentration larger by as much as 10^3. Laboratory work [*Roberts and Hallett*, 1968] showed that preactivation of natural nuclei readily occurred but was lost when nuclei were heated or dried out.

Two other possibilities for the nuclei-crystal discrepancies should be carefully examined. First, techniques of ice nuclei measurement were inadequately simulating the processes that occurred in clouds, and thus led to lower (or occasionally higher) counts. This situation improved with the introduction by *Stevenson* [1968] of a millipore filter technique in which the nuclei could be exposed to controlled temperature and humidity in an apparatus comparable with that used earlier for crystal growth studies. Even this technique, however, could not adequately simulate natural clouds, where, for example, contact nucleation by Brownian capture of nuclei could occur with quite different nucleation temperature. The second possibility was that some kind of crystal splintering mechanism was occurring. Laboratory studies showed that single drop freezing was not a copious source of ice splinters [*Dye and Hobbs*, 1968; *Hobbs and Alkezweeny*, 1968; *Johnson and Hallett*, 1968] but suggested the possibility of splintering during accreation [*Brownscombe and Hallett*, 1967]. Another mechanism for nucleation of ice crystals has been a cause of some controversy. *Plooster* [1968] and *Gitlin and Lin* [1969] have shown that nucleation is associated with collapse of a vapor cavity at temperatures a few degrees below 0°C. *Edwards et al.* [1969], on the other hand, suggest that the nucleation process is associated with the shearing of water in contact with a solid surface. *Goyer and Plooster* [1968] concluded that the shock waves from a lightning discharge were not sufficiently intense to cause significant nucleation. *Schaefer* [1968*b*], however, found that other electrical effects could give rise to ice large numbers of crystals formed from the tips of growing dendrites in the presence of electric fields caused by application of 5000 volts to the crystal.

Particles from auto exhausts have been examined as a possible means of inadvertent weather modification through their action as ice forming nuclei. *Schaefer* [1968*a*] and *Morgan and Allee* [1968] suggested that lead present in most fuels could react with traces of iodine to give PbI_2. *Parungo and Rhea* [1970*a*] measured the lead content in air in the neighborhood of Denver, Colorado, and in snow collected from the Park Range AgI seeding project. They found that there was an increase of ice nuclei (tenfold) in association with high lead content of the Denver air and that the lead content of the snow exceeded its silver content by a factor of 10.

Microphysics

The microphysical processes in clouds have received considerable attention during the period covered by this report. New studies of the input variability of the initial conditions for condensation growth have been successful in some instances in broadening the understanding of initial drop distribution. Considerable progress has been made in numerical models of cloud drop growth by collision and coalescence. Collision efficiency calculations for small drops have been greatly improved, but confirming experimental data are scarce or lacking. Numerical models of cloud electrification processes attributable to particle interaction are now possible and give reasonable results, but the over-all complexity of the problem demands that many of the processes now handled as constant or parametrically changing be allowed to vary in a more realistic manner.

Condensation Growth of Cloud Droplets

Condensation on soluble nuclei in a closed parcel of air rising with constant updraft has been studied by *Koenig* [1968*c*] and *Arnason et al.* [1969]. A more extended model that includes entrainment has been developed by *Chen* [1970]. The drop size spectrum obtained in the above computations is generally narrower than the observed cloud droplet spectrum. Various approaches have been used to explain the observed broad droplet size distributions. Condensation on a heterogeneous population of condensation nuclei, including soluble and insoluble nuclei, has been studied by *Kornfeld* [1970*b*]. *Carstens et al.* [1970] have investigated diffusional interaction between two growing droplets and found the effect to be of minor importance in clouds. The effect of modified diffusion and heat conduction coefficients on droplet growth by condensation in the first few hundred meters above cloud base has been studied by *Fitzgerald* [1970*a*]. *Paluch* [1970*a*] has worked on a numerical model that depends on small variations in the initial relative humidity, which coupled with droplet sedimentation can produce inhomogeneities in droplet number concentration and thus result in broader droplet size distributions.

Coalescence

There has been an upsurge in interest in the coalescence and disruption of drops and in the role electrical forces play in these processes [*Cotton and Gokhale*, 1967; *Damon*, 1967; *Sartor*, 1967; *Adam et al.*, 1968; *Sartor and Abbott*, 1968; *List and Whelpdale*, 1969; *Whelpdale and List*, 1970; *Blanchard and Spencer*, 1970, *Foote*, 1970; *Park*, 1970]. Some laboratory studies have been made of very limited drop sizes, but the range of sizes (over which the physical consequences vary greatly) that must be covered for cloud physics application is so great that it may be a long time before all the results are in. *Damon* [1967], *Park* [1970], and *Foote* [1970] attempt to fit the limited measurements with general theories from which the information gaps can be closed.

Collection and Growth

The collection equation (frequently referred to as the coalescence equation) for the growth of droplets in well-mixed clouds suffers from the same kind of 'closure problems' as the field of turbulence [see *Drake*, 1970]. The problem of closure has been discussed by *Warshaw* [1967] and *Scott* [1967]. A more comprehensive model for the time evolution of a cloud droplet spectrum was given by *Berry* [1969]. This includes the effects of condensation, evaporation, collection, sedimentation, and ambient air motions. A different statistical approach to the collection problem, which may well lead to the most rigorous formulation of the collection problem, was given by *Knight* [1970]. He considered the collection process as a *McKean* [1966] type Markov process and the resulting equation is somewhat similar to that given earlier by *Muller* [1928*a*, *b*]. The Muller equation describing the collection of droplets is an integro-differential equation whose kernel may be thought of as the parameter of the system. For cloud physics this kernel is a function of the terminal velocities of the droplets, the collision and coalescence efficiencies, the cross-sectional areas of the droplets, and the physical properties of the air. Since the solutions of this integro-differential equation are very sensitive to the form of the kernel, any improvement in the description of the kernel is very important.

The integro-differential equation of Muller possesses exact solutions for certain formulations of the kernel. *Scott* [1968*a*] obtained solutions for the constant kernel, the sum, and the product kernels. *Drake* [1970] extended the results of Scott by obtaining exact solutions for linear combinations of these kernels. However, the kernels that correspond to physical situations require approximate solution techniques. *Drake* [1970] discusses these methods in detail. *Rice and Whitehead* [1967] have used power series methods, but the method has a serious drawback since many terms are required to describe accurately the 'tail' of the droplet spectrum. The use of similarity methods has been considered for various kernels in the papers of *Wang and Friedlander* [1967], *Friedlander and Hidy* [1969], *Suzuki et al.* [1969], and *Hidy* [1970]. *Scott* [1968*a*], using the saddlepoint method, obtained asymptotic solutions for several different kernels. The use of transforms and integral power moments is discussed by *Scott* [1968*a*], *Thompson* [1968], and *Drake* [1970].

The most useful and productive approximate solution technique has been that of finite differences and sums. The most comprehensive set of computations were made by *Berry* [1967] for twelve different kernels. From this study, *Berry* [1968] formulated a new autoconversion rate for liquid water from cloud droplets to water drops useful in the modeling of cumulus clouds. *Mockros et al.* [1967] solved a system describing an evolving aerosol spectrum that was continuously reinforced by a new supply of particles. *Srivastava* [1967*b*] considered a model for the coalescence of raindrops, and *Austin and Kraus* [1968] discussed a model for snowflake aggregation. *Kaniel et al.* [1968] and *Kovetz and Olund* [1969] devised models for the formation of rain in warm clouds. *Warshaw* [1967] considered the coalescence of droplets in warm clouds, allowing for the influence of one-dimensional sedimentation, and studied the effects of the Davis-Sartor collision efficiencies on cloud droplet growth. His calculations show that, although the absence of a cutoff can be critical in allowing the coalescence process to get started, once underway the Davis-Sartor collision efficiencies give somewhat slower rates. (It should be noted that for droplets of radii less than 20 μm the actual value of the collision efficiency is in doubt by certainly a factor of 2 because of uncertainties in the gas-kinetic effects when the droplets approach closely). *Nelson* [1970], using *Melzak's* [1957] coalescence equation with breakup, simulated the effects of water spray seeding on the warm rain process.

Other approximate solution techniques for the collision coalescence problem are the direct simulation by the Monte Carlo methods of *Kornfeld et al.* [1968] and *Chin* [1970], the use of a linearized form of the coalescence equation of *Scott* [1968*b*] and the 'mean-value theorem' approach of *Bleck* [1970]. The solution technique of Bleck has been applied in simulating hail growth in a one-dimensional cumulus cloud model [*Danielsen et al.*, 1970].

Hocking [1959] computed collection efficiencies for very small droplets in Stokes flow. One result of these computations was the 'famous' 19 -μm cutoff. The improved computations of *Davis and Sartor* [1967] showed that this cutoff is nonexistent. Other improvements in the collision efficiency computations for droplets in a viscous fluid are given by *M. H. Davis* [1969*b*] and *Davis et al.* [1970]. These theoretical calculations confirm the nonexistence of the 'Hocking cutoff' and, further, predict an enhanced collision efficiency for droplets of nearly equal size. The basis of the new results in the paper by Davis et al. is the new terminal velocity and drag results for small water droplets in low and intermediate Reynolds number flows reported by *Pruppacher and Steinberger* [1968], *Beard and Pruppacher* [1969], *Hamielec et al.* [1967], *Rimon and Cheng* [1969], and *LeClair et al.* [1970]. Recent unpublished laboratory results of Pruppacher for collisions between large droplets ($r > 60$ μm) and small droplets ($r < 10$ μm) have established the validity for this size range of the modified Langmuir results reported by *Mason* [1957]. *Scott and Chen* [1970] derived empirical formulas for the collision efficiency curves for the *Shafrir and Neiburger* [1963] and *Davis and Sartor* [1967] kernels.

The growth rate of droplets can be enhanced or retarded by the presence of electric fields and charges. These effects have been considered by *Rice and Whitehead* [1967], *Sartor* [1967, 1970], and *Paluch* [1970*b*].

Glaciation of Clouds

Aircraft and ground observations within clouds have continued to show that the concentration of ice crystals can be as much as 10^3 or 10^4 times as great as the concentration of counted ice nuclei [*Grant*, 1968, *Koenig*, 1968*a*; *Hobbs*, 1969; *Auer et al.*, 1969, *Burrows and Robertson*, 1969]. *Hobbs* [1969] and *Auer et al.* [1969] have suggested that the ratio of ice crystals to ice nuclei decreases with decreasing temperature, being 1 at about −25°C. However, *Mossop et al.* [1970] indicate that the apparent temperature variation may be primarily due to the fact that the maximum ice crystal concentrations found are of the order of 100 liter^{-1}, whereas the ice nuclei concentration increases with decreasing temperature. Even considering the uncertainty and difficulty in obtaining realistic measurements of ice nuclei concentrations, there is little doubt that an ice multiplication mechanism is operating in some clouds. The explanation of this mechanism and the conditions under which it occurs is one of the more important problems in cloud physics. Some of the more likely mechanisms that have been considered are fragmentation of freezing drops, mechanical breakup of ice crystals (such as dendrites), and breakup or splintering during riming. Recent work indicates that the fragmentation of freezing drops is probably not important as a rapid mechanism for crystal multiplication or as a major cloud electrification process [*Dye and Hobbs*, 1968; *Johnson and Hallett*, 1968; *Brownscombe and Thorndike*, 1968; *Hobbs and Alkezweeny*, 1968]. The mechanical breakup of crystals has been suggested by *Koenig* [1968*a*, *b*], but no laboratory confirmation has been attempted. Riming also needs unequivocal laboratory confirmation.

Electrification of Clouds due to Microphysical Processes

Pruppacher et al. [1968] and *Cobb and Gross* [1969] summarized much of the work on the electrical potentials developed during the freezing of water and conducted experiments that give a comprehensive picture of application of freezing potentials and thermoelectric effects to the electrification of clouds. When their results are applied to collisions between ice particles in clouds, their work can be summarized as follows. Collisions between ice particles result in a negative charge on the warmer (usually larger) particle and a corresponding positive charge on the colder particle at temperatures below −8°C. Above −8°C the charge reverse signs. Collisions between particles of ice doped with salts (concentrations of 10^{-6} to 10^{-3} mole per liter) commonly found in the atmosphere produce a negative sign on the warmer (usually larger) particle. As with all particle interaction processes, contact charging is limited by the time the particles are in contact and the electrical relaxation time of the hydrometeor. Since the conductivity of ice decreases with decreasing temperature, there is a corresponding increase in the relaxation time that limits the effectiveness of charge transfer at the colder temperatures [*Camp et al.*, 1967, *Sartor*, 1967]. The field observations of the charging events due to collisions of natural ice crystals with ice spheres by *Scott and Hobbs* [1968] and *Burrows and Hobbs* [1969] show this temperature effect and the effect of inductive charging in a polarizing field which sometimes masked other charging events. *Scott and Levin* [1970] found experimentally that the charging of snow crystals due to collisions with an ice sphere in an electric field was higher than predicted by theory.

Laboratory studies of charge transfer between colliding water drops in an electric field are reported by *Montgomery and Dawson* [1969] and *Sartor and Abbott* [1968]. The results are found to agree well with theoretical calculations by *M. H. Davis* [1964, 1969*a*]. *Shewchuck and Iribarne* [1970] and *Iribarne and Klemes* [1970] studied the electrification associated with drop breakup, and *Levin and Hobbs* [1970] reported on the charge separation due to the splashing of water drops in electric fields and in the absence of electric fields.

The numerical model of the cloud electrification processes due to particle interactions [*Sartor*, 1961*a*, *b*] was further generalized to include thermoelectric as well as inductive charging processes and cloud air conductivity that varies with the field [*Sartor*, 1967]. The electric field growth curves prepared by using particle distributions observed in thunderstorms compare favorably in time and shape with observed traces. *Kamra* [1970] points out that charge exchanging collisions between ice crystals and hail pellets (or graupel) in high electric fields can reverse the direction of the motion of the ice crystal in the field, thereby limiting the field. The limiting fields are functions of the particle size and precipitation rates and are generally above 100 v cm^{-1}, these fields, although rare, are observed in active thunderstorms according to the recent rocket observations of *Winn and Moore* [1970].

Phillips [1967] finds an important role for the conductivity gradient at the edge of cumulus clouds in separating charge so that it eventually can control the behavior of an initially independent charging mechanism.

Using the laboratory observations of *Atkinson and Paluch* [1966] and *Keeney* [1970] on the intensity of the microwave radio emission from sparking charged drops when they collide, *Sartor and Atkinson* [1967] made calculations of the quasi-thermal noise temperatures from a wide variety of possible combinations of particle drop sizes, drop charges, and electric fields in thunderstorms. *Penzias and Wilson* [1970] found 1° to 5°K microwave noise temperatures from rainstorms attributable to this source. In the Sartor and Atkinson calculations, this result would correspond to collisions between particles of at least 0.6- and 0.8-mm radius with an average charge of ±0.2 esu per particle in concentrations of 142 particles m^{-3} Other combinations of charge, particle size, and concentration would give the same results. Additional laboratory information on sparking thresholds could lead to the remote sensing of thunderstorms for microphysical information by microwave radiometers.

Mesoscale Numerical Cloud Models

As evidenced by the number of papers now appearing, the numerical modeling of mesoscale cloud phenomena is on the increase. The dynamics of cloud processes, the airflow over lakes, islands, and mountains with the attendant cloud and rain formation, and the development of hurricanes have all been simulated numerically in the past few years. A greater emphasis than before has been placed on the interaction of cloud, rain, snow, and hail processes with these atmospheric flows.

The modeling of cloud processes has proceeded in one-, two-, and three-dimensional models, both steady state and time dependent. Papers by *Simpson et al.* [1967], *Weinstein and MacCready* [1969], *Simpson and Wiggert* [1969], and *Marwitz et al.* [1970], have dealt with one-dimensional steady-state models of clouds. These models predict the steady-state profiles of vertical velocity, excess virtual temperatures, cloud and hydrometeor water, and cloud-top height. *Warner* [1970] has shown that the models can do well in predicting the cloud-top height, but will in general fail in predicting the internal parameters of the cloud. The prediction of cloud-top height was used by Simpson et al. and Weinstein and MacCready to give excellent correlation with field experiments on the silver iodide seeding of cumulus clouds. These models are simple computationally, requiring small amounts of computer time; hence they are extremely valuable for field operations. In general the microphysics in these models is parameterized by means of the techniques of *Kessler* [1969] in which autoconversion of cloud water to rain and accretion of the cloud by the rain is modeled.

Several one-dimensional time-dependent models are appearing in the literature and are being reported at scientific meetings [*Srivastava,* 1967*a*, *Weinstein,* 1970, *Wisner,* 1970; *Ogura and Takahashi,* 1970]. These models predict in time and height the development of the various dynamic and cloud physics properties of a cloud mentioned above in connection with the steady-state models. Srivastava treated an all-liquid cloud and rain process but did not include mixing explicitly in his model. The more recent papers do have a mixing process similar to that used in the steady-state models. That is, mixing is assumed to be inversely proportional to the radius of the cloud element. Weinstein's paper also adds a cloud-ice process to the model, Wisner has no cloud-ice process but includes hail and Ogura and Takahashi include a snow process in their model. *Bleck* [1970] calculates the growth of rain particles via coalescence equations. His method is being applied in a time-dependent numerical cloud model. This deviation from the Kessler technique requires a large amount of computer time and adds great complexity to the problem, but is an approach to realism that may be needed to explain some of the more detailed aspects of cloud motion and cloud particle dynamic interaction.

The two-dimensional time-dependent models are becoming more complex and are simulating, for the first time, the growth of large clouds that are an aggregate of several smaller convective elements. Papers by *Arnason et al.* [1968], *Liu and Orville* [1969], and *Orville and Sloan* [1970*b*] are concerned with the interaction of the cloud dynamics and precipitation physics. The equations for conservation of momentum, energy, and air and water mass are integrated numerically Kessler's precipitation techniques are used in Arnason's papers. Orville uses a method for autoconversion developed by *Berry* [1968]. *Murray* [1970] shows that a perturbation in the relative humidity is an important initiator of convection; this situation also existed in *Orville's* [1968] work where an active lower boundary surface was thought to produce the convection, via heating and evaporation at the earth's surface. *Kessler* [1969] applies his precipitation techniques to a presupposed dynamic situation, so that the dynamic interaction of the airflow and the precipitation is uncoupled. Kessler's monograph is an excellent description of his methods for modeling precipitation developed over the past 10 years.

Conceptual three-dimensional steady-state models of storms have been constructed by *Goldman* [1968] and *Fujita and Grandoso* [1968]. Goldman uses a five-layer model to describe a thunderstorm He uses aerodynamic flows of translation, sources and sinks and assumed vertical motion profiles. Hence, the thermodynamics and dynamics are decoupled. Fujita and Grandoso model a rotating thunderstorm and predict the motion of anticyclonic and cyclonic storms imbedded in a uniform airflow.

Three-dimensional time-dependent numerical models have not as yet been applied to cloud growth but are being used to simulate dry convection and motion in the planetary boundary layer [*Fox,* 1970; *Deardorff,* 1970]. To fully simulate cloud motions, further work in cloud modeling will need to expand to three-dimensional time-dependent numerical models.

The numerical simulation of thunderstorm downdrafts has been attempted by *Das and Rao* [1968] and

Caplan [1969]. In addition, *Asai and Kasahara* [1967] have studied the influence of the downdraft on the growth of a cloud column in a nearly one-dimensional time-dependent model. Both Das and Caplan investigate the influence of rain particles on the downdraft. Caplan concludes that the cooling from small drops is offset by adiabatic warming in the downdraft, whereas Das does not show such a compensation. Both authors show that an unsaturated downdraft is a consequence of too few particles' being available in the downdraft to saturate the draft. *Das* [1969] develops a thermodynamic equation that explicitly takes into account the effect of particles on the lapse rate underneath and in a cloud.

A few numerical papers relate to the problem of cloud modeling [*Crowley,* 1968; *Molenkamp,* 1968; *Orville and Sloan,* 1970*a*]. Crowley and Molenkamp investigate how the fluid motion is influenced by various finite difference techniques used in the advection terms of the prognostic equations. Orville and Sloan apply Crowley's technique and show that it is successful in the modeling of cumulus clouds where grid intervals of 100 meters are used.

There were a few papers on the numerical modeling of stratus clouds [*Gerrity,* 1967; *Lilly,* 1968; *LaBlanc and Brundidge,* 1969]. Gerrity attempted to forecast low clouds over the eastern United States via a numerical model with real data as input. The equations were applied in the planetary boundary layer and predictions of the temperature, specific humidity, and specific moisture content were made. Lilly modeled a radiatively active turbulent cloud layer over the sea and under a strong subsidence inversion. Steady-state solutions are found with results that agree with observations of the trade wind inversion near California. LaBlanc and Brundidge use a hydrostatic two-dimensional model for the numerical simulation of nocturnal stratus over the Texas coast. A sloping lower boundary is used and is shown to be important for cloud formation. Three different values of the eddy coefficient were used and shown to have a significant effect on the cloud types.

Hurricane modeling has been pursued by *Ooyama* [1969], *Rosenthal and Koss* [1968], and *Rosenthal* [1970]. Ooyama parameterizes the effects of cumulus convection in a three-layer hurricane model and simulates the life history of a tropical cyclone. In Rosenthal's study an explicit water vapor cycle is modeled and rainfall from both convective and nonconvective sources is considered. The nonconvective portion of the rain is significant. Rosenthal also attempted to use the Crowley technique for differencing the advection term in the hydrodynamic equations but found it insufficient for a model with grid intervals of 10 km (the interval of the hurricane model). The Rosenthal model uses upstream differencing in the advection terms.

Several numerical studies of land and sea breeze or lake breeze phenomena [*McPherson,* 1970, *Geisler and Bretherton,* 1969; *Moroz,* 1967; *Hsu,* 1970; *Estoque and Bhumralkar,* 1969; *Lavoie et al.,* 1970; *Chang and Orville,* 1970] have been conducted. Only Lavoie et al. and Chang and Orville include a cloud or rain process at this time. However, McPherson's work, truly a three-dimensional time-dependent study, shows that enhanced convection would occur to the northwest and northeast of a box-shaped bay area. The results agree with the cloud observations of Hsu and with satellite data. Lavoie's work considers the airflow over Lake Erie and the dynamics of the lake effects storms. The physical effects of heating by the warm water surface, differential friction between the land and water, and topographical effects are included in the model. A simple precipitation process is postulated, and the results of the snowfall downwind of the lakes agree well with observations. Chang and Orville added a condensation process to Lavoie's model and applied it to airflow over the Black Hills of South Dakota.

BIBLIOGRAPHY

Abraham, F. F., A reexamination of homogeneous nucleation theory: Thermodynamic aspects, *J. Atmos. Sci.*, *25,* 47–53, 1968.

Abraham, F. F., and G. M. Pound, Reexamination of homogeneous nucleation theory: Statistical thermodynamic aspects, *J Chem. Phys.*, *48,* 732–740, 1968.

Adam, J. R., N. R. Lindblad, and C. D. Hendricks, The collision, coalescence and disruption of water droplets, *J. Appl. Phys.*, *39,* 5173–5180, 1968.

Allee, P. A., H. Gerber, and H. K. Weickmann, Measurements of ice nuclei size distribution with an aerosol spectrometer, in *Proceedings of the 7th International Conference on Condensation and Ice Nuclei,* pp. 262–267, Czchoslovak Academy of Sciences, Prague, 1969.

Arnason, G., R. S. Greenfield, and E. A. Newburg, Numerical experiment in dry and moist convection including the rain stage, *J. Atmos. Sci.*, *25,* 404–415, 1968.

Arnason, G., P. S. Brown, R. T. Chu, and R. S. Greenfield, Numerical simulation of macrophysical and microphysical processes of moist convection, Final Report to the NSF, grant GA-1114. 1969.

Asai, T., and A. Kasahara, Theoretical study of the compensating downward motions associated with cumulus clouds, *J. Atmos. Sci.*, *24,* 487–496, 1967.

Atkinson, W. R., and I. Paluch, Electromagnetic emission from pairs of water drops exchanging charge, *J. Geophys. Res.*, *71,* 3811–3816, 1966.

Auer, P. A., D. L. Veal, and J. D. Marwitz, Observations of ice crystal and ice nuclei concentrations in stable cap clouds, *J. Atmos. Sci.*, *26,* 1342–1343, 1969.

Austin, P. M., and M. J. Kraus, Snowflake aggregation: A numerical method, in *Proceedings of the International Conference on Cloud Physics, Canada,* pp. 300–304, University of Toronto, Toronto, 1968.

Beard, K. F., and H. R. Pruppacher, A determination of the terminal velocity and drag of small water drops by means of a wind tunnel, *J. Atmos. Sci.*, *26,* 1066–1072, 1969.

Berry, E. X., Cloud droplet growth by collection, *J. Atmos. Sci.*, *24,* 668–701, 1967.

Berry, E. X., Modification of the warm rain process, in *Proceedings of the First National Conference on Weather Modification, Albany, New York,* pp. 81–88, American Meteorological Society, Washington, D.C., 1968.

Berry, E. X., A mathematical framework for cloud models. *J. Atmos. Sci.*, *26,* 109–111, 1969.

Bigg, E. K., and J. Giutronich, Ice nucleating properties of meteoritic material, *J. Atmos. Sci.*, *24,* 46–49, 1967.

Blair, D. N., and B. L. Davis, Aging of AgI–sodium iodide generator effluent in moist dry air, *J. Appl. Meteorol.*, *8,* 551–555, 1969.

Blanchard, D. C., Surface active organic material of airborne salt particles, in *Proceedings of the International Conference on Cloud Physics, Canada,* University of Toronto, Toronto, 1968.

Blanchard, D. C., The oceanic production rate of cloud nuclei, *J. Rech. Atmos.*, *4*, 1–6, 1969.

Blanchard, D. C., and A. T. Spencer, Experiments on the generation of raindrop-size distributions by drop breakup, *J. Atmos. Sci.*, *27*, 101–108, 1970.

Bleck, R., A fast approximative method for integrating the stochastic coalescence equation, *J. Geophys Res.*, *75*, 5165–5172, 1970.

Brownscombe, J. L., and J. Hallett, Experimental and field studies of precipitation particles formed by the freezing of supercooled water, *Quart. J. Roy. Meteorol. Soc.*, *93*, 455–473, 1967.

Brownscombe, J. L., and N. S. C. Thorndike, The freezing of water droplets in free fall, in *Proceedings of the International Conference on Cloud Physics, Canada*, pp. 280–284, University of Toronto, Toronto, 1968.

Burrows, D. A., and P. V. Hobbs, Charging of ice spheres due to collisions with ice crystals and the electrification of thunderstorms, *J. Atmos. Sci.*, *26*, 560–565, 1969.

Burrows, D. A., and C. F. Robertson, Comments on 'ice multiplication in clouds,' *J. Atmos. Sci.*, *26*, 1340–1341, 1969.

Camp, P. R., W. Kiszenick, and D. A. Arnold, Electrical conduction in ice, *Res. Rep. 197*, 52 pp., Cold Regions Research and Engineering Laboratory, Hanover, N. H., 1967.

Caplan, Peter M., On thunderstorm downdrafts, preprints of the *Sixth Conference on Severe Local Storms*, pp. 68–70, American Meteorological Society, Chicago, Ill., 1969.

Carstens, J. C., and J. L. Kassner, Jr., Some aspects of droplet growth theory applicable to nuclei measurements, *J. Rech. Atmos.*, *3*, 33–39, 1968.

Carstens, J. C., A. Williams, and J. T. Zung, Theory of droplet growth in clouds, 2, Diffusional interaction between two growing droplets, *J. Atmos. Sci.*, *27*, 798–803, 1970.

Chang, C. B., and H. D. Orville, A mesoscale numerical model of airflow over the Black Hills, in *Proceedings of the Conference on Cloud Physics, Ft. Collins, Colorado*, pp. 197–197, American Meteorological Society, Washington, D.C., 1970.

Chen, G. S., Drop growth by condensation in the entraining updraft, in *Proceedings of the Conference on Cloud Physics, Ft. Collins, Colorado*, pp. 113–114, American Meteorological Society, Washington, D.C., 1970.

Chin, H. C., Simulation of cloud droplet collection process, in *Proceedings of the Conference on Cloud Physics, Ft. Collins, Colorado*, pp. 119–120, American Meteorological Society, Washington, D.C., 1970.

Cobb, A. W., and G. W. Gross, Interfacial electrical effects observed during the freezing of dilute electrolytes in water, *J. Electrochem. Soc.*, *116*, 796–804, 1969.

Conover, J. H., New observation of anomalous cloud lines, *J. Atmos. Sci.*, *26*, 1153–1154, 1969.

Corrin, M. L., J. A. Nelson, B. Cooley, and B. Rosenthal, The preparation of 'pure' AgI for nucleation studies, *J. Atmos. Sci.*, *24*, 594–595, 1967.

Cotton, W. R., and N. R. Gokhale, Collision, coalescence, and breakup of large water drops in a vertical wind tunnel, *J. Geophys. Res.*, *72*, 4041–4049, 1967.

Crowley, W. P., Numerical advection experiments, *Mon Weather Rev.*, *96*, 1–11, 1968.

Damon, K. G., An analytical study of the collision of liquid drops, Ph.D. thesis, University of Wisconsin, Madison, 1967.

Danielsen, E., R. Bleck, and D. Morris, Hail growth by stochastic coalescence in a cumulus model, to be submitted to *J. Atmos. Sci.*, 1970.

Das, P., Thermodynamics equation in cumulus dynamics, *J Atmos. Sci.*, *26*, 399–407, 1969.

Das, P., and M. C. Subba Rao, Unsaturated downdraught, in *Proceedings of the International Conference on Cloud Physics, Canada*, pp. 592–596, University of Toronto, Toronto, 1968.

Davis, B. L., Chemical complexing of AgI-NaI aerosols, *J. Atmos. Sci.*, *26*, 1042–1048, 1969.

Davis, C. I., and R. L. Steele, Performance characteristics various artificial ice nuclei sources, *J. Appl. Meteorol.*, *7*, 667–673, 1968.

Davis, M. H., Two charged spherical conductors in a uniform electric field. Forces and field strength, *Quart. J. Mech. Appl Math.*, *17*, 499–511, 1964.

Davis, M. H., Electrostatic field and force on a dielectric sphere near a conducting plane: A note on the application of electrostatic theory to water droplets, *Amer. J. Phys.*, *37*, 26–29, 1969*a*.

Davis, M. H., The slow translation and rotation of two unequal spheres in a viscous fluid, *Chem. Eng. Sci.*, *24*, 1769–1776, 1969*b*.

Davis, M. H., and J. D. Sartor, Theoretical collision efficiencies for small cloud droplets in Stokes flow, *Nature*, *215*, 1371–1372, 1967.

Davis, M. H., J. D. Klett, and M. Neiburger, Collision efficiencies of cloud droplets at small Reynolds numbers, in *Proceedings of the Conference on Cloud Physics, Ft. Collins, Colorado*, pp. 115–116, American Meteorological Society, Washington, D.C., 1970.

Deardorff, J. W., A numerical study of three-dimensional turbulent channel flow at large Reynolds numbers, *J. Fluid Mech.*, *41*, 453–480, 1970.

Dinger, J. E., H. B. Howell, and T. A. Wojciechowski, On the source and composition of cloud nuclei in a subsident air mass over the North Atlantic, *J. Atmos. Sci.*, *27*, 791–797, 1970

Drake, R., A general mathematical survey of the coagulation equation, to be published in *International Reviews in Aerosol Physics and Chemistry*, edited by G. Hidy and J. Brock, Pergamon, New York, 1970.

Dye, J. E., and P. V. Hobbs, The influence of environmental parameters on the freezing and fragmentation of suspended water drops, *J Atmos. Sci.*, *25*, 82–96, 1968.

Edwards, G. R., and L. F. Evans, Ice nucleation by AgI, 3, The nature of the nucleating site, *J Atmos Sci.*, *25*, 249–256, 1968.

Edwards, G. R., L. F. Evans, and S. D. Hamann, Nucleation of ice by mechanical shock, *Nature*, *223*, 390–391, 1969.

Estoque, M. A., and C. M. Bhumralkar, Flow over a localized heat source, *Mon. Weather Rev.*, *97*, 850–859, 1969

Fitzgerald, J. W., A reexamination of the classical theory of the growth of a population of cloud droplets by condensation, in *Proceedings of the Conference on Cloud Physics, Ft. Collins, Colorado*, pp. 111–112, American Meteorological Society, Washington, D.C., 1970*a*.

Fitzgerald, J. W., Non-steady-state supersaturations in thermal diffusion chambers, *J. Atmos. Sci.*, *27*, 70–72, 1970*b*.

Fletcher, N. H., Ice nucleation behavior of AgI smokes containing a soluble component, *J Atmos. Sci.*, *25*, 1058–1060, 1968.

Fletcher, N. H., Active sites and ice crystal nucleation, *J. Atmos. Sci.*, *26*, 1266–1271, 1969

Foote, G. G., A theoretical investigation of the dynamics of liquid drops, Ph.D. thesis, University of Arizona, Tucson, 1970.

Fox, D. G., Numerical simulation of three-dimensional convective elements, in *Proceedings of the Conference on Cloud Physics, Ft. Collins, Colorado*, pp. 157–158, American Meteorological Society, Washington, D. C., 1970.

Friedlander, S. K., and G. M. Hidy, New concepts in aerosol size spectrum theory, to be published in *Proceedings of the Seventh International Conference on Condensation and Ice Nuclei*, 5 pp., 1969

Fujita, T., and I. Grandoso, Split of a thunderstorm into anticyclonic and cyclonic storms and their motion as determined from numerical model experiments, *J. Atmos. Sci.*, *25*, 416–439, 1968.

Garrett, W. D., The influence of monomolecular surface films on the production of condensation nuclei from bubbled sea water, *J. Geophys. Res.*, *73*, 5145–5150, 1968.

Geisler, J. E., and F. P. Bretherton, Sea-breeze forerunner, *J. Atmos. Sci.*, *26*, 82–95, 1969.

Gerrity, J. P., Jr., Physical-numerical model for the prediction of synoptic-scale low cloudiness, *Mon. Weather Rev.*, *95*, 261–282, 1967.

Gitlin, S. N., and S. S. Lin, Dynamic nucleation of the ice phase in supercooled water, *J. Appl. Phys.*, *40*, 4761–4767, 1969.

Gokhale, N. R., and J. Goold, Jr., Droplet freezing by surface nucleation, *J. Appl. Meteorol.*, *7*, 870–874, 1968.

Goldman, J. L., The high speed updraft–the key to the severe thunderstorm, *J. Atmos. Sci.*, *25*, 222–248, 1968.

Goyer, G. G., and M. N. Plooster, On the role of shock waves and adiabatic cooling in the nucleation of ice crystals by the lightning discharge, *J. Atmos. Sci.*, *25*, 847–862, 1968.

Grant, L. O., The role of ice nuclei in the formation of precipitation, in *Proceedings of the International Conference on Cloud Physics, Canada*, pp. 305–310, University of Toronto, Toronto, 1968.

Hamielec, A. E., T. W. Hoffmann, and L. L. Ross, Numerical solution of the Navier-Stokes equations for flow post spheres, *AIChE J. 13*, 212–219, 1967.

Hidy, G. M., The dynamics of aerosols in the lower troposphere, paper presented at *Third Conference on Environmental Toxicology*, Rochester, New York, 1970.

Hobbs, P. V., Ice multiplication in clouds, *J. Atmos. Sci.*, *26*, 315–318, 1969.

Hobbs, P. V., and A. J. Alkezweeny, The fragmentation of freezing water droplets in free fall, *J. Atmos. Sci.*, *25*, 881–888, 1968.

Hobbs, P. V., L. T. Radke, and S. E. Shumway, Cloud condensation nuclei from industrial sources and their apparent influence on precipitation in Washington State, *J. Atmos. Sci.*, *27*, 81–89, 1970.

Hocking, L. M., The collision efficiency of small drops, *Quart. J. Roy. Meteorol. Soc.*, *85*, 44–50, 1959.

Hsu, S. A., Coastal air-circulation system: Observations and empirical model, *Mon. Weather Rev.*, *95*, 487–509, 1970.

Iribarne, J. V., and M. Klemes, Electrification associated with breakup of drops at terminal velocity in air, *J. Atmos. Sci.*, *27*, 927–936, 1970.

Jiusto, J. E., and W. C. Kocmond, Condensation on nonhygroscopic particles, *J. Rech. Atmos.*, *3*, 19–24, 1968.

Jiusto, J. E., R. J. Pilié, and W. C. Kocmond, Fog modifications with giant hygroscopic nuclei, *J. Appl. Meteorol.*, *7*, 860–869, 1968.

Johnson, D. A., and J. Hallett, Freezing and shattering of supercooled water drops, *Quart. J. Roy. Meteorol. Soc.*, *94*, 468–482, 1968.

Kamara, A. K., Effect of electric field on charge separation by the falling precipitation mechanism in thunderclouds, *J. Atmos. Sci.*, *27*, 1182–1185, 1970.

Kaniel, S., A. Kovetz, and B. Olund, Rain formation in a warm cloud, in *Proceedings of the Conference on Cloud Physics, Canada*, pp. 379–383, University of Toronto, Toronto, 1968.

Kassner, J. L., Jr., and J. C. Carstens, et al., Expansion cloud chamber technique for absolute Aitken nuclei counting, *J. Rech. Atmos.*, *3*, 45–62, 1968*a*.

Kassner, J. L., J. C. Carstens, and L. B. Allen, Analysis of the heat and vapor propagation for the walls of the Nolan, Pollack and Gardner type condensation nucleus counters, *J. Atmos. Sci.*, *25*, 919–926, 1968*b*.

Kassner, J. L., J. C. Carstens, and L. B. Allen, The myth concerning the condensation nucleus counters, *J. Rech. Atmos.*, *3*, 25–31, 1969.

Keeney, J., Observations on the microwave emission from colliding charged water drops, *J. Geophys. Res.*, *75*, 1123–1126, 1970.

Kessler, E., On distribution and continuity of water substance in atmospheric circulations, *Meteorol. Monogr.*, *10*(32), 84 pp., 1969.

Knight, C. A., Small particle detection and identification by crystal growth: Preliminary work on AgI particle detection, *J. Appl. Meteorol.*, *8*, 705–707, 1969.

Knight, F. B., Some condensation processes of the McKean type, unpubl. notes, 1970.

Knollenberg, R. G., A study of the local cooling resulting from the dissolution of soluble ice nuclei having endothermic heats of solution, *J. Atmos. Sci.*, *26*, 115–124, 1969*a*.

Knollenberg, R. G., The local cooling ice nucleation model, *J. Appl. Sci.*, *26*, 125–129, 1969*b*.

Koenig, L. R., Some observations suggesting ice multiplication in the atmosphere, *J. Atmos. Sci.*, *25*, 460–463, 1968*a*.

Koenig, L. R., Comments on atmospheric ice multiplication measurements, in *Proceedings of the International Conference on Cloud Physics, Canada*, pp. 460–463, University of Toronto, Toronto, 1968*b*.

Koenig, L. R., Numerical modeling of condensation, *Memo RM-553-NSF*, Rand Corp., Santa Monica, Calif., 53 pp., 1968*c*.

Kornfeld, P., Some numerical experiences for warm fog clearing by seeding with hydroscopic nuclei, *J. Appl. Meteorol.*, *9*, 459–463, 1970*a*.

Kornfeld, P., Numerical solution for condensation of atmospheric vapor on soluble and insoluble nuclei, *J. Atmos. Sci.*, *27*, 256–264, 1970*b*.

Kornfeld, P., U. Shafrir, and M. H. Davis, A direct numerical simulation experiment of cloud droplet growth by accretion, in *Proceedings of the International Conference on Cloud Physics, Canada*, pp. 107–110, University of Toronto, Toronto, 1968.

Kovetz, A., and B. Olund, The effect of coalescence and condensation on rain formation in a cloud of finite vertical extent, *J. Atmos. Sci.*, *26*, 1060–1065, 1969.

Kuhns, I. E., The nucleation of water droplets of deep supercooling in different gaseous environments, *J. Atmos. Sci.*, *25*, 878–880, 1968.

Kunkel, B. A., and B. A. Silverman, A comparison of the warm fog clearing capabilities of some hygroscopic materials, *J. Appl. Meteorol.*, *9*, 459–463, 1970.

LaBlanc, L. L., and K. C. Brundidge, Numerical experiment in predicting stratus clouds, *J. Appl. Meteorol.*, *8*, 177–189, 1969.

Lavoie, R. L., W. R. Cotton, and J. B. Hovermale, Investigations of lake effect storms, Final Report to ESSA, Atmospheric Physics and Chemistry Laboratory, Boulder, Colorado, contract E22-103-68(N), 1970.

Layton, R. G., and M. Lavign, The decay and rejuvenation of AgI surfaces, *J. Rech. Atmos.*, *4*, 113–114, 1969.

LeClair, B. P., A. E. Hamielac, and H. R. Pruppacher, Numerical study of the drag on a sphere at low and intermediate Reynolds numbers, *J. Atmos. Sci.*, *27*, 308–315, 1970.

Levin, Z., and P. V. Hobbs, Charge separation due to the splashings of water drops, in *Proceedings of the Conference on Cloud Physics, Fort Collins, Colorado*, pp. 145–146, American Meteorological Society, Washington, D. C., 1970.

Lilly, D. K., Models of cloud-topped mixed layers under a strong inversion, *Quart. J. Roy. Meteorol. Soc.*, *94*, 292–309, 1968.

List, R., and D. M. Whelpdale, A preliminary investigation of factors affecting the coalescence of colliding water drops, *J. Atmos. Sci.*, *26*, 305–308, 1969.

Liu, J. Y., and H. D. Orville, Numerical modeling of precipitation and cloud shadow effects on mountain-induced cumuli, *J. Atmos. Sci.*, *26*, 1283–1298, 1969.

Long, A. B., A thermodynamic study of homogeneous nucleation, *Advan. Geophys.*, *7*, 595–621, 1969.

Low, D. H., A theoretical study of 19 condensation nuclei, *J. Rech. Atmos.*, *4*, 65–78, 1969.

MacCready, P. B., Jr., and R. G. Baughman, The glaciation of an AgI seeded cumulus cloud, *J. Appl. Meteorol.*, *7*, 132–135, 1968.

McKean, H. P., Jr., A class of Markov processes associated with nonlinear parabolic equations, *Proc. Nat. Acad. Sci.*, *56*, 1907–1911, 1966.

McPherson, R. D., A numerical study of the effect of a coastal irregularity on the sea breeze, *J. Appl. Meteorol.*, *9*, 767–777, 1970.

Marwitz, J. D., J. R. Middleton, A. H. Auer, Jr., and D. L. Veal, The dynamics of updraft vaults in hailstorms as inferred from the entraining jet model, *J. Atmos. Sci.*, *27*, 1099–1102, 1970.

Mason, B. J., *The Physics of Clouds*, 481 pp., Clarendon, Oxford, 1957.

Melzak, Z. A., A scalar transport equation, *Trans. Amer. Math. Soc.*, *85*, 547–560, 1957.

Mockros, L. R., J. E. Quon, and A. T. Hjelmflet, Jr., Coagulation of continuously reinforced aerosol, *J. Colloid Interface Sci.*, *23*, 90–98, 1967.

Molenkamp, C. R., Accuracy of finite-difference methods applied to the advection equation, *J. Appl. Meteorol.*, *7*, 160–167, 1968.

Montgomery, D. N., and G. A. Dawson, Collisional charging of water drops, *J. Geophys. Res.*, *75*, 962–972, 1969.

Morgan, G. M., Jr., and P. A. Allee, The production of potential ice nuclei by gasoline engines, *J. Appl. Meteorol.*, *7*, 251–256, 1968.

Moroz, W. J., A lake breeze on the eastern shore of Lake Michigan: Observations and model, *J. Atmos. Sci.*, *24*, 337–355, 1967.

Mossop, S. C., Concentrations of ice crystals in clouds, *Bull. Amer. Meteorol. Soc.*, *51*, 474–479, 1970.

Mossop, S. C., R. E. Ruskin, and K. J. Hefferman, Glaciation of a cumulus at approximately –4°C, *J. Atmos. Sci.*, *25*, 889, 1968.

Mossop, S. C., A. Ono, and E. R. Wishart, Ice particles in maritime clouds near Tasmania, *Quart. J. Roy. Meteorol. Soc.*, *96*, 487–508, 1970.

Muller, H., Zur Theorie der elektrischen Ladung und der Koagulation der Kolloide, *Kolloidchem. Beith.*, *26*, 257–311, 1928*a*.

Müller, H., Zur allgemeinen Theorie der raschen Koagulation, *Kolloidchem. Beih.*, *27*, 223–250, 1928*b*.

Murray, F. W., Numerical models of a tropical cumulus cloud with bilateral and axial symmetry, *Mon. Weather Rev.*, *98*, 14–28, 1970.

Nelson, L. D., A numerical simulation of the effects of water spray seeding on the warm-rain process, in *Proceedings of Second National Conference on Weather Modification, Santa Barbara, Calif.*, pp. 18–23, American Meteorological Society, Washington, D. C., 1970.

Odencrantz, F. K., Freezing of water droplets: Nucleation efficiency at temperatures above –5°C, *J. Appl. Metorol.*, *8*, 322–325, 1969.

Ogura, Y., and T. Takahashi, Numerical simulation of the life cycle of a thunderstorm cell, in *Proceedings of the Conference on Cloud Physics, Fort Collins, Colorado*, pp. 183–184, American Meteorological Society, Washington, D. C., 1970.

Ooyama, K., Numerical simulation of the life cycle of tropical cyclones, *J. Atmos. Sci.*, *26*, 3–40, 1969.

Orville, H. D., Ambient wind effects on the initiation of cumulus clouds over the mountains, *J. Atmos. Sci.*, *25*, 385–403, 1968.

Orville, H. D., and L. J. Sloan, Effects of higher order advection techniques on a numerical cloud model, *Mon. Weather Rev.*, *98*, 7–13, 1970*a*.

Orville, H. D., and L. J. Sloan, A numerical simulation of the life history of a rainstorm. *J. Atmos. Sci.*, *27*, 1148–1159, 1970*b*.

Paluch, I. R., A model for cloud droplet growth by condensation in an inhomogeneous medium, submitted to *J. Atmos. Sci.*, 1970*a*.

Paluch, I. R., Theoretical collision efficiencies of charged cloud droplets, *J. Geophys. Res.*, *75*, 1633–1640, 1970*b*.

Park, R. W., Behavior of water drops colliding in humid nitrogen, Ph.D. thesis, University of Wisconsin, Madison, 1970.

Parungo, F. P., and J. P. Lodge, Jr., Amino acids as ice nucleators, *J. Atmos. Sci.*, *24*, 274–277, 1967*a*.

Parungo, F. P., and J. P. Lodge, Jr., Freezing of aqueous solutions of nonpolar gases, *J. Atmos. Sci.*, *24*, 439–441, 1967*b*.

Parungo, F. P., and J. O. Rhea, Lead measurement in urban air as it relates to weather modification, *J. Appl. Meteorol.*, *9*, 468–475, 1970*a*.

Parungo, F. P., and J. O. Rhea, Field use of a simple technique for identifying AgI particles as snow crystal nuclei, *J. Appl. Meteorol.*, *9*, 651–656, 1970*b*.

Penzias, A. A., and R. W. Wilson, Microwave noise from rainstorms, *Science*, *169*, 583–584, 1970.

Phillips, B. B., Ionic equilibrium and the electrical conductivity in thunderclouds, *Mon. Weather Rev.*, *95*, 854–862, 1967.

Plooster, M. H., Nucleation freezing in supercooled water by cavitation, *Nature*, *217*, 1246–1247, 1968.

Pruppacher, H. R., and E. H. Steinberger, An experimental determination of the drag on a sphere at low Reynolds numbers, *J. Appl. Phys.*, *39*, 4129–4132, 1968.

Pruppacher, H. R., E. H. Steinberger, and T. L. Wang, On the electrical effects that accompany the spontaneous growth of ice in super-cooled aqueous solutions, *J. Geophys. Res.*, *73*, 571–584, 1968.

Radke, L. F., and P. V. Hobbs, Measurement of cloud condensation nuclei, light scattering coefficient sodium-containing particles and Aitken nuclei in the Olympic Mountains of Washington, *J. Atmos. Sci.*, *26*, 281–288, 1969*a*.

Radke, L. F., and P. V. Hobbs, An automatic cloud condensation nuclei counter, *J. Appl. Meteorol.*, *8*, 105–109, 1969*b*.

Reiss, H., J. L. Katz, and E. R. Cohen, Translation–rotation paradox in the theory of nucleation, *J. Chem. Phys.*, *48*, 5553–5560, 1968.

Rice, C. L., and R. Whitehead, The theory of the coagulation of emissions, *J. Coll. Interface Sci.*, *23*, 174–181, 1967.

Rimon, Y., and S. I. Cheng, Numerical solutions of a uniform flow over a sphere at intermediate Reynolds numbers, *Phys. Fluids*, *12*, 949–959, 1969.

Roberts, P., and J. Hallett, A laboratory study of the ice nucleating properties of some mineral particulates, *Quart. J. Roy. Meteorol. Soc.*, *94*, 25–34, 1968.

Rosenthal, S. L., A circulatory symmetric primitive equation model of tropical cyclone development containing an explicit water vapor cycle, *Mon. Weather Rev.*, *98*, 643–663, 1970.

Rosenthal, S. L., and W. J. Koss, Linear analysis of a tropical cyclone model with increased resolution, *Mon. Weather Rev.*, *96*, 858–866, 1968.

Sartor, J. D., Calculations of cloud electrification based on a general charge-separation mechanism, *J. Geophys. Res.*, *66*, 831–838, 1961*a*.

Sartor, J. D., Recalculations of cloud electrification based on a general charge-separation mechanism, *J. Geophys. Res.*, *66*, 3070–3071, 1961*b*.

Sartor, J. D., The role of particle interactions in the distribution of electricity in thunderstorms, *J. Atmos. Sci.*, *24*, 601–615, 1967.

Sartor, J. D., Accretion rates of cloud drops, raindrops and small hail in mature thunderstorms, *J. Geophys. Res.*, *75*, 7547–7558, 1970.

Sartor, J. D., and C. E. Abbott, Charge transfer between uncharged water drops in free fall in an electric field, *J. Geophys. Res.*, *73*, 6415–6423, 1968.

Sartor, J. D., and W. R. Atkinson, Charge transfer between raindrops, *Science*, *157*, 1257–1269, 1967.

Sax, R. I., The importance of natural glaciation on the modification of tropical maritime cumuli by AgI seeding, *J. Appl. Meteorol.*, *8*, 92–104, 1969.

Saxena, V. K., J. N. Burford, and J. L. Kassner, Jr., Operation of a thermal diffusion chamber for measurements on cloud condensation nuclei, *J. Atmos. Sci.*, *27*, 73–80, 1970.

Schaefer, V. J., Ice nuclei from auto exhaust–organic vapors, *J. Appl. Meteorol.*, *7*, 148–149, 1968*a*.

Schaefer, V. J. The generation of large numbers of ice crystals in an electric field, *J. Appl. Meteorol.*, *7*, 452–455, 1968*b*.

Scott, W. D., and P. V. Hobbs, The spectra of charging events due to the collision of natural ice particles with an ice surface, *Quart. J. Roy. Meteorol. Soc.*, *94*, 510–522, 1968.

Scott, W. D., and Z. Levin, The effect of potential gradient on the charge separation during interactions of snow crystals with an ice sphere, *J. Atmos. Sci.*, *27*, 463–473, 1970.

Scott, W. T., Poisson statistics in distributions of coalescing droplets, *J. Atmos. Sci.*, *24*, 221–225, 1967.

Scott, W. T., Analytic studies of cloud droplet coalescence, I, *J. Atmos. Sci.*, *25*, 54–65, 1968*a*.

Scott, W. T., On the connection between the Telford and kinetic-equation approaches to droplet coalescence theory, *J. Atmos. Sci.*, *25*, 871–873, 1968*b*.

Scott, W. T., and C. Y. Chen, Approximate formulas fitted to the Davis-Sartor-Shafrir-Neiburger droplet collision efficiency calculations, *J. Atmos. Sci.*, *27*, 698–700, 1970.

Shafrir, U., and M. Neiburger, Collision efficiencies of two spheres falling in a viscous medium, *J. Geophys. Res.*, *68*, 4141–4147, 1963.

Shewchuk, S. R., and J. V. Iribarne, Electrification associated with drop splashing, *Trans. Faraday Soc., 66,* 2092–2105, 1970.

Silverman, B. A., and B. A. Kunkel, A numerical model of warm fog dissipation by hygroscopic particle seeding, *J. Appl. Meteorol., 9,* 627–633, 1970.

Simpson, J., and V. Wiggert, Models of precipitating cumulus towers, *Mon. Weather Rev., 97,* 471–489, 1969.

Simpson, J., G. W. Brier, and R. H. Simpson, Stormfury cumulus seeding experiment 1965: Statistical analysis and main results, *J. Atmos. Sci., 24,* 508–521, 1967*a*.

Srivastava, R. C., Study of the effect of precipitation on cumulus dynamics, *J. Atmos. Sci., 24,* 36–45, 1967.

Srivastava, R. C., On the role of coalescence between raindrops in shaping their size distribution, *J. Atmos. Sci., 24,* 287–292, 1967*b*.

Steele, R. L., and C. I. Davis, Variation of ice nuclei effectiveness with liquid water, *J. Atmos. Sci., 26,* 329–330, 1969.

Stevenson, C. M., An improved Millipore filter technique for measuring the concentrations of freezing nuclei in the atmosphere, *Quart. J. Roy. Meteorol. Soc., 94,* 35–43, 1968.

Suzuki, A., N. F. H. Ho, and W. I. Higuchi, Predictions of the particle size distribution changes in emulsions and suspensions by digital computations, *J. Coll. Interface Sci., 29,* 552–564, 1969.

Thompson, P. D., A transformation of the stochastic equation for droplet coalescence, in *Proceedings of the International Conference on Cloud Physics, Canada,* pp. 115–126, University of Toronto, Toronto, 1968.

Twomey, S., Measurements of natural cloud nuclei, *J. Rech. Atmos., 1,* 101–105, 1963.

Twomey, S., On the composition of cloud nuclei in the N.E. United States, *J. Rech. Atmos., 3,* 281–285, 1968.

Twomey, S., The oceanic production of cloud nuclei, *J. Rech. Atmos., 4,* 179–181, 1969.

Twomey, S., and J. Warner, Comparison of measurements of cloud droplets and cloud nuclei, *J. Atmos. Sci., 24,* 702–703, 1967.

Twomey, S., and T. A. Wojciechowski, Observations of the geographical variation of cloud nuclei, *J. Atmos. Sci., 26,* 684–688, 1969.

Wang, Chiu-sen, and S. K. Friedlander, The self-preserving particle size distribution for coagulation by Brownian motion, 2, Small particle slip connection and simultaneous shear flow, *J. Colloid. Interface Sci., 24,* 170–179, 1967.

Warner, J., A reduction in rainfall associated with smoke from sugarcane fires—an inadvertent weather modification?, *J. Appl. Meteorol., 7,* 247–251, 1968.

Warner, J., On steady-state one-dimensional models of cumulus convection, *J. Atmos. Sci., 27,* 1035–1040, 1970.

Warner, J., and S. Twomey, The production of cloud nuclei by cane fires and the effect on cloud droplet concentration, *J. Atmos. Sci., 24,* 704–706, 1967.

Warner, J., and W. G. Warne, The effect of surface films in retarding the growth by condensation of cloud nuclei and their use in fog suppression, *J. Appl. Meteorol., 9,* 639–650, 1970.

Warshaw, M., Cloud droplet coalescence: Statistical foundations and a one-dimensional sedimentation model, *J. Atmos. Sci., 24,* 278–286, 1967.

Weickmann, H., U. Katz, and R. Steele, AgI–sublimation or contact nucleus? in *Proceedings of the Second National Conference on Weather Modification, Santa Barbara, Calif.,* pp. 332–336, American Meteorological Society, Washington, D.C., 1970.

Weinstein, A. I., A numerical model of cumulus dynamics and microphysics, *J. Atmos. Sci., 47,* 246–255, 1970.

Weinstein, A. I., and P. B. MacCready, Jr., An isolated cumulus cloud modification project, *J. Appl. Meteorol., 8,* 936–947, 1969.

Whelpdale, D. M., and R. List, The coalescence process in raindrop growth, *J. Geophys. Res., 76*(12), 1971.

Winn, W. P., and C. B. Moore, Thundercloud electric field measurements using instrumented rockets, paper presented at Fifty-First Annual Meeting of the American Geophysical Union, Washington, D. C., 1970.

Wisner, C., A numerical model of hail-bearing convective storms in *Proceedings of the Conference on Cloud Physics, Ft. Collins, Colorado,* pp. 187–188, American Meteorological Society, Washington, D. C., 1970.

The Electrical Shielding Layer Around Charged Clouds and its Role in Thunderstorm Electricity

W. A. HOPPEL

Naval Research Laboratory, Washington, D. C.

AND B. B. PHILLIPS

Environmental Research Laboratories, NOAA, Boulder, Colo.

(Manuscript received 14 December 1970, in revised form 28 May 1971)

ABSTRICT

The system of differential equations which governs the equilibrium charge distribution around a charged cloud located in an atmosphere with constant ionization is solved numerically for clouds with differing water content. The equations include the effects of ionic recombination, and the ionic conduction currents to cloud droplets. The results show that the electric field external to the cloud is greatly reduced by a shielding charge distribution which first develops at the clear air-cloud boundary and then slowly moves inward toward the charge center. If ions are generated locally within the cloud, they produce an inner region of charged droplets of opposite polarity to the outer screening layer. An increased electric field maximum will exist between the regions of charge. The effects of turbulence and electroconvection within boundary layers and the time-dependence of the shielding layer charging with and without turbulent transport are discussed. The role of the shielding charge in determining the electric field recovery time following lightning discharges is specified and the ionic concentration and electrical conductivity within thunderstorms is considered.

1. Introduction

Electric field data around and below thunderstorms have been taken for many years, yet the charge generation and transport of charge within the thundercloud are still not well understood. In existing theories, charge separation is associated with either gravitational separation in the precipitation zone or convective separation by drafts. In addition to the destruction of charge centers by lightning, there is dissipative loss resulting from atmospheric conductivity. A change in the conductivity at the cloud boundary results in a screening charge about the cloud. The interaction among the time-dependencies of the primary generator, the dissipation currents, and the development of the screening layer makes it difficult to interpret measurements of the electric field taken outside the cloud. A recent discussion of the charge distribution in screening layers and transport mechanisms was given by Phillips (1967). An initial description of the screening layer and its possible role in thunderstorms was given by Grenet (1947); subsequent discussions were given by Vonnegut (1955) and by Gunn (1956).

The purpose of this paper is to present numerical solutions to the system of equations which governs the ion flux, electric field and droplet charge for the steady-state case of a quiescent cloud. The solutions are then used to describe the development of the screening layer at the cloud boundary and to obtain some insight into the interaction between ions and cloud droplets in an electric field.

Since we are principally interested here in the electrification processes which occur in cloud boundary regions, a very simple spherical cloud model is assumed for the numerical analysis. In this model a homogeneous cloud surrounds a central cloud charge distribution which is maintained at a constant total charge by the thunderstorm charging mechanism. Initially, the central charge core is considered to be a conducting sphere which receives ion current flow from the surrounding cloud boundary region but from which there is no outward (repelled) ion current. This corresponds to a centrally charged thunderstorm cloud in which the

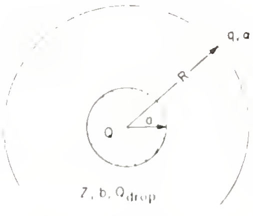

FIG. 1. Spherical cloud model.

cloud core has a sufficiently large droplet density that ion capture by the droplets, which are polarized in the presence of the electric field, is so great as to render the inner cloud non-conductive. Later this restriction is removed and the system of equations is solved for the case where the concentration of both sign ions are finite in the central core of the cloud, corresponding to a thunderstorm cloud with finite conductivities throughout the cloud. These solutions provide quantitative estimates of the electric structure and mechanisms within boundary layers which can be transposed to clouds which exhibit the primary dipole charge distributions observed in thunderstorms. The effects of turbulence and electroconvection within boundary layers and the time-dependency of shielding layer charging with and without turbulent transport are considered.

2. Theoretical considerations

In order to obtain a quantitative picture of the ionic flow and the development of the screening layer in real clouds the following problem is considered. A conducting sphere of radius a and charge Q is surrounded by a spherical cloud of radius R (see Fig. 1). The cloud is characterized by particles of radius b and number density Z. Outside a distance R, the air is free of cloud particles. Ions are formed within the cloud and free atmosphere at a rate q per unit volume. The problem is to calculate the electric field, $\mathbf{E}$, the ion densities, $n_{1,2}$, and the charge on the aerosol, $Q_{\rm drop}$, in and about the cloud. Spherical geometry is used because the cloud dome is better represented by a spherical surface than a plane surface. This model is recognized as a gross oversimplification of natural occurring clouds, but the procedure here is to start with a simple model which can be solved numerically and then progress to more complicated situations. The charge Q is maintained on the central sphere by some interior charging mechanism which need not be specified in the present discussion.

The equations which govern the nonturbulent case are

$$\frac{\partial n_1}{\partial t}+\nabla\cdot\mathbf{J}_1=q-\alpha n_1 n_2-\beta_1 n_1 Z, \qquad (1)$$

$$\frac{\partial n_2}{\partial t}+\nabla\cdot\mathbf{J}_2=q-\alpha n_1 n_2-\beta_2 n_2 Z, \qquad (2)$$

$$\nabla\cdot\mathbf{E}=\frac{e(n_1-n_2)+ZQ_{\rm drop}}{\epsilon_0}, \qquad (3)$$

where

$$\mathbf{J}_{1,2}=\pm k_{1,2}\mathbf{E}n_{1,2},$$

$k_{1,2}$ is the mobility of the positive and negative ions respectively, α the recombination coefficient, and $\beta_{1,2}$ the combination coefficient between the small ions and the aerosol particles. The ionic charge is e and ϵ_0 is the permittivity of free space. The electrical mobility of the charged cloud particles is much smaller than that of the small ions and is therefore neglected.

Movement of the ions toward the aersol particles will result from the induced dipole field and the field resulting from any net charge, $Q_{\rm drop}$, on the particle. The ionic current which flows to the droplet under the influence of the resultant field represents the loss of ions to the droplet. The combination coefficient is given by Gunn (1956) as

$$\beta_{1,2}=\frac{\pi k_{1,2}}{3Eb^2}\left(3Eb^2\mp\frac{Q_{\rm drop}}{4\pi\epsilon_0}\right)^2. \qquad (4)$$

If the electric field is sufficiently small, the loss of ions to the particles by diffusion cannot be neglected and additional terms representing diffusional loss must be included in (1) and (2). In general, there will be statistical charging of the particles and each charge species must be taken into account. Also, since the diffusion coefficients are different for the positive and negative ions, the average droplet charge is not quite zero for $E=0$. For the purpose of this paper however, when the inclusion of diffusive loss is necessary, it is sufficient to represent it by a term, $4\pi bDZn_{1,2}$, where D is the diffusion coefficient for either small ion.

The governing equations above are macroscopic equations in the sense that they are valid only over regions which are large compared to the cloud particle. The loss of ions on the microscale occurs at the surface of the particle. As is customary in macroscopic equations, the effect of microscopic processes is here represented as a bulk coefficient in the macroscopic equations.

Eqs. (1), (2) and (3) for steady-state and spherical geometry are

$$\frac{k_1}{r^2}\frac{d}{dr}(r^2En_1)=q-\alpha n_1 n_2-\beta_1 n_1 Z, \qquad (5)$$

$$-\frac{k_2}{r^2}\frac{d}{dr}(r^2En_2)=q-\alpha n_1 n_2-\beta_2 n_2 Z, \qquad (6)$$

$$\frac{1}{r^2}\frac{d}{dr}(r^2E)=\frac{1}{\epsilon_0}[e(n_1-n_2)+ZQ_{\rm drop}]. \qquad (7)$$

Subtracting (6) from (5) gives

$$\frac{1}{r^2}\left[\frac{d}{dr}(k_1r^2En_1+k_2r^2En_2)\right]=\beta_2 n_1 Z-\beta_1 n_1 Z. \qquad (8)$$

For equilibrium conditions, charge continuity requires that $\nabla\cdot\mathbf{j}=0$, where $\mathbf{j}$ is the current density. The left side of (8) is just $\nabla\cdot(\mathbf{j}/e)$ so that

$$\beta_1 n_1=\beta_2 n_2. \qquad (9)$$

When the explicit expressions for $\beta_{1,2}$ are substituted

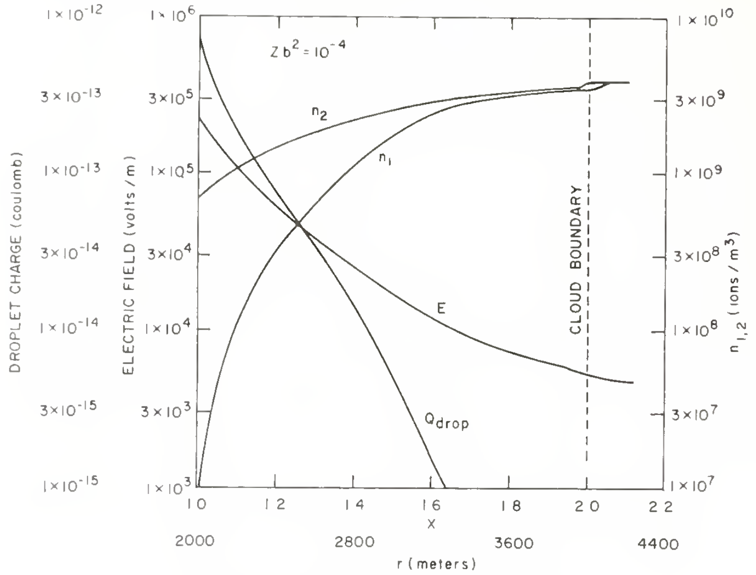

FIG. 2. Solution for $Zb^2=10^{-4}$, $Z=10^4$, $b=10^{-4}$.

into (9), the following formula is obtained for $Q_{\rm drop}$:

$$Q_{\rm drop}=4\pi\epsilon_0(3Eb^2)\left[\frac{(k_1n_1/k_2n_2)^{\frac{1}{2}}-1}{(k_1n_1/k_2n_2)^{\frac{1}{2}}+1}\right]. \qquad (10)$$

This expression, which gives the steady-state charge on the aerosol particle of radius b, has been derived in a somewhat different manner by Gunn (1956) who referred to this charging process as "hyperelectrification" of cloud or precipitation drops.

Eqs. (5), (6) and (7) form a system of nonlinear differential equations for the three dependent variables, E, n_1 and n_2. The asymptotic boundary conditions as r goes to infinity are that $n_{1,2}$ approach $\sqrt{q/\alpha}$ and r^2E becomes constant. The asymptotic condition for E is equivalent to requiring that a monopole field predominates at large distances. At the surface $r=a$, E is determined by the charge Q. If the sphere is positively charged and no positive ions can flow out of the sphere, then $n_1(a)=0$. In the case of a cloud $n_1(a)$ may be finite; this introduces no additional computational difficulties as will be demonstrated later. The negative ion density is unspecified at the surface and must be picked such that the asymptotic boundary conditions are satisfied. For a highly electrified cloud under steady-state conditions, the requirement that $n_1(a)\approx 0$ is not unreasonable because ions formed in small numbers by cosmic rays within the inner sphere will readily attach to the cloud particles. The negative ion density $n_2(a)$ is maintained by the influx of ions from outside the cloud or from more remote regions of the cloud with low values of electric field.

The Runga-Kutta method for the numerical solution of a system of differential equations has been used to program this set of equations for the digital computer. The negative ion number density, $n_2(a)$, must be varied until the asymptotic boundary conditions are realized. In practice, this means that many solutions to this

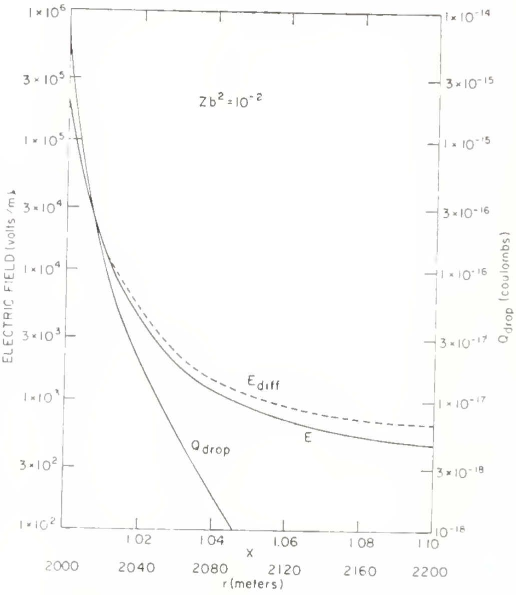

FIG. 3. Solution for $Zb^2=10^{-2}$, $Z=10^3$, $b=10^{-5}$.

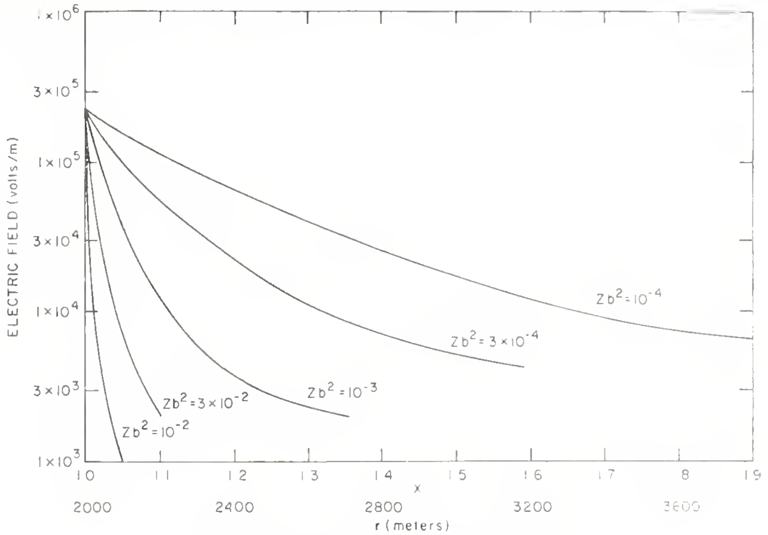

FIG. 4. Electric fields for various values of Zb^2.

system must be generated before the solution which very nearly satisfies the desired boundary conditions is obtained.

A close examination of the governing equations shows that b and Z appear in the equations only as the product Zb^2, thus, a solution for one set of values for b and Z will also be a solution for any other combination provided the product Zb^2 is the same. It is therefore convenient to classify the solutions in terms of the product Zb^2 (in units of meter^{-1}).

The solutions to the governing equations for the given problem with $a=2000$ m, $R=4000$ m, $Q=100$ C, $k_{1,2}=2.3\times10^{-4}$ m^2 (V-sec)$^{-1}$, $q=18\times10^6$ m^{-3} sec^{-1}, and $\alpha=1.8\times10^{-12}$ m^3 sec^{-1} are shown in Figs. 2 and 3 as functions of r and $x=r/a$. Values of k, q, and α are typical of those found at about 6–7 km. Fig. 2 shows the solution for the case when $Zb^2=10^{-4}$. This represents a very light cloud. In thunderstorms this would be the order of magnitude of Zb^2 which might be expected at the cloud top. In this steady-state model, it is evident that most of the shielding occurs near the inner boundary of the cloud and is caused by the charge on the cloud droplets. The field at the outer boundary is greatly diminished. Although the dependent variables n_1, n_2 and E depend only on the product Zb^2, values of Z and b must be chosen in order to calculate the charge on the drop. In Fig. 2 the scale on Q_{drop} is obtained by assuming particles of 10^{-4} m radius and concentration of 10^4 m^{-3}. If a different value of Z is chosen, Q_{drop} must be changed inversely.

For the cloud base, the order of magnitude of Zb^2 is probably between 10^{-2} and 10^{-3}. Fig. 3 shows the solution for the case of $Zb^2=10^{-2}$. The charge, Q_{drop}, is based here on particles of radius 10^{-5} m and density 10^8 m^{-3}. This cloud has a much larger water content and is thus a more effective shield. Here the charge is nearly shielded in the first 50 m. Beyond 50 m the field is so weak that diffusional loss is more important than conductional loss. When the diffusional loss is included, the equations no longer depend upon Z and b only through the product Zb^2. The ion density in such a cloud, free of an electric field, is smaller than the ion density in the free atmosphere. The dashed curve labeled E_{diff} is the solution when the diffusional loss is included. Fig. 4 shows the shielding of the field for various values Zb^2.

If conductivity is defined in the conventional manner as

$$\lambda=e(n_1k_1+n_2k_2),$$

then within the cloud it is obvious that λ depends upon the electric field because $n_{1,2}$ depends upon the field. The current density is no longer linearly related to the electric field, i.e., Ohm's law is invalid. This, of course, results largely from the fact that the effectiveness with which cloud particles act as centers of recombination is field-dependent. Also the time-dependencies which govern the relaxation of the variables to the steady-state values do not separate into an exponential function depending only upon time as is usually the case for ohmic conduction. Therefore, the "relaxation time" in the cloud cannot be defined conventionally in terms of the conductivity, but is itself a complicated function of time, space, and the electric field.

It is important to recognize that the solutions which have been obtained are for the steady-state case and are valid only after the relaxation time of the medium has transpired. Since the relaxation time in the cloud is much longer than that of the free atmosphere, the total relaxation time will be approximately that of the cloud. If the establishment of the charged core within the cloud is much faster than the relaxation time of the cloud, there will be an initial buildup of a screening at the clear air-cloud boundary. The position of the screening charge will then move inward at a rate determined by the relaxation time of the cloud until the steady-state solution if realized. The steady-state solution is probably not reached in natural clouds, but should be realizable in laboratory clouds provided adequate precautions are taken.

Even though a steady-state solution is not reached, certain conclusions regarding the screening at the clear air-cloud boundary can be made from the steady-state solutions. Consider a thin layer of cloud at the clear air-cloud boundary after a charge is instantaneously placed at the center of the cloud. Initially, the charged layer under consideration is so thin that the electric field is not reduced significantly even if every cloud particle has its maximum charge given by (10). A short time later negative ions entering the cloud have penetrated a somewhat deeper layer such that the field at the surface has been reduced and the rate at which negative charge enters the cloud has been reduced. The reduction of the field at the surface also reduces the charge which the cloud particles near the surface can maintain [by Eq. (10)]. A short distance into the cloud, the field is still large; the cloud particles are not fully charged, and they have very large cross sections for attaching negative ions. Negative ions have not yet penetrated the inner cloud. This produces an outer shielding layer which is similar to the inner layer which exists in the steady state. The width of the steady-state shielding layer can be used to estimate the thickness of the shielding layer at the outer boundary for times longer than the free-air relaxation time but shorter than the cloud relaxation time.

If the distance Δ over which the field falls to some fraction of its value at $x=1$ (see Fig. 4) is plotted against Zb^2, the equation of the line is given approximately as

$$\Delta=\frac{B}{(Zb^2)^{0.89}}, \tag{11}$$

where $B=0.26$ for a tenfold reduction in the field and 0.096 for a reduction of e^{-1}. It is interesting to compare these values with those given by Vonnegut *et al.* (1966) and Phillips (1967) based upon more intuitive approaches. These expressions can be written as

$$\Delta=\frac{A}{Zb^2},$$

where $A=0.083$ for the Vonnegut expression and 0.32 for that of Phillips. The width Δ in the Phillips expression is for the reduction of e^{-1} and in the Vonnegut expression for "complete" screening. The constants in (11) undoubtedly depend upon the values of q and k and to a lesser degree upon α.

The rigorous solution to the time-dependent equations is difficult because the time and space coordinates do not separate. However, a good approximation to the initial decay rate of the electric field outside the cloud can be obtained by calculating the rate of flow of charge into the cloud boundary from the clear air. The change in the electric field at the cloud boundary can be written as

$$\frac{dE}{dt}=\frac{e}{\epsilon_0}[J_1(R)-J_2(R)], \tag{12}$$

where $J_1(R)$ will be the flux of positive ions out of the cloud and $J_2(R)$ the flux of negative ions into the cloud (for positive charge center). If the cloud is dense and the electric field large, the initial ion density within the cloud will be small and $J_1(R)=0$. The inward flow is determined by the clear-air ion density, $(q/\alpha)^{\frac{1}{2}}$. In this case the solution to (12) is

$$E=E_0\exp\left(\frac{ek\sqrt{q/\alpha}}{\epsilon_0}t\right)=E_0\exp(\lambda t/2\epsilon_0), \tag{13}$$

where λ is the free-air conductivity. Thus, the time constant is equal to one-half the clear-air time constant. The factor of one-half enters because the field was evaluated at the cloud boundary. If the same analysis is applied to an imaginary surface far enough from the cloud so that ionic equilibrium exists and $n_1=n_2=\sqrt{q/\alpha}$, then the field decays initially with a time constant which is equal to the free-air relaxation time. External to the boundary of thick clouds, a space charge layer will develop where $n_1\neq n_2$ because of the diminished concentration of the outward ion flow. This charge is analogous to the "electrode effect" which develops at boundaries of ionic discontinuities. For clouds which are electrically thin, the outward moving ions cannot be neglected and the field decay of the boundary will proceed at a rate between the free-atmosphere relaxation rate and one-half the free atmosphere value. The above agruments hold only for times which are short compared to the relaxation time of the cloud.

An approximate time-dependent solution for the electric variables at a given time can be obtained by forcing the electric field to be large throughout most of the cloud except in a region close to the boundary. The distance inside the boundary at which the field is forced to be large uniquely determines a value of the field at the cloud boundary and the value of the field at the boundary is associated with a time as specified by (13). Using this artifice, the field profiles have been calculated and plotted in Fig. 5 for several different times and $Zb^2=10^{-3}$. The existence of a large shielding charge (gradient of the field) is clearly evident even after a relatively short time. For short times (the order of magnitude of the free-atmosphere relaxation time) considerable amounts of space charge reside in the free atmosphere outside the cloud boundary. This, of course, is caused by the depletion of positive ions near the cloud boundary. Positive ions in the vicinity of the cloud are propelled away from the cloud by the strong electric field and no compensating outward flow of positive ions can originate within the cloud because the ion densities are extremely low within the cloud. The dotted line inside the cloud shows the solution of the steady-state equations if the inner boundary were placed at the point where the dotted line ends. Since there is no real boundary at this point, the inflowing ions will penetrate beyond this point, but certainly no farther than the distance given by the product of their velocity (kE) and the given time. For the longer times, it is obvious from the slope of the curves in Fig. 5 that the region of maximum charge density has moved inside the boundary (note that the ordinate of Fig. 5 is logarithmic). It should be emphasized that the values of the constants appearing in the equations are those typical of 6–7 km.

It is certain that ions are formed within the charge center of the cloud. In addition to the cosmic ray ionization mechanism, formation may be accomplished by corona discharge or by processes similar to those which produce small ions in spray and bubble electrification (Chapman, 1938). In this case, the boundary condition imposed upon the positive ion density at the inner boundary must be changed. Fig. 6 shows the solution for various values of the positive ion density at the inner boundary. The solution with the correct asymptotic behavior is again found by varying the negative ion density at the inner boundary. Fig. 6 shows that the production of positive ions within the cloud will result in the hyperelectrification of cloud droplets near the region of charge generation. (It is clear that a reversal of the polarity of the central charge requires a reversal of the sign on the small ions and cloud droplets.)

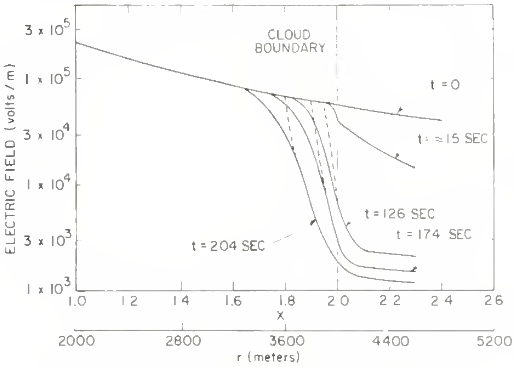

FIG. 5. Electric field profiles as a function of time.

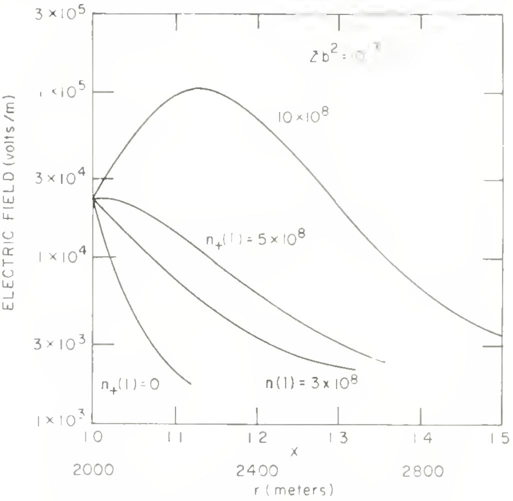

FIG. 6. Electric field profiles for a finite positive ion density at the inner boundary.

The solution for all the electric variables is shown for the case of $Zb^2 = 10^{-3}$ and $n_1 = 1 \times 10^9$ at the inner boundary in Fig. 7. The particle charge, Q_{drop}, is computed on the basis of $Z = 10^5$ m^{-3} and $b = 10^{-4}$ m. The cloud is positively charged near the inner boundary but the droplet charge reverses sign at a point where the surplus of small positive ions injected at the inner boundary is overcome by the negative ions supplied by the outer boundary. In the intermediate region, the conductivity is a minimum because the high electric field increases the attachment coefficient. That this type of field behavior does exist when surface ionization is present on the boundary surfaces of a cloud has been shown in the laboratory by Hoppel and Gathman (1970). This behavior is discussed later in connection with Fig. 10.

Again the solution will be different at times that are short compared to the relaxation time of the cloud. In this case, a positive charge will develop at the inner boundary and a negative shielding layer will develop at the outer boundary; in between, the electric field will have a maximum and the conductivity a minimum across a much broader region of the cloud. This is shown schematically in Fig. 8 where the radial dependence ($1/r^2$) of the field has been neglected.

3. Turbulence and electroconvection

All the considerations in the last section were based upon a quiescent model of a cloud. A condition of quiescence rarely occurs in natural clouds (except in certain stratus formations). It has been shown both experimentally and theoretically (Hoppel, 1969) that the turbulent transfer is important in mixing of the space charge near the earth's surface. Turbulence dramatically alters the so-called "electrode effect."

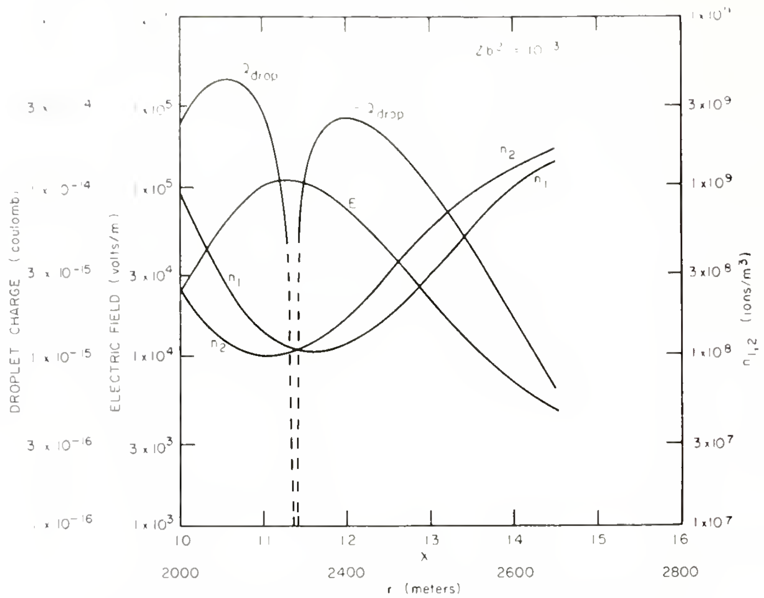

FIG. 7. Solution for electric variables when $Zb^2 = 10^{-3}$ and $n_+(1) = 10^9$ ions m^{-3}.

There is little doubt that turbulent transport of charge is also important in clouds. Almost all treatments of the thunderstorm electric circuit have neglected the effects of turbulent transport of charge and considered only the conduction of small ions. Here only the case of turbulent transport which can be described statistically in terms of the turbulent diffusion coefficient $K(r)$ is considered; convection will be considered later. A quasi-steady state then exists and the governing equations are still given by (1), (2) and (3); now, however,

$$\mathbf{J}_{1,2} = \pm k_{1,2}\mathbf{E}n_{1,2} - K(r)\nabla n_{1,2}, \qquad (14)$$

$$\nabla\cdot\mathbf{j} = \nabla\cdot[(\mathbf{J}_1 - \mathbf{J}_2)e - ZK(r)\nabla Q_{\text{drop}}] = 0, \qquad (15)$$

where $\mathbf{j}$ is the total current density. The electrical mobility of the charged droplet is assumed to be negligible compared to the ionic mobility. Eq. (15) leads to a second-order differential equation for Q_{drop} in addition to the second-order equations for n_1 and n_2. It is difficult to vary, simultaneously, several derivatives at one boundary, to obtain the correct behavior at the other boundary. [For a more detailed discussion, see Hoppel (1969).] The effect of turbulence can be predicted, however, by rewriting (15) in the form

$$ek\mathbf{E}(n_1 + n_2) - C\nabla q_T = \mathbf{j}, \qquad (16)$$

where $K(r) = C$ is constant and q_T, the total space charge density, is given by

$$q_T = e(n_1 - n_2) + ZQ_{\text{drop}}. \qquad (17)$$

For times which are short compared to the relaxation time of the cloud, ∇q_T is negative inside the cloud boundary since the negative charge increases in the positive direction. If there is a source of ions at the inner boundary, ∇q_T is also negative at the inner boundary. The total current density, $\mathbf{j}$, is therefore increased by the existence of turbulence. If the polarity of the cloud is reversed the same argument holds for the aboslute value of the current.

The preceding conclusions can be easily demonstrated in the laboratory. The laboratory experiments (Hoppel and Gathman, 1970) on artificial clouds between

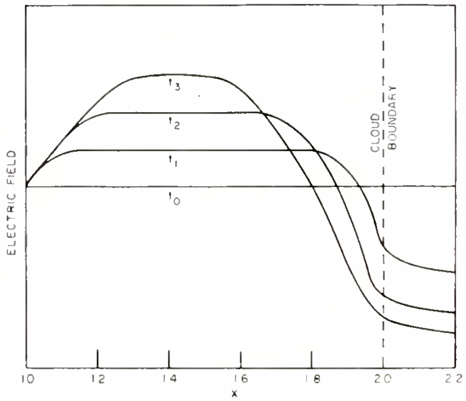

FIG. 8. Schematic of the development of the inner and outer charged layers.

parallel plate electrodes show: 1) that quiescent clouds do sustain highly charged shielding layers which act to reduce the current flow in the cloud; 2) the electric fields in a quiescent cloud are accurately described by (1)–(4); and 3) the effect of turbulence upon charge transport depends upon the ionization profile. For volume ionization, the turbulent transport opposes the conduction current and reduces the total current, while for surface ionization the turbulent transport greatly enhances the total current. The case of cloud-clear air boundary is similar to the case of surface ionization since the clear air outside the cloud is able to supply ions to the cloud surface. Likewise, any ion source within the cloud behaves as surface ionization. Fig. 9 shows the current-voltage characteristics for an aerosol cloud in a parallel plate chamber with 20-cm plate separation and an α source (Po^{210}) on each electrode. If turbulence is generated within the cloud by a small fan, the current increases dramatically as predicted by (16).

If no forced turbulence is generated within the cloud and the voltage on the chamber is increased to several kilovolts, then electrically driven turbulence develops in the region between the two α sources. Fig. 10 for a dry ice cloud shows the electric field profile calculated numerically from the equations governing the quiescent cloud together with the measured electric field profile prior to the occurrence of electroconvection. Centers of positive and negative charge exist in the regions where the magnitude of the slope is greatest. As the voltage between the plates is increased, the interaction of the electric field and the charged aerosol produces electroconvection when the electrical stress exceeds the stabilizing forces. Some streaming motion can be observed at voltages below 1 kV, and at several kilovolts turbulence is dominant in the region between the sources. Concurrent with the onset of electroconvection there is an increase in the current through the chamber and a decrease in the electric stress as indicated by a more uniform electric field profile. Thus, long before the field in the center of the chamber reaches breakdown proportions the electric stress is relieved by electroconvection. [For details see Hoppel and Gathman (1970).]

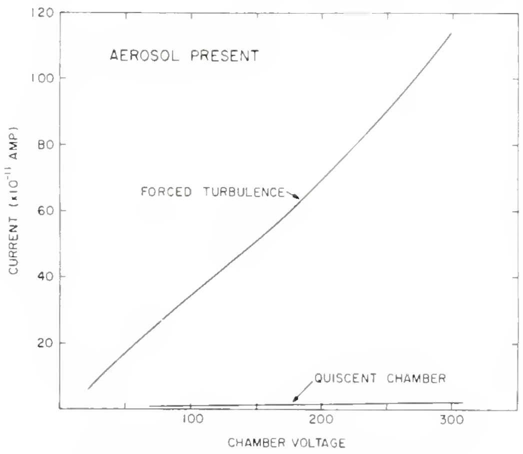

Fig. 9. Current voltage characteristic with and without forced turbulence.

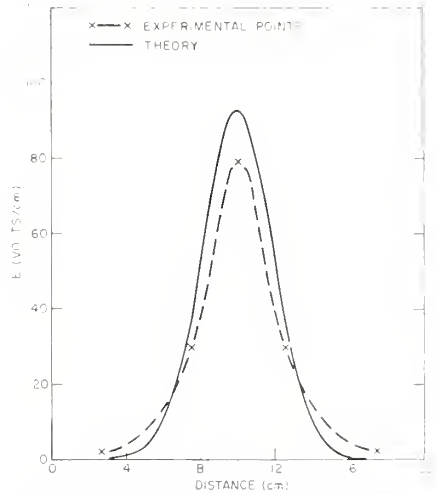

Fig. 10. Electric field profile in chamber prior to electroconvection.

4. Application to thunderstorm electricity

The existence of a shielding layer around natural clouds has been established by several investigators. Gunn (1955) found from aircraft measurements that the electric field outside thunderclouds was typically ~ 200 V cm^{-1} maximum and that upon entering the cloud, the field jumped by a factor of 2–4. This he attributed to a free charge near the boundary. Reiter (1969) reports that the average electric field under a stratus deck which is turbulent has about the same value as the fair weather field, but if the turbulence subsides and the cloud becomes stably stratified, then the field below the cloud is very small. Positive ions collect on the upper surface of the cloud and a negative charge collects on the lower surface such that the potential which ordinarily exists between earth and the electrosphere is now predominantly across the cloud deck. Aircraft measurements of electric field above thunderstorms were interpreted by Vonnegut *et al.* (1966) to infer that an electrical shielding layer exists above the thunderstorm except in regions where strong convective activity disperses the shielding layer and exposes the positive charge which exists in the cloud top. The latter two examples not only substantiate the existence of a shielding layer but also show that turbulent and convective transfer of charge is important. Further evidence of the existence of the screening layer is the well known reversal of the electric field immediately following a lightning stroke. When the central negative charge is destroyed by the return stroke, the field at the ground often is momentarily strongly reversed, indicating that an opposite sign charge distribution exists. Similar reversal effects associated with discharges occur at cloud altitudes and above clouds as measured during aircraft investigations of thunderstorm electric fields (Vonnegut *et al.*, 1966; Imyanitov *et al.*, 1969). The development of a shielding layer which diminishes the field outside the cloud requires that the conductivity just inside the cloud be smaller than the conductivity outside the cloud. If the reverse were true, the field would increase outwardly at the cloud boundary.

The initial transfer of charge from the free air to the shielding layer following an alteration of either or both of the spatial or time coordinates of the internal cloud charge distribution occurs at a rate which is determined principally by the conductivity at and exterior to the boundary. The net charge within the screening layer at any given cloud level acquires 63% of its equilibrium value in the time $\tau=\epsilon_0/\lambda$, where λ is the total free air conductivity. Fig. 11 shows the free-air relaxation times as a function of altitude as derived from measured conductivity data of Woessner *et al.* (1958) at Washington, D. C. (39N). From this it is seen that shielding at lower cloud levels require periods of approximately 1 min. For the upper cloud, 63% of the shielding is established in 10 sec and less. More will be said about cloud relaxation time and conductivity later.

a. Turbulent charge transport

In order to discuss the effect of turbulence upon the charge transport, it is assumed that the turbulence can be described by a statistical turbulent diffusion coefficient C. From (16) the current in the cloud is given by

$$\mathbf{j}_c=\lambda_c\mathbf{E}-C\nabla q_c, \tag{18}$$

where $\lambda_c=(n_1+n_2)ek$ is the conventional definition of conductivity and q_c is the space charge density given by (17). Likewise the current in the clear air is

$$\mathbf{j}_a=\lambda_a\mathbf{E}_a-C_ae\nabla(n_1-n_2). \tag{19}$$

If the geometric factors are neglected (assume a plane boundary between cloud and clear air), then Gauss' law requires that

$$E_a=\frac{\sigma_s}{\epsilon_0}+E_c,$$

where σ_s is the charge per unit area contained in the boundary layer. For quasi-steady-state conditions, the currents must be equal. Equating the currents yields

$$\sigma_s=-\epsilon_0\left(1-\frac{\lambda_c}{\lambda_a}\right)E_c-\frac{\epsilon_0 C}{\lambda_a}\nabla q_c, \tag{20}$$

where the term $\nabla(n_1-n_2)$ is assumed to be small, i.e., the charge resides on the cloud particles and not on small ions. If $C=0$, (20) is similar to the expression given by Kasemir (1965). The additional term containing C will decrease the boundary layer strength by increasing the charge transport through the cloud. This increase in charge transport will make the cloud appear to have a somewhat higher conductivity λ_{eff} than that given by λ_c, such that

$$\lambda_{\text{eff}}=\lambda_c-\frac{C}{E}\nabla q_c, \tag{21}$$

where ∇q_c is negative and q_c depends upon E.

If the width of the charged boundary layer is d, then

$$\nabla q_c\approx\frac{\sigma_s}{d^2},$$

and

$$\sigma_s=-\frac{\epsilon_0 E_c(1-\lambda_c/\lambda_a)}{1+(\epsilon_0/\lambda_a)(C/d^2)}. \tag{22}$$

From the previous discussion, it would be anticipated that inside the cloud, where the field is large, $\lambda_c\ll\lambda_a$. It is difficult to evaluate (22) because the ratio C/d^2 is unknown. As the turbulent diffusion coefficient C increases, d will also increase. Values of C from 5–500 m^2 sec^{-1} are considered reasonable. For the higher values of C, d could hardly be less than 500 m. Any value of the ratio C/d^2 which seems reasonable at the present time is too small to change σ_s appreciably. However,

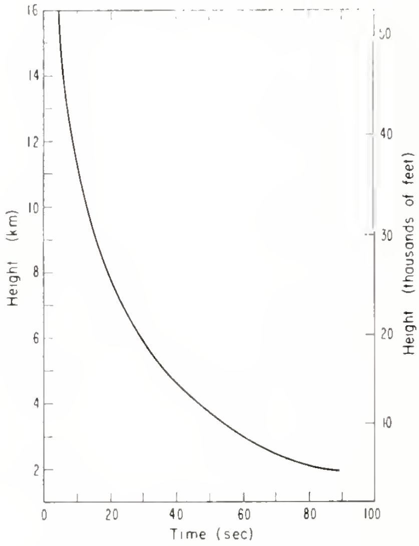

FIG. 11. Free-atmosphere relaxation time as a function of altitude.

the turbulence would disperse the space charge over a much larger region than that given by (11). This conclusion is in agreement with the results of the turbulent electrode effect; i.e., the net charge in the electrode layer is not affected, but the height of the layer is greatly increased by increasing values of eddy diffusivity (Hoppel, 1969). The effective conductivity as given by (21) is considerably less than the free-air conductivity, but the two terms on the right-hand side are the same order of magnitude.

From these arguments we conclude that a shielding charge will exist even in cases of considerable turbulence. However, with turbulence, the charge will not appear as a well-defined layer but rather as a more diffuse transition region within the cloud boundary. Throughout this region, the electric field will decrease more rapidly than would be expected from the $1/r^2$ law of electrostatics.

In active storms the turbulent transfer mechanism may transport charge from the cloud boundary layer without appreciable loss of charge density. The result of this larger scale turbulent motion will be to develop a chaotic distribution of charges within thicker cloud boundary layers, especially so in cloud tops where charging periods are near or less than the period between successive lightning discharges. Such random charge distributions are reported in upper levels of storms (Fitzgerald and Cunningham, 1965). When lightning discharges result in electric field reversals at the cloud boundary, the enfolding and transport of the high-density space charge of cloud surfaces by the larger scale motion may cause strong local field enhancement and contribute to continued lightning activity.

It is not believed that electroconvection contributes significantly to the turbulence in a thunderstorm cloud. This conclusion is suggested by the following arguments: 1) a rough calculation indicates that the electrical dissipation resulting from turbulence is much smaller than mechanical dissipation of energy; 2) the electrical forces are much smaller than buoyancy forces; and 3) the volume forces are at least a factor of 100 below that required in laboratory experiments to sustain electroconvection against viscous dissipation.

b. *Cloud conductivity and relaxation time*

When there is a source of ions in the central region of the cloud, these ions will move outward and attach to the cloud particles in the intermediate region of the cloud as discussed in connection with Figs. 7 and 8. This enlarges the region of the central charge and, as the ion-generating mechanism increases, the maximum field does not occur in the central region where the ions are produced but in a region around the generating area. This is because the positive ions which move outward attach to the cloud particles and the magnitude of the field depends upon the cumulative charge inside the Gaussian surface. As is evident from the values of $n_1(1)$ in Fig. 6, it does not take a very strong source of ions in the center to produce a large field in the intermediate region of the cloud (for the steady-state case).

Processes other than cosmic ray ionization which produce small ions are undoubtedly present in the precipitating portion of the cloud. Chapman (1953) has found that enough small ions of both polarities are formed in the disruption of droplets to produce sufficient charge of both polarities to account for the necessary amount of charge in thunderstorms. Sartor (1967) has observed discharge between charged droplets which occurs in air and undoubtedly forms many small ions of both signs.

An additional source of ions in the precipitating portion of the cloud would increase the conductivity in this region. Freier (1963) argues that the observed electric field recovery period after a lightning stroke requires a high conductivity inside the cloud. This is based upon the questionable assumption that the thunderstorm generates a constant current. Measurements in the thunderstorm are interpreted by Evans (1969) to indicate that the conductivity inside the thunderstorm is a factor of 10 larger than the conductivity outside the cloud, but because of possible inaccuracies in the measuring method, we must agree with Evans' own evaluation that this result is "highly tentative." If significant numbers of ions are formed within the precipitating region of the cloud, then ions under the influence of the electric field must move outward from this region. The existence of the observed outer shielding layer requires that the outer nonprecipitating region of the cloud has a lower conductivity and, consequently, a higher field. The picture would then be roughly that given by Fig. 8.

The preceding picture is similar to the qualitative description deduced by Imyanitov *et al.* (1969) from aircraft measurements in the Soviet Union. They picture the thunderstorm as a central turbulent region of high conductivity surrounded by a relatively low conducting medium. The large horizontal component of the electric field in the intermediate region of the thunderstorm could account for the horizontal component of many of the lightning strokes observed by Brook and Vonnegut (1960) and Ogawa and Brook (1969).

An argument can be given in support of increased conductivity in the precipitation regions of clouds. In recent years, cloud physicists have recognized that the growth of precipitation in the updraft of convective clouds is associated with an effective filtering of the cloud water content from the updraft flow (Iribarne and De Pena, 1962; Iribarne, 1968). This can be illustrated simply in the following way. The precipitation falling within the cloud droplet distribution possesses an effective capture cross section given by

$$\sigma=\int_0^\infty \pi b^2\Gamma(b)N(b)db, \qquad (23)$$

where $N(b)$ is the distribution function and $\Gamma(b)$ the collection efficiency of the precipitation particles. The cloud water loss with height is given by $dm/dz=-\sigma m$, and the fractional cloud water remaining at a given height is

$$\frac{m}{m_0}=\exp[-\sigma(z-z_0)], \tag{24}$$

where m_0 is the initial cloud water content at level z_0. Thus, it can be shown (Phillips, 1969), that 63% of the cloud water is captured within a vertical distance of little more than 1 km when the precipitation water content is 1 gm m^{-3}. As the cloud droplets are captured, the condensation processes in the updraft transfer to the precipitation particles and few new cloud droplets are born. Thunderstorms evidence precipitation radar echoes which are typically 6–16 km in cross section and height. In much of this volume we expect that because of effective cloud droplet capture, the primary particle distribution is that of precipitation rather than cloud, the significant difference being that the mean particle size is of the order of 1–2 mm, much larger than the cloud droplet size range of 10–20 μ commonly referenced for cumulonimbus-type clouds.

The Zb^2 product for a precipitation water content of 1 gm m^{-3}, distributed uniformly in 1-mm drops, is 2.39×10^{-4} m^{-1}. Such a cloud is thus electrically "thin" and will consequently possess appreciable ion concentrations and conductivities even when only cosmic ionization is present. If the current divergence term is negligible, the equilibrium ion concentration in the precipitation region can be approximated from (5). Taking $Zb^2=2.39\times10^{-4}$ m^{-1}, $E=3\times10^4$ V m^{-1}, $k=2.3\times10^{-4}$ m^2 V^{-1} sec^{-1}, and $q=18\times10^6$ m^{-3} sec^{-1} as representative for a 6–7 km height, then the ion concentration is 10^9 m^{-3}. By comparison, the concentration in the free atmosphere at the same height is $n_{1,2}\approx3.9\times10^9$ m^{-3}. The rate of ionization needed to provide this same concentration in the precipitation core can be evaluated to be 79×10^6 m^{-3} sec. This means that an ion production increase of less than a factor of 5 above the cosmic ray ionization rate is needed to yield a central cloud conductivity equal to that of the free air at this same altitude. Such a factor may be possible by the additional ionizing mechanisms already mentioned.

Using the well-known Marshall-Palmer relation, the number of raindrops $N(D)$ in the drop diameter increment δD is given by

$$N(D)\delta D=N_0e^{-\lambda D}\delta D,$$

where $N_0=0.08$ cm^{-4} for all distributions, $\lambda=41R^{-0.21}$ cm^{-1}, and R is the rate of rainfall (mm hr^{-1}). The Zb^2 product of the distribution is therefore

$$Zb^2=\int_{D_{\min}}^{D_{\max}}\frac{D^2}{4}N(D)\delta D. \tag{25}$$

For thunderstorm rain a representative value of $R=25$ mm hr^{-1} can be assumed along with values of $D_{\min}=0.05$ cm and $D_{\max}=0.6$ cm. The lower limit of 250 μ radius for the raindrop spectrum is reasonable for cloud precipitation levels, the smaller cloud drops having been filtered by raindrop capture in all but the lowest cloud levels. Using these values, the Zb^2 product is found to be 4×10^{-4} m^{-1} for thunderstorm rain of 1 inch hr^{-1} rainfall rate. Thus, the whole of the thunderstorm precipitation core may be classified as electrically "thin." As a result, ions transported outward from the central charge centers can be expected to increase the electric field intensity (horizontal) in the non-precipitating cloud region as indicated in Fig. 8.

c. *Thunderstorm electric field recovery time*

Continuous records of the electric field beneath active thunderstorms show that the lightning discharge causes a near instantaneous alteration of the field which is followed by an approximate exponential field recovery toward the initial value prior to the discharge. The recovery time to 63% of the initial value is commonly in the range of 10–20 sec with a mean period of around 15 sec. This recovery period has been subjected to several interpretations both as to charging mechanisms and discharging (conduction) mechanisms within and exterior to the cloud.

Phillips (1967) has shown that the net charge as a function of time for either the upper or lower dipole cloud charge can be represented by

$$Q(t)=\frac{I\epsilon_0}{\lambda}[1-\exp(-\bar{\lambda}t/\epsilon_0)], \tag{26}$$

where I is the thunderstorm generator current between the upper and lower cloud and $\bar{\lambda}$ is the mean conductivity *of the free air* sruronding the charge centers. This assumes that I, which may be equated to the product of the mean precipitation particle charge and fall velocity, is constant over the period of recovery. Eq. (26) may be put in terms of the electric field exterior to the cloud by Gauss' law by which

$$E(t)=\text{constant}\times\frac{I\epsilon_0}{\bar{\lambda}}[1-\exp(-\lambda t/\epsilon_0)], \tag{27}$$

showing that the electric field recovery time is $\Upsilon=\epsilon_0/\bar{\lambda}$.

The thunderstorm can be pictured as a dipole with primary charge centers and shielding charge distributions. Prior to discharge, the net upper and lower charges Q_1 and Q_2 may be approximately equal (Fig. 12a). With the return stroke the lower charge is essentially neutralized, reducing the electric field at the earth's surface to near zero (Fig. 12b). The electric field lines originating on the upper charge which were tied to the lower charge center within the cloud are now released; i.e., the radial electric field is suddenly in-

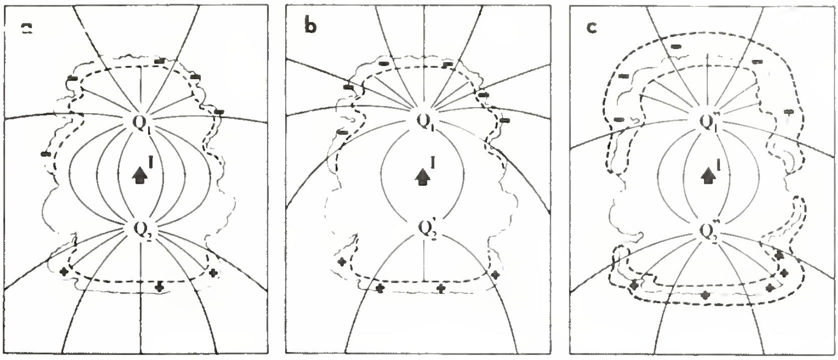

FIG. 12. Schematic of the electric charge and field distribution: before lightning discharge, a., immediately after lightning discharge, b., and after establishment of a shielding charge distribution in a period equal to the recovery time of the electric field at the ground, c.

creased, principally about the upper cloud surface. The primary charge readjustment that occurs is the establishment of the shielding charge distribution about the upper cloud surface. As discussed previously, this initial shielding layer is at the cloud surface, partially within the cloud on particles and as net charge due to the unequal ion concentrations and partially as an electrode layer exterior to the cloud. Mathematically, the exterior charge layer extends to infinity; practically, it is limited to a much shorter radius about the cloud.

The electric field beneath the storm reflects the charge readjustments of both the upper and lower poles which occur because of the charging current I and the conduction current to the shielding layers. As the primary shielding layer adjustment is that of the upper cloud, the recovery time by (27) is determined more by the mean relaxation time of the free air at these upper cloud levels. In reality, the observed result is the superposition of relaxation periods from all cloud levels; however, since the major shielding layer adjustment is across the upper cloud and since these adjustments are at more rapid rates, the recovery times appear largely determined by $\bar{\lambda}$ of the higher levels. Fig. 12c represents the situation near the end of the recovery time, ϵ_0/λ. The net upper charge Q_1'' and net lower charge Q_2'' reflect the charge transfers from the generator and conduction currents.

The free air conductivity as a function of altitude can be formulated by $\lambda=\lambda_h \exp(kz)$, where λ_h is the conductivity at height h and $k=0.22$ km^{-1}. From Woessner *et al.* (1958) the mean conductivity for the region between 6 and 12 km, 6 and 13 km and 6 and 14 km, and the respective relaxation times ϵ_0/λ are determined as follows:

$$\left.\begin{array}{l}\lambda_{6-12}=5.8\times10^{-13}\,\Omega^{-1}\,\mathrm{m}^{-1};\ \Upsilon_{6-12}=15.3\ \mathrm{sec}\\ \lambda_{6-13}=6.6\times10^{-13}\,\Omega^{-1}\,\mathrm{m}^{-1};\ \Upsilon_{6-13}=13.3\ \mathrm{sec}\\ \lambda_{6-14}=7.5\times10^{-13}\,\Omega^{-1}\,\mathrm{m}^{-1};\ \Upsilon_{6-14}=11.7\ \mathrm{sec}\end{array}\right\}.$$

Note that the 6–14 km interval may be appropriate for cloud heights <14 km as the electrode layer is partly in the free air during the initial recovery period.

The results show clearly that the observed recovery times for the electric fields associated with storms can be adequately explained on the basis of shielding layer charge readjustments from the free air environment. From this it appears that it is not necessary to postulate an in-cloud conductivity considerably greater than the free air conductivity in order to yield field recovery periods of the order of 15 sec. (Freier, 1963).

d. Large-scale cloud motion

If only smaller eddies were present, the effect of turbulence could be approximated by the treatment given. However, for the case of drafts which are continuous over a region as large as the thunderstorm itself, the treatment is not so simple and the exact circulation and time-dependent equations would be necessary. The initial stage of the thundercloud development is characterized by an updraft throughout the entire cloud. By the time the cloud reaches maturity, a downdraft develops in the region of heavy precipitation and the updraft moves to the leading edge of the thunderstorm. It is during the mature stage that the thunderstorm is most active electrically, and Byers (1965) suggests that the downdraft is what distinguishes the thunderstorm from a simple convective cell. The region of heaviest precipitation was also identified by Byers and Braham (1949) as the seat of negative charge.

It is interesting to speculate on what influence the large-scale drafts might have on the shielding layer. If the central charge during the initial convective stage of the thundercloud is of negative polarity (opposite to that shown in the figures), then a positive shielding layer will develop around the cloud. The net shielding charge will be smaller but of the same order of magnitude as the central charge. As the cloud matures, the updraft shifts toward the leading edge of the cloud and a downdraft develops in the region of heavy precipitation. The updraft will carry the entrained positive charge aloft. The downdraft will transport negative charge downward and help to contain the dispersal of negative charge formed by the precipitation. The free atmosphere along the flank of the cloud is now exposed to the electric field and will supply positive ions to reestablish the screening layer. These ions will also be captured by cloud particles in the updraft and will be carried aloft. In the mature stage, the net result is positive charge above the central negative charge.

The preceding speculations could be the possible explanation for the following experimental observations: 1) the change of polarity of thunderstorms upon maturing as observed above the cloud by Imyanitov *et al.* (1969), 2) the most frequent polarity of mature storms found by most observers, 3) the positively charged convective plume above an active thundercloud observed by Vonnegut *et al.* (1966), 4) the necessity of both precipitation and strong drafts to produce thunderstorms, and 5) the strong horizontal component of many lightning strokes.

It has been assumed here that a central charge separation mechanism exists and is presumably associated with gravitational separation of charge with positive charge falling to the ground. [Most measurements of net precipitation charge at the ground have recorded positive charge (Chalmers, 1967)]. A simple calculation shows that the total current entrained into the cloud updraft is only of the order of magnitude of the charging current found above the thunderstorm and is probably not sufficient to sustain the charge separation against the dissipative effects in the cloud. It would thus appear that the central charging mechanism must supply the bulk of the current dissipated in the thunderstorm.

5. Conclusions

Based on a simple cloud model, numerical solutions of the governing system of nonlinear equations have been obtained for the ion concentrations, electric field and cloud droplet charge within the shielding charge layer which exists in the cloud boundary regions of electrified clouds. The shielding charge distribution exists principally within the cloud where the charge resides primarily on the cloud particles which are hyperelectrified in the presence of electric fields and unequal ionic concentrations.

The "steady-state" shielding layer should exist at considerable depth within stable clouds; however, the "steady-state layer" is probably not physically possible in natural electrified clouds. In actual clouds, the shielding charge distributions are established nearer the cloud boundary in times approximating the relaxation time of the free-air cloud environment, $\tau=\epsilon_0/\lambda$, where λ is the total conductivity. The relaxation time of the free-air environment is believed to determine the recovery time of the electric field beneath storms. In the absence of continuing charge accumulation within the central thunderstorm cloud core, the shielding charge accumulation would render the external cloud electric field and conduction current near zero after a time period equal to a few multiples of the free-air relaxation time. The existence of continuing fields and currents—as have been measured above storms, for example—necessitates, in turn, a continuing current within the cloud proper, either as a generator current effecting charge accumulation or as a convection current which effectively passes the free air conduction current to earth.

The thickness of the cloud-shielding layer in quiescent clouds can be represented in the form $\Delta=B/(Zb^2)^p$, where the constants B and p depend on factors such as the rate of ionization and ion recombination, and the ionic mobilities. When ion concentrations within the central cloud are appreciable fractions of or equal to the free air concentrations, then an intermediate region of maximum electric field will develop as the result of charge distributions of opposing signs.

The effect of turbulence within cloud boundaries is to add an eddy transport current to the normal conduction current so that the total current density is increased. The turbulent charge transport from cloud boundaries parallels the turbulent charge transport which has been observed in laboratory experiments employing surface ionization. The resulting charge transport makes the cloud appear to have a higher conductivity than that given by the normal ionic conductivity. The increase caused by turbulence cannot be accurately determined because accurate values of the turbulent diffusion coefficient and eddy size are not known; however, it can be estimated that the effective conductivity in clouds may be increased by a factor of 2 as the result of turbulence in the boundary layers. In active sotrms, a second effect of turbulent charge transfer may be local electric field enhancement and local field reduction in clouds as the result of the large-scale motions of adjacent charged boundary layers.

It is believed that electroconvection is not a significant contributor to turbulent motion in thunderstorms. This conclusion appears valid based on the relative magnitudes of energy dissipation, a comparison of electrical and buoyancy forces in clouds, and an order-of-magnitude extrapolation from laboratory experiments.

REFERENCES

Brook, M., and B. Vonnegut, 1960: Visual confirmation of the junction process in lightning discharges. *J. Geophys. Res.* 65, 1302–1303.

Byers, H. R., 1965: *Problems of Atmospheric and Space Electricity.* New York, Elsevier pp. 314, 494.

——, and R. R. Braham, Jr., 1949: *The Thunderstorm.* U. S. Dept. of Commerce, Government Printing Office, Washington, D. C., p. 85.

Chalmers, J. A., 1967: *Atmospheric Electricity,* 2nd ed. Oxford, Pergamon Press, 515 pp.

Chapman, S., 1938: Carrier mobility of liquids electrified by bubbling. *Phys. Rev.*, 54, 494.

Reprinted with permission from Journal de Recherches Atmosphériques *V*, No. 2, 1971.

CRYSTAL DEVELOPMENT AND GLACIATION OF A SUPERCOOLED CLOUD

by

James E. JIUSTO

State University of New York, Albany, N. Y., U.S.A.

RÉSUMÉ

Un modèle numérique simple a été développé pour évaluer la croissance des cristaux de glace et le taux de glaciation des nuages surfondus en fonction de la vitesse du courant ascendant et de la concentration en noyaux glaçogènes. Les conditions choisies représentent au mieux les tempêtes de neige des Grands Lacs. Les données indiquent que, dans des circonstances typiques (courants ascendants $\leqslant$ *3 m/s), le givrage devient le mécanisme dominant de la croissance du cristal après seulement quelques minutes, et avec des concentrations en noyaux glaçogènes inférieures à quelques dizaines par litre, de la neige roulée devant se former par la suite. Avec des concentrations en noyaux dépassant 50 à 100 par litre, les nuages surfondus se congèlent rapidement (en moins de 15 minutes) avant qu'un givrage effectif puisse se produire. Alors qu'on pourrait ensuite s'attendre à des cristaux individuels qui grossiraient uniquement par diffusion de vapeur d'eau, les concentrations élevées en cristaux conduisent à une agrégation prononcée de flocons de neige. Le fait que des agrégats de flocons de neige s'observent dans la plupart des tempêtes d'hiver suggère l'existence de concentrations en cristaux bien supérieures à celles indiquées par les mesures de noyaux en chambre froide, et probablement l'existence de zones d'accumulation de cristaux dans les nuages. Il s'ensuit certaines implications concernant l'ensemencement des nuages.*

ABSTRACT

An unsophisticated numerical model was developed to estimate the growth of ice crystals and the glaciation rate of supercooled clouds as a function of updraft speed and ice nucleus concentration. The conditions chosen best represent Great Lakes snowstorms. The data indicate that under typical circumstances (updrafts $\leqslant$ *3 m/sec) riming becomes the dominant crystal growth mechanism after only a few minutes time, and with ice nucleus concentrations less than a few tens per liter, graupel will subsequently form. With nucleus concentrations in excess of 50—100* l^{-1}*, the supercooled clouds rapidly glaciate (*$<$ *15 minutes time) before substantial riming can take place. While one might then expect individual crystals that grow strictly by diffusion of water vapor, the high crystal concentrations lead to pronounced snowflake aggregation. The common occurrence of snowflake aggregates in most winter snowstorms suggest crystal concentrations well in excess of that indicated by cold-box nucleus measurements, and probably preferred cloud regions of high crystal congregation. Certain cloud seeding implications readily follow.*

I. INTRODUCTION.

The mathematical modeling of a mixed-phase cold cloud has not received attention comparable to that of warm clouds, although some partial formulations have been reported (e.g., Houghton [1], Jiusto [2], Podzimek [3], Cotton [4]). Adding to the complexity of these clouds are such factors as varied crystal geometry, associated variations in vapor diffusion fields and crystal fall velocity, and the uncertainties of collision relationships in crystal-droplet interactions (riming) and crystal-crystal interactions (snowflake aggregation). Yet such mixed-phase clouds probably represent the most general type at mid-latitudes, and certainly are basic to a number of weather modification concepts.

Often there are insufficient ice nuclei present to glaciate supercooled clouds. This is especially true of highly convective systems where the supply rate of water vapor can exceed the extraction rate by deposition onto available ice crystals. There is a critical ice-to-water ratio beyond which the cloud will completely glaciate in a given period of time. This ratio, which varies with cloud updraft intensity, temperature, and crystal size and type, is important in studying the development of natural and seeded clouds.

Twomey [5] and Todd [6] have expressed the critical ice concentration for complete glaciation of a cloud in terms of fixed values of liquid-water content. A general expression for the critical concentration was obtained (Jiusto [2], [7]) that accounted for the variable generation rate of water vapor in a cloud and the rate of extraction of vapor onto crystals of given type and size. The results obtained were useful in evaluating the relative importance of the three mechanisms of ice crystal growth diffusion, accretion of drops (riming), and snowflake aggregation during the evolution of a mixed cloud.

The key expression in this derivation was the standard equation for supersaturation change with time, dS/dt, in a cloud :

$$dS/dt = \varphi_1 u - \varphi_2 dm/dt, \tag{1}$$

where u is updraft intensity, dm/dt is condensation rate, and φ_1 and φ_2 are thermodynamic functions defined in the list of symbols (Appendix). It was shown that the specification dS/dt = 0 implied that all water vapor generated in an updraft would be consumed by growing ice crystals (or droplets). Thus, the mass of water produced by a given updraft could be determined, and this quantity divided by the rate of vapor extraction per given crystal to yield the concentration of crystals N_c required for complete cloud glaciation in some desired time interval :

$$N_c = \frac{dm/dt}{dm/dt}\ \frac{(\text{Supply})}{(\text{Extraction})} = \frac{\varphi_1 u/\varphi_2}{4\pi C G^{1} S_i \varphi_i} \tag{2}$$

Table I illustrates the nucleation requirements as a function of temperature indicated by a solution of equation (2) for an updraft of 0.5 m/sec and planar crystals of 0.1 mm radius. Note that the critical number of nuclei N_c is directly proportional to the updraft and can be readily adjusted for other values.

TABLE I

Critical concentration of ice nuclei (N_c) for complete cloud glaciation within ~ 5 minutes
(Updraft u = 0.5 m/sec)

T (°C)	φ_1/φ_2 (g cm^{-4})	Vapor supply dm/dt (g sec^{-1} cm^{-3})	Vapor extraction per crystal (0.1 mm r)	Critical ice nuclei N_c
5	1.285×10^{-11}	6.42×10^{-10}	1.9×10^{-9} g sec^{-1}	340 l^{-1}
10	1.045	5.23	2.9×10^{-9}	180
20	0.623	3.12	3.0×10^{-9}	105
30	0.323	1.62	1.9×10^{-9}	85
40	0.147	0.735	0.92×10^{-9}	80

The following work represents an extension of the above calculations with a numerical model that allows considerably greater variation of parameters. Notably, supersaturation changes in a mixed-phase cloud are determined as a function of ice nucleus concentration and the continuous interplay among the updraft, the growth of crystals, and the growth or evaporation of droplets.

II. — FORMULATION.

At this stage, the cloud model is single layered with constant temperature and uniform hydrometeor distribution. The goal was to realistically represent snow crystal morphology and cloud microphysics on a local scale before adding the complexities of spatial variations. Owing to the limited vertical development (< 3.5 km) of most Great Lakes snowstorms, this approach appears permissible. Also verification of seeding effectiveness in a NOAA field program (Weickmann et al. [8]) relied heavily on the size, type, and concentration of falling snow crystals, giving added impetus for stressing these variables in the numerical model.

Crystals are allowed to grow by diffusion of water vapor and by accretion of supercooled droplets, with the dominant growth mechanism being indicated by the model. A distinction is made between nonrimed crystals ; partially rimed crystals, where the initial crystal form (hexagonal plates and plane dendrites) is preserved ; and heavily rimed three-dimensional pellets (graupel). Two key input quantities are updraft intensity and concentration of ice nuclei, both being specified for a given run of, typically, 55-60 minutes of cloud development time. Ice nucleus concentrations of 1 l^{-1} to 1000 l^{-1} have been considered. Output variables as a function of time include : cloud saturation with respect to ice ; crystal type ; crystal mass, size, and fall velocity ; droplet size and cloud liquid-water content ; ice water content ; and total fall distance of crystals.

1°) *Equation set.*

The main equations used in the program are discussed below, with symbols defined there and/or in the Appendix. The c.g.s. system of units is used throughout unless otherwise indicated.

a) Cloud supersaturation.

Amplifying upon equation (1) to include both droplets (d) and crystals (c) in a mixed-phase cloud yields :

$$(dS_i/dt) = \varphi_1 u - \varphi_2 N_c (dm/dt)_c - \varphi_3 N_d (dm/dt)_d \qquad (3)$$

where S_i is supersaturation with respect to ice and N_c and N_d are the concentrations of ice crystals and cloud droplets respectively. Note that the third term on the right can be either positive or negative, depending on whether droplets are evaporating (vapor source) or growing (vapor sink). The latter occurs when the updraft is vigorous and the ice crystals are too few or growing too slowly to prevent supersaturation with respect to water.

b) Crystal growth by diffusion.

The mass growth of an ice crystal by diffusion of water vapor is given by the so-called classic equation :

$$(dm/dt)_c = 4 \pi C G' S_i \rho_I \qquad (4)$$

where C is the crystal shape factor, G′ a thermodynamic function accounting for latent heat and vapor diffusivity, and ρ_I the density of ice.

To convert from crystal mass to size (radius r_c) at any given point, the empirical relationships of Nakaya and Terada [9] were used. These are listed in Table II, along with values of the shape factor C assumed for each crystal type.

TABLE II

Crystal mass-size relationships and C values

Crystal habit	C	Mass vs. size
Planar unrimed	$2 r_c/\pi$	$r_c = (m_c/0.00152)^{1/2}$
Partially rimed	$0.8 r_c$	$r_c = (m_c/0.0108)^{1/2}$
Heavily rimed	r_c	$r_c = (m_c/0.52)^{1/3}$

c) Droplet evaporation (or growth).

The equation used for droplet growth by diffusion is that given by Fletcher [10] :

$$(dm/dt)_d = 4 \pi \rho_l G r_d \left(S - \frac{a}{r_d} + \frac{b}{r_d^3}\right), \qquad (5)$$

where ρ_l is the density of water, S the supersaturation with respect to water, a the Kelvin curvature term, and b the nucleus solubility term. It was assumed that droplets form on 0.1 μ radius sodium-chloride condensation nuclei.

d) Crystal growth by riming.

The rate of increase of mass m of a falling crystal by accretion of supercooled cloud droplets is commonly given by

$$(dm/dt)_R = \pi r^2_c E \omega (v_c - v_d), \qquad (6)$$

where r_c is the crystal radius, E the collection efficiency, ω the liquid water content, and $(v_c - v_d)$ the difference in fall velocity of crystal and collected droplets, respectively. (Droplet fall velocity $v_d \ll v_c$, and can be neglected).

Collection efficiencies of ice crystals for cloud droplets are not well known. A collection efficiency of 0.5 was assumed for disc type crystals (hexagonal plates, solid stellars) and an E of 1 for dendrites, where the capture cross-section area reduces to approximately $\pi r_c^2/2$. Based on the collection theory of Ranz and Wong [11] for discs and representative cloud drops of 10-20 μ, and dendrite collection estimates of Weickmann [12], these E values appear reasonable.

The conversion to partially rimed crystals is specified when the droplet accretion growth rate (eqn. 6) exceeds the vapor diffusion growth rate (eqn. 4) of the crystals. When the crystal mass equals an equivalent sphere radius of 1 mm (occurring approximately when the crystal c axis exceeds the a axis), graupel growth is assumed.

e) Fall velocity of crystals.

The fall velocity of unrimed planar crystals is taken as a constant 30 cm/sec, as given by Nakaya [13]. Based on the cited crystal-mass relationships and some measured velocity data of Langleben [14], the terminal velocity of riming crystals can be expressed [2] as

$$v_{cR} = 210\, r_c^{0.3} \text{ cm/sec.}$$

This expression appears quite valid for partially rimed crystals, but underestimates the fall velocity of graupel.

A number of other standard equations are used in the program. These include expressions for the cloud liquid water content, ice content, net vertical velocity and vertical displacement of crystals, and water vapor pressure.

2°) *Computer program.*

A fourth-order Runge-Kutta method was used to numerically solve the foregoing set of equations with a Univac 1108 computer. While the model is capable of generating a cloud from an initial updraft, the computations reported here are begun with an established supercooled cloud at water saturation. Then the effects of introducing given concentrations of ice nuclei are examined. The starting conditions for all the cases discussed in the next section are as follows :

$T = -20$ °C $\qquad N_d = 300$ cm^{-3}

$p = 800$ mb $\qquad r_d = 7\ \mu$

$S_1 = 21.5\ \%$ $\qquad \omega = 0.43$ g/m^3

III. - RESULTS.

Five ice nucleus concentrations ($N_c = 1, 10, 50, 100,$ and 1000 l^{-1}) were successively run for each specified updraft case. The low concentrations of 1 and 10 l^{-1} (and sometimes even 50 l^{-1}) are fairly representative of natural precipitating clouds while concentrations of 100 and 1000 l^{-1} simulate heavily seeded clouds. Nonprecipitating supercooled clouds can, of course, have ice nucleus concentrations substantially lower than 1 l^{-1}.

Four fixed updraft cases were treated ; 5 cm/sec, 20 cm/sec, 1 m/sec, and 3 m/sec. One might think of these values as representing average updraft conditions in winter cloud types varying from weak stratus to vigorous cumulus clouds. In a given intense Great Lakes snowstorm, all these values can and do occur.

Based on calculations of precipitation rate for given updrafts, it is felt that an overall average value of 0.5 m/sec represents quite well the typical Great Lakes snowband. For example, with such an updraft and an average cloud temperature of —15 °C, Table I predicts a cloud-water generation rate of 4.18×10^{-10} g/sec cm^3. Assuming a cloud depth of 3 km and that 50 % of the condensate falls out as precipitation, this yields a precipitation rate of 0.226 g/cm^2 hr, which translates to a snowfall rate of approximately 1 to 3 inches per hour -- commonly measured values in these intense snowstorms. Thus the updraft values chosen for the model seemingly bracket quite well average lake storm conditions. The 3 m/sec updraft case would apply best to buoyant turrets in the narrow core of an intense storm cell.

The time history of cloud supersaturation and liquid water content are shown in Figures 1 through 3 as a function of updraft and ice nucleus concentration. Also shown on the supersaturation traces are the times when crystals (which initially grow strictly by diffusion of water vapor) commence to partially rime (P) and then heavily rime (R). If sufficient crystals are present, a return to strict vapor diffusion growth (D) may occur as the cloud glaciates.

Examining the figures, it is evident that one ice nucleus per liter of air is not adequate to glaciate the model cloud even in a weak updraft of 5 cm/sec (extending the time to 60 minutes produced little change). A crystal concentration of 10 l^{-1} will consume all the cloud liquid water in approximately 20 to 55 minutes, depending on updraft strength. Complete cloud glaciation occurs in approximately 8 to 12 minutes for $N_c = 100$ l^{-1}, and in 3-5 minutes for $N_c = 1000$ l^{-1}.

It should be noted that the model does not presently account for droplet population decreases by riming. While it can be argued that new drops are constantly being generated in the updraft, these neophyte droplets would not be as large as those lost through riming. Hence, this model deficiency tends to exaggerate cloud liquid water (and riming) in some cases. Clearly it causes no error when $N_c = 1000$ l^{-1} and riming never occurs, and only slight water exaggeration in the low updraft cases of 5 and 20 cm/sec. For the 1 and 3 m/sec updraft cases and intermediate N_c values of 10-100 l^{-1}, the glaciation times noted should be considered conservative.

Figures 1 and 2 indicate that light riming in the model cloud commences in about 2 minutes almost independent of updraft strength and crystal concentration ($\leq$ 100 l^{-1}). For example, the onset of riming occurs at 1.7 minute when $u = 3$ m/sec and about 2.6 minutes when $u = 5$ cm/sec. Thus, some light riming of crystals in clouds of such liquid water content is to be expected and theoretically, if perhaps not practically, can be avoided only by seeding with massive concentrations of ice nuclei.

Heavy riming to the graupel stage, however, can be avoided with ice nucleus concentrations of about 50 l^{-1} for updrafts up to 1 m/sec and 100 l^{-1} for 3 m/sec updrafts. The onset time of heavy riming, if it is to occur at all, and its cessation time vary considerably with updraft strength and crystal concentration.

For comparison purposes, certain model output parameters are listed in Table III after 30 minutes of cloud development time, a reasonable lifetime for a given cloud cell. The data trends are probably more useful than the absolute numerical values, owing to the specification of realistic but singular initial cloud conditions and to model limitations. Some of the relevant items that might be pointed out are as follows :

a) Crystal sizes predicted by the model for updrafts $u \leq 100$ cm/sec and natural cloud crystal concentrations of 1-10 l^{-1} are approximately 2 to 4 mm in size. This is consistent with our field measurements of single crystals in natural storms.

b) N_c must be increased by about three orders of magnitude to decrease crystal

TABLE III

Cloud model variables after 30 minutes

(Model cloud : T = —20 °C, p = 800 mb ; initial conditions, $S_i = 21.5$ %, $\omega = 0.43$ g/m^3)

	Ice crystal concentration N_c (l^{-1})				
	1	10	50	100	1000
a) u = 5 cm/sec					
Crystal type	Graupel	Rimed C.	Rimed	Ligth rime	Unrimed
Crystal radius (mm)	1.7	1.6	1.0	0.5	0.20
Drop radius (μ)	6.9	0	0	0	0
Liquid water (g/m^3)	0.41	0	0	0	0
Supersaturation-ice (%)	21.5	0.4	0.3	0.2	0.1
Crystal fall velocity (cm/sec)	210*	133	94	84	30
Riming to diffusion (min)	—	22	11	8	D only
b) u = 20 cm/sec					
Crystal	Graupel	Graupel	Rimed	Light rime	Unrimed
r_c (mm)	1.8	1.6	1.1	0.6	0.23
r_d (μ)	7.7	0	0	0	0
ω (g/m^3)	0.58	0	0	0	0
S_i (%)	21.5	5.0	0.9	0.8	0.3
v_T (cm/sec)	220*	210*	97	84	30
R→D (min)	—	27	11	8	D only
c) u = 100 cm/sec					
Crystal	Graupel	Graupel	Rimed	Rimed	Unrimed
r_c (mm)	2.6	1.9	1.3	1.0	0.32
r_d (μ)	10.4	8.0	0	0	0
ω (g/m^3)	1.44	0.63	0	0	0
S_i (%)	21.6	21.5	2.1	2.3	1.2
v_T (cm/sec)	260*	230*	113	94	30
R→D (min)	—	51	15	10	D only
d) u = 300 cm/sec					
Crystal	Graupel	Graupel	Graupel	Rimed	Unrimed
r_c (mm)	5.7	4.4	1.5	2.0	0.48
r_d (μ)	14.2	12.0	0	0	0
ω (g/m^3)	3.61	2.19	0	0	0
S_i (%)	21.7	21.5	2.2	2.1	2.3
v_T (cm/sec)	>400*	>300*	200*	126	30
R→D (min)	—	56	22	12	D only

* Velocities from Nakaya [13] graupel data.

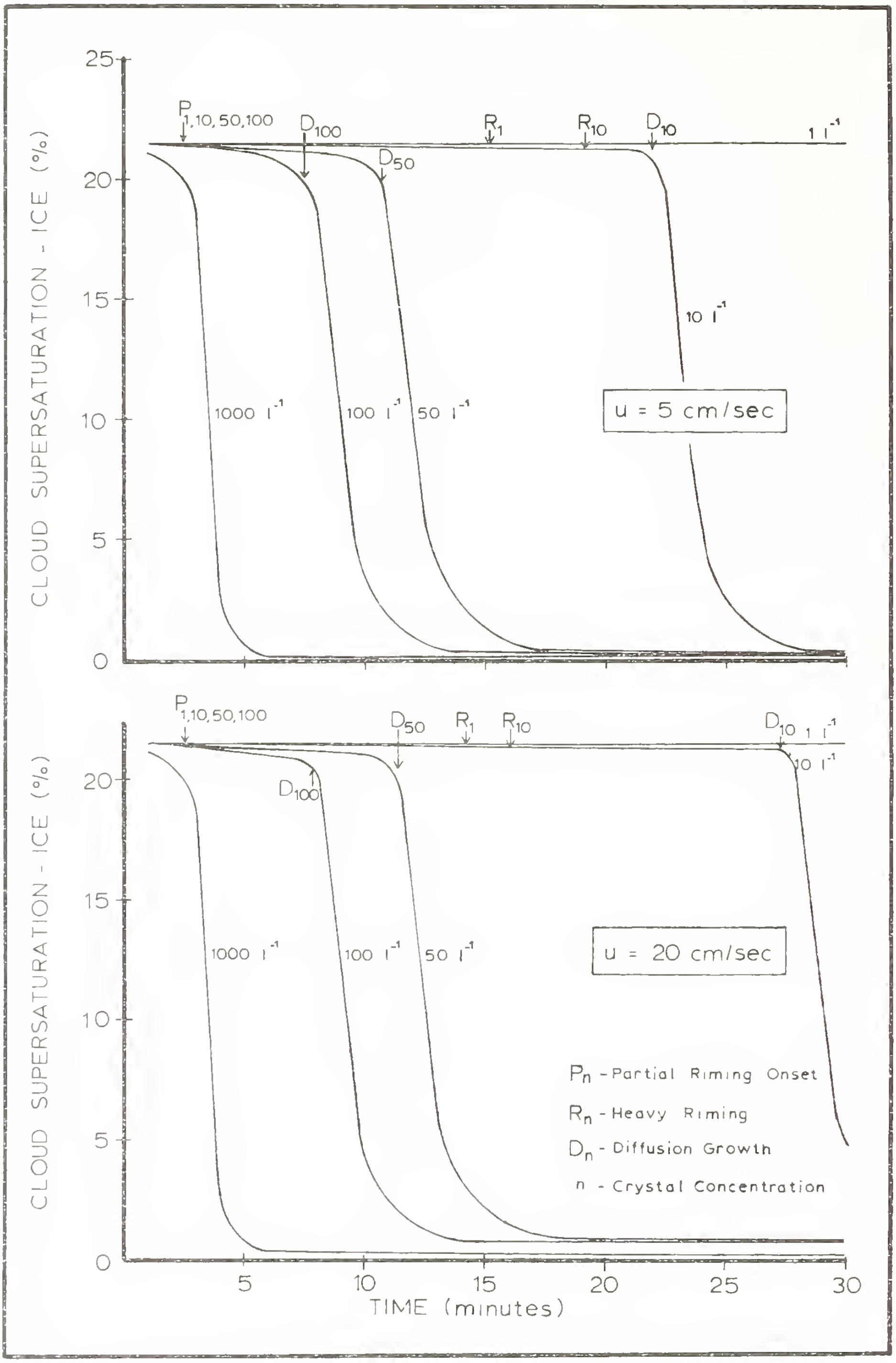

FIG. 1. — Cloud supersaturation (ice) vs. crystal concentration N_c and time (model cloud — 5 and 20 cm/sec updraft cases).

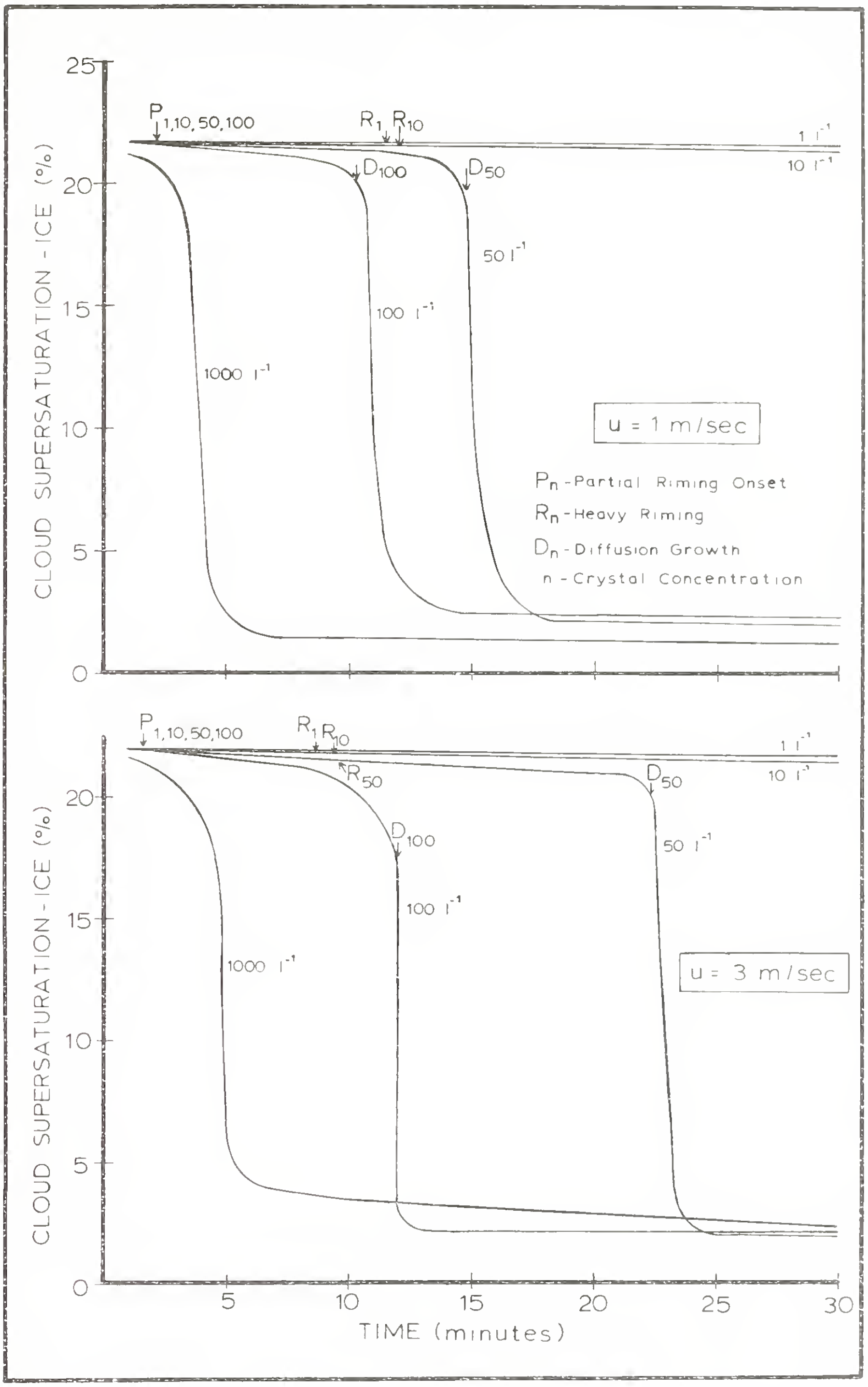

FIG. 2. — Cloud supersaturation (ice) vs. crystal concentration N_c and time (model cloud — 1 and 3 m/sec updraft cases).

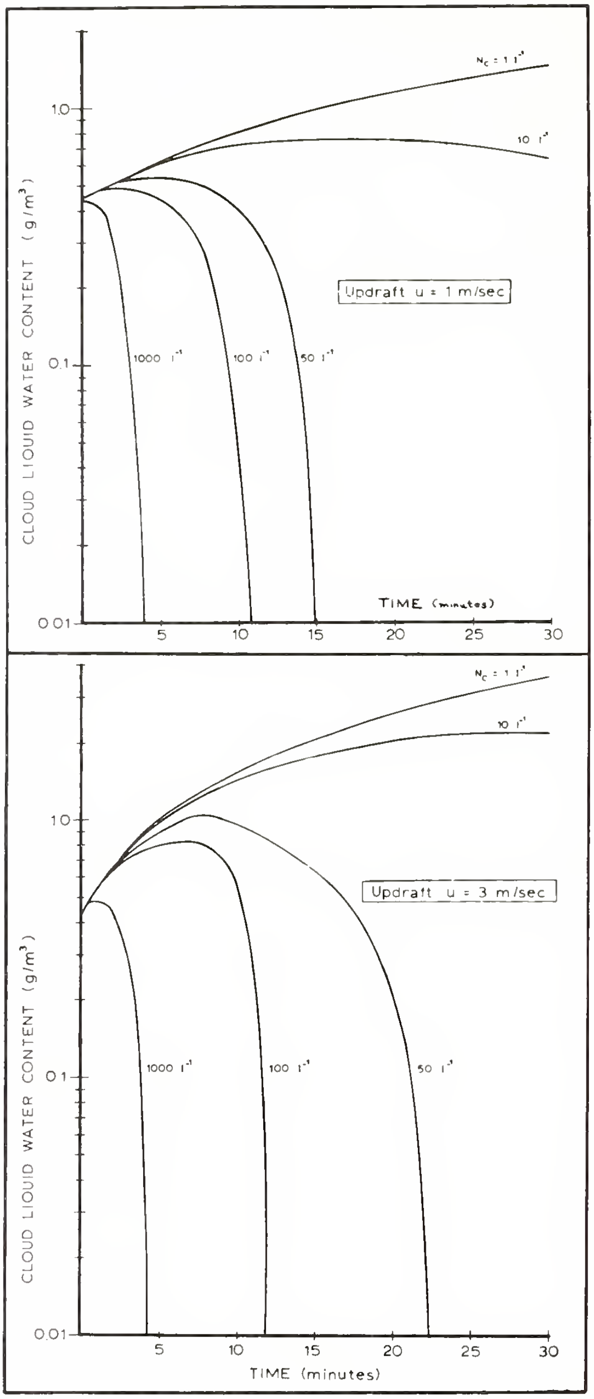

FIG. 3. Cloud liquid water vs. crystal concentration N_c and time (model cloud – 1 and 3 m/sec updraft cases).

size by one order of magnitude. The largest nucleus concentrations (1000 l^{-1}) limit individual planar crystals to approximately 0.4 to 1 mm sizes.

c) The data suggest that a seeding concentration of the order of 100 l^{-1}, while not capable of suppressing light riming, will reduce the fall velocity of crystals by a factor of 2 to 3 over graupel pellets. The restriction of fall velocities to 30-50 cm/sec, characteristic of unrimed planar crystals, suggests massive seeding concentrations of the order of several 100 to 1000 l^{-1}.

Note that the critical concentrations given simply by Equation (2) and Table I are roughly comparable to these more detailed model estimates.

Table IV lists the approximate time and cloud layer thickness required for the formation of graupel of 1 mm radius. Again, the initial cloud model conditions of Section II 2°) were assumed. Note that the stronger the updraft, the less is the time required for graupel to form. This is due to the corresponding increase in cloud liquid water and, hence, increase in crystal riming rate as the updraft becomes more intense.

Of particular interest is the fact that the required cloud layer thickness can be as shallow as about 0.18 km, which occurs with updrafts of 1 m/sec. Such updraft magnitudes correspond rather closely with the terminal fall velocity of partially rimed crystals so that a growing crystal remains relatively « stationary » with respect to the ground. It is also evident from the table that ice nucleus concentrations of 50-100 l^{-1} can prevent the formation of graupel.

TABLE IV

Required cloud layer depth (km) and time (min) for graupel (r = 1 mm) formation

(Model cloud conditions of section II 2°)

Updraft	Ice nucleus concentration N_c (l^{-1})			
	1	10	50	100
u (cm/sec)	km (min)	km (min)	km (min)	km (min)
5	0.70 (15.2)	0.96 (19.2)	*	*
20	0.51 (14.2)	0.62 (16.0)	*	*
100	0.18 (11.4)	0.18 (11.9)	*	*
300	1.17 (8.7)	1.20 (8.9)	1.30 (9.6)	*

* Graupel does not form.

Thus far we have not considered the implications of crystal aggregation on the cloud development process. As will be shown in the following section, high concentrations of ice nuclei lead to enhanced crystal aggregation and snowflake fall velocities of 1-1.5 m/sec. In terms of merely glaciating the cloud, the model predictions indicate that the nucleus concentrations of 100 l^{-1} will do almost as well as 1000 l^{-1} except that a bit more time is needed (4 to 8 minutes). Conversely, the extreme concentration conceivably could produce snowflakes with a higher fall velocity than individual lightly rimed crystals (see Table III velocity values.) In a practical sense, then, there appears to be little virtue in attempting to seed Great Lakes snowstorms with nucleus concentrations greater than 100 l^{-1} or so.

If the goal merely is to stimulate snowfall in nonprecipitating supercooled clouds, the model suggests that nucleus concentrations of 1-10 l^{-1} will suffice.

IV. — SNOW CRYSTAL AGGREGATION.

Snow crystal aggregation — even in the absence of seeding — is very common in lake storms, increasing in importance as ambient temperature decreases and as inland distance increases. In general, it appears that in the north-eastern United States, snowflake aggregates constitute the most common type of snowfall. Dendritic crystals, formed at temperatures near —15 °C and humidities close to water saturation, favor the aggregation process as probably does some light riming of these crystals. Field observations of snowflakes invariably revealed dendritic forms with sometimes hundreds of crystals per cm-size snowflake.

Snow crystal concentrations measured at ground level often ran high, i.e., tens per liter of air. Freezing nucleus concentrations at —18 to —20 °C were at least an order of magnitude lower. This not uncommon paradox in clouds has been reviewed by Mossop [15].

Explanations for the discrepancy usually invoke some type of droplet splintering mechanism (Koenig [16], Hobbs [17]), cirrus seeding of lower cloud layers (Braham [18]), or doubts as to the relevance of cold box measurements of ice nuclei. Another mechanism, that of an accumulation of crystals within the cloud where they are approximately balanced by the updraft, is rather appealing, at least for lake storm bands. Also appealing is some type of crystal fragmentation process. The common occurrence of snowflake aggregates requires a mechanism whereby high concentrations of crystals are produced within a cloud.

1°) *Snow crystal congregation.*

The idea of storage or accumulation of water in excess of the moist adiabatic production in certain restricted regions of a warm cloud is by no means new. Such observations have been reported by Weickmann and aufm Kampe [19], Battan and Reitan [20], and others. Warner and Squires [21] concluded that these somewhat rare observations would have to be restricted to layers almost negligible in size by comparison with the cloud as a whole. Squires [22] also inferred that such water accumulation could only be explained by selective droplet sedimentation that enriched some parts of the cloud. Gokhale and Rao [23], with an idealized physical model of a thunderstorm, argue that water accumulation is likely in the upper portion of the cloud where settling drops are balanced as they descend into layers of stronger updrafts.

Recognizing that the foregoing observations and interpretations are not universally accepted, it is suggested that *if* some updraft balance-type mechanism possibly can operate in convective warm clouds to explain large liquid water concentrations, it is more than likely to occur in cold clouds to produce high crystal concentrations. The conditions for ice crystal congregation appear far more favorable as reasoned by the following :

a) The terminal fall velocities of ice crystals comprise a much narrower spectrum than water droplets. Most ice crystals possess fall velocities less than 1.5 m/sec, with the average likely between 0.5 and 1.0 m/sec.

b) Average updrafts in these lake storm bands (and probably many winter snow clouds), as inferred from precipitation rate computations, closely coincide with typical crystal fall velocities. In intense cloud cores, more vigorous updrafts carry the crystals to the upper cloud levels.

c) One implication of *a*) and *b*) seems rather obvious — a substantial percentage of the ice crystal population could become concentrated in certain (probably upper) cloud layers to facilitate snowflake aggregation. (Lateral divergence would obviously tend to dilute crystal concentrations).

d) The occurrence of large snowflakes mathematically precludes (section IV 2°) a homogeneous distribution of ice crystals of say 0.01 to 1 l^{-1}, as suggested by ice nucleus measurements.

e) While observations of large water accumulations in warm clouds are rare, high crystal concentrations in cold clouds and at the ground appear common.

Crystal fragmentation by collisions with droplets and other crystals must account for some of the observed high crystal concentrations, as might the sublimational break-up of crystals suggested by Schaefer and Cheng [24]. Large numbers of crystal fragments are observed in some lake storms ; in one case, 80 % of the replicated crystals consisted of fragments (Jiusto and Holroyd [25]). Supercooled drop splintering also must occur to some extent in clouds, but the difficulty of duplicating this phenomenon in the laboratory tends at present to make one skeptical of its common occurrence in the atmosphere. Further the cold temperature of typical lake storm clouds results in small droplets less likely to shatter.

2°) *Snowflake aggregation rates.*

The collision rate (dC_o/dt) of a snowflake falling through a population of individual crystals can be expressed as,

$$(dC_o/dt) = \pi\, r_f^2\, E\, N_c\, (v_f - v_c), \tag{8}$$

where r_f is the radius of the flake, N_c the concentration of individual ice crystals in the cloud, and v_f and v_c the fall velocity of flake and crystals, respectively.

Derived equations (Jiusto and Holroyd [25]) for the terminal fall velocity v_f of snowflakes, and of flake radius r_f as a function of crystal concentration n_c per flake and individual crystal radius r are as follows :

$$v_f = 150\, r_f^{0.2}, \tag{9}$$

$$r_f = 0.25\, n_c^{1/2}\, r. \tag{10}$$

These equations permit, with some simplifying starting assumptions, an estimation of crystal aggregation rates and the size and velocity changes of falling snowflakes. It was assumed that a three-crystal snowflake initially existed, that $v_c = 30$ cm/sec, and $E = 1$. The equation set was then solved numerically for the following cloud crystal concentrations (N_c) and fixed crystal sizes (r) :

a) $N_c = 1, 10\ l^{-1}$ $r = 1$ mm
b) $N_c = 10, 50, 100\ l^{-1}$ $r = 0.5$ mm
c) $N_c = 100\ l^{-1}$ $r = 1.0$ mm
d) $N_c = 1000\ l^{-1}$ $r = 0.2$ mm

Cases a) and b) represent conditions predicted by the microphysics model after about 10 minutes of cloud development time in updrafts varying from 5 cm/sec to 1 m/sec. Case c) represents crystal growth in an extreme 3 m/sec updraft while case d) is intended

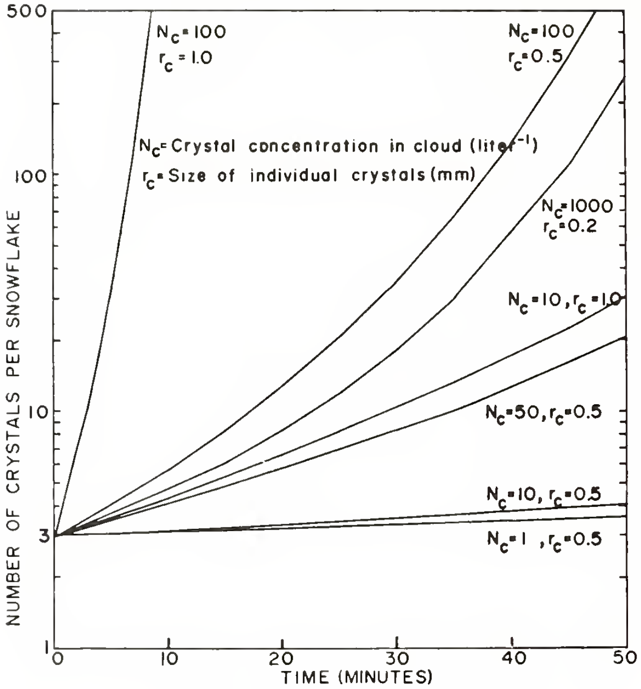

Fig. 4. — Snowflake aggregation rates (preliminary model).

to simulate a NOAA overseeding experiment of 7 December 1968, in which cloud properties and crystal type and sizes were reported (Holroyd and Jiusto [26]) to change in the manner predicted by the microphysics model.

Figure 4 shows the degree of aggregation predicted in each case, expressed as the number of crystals per snowflake with time. A fixed population of cloud crystals was assumed in this first-approximation calculation. Without a depletion term, the results tend to exaggerate aggregation. Nevertheless, certain informative points emerge, as follows :

a) with cloud crystal concentrations of 1 l^{-1}, aggregation is slight to nonexistent ;

b) the same is true for concentrations of 10 l^{-1} until individual crystal sizes reach radii of 1 mm or so ;

c) with crystal concentrations of about 50 l^{-1} or more, aggregation is apparently the dominant growth mechanism overshadowing riming and diffusion growth ;

d) the simulated overseeding case ($N_c = 1000\ l^{-1}$) shows crystal aggregation values after 30 minutes that are quite compatible with those observed (several tens to several hundreds of crystals per snowflake).

V. — Summary.

The relatively simple microphysics model presented enables one to evaluate the respective importance of crystal growth by diffusion, riming, and snowflake aggregation. With clouds of the type involved in Great Lakes snowstorms (i.e., $\omega \simeq 0.5 - 1$ g/m^3 ; u $\simeq$ 3 m/sec), certain generalizations appear valid :

a) Crystal concentrations of only 1 l^{-1} are not sufficient to glaciate these clouds. Even with 10 l^{-1}, riming is the dominant growth mechanism leading to the formation of graupel in times as short as 8 minutes (and cloud layer depths as shallow as 180 m).

b) Ice nucleus concentrations in the neighborhood of 100 l^{-1} will prevent graupel and quickly glaciate a cloud but some crystal riming still is to be expected. Massive seeding of several 100 to 1000 nuclei per liter is needed to completely eliminate riming.

c) Snowflake aggregation becomes the dominant growth mechanism when crystal concentrations exceed about 50 l^{-1}. Hence, massive cloud seeding which formerly was felt might stabilize clouds, will only succeed in accentuating aggregation (and in producing snowflakes that precipitate at about 1 m/sec).

d) The common observation of snowflake aggregates in the north-eastern United States suggests regions within clouds where high concentrations of individual crystals congregate. An updraft balance mechanism appears reasonable. Crystal fragmentation within a mixed phase cloud involving dendritic forms could considerably enhance concentrations, as might also in rare cases the often speculated but tenuous droplet shattering.

ACKNOWLEDGMENTS.

This work was sponsored by the National Oceanic and Atmospheric Administration (Atmospheric Physics and Chemistry Laboratory) under Grants E22-13-69 (G) and E22-49-70. Substantial support was also received from the State University of New York at Albany. Mr. Richard Schmitt, of the latter organization, did all of the computer programming of the microphysics model. Gratitude is also expressed for contributions made by Mr. Edmond Holroyd of SUNY and Dr. Helmut Weickmann of NOAA.

*

REFERENCES

[1] Houghton H.G. (1950). — A preliminary quantitative estimate of precipitation mechanisms. *J. of Met.*, 7, p. 363.

[2] Jiusto J.E. (1967). — Nucleation factors in the development of clouds. Ph.D. Dissertation, Penn. State Univ., 124 p.

[3] Podzimek J. (1969). — Le modèle théorique d'un nuage de précipitation. *Ann. Ist. Univ. Navale di Napoli*, XXXVII, 12 p.

[4] Cotton W.R. (1970). — A numerical simulation of precipitation development in supercooled cumuli. Rep. n° 17, to Nat. Sc. Foundation, NSF Grant GA-13818, Dept. of Meteor., Penn. State Univ., 178 p.

[5] Twomey S. (1958). — Quantitative aspects of seeding rates for use in supercooled clouds. *Bull. Obs. Puy de Dôme*, n° 2, p. 33.

[6] Todd C.J. (1964). — A system for computing ice phase hydrometeor development. Meteorology Research Inc., Rep. ARG 64 Pa.-121.

[7] Jiusto J.E. (1968). — Snow crystal development in supercooled clouds. Proc. 1st Nat. Conf. on Weather Modification, Albany, Am. Met. Soc., p. 287.

[8] Weickmann H.K., Jiusto J.E., McVehil G.E., Pilie R.J. and Warburton J. (1970). — The Great Lakes Project. Proc. 2nd Nat. Conf. on Weather Modification, Santa Barbara, p. 34.

[9] Nakaya U. and Terada T. (1934). — Simultaneous observations of the mass, falling velocity and form of individual snow crystals. *J. Fac. Sci. Hokkaido Univ.*, Ser. II, 1, p. 191.

[10] Fletcher N.H. (1962). — The physics of rainclouds. Cambridge Univ. Press, 386 p.

[11] Ranz W.E. and Wong J.B. (1952). — Impaction of dust and smoke particles on surface and body collectors. *Industr. and Engineering Chem.*, 44, p. 1371.

[12] Weickmann H.K. (1957). — A nomogram for the calculation of collision efficiencies. Proc., Artificial Stimulation of Rain, Pergamon Press, p. 161.

[13] Nakaya U. (1954). — Snow crystals, natural and artificial. Harvard Univ. Press, 510 p.

[14] Langleben M.P. (1954). — The terminal velocity of snowflakes. *Q.J.R.M.S.*, 80, p. 174.

[15] Mossop S.C. (1970). — Concentrations of ice crystals in clouds. *Bull. Am. Met. Soc.*, 51, n° 6, p. 474.

[16] Koenig L.R. (1963). — The glaciating behavior of small cumulonimbus clouds. *J. Atm. Sc.*, 20, p. 29.

[17] Hobbs P.V. (1969). — Ice multiplication in clouds. *J. Atm. Sc.*, 26, p. 315.

[18] Braham R.R., Jr. (1967). — Cirrus cloud seeding as a trigger for storm development. *J. Atm. Sc.*, 24, p. 311.

[19] Weickmann H.K. and aufm Kampe H.J. (1953). — Physical properties of cumulus clouds. *J. of Met.*, 10, p. 204.

[20] Battan L.J. and Reitan C.H. (1957). — Droplet size measurements in convective clouds. In : Artificial stimulation of rain, ed. H.K. Weickmann and W. Smith, Pergamon Press.

[21] Warner J. and Squires P. (1958). — Liquid water content and the adiabatic model of cumulus development. *Tellus*, 10, p. 390.

[22] Squires P. (1962). — The dynamics of clouds. In : The physics of rainclouds, N. Fletcher, Cambridge Univ. Press, p. 1.

[23] Gokhale N.R. and Rao K.M. (1969). — Theory of hail growth. *J.R.A.*, IV, 1re année, n° 4, p. 153.

[24] Schaefer V.J. and Cheng R.J. (1971). — The production of ice crystal fragments by sublimation and electrification. *J.R.A.*, V, n° 1, p. 5.

[25] Jiusto J.E. and Holroyd E.W. (1970). — Great Lakes snowstorms — Part 1 : Cloud physics aspects. ASRC, State Univ. of New York at Albany, ESSA Grant n° E22-49-70, 142 p.

[26] Holroyd E.W. and Jiusto J.E. (1971). — Snowfall from a heavily seeded cloud. *J. Appl. Met.*, 10, n° 3, p. 266.

*

[*Reçu le* 13 *avril* 1971]

APPENDIX — LIST OF SYMBOLS

a	droplet curvature term ($a = 3.3 \times 10^{-5}/T$)
b	droplet solubility term ($b = 4.3\ i\ m_s/M_s$)
c_p	specific heat of air at constant pressure
C	crystal shape (capacitance) factor ; degrees centrigrade
C_o	number of collisions of falling snowflake with ice crystals
D	diffusivity of water vapor
e	vapor pressure of the environment
E	collection efficiency of a falling hydrometeor
f	subscript denoting snowflake
g	gravitational acceleration ; or subscript denoting graupel
G	thermodynamic function in drop growth equation

$$G = \frac{D\rho_v}{\rho_l}\left[1 + \frac{DL^2\ \rho_v\ M_o}{RT^2\ \varkappa}\right]^{-1}$$

G'	thermodynamic function in ice crystal growth equation (like G above except ρ_v, ρ_l, and L are replaced by ρ_{vi}, ρ_i, and L_s, respectively)
i	van't Hoff factor ; or size interval
L, L_s	latent heat of condensation, and of sublimation
m	mass
M_a, M_o, M_s	molecular weight of air, water vapor, and soluble condensation nucleus, respectively
n_c	number of crystals per snowflake aggregate
N_c, N_d	concentration of ice crystals, and of cloud droplets, per unit volume of air
p	atmospheric pressure
r_c, r_d, r_f	radius of crystal, droplet, and snowflake, respectively
R	universal gas constant ; or subscript denoting riming
S, S_i	supersaturation with respect to water, and ice
t	time
T	temperature
u	updraft velocity
v, v_T	fall velocity (often with a subscript denoting object)
$\varkappa$	thermal conductivity of air
ρ_{air}, ρ_f	density of air, and of a snowflake
ρ_i, ρ_l	density of ice, and of water
ρ_v, ρ_{vi}	saturation vapor density over water, and over ice
$\varphi_1, \varphi_2, \varphi_3$	thermodynamic functions in supersaturation equation (3)

$$\varphi_1 = \frac{g}{RT}\left[\frac{L\ M_o}{T\ c_p} - M_a\right]$$

$$\varphi_2 = \frac{L_s{}^2\ M_o}{T\ p\ M_a\ c_p} + \frac{RT}{M_o\ e}$$

φ_3 : like φ_2 except L_s is replaced by L

ω	liquid water content of cloud

U.S. DEPARTMENT OF COMMERCE
National Oceanic and Atmospheric Administration
Environmental Research Laboratories

NOAA Technical Memorandum ERL APCL-12

BASIC THEORY AND PILOT EXPERIMENTS TO THE PROBLEM OF TRIGGERING LIGHTNING DISCHARGES BY ROCKETS

H. W. Kasemir

Atmospheric Physics and Chemistry Laboratory
Boulder, Colorado
April 1971

TABLE OF CONTENTS

Page

ABSTRACT iv

ABBREVIATIONS AND SYMBOLS v

1. ELECTROSTATIC THEORY OF THE CHARGED ROCKET PENETRATING A THUNDERCLOUD 1
    - 1.1 The Charged Rocket 1
    - 1.2 The Uncharged Rocket in the External Field F 7
    - 1.3 The Charged Rocket in the External Field F 13
    - 1.4 Simulation of a Large Rocket By a Small Rocket With a Trailing Wire 22
2. EXPERIMENTAL TESTS 25
3. THE LIGHTNING TOWER 33
4. RECOMMENDED RESEARCH AND DEVELOPMENT 37
    - 4.1 FFAR Firings at Socorro and KSC 38
    - 4.2 Use of Larger Rockets 39
    - 4.3 Dropsondes 39
    - 4.4 Determination of the Electric Charge of the Apollo Rocket in Flight 40
5. REFERENCES 42

ABSTRACT

The objective of this contract was to determine the feasibility of discharging electrified clouds with triggered lightning. As a first step towards this goal, the conditions have been calculated under which lightning may be triggered by different types of rockets. For instance the breakdown field value is reached at the tip of the Apollo-Saturn V rocket in a cloud field of about 10 kV/m, whereas a cloud field of about 125 kV/m is necessary to produce breakdown field at the folding fin aircraft rocket Mighty Mouse tipped with a trigger sphere of about 3.5 cm radius. The field concentration factor η at the tip of the rocket which augments the external cloud field to the field at the rocket tip is a function of the ratio of the length of the rocket a to the radius of curvature at the tip ρ. In the case of the Apollo rocket, $a/\rho = 1000$ and in the case of the Mighty Mouse rocket, $a/\rho = 34$, with $a = 120$ cm and $\rho = 3.5$ cm. To simulate the Apollo by the Mighty Mouse rocket, it is necessary either to increase the length a or decrease the radius of curvature ρ of the Mighty Mouse rocket in such a way that $a/\rho = 1000$. This leads to $a = 35$ m or $\rho = 1.2$ mm. It is shown in section 1.4 that the length a may be further reduced to about 26 m. The radius of curvature ρ determines the type of discharge. For $\rho > 2$ cm the discharge will be in the form of a spark and for $\rho < 2$ cm in the form of corona discharge. The corona current is a function of the electric field strength. Using the corona current on a sharp needle as a field indicator, an instrument has been designed (measuring payboard) which can be attached to the Mighty Mouse rocket [L. H. Ruhnke, 1971]. This instrument measures and transmits to ground the electric field values along the rocket path.

U.S. DEPARTMENT OF COMMERCE
National Oceanic and Atmospheric Administration
Environmental Research Laboratories

NOAA Technical Memorandum ERL APCL-11

CALIBRATION OF ATMOSPHERIC ELECTRIC FIELD METERS AND THE DETERMINATION OF FORM FACTORS AT KENNEDY SPACE CENTER

H. W. Kasemir

Atmospheric Physics and Chemistry Laboratory
Boulder, Colorado
April 1971

TABLE OF CONTENTS

Page

1. INTRODUCTION 1

2. THE DIFFERENT CALIBRATION DEVICES 2
   - 2.1 The Plate Condenser in General 4
   - 2.2 The KSC Plate Condenser 18
   - 2.3 The Sweeney Calibration Plate 43
   - 2.4 Calibration With a Charged Wire 49

3. DETERMINATION OF THE FORM FACTORS AT THE DIFFERENT FIELD SITES IN THE KSC AREA 52

4. APPENDIX 62

5. RECOMMENDATIONS 80

6. ACKNOWLEDGEMENT 87

7. REFERENCES 88

ABSTRACT

Eight potential gradient meters have been installed in the Kennedy Space Center area to monitor the buildup of the atmospheric electric field during the formation of shower and thunderclouds. It is necessary to calibrate these instruments at the different locations in absolute units (kV/m) if the lightning danger during the launch of larger rockets is to be determined. An official standard procedure for the calibration of field or potential gradient meters does not exist. Therefore there is widespread confusion about the size and construction of adequate calibration devices and the accuracy which can be achieved. It is the main objective of this report to determine the design criteria of a plate condenser which permits the absolute calibration of instruments of different sizes with an accuracy of better than 5 percent, to explain the errors of the present calibration procedure and to determine the correction factors. The correction factor of the KSC plate condenser was found to be 0.4.

No further correction is required if the instrument is placed on flat ground at the field site far enough away from telephone poles, power lines, buildings or other field-distorting objects. However, as this is not the case at the location of any of the instruments in the KSC area, the local form factor has been determined for each individual instrument. These form factors range from 0.08 to 1.1. They have been combined with the calibration correction factor and are listed as reduction factors in table 1 of this report for each field site. With these reduction factors the field records of the Sweeney network during the APOLLO 12 launch have been reevaluated. The maximum field values reduced to a plane surface before the launch are ± 4 kV/m, during launch ± 3 kV/m, and after

launch +3.7, -1.5 kV/m. These values indicate an upper limit of about ± 3 kV/m for a definite lightning hazard during the launch of larger rockets. However, it should be emphasized that these values cannot be used to determine the threshold value of the field for safe cloud penetration. We can say that this threshold value should be lower than ± 3 kV/m but not how much lower. To determine this threshold value, a much more extensive study and a more elaborate measuring network would be necessary. Recommendations for such a study and such a network are given at the end of this report.

Sonderdruck aus
„Meteorologische Rundschau" 25. Jahrgang, 2. Heft, 1972
Seite 33—38

© by Springer-Verlag 1972
Printed in Germany

The Cylindrical Field Mill*

H. W. Kasemir
Boulder, Colorado

Summary. A field-mill-type instrument is described which is especially suited to recording the atmospheric electric field from an airplane. The instrument measures the two components of the electric fields vertical to its axis and rejects the component in the direction of the axis. This feature can be used to eliminate the influence of the airplane charge on the measurement of the atmospheric electric field so that weak fields down to the order of 2 volts per meter can be recorded. Furthermore, each cylindrical field mill delivers two components of the electric field so that only two field mills of the cylindrical type are required to obtain all 3 components of the atmospheric electric field. Problems involving the correct places for mounting the field mills on the plane and the determination of the calibration factor are discussed. A brief analysis of the field records is given for the simple case of an electric charge of one sign in different positions to the airplane path. Ways are pointed out to either avoid strong electric fields during the flight or locate and penetrate thern.

Zusammenfassung. Es wird eine Feldmuhle beschrieben, die zur Messung des elektrischen Felds der Atmosphare vom Flugzeug aus entwickelt wurde. Das Gerat mißt die beiden Komponenten des elektrischen Felds senkrecht zu seiner Achse und berucksichtigt nicht die Komponente in Richtung der Achsen. Diese Tatsache kann benutzt werden, um den Einfluß der Ladung des Flugzeugs auf das elektrische Feld der Atmosphare auszuschalten, und damit konnen schwache Felder bis herab zu 2 V m registriert werden. Da weiterhin jede zylindrische Feldmuhle zwei Komponenten des elektrischen Felds mißt, konnen mit zwei Feldmuhlen alle 3 Komponenten in der Atmosphare erfaßt werden. Es werden die Fragen diskutiert, die sich aus der Anbringung der Feldmuhle am Flugzeug und aus der Eichung ergeben. Eine kurze Analyse von Feldmessungen fur den einfachen Fall einer elektrischen Ladung eines Vorzeichens an verschiedenen Punkten des Flugwegs wird gegeben. Moglichkeiten werden angegeben, um entweder starke Felder wahrend eines Flugs zu vermeiden oder sie zu orten und zu durchfliegen.

1. Introduction

In general the field mill is a device that measures a surface charge density q. The surface charge density is proportional to the electric field E on that surface. With ε being the dielectric constant, the following relation holds

$$E = q/\varepsilon \,. \tag{1}$$

As ε is constant in most cases, in space and time, the quantity measured by the field mill can be calibrated in terms of the electric field as well as in terms of the surface charge density. A field calibration is usually preferred. The working principle of the common type field mill is as follows: A certain area of the surface of the instrument is periodically shielded and exposed to the electric field by a rotating shutter (this type will be called, in the following, the shutter field mill). The surface charge flowing from the ground to the surface in the exposed position, and back to the ground in the shielded position, is measured either as current flow or as voltage drop over a resistor or a capacitor connecting the sensitive area with the ground. The purpose of this set-up is to change a constant electric field into an alternating current or voltage, which can be easily amplified and recorded. The energy for the movement of the surface charge is supplied by the motor, which drives the rotating shutter. No energy is bled from the field to be measured, so the measurement is truly electrostatic. The difference in the working mechanism of the cylindrical field mill compared to the shutter field mill is that the sensitive area is not shielded and exposed to the electric field by a shutter, but is moved periodically between two positions in which the surface charge induced by the electric field is different (Kasemir [2, 3]; Matthias [1]). The difference in the surface charges, which is also proportional to the influencing electric field, is then amplified and recorded. The cylindrical field mill has a number of advantages over the shutter field mill which will be discussed in detail in this paper. Furthermore, it has the peculiar feature of being capable of measuring two components of an electric field vector and rejecting the third. This makes the cylindrical field mill especially suited for field measurements from an airplane because it can be constructed and mounted in such a way that the influence of the airplane charge is automatically cancelled.

2. Theory

The sensor areas of the cylindrical field mill are the two halves of a cylinder mantle as shown in Figs. 1a and b. Figs. 2a and b are photographs of the finished instrument in which the two segments can be easily recognized

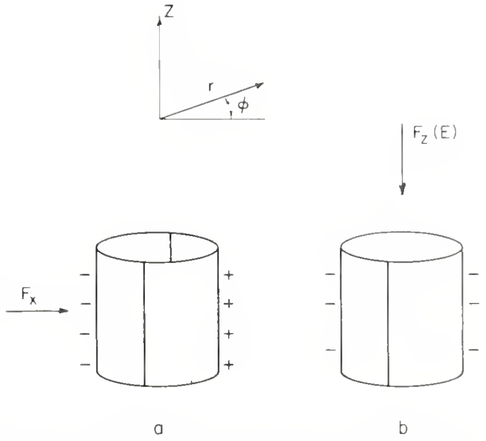

Fig. 1. Cylinder segments influenced by: a horizontal field F_x (a) and a vertical field F_z, or the field E of the airplane charge (b)

---

* H. Israël zum Gedenken gewidmet.

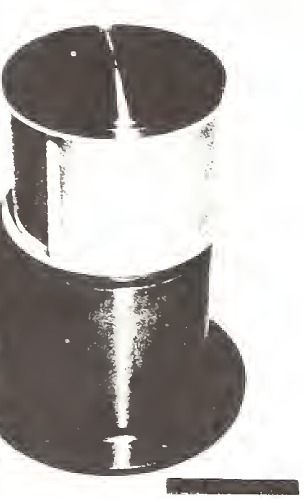

Fig. 2a. The cylindrical field mill

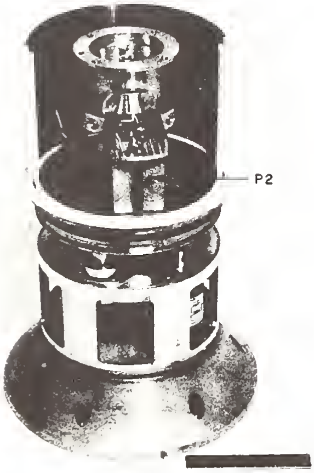

Fig. 2b. The cylindrical field mill, with top and one cylinder segment removed ($P2$ = operational amplifier)

in the head of the cylinder. The head rotates at 30 revolutions per second. Exposed to a horizontal electric field F_x (Fig. 1), negative and potive influence charges will flow to the two cylinder segments alternating in sign with the rotation of the head. The current flow caused by the influence charges is amplified, rectified, and recorded. The calculation will show that the amplitude of this alternating current is proportional to the electric field F.

To calculate the charge density on the surface, the field mill may be substituted by an infinitely long cylinder of radius a, exposed to a homogenous electric field F vertical to its axis. However, in reality, the field mill is only a short piece of this infinitely long cylinder, and a better approximation can be achieved if at least half of the infinite cylinder is cut away and the charge density on the end piece is calculated. As this calculation is rather tedious, and in practice the field mill is calibrated in an artificial field of known strength, the simple calculation using the infinite cylinder is sufficient for our purposes here.

The potential function Φ of an infinite cylinder placed in a homogeneous field F is given by the equation

$$\Phi = -F\, r \cos\varphi\, (1 - a^2/r^2)\,. \tag{2}$$

Here, cylindrical coordinates z, r, φ are used, with the axis of the cylinder being the z axis of the coordinate system (Fig. 1a). By differentiation with respect to r and then setting $r = a$, the electric field and, with equation (1), the charge density q on the cylinder surface are obtained

$$q = 2\,\varepsilon\, F \cos\varphi\,. \tag{3}$$

Integration along the z axis over a length L and between angles φ_1 and φ_2 yields the charge Q of the so defined area of the cylinder mantle.

$$Q = -2\,a\,L\,\varepsilon\,F\,(\sin\varphi_2 - \sin\varphi_1)\,. \tag{4}$$

If $\varphi_2 = \varphi_1 + \pi$, the charge of a half segment of the cylinder mantle is obtained.

$$Q = -2\,\varepsilon\,F\,2\,a\,L \sin\varphi_1\,. \tag{5}$$

This, then, would give the influence charge of one of the sensitive areas of the field mill, whereby φ_1 is the angle of the cut of the cylinder with respect to the direction of the field. If the cylinder rotates with a circular frequency ω, φ_1 increases by $\omega\, t$, where t is the time, and from equation (5) follows

$$Q = -2\,\varepsilon\,F\,2\,a\,L \sin(\omega\, t + \varphi_1)\,. \tag{6}$$

Differentiation with respect to time t yields the current I caused by the flow of the charge Q.

$$I = -2\,\varepsilon\,F\,2\,a\,L\,\omega \cos(\omega\, t + \varphi_1)\,. \tag{7}$$

This current is used to drive an operational amplifier with the feedback resistor R (Fig. 3). The resulting output voltage U_o of the amplifier is then given by

$$U_o = -IR = 2\,\varepsilon\,F\,2\,a\,L\,\omega\,R \cos(\omega\, t + \varphi_1)\,. \tag{8}$$

The rotating cylinder head of the instrument has a radius of $a = 5$ cm and a length $L = 10$ cm. The feedback resistor is 22 MΩ. The amplitude of the output voltage U_o for an electric field of 100 volts per meter is in this case $U_o = 77$ millivolts.

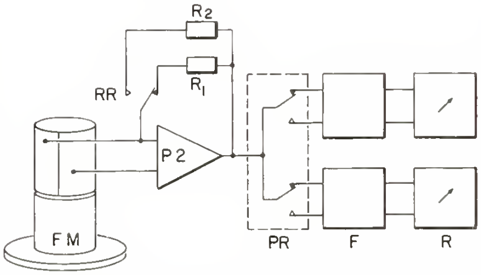

Fig. 3. Block diagram of the electric circuit of the two-component cylindrical field mill. FM cylindrical field mill, $P2$ operational amplifier, RR range relays, R_1, R_2 feedback resistors, PR phase-sensitive rectifier, F filter, R recorder

The amplitude of the output voltage U_0 is proportional to the absolute value of the field vector of an electric field in a plane vertical to the axis of the field mill. The direction of the field vector with reference to the field mill coordinates can be obtained by recording the phase shift between U_0 and a fixed voltage U of an auxiliary generator mounted on the axis of the field mill. This means that the absolute value and the direction of the field vector are the natural outputs of the cylindrical field mill. Using two phase-sensitive rectifiers and filters, the output voltage U_0 of the amplifier can be split up into two parts, one of which is proportional to $F_x = F\cos\varphi_1$, and the other one to $F_y = F\sin\varphi_1$, as will be shown in the next section. In this way the two components of the electric field vertical to the axis of the field mill can be obtained.

To calculate the influence charge of the field component F_z parallel to the axis of the cylinder, the field mill cannot be represented by a cylinder of infinite length. Half of the cylinder has to be cut away and the open end closed by a circular disc.

An equal amount of field lines will end on each sensitive area, and a proportional amount of influence charge is thus induced (Fig. 1b). But the difference to the prior case of the horizontal field is that the amount of influence charge due to the axial field remains constant even if the cylinder head is rotating. This follows immediately from the rotational symmetry of the instrument. Therefore, the differentiation with time of the constant charge yields zero output current. This is the reason the cylindrical field mill will not respond to the component of the electric field in the direction of the cylinder axis. The same is true if the field mill should carry a charge of its own as would occur if attached to an airplane charged by the exhaust fumes. An equal amount of charge will flow to the sensitive areas, but this charge will not be modulated by the rotation of the field mill and therefore will not contribute to the current of the horizontal field. Only sudden field changes will generate short pulses of the output voltage. These transient currents would be suppressed by the filter network of the phase-sensitive rectifier.

A certain precaution must be exercised in choosing the spot on which to mount the field mill on the plane. The criterion for a good place is one where the charge density at the sensor areas of the cylindrical field mill, which results from the airplane charge, does not change by the rotation of the cylinder head. This can be checked by measuring the capacity of the sensor at different positions of the cylinder head. The best places are those where the rotational symmetry is greatest, for instance, at the nose or in the middle of the fuselage of the plane.

3. Instrument

In general, the field mill consists of four parts: 1. the field mill proper with the sensitive areas and the drive mechanism, which either rotates a periodically screening shield above the sensitive areas in the case of a shutter field mill or which rotates the cylinder head with its two sensitive segments as is the case of the cylindrical field mill; 2. the amplifier, which amplifies the electric signal, delivered by the field mill, to a level necessary to drive a recorder; 3. phase-sensitive rectifier, which rectifies the *ac* output of the amplifier to *dc* (in the case of the cylindrical field mill, there are two phase-sensitive rectifiers 90 degrees out of phase to each other, which produce outputs proportional to the x and y components of the electric field), and 4. one- or two-channel recorder.

The compactness of the amplifier P_2 allows it to be housed inside the cylinder head (Fig. 2h). This has two advantages: 1. The leads from the sensitive areas to the input of the amplifier can be kept extremely short. Excessive stray or cable capacity is so avoided and therefore the capacity load is very small. 2. Slip rings have to be used to transduct the signal from the rotating head to the fixed base of the field mill. If this can be done at the output of the amplifier instead of at the input, the noise introduced by the slip rings becomes negligible. Recently a rotating capacitor has been used to transmit the signal from the receiving segment in the field mill head to the input terminal of the amplifier, which in this case is located in the base of the field mill. This has all the advantages of short leads and low stray capacity and avoids signal transmission through slip rings.

The disadvantage of placing the amplifier in the cylinder head is that range switching becomes more difficult. The large dynamic range and the extremely low drift and noise level of the amplifier permit range switching at the output for about 10^2. However, the atmospheric electric field may change by a factor of 10^4. To accommodate this wide range, a range relay *RR* is incorporated in the feedback circuit of the amplifier, which can be operated by remote control and which reduces the feedback resistor by a factor of 100 (Fig. 3). In this way the dynamic range can be used twice. The range switch of this instrument permits the following settings: full deflection of the recorder for 50, 150, 500, 1500, 5000, 15000, 50000, 150000, and 500000 volts per meter.

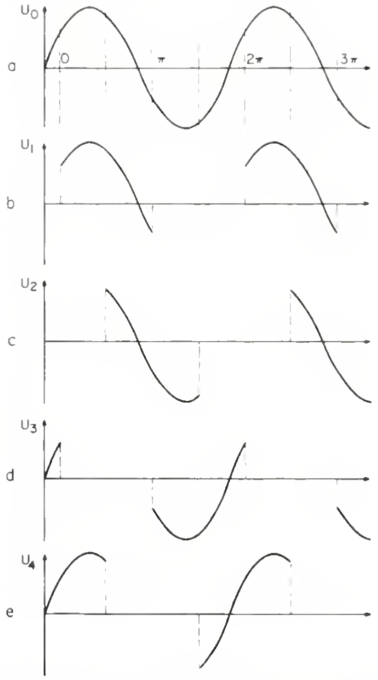

Fig. 4. Output voltage of (a) operational amplifier, (b) rectifier 1, (c) rectifier 2, (d) rectifier 3, (e) rectifier 4

Fig. 4a shows the sinusoidal output voltage U_o of the amplifier P_2. The vertical dashed lines indicate the make and hreak points of four phase sensitive rectifiers marked *PR* in Fig. 3. The output voltages U'_1 to U'_4 of these rectifiers are shown in Figs. 4b—e. These voltages are smoothed hy the filter network *F*, paired and recorded on two strip chart recorders *R* (Fig. 3). The *dc* component U_{n0} of the voltage U'_n ($n = 1, 2, 3, 4$) can he calculated by the first term of a Fourier expansion.

$$U_{n0} = 2\varepsilon F 2 a L \omega R \frac{1}{2\pi} \int_{c\pi}^{b\pi} \cos(\omega t + q_1)\, d\omega t\,. \quad (9)$$

Usually the houndaries of the Fourier integral are 0 and 2π, but as evident from Fig. 4b—e, the functions $U'_1 \ldots U'_4$ are different from zero only at certain intervals. These intervals are given by the boundaries $c\pi$ and $b\pi$, wherehy c and b can he expressed in the following manner:

$$c = \frac{n-1}{2}\,; \quad b = \frac{n+1}{2}\,; \quad n = 1, 2, 3, 4\,. \quad (10)$$

The solution of (9) with (10) yields

$$\begin{aligned} U'_1 &= AF \sin q_1 \\ U'_2 &= -AF \cos q_1 \\ U'_3 &= +AF \sin q_1 \\ U'_4 &= +AF \cos q_2 \end{aligned} \quad (11)$$

$$\text{when } A = 2\varepsilon 2 a L \omega R/\pi$$

U'_1 and U'_3 are proportional to $F \sin q_1 = F_y$ and therefore measure the y component of the electric field; while U'_2 and U'_4 proportional to $F \cos q_1 = F_x$ measure the x component. As U'_1 and U_3 as well as U'_2 and U'_4 have opposite signs, they are paired and fied into the imput terminals of a halanced potentiometer recorder. Thereby the signal strength is doubled, and any *dc* drift of the operational amplifier is cancelled. With the dimensions and the electrical circuit of the field mill discussed here, a field $F = 100$ volts per meter would produce ±10 millivolts at the input terminals of the recorder. The recorder sensitivity is adjustable between 10 and 100 millivolt full deflection, which makes it possible to compensate for the different model factors of the different field components.

A few remarks are devoted to the noise voltage introduced by the contact potential. In the case of the shutter field mill, the screening shutter moves closely over the sensitive segments alternately shielding and exposing them to the external field. Any existing contact potential hetween the shutter and the segments is modulated in the same way as the external field and therefore cannot he cancelled out by a phase-sensitive rectifier. To keep the contact potential low, the shutter and the segments are usually gold or chrome plated. But the slightest scratch in the plating that exposes the substratum material will introduce the contact potential between the substratum material and the gold or chrome, and generate a high noise level. In the case of the cylindrical field mill, the screening shutter is absent. The two sensitive areas do not change their position with respect to each other, even if the cylinder head is rotating. Therefore, an existing contact potential between them is not modulated and cannot introduce an output signal. This is the reason the noise level of the cylindrical field mill even without gold plating is lower at least by a factor 10 than that of a shutter field mill.

The sensitive areas of the described instrument are made from stainless steel. This brings a decisive advantage if the field mill is used in thunderstorm research. Hailstones impinging on the surface of the field mill with the airplane velocity of about 50 m per second would probably chop off the gold plating, hut have no effect on a surface of solid stainless steel.

4. The Calibration Factor

If the field mill is placed in the middle of a sufficiently large plate condenser with the field mill axis parallel to the equipotential lines, the applied field can be calculated from the distance of the plates and the voltage difference between them. In this way the basic calibration can he obtained. For airplane measurement, the field distortion factor of the plane itself has to be determined. In our case, one field mill was mounted on the nose and one centered on the lower fuselage (belly) of the plane (Fig. 5). These spots were chosen for their relatively good symmetry with respect to the main axis of the plane, insuring the cancellation of the field of the airplane charge. The nose field mill measures the horizontal and the vertical component F_x and F_z of the atmospheric electric field. The x axis is in the direction of the wings, and the z axis is in the direction upper to lower part (back to belly) of the plane. The fuselage field mill measures the x and y components in the horizontale plane, whereby the x component is again in the direction of the wings and the y component in the direction from the mose to tail of the plane.

Each of these components is affected by a different model factor. The following procedure for their determination was applied.

The atmospheric electric fair weather field is assumed to he vertical. This assumption was proved correct by most of the fair weather flights. The fair weather field was recorded by an atmospheric electric radiosonde, which had been calibrated in a plate condenser at the ground. The model factor M_z for the vertical component of the nose field mill had been obtained by having the airplane circle around the slowly rising radiosonde balloon and comparing the two recorded values. The model factor M_x of the nose field mill was then determined by banking the airplane to a 45-degree angle, which splits the vertical fair weather field into two equal components F_x and F_z with regard to the coordinate system x, y, z fixed to the main axis of the plane. M_x was then determined from M_z. The same method also yielded the model factor M_{x_1} of the fuselage field mill. An attempt was made to obtain the remaining model factor M_y by diving, but the airplane could not be tilted down to a

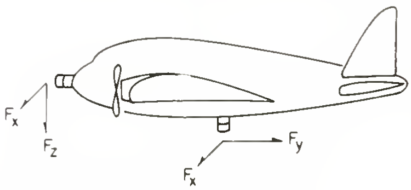

Fig. 5. Nose and fuselage field mill on airplane

45-degree angle. Especially, such a maneuver could not be performed near the ground, where the atmospheric electric field is strongest.

More successful was the method where the plane was flown near a thunderstorm at an altitude where large horizontal fields were present. The plane described a figure 8 where it crosses its previous path by a 90-degree angle. F_y of one path is F_x of the following path and vice versa, so that M_y can be determined from M_x. The figure 8 was run through several times to make sure that the field has not changed during the time necessary to perform the loop.

It should be mentioned that even if the model factors M_x, M_y, M_z are not equal, they are constant; and the phase-sensitive rectifier delivers each component with its correct model factor. This follows very clearly from the principle of superposition of electric fields.

5. The Interpretation of the Record of the Field Cylindrical Field Mill in Flight

The records of the three components of the electric field during actual flight were at first rather confusing and difficult to interpret until the basic pattern had been worked out. Fig. 6 gives 12 pictures of records as they appear if a single positive or negative space charge is approached and passed. The charge may be dead-center to the approaching plane up or down or right or left. For each of these cases a specific combination of the three component traces F_x, F_y, F_z will appear. These combinations are shown in Fig. 6a—l. On each small picture the airplane (seen from the back) is shown at the top with the charge marked by a plus or a minus sign according to its polarity. In the different pictures the charge is now placed in different positions with respect to the plane and the resulting traces of the F_x, F_y, and F_z recorder are shown underneath.

The first 6 pictures (Fig. 6a—f) deal with a positive charge, and the last 6 pictures (Fig. 6g—l) with a negative charge. The shape of the trace of F_y is the same for all pictures with a positive charge. F_y increases from zero to a positive maximum, then crosses the zero line and goes rapidly to a negative maximum after which it decays to zero again. The zero crossing between the positive and the negative maximum indicates the point when the airplane passes through or sideways of the charge center.

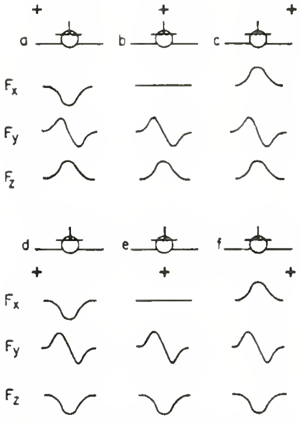

Fig. 6a—f. Records of the field components F_x, F_y, F_z by passing a positive charge (6a—f). The plus sign indicates the position of the charge with respect to the airplane

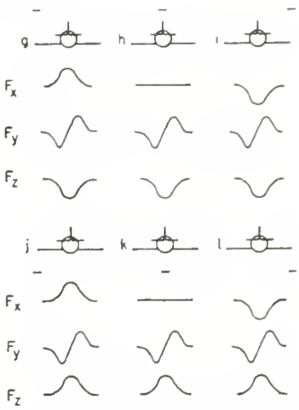

Fig. 6g—l. Records of the field components F_x, F_y, F_z by passing a negative charge (6g—l). The minus sign indicates the position of the charge with respect to the airplane

The trace of F_y of a negative charge is the mirror image to that of a positive charge (Fig. 6g—l). It goes from zero to a negative maximum, crosses the zero line to a positive maximum, and decays to zero afterwards. Therefore, the sign of the first maximum of F_y identifies the polarity of the charge which the airplane approaches. It is pointed out that under static conditions it is not possible to determine if a positive deflection of F_y is caused by a positive charge in front or by a negative in back, but the movement of the airplane supplies the necessary information to resolve this ambiguity.

With the polarity of the charge determined from the F_y trace, it is easy to interpret the significance of the F_x and F_z traces. These are always simple excursions to one side. either positive or negative. If, for instance, the maximum of the F_z trace has the same polarity as the first maximum of the F_y trace, the charge is located above the airplane level. If the F_z trace remains zero during the excursion of the F_y trace, the charge center is at the same altitude as the plane. Similar simple rules can be worked out for the F_x component. If the F_x trace remains zero (Fig. 6b, e, h, k), the plane moves exactly above, below, or through the center of the space charge. If the maximum of F_x has the same polarity as the first maximum of F_y, the charge center is to the right of the plane; and in case of opposite polarity, it is to the left. These rules are valid for positive as well as negative charges.

It is possible to direct the airplane during the flight towards the charge center or away from it, whichever case is desirable. For instance, in thunderstorm research, where it is essential to locate the main charge centers, the field records may start out as those in Fig. 6c as the plane approaches the storm center. If F_y is still before its first positive maximum, the positive field increase of F_x, F_y, and F_z indicates that a positive charge center is located in front, above, and to the right of the plane. A right turn is then made until F_x becomes zero, as in Fig. 6b. The airplane then flies straight ahead, always keeping $F_x = 0$. At the same time, the plane should climb until $F_z = 0$ and then level off. If the F_y trace has now passed its positive maximum and changed its polarity to the negative maximum, the zero crossing indicates that at this moment the plane is in the center of the positive charge.

In commercial air traffic it will be desirable to avoid the strong electric fields of thunderstorms because they are the birthplaces of lightning discharges. If in this case the field records indicate that a positive charge is above and to the right of the plane, the flight direction has to be changed to the left until again the F_x component is zero. During the left turn the F_y component passes through zero to its negative maximum, which indicates that the charge center is now to the rear of the plane. The flight is then continued in a straight direction until the field is sufficiently diminished.

Thunderstorms usually contain not only one but different charge centers of different polarities and in different altitudes. In this case the traces of the F_x, F_y, F_z components will be more complex than the simple forms of Fig. 6a—l. But any complex pattern can be analyzed or synthesized by a superposition of the basic patterns of Fig. 6.

It shall be mentioned that a similar analysis can be worked out for the field components in spherical coordinates. Such a representation would conform better to the vector character of the electric field given by vector amplitude and direction. However, the field distortion by the airplane, which results in different model factors for the different x, y, z components, would change the spherical to spheroidal coordinates. To correct this distortion by adjustment of individual amplifiers one would have to use first the representation in F_x, F_y, F_z components and after correction of the model factors calculate electronically the spherical components of the electric field.

References. Matthias, A.: Fortschritte in der Aufklärung der Gewittereinflüsse auf Leitungsanlagen. Elektrizitätswirtschaft **25**, 297—308 (1926). — Kasemir, H. W.: Die Zylinderfeldstärkenmühle mit kleinen Segmenten. Flugfunkforschungsinstitut Oberpfaffenhofen e.V., Außenstelle Gräfelfing. Beauftr. Hochfreque. Fragen. Ref. III A/1306 (1944); — Die Feldkomponentenmühle. Tellus **3**, 240—247 (1951).

U.S. DEPARTMENT OF COMMERCE
National Oceanic and Atmospheric Administration
Environmental Research Laboratories

NOAA Technical Memorandum ERL APCL-14

1972

DESCRIPTION AND INSTRUCTION MANUAL FOR THE CYLINDRICAL FIELD MILL SYSTEM

NASA, Kennedy Space Center, Contract CC-59753

Heinz W. Kasemir, Project Leader
F. James Holitza, Prinicpal Investigator
(303) 499-1000

Atmospheric Physics and Chemistry Laboratory
Boulder, Colorado
February 1972

TABLE OF CONTENTS

Section	Title	Page
I	SPECIFICATIONS	1
II	THEORY OF OPERATION	2
III	THE INSTRUMENT	7
	A. The Field Mill System	7
	B. The Field Mill	8
	C. Interconnecting Cables	10
	D. The Control Panel	11
	1. Gating Signals	11
	2. AC Gain	13
	3. Phase Sensitive Rectification	14
	4. DC Outputs	16
	5. Input Power	16
	6. Front Panel Controls	18
	7. Rear Panel Connectors	18
	E. Recorder	19
IV	MAINTENANCE	19

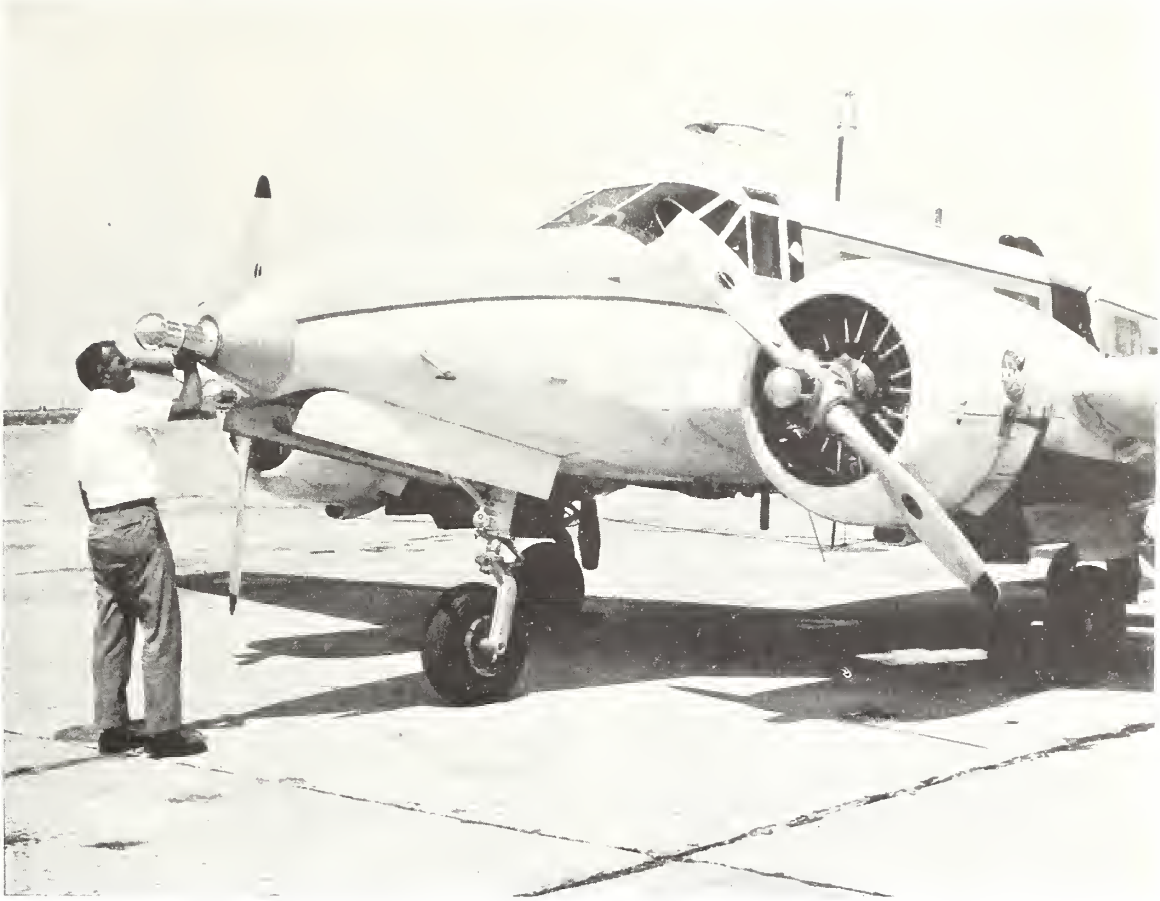

The most recent installation of the atmospheric electric field mill system is on the NASA 6 aircraft. NASA's veteran thunderstorm research pilot, Lindy Mason, is shown in a preflight check of the nose field mill that measures two components of the electric field in a horizontal plane.

Reprinted with permission from Third Conference on Weather Modification, June 26-29, 1972, Rapid City, South Dakota, © American Meteorological Society.

STATISTICAL EVIDENCE OF ELECTRICAL MODIFICATION OF THUNDERSTORMS BY ARTIFICIALLY TRIGGERED LIGHTNINGS

E. L. Magaziner

National Oceanic and Atmospheric Administration
Boulder, Colorado

1. INTRODUCTION

The interaction of rockets with the electrical environment of thunderstorms and other electrified clouds has, since the Apollo 12 "incident," captured wide interest. The artificial triggering of lightnings by rockets in high electric fields is the primary concern. Theoretical calculations based on electrostatics have been somewhat informally discussed by several atmospheric electricians; one of the conclusions was that small rockets may be as capable of triggering lightnings as the Apollo launch vehicle. An experiment in which small rockets were launched from the ground into thunderstorms was performed by Kasemir (1972) at the Kennedy Space Center in June of 1971. This paper discusses the evaluation of this experiment and presents evidence in favor of the lightning triggering capability of small rockets.

2. DESCRIPTION OF DATA COLLECTED

Several instruments are in use or are being developed for collecting data during Kasemir's lightning triggering rocket flights. These include a capacitively loaded antenna to record primarily the occurrence of lightning, a lightning plotting system to determine the positions of lightnings, and a transmitter borne by the triggering rocket to signal a lightning strike to the rocket. When all three instruments are operational, the triggering of a lightning by a rocket can be unambiguously determined. The occurrence of the lightning can be verified by the antenna. The lightning plotter can verify that the lightning position coincides with that of the rocket. The rocket borne transmitter signal can verify that the lightning stroke was not a near miss.

Data available at the time of writing consist entirely of lightning occurrence recordings; that is, the occurrence of lightning versus time was recorded in a time interval encompassing the experiment. Nevertheless, even this crude information already contains evidence of lightnings triggered by the small rockets.

Lightning occurrence data for periods during 18 rocket flights, each lasting approximately 60 seconds, were organized as follows. Thirty-six 60-second portions were extracted from the data, 18 from T_0 to $T_0 + 60$ for each launch time T_0, and 18 randomly chosen 60-second portions during which no rockets were in flight. The 60-second intervals from the first group were superimposed so that the launch times coincide and the number of lightnings from T - 1 to T + 1 for each T from T_0 to $T_0 + 60$ were counted. The results of this appear in Fig. 1, third from the top, and are called the experimental group. The intervals from the second group were also superimposed obtaining the control group which appears in Fig. 1, bottom.

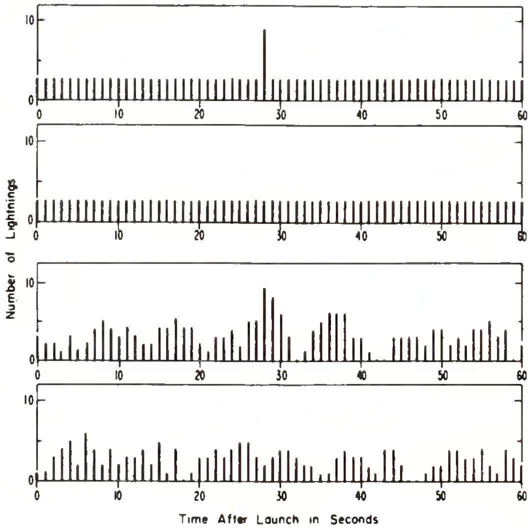

Fig. 1. Mathematical idealizations (top) and actual data (bottom) of the experimental and control groups.

3. ANALYSIS OF THE DATA

The control group represents a natural, undisturbed record of lightning activity during the experiments. In a mathematically ideal sense, this would be expected to appear as Fig. 1, second from the top, with some constant mean number of lightnings in any of the 2-second intervals. The actual control group, of course, exhibits variations about its mean value. Statistically, the control group can be described by a mean of 2.79 with standard deviation 1.36. Since this is the composite of 18 cases, the mean represents 0.156 lightnings in any 2-second interval. The frequency distribution histogram and the cumulative distribution function of the control group appear on the left side of Fig. 2.

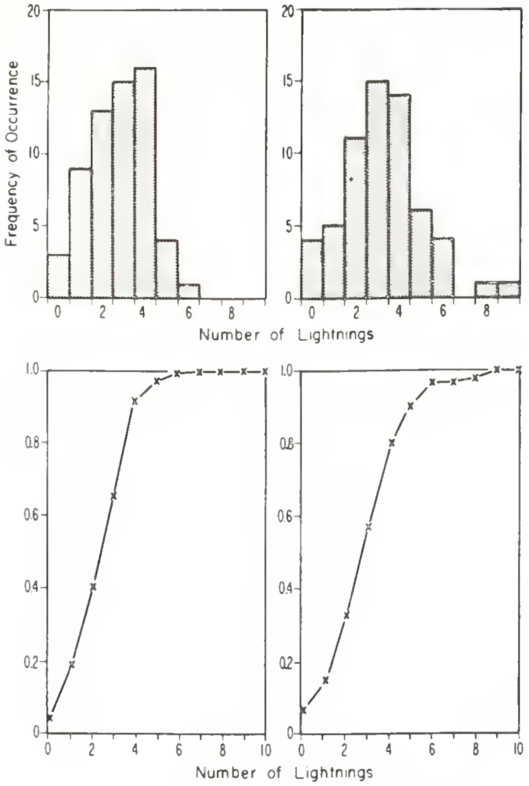

Fig. 2. Frequency distribution histograms and cumulative distribution functions for the control (left) and experimental (right) groups.

The experimental group should contain information on the effect of the rockets on the lightning activity of the thunderstorms. It is expected that, on the average, the number of lightnings would be increased, that is, the experimental group would possess a mean larger than that of the control. The mean of the experimental group is 3.26 with a standard deviation of 1.82. The frequency distribution histogram and the cumulative distribution function of this group appear on the right side of Fig. 2. Instead of computing a statistic to determine the significance of the difference between the two means, it is noted that the cumulative distribution function of the control group is larger than that of the experimental group. This means that (1) not only is the mean of the experimental group larger, but (2) the experimental group is a sample from a population stochastically larger than that of the control group. Therefore, the statistical significance of the increase of the number of lightnings by the rockets may be preferably determined without any assumptions regarding the distributions of the control and experimental groups. The nonparametric Mann-Whitney (1947) test was used to establish significance of the increase in lightnings at the 0.09 level.

The experimental group also indicates that the rockets effected a redistribution of the lightning activity of the thunderstorms. In a mathematically ideal sense, one may expect the experimental group to appear as at the top of Fig. 1; that is, the rocket would trigger lightning as it entered the region of high field at some point in its trajectory. The experimental group does exhibit such a peak distributed about $T_0 + 28$. It is extremely unlikely that this is a chance occurrence, since the magnitude of the peak is more than four standard deviations from the control mean. The decrease below the mean after $T_0 + 30$ can probably be attributed to a temporary discharging of the cloud by the rocket triggered lightning and, together with the next peak and valley, may be thought of as "transients" caused by the "pulse" at $T_0 + 28$.

4. CONCLUSION

The data acquisition system for this experiment in which lightnings are triggered in thunderstorms by small rockets is still under development. Nevertheless, even the most primitive data, namely a record of lightning occurrence versus time during the experiment, already indicate that the rockets increase and modify the lightning activity of the thunderstorms.

5. ACKNOWLEDGEMENT

The experiment cited in this paper, as well as the evaluation of its results, was sponsored by Kennedy Space Center, National Aeronautics and Space Administration.

6. REFERENCES

Kasemir, H. W., 1972: Theory and experiments to the problem of rocket triggered lightning discharges, *Proc. of Third Conference on Weather Modification*, Rapid City, S. D.

Mann, H. B. and Whitney, D. R., 1947: On a test whether one of two random variables is stochastically larger than the other, *Ann. Math. Statist.* 18, 50-60.

Reprinted with permission from Third Conference on Weather Modification, June 26-29, 1972, Rapid City, South Dakota, © American Meteorological Society.

NOAA OBJECTIVES AND RESULTS WITHIN NHRE

B. B. Phillips, H. H. Grote, P. M. Kuhn, and H. K. Weickmann

Atmospheric Physics and Chemistry Laboratory
Environmental Research Laboratories
National Oceanic and Atmospheric Administration
Boulder, Colorado

1. INTRODUCTION

NOAA's Atmospheric Physics and Chemistry Laboratory participated in the National Hail Research Experiment (NHRE) in Northeastern Colorado during the 1971 summer hail season (May to August) in extension of previous years' research with the Joint Hail Research Project (Weickmann, 1969). NOAA objectives within NHRE were threefold: (1) Aircraft mesometeorological analysis of storm fluxes and processes; (2) design and operation of the surface precipitation network and chase crews; and (3) hailstreak mapping using remote sensing IR scanning radiometric measurement from aircraft. In addition to these field efforts, NOAA scientists participated with members of NHRE in the operational control responsibility at the project control center in Grover, Colorado.

The results of the NOAA participation can be briefly summarized as follows:

1. The low level air and water flux to storms have been measured using the DC-6 NOAA aircraft flying at and below cloud base. This continued the analysis of storm influx begun in previous years.
2. A 420-station precipitation network was established and operated during the NHRE program period. The network included recording rain gages and hail momentum-rate recording gages to determine the areal and temporal precipitation distribution.
3. The precipitation network measurements were supplemented by radio controlled truck chase crews and by aircraft remote scanning radiometer measurements of the surface temperature fields for the mapping of hailstreaks.
4. Upper level divergence and the storm's vertical transport and tropospheric-stratospheric exchange of water vapor, ozone and aerosols were measured at altitudes between 40,000 feet and 45,000 feet during flights of NASA's Convair 990 aircraft.
5. A strong beginning has been made toward programming for the computer analysis and plotting of the very considerable data inputs in order to provide for a "contemporary-time" data analysis within the NHRE in succeeding years.

NOAA and the National Center for Atmospheric Research (NCAR) cooperated in the surface network, the chase crew and the aircraft scanning radiometric measurements with principle funding for these coordinated efforts from the National Science Foundation.

A summary of the procedures, schedules, operational highlights and results appropriate to these program areas is given below.

2. DC-6 AIRCRAFT PROGRAM

NOAA's Research Flight Facility instrumented DC-6 aircraft conducted mesoscale storm analysis flights during the period June 1 to July 1. The objectives of these flights were the measurement of the storm air and water fluxes, the analysis of the boundary layer inflow and outflow velocity fields, and the computation of the storm's precipitation efficiency and water budget. The Doppler navigation unit on the aircraft provided data on aircraft position, true air speed, drift angle, ground speed, wind direction and wind speed at flight level, and distance traveled. Other instrumentation provided radar altitude, pressure altitude, pressure at flight levels, air temperature and specific humidity. This flight information is recorded on magnetic tape and the data is analyzed after the flight by numerical computer for the flight level divergence and the air and water mass inflows and velocity field to the storm. When storms occurred over the NHRE precipitation network, then computations of the precipitation efficiency could be made utilizing the combined aircraft and network data. The plane has two onboard radars to assist in flight direction and real-time and post flight analysis.

A total of eight DC-6 aircraft flights were made including the tower fly-by and aircraft intercomparison flights. On two days, June 11 and June 16, multi-level flights were made around developed hail storms. Four flights were conducted during marginal storm days.

2.1 Storm of June 11

Figure 1 shows the aircraft flight track about a hailstorm over the central part of the NHRE precipitation network on June 11, 1971. The numbers along the flight path specify the time (GMT). The four storm circumnavigations between 1540 Local Daylight Time (2140 GMT) and 1720 LDT (2320 GMT) were at flight levels of 9000 feet msl and 7000 feet msl corresponding to 1000 feet below cloud base and 2000 feet above the local terrain. The wind vectors terminate on the flight path, for example, the flight level winds are generally from the southeasterly quadrant during the northbound flight legs along the eastern side of the storm.

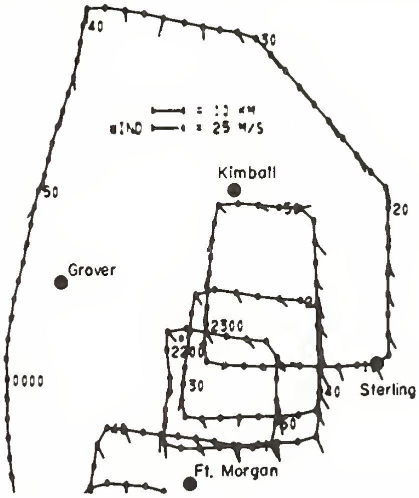

Figure 1. Computer plot of aircraft flight track about the hailstorm of June 11.

During the first circumnavigation, the aircraft's forward-looking radar showed an elongated storm structure oriented nearly west-east as seen in fig. 2. Flight control radar reported storm tops at 36,000 feet with reflectivity factor 10 log Z = 56, indicating at least light to moderate hail. The first and second "boxes" were flown at 9000 feet msl at a radius of 5 to 10 miles from the iso-echo radar reflective center. Usually, the flight path was underneath the cloud. The inflow area of this storm was clearly along the southeast and east sides. By the time of the second circumnavigation, two developing cells were apparent to the north of the initial cell. These continued to develop, changing the orientation of the storm system to north-south. This pattern was reflected in the surface precipitation. During the first box a single precipitation area was centered east of Raymer, Colorado; by the period of the third box, a north-south precipitation pattern existed over the eastern half of the NHRE network. The aircraft RHI radar showed a consistent overhang toward the east and a similarity of structure of the three major cells. The horizontal PPI during the northbound 9000 feet second flight pass along the eastern edge of the three cells is shown in fig. 3. Figure 4 shows three vertical RHI pictures obtained through these cells during the same northbound flight leg at approximately the orientation of the dashed lines indicated in fig. 3.

The third box about the storm system and the final south and east legs of the fourth box were flown at 7000 feet msl at an increased distance from the storm. The cells produced sporadic small hail during their lifetime as determined by the surface observations. A well developed hail shaft could be seen on the southwestern corner of the system during the third box

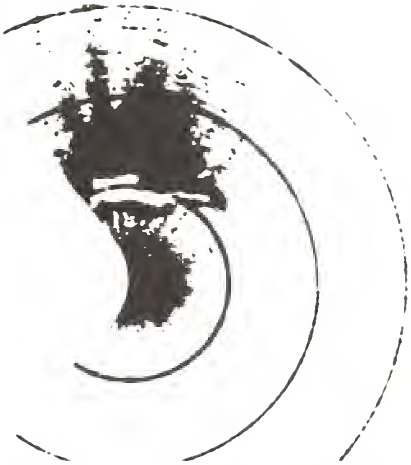

Figure 2. Horizontal PPI of June 11 storm obtained heading ~~from~~ south during initial flight around storm, (10 mile range marks)

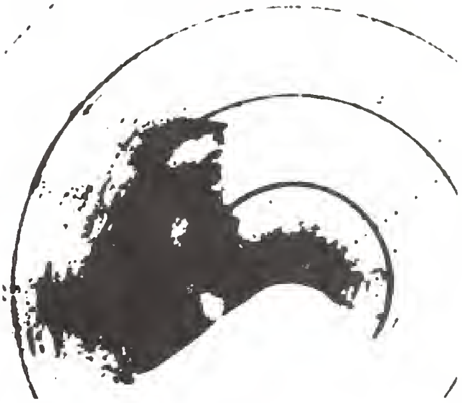

Figure 3. Horizontal PPI of June 11 storm obtained from east during second flight around storm.

about the storm. Strong outflow was evidenced by a "dust-front" which rose above the 9000 foot msl level of the aircraft during our final pass north of the system. By 1740 the storm had weakened markedly and the mission was terminated.

2.2 STORM OF JUNE 16

A similar storm of somewhat more severe intensity occurred on June 16. The remnants of a stationary front lay across the NHRE area in a NNE to SSW orientation with weak generally westerly flow. Although fairly dry along the mountains, the moisture increased considerably across eastern Colorado and by mid-afternoon cumulus buildups were evident from Greeley eastward. With the aid of the Greeley flight control radar and chase crews, the

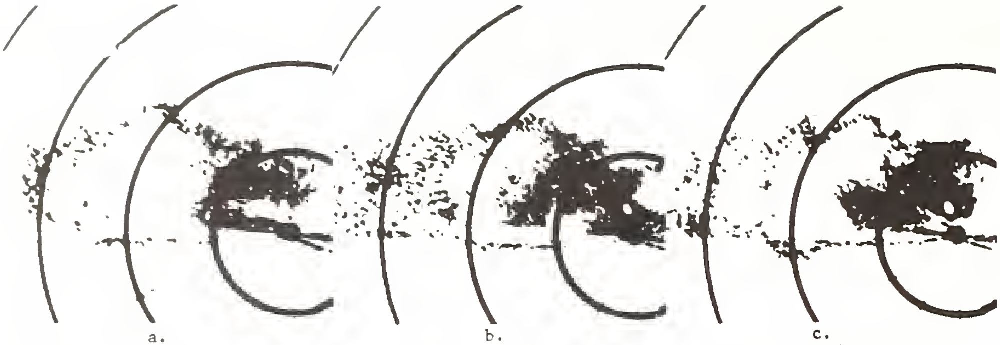

Figure 4. Vertical cell structure indicated by the aircraft RHI radar during the ~~second~~ third flight pass east of the June 11 storm (5 mile range marks).

DC-6 conducted quite successful measurements of a storm which persisted for 1½ hours over the north central precipitation network area. Two storm circumnavigations were flown at 9000 feet msl at radii of 5 and 10 miles from the storm and one flight at 7000 feet msl at 5 mile radius. Storm tops were between 45,000 and 52,000 feet and reflectivities $10 \log Z > 55$ were reported by Greeley radar for much of the lifetime of the storm. Surface chase crews confirmed moderate and light hailfall within the precipitation.

The measurement results from these flights of June 11 and June 16 will be discussed in more detail at the conference presentation.

3. SURFACE PRECIPITATION ANALYSIS PROGRAM

The precipitation surface network and hailstorm chase vehicle observational programs within NHRE are required in order to give the yes-no answer as to the occurrence of hail with and without seeding, to define the hailstreak and rainstreak areas of storms, to determine the time and location of hailfall with respect to radar echo and storm structure, and to relate the rain and hail rates to radar reflectivity analyses. At the same time, the precipitation measurements are necessary for any attempt at the difficult assessment of what effect hail suppression seeding produces on the rainfall.

The 1971 network array (seen in figs. 6, 7, and 8) covered an area of approximately 50x50 miles and included 120 stations with recording weighing rain gage, recording hail momentum-rate gate, and hail pad; 100 stations with non-recording rain gage and hail pad; and 200 stations with hail pad only. Some 60 of these stations were equipped with a dry-ice refrigerated hail catcher for catching hail without it having fallen on the ground. Samples of hail from these refrigerated catchers are being analyzed at NCAR for their "background" ice nucleus content.

The hail momentum-rate gage is shown in fig. 5 with the wind shield removed. The hail receiving surface is an expanded aluminum screen having a cross-sectional area of 1/10 of a square meter, equal to that of the hail pad, so that a comparison can be made between the two sensors. The impact gage gives the added information of the time of hailfall and the hailstone mass distribution during the hail period. The gage is activated by any stone of size 8 mm or larger. Once started, the recorder continues to run until two minutes after the last 8 mm hailstone strikes the receiving screen. The unit is mechanically damped and can resolve three to four hailstone impacts per second.

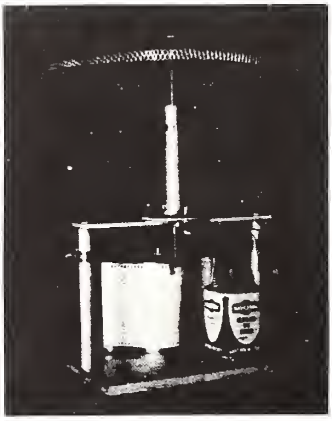

Figure 5. Recording hail gage.

Much of the network rain and hail data have been punched on data cards for machine analysis and programs written to provide computer generated analysis. The rainfall amounts and occurrence of hail are machine plotted for manual analysis. The hailstone size distributions can be graphically plotted.

Figure 6 is a computer plot of the 4-minute rainfall rates for storms of July 14 and July 15. As indicated in the lower right hand legend, the time scale in hours is given along a horizontal bar, the 4-minute rain rates are given by vertical bars projected in proper time sequence for each recording rain rate gage having precipitation during the time period prescribed. The log-scale of the vertical rain rate bars is also indicated in the legend for each plot. These graphs vividly display the track and the time sequence of rainfall.

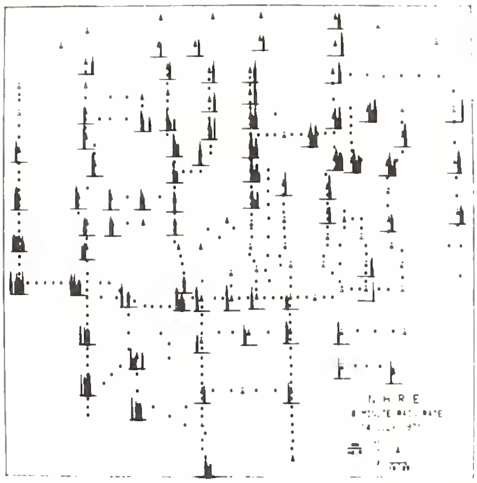

Figure 6a. Computer plot of eight-minute rainfall rates for storms of July 14, 1971.

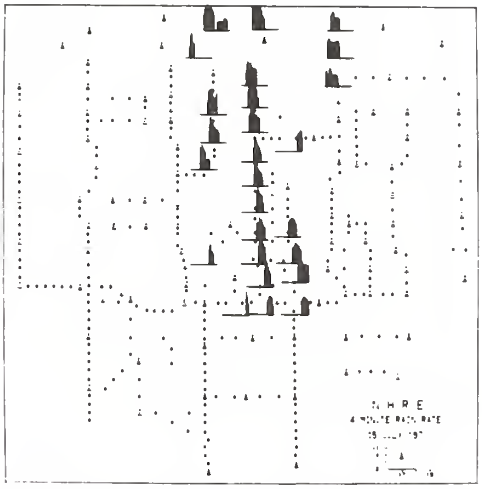

Figure 6b. Computer plot of four-minute rainfall rates for storm of July 15, 1971.

Figures 7, 8, and 9 show precipitation network results obtained during the storms which occurred on successive days, July 14 and July 15, 1971. Figure 7 shows the hailfall from a severe late evening storm which formed to the west of the NHRE research area and passed eastward over the network between 2030 and 2200 hours MDT. The curves are isolines of the maximum hailstone diameter in millimeters as indicated by the network hailpad array. The largest stones from this storm exceeded 70 mm or nearly three inches in diameter. This storm provided the best defined hailstreak that has occurred in the past two years.

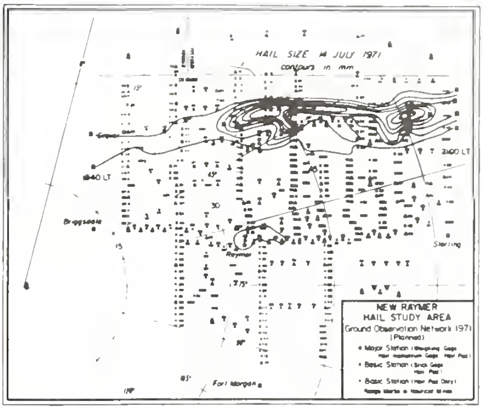

Figure 7. Hailstreak of July 14, 1971.

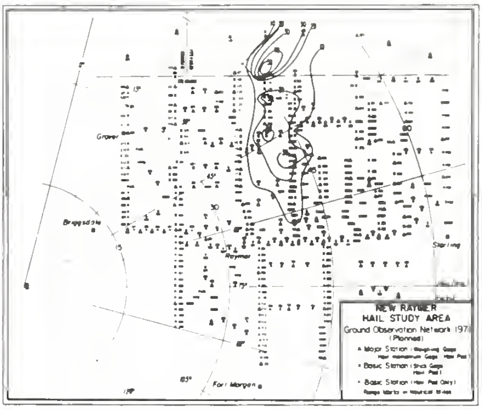

Figure 8. Hailstreak of July 15, 1971.

On July 15, a severe storm formed immediately north of the NHRE area and moved due south. The maximum hailstone size analysis for this storm is shown in fig. 8. The area of hail seen in fig. 8 can be correlated with the rainfall rate pattern for the same storm shown in fig. 6.

Figure 9 details the data from the hail rate-momentum recording gages for the storm of July 15, 1971. As can be seen from fig. 6, this storm entered the north central NHRE network area at approximately 1600 MDT and progressed with time southward, finally dissipating around 1800 MDT within the network. The hailfall associated with this storm shows a similar area-time pattern as seen in fig. 9, where the plotted stations are arrayed in the approximate orientation as exists geographically in fig. 6. For each station recording hail the distribution of stone size is indicated for each minute of hailfall. The time of the hail to the nearest minute is given above the distributions, the station shown below.

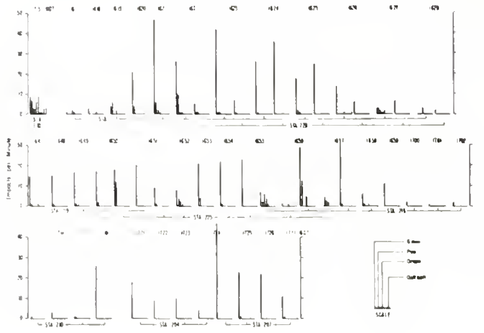

Figure 9. Hail size-time distribution recorded by the network hail momentum-rate gaged during storm of July 15, 1971.

4. CONVAIR 990 AIRCRAFT PROGRAM

A series of flights were conducted in mid-July by scientific and flight crew personnel of NOAA and NASA aboard NASA's Convair 990 aircraft. A prime objective of this field study was to determine, from measurements aboard the aircraft, the amount of water vapor and particulate matter injected into the stratosphere by plains thunderstorms, and to investigate the downward transport of ozone across the tropopause in areas of thunderstorm activity. In addition, the aircraft's inertial navigation system and instrument package which included the measurement of the meteorological parameters offered the possibility of obtaining divergence and mass outflow data around the upper elevation of the storms. A series of three 200-mile circumnavigations at altitudes of 12.4, 12.6 and 13.3 km were made around a storm which occurred during the afternoon of July 14 (0000 to 0130 GMT, July 15). This flight data supplements flight data obtained on this same storm during the same period by the NCAR Buffalo and Sabreliner in the altitude ranges of below cloud base and from 8 to 10.5 km respectively, thus constituting the first time that three-level aircraft divergence data have been obtained from a single storm. It is of additional interest that this was a splitting type storm which persisted for nearly one hour after splitting. The prime objective results of the CV 990 flight data are reported by Kuhn et al. (1971).

5. AIRBORNE INFRARED IMAGING PROGRAM

The installation of a Texas Instruments, Inc., infrared line scanner (Model RS-310) aboard NCAR's Queenaire aircraft provided the NHRE project with a passive, airborne infrared imaging system. This infrared mapper scans the ground along and to both sides of the flight path and produces a continuous thermal image of the scanned interface. Radiant power is received by the scanner from the ground, focused on cryogenic cooled detectors, converted to visible light through the use of light-emitting diodes and with a mechanically-coupled recorder exposes photographic film, transported at a rate proportional to the velocity and height of the aircraft. This produces a continuous photographic record of the radiant energy detected.

The infrared imager was employed to map hail swaths during the 1971 NHRE field program with a twofold purpose: (1) To determine the percent hail coverage, and (2) to determine hail deposition patterns in relation to radar location of the parent storm cells. Temperature contouring necessary in hail coverage analysis even within the hail swaths was possible by setting eleven gray wedge steps on the film leader calibrated against gain and level settings on the Imager console. A three temperature target system covering the maximum, average and minimum temperatures for each gain setting provided temperature contour control to ±0.5C, relative error.

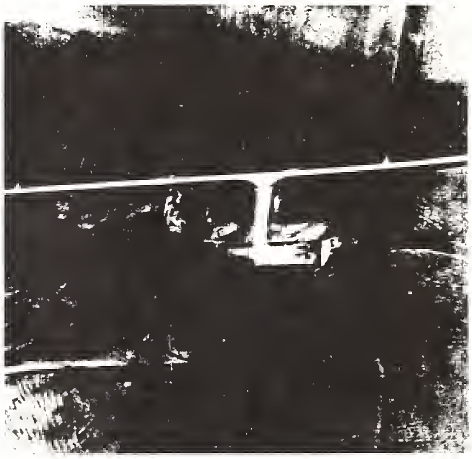

Figure 10. Scanning radiometer thermal image of hailstreak (dark areas), storm of June 15, 1971.

Figure 10 is a section of an infrared thermal image of a hail swath area on either side of a secondary road in the NHRE target area from a storm that occurred on June 15, 1971. The hot areas are light in color (i.e., the asphalt road indicating 41C) and the cold areas are dark (i.e., the hail swath in the upper center of the figure indicating a brightness temperature in the 8.0 to 13.0 μm spectral band of +2C). The 40C apparent temperature range can be contoured by an eleven step grey wedge and a three point temperature calibration into 3.7C intervals. Magnetic tape wide band FM recording of the imagery can be amplitude sliced to much higher resolution. The temperature range can be gain and level set to a much narrower span but will result in film saturation and cutout.

This airborne IR imaging program was conducted in cooperation with Dr. G. Gayer of NCAR.

6. AIRCRAFT METEOROLOGICAL SYSTEM CALIBRATION

DC-6 aircraft tower fly-bys and aircraft intercomparison with the NCAR instrumented de Haviland Buffalo were flown on June 11 and June 24 respectively. The purpose of these flights was first, to obtain a reference for the meteorological instrumentation accuracy and an analysis of mean differences and standard deviations of the various aircraft data, and second, to determine whether or not systematic biases exist in order to allow that corrections can be made of the obtained data and of the instrument performances. The results suggest that the meteorological state parameters including pressure, temperature, dewpoint were obtained with the expected precisions. The indicated air speed and true air speed differences (DC-6 and Buffalo) were approximately 5 and 7 kts respectively; however, the variation over the flight was small (±½ kt) strongly suggesting the feasibility of removing a relative bias. An argument can be made from the intercomparison flight data that the DC-6 air speed is low while the drift angle is reasonably correct, whereas the Buffalo air speeds are correct, but the drift angle may be in error. Since these are primary inputs to the computation of flight level winds, it is important to further analyza the system accuracies. Improved intercomparison flight paths and a more accurate daily flight calibration method are suggested for 1972.

7. REFERENCES

Duchon, C. E., 1972: *Preliminary Report on Analysis of Mean Differences and Standard Deviations of Meteorological Aircraft Data Acquired from Interaircraft Comparison Flights* (unpublished).

Kuhn, P. M., M. S. Lojko, and E. V. Petersen, 1971: Water vapor: Stratospheric injections by thunderstorms, *Science* **174**, No. 4016, pp. 1319-1321.

Weickmann, H. K., 1969: ESSA-1968 Colorado hail research, Sixth Conference on Severe Local Storms, Preprints, Chicago, Illinois, 8-10 April 1969, pp. 314-319.

Sonderdruck aus
„Meteorologische Rundschau", 25. Jahrgang, 2. Heft, 1972
Seite 38—41

© by Springer-Verlag 1972
Printed in Germany

Atmospheric Electric Cloud Modelling[*]

L. H. Ruhnke
Boulder, Colorado

Summary. Numerical methods are used to calculate electric charges and electric fields in an atmosphere where data on convection and conductivity are available in parameter form. The influence of updraft on the charge and field distribution in fair weather and in the presence of nonraining clouds is shown in examples. It is concluded that no strong generation of electricity is likely in the atmosphere by convective mechanisms and inhomogenities of conductivity alone.

Zusammenfassung. Es werden numerische Methoden benutzt, um die elektrischen Ladungen und das elektrische Feld in einer Atmosphäre zu berechnen, in der in Parameterform die Werte der Konvektion und der Leitfähigkeit vorliegen. An Beispielen wird der Einfluß des Aufwindes auf Ladung und elektrisches Feld bei Schönwetterlagen und beim Vorhandensein nicht regnender Wolken gezeigt. Es wird gefolgert, daß wahrscheinlich in der Atmosphäre keine erhebliche Bildung von Elektrizität allein durch Konvektionsvorgänge und Inhomogenitäten der Leitfähigkeit erfolgt.

1. Introduction

Simulation of atmospheric processes by elaborate mathematical equations is used successfully in many areas of meteorology. Also in atmospheric electricity, significant progress has been made towards understanding of sources and sinks of electricity by relating measured variables to physical and statistical laws. Unfortunately the complexity of the atmospheric electric state has limited theoretical studies to crude approximations in many important areas. Before the advent of large digital computers, it was necessary to approximate the number of variables, their mutual interaction, as well as their spatial extent, such that closed analytical solutions were possible. The results were still very valuable to understand general features of the electric field and current distribution, but descrepancies often developed if one attempted to predict the outcome of particular experiments.

Israel *et al.* [2, 3], in particular Kasemir [4, 5, 6] have tried to describe atmospheric electrical phenomena by relating experimental data to a theory of current flow based on air conductivity, potentials, and currents. This was a considerable improvement over earlier theories that mainly considered electrostatics. But several important aspects of experimental findings could not be satisfactorily explained by their electrodynamic theory, such as the fullfillment of Ohm's law by experiment, the difficulties to detect large scale features on a synoptic scale without long time averaging, and generator processes. The difficulties are not due to inaccuracies in the theories used but rather due to mathematical difficulties to obtain closed solutions for cases that include charge generation processes, convection, turbulence, and nonlinear effects. It can be expected that large computers will make it feasible to include parameters and physical assumptions of such complexity that a numerical description will be found accurate enough to be related to detailed experimental data. Such comparisons of numerical solutions to experimental data can undoubtedly be used to verify existing hypotheses on charge separation, to separate local from global variations, or to obtain a realistic assessment of the global current flow pattern, to name just some.

This study is of preliminary nature and is concerned with the influence of orderly convection on the charge and potential distribution in regions of the atmosphere where no active charge separation processes take place. Therefore, nonlinear effects are excluded as well as random motions. A steady state is assumed not necessarily to simplify mathematics but to keep the study short and concise. No restrictions are needed for the spatial distribution of conductivities and air velocities.

---

[*] H. Israël zum Gedenken gewidmet.

2. Theory

Electrical charges have a quasi-conservative property, i.e., charges can be transported in the atmosphere by convection, but significant effects of charge transport are evident only if the transport times are smaller than the relaxation time of air. Therefore, the equation of continuity of current should include convection currents if space charges and convection exist. In steady state we can assume:

$$\operatorname{div}(q V + \lambda E) = 0. \tag{1}$$

Here q is the space dependent charge concentration per unit volume, V the vector field of the air velocity, λ the space dependent bipolar conductivity, and E the electric field. V and λ are assumed independent variables. The dependence of E on the distribution of q is expressed by Poisson's equation

$$\operatorname{div} E = q/\varepsilon. \tag{2}$$

The permittivity ε is assumed constant ($\varepsilon = 8.859 \cdot 10^{-12}$ A sec/V m is mks units). The velocity distribution can be assumed known in parameter form from measurements, from mathematical equations, or from other numerical simulation models. For the conductivity outside clouds experimental data can be taken, but a simple exponential increase of conductivity with altitude will give reasonable results if most conductivity gradients are confined to regions inside clouds. Cloud conductivities can be estimated from the droplet size distribution and certain assumptions regarding ion combination processes. Boundary conditions for potentials can be obtained from electric field data of fair-weather areas or from data on the density of global currents. For a numerical model, a limited space has to be assumed. Any air entering this space has to have a known space charge concentration at the boundary. To avoid this difficulty we will assume a closed circulation. To allow simulation of simple rotationally symmetric clouds at some altitude above flat ground, we chose conveniently a cylindrical coordinate system with z the altitude coordinate and r the radial distance from the center of the cylinder. Assuming a non-compressable fluid one can rewrite (1):

$$V \cdot \nabla q + \frac{\lambda q}{\varepsilon} + E \cdot \nabla \lambda = 0. \tag{3}$$

For solving (2) and (3) numerically, one can make a first guess for q and solve (2) for E by a relaxation procedure. These values for E can be used to solve in another procedure (3) numerically. A successfull procedure to obtain the next better value of q is to calculate the next value by forward stepping in direction of V. Both procedures are repeated sequentially until both equations are sufficiently fullfilled. Values of q and E converge if the conductivity change over one stepping increment is sufficiently small. Small stepping increments naturally increase the time needed for (2) to converge by relaxation, and a few trial computations are normally needed to decide on a grid size that gives results with sufficient accuracy but still can be used economically. For this study a spacing of 400 m was chosen. The space under consideration is a cylinder with 8 km diameter between ground level and 10 km altitude.

For a closed circulation it is convienient to assume $V = \nabla \times A$, where A is a specified vector field. For our model we use $A = 0$ at all boundaries and a sinusoidal increase of A towards the center of the space where a maximum updraft is assumed. Fig. 1 shows the streamline pattern used. The maximum updraft velocity can be used as a parameter in the calculations to show the influence of convection.

Air conductivity λ_0 in the absence of clouds is assumed to increase exponentially with altitude h:

$$\lambda_0[\Omega^{-1}\,\mathrm{m}^{-1}] = 10^{-14} \exp(2.3 \cdot 10^{-4} \cdot h[\mathrm{m}]). \tag{4}$$

If clouds are present, conductivity will decrease due to the attachment of small ions to cloud droplets. An estimate of the influence of cloud droplets on air conductivity can be made from the steady-state equation of ion balance. Neglecting recombination between small ions (as can be assumed in the troposphere), one can relate the undisturbed conductivity λ_0 to the conductivity λ in the presence of cloud droplets by:

$$\lambda = \frac{\lambda_0}{1 + \dfrac{4 \pi r D Z n_0}{q_0}}. \tag{5}$$

D = diffusion constant for small ions ($3.4 \cdot 10^{-6}$ m²/sec), n_0 = small ion density in cloud free air (m^{-3}), q_0 = rate of ionization (10^7 m^{-3} sec^{-1}), r = cloud droplet radius (m), and Z = cloud droplet concentration (m^{-3}).

Expressing (5) in terms of the liquid water content of clouds w (g · m^{-3}) (a measure usually available in parameter form from measurements or simulation models) one obtains for clouds with an effective droplet diameter of 10 micron:

$$\lambda = \frac{\lambda_0}{1 + \alpha w}$$

with

$$\alpha \cong 50.$$

The value of 50 for α appears reasonable when compared to estimates of Chalmers [1] for conductivity in fog.

3. Numerical Experiments

In a first experiment we assumed a cloudless atmosphere. Convective cells as assumed in Fig. 1 do appear often during daytime heat-up, and it is of interest what effect such convection has on the distribution of space charges

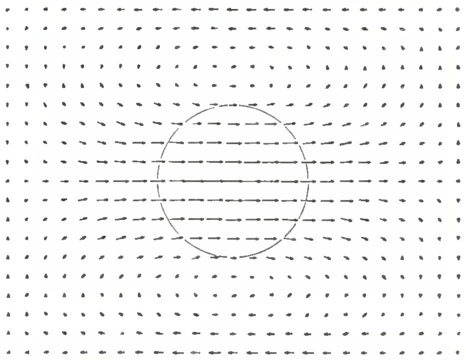

Fig. 1. Field of velocity vectors in the assumed convection model. Maximum updraft velocity is in the center of the cloud

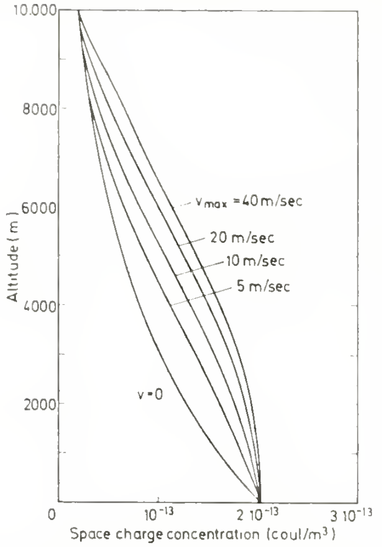

Fig. 2. Altitude profile of spacecharge concentrations in fair weather without clouds to show the influence of convection

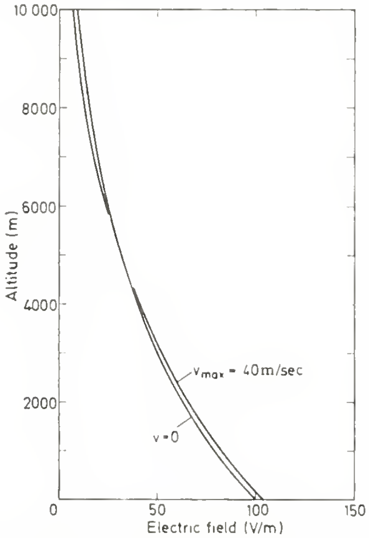

Fig. 3. Altitude profile of electric field in fair weather without clouds. Little influence of convection on electric field can be noticed

and electric fields. Vonnegut [8] has speculated that space charges as they appear in fair weather regions can accumulate through strong updrafts to a point where electric fields at the ground increase such that corona currents develop. Fig. 2 and Fig. 3 show the charge and electric field distribution versus altitude for different values of maximum updraft. It is apparent that a significant change in the charge profile is produced by updrafts; however, even at updraft speeds of 40 m sec^{-1}, no strong increase in surface fields can be noticed, certainly not enough to produce additional ionization by corona.

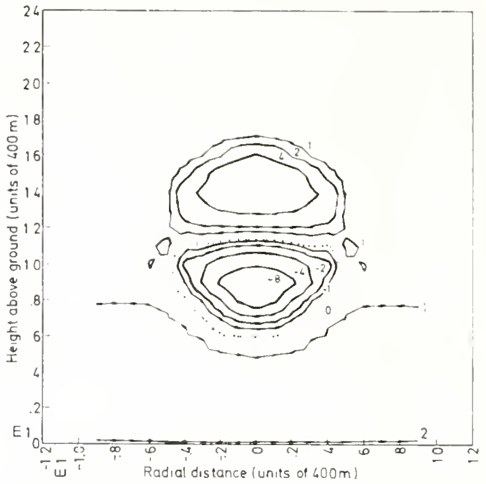

Fig. 4. Isolines of spacecharge concentrations of an atmosphere with a nonraining cloud when convection is neglected. Numbers on isolines denote units of 10^{-13} *A* sec m^{-3}

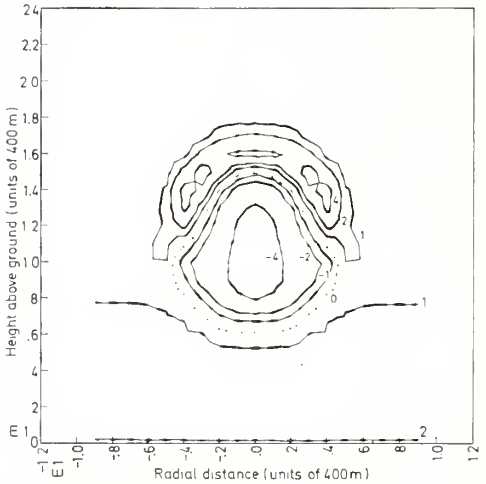

Fig. 5. Same as Fig. 4 except for a maximum updraft velocity of 1 m sec^{-1} in the center of the cloud

In another experiment we assumed a spherical cloud of different dimensions and various values of liquid water content. Fig. 4 shows the charge distribution in the absence of convection for a cloud with maximum liquid water content of 1 g · m^{-3} in the center of the cloud. In the lower part negative space charges accumulate, and in the upper part of the cloud a similar positive space charge develops. This distribution does not change very much if different values for α or w are used as long as their product is larger than 3. This can be explained by the spherical form of the cloud. Similar conditions exist for the electric field distribution. Kasemir [5] has shown generally for a homogeneous cloud that the electric field inside clouds is mainly determined by the form of the cloud if the ratio of conductivity outside the cloud to inside is

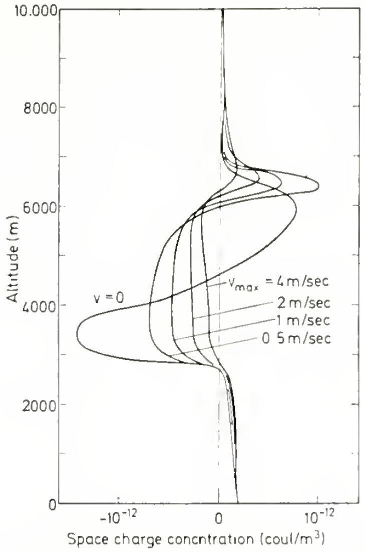

Fig. 6. Vertical profile of space charge concentration through the center of a cloud with maximum updraft velocity as parameter

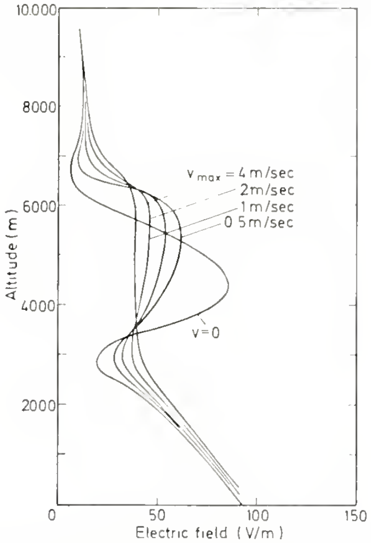

Fig. 7. Vertical profile of electric field through the center of a cloud with maximum updraft velocity as parameter

large. Fig. 5 shows the charge distribution of the same cloud when a circulation with a maximum updraft of only 1 m · sec^{-1} exists. Such conditions might exist in growing cumulus clouds if no precipitation is there.

Figs. 6 and 7 show the charge and electric field distribution, respectively, as a function of altitude in the center of the updraft. Significantly, updrafts tend to decrease the positive as well as the negative charge. However, as already shown earlier with a more primitive model (Ruhnke [7]), the negative charge decreases not as pronounced as the positive charge. The electric field inside the cloud or in its neighborhood does not increase with convection in the model used. It seems unlikely that reasonable parameters for wind velocity or conductivity can be found which produce electric fields at the ground sufficient to generate space charges by corona or to generate electricity in an amount as is evident in thunderstorms.

Literatur. 1. Chalmers, J. A.: Atmospheric Electricity. 2nd Edition, p. 212. London: Pergamon Press 1967. — 2. Israel, H., Kasemir, H. W.: Studien über das atmosphärische Potentialgefalle VI: Beispiele fur das Verhalten luftelektrischer Elemente bei Nebel. Arch. Meteor., Geophys. Bioklim., Serie A **5**, 71 (1952). — 3. Israël, H., Kasemir, H. W., Wienert, K.: Luftelektrische Tagesgänge und Massenaustausch im Hochgebirge der Alpen. Die luftelektrischen Verhältnisse am Jungfraujoch (3472 m) I. Arch. Meteor., Geophys. Bioklim., Serie A **3**, 357 (1951). — 4. Kasemir, H. W.: Studien über das atmosphärische Potentialgefälle. IV: Zur Strömungstheorie des luftelektrischen Feldes I. Arch. Meteor., Geophys. Bioklim., Serie A **3**, 84 (1950); — 5. Studien uber das atmosphärische Potentialgefälle V: Zur Strömungstheorie des luftelektrischen Feldes II. Arch. Meteor., Geophys. Bioklim., Serie A **5**, 56 (1952); — 6. On the theory of the atmospheric electric current flow, IV. USAELRDL Technical Report 2394, U.S. Army Electronics Research and Development Labs., Fort Monmouth, New Jersey, 1963. — 7. Ruhnke, L. H.: A simple model of electric charges and fields in non-raining convective clouds. J. Applied Meteorology **9**, 947 (1970). — 8. Vonnegut, B.: Possible mechanism for the formation of thunderstorm electricity. Proc. Conf. Atmosph. Electr. Wentworth-by-the-Sea. Geoph. Res. Pap. **42**, 169 (1955).

Reprinted with permission from Proc. Eighth Space Congress,
April 19-23, 1971.

ATMOSPHERIC ELECTRICITY PROBLEMS AT KENNEDY SPACE CENTER

Dr. Lothar H. Ruhnke
Physicist
National Oceanic and Atmospheric Administration
Environmental Research Laboratories
Atmospheric Physics and Chemistry Laboratory
Boulder, Colorado

ABSTRACT

The problems encountered when protecting rockets and launch operations from the dangers of lightning are discussed. This reveals the need for a mesoscale network for observing important parameters that indicate lightning danger, as well as the need to develop a set of rules for forecasting potential lightning danger. Before developing methods to inhibit the generation of electricity inside thunderclouds, it is imperative that the charge separation mechanism be thoroughly understood. The present state-of-the-art of lightning suppression uses either metallic chaff fibers to produce a continuous discharge current or rocket propelled projectiles to discharge the thundercloud with artificially triggered lightning.

PRESENTATION

Lightning, either by direct hits or by electric or magnetic induction, endangers launch vehicles as well as ground support operations. Nearby lightning strikes, through induced currents, can easily affect complex electronic equipment and cause time-consuming checking and repair procedures. Explosives can also be ignited by electrical sparks and strong currents. Last but not least, lightning endangers people.

There are three ways to cope with these dangers: protection, prediction, and modification. Protection against lightning is an engineering problem. Usually equipment as well as people are considered to be sufficiently protected against lightning currents as well as against electrical induction when they are inside a Faraday cage. Such shielding is usually insufficient protection against magnetic induction, unless special precautions are used. The problems of protection become particularly difficult if a direct hit by lightning must be anticipated. Electrical currents of lightning strokes are in the order of 10,000 to 100,000 A and last for about 100 microseconds. Even a small fraction of this current can burn out switches, cables, and connectors, not to speak of sensitive components of electronic circuitry, as semiconductors, capacitors, or induction coils. Although engineering techniques can cope with many of the protection problems, one must realize that there are limits in the procedures to protect against lightning.

For predicting lightning danger, one needs, as in weather forecasting, a network to survey a suitable set of parameters and, additionally, a set of rules based either on physical laws or on a history of observations. Then, when potential lightning danger is forecast, equipment and people can be moved to a safe place and the operation delayed until the danger is over. The effectiveness of this approach is limited, because delays are often intolerable or very costly, and equipment sometimes cannot be moved or only moved very slowly. Furthermore, forecasts of lightning danger are not very accurate with the present state-of-the-art, which leads to a high rate of false alarms as well as to insufficient warning of real danger.

The design of a prediction system for lightning danger is not a straightforward engineering task, because some of the instrumentation needed is not commercially available and needs to be designed; also the forecast rules still need to be developed either empirically from observational data or from the physical laws that govern the development of thunderstorms and lightning. In contrast to the prediction system for large scale weather phenomena, thunderstorms have lifetimes of only about 1 hour and extend over only about 5 miles. This makes it necessary to establish a mesoscale observational network with sensors spaced about 2 to 5 miles apart and to gather a set of data for each 10-minute period. This necessitates a rapid data processing and analysis system which has not been developed yet.

Once a good system for surveying and forecasting lightning danger exists, it is necessary to ask whether we must let nature take its course or whether we can purposefully modify and influence that what causes danger to life and equipment. Here we go to the root of the problem by treating the cause. This approach is relatively new, if we neglect all the attempts to modify lightning danger by praying or by wishful thinking. Unfortunately, the cause for lightning and high electric fields inside clouds is as yet unknown. Therefore, our efforts to eliminate or diminish occurrences of lightning should be directed strongly towards basic research on the fundamental processes of the generation of electricity inside clouds. Such an approach, however, is not likely to be favored by an organization like the Kennedy Space Center, in which launch operations, engineering, and technology are the major theme. Yet, without basic research, there can be no significant progress toward eliminating lightning danger to launch vehicles and launch support installations.

We should therefore attempt to explore the mechanism by which electrical charges are generated in clouds. This 200 year old problem has persistently resisted a solution despite the sincere efforts of many noted scientists. A strongly mission oriented research project is necessary; it must be founded on sound physical concepts and make use of modern philosophies and technologies. Such a research effort should be well directed by competent management and should involve the major U.S. centers of competence in atmospheric electricity. As is generally true in basic research, one cannot predict with certainty success as well as time and money expenditures. But I believe the time is right to solve the problem of charge generation and to find a means to eliminate charge accumulations.

At present, the approach to diminish lightning strikes at KSC is also a mission oriented one. Whenever hazardous conditions exist inside a cloud, e.g., electric fields of such a magnitude that they cause natural lightning or lightning that can be triggered by a rocket and thereby endangering the rocket, the cloud or some portion of it should be discharged artificially.

To discharge a cloud one can disperse small metallic fibers, which produce electrical corona currents in strong electric fields. Such corona currents will dissipate the cloud charges and will inhibit the buildup of dangerous conditions. Preliminary field tests by the Atmospheric Physics and Chemistry Laboratory of NOAA have shown the feasibility of suppressing lightning by this method (1). The disadvantage of this method is that such metallic fibers scatter certain electromagnetic waves, which can interfere with vital communications between a rocket and the ground. Using this method therefore requires good coordination between communication engineers and cloud physicists in the design of a workable lightning suppression system.

Other schemes that promise success include the use of projectiles to trigger lightning in a controlled manner, such that no natural or unintended lightning occurs. Feasibility studies were made using small rockets that were connected to the ground during flight by a wire which triggered lightning (2).

One project conducted by Atmospheric Physics and Chemistry Laboratory of NOAA, under NASA sponsorship, uses a small rocket, "Mighty Mouse," that triggers, at will, lightning inside clouds. Tests conducted in 1970 at Socorro, N. M., (3) showed very encouraging results not only to discharge some portion of the thundercloud but also to study, in general, the mechanism by which rockets trigger lightning. Such studies are necessary to assess the danger of large rockets, like the Saturn V, unintentionally triggering lightning. The Apollo 12 lightning incident showed the necessity to understand fully the physcal conditions that lead to lightning.

It is certain that in the future more concepts will be proposed and tested to harmlessly dissipate electricity that is produced and stored in a thunderstorm. It is also certain to me that the atmospheric electric problems at KSC will be solved sufficiently only when the physics of the charge separation process inside clouds is well understood, and a means to control this process is found.

REFERENCES

(1) Kasemir, H. W. "Lightning Suppression by Chaff Seeding." ESSA Final Report on USAECOM Project 67-93906, June 1968.

(2) Newman, M. M. "Use of Triggered Lightning to Study the Discharge Process in the Channel and Application V L F Propagation Studies." *Problems of Atmospheric and Space Electricity*. S. C. Coroniti ed. (Elsevier Publ. Co. Amsterdam.) 482-490, 1965.

(3) Kasemir, H. W. "Basic Theory and Pilot Experiments to the Problem of Discharging Electrified Clouds by Rocket-Triggered Lightning Discharges." NOAA Technical Report (U. S. Government Printing Office, Washington, D. C.), April 1971.

U.S. DEPARTMENT OF COMMERCE
Maurice H. Stans, Secretary

NATIONAL OCEANIC AND ATMOSPHERIC ADMINISTRATION
Robert M. White, Acting Administrator
ENVIRONMENTAL RESEARCH LABORATORIES
Wilmot N. Hess, Director

NOAA TECHNICAL REPORT ERL 195-APCL 16

Determining Distance to Lightning Strokes From a Single Station

LOTHAR H. RUHNKE

ATMOSPHERIC PHYSICS AND CHEMISTRY LABORATORY
BOULDER, COLORADO
January 1971

TABLE OF CONTENTS

Page

ABSTRACT iv

1. INTRODUCTION 1

2. THEORY 2

3. INSTRUMENT DEVELOPMENT 11

4. EXPERIMENTS 18

5. ACKNOWLEDGMENTS 24

6. REFERENCES 24

APPENDIX A 25

ABSTRACT

A study has been made to use the differences between the decay of electric and magnetic fields near lightning strokes to determine the distance from a single station to the lightning. In our analysis a model of a return stroke is used to compute the waveform of electric and magnetic fields, between 1 km and 100 km distance, and the associated frequency spectrum. At distances small compared with the length of the return stroke channel, the electric field and also the magnetic field decrease inversely with distance from the stroke. From 3 km to 30 km the electric field, when observed at 1 kHz decreases approximately with the cube of the distance, while the magnetic field decreases with the square of the distance. For distances farther than 30 km, both signals decay inversely with distance. On an observation frequency of 1 kHz, it is possible to determine distances to return stroke channels between 3 km to 30 km by using the ratio of magnetic field to electric field. For this range, this ratio is independent of waveform and magnitude of the lightning signal. A prototype instrument was designed and tested during one thunderstorm season. The instrument uses loop antennas for sensing magnetic fields and horizontal wire antennas for sensing the electric field, and contains sharp filters, amplifiers, and peak voltage detectors. For the output, strip chart recorders are used. Data obtained with this instrument verify the predicted possibility of determining from a single station the distance to lightning strokes.

U.S. DEPARTMENT OF COMMERCE
Maurice H. Stans, Secretary

NATIONAL OCEANIC AND ATMOSPHERIC ADMINISTRATION
Robert M. White, Administrator
ENVIRONMENTAL RESEARCH LABORATORIES
Wilmot N. Hess, Director

NOAA TECHNICAL REPORT ERL 206-APCL 20

A Rocket Borne Instrument to Measure Electric Fields Inside Electrified Clouds

L. H. RUHNKE

BOULDER, COLO.
May 1971

TABLE OF CONTENTS

Page

ABSTRACT 1

1. INTRODUCTION 1

2. DESIGN CRITERIA 3

3. PRELIMINARY TESTS AND DEVELOPMENT PROCEDURE 4

4. INSTRUMENT DESCRIPTION 12

5. TESTS FLIGHTS 25

6. ACKNOWLEDGMENTS 26

7. REFERENCES 27

APPENDIX 28

A ROCKET BORNE INSTRUMENT TO MEASURE ELECTRIC FIELDS INSIDE ELECTRIFIED CLOUDS

L. H. Ruhnke

Development of a rocket borne instrument to measure electric fields in thunderstorms is described. Corona currents from a sharp needle atop a small rocket are used to sense the electric field. A high ohm resistor in series with the corona needle linearizes the relationship between corona current and electric field. The corona current feeds a relaxation oscillator, whose pulses trigger a transmitter which operates in the 395 to 410 MHz meteorological band. The instrument senses fields between 5 kV/m and 100 kV/m.

Reprinted with permission from EDN/EEE *16*, No. 16, Aug 1971.

Variable dc offset using a current source

To Vote For This Circuit
Circle 162

by **P. Bruce Uhlenhopp**
NOAA
Boulder, Colo.

In many circuit applications it is useful to offset ac signals at varying dc levels. Some designs call for offsetting signals that are to be fed into a moderately high input impedance. A dc offset can be added to an ac signal without significant interaction by using a high-impedance current source to provide the desired level shift as illustrated in the figure.

Transistor Q_4 and its resistive network form a high-impedance adjustable current source. The input signal and the offset signal are fed to the base of Q_3 which drives Q_1 and Q_2, a complementary-symmetry emitter follower.

For the values shown, the level can be shifted about ±7V dc. This is particularly useful in a video circuit whose dc level controls the intensity of a CRT. DC level can be controlled from a panel-mounted potentiometer since the high-frequency video signal does not pass through the pot.

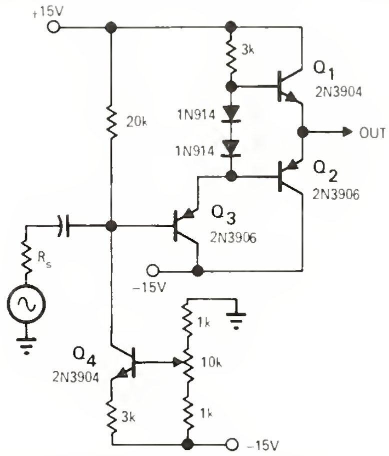

This simple circuit, using an adjustable current source, allows a video signal to be offset ±7V dc.

U.S. DEPARTMENT OF COMMERCE
National Oceanic and Atmospheric Administration
Environmental Research Laboratories

NOAA Technical Memorandum ERL APCL-15

DESIGN, EXECUTION, AND RESULTS OF A MESOSCALE SNOWSTORM MODIFICATION PROJECT

Helmut K. Weickmann

Atmospheric Physics and Chemistry Laboratory
Boulder, Colorado
May 1972

TABLE OF CONTENTS

Page

ABSTRACT 1

1. INTRODUCTION 2
2. DISCUSSION 2
    a. Mesoscale numerical model 5
    b. The problem of snowcrystal aggregation 13
    c. Results of seeding activities during two winter seasons, 1968 to 1969. 15
    d. Problem of targeting the seeding effect 17
    e. Case of 7 December 1968 18
    f. Case of 3 December 1969 19
    g. Case of 4 December 1969 23
3. CONCLUSION 24
4. ACKNOWLEDGEMENTS 25
5. REFERENCES 26

FIGURE CAPTIONS 28

FIGURES 32

DESIGN, EXECUTION, AND RESULTS OF A MESOSCALE SNOWSTORM MODIFICATION PROJECT

Helmut K. Weickmann
Atmospheric Physics and Chemistry Laboratory
National Oceanic and Atmospheric Administration
Boulder, Colorado

In the Great Lakes region of the U.S.A., shallow but intensive winter storms form through a combination of cold continental air moving over still unfrozen and even warm, large water surfaces. Depending on their trajectories over the lakes and their persistence, these storms may dump large amounts of snow onto the downwind shorelines. The natural freezing nuclei concentration causes the formation of heavily rimed crystals; seeding shall increase their number and prevent riming, causing smaller crystal fall velocities and consequently a larger transport of snow downwind and away from the urban and industrial centers near the shores. The experiment is designed around a mesoscale numerical model and microphysical model of snow crystal formation. The great variability of the cloud systems prevents a clear definition of a homogeneous sample of comparable experiments and makes, therefore, a clear statistical design impossible. The execution employs seeding from the ground and from the air, tracking of the seeding agent through the cloud system by an airborne freezing nucleus counter, and analyzing the AgI nuclei in the precipitated snow crystals. The analysis includes radar, surface observation stations, and airborne observations. Results indicate the capability to affect the snowfalls in the desired mode strongly depends on the cloud temperature, indicating that snowfall can be initiated, redistributed, or not be affected at all. The project continues.

Reprinted from WEATHERWISE, Vol. 25, No. 6, December 1972
American Meteorological Society
Printed in U. S. A.

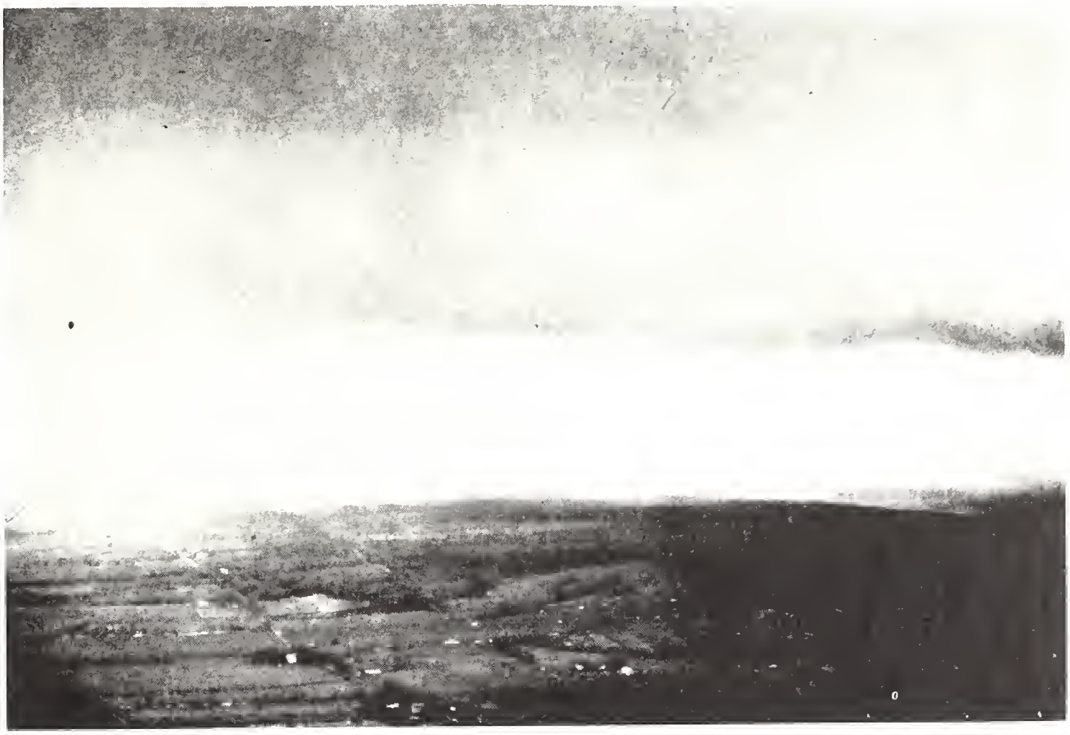

Fig. 1. Artificial snowshower over the southern shore of Lake Erie on 25 November 1968.

Man-made Weather Patterns in the Great Lakes Basin

HELMUT WEICKMANN, *Director, Atmospheric Physics and Chemistry Laboratory, NOAA, Boulder, Colorado*

IN the heartland of the North American Continent is the Great Lakes Basin. It is not only a most interesting region for its hydrology, its population density, and its industrial growth, but also it is fascinating for its weather systems as it produces much of its own climate (Changnon, 1968).

The Great Lakes Basin encloses an area of more than 750,000 km^2 and has a water surface of 250,000 km^2. Thirty-two million people live within the lake boundaries—twenty-eight million of them take their water requirements directly from the hydrological system of the Great Lakes Basin. This makes a daily total water consumption for industrial and private use of 15,600 million gallons. It is interesting to note that the average amount of snow falling from a typical Lake Erie "lakestorm" is 250,000 millions of gallons, or a 16-day supply of water for the population. During the period 4 November 1966 through 25 January 1969, 23 storms occurred (Jiusto and Kaplan, 1972); this was a water supply for one year. As the hydrology of all the lakes is delicately balanced, it is obvious that the artificial manipulation of atmospheric resources over the lakes may have a very significant influence on various human activities.

Climatologically, the Great Lakes region is peculiar in that its numerous relationships between the water surfaces and the air exert particularly strong influences in the atmospheric boundary layer. In winter the entire Great Lakes Basin has a high frequency of shallow cloud layers which, upon travelling across the still unfrozen and warm lakes, form the basic ingredient for the development of lake-effect storms (Lavoie, 1972).

Figure 2 shows the mean cloudiness of North America in January. The Great Lakes Basin stands out with high cloudiness like an island. The reason for this high cloudiness is the annual course of evapotranspiration which shows over land a minimum in December and January and a maximum in June and August, while the Great Lakes have often negative evaporation during May and June, but they have maximum evaporation in late fall and early winter due to storage of solar energy as sensible heat content during the summer months, with extreme values during days with lake storm events. The low level water source leads to the frequent occurrence of shallow supercooled cloud layers within the boundary layer. These cloud layers are generally 1700–1800 meters thick and often have cloud top temperatures warmer than −15°C. Few natural freezing nuclei are active at these warm temperatures and consequently there is a poor natural release of precipitation. Precipitation from these clouds can be released through artificial seeding. Their precipitation potential can be estimated from the rate of condensation in convective cloud layers based upon updraft speeds measured with a doppler radar. Table 1 gives hourly values of induced precipitation for various conditions of cloud thickness and temperature, assuming a 50% effectiveness of the seeding effort.

TABLE 1

ESTIMATE OF INDUCED PRECIPITATION—
50% EFFICIENCY

Geographic area	Stratus cloud thickness (meters)	Temperature range (°C)	Updraft velocity (cm/sec)	Induced precipitation (mm/hr)
Great Lakes	3000	0 to −22	10	1.73
	3000	0 to −22	50	8.05
	2000	0 to −15	50	4.50

For the past 5 years the National Oceanic and Atmospheric Administration has studied the weather modification potential of the Great Lakes region. Numerous observations of artificial rain and snowfall have been made in the Buffalo region of Lake Erie. Several cases are listed in table 2.

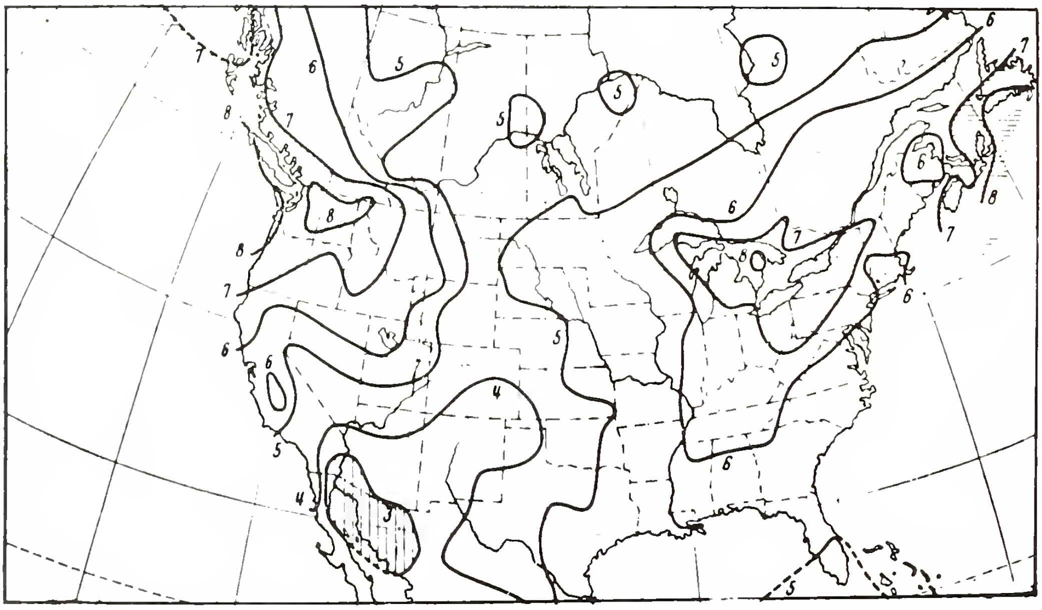

Fig. 2. Average January daytime cloudiness over North America in tenths (after R. De C. Ward, et al., 1936).

TABLE 2

INITIATION OF PRECIPITATION

Date	Convective layer				Stratiform layer				Seeding	
	Base		Top		Base		Top		Type	Result*
	m	°C	m	°C	m	°C	m	°C		
13 Nov 68	900	−7	2000	−9					650 lb dry ice racetrack	$\overset{*}{\nabla}$ 35 min. A.S.
25 Nov 68	900	−2	1800	−9.5	2100	−10	2400	−10.8	250 lb dry ice circle	$\overset{*}{\nabla}^1$ 26 min. A.S.
29 Nov 68	700	−2	1800	−10.8					450 lb dry ice 3 legs	$\overset{*}{\nabla}^1$ 1/3"/hr
2 Dec 68	300	+1	2400	−11					550 lb dry ice	$\overset{\cdot}{\nabla}$ over lake
3 Dec 68	1000	+1.5	2600	−8	2700	−11.3	2900	−12.3	2400g AgI fusees	$\overset{\cdot}{\nabla}$ over lake
6 Dec 68	300	−6.5	1500	−12.0	1800		2100	−14.5	2400g AgI fusees 700 lb dry ice	$\overset{\cdot}{\nabla}^{1-2}$ over lake $\overset{\cdot}{\nabla}^{1-2}$ 36 min A.S.

* Legend: $\overset{*}{\nabla}$ snow shower; $\overset{\cdot}{\nabla}$ rain shower; A.S. after seeding; and exponent ^{1} or ^{2} indicates intensity: ^{1} moderate and ^{2} heavy.

Intentionally-produced, man-made snowshowers of 25 November 1968 are shown in figure 1. See table 2 for cloud data. Note the optical density of the showers. Radar echoes of similar showers on 29 November are shown in figure 3. On this day the clouds snowed out completely letting the sunshine come through. On 25 November other man-made snowshowers were discovered; these were, however, inadvertently caused by industrial pollution. The Basin is the seat of many industries whose pollution potential not only affects the hydrology and ecology but also the weather. For instance, large concentrations of highly effective freezing nuclei have been found downwind of the Bethlehem Steel Plant in Lackawanna near Buffalo. These nuclei have released downwind snowshowers on several occasions (fig. 4). Of course, the famous La Porte, Indiana, anomaly may be another case of a possible pollution effect.

Figure 4 shows the flight path after the seeding experiment; the numbers written along the flight path are freezing nuclei concentrations measured with a carefully calibrated airborne acoustic ice nuclei counter. Note that downwind of Buffalo, Toronto, and the industrial center of Oshawa snowshowers formed, visible as radar echoes which were clearly related to the high concentration of artificial ice nuclei. The showers which developed on 6 December following seeding were much more intense; they withstood on the National Weather Service 10 cm WSR-57 radar an attenuation of 36 db, and during penetration with the aircraft we encountered gustiness and heavy precipitation as in a miniature squall line. The development of the echo areas following dry ice and AgI seeding is shown on figures 5 and 6. The spreading of the seeding effect throughout the cloud deck by careful planimeterization of the radar echo areas is shown in figure 7. It illustrates the superiority of the dry ice seeding from the cloud tops over the AgI seeding at cloud base: Dry ice forms a curtain of ice crystals throughout the cloud layer, while AgI seeding produces only a line of crystals. The latter method takes about 20 minutes before the areal growth of its seeding parallels the dry ice growth. It must be mentioned, though, that after 20 minutes, the dry ice area contained about 60 crystals/l, while the AgI area contained about

20/l. The larger number of nuclei from dry ice seeding may have contributed to accelerating the spreading of the seeded area.

A similar squall line after seeding has been observed to form during earlier experiments over Lake Michigan (Weickmann, 1957).

An efficient vertical transport mechanism exists for seeding material which is released at the surface. The formation of snowshowers in anthropogenic nuclei plumes as in figure 4 testifies to this mechanism. We have explored this mechanism in an experiment on 4 December 1969 where a surface generator was placed at Millers Point, Canada, on the north shore of Lake Erie. AgI was released at a rate of 20 g/min from 1200–1330 EST. The plume was tracked across the Lake with an airborne ice nuclei counter mounted in the NOAA DC-6 aircraft, and figure 8 indicates the result. The plume boundaries are marked

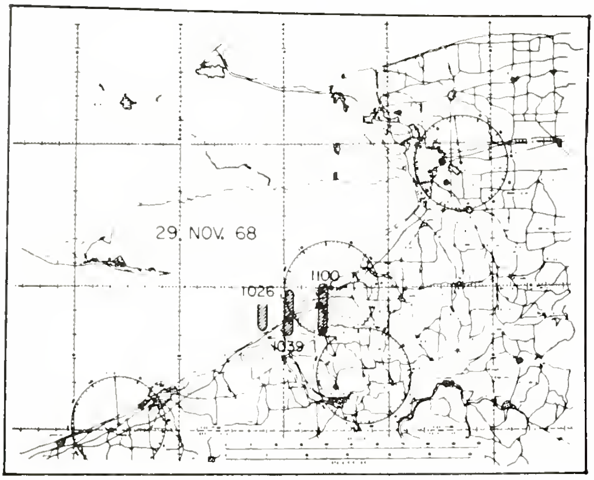

Fig. 3. Radar echoes of snow showers on 29 November 1968.

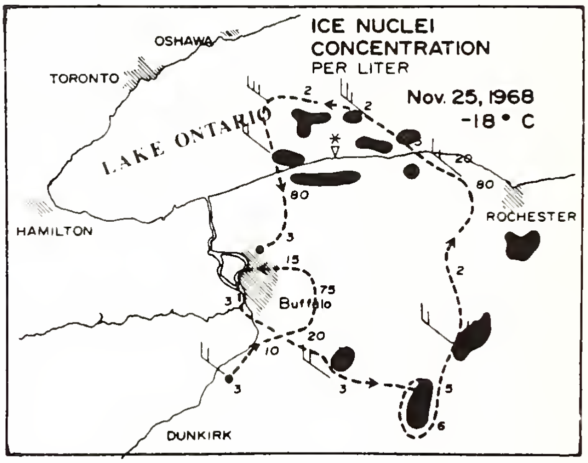

Fig. 4. Radar echoes of snow shower produced inadvertently by anthropogenic nuclei downwind of industrial centers, 25 November 1968. The figure gives the flight path of the NOAA DC-6 and ice nuclei concentrations measured along the flight path.

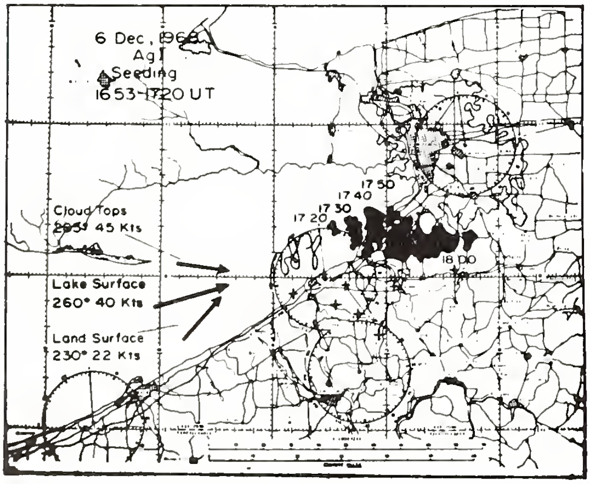

Fig. 5. The effect of AgI seeding on 6 December 1968. Note flight path during seeding and development of radar echoes following seeding.

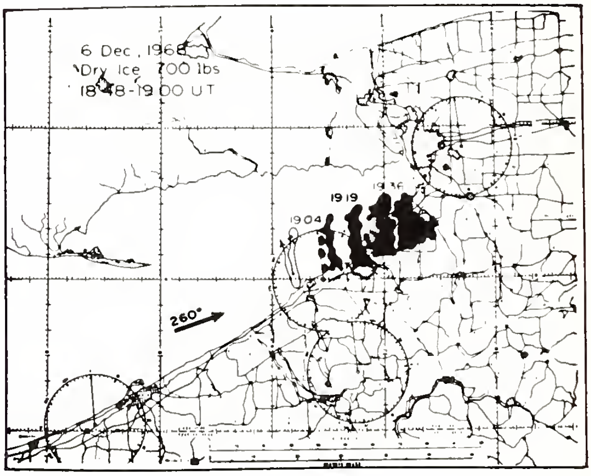

Fig. 6. The effect of dry ice seeding on 6 December 1968. Note flight path during seeding and development of radar echoes following seeding.

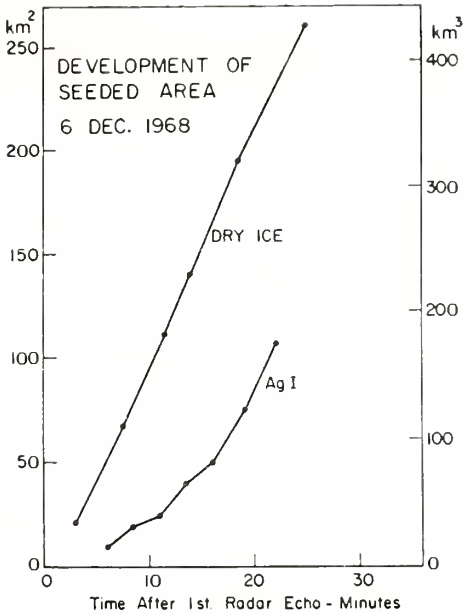

Fig. 7. Areal spreading of AgI and dry ice seeding.

and so are snowshowers that have begun to form near the southern shoreline. They appeared clearly on the Dunkirk radar operated by the Cornell Aeronautical Laboratory and their precipitation particles have been observed over land by ground teams of the State University of New York. Snowfall augmentation amounted to about 0.5-inch per hour. No clouds existed over the northern shore while clouds formed as the air moved across the warm lake.

The understanding of the mechanism of intensive lake storms has been considerably enhanced by the Lavoie numerical model (Lavoie, 1972). Lavoie describes the applicability of his model for a study of precipitation processes which has been applied for a specific case by Magaziner (1972). He assumed an airflow along the axis of Lake Erie, wind speed 15 m/sec, and a lake-air temperature difference of 12°C while the upstream inversion height was at 2000 m. He incorporated the formation of precipitation particles due to diffusion, due to riming, and due to crystal aggregation. Figure 9 illustrates the water equivalent of precipitation in the natural unseeded case. This pattern agrees well with observations made during similar storms, for instance, during the storm of 15–16 November 1969. When seeding was accomplished using dry ice or AgI cartridges released at cloud top and generating 100 crystals/l along the line marked "seed" (fig. 10), the distribution of precipitation changed drastically and most of it was discharged into the lake before reaching the shore and metropolitan area of Buffalo.

The result of this numerical field experiment seen against the background of verification of the Lavoie model as reported by Lavoie (1972) may be a very real solution. It may,

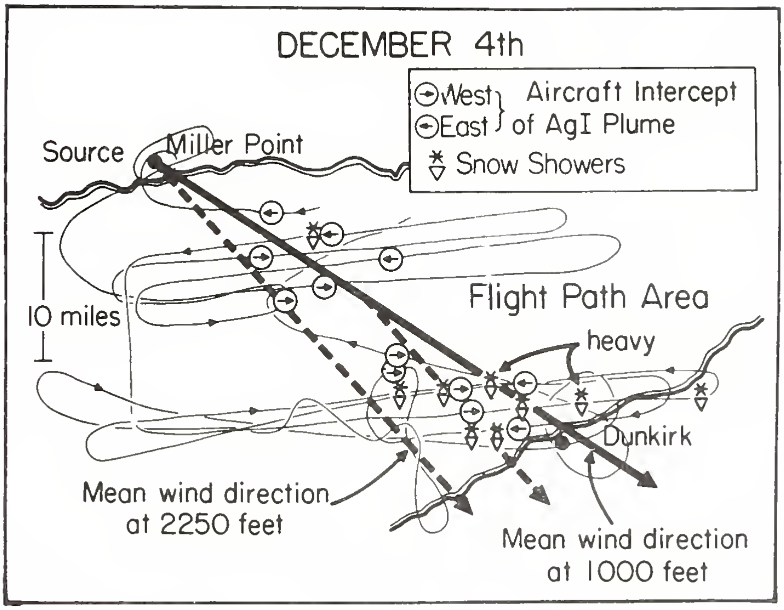
DECEMBER 4th
West
East
Aircraft Intercept of AgI Plume
Snow Showers
Source
Miller Point
10 miles
Flight Path Area
heavy
Dunkirk
Mean wind direction at 2250 feet
Mean wind direction at 1000 feet

Fig. 8. Analysis of seeding effect when seeding was carried out with ground based AgI generator from Millers Point (Canada) on northern shore of Lake Erie, 4 December 1969.

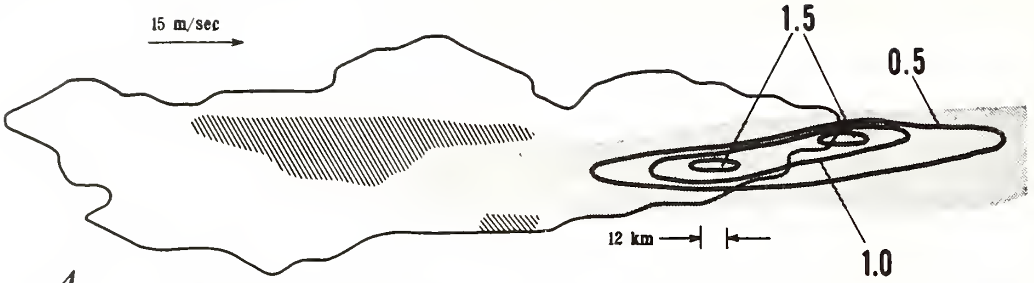
15 m/sec
1.5
0.5
1.0
12 km
N
Precipitation in mm/hr of melt.
Crosshatched areas indicate primarily diffusional crystal growth,
screened areas primarily accretional growth. Unseeded case.

Fig. 9. Result of numerical experiment of Lake-Effect Storm. Development of natural precipitation (Magaziner, 1972).

of course, not be the only solution that nature finds. But, if we were able to verify this solution on a naturally occurring storm, we would very well be on our way to manipulating artificially the lake level and contributing significantly to the water needs of millions of people. It is known that the lake levels undergo considerable annual variations reaching several feet in both directions for a mean level. Fortunately, the response time of the lake levels to precipitation and evaporation—the two main contributors—has a delay of about one year. Therefore, sufficient lead time is available for the effective experimental planning of water recycling into the lakes.

Cloud Dissipation

Another interesting weather modification potential over the Great Lakes Basin exists through the dissipation of extended supercooled cloud layers. This will not only contribute to the amelioration of the frequently dreary winter climate, but it will directly affect the albedo of the weather system and through the albedo the energy source, namely the sun radiation, which ultimately drives the weather mechanism. Figure 11 shows a man-made weather scene over Thunderbay, Lake Michigan, after dissipation of about 175 km² of an extended supercooled cloud deck of the following characteristics: base 1350 m, −7.5°C, top 2100 m, −9.0°C. Seeding was done with 12 lbs of dry ice per mile along three parallel legs with three miles separation between each leg. Man-made blue sky is visible on top of the photograph which had been taken after descending through the opening in the cloud deck. Man-made snowshowers from a fourth seeding run are still visible in the background, while in the center of the picture cumulus clouds are forming due to initiation of convection and downward

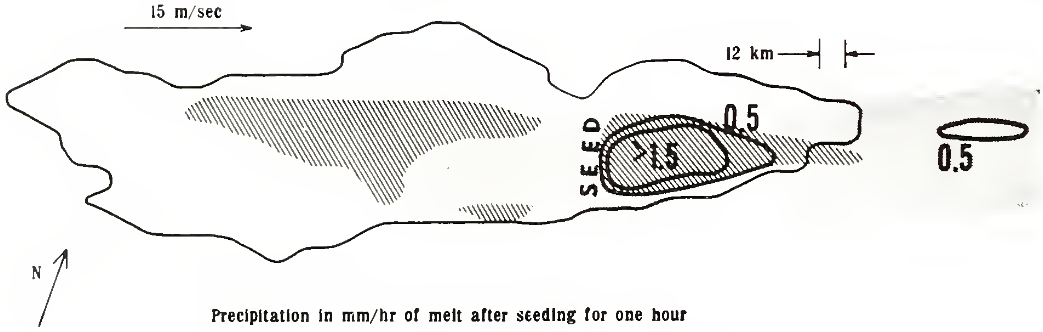
15 m/sec
12 km
SEED
0.5
>1.5
0.5
N
Precipitation in mm/hr of melt after seeding for one hour
with maximum concentration of 100 nuclei/liter.
Crosshatched areas indicate primarily diffusional crystal growth,
screened areas primarily accretional growth.

Fig. 10. Result of numerical experiment of Lake-Effect Storm. Development of precipitation after seeding (Magaziner, 1972).

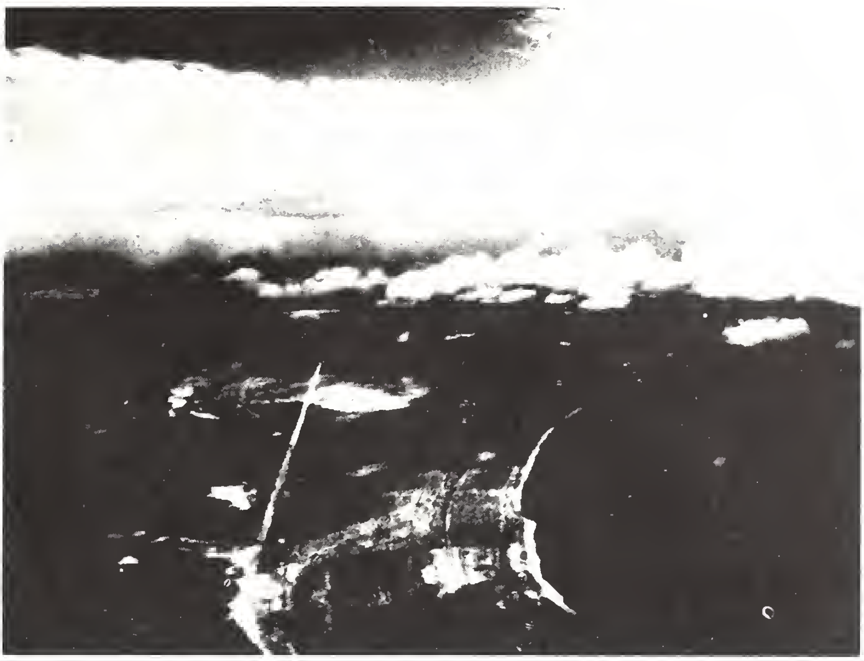

80 MIN AFTER SEEDING

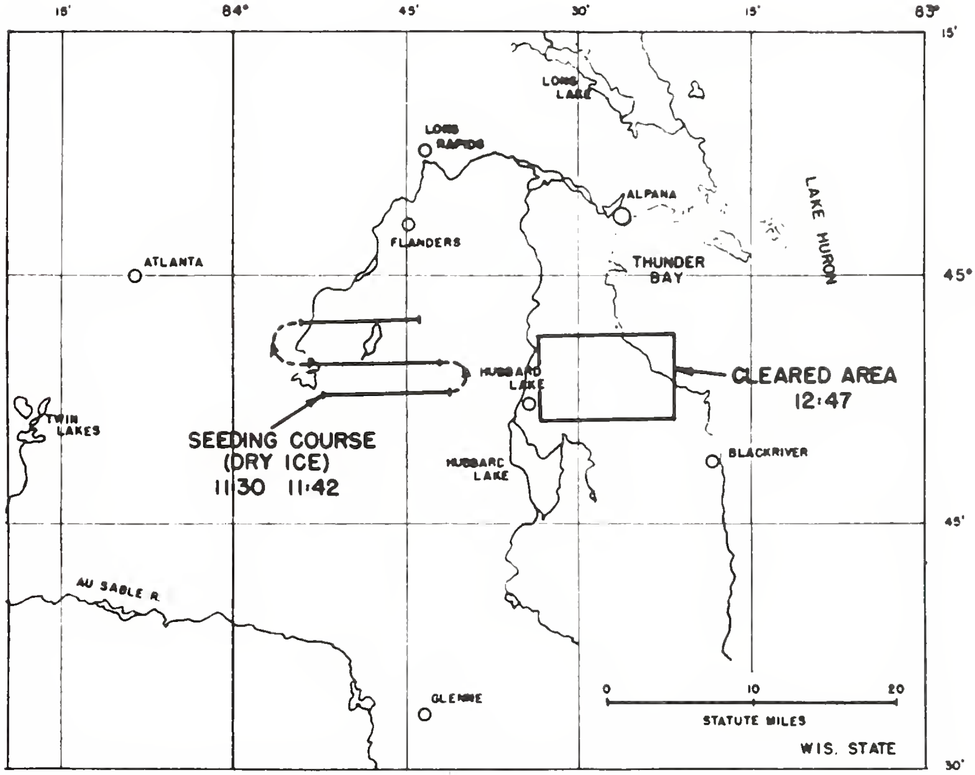

Fig. 11. A man-made weather scene over Thunderbay, Lake Michigan.

transport of moisture from the snowed out cloud deck. Numerous additional cases of cloud dissipation have been described elsewhere (aufm Kampe et al., 1957).

Outlook

The potential of cloud modification during winter in the Great Lakes Basin has been sketched above. There is no doubt that the research accomplished so far is most promising for the application of seeding methods in a beneficial way for the population. How can "beneficial" be defined? Along the southern shore of Lake Erie and elsewhere, skiing areas exist. For these areas snowfall is beneficial while it may not be so for the communities in their environment for which snow is often a nuisance. During years of low lake level recycling of water back into the lakes would be beneficial for the water needs of the Great Lakes Basin population, industries, and water power requirements. The water needs of the City of Chicago constitute a special case. The tightly-controlled lake hydrology causes problems with the water supply of the City of Chicago which has a water allotment from Lake Michigan of 1700 cubic feet/sec (CFS) while its needs are 3200 CFS.

Through systematic cloud seeding activities substantial amounts of precipitation could be added to Lake Michigan during wintertime which could easily accumulate to a 10-day supply at a present cost to the consumer of $3 million. During years of high lake level atmospheric water can be exported to other neighboring water sheds, or artificial snowfall can be targeted over skiing areas or cloud dissipating can be accomplished for the improvement of the climate.

It is conceivable that the Great Lakes Basin offers also during summer interesting possibilities for weather modification.

The many different configurations in the geographic boundaries between water and land cause natural convergences in the low level, so-called, Ekman flow. These areas are predestined for the development of clouds and the organizations of showers. We believe that La Porte, Indiana, is located in such an area. For the prevailing westerly flow, the land area around the southeast lake corner will be an area of natural convergency of air coming across the water and air coming over land along the southern shore region. This will cause *a priori* a high year-round shower activity, and it is entirely plausible that the ice nuclei sources in the Gary, Indiana, industrial complex contribute to enhance the precipitation efficiency in that area. Figure 12 shows the area of increased precipitation in that region (Huff and Changnon, 1972). Most likely more such areas of natural convergence exist in the Basin.

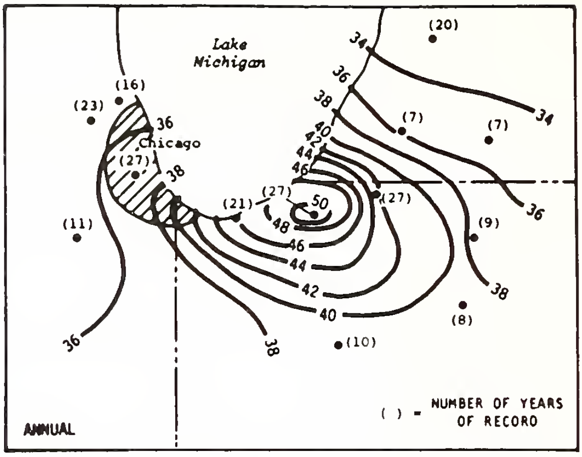

Fig. 12. Average annual pattern of number of thunder days at Chicago-La Porte area based on 1942–1968 period (Huff and Changnon, 1972).

The exploration of all these possibilities of precipitation enhancement is planned by NOAA in a program designed and executed jointly with universities and private research institutions in that region. A thorough assessment of not only the meteorological and climatological problems, but also of the legal, international, socio-economic, and ecological implications is planned before major seeding experiments can be designed.

Weather modification of the future will look entirely different from the first steps that we are taking now: In order to do justice to the numerous different requirements for weather modification which may develop in an area of the potential of the Great Lakes Basin, such as, to make snow over skiing areas, to mitigate lake winter storms, to recycle cloud water back into Lake Michigan, to dissipate supercooled cloud layers, we realize that a new dimension in the scale of such operation is required.

The impressive seeding events described above have been encountered more or less accidentally and without the need to direct

(*Continued on page 285*)

Man-made Weather

(*Continued from page 267*)

them over a certain target. This need becomes immediately a reality as soon as an operational large-scale weather modification effort in the Great Lakes Basin is planned. Then, above all other experimental requirements, a complete forecasting capability of seeding potentials must be developed. It is almost certain that the accuracy requirements with which this forecasting service is confronted are much more ambitious than those for present-day forecasting, as ground generators for nuclei must be turned on at a certain time and location, aircraft crews alerted, and numerical models must be studied in order to be able to target various effects over certain areas. These model computations must be continuously updated as the seeding time approaches on the basis of incoming refined weather reports. These reports must make use of the most modern means of weather analysis through satellites, radar systems, and remote probing capabilities. Likewise socioeconomic considerations will require a complete analysis capability of the seeding effect. NOAA is planning to develop these capabilities step by step by centering its weather modification efforts into certain areas.

Credit

Credit is due to our contractors at Cornell Aeronautical Laboratories, at State University of New York, at Pennsylvania State University, at Desert Research Institute, to the pilots and crew members of the NOAA Research Flight Facility and last but not least to my co-workers at the Atmospheric Physics & Chemistry Laboratory.

References

Changnon, S. A., 1968: *Precipitation Climatology of Lake Michigan Basin, Bulletin 52,* State of Illinois, State Water Survey Division, Urbana, 46 pp.

Huff, F. A., and S. A. Changnon, 1972: *Climatological Assessment of Urban Effects on Precipitation, Final Report, Part I—Summary and Conclusions.* Illinois State Water Survey, Urbana, NSF-GA 18781, 34 pp.

Jiusto, J. E., and M. L. Kaplan, 1972: Snowfall from Lake-effect Storms, *Mon. Wea. Rev.* **100**, 62–66.

Lavoie, R. L., 1972: A Mesoscale Numerical Model of Lake-Effect Storms, *J. Atm. Sc.* **29**, 1025–1040.

Magaziner, E., 1972: A Numerical Model of the Effects of Seeding on the Evolution of Lake Effect Storm, submitted for publications to *J. Atm. Sc.,* November 1972.

Ward, R. DeC., C. F. Brooks, and A. J. Connor, 1936: *The Climates of North America—Handbuch der Klimatologie.* Vol. II, Part J, Gebr. Borntraeger, Berlin, 325 pp.

Weickmann, H., 1957: Current Understanding of the Physical Processes Associated with Cloud Nucleation. *Beitr. Phys. Atmo.* **30**, 97–118.

Reprinted with permission from Journal de Recherches Atmosphériques *VI*,
Nos. 1,2,3, Dessens Memorial, Jan-Sept 1972.

SNOW CRYSTAL FORMS AND THEIR RELATIONSHIP TO SNOWSTORMS

Helmut K. WEICKMANN

Atmospheric Physics and Chemistry Laboratory
Environmental Research Laboratories
National Oceanic and Atmospheric Administration
Boulder, Colorado, U.S.A.

RÉSUMÉ

On discute de plusieurs formes typiques de cristaux de neige, et on montre leur relation avec la structure à grande échelle des orages. La formation de formes spécifiques, par exemple les étoiles dendritiques et les cristaux spatiaux, est discutée de façon plus détaillée.

ABSTRACT

Several typical snow crystal forms are discussed and it is shown how they are related to the large scale storm structure. The formation of specific forms, for instance, dendritic stars and spatial crystals are discussed in more detail.

In the past years we have studied precipitation systems that occur during winter in the Great Lakes Basin. We have observed the occurrence of three basic precipitation systems which can be clearly separated due to the particle type that they discharge as well as due to the typical cloud system in which these originate. Figure 1, which shows the dependence of major crystal forms on temperature in a water-saturated environment, will assists the reader in the following discussion.

THE PRECIPITATION SYSTEMS.

System No. 1 : System 1 occurred typically on February 13, 1971. It is a synoptic scale precipitation system whose center moved north-eastward and was located east of the Great Lakes region. Overriding warm air over the cold air on the back side of the large depression caused the formation of a deep altostratus layer which continuously discharged very fine snow crystals. A typical radiosonde cross section is shown on Figure 2. The overriding warm air is clearly shown from the inversion (temperature increase at 900 mb) ; in the shallow layer below the inversion, clouds may form but no ice crystals as the temperature is not sufficiently low. Lake Erie being frozen did not introduce warm convection. Yet from the homogeneously overcast sky, fine snow fell whose crystals have the typical shapes of low temperature origin which are typical of cirrus and altostratus. The ice character of the cloud follows from the dewpoint which represents ice saturation for the environmental temperature. The following log entries testify to the cirrostratus character of the crystals.

Buffalo, New York — 13-14 *February* 1971.

08.10 EST. Small flakes of small rimed prism bundles ; individual crystal sizes about 0.1 mm diameter, flakes 1 to 2 mm, 20 to 30 crystals per flake. Note from Figure 2 that the occurrence of a thin sc-layer at the inversion is possible due to the steep gradient and the high humidity. The temperature however is too warm for the formation of crystals therefore only riming of the high level crystals occurs. As the Buffalo region remains on the edge of the large scale depression as it moves north-eastward, the crystal shape does not change all day.

Niagara, New York.

09.55 EST. Still typical As, Cs particles now unrimed in small flakes, less than 10 individual crystals consisting of hollow prism bundles with numerous individual crystals, 0.1 to 0.2 mm ; some crystals indicate the beginning of the formation of end plates. (The formation of end plates on prisms indicates the existence of layers of higher humidity at the temperature range where normally plates would form).

On road between Niagara and Buffalo.

14.55 EST. Still same type of snowfall, essentially unflaked As particles, prisms, on and off rimed (were rimed at 14.30 EST, not now), but have acquired thick plates.

Buffalo, New York.

16.00 EST. Still the same fine prism bundles. As the low pressure area moved northward, the lower cold air layer became deeper, while the altostratus layer dried up. Consequently, during the night the particle habit changed, as was observed the next morning.

Buffalo, New York.

07.50 EST. Light snowfall from clear sector plates and stars. On car are sector stars with droplet in center, and sector spatial stars, partially very lightly rimed; there are also a few graupel in between.

The total snow accumulation in 24 hours in the Buffalo area was light and not more than 2 to 3 inches ; traffic problems were caused by icy roads and drifting snow. In Bergeron's terminology [1] the snowfall was characterized by the existence of a « releaser cloud » but the absence of a low level « spender-cloud ». More toward the center of the storm where the latter was present 12 inches and more accumulated. Note that at this time Lake Ontario was unfrozen, while Lake Erie was frozen.

System No. 2 : The synoptic situation of this system is very similar as before ; again northerly winds prevail, but we are located closer to the center of the depression, the lakes are warm (Lake Erie temperature is 11 °C !) which increases the tendency for the formation of low level convective clouds. The observation was made on November 12, 1968, along the south shore of Lake Erie while driving from Dunkirk back to Buffalo, along a 20 mile stretch near Hamburg, New York.

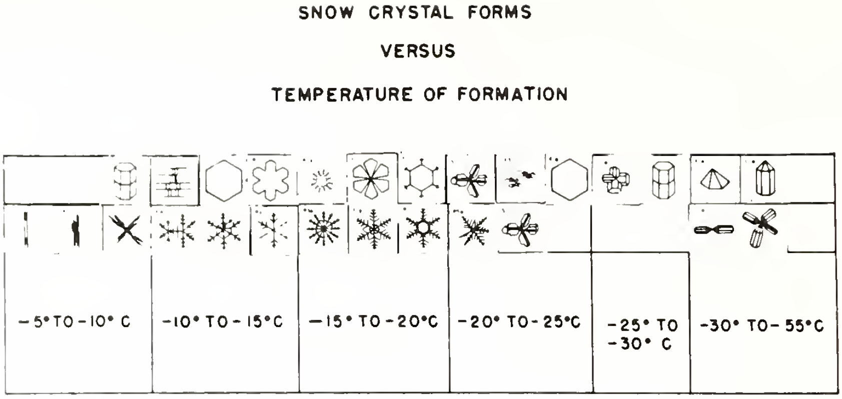

FIG. 1. — Major snow crystal forms and their dependence on temperature when growing at water saturation (lower line of crystals) or below water saturation and above ice saturation (upper line of crystals).

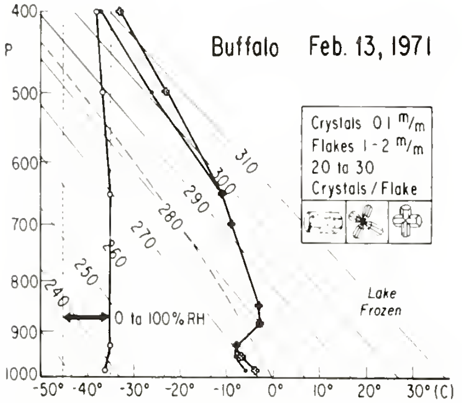

FIG. 2. — Atmospheric temperature and humidity profile connected with the precipitation of high level altostratus crystals. Note that water saturation exists up to about 650 mb air pressure (ordinate) but temperature at this points is below −10 °C which is too warm for crystal formation.

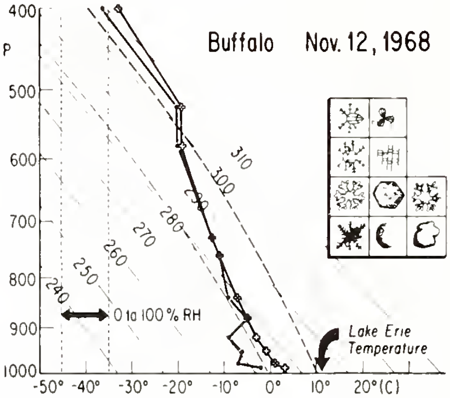

FIG. 3. — Temperature and humidity profile on Nov. 12, 1968, over Buffalo, N. Y., a.m. Prism forms indicate the existence of a deep moist layer reaching above 400 millibar (ordinate). Dotted line from lake temperature crossing temperature profile at about 550 millibar indicates approximate temperature profile of convective clouds forming over the warm lake surface. In these clouds dendrites, spatial aggregates and graupel form in agreement with Fig. 1.

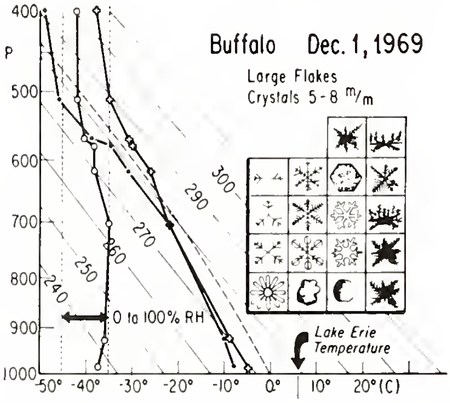

FIG. 4. Temperature and humidity profile on Dec. 1, 1969, over Buffalo, N. Y. Dotted line emerging from surface at 0 °C and crossing temperature profile at 650 millibar (ordinate) indicates the approximate temperature profile of the convective lake clouds. Crystal forms are in agreement with this profile.

15.05 EST. Heavily rimed prisms with little rimed plates and dendritic branches or appendices, also stars and graupel. Snowfall intensity light to moderate.

15.13 EST. Forms are now very difficult to distinguish : all are rimed consisting of dendritic and sector stars, prisms with side plates, and graupel. Moderate snowfall intensity mixed with showers, visibility less than one kilometer.

15.20 EST. Moderate snowfall, visibility less than 1 km, snow consisting of all possible forms, graupel, spatial dendrites, prism bundles with side plates completely and partially rimed.

15.35 EST. Now rimed spatial plate crystals, small prisms with end plates, dendrites, but no graupel.

These forms are consistent with the temperature and humidity profile of this day (Fig. 3, note legend). The warm lake temperature explains the formation of low convective clouds with some graupel formation. The morning radiosonde indicates the existence of a deep moist layer which is ice saturated in its upper parts and has caused the formation of the prismatic crystals, while the evening radiosonde showed drying out from above, but saturation up to −20 °C, which accounts for the formation of spatial dendrites. With the presence of a lower « spender cloud » the precipitation efficiency is increased compared with the case of System No. 1, as is qualitatively evident from the low visibility.

System No. 3 : This system is a typical moderate lake storm which formed over Lake Ontario on 1 December 1969. The airflow was from the north-west turning north and as the morning as well as the evening radiosonde indicate the lapse rate was nearly moist adiabatic. The lake was still warm (+6 °C) causing the formation of a convective stratocumulus layer whose tops must have reached the 650 mb level. A survey of the precipitation particles was made from the edge of the band to its center along an east-western direction on driving from downtown Buffalo to Batavia about 30 miles east of Buffalo. Every 2 to 3 miles we stopped the car and investigated the snow crystals using a hand-held microscope (Fig. 4).

15.25 EST. 0 mile, downtown Buffalo : Snow flurries consisting of sector stars, dendrites, and spatial sector stars and spatial dendrites, partly flaked, no riming.

15.34 EST. 2.9 miles. After driving through a locally heavier shower, the particles are now the same as before and fall in flurries.

15.39 EST. 5.7 miles. Same forms but indicating a more intensive precipitation process through heavier riming. Sector stars are rimed essentially along their periphery.

15.49 EST. 8.1 miles. Small concentration of snow crystals, sector stars again rimed at periphery.

15.55 EST. 12.0 miles. Snow flurries, again consisting of rimed sector stars.

16.01 EST. 15.1 miles. Snow flurries, sector stars in all riming stages, mostly double stars.

16.11 EST. 19.0 miles. Light to moderate snowfall ; sector stars, spatial sector branches, all in flakes, little riming.

16.17 EST. 21.1 miles. Moderate snowfall of large dendritic stars (diameter larger than 5 mm), bi-level sector stars, few spatial sector or dendritic crystals, unrimed or slightly rimed, moderate flaking.

16.20 EST. 23.1 miles. Moderate snowfall, flakes or large dendritic stars (larger than 5 mm), some spatial dendrites, visibility 1 to 2 miles.

16.35 EST. 26.4 miles. City Batavia. Light snowfall, spatial dendrites, rimed.

16.55 EST. 31.2 miles. Moderate to heavy snowfall ; large flakes from large dendrites and spatial dendrites, diameter of dendrites 7-8 mm, moderate riming ; fall velocity more than 1 m/sec.

17.05 EST. 36.9 miles. Moderate to heavy snowfall : large rimed dendrites and spatial dendrites in flakes, riming considerably, causing new branches to grow from crystal surfaces. Fall velocity more than 1 m/sec.

17.16 EST. 41.5 miles. Moderate to heavy snowfall. Heavily rimed dendrites and spatial dendrites, large individual crystals, higher fall velocities than before.

Return trip :

17.35 EST. 31.2 miles from downtown Buffalo. Dendrites and spatial dendrites, all moderately rimed, large crystals.

17.45 EST. 26.4 miles from downtown Buffalo. Heavy snowfall or large flakes (> 1 cm) consisting of large dendrites and spatial dendrites, with branches emerging from rimed droplets, all moderately rimed, sizes of individual crystals 5-7 mm diameter. The flakes are loosely aggregated causing a very moderate fall velocity.

18.11 EST. 16.7 miles from downtown Buffalo. Moderate snowfall, spatial dendrites rimed, individual crystals smaller than before.

18.41 EST. 6.2 miles from downtown Buffalo. Snowfall slowly diminishing. There could be no question that this snowfall originated in a squall from Lake Ontario.

Figure 4 gives the temperature lapse rate of the Buffalo radiosonde for this day and the schematic drawings of the crystal forms in Nakaya's classification. Note that the humidity decreases above the 700 mb level. The arrow indicates the water temperature, and we have shown an intermediate moist-adiabate line which may have been caused by the heat transfer from the warm water surface. Convective clouds may have formed along this moist adiabate, causing some of the cloud tops to reach beyond the 700 mb level.

The precipitation process that is active in this cloud system is no longer compatible with the Bergeron mechanism of a spender and releaser cloud. Apparently here the releaser cloud is missing and the release of precipitation has to be accomplished by the spender cloud. While the precipitation intensity is always light when the releaser cloud is present and the spender cloud missing, this is not necessarily true as long as only the spender cloud is available since the rate of condensation in the convective cloud system is high, therefore, as long as the temperature is low enough, heavy precipitation from even shallow systems may fall. As this important precipitation mechanism has not as yet been described in the literature, it shall be accomplished subsequently.

Microphysics of crystal habit formation.

The ice forming mechanism in these cloud systems is as follows :

The cloud droplets which rise with the cloud have a freezing nucleus embedded or come into contact with one. When the threshold temperature of the nucleus is reached, the droplet freezes. The subsequently developing crystal habit is a function of the temperature at which the droplet froze, of its size, and of the temperature and humidity of the atmospheric layers which it passes through. The temperature and size determine whether it will form a single crystal or a polycrystal and this determines whether a plane star or a spatial star will form. This process depends on temperature and size of the frozen cloud drop in a way which has been explored by Magono and Aburakawa [2]. These authors used as nucleant an ice surface whose C-axis was perpendicular to the surface orientation, and sprayed on that surface droplets of various sizes and temperatures. Using polarized light they then studied the crystalline structure of the frozen droplet. Their results for various temperatures and droplet sizes are shown in Figure 4. Different hatching of the block diagrams indicate whether the droplets on impact formed single crystals or polycrystals. In the case of a freezing nucleus embedded into the droplet it will replace the ice surface of the experiment. As long as the nucleus has one active nucleation site, a unit crystal will grow as in the Magono and Aburakawa experiment. Whether this is indeed just one site or whether one site wins in the competition of a number of sites is immaterial. Furthermore, the formation of a unit or of a polycrystalline crystal when a drop freezes is not only a function of the threshold temperature, i.e. of the nucleus, but also a function of drop size, consequently a function of the post-nucleation crystallization process. At lower temperatures, it would be possible that several nucleation sites become active, but it can also occur that dendritic growth emerging from one nucleation site on the nucleus causes the polycrystalline structure of the drop. This latter process has been observed for large drops (1 mm diameter) as the reason for polycrystallinity [3]. It is conceivable that droplets which have crystallized into a single crystal form double stars or dendrites as shown schematically in Figure 6 [4], while polycrystals will accordingly initiate the formation of spatially arranged dendritic branches (Fig. 7). Figures 8a and 8b show all double crystals which have formed in a cloud chamber after seeding with differently prepared AgI crystals. The temperatures were between 15.5 and - 17.5 °C. Figure 9 shows spatial aggregates which have formed after freezing nuclei seeding with AgI in a supercooled cloud at − 22 °C [5] according to the scheme of Figure 7.

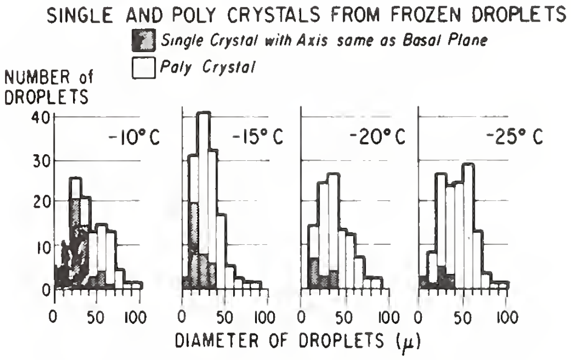

Fig. 5. — Development of single and polycrystals from supercooled droplets on crystallization (acc. to Magono and Aburakawa [2]).

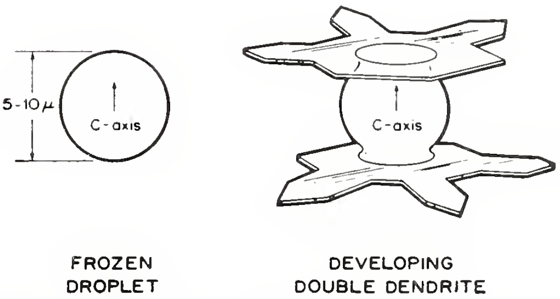

IG. 6. — Schematic drawing indicating the development of a double dendrite from a droplet frozen to a unit crystal. Note that due to competition for water vapor the upper and the lower crystal may develop alternate branches.

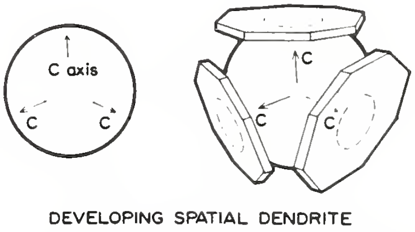

Fig. 7. — Dendrite development from polycrystal. Form of macroscopic crystal is that of a spatial dendrite.

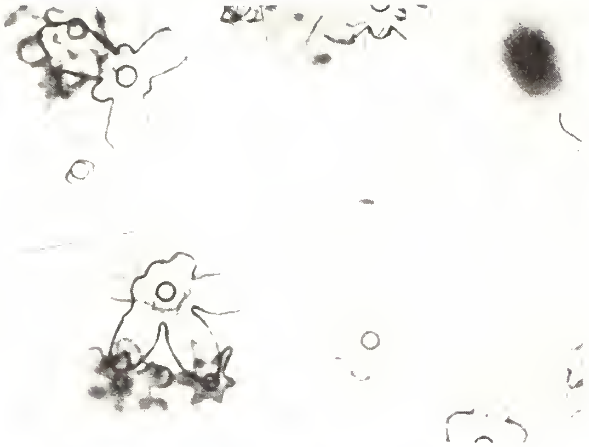

FIG. 8 a (above). — Double dendrites formed in cloud chamber at —15.5 °C after seeding with AgI evaporated from hot plate.

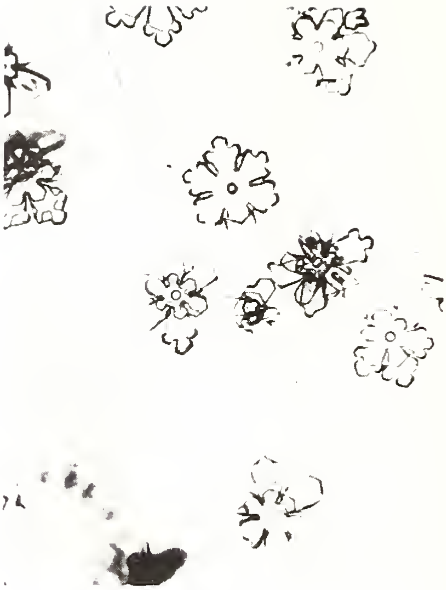

FIG. 8 b (right). — Double dendrites formed in cloud chamber at —17 °C after seeding with 2 % AgI - isopropylamine mixture.

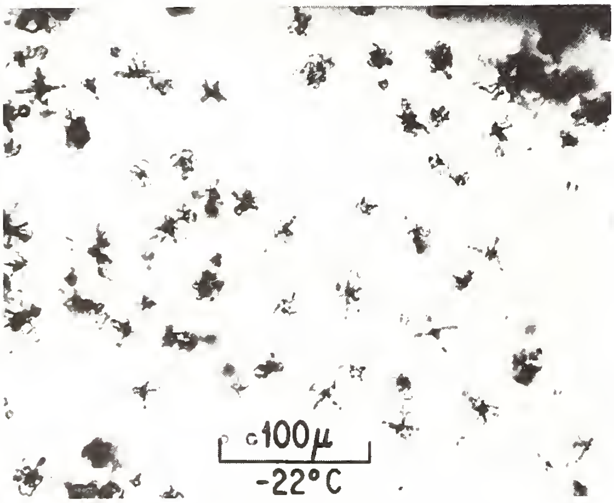

FIG. 9 (above). — Spatial dendrites formed in cloud chamber after seeding with AgI.

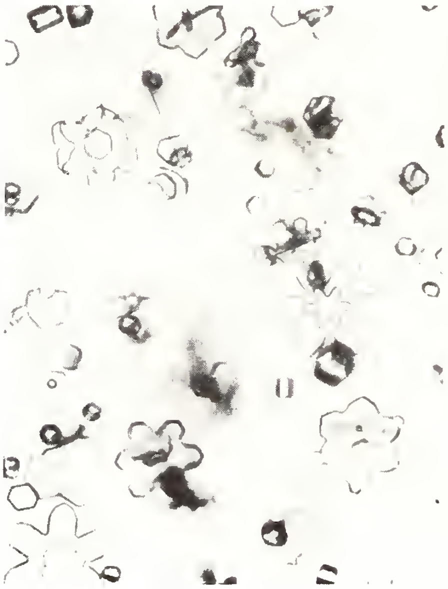

FIG. 10 (right). — Crystals formed in cloud chamber at —17.5 °C after seeding with dry ice. Crystallization process is due to homogeneous nucleation and not due to droplet freezing.

Figure 10 shows for comparison the ice crystals which form after dry ice seeding due to homogeneous nucleation. Note that none has a frozen droplet in the center. Cloud temperature was — 17.5 °C.

We can now make an important statement related to the origin of various crystal types in convective cloud systems: Planar double dendrites and spatial dendrites form through freezing of cloud droplets which are carried in the water saturated updraft to their threshold temperature ; their size and the temperature at crystallization will determine whether a planar double dendrite or a spatial multi-branch dendrite will form. The lower the temperature the more likely becomes the formation of a polycrystal for any droplet size. The great importance of these irregular types of snow crystals, which nevertheless are found in a number of typical varieties [6] for the efficient formation of precipitation follows from the fact that they offer a large surface area. We have planimetered the surface area of dendritic stars from the collection of Magono and Lee [6] and have found that expressed in terms of effective surface area their equivalent radius as hexagonal plate crystal is about 1 /2 of the circumscribed circle. At the same time, they have a great riming efficiency and the frozen droplets can again form centers of new branches [6]. This explains why deep cloud systems can effectively be snowed out by crystals as few as 1 to 10 per liter — concentrations which can in nature be expected to form in the temperature range —20 to —25 °C.

We like to emphasize here an important mechanism that determines, as we will see later, the efficiency of the precipitation mechanism. This mechanism is the self-cleaning process of the clouds ; they free themselves from the ice crystals generated within them during their active stage. These ice crystals, because of their small fall velocity, are taken with the updraft to the cloud top, leaving the cloud beneath ice-free, and on top they are dispersed horizontally in a shallow layer and away from the cloud in a stratocumulus cumulo-genitus mechanism. The ice crystals which have formed throughout the depth of the cloud are now concentrated in a shallow layer in and around the cloud top and are ready to snow-out a neighboring cloud whose updraft has ceased. We believe that this concentration process of the ice crystals is an important mechanism for the effective snow-out of these cloud systems whose releaser cloud is missing. From there they may fall into another cloud which has ceased to be active, and whose internal structure is determined by large energy consuming eddies. In the meantime, the original cloud has become inactive also, air no longer ascends through it and the organized updraft is decaying into eddies and turbulence. Ice crystals that fall into these clouds have excellent conditions for growth because their fall velocities are well within the velocities of the turbulent eddies. The precipitation process described in our case study No. 3 and those which are related to the typical lake storm cloud systems (Fig. 4), resemble most nearly the « generating cell » mechanism which has been described by Marshall [7], Langleben [8], Gunn et al. [9].

It appears that the primitive equipment, usually a vertically pointing antenna whose return signal was recorded on a simple paper recorder, was superior in displaying the profile of the precipitation structure than the modern equipment presently used. It would be desirable to resume this research with present day sophisticated equipment and under due consideration of the effects on radar pattern of rising and falling precipitation particles. It is conceivable that the vertical echo pattern of the generating cells proper is due to the presence of both rising and falling snow crystals. It is interesting that this possibility is mentioned only in Marshall's original paper on that subject, while in later publications this important echo characteristic is no longer considered.

THE INTERRELATING, COMPARATIVE SNOW CRYSTAL ANALYSIS.

After having described the system of snow crystals which are discharged from shallow lake storms, we only have to study the snow precipitation at other locations in order to be able to draw conclusions about the occurrence or non-occurrence of similar systems. Of course, it is known from the extensive snow crystal observations made by Japanese scientists on the peninsula Hokkaido that the same storms occur there when the air is moving from the warm Japan Sea over Hokkaido. We have, however, also frequently observed that orographic systems in Colorado and Bavaria north of the Alps occur also as shallow storms. Before we describe some of the precipitation systems related to this problem, we will show how snow crystal observations can be used to determine similarities in the cloud structure. It must be admitted that to date no numerical snow crystal model exists which is able to describe satisfactorily the infinite variety of natural snow crystal habit and its modifications in the riming process. Numerical models have been proposed by Koenig [10] and Cotton [11], but the forms modeled are simple elementary crystal forms which do not occur in nature except in seeded clouds. In the cases where overseeding is effective so that simple forms occur and riming is excluded, the models probably describe quite well the precipitation efficiency of the cloud. When compared with the so-called natural conditions using the same crystal forms, the natural efficiency turns out to be much less. In natural conditions of crystal growth and riming, nature has however infinite possibilities of increasing the collecting surface for both vapor through diffusion and cloud water through riming so that the natural efficiencies must be greatly underestimated in existing numerical models. This deficiency should always be kept in mind when such simplified numerical models of crystal habit are being used for the evaluation of precipitation efficiency in seeded and unseeded clouds.

The great sensitivity of the crystal habit to temperature and humidity conditions follows clearly from the fundamental work of Nakaya on crystal growth and from the Magono and Lee [6] crystal classifications. The diagrams of these investigators show that for instance in the temperature range from —15 to —20 °C any habit from solid columns to dendrites can form depending on the humidity conditions. This has been confirmed for natural conditions in our seeding experiments where the seeding rate caused the formation of 1000 crystals per liter. These effectively overseeded the cloud causing crystal growth at ice saturation and consequently the formation of columns. The crystal habit in a natural cloud is related sensitively to dynamic cloud parameters such as temperature, humidity and liquid water content, which in turn depend on other cloud parameters like updraft velocity etc., but also to microphysical parameters like concentration of freezing nuclei. In winterly cloud systems with identical nuclei concentrations, the crystal habit depends on the cloud dynamics; consequently, identical crystal habits point to the action of identical cloud systems.

DESCRIPTION OF CRYSTAL HABITS IN OTHER TYPES OF SHALLOW WINTER SNOW STORMS.

Subsequently, we bring a few examples of snow storms which have produced identical crystal habits as lake winter storms:

Boulder, Colorado, 2 *March* 1968, *upslope condition: Radiosonde data* (*Fig.* 11).

16.15 MST: Continuous moderate snowfall since A.M. Snow crystals 6 miles east of Foothill range are flaked and slightly rimed, not all crystals in a flake are rimed. Most forms are dendritic stellars, or a mean habit between sectors and dendrites. Original habits are spatial dendrites, spatial sector stars, but no prisms.

16.25 MST: Intensification of snowfall. Both, flakes and individual crystals are larger, rimed as before, no prism forms.

16.30 MST: The flakes consist of about 20 to 50 single crystals. The individual crystals are between large (diameter about 5 mm) sector stars with few rimed droplets to small spatial plate particles. (One big sector star contains perhaps as much ice as one small spatial dendrite).

17.00 MST : Continuously heavy snowfall. Particles are flakes, but now consisting of many small spatial plate aggregates, small sector or dendritic stars, but more numerous flakes and crystals. It seems as if either the generating level or the freezing nuclei concentration has increased with altitude ; for either one of these reasons more particles are generated and all remain smaller without reducing or increasing overall rate of snowfall.

17.20 MST at base of Foothills, Boulder, Colorado : Heavy snowfall, large flakes consisting of spatial dendrites, partly heavily rimed, one graupel (snow pellet). Stars are dendrites rather than sectors. The most intensive riming is in the center of the spatial aggregates.

Boulder, Colorado, November 2, 1969 ; *Radiosonde data* (*Fig.* 12).

12.00 MST : Snowfall with rimed flakes changes to snowfall with very large flakes. Before the change the forms were spatial plate aggregates rimed and flaked together. After the intensification to large flakes the forms were : spatial aggregates of large dendrites, rimed and flaked. The only basic difference was that the fundamental habit had changed from spatial plate and sector aggregates to large spatial dendrites. Large flake precipitation lasted for about 5 minutes.

Boulder, Colorado, March 20, 1968 ; *Radiosonde data* (*Fig.* 13).

18.00 MST : Very dense intensive snowfall. Snowflakes consist of heavily rimed spatial dendrites.

Boulder, Colorado, April 3, 1968 ; *Radiosonde data* (*Fig.* 14).

07.00 MST : Heavy snow storm from north. Flakes consisting of spatial dendrites which are slightly rimed. 10-15 crystals fall in 10 seconds per cm². They are large spatial dendrites ; flakes have about 1/2 inch diameter and consist of 10-20 single dendrites.

Other similar log entries are from snow observations in New Jersey, in Northern Main, in Bavaria (Germany), in Alaska. Quite often the shallow storm type constitutes the main body of a typical front, then the crystal sequence is as described by Grunow [12] and Weickmann [13]. The storm begins with high level low temperature prism bundles and ends with the typical shallow storm crystals, such as spatial dendrites in flakes and rimed and mostly mixed with sector or dendritic stars.

Subsequently we would like to quote one observation sequence of such a storm, as observed on January 16, 1965, in Asbury Park, New Jersey ; radiosonde data are from New York, New York, Figures 15a, b.

Figures 15 a, b, present the typical As-Ns (altostratus-nimbostratus) phase of the storm during which high-level prism forms are predominant. Figure 15b indicates that an inversion has formed just above the 700-mb level, and that the typical convective Sc (Strato-cumulus) particles are being discharged through many hours as described subsequently :

18.50 EST : Particles are now crystalline and small and numerous, reaching from a few plates over many plate aggregates to prisms.

Same forms fell for hours ; but in the morning they were rimed, larger, and partly in flakes. During the forenoon sometimes large stars fell also.

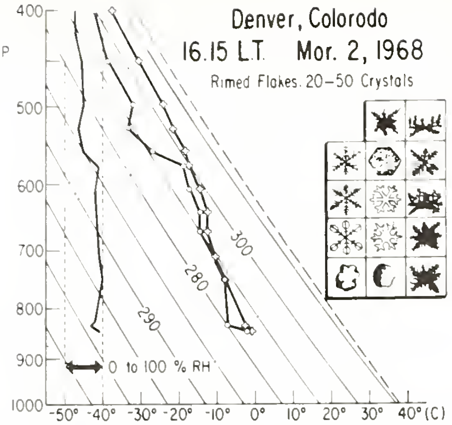

Fig. 11. — Temperature and humidity profile on 2 March 1968, Denver, Colo. Crystal forms agree with diagram of Fig. 1.

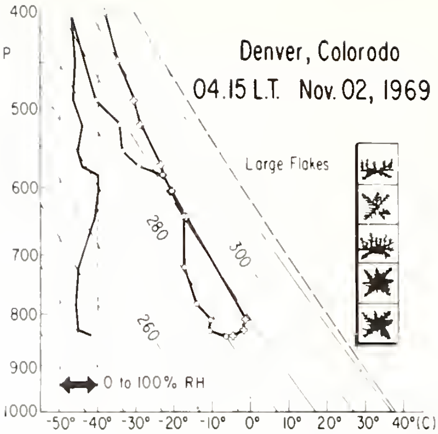

Fig. 12. — Temperature and humidity profile on 2 November 1969, Denver, Colo.

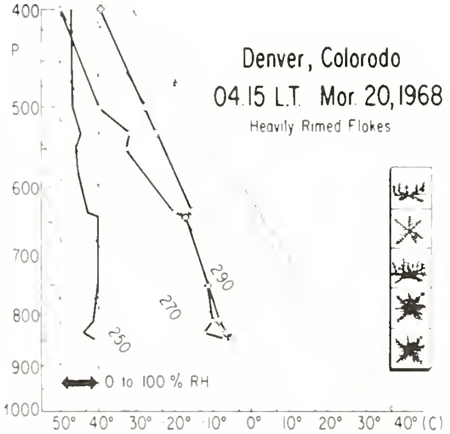

Fig. 13. — Temperature and humidity profile on 20 March 1968, Denver, Colo.

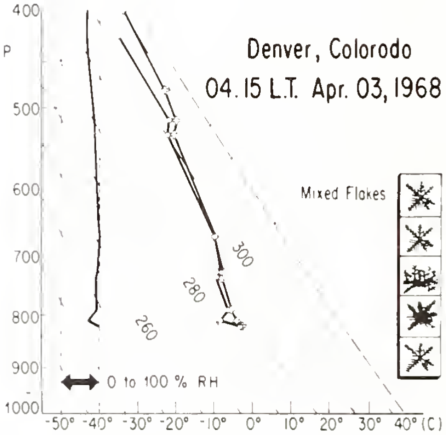

Fig. 14. — Temperature and humidity profile on 3 April 1968, Denver, Colo.

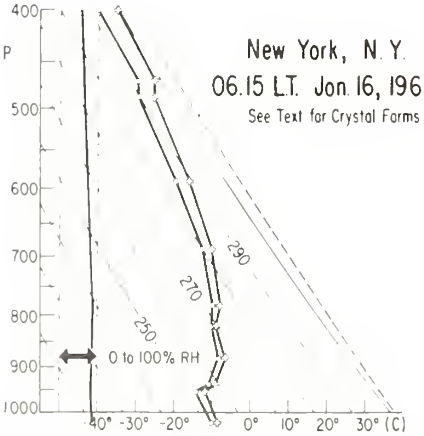

Fig. 15 a. — Temperature and humidity profile on 16 January 1965, New York City, N. Y., 06.15 local time.

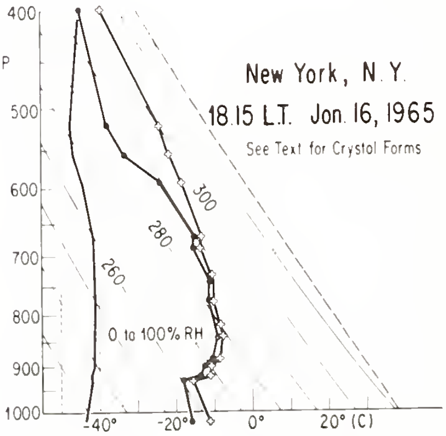

Fig. 15 b. — Temperature and humidity profile on 16 January 1965, New York City, N. Y., 18.15 local time.

14.45 EST : Renewed intensification of snowfall. All particles are larger and rimed and form flakes. Sector stars, not heavily rimed, fall also. Most particles are spatial aggregates.

15.20 EST : Snowfall intensified. Large rimed dendrites and large rimed dendritic spatial aggregates. Dendrites and spatial dendrites fall, single and in small flakes. Double stars also.

15.45 EST : Heavily rimed dendrites in greater frequency than spatial aggregates. The dendrites are homogeneously rimed over the whole surface. Sometimes the rimed drops have grown into crystals (prisms).

19.30 MST : Still considerable snowfall (10 °C) from flakes. Particles are dendrites as stars and as spatial dendrites, both rimed and unrimed.

Here for the whole afternoon the shallow storm character was in progress.

We have called attention to these observations because they permit the conclusion that the non-precipitating shallow cloud systems will occur as well in other places, though probably less frequently, than over the Great Lakes Basin. They may present a seeding potential which is hitherto unexploited.

GENERAL COMMON FEATURES OF SHALLOW WINTER SNOW STORMS.

It appears that shallow winter storms originate within the boundary layer flow in connection with a moisture source. Preferably the flow becomes established before condensation occurs. This permits the establishment of neutral stability in the boundary layer, which leads to convective instability as condensation occurs. A cloud thickness of 1500 meters is sufficient to cause moderate to heavy snow falls according to our experiences in the Great Lakes region. Condensation in the boundary layer flow occurs for several reasons : in the Great Lakes and related areas due to the flow of the air over a warm lake surface ; in orographic precipitation, as per example, for easterly flow from Kansas to Colorado against the Rocky Mountains due to the lifting of the airmass by several thousands of feet, and finally in synoptic cyclonic systems due to the cyclonic vorticity present in the storm.

The artificial beneficial exploitation of these storm systems is particularly desirable in regions where the upslope flow occurs over normally downslope or dry areas, such as in the United States, in Colorado, Wyoming, and New Mexico. Exploitation of these systems, which occur according to our observations between 2 to 5 times per season, depends largely on our ability to forecast and recognize the systems early enough, so that seeding plans can be initiated.

REFERENCES

[1] Bergeron T. (1949). — The problem of artificial control of rainfall on the globe. 1. General effect of ice nuclei on clouds. *Tellus*, 1 (1), pp. 32-43.

[2] Magono Ch. and Aburakawa H. (1968). — Experimental studies on snow crystals of plane type with spatial branches. *J. Fac. Sci.*, Hokkaido Univ. of Japan, Series VII, 3, pp. 85-97.

[3] Brownscombe J.L. and Hallett J. (1967). — Experimental and field studies of precipitation particles formed by the freezing of supercooled water. *Quart. J. Roy. Met. Soc.*, 93, pp. 455-73.

[4] Weickmann H.K., Katz U. and Steele R. (1970). — AgI - sublimation or contact nucleus. Second National Conf. on Weather Modification, Santa Barbara, Calif., pp. 332-6.

[5] aufm Kampe H.J., Weickmann H.K. and Kelly J.J. (1951). — The influence of temperature on the shape of ice crystals growing at water saturation. *J. of Meteor.*, 8, pp. 168-74.

[6] Magono Ch. and Lee Ch. W. (1966). — Meteorological classification of natural snow crystals. *J. Fac. Sci.*, Hokkaido Univ., Series VII, Geophysics, vol. 2, pp. 321-35.

[7] Marshall J.S. (1953). — Precipitation trajectories and patterns. *J. of Meteor.*, 10, pp. 25-9.

[8] Langleben M.P. (1954). — The terminal velocity of snowflakes. *Quart. J. Roy. Met. Soc.*, 80, pp. 174-81.

[9] Gunn K.L.S., Langleben M.P. and Dennis A.S. (1954). — Radar evidences of a generating level for now. *J. of Meteor.*, 11, pp. 20-6.

[10] Koenig L.R. (1971). — Numerical modeling of ice deposition. *J. Atm. Sci.*, 28, 2, pp. 226-37.

[11] Cotton William R. (1970). — A numerical simulation of precipitation development in supercooled cumuli. NSF Grant GA-13818, Report No. 17 to NSF, Dept. of Meteorology, The Pennsylvania University, University Park, Penn.

[12] Grunow J. (1960). — Snow crystal analysis as a method of indirect aerology. AGU Geophys., Monograph No. 5, Physics of Precipitation, Waverly Press, Inc., Baltimore, Md., pp. 130-41.

[13] Weickmann H.K. (1957). — The snow crystal as aerological sonde. Artificial stimulation of rain, Proc., First Conference, Physics of Cloud and Precipitation Particles, Woods Hole Oceanographic Institution, Woods Hole, Mass., pp. 315-26.

*

Reprinted with permission from Third Conference on Weather Modification, June 26-29, 1972, Rapid City, South Dakota, © American Meteorological Society.

PROGRESS OF THE GREAT LAKES WEATHER MODIFICATION PROGRAM

Helmut K. Weickmann
Byron B. Phillips
Peter M. Kuhn

Atmospheric Physics and Chemistry Laboratory
Environmental Research Laboratories
National Oceanic and Atmospheric Administration
Boulder, Colorado 80302

William J. Eadie

Applied Physics Department
Cornell Aeronautics Laboratory
Buffalo, New York 14221

1. INTRODUCTION

The Lavoie model of the Great Lakes snow storm has been extended to represent both, Lake Erie and Lake Ontario. A remarkable verification has been obtained of special features of the heavy storm over both lakes on 15/16 November 1969. With the inclusion of condensation the model permits a qualitative prediction of the rate of precipitation. In the field program the cloud systems of the lake storms have been studied extensively; it was found that they belong to frequently occurring, but as yet little explored shallow precipitation systems which are not limited to the Great Lakes Basin. Their modification potential will be discussed.

2. DEVELOPMENT OF A LAKE ERIE-LAKE ONTARIO MODEL

Lake Erie generally freezes over by mid-January, effectively terminating lake-effect activity until spring when the ice begins to melt. Since Lake Ontario remains unfrozen, a longer period of suitable lake-effect weather for future NOAA modification experiments might be achieved by working with short-trajectory storms off the west end of Lake Ontario after the Lake Erie lake-effect season is over. To provide for such a possibility and to permit the mesoscale modeling of Lake Ontario storms in general, the CAL moist version of the Lavoie model was modified to simulate the mesoscale influences of the joint Lake Erie-Lake Ontario system. The more general two-lake model was developed, rather than an additional one-lake model for Lake Ontario because the influences of Lake Erie and Lake Ontario are not clearly separable under many wind conditions.

The two-lake model has a 60 x 40 point rectangular grid system covering the Lake Erie-Lake Ontario area. In order to avoid a large increase in computational requirements accompanying the increase in the area covered by the model, the horizontal grid spacing is increased 33% over that employed in the Lake Erie model. The grid spacing in the 45 x 25 point interior grid spanning the two lakes and immediately adjacent land areas is 16 km in the direction parallel to the long axes of the lakes (approximately WSW-ENE) and 8 km in the direction perpendicular to the long axes of the lakes (approximately NNW-SSE). It was felt that this increased spacing would still delineate the boundaries of the two lakes, including the Niagara Peninsula, with sufficient precision to represent the important mesoscale influences of the lakes.

As in the Lake Erie model, outside the interior grid system, the grid spacing is increased exponentially to minimize the propagation of any deleterious effects from the boundaries of the grid system into the region of interest during the period of integration. Orographic effects were not included in the two-lake model.

The two-lake model was tested by carrying out a numerical experiment based upon a set of initial and boundary conditions which had previously been utilized in an experiment with the Lake Erie model. Since the initial wind direction was westerly, the disturbances produced by Lake Erie and Lake Ontario were for the most part separable. The steady state solutions computed from the two-lake model show disturbance patterns produced by Lake Erie which were quite similar to those obtained from the Lake Erie model. Quantitatively, the values predicted by the two models for the deformation of the inversion surface produced by Lake Erie differed by as much as 30 to 40% with more typical differences on the order of ±15%. It is believed that these differences resulted primarily from upwind influences of Lake Ontario on the Lake Erie disturbance, although the effects of the increased grid spacing upon the resolution of Lake Erie and the integration of the finite difference equations undoubtedly contributed.

Using moist modifications of the two-lake model, numerical experiments were carried out on the intense 15 November 1969 lake-effect snowstorm, which had been previously simulated with considerable success using the Lake Erie model (Eadie et al., 1971). The results are described in the following section.

3. NUMERICAL EXPERIMENTS WITH THE LAKE ERIE-LAKE ONTARIO MODEL

A series of numerical experiments were carried out with the joint Lake Erie-Lake Ontario model based upon a lake-effect storm which occurred on 15 and 16 November 1969 and deposited 12 to 15 inches of snow just north of Buffalo, New York over Grand Island, Tonawanda, and Niagara Falls. Fig. 1 shows the satellite picture of the storm situation and Fig. 2 the precipitation echo contours for the same time as measured by the Buffalo WSR-57 radar at 2243Z on the 15th. The maximum radar tops measured for the storm ranged from 8,000 to 9,000 feet. The Buffalo sounding at 0000Z on the 16th shows a capping inversion at 11,000 to 12,000 feet. The -20°C level was at approximately 9,000 feet.

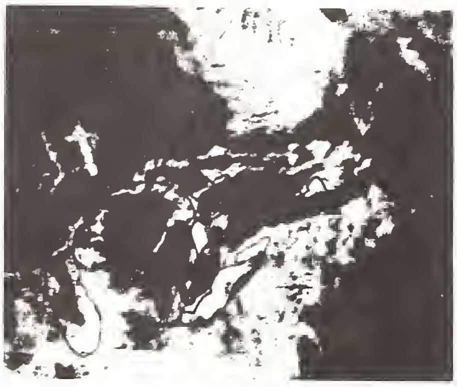

Figure 1.

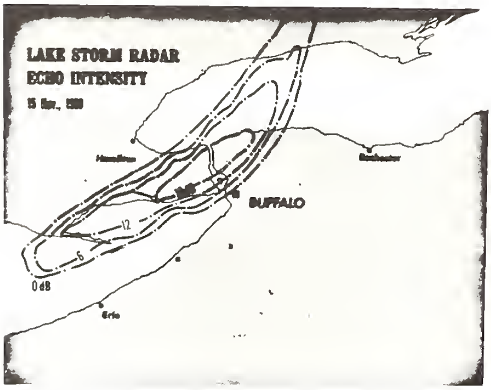

Figure 2.

In order to provide an example of results from the two-lake model based on the 15 and 16 November 1969 storm, a numerical experiment which yielded strong disturbances from both Lake Erie and Lake Ontario will be discussed. Following Lavoie et al. (1970), the effective potential temperature of the upper layer was chosen to be

$$\theta_u = \theta_h + \frac{\Gamma}{4} \Delta H^* \qquad (1)$$

where $\theta_h = 273^\circ K$ is the potential temperature above the inversion surface, $\Gamma = 2^\circ K$ per kilometer is the average rate of increase in potential temperature with height in the stable upper layer, and ΔH^* is the instantaneous maximum upward deformation of inversion surface from its initial uniform value. The initial potential temperature θ in the well-mixed layer of the model was assumed to be $268^\circ K$, giving an initial capping inversion of $5^\circ K$. However, when heating of the well-mixed layer produced a potential temperature $\theta \geq 273^\circ K$, θ_h in Eq. (1) was replaced by θ, yielding

$$\theta_u = \theta + \frac{\Gamma}{4} \Delta H^* \qquad (2)$$

This procedure yields bounded solutions for any degree of heating and had the effect of permitting the Lake Erie disturbance to intensify.

In order to investigate the effects of greater condensation on the precipitation predictions generated by the model, the parameterization of condensation in the moist modification of the Lavoie model developed at CAL (Edie et al., 1971) was changed in this experiment to

$$\begin{aligned} \text{COND} &= rW_H\ , \quad W_H > 0 \\ &= 0\ , \quad W_H \leq 0 \end{aligned} \qquad (3)$$

where COND is the condensation rate in a unit column of the layer, r is the average mixing ratio for the layer, and $W_H = -H\nabla \cdot V$ is the vertical velocity at the inversion surface H. This in effect assumes that all of the water vapor convergence in the layer as a result of convergence in the horizontal velocity field is converted into liquid water.

Finally, the empirical expression

$$N = .216e^{-.216T} \qquad (4)$$

for the number of ice nuclei per liter active at temperature T in °C was substituted in the diagnostic expression for precipitation production by riming growth of snowfall in an attempt to account for ice crystal multiplication at warmer temperatures (Lavoie et al., 1970).

The steady state solution computed in the numerical experiment for inversion height deformation ΔH is shown in Figure 3. It is important to note the extremely strong narrow band disturbances produced by both lakes. Although the upwind location of the Lake Erie disturbance is in good agreement with the radar echoes shown in Figure 3, the extension of the Lake Erie disturbance over Lake Ontario is apparently limited by the presence of the strong disturbance field generated by Lake Ontario. The maximum inversion height of four kilometers or over 13,000 feet predicted for the Lake Erie band is compatible with the radar and radiosonde observations at Buffalo during the storm.

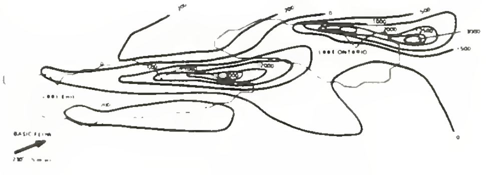

DEFORMATION OF INVERSION SURFACE (m) PREDICTED FOR 15-16 NOVEMBER 1969 STORM (INITIAL HEIGHT 1000 m)

Figure 3.

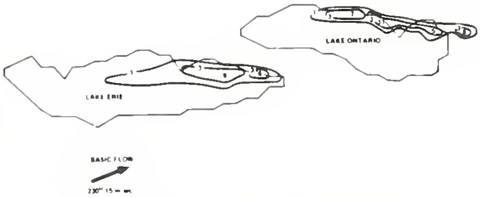

DISTRIBUTION OF PRECIPITATION RATE (mm hr^{-1} OF MELT WATER) PREDICTED FOR 15-16 NOVEMBER 1969 STORM

Figure 4.

The distributions of the computed precipitation rate in mm of melt water per hour are shown in Figure 4. Jiusto et al. (1970) suggest a snow to melt water ratio between 6 and 15 for rimed crystals. Adopting a mean ratio of 10, precipitation rate of 2.5 mm per hour corresponds to a snowfall rate of one inch per hour. The predicted precipitation rate distributions from both bands are, therefore, generally representative both in size and intensity of snowfall from intense lake-effect bands. It is obvious, however, that the precipitation from the Lake Erie band was released too far upstream to be in good agreement with snowfall and radar observations from the actual storm. Horizontal advection of snow in falling to the surface is neglected in the present model. If a 45 kilometer advection distance were introduced, based on snow crystals falling 3 km from a generation level to the surface at an average fall speed of one meter per second in a horizontal wind of 15 meters per second, it would bring the predicted precipitation distribution from the Lake Erie band into reasonable agreement with observations.

4. GENERAL OCCURRENCE OF THE SHALLOW LAKE STORM SYSTEMS.

Bergeron has postulated that for the efficient rain-out of large scale stratiform precipitation systems a releaser cloud is required which releases a sufficient number of ice crystals. These ice crystals then fall, growing by diffusion and riming through a spender cloud which is at lower levels and which forms the supply of precipitable water. The releaser cloud may very well be a Cirrostratus of Altostratus, i.e., an ice cloud, while the spender cloud belongs to the classes of Stratus and Stratocumulus and may reach from warmer than freezing at the base to -10 or even -20°C at the top. In observing the crystal concentrations which are discharged by such a system and which apparently cause an efficient rain-out one finds in general about 50 crystals per liter. This must be viewed against the general background of ice nuclei in the troposphere which is according to unpublished measurements of P. Allee about 1/2 per liter at -20°C (Table 1).

Table 1.

AVERAGE ICE NUCLEI CONCENTRATIONS FROM AIRCRAFT MEASUREMENTS (P.Allee)

Location	ICN l^{-1}, -20°C Background	ICN l^{-1}, -20°C Urban
Barbados, 1969	1 to 2	
Colorado	0.5	20
Great Lakes	5	180
Great Lakes (above inversion)	<0.5	<0.5

As the natural concentration of ice nuclei increases roughly by one order of magnitude for every 4°C temperature decrease, efficient precipitation requires a deep system whose top temperature nears -30°C.

In the shallow precipitation systems of about 2 km depth that we observed in the Great Lakes region we have in Bergeron's terminology a spender cloud only whose top temperature at best is near -20°C but it can be warmer. How will such a cloud system produce a sufficient number of ice crystals? Assuming that the mesoscale structure of the cloud system can be approximated by a hexagonal Benard cell pattern then each convective cloud element has 6 neighbors. Radar studies have shown a cloud diameter of about 3 to 8 km. The ice crystals produced in the actively convective stage of a cloud element are carried to its top as in the cases of interest here the updraft exceeds the fall velocity of the crystals. On top, due to the frequently existing inversion, each cloud diverges in a Stratocumulus cumulogenitus process in a thin layer, mostly around 300 m thick and from this layer the convective clouds beneath are "seeded" when their updraft has ceased. As an example we may assume a cloud layer which consists of individual cells of 4 km radius, 2 km depth whose active updraft exceeds 2 m/sec and lasts for 15 minutes. Divergence on top and spreading into a 300 m thick layer will cause a diameter of 20 km for the Stratocumulus cumulo-genitus. Since each cloud has 6 neighbors seven Stratocumulus cumulogeniti mix with each other and add their nuclei to snow out the cloud beneath whose updraft has ceased. If each liter furnishes 5 nuclei (Table 1 for Great Lakes background value) then at best 35 crystals formed at -20°C are available in each m^3 of the 300 m thick Stratocumulus layer. In descending with 1/2 to 1 m/sec a shower of 5-10 minutes duration forms with each Benard cell element. Lateral mixing in between the cloud system elements will distribute the crystals horizontally and eliminate the character of short-lived showers. Both the formation of the Stratocumulus cumulogenitus seeder cloud as well as the efficient lateral mixing within the cloud layer has been observed in the Great Lakes Project experiments. A look at Table 1 makes clear that in an urban or industrial environment where the major part of the freezing nuclei spectrum is antropogenic, an oversupply of nuclei at the specified temperature exists while in an unpolluted environment (see background value for Colorado or Barbados) an undersupply prevails. Neither one of these conditions must be alarming since nature has sufficient means for compensation over a wide range of nuclei supply, such as the process of aggregation of crystals for oversupply and the development of special forms - dendrites, spatial dendrites and riming for undersupply. Only if the top temperature becomes warmer the rapid decrease of the threshold nuclei concentration makes the natural precipitation process insufficient and seeding results in additional moisture at the surface.

It has been observed in connection with the work on Great Lakes snow storms that these storms belong to a kind of winter-storm which we like to call the "shallow winter snowstorms". They consist of cloud systems which develop in the boundary layer. They not only originate over lakes and oceans with adjacent land areas but occur as well over the semi-arid areas east of the Rocky Mountain chain. Here easterly flow causes orographic lifting over the entire region of the high plains and cloud systems develop over large areas from which additional rain or snow can easily be obtained through seeding. While condensation from the warm lake surface causes Stratocumulus formation for the Great Lakes cloud systems, condensation due to large scale orogenic lifting causes Stratocumulus layer in the High Plains region. The identical structure of both cloud systems is revealed by the comparative analysis of the snow crystal habit discharged from both cloud systems. Identical crystal forms fall from both systems and, since snow crystals are extremly sensitive minute aerological sondes (nature's "analogue computers") of cloud conditions, one can conclude that identical crystal forms are caused by identical cloud systems. Figure 5 shows a satellite picture of such an upslope cloud system which occurred on 16 September 1971. The Denver radiosonde whose location is next to the center cross mark of the satellite picture is shown also.

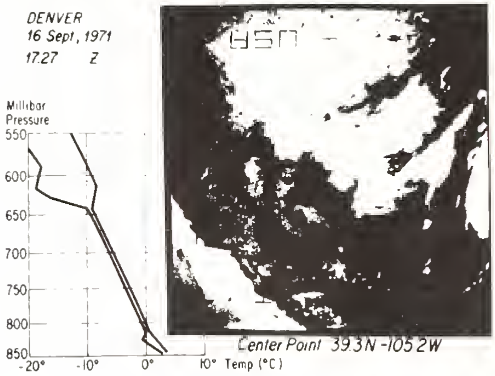

Figure 5.

While the cloud deck is deep enough in order to produce precipitation and the updraft caused by the upslope condition (2 to 10 cm/sec) sufficiently strong to sustain it - the temperature is too warm for natural release. It is clear that on this day, rain could have been released artificially over a large region of semi-arid climatic characteristic (note satellite picture). Another very similar case of upslope cloud system occurred on 28 and 29 October 1971. The climatological frequency of such large seedable cloud systems to increase precipitation in a semi-arid area has not been established but according to our experiences one half dozen opportunities per winter season appears to be a good estimate. A study of the occurrences of such cloud systems during the last ten years has been conducted for a number of radiosonde stations around the Great Lakes with the specifications that the top temperatures must be between -5 and -14°C. The average thickness of these shallow systems turned out to be 1700 to 1800 m, and their yearly frequency of occurrence is of the order of one half dozen.

In Colorado such cloud systems according to our observations of the last 5 years occur frequently enough to consider them as potential water producers over large regions.

The long trajectory over land contributes to the development of the deep boundary layer, so that the cloud system will become about 2000 m thick. Using the rate of condensation as derived from temperature, updraft and elevation and assuming an artificial precipitation potential of 50% efficiency, one finds that precipitation rates of 2 to 8 mm per hour are possible for updraft speeds which have been measured in Lake storms or which can be derived from the upslope windspeed (Table 2). If a total of 1/5 inch of precipitation were generated over an area of 100 miles long and 10 miles wide, 10,000 acre feet of water were deposited.

The typical orographic systems, known for a long time as potential sources of artificial precipitation belong to the same shallow cloud systems. Figure 6a, b shows satellite pictures of the Rocky Mountains during (a) and after (b) a

TABLE 2

ESTIMATE OF INDUCED PRECIPITATION

GEOGRAPHIC AREA	STRATUS CLOUD THICKNESS (METERS)	TEMPERATURE RANGE (OC)	UPDRAFT VELOCITY (cm/sec)	INDUCED PRECIPITATION (mm/hr)
	3000	0 to -22	10	1.73
GREAT LAKES	3000	0 to -22	50	6.05
	2000	0 to -15	50	4.50
COLORADO	2000	0 to -10	10	0.46
(FRONT RANGE)	2000	0 to -10	50	2.30

FOOTNOTE 50% PRECIP EFFICIENCY

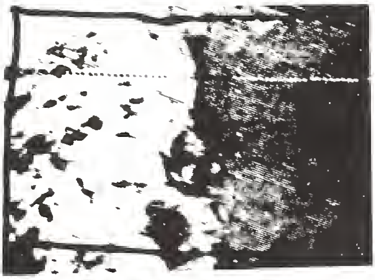

Figure 6a.

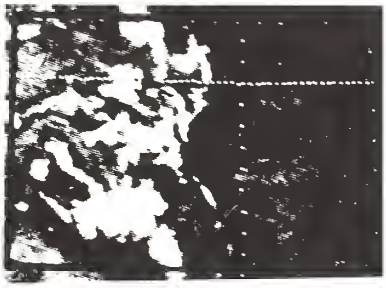

Figure 6b.

heavy snowstorm at the opening day of the hunting season 1971 which caught hunters unaware and trapped many. The upstream conditions are shown by the Grand Junction Radiosonde Figure 7. Figure 6a. clearly shows the shallow character of the storm as valleys are plainly seen where the storm cloud dissolved in local downdrafts.

We would like to mention that we have observed similar storm systems in New Jersy, in Bavaria, Germany, and that they have been described from crystal observations by Dobrowolski (1904) in the Antarctic. As these systems are potential sources of large scale precipitation enhancement their further study is warranted.

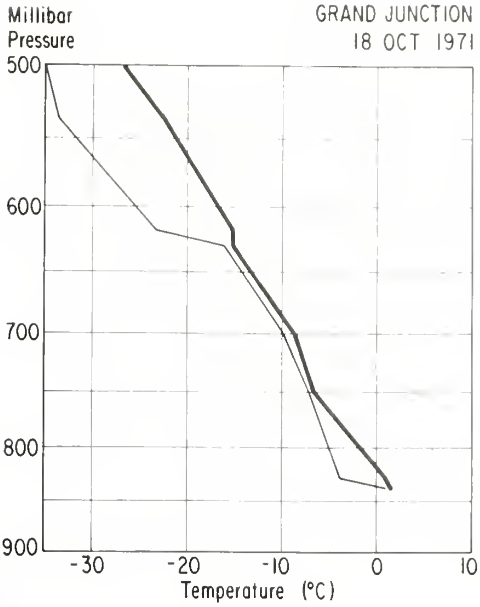

Figure 7.

5. REFERENCES

Eadie, W. J., R. J. Pilié, and W. C. Kocmond, 1971: Modification and modeling of lake-effect weather, Final report on Contract No. E22-39-70(N), CAL Report No. VC-2898-P-2, Cornell Aeronautical Laboratory, Inc., Buffalo, New York.

Dobrowolski, A., 1904: La neige et le givre. Résultats du voyage du S.Y. "Belgica" en 1897-1898-1899. Météorologie 1904.

Jiusto, J. E., D. A. Paine, and M. L. Kaplan, 1970: Great Lakes snowstorms, Part 2. Synoptic and climatological aspects, Report on Grant No. E22-49-70, Atmospheric Sciences Research Center, State University of New York at Albany.

Lavoie, R. L., W. R. Cotton, and J. B. Hovermale, 1970: Investigations of lake effect storms, Final Report on Contract No. E22-103-68(N), Department of Meteorology, Pennsylvania State University.

Reprinted with permission from Solar Energy *13*, 1971 © Pergamon Press.

DEPLETION OF SHORT-WAVE IRRADIANCE AT THE GROUND BY PARTICLES SUSPENDED IN THE ATMOSPHERE*

EARL W. BARRETT†

(*Received* 10 *September* 1970; *in revised form* 9 *November* 1970)

Abstract—Changes in concentration of those atmospheric constituents which contribute to the planetary albedo can give rise to climatic alterations. Suspended particles in the atmosphere contribute to the albedo by virtue of their light-scattering power. This paper presents a mathematical model of the effect of particulate loading on daily totals of irradiance at the ground at various latitudes and seasons, under the assumptions of: (a) Rayleigh scattering by the gaseous constituents of the atmosphere, and (b) Mie scattering by a uniform layer of polydisperse particles having a power-law size-distribution function. These computations show that substantial depletions of irradiance can result from moderate to heavy particulate loadings, and that an increase in man-made particulate emissions by a factor of 50 or more could give rise to a general cooling of serious magnitude.

Résumé—Les changements de concentration des constituants atmosphériques qui contribuent à l'albédo planétaire peuvent donner lieu à des modifications climatiques. Les particules en suspension dans l'atmosphère contribuent à l'albédo en vertu de leur pouvoir de dispersion de la lumière. Cet article présente un modèle mathématique en vue du chargement particulaire des totaux quotidiens de radiation au sol, sous des latitudes et pendant des saisons variées, selon l'hypothèse de: (a) la dispersion de Rayleigh par les constituants gazeux de l'atmosphère et (b) la dispersion de Mie par une couche uniforme de particules dispersées ayant une fonction de loi de puissance du rapport taille/distribution. Ces calculs montrent que des chargements particuliers variant de modérés à importants peuvent entraîner un épuisement substantiel des radiations et qu'une augmentation par un coefficient de 50 ou plus des émissions artificielles particulières peuvent donner lieu à une élévation importante du refroidiseement général.

Resumen—Las variaciones en la concentracion de aquellos constituyentes atmosféricos que contribuyen al albedo planetario pueden dar lugar a alteraciones climáticas. Las partículas suspendidas en la atmósfera contribuyen al albedo en virtud de su poder fotodispersor. Esta ponencia presenta un modelo matemático del efecto que ejerce la carga particulada sobre los totales diarios de irradiancia en la tierra en diversas latitudes y estaciones, bajo los supuestos de: (a) dispersión Rayleigh por los constituyentes gaseosos de la atmósfera, y (b) dispersión Mie por una capa uniforme de partículas polidispersas con función de distribución de tamaños por ley cuadrática. Estos cóputos indican que pueden producirse sensibles agotamientos de irradiancia como consecuencia de cargas particuladas entre moderadas y pesadas, y que el aumento de las emisiones particuladas creadas artificialmente por un factor de 50 o más podría dar lugar a un enfriamiento general de seria magnitud.

INTRODUCTION

It is an obvious and familiar fact that the primary energy input to the atmospheric heat engine is the irradiance from the Sun and sky which is absorbed by the Earth's surface and transferred to the atmosphere by convection and longwave radiation. Geographical differences in this irradiance provide the potential energy which is, in part, converted into the kinetic energy of the general circulation, giving rise to the existing patterns of climate. It follows that any factors which operate to change the amount or geographical distribution of insolation will cause climatic alterations.

---

*Solar Energy Society Conference paper.

†Atmospheric Physics and Chemistry Laboratory, NOAA Research Laboratories, Boulder, Colorado, U.S.A., 1970 International.

The subject of inadvertent weather and climate modification by large-scale human activity is one which is beginning to receive well-deserved attention. The rather steady increase in atmospheric carbon-dioxide concentration, first noted by Callendar[1], is now well-documented. The effects of this rise on atmospheric temperatures have been modelled mathematically by several researchers; one of the most recent models is that of Manabe and Wetherald[2], which yields the result that, in a static atmosphere with statistical-mean profiles of temperature and water vapor, doubling of the CO_2 concentration should produce a temperature rise of about 2°C at the surface, and a drop of about 15°C in the stratosphere. Since the exponential doubling time for CO_2, extrapolated from observed data, is about 340 years, and since the convective stability of the atmosphere would be decreased (permitting more effective heat exchange between the surface and the free atmosphere), it does not appear that the CO_2 increase (presumed due to fossil-fuel combustion) will have a marked effect on climatic patterns in the near future.

In contrast to the situation for CO_2, the possible climatic effects of changes in the amount of suspended particulate matter in the atmosphere have not been explored to a great extent. Observational evidence for such effects does exist; for example, the extremely cold summer of 1816 has been attributed to a heavy particulate loading from a series of volcanic eruptions during the preceding several years. Ludwig and McCormick [3] have discussed the possible cooling effects of long-residence-time aerosols by virtue of their extinction of the direct solar beam, but did not attempt to make quantitative calculations of the effect.

The purpose of this paper is to present a mathematical model of the effect of suspended particles on the total short-wave irradiance received at the Earth's surface. It is qualitatively evident that the principal effect of these particles is to scatter the incident radiation; a portion of the energy arriving from the Sun is thereby returned to space. For most particles found in the atmosphere, the scattering per particle greatly exceeds the absorption, so that the net effect is a decrease in available energy; the planetary albedo increases with increase in particulate loading. If no other factors are operative, an increase in particulate loading will produce a general climatic cooling.

Since the particles also scatter and absorb long-wave radiation emitted from the ground and the atmosphere below, it may be argued that a net warming (enhanced "greenhouse effect") similar to that due to CO_2 should be expected. The scattering efficiency at long wavelengths is, however, much lower than that in the visible range, so that it appears probable that the net effect will be an energy loss. A mathematical model of the effect at long wavelengths is more complicated than the one presented here; work on this is in progress and will be reported in a later paper.

No claim is made for complete physical or mathematical rigor in the model presented below. Even with the fastest computers in existence, it is not possible to achieve perfection in these respects. Simplifying assumptions have therefore been introduced when necessary to make the computation feasible. It should also be understood that the objective is to determine the fractional decrease in available energy as a function of particulate loading; these estimates can be compared with experimental data such as those of Marlatt[4], and, if found to be valid, can provide a basis for computing particulate loading (on cloud-free days) from solarimeter data. Although absolute values of irradiance are computed and presented, no claim is made that these possess a higher absolute accuracy than estimates made by others.

DERIVATION OF THE MODEL

Solar and astronomical factors

In this model, the solar constant is taken to be 1·97 langleys per min (137·4 mW cm^{-2}). The solar spectrum is taken to be the Planck function for 6000°K with abrupt cutoff at 0·3 micrometer (μm). The absorption by ozone in the stratosphere is thus incorporated, but water-vapor absorption in the visible spectrum is ignored; the results apply to a completely dry atmosphere. The specific intensity $I_0\lambda$ as a function of wavelength λ, in ly min^{-1} μm^{-1}, is therefore

$$I_0(\lambda) = 9{\cdot}8445\lambda^{-5} \exp\,(2{\cdot}3866\lambda^{-1}-1)\,. \tag{1}$$

Eccentricity of the Earth's orbit is ignored in computing annual means and in computing duration of daylight. Also, no attempt is made to model the complex situation of the partially-illuminated atmosphere at dawn and twilight; illumination is terminated abruptly at solar zenith angle $Z = 90°$. The zenith angle is computed from the latitude ψ, solar declination δ, and hour angle H by

$$x = \cos Z = \cos\psi \cos\delta \cos H + \sin\psi \sin\delta \tag{2}$$

and the hour angle at sunrise H_0 is given by

$$H_0 = \cos^{-1}(-\tan\psi \tan\delta) \tag{3}$$

when $\tan^2\psi \tan^2\delta \leq 1$. When $\tan\psi \tan\delta < -1$, H_0 is taken as zero (polar night); when $\tan\psi \tan\delta > 1$, H_0 is taken as 180° (24 hr of daylight).

Earth curvature is taken into account by Bemporad's function B for a homogeneous atmosphere having the same scale height as the assumed model atmosphere (7991 m) and an Earth radius of 6371 km,

$$B = (0{\cdot}997496x^2 + 0{\cdot}002504)^{-1/2} \tag{4}$$,

in place of $x^{-1} = \sec Z$ in computing slant-path extinctions. For convenience in presentation, however, $x = \cos Z$ will be used in derivations of equations in the subsequent discussion.

The model atmosphere

The pressure, temperature and density as functions of height in the atmosphere are those of the ICAO standard atmosphere at pressures above 200 mb; in the stratosphere, the temperature is taken as constant at 218·5°K. The pertinent optical properties of this atmosphere are: the scattering extinction factor (optical thickness) s_1 for a layer of the atmosphere bounded by pressures p_1 and $p_2 < p_1$

$$s_1(q_1, q_2, \lambda) = 9{\cdot}0613 \times 10^{-3}\lambda^{-4}(q_1 - q_2) \tag{5}$$

and the scattering cross-section per unit volume (m^{-1} sterad^{-1}) f_R at a scattering angle β with respect to the direction of the incident radiation

$$f_R(q, \beta, \lambda) = (3/16\pi)(1+\cos^2\beta)(qg/RT)\mathrm{d}s_1/\mathrm{d}q\,. \tag{6}$$

In these formulae, obtained from the well-known Rayleigh theory, q is nondimensional pressure p/p_0, p_0 is the standard pressure at sea level, 1013·3 mb, g is the acceleration of gravity, R the specific gas constant for dry air, T the temperature, and λ the wavelength in micrometers. For the model atmosphere, Eq. (6) is given numerically in the stratosphere by

$$f_R(q \leqslant 0{\cdot}1987) = 0{\cdot}8450 \times 10^{-7}\lambda^{-4}q(1+\cos^2\beta) \tag{6a}$$

and in the troposphere by

$$f_R(q \geqslant 0{\cdot}1987) = 0{\cdot}6414 \times 10^{-7}\lambda^{-4}q^{0{\cdot}8098}(1+\cos^2\beta)\,. \tag{6b}$$

The model aerosol

The suspended particles are assumed to be spherical, to be contained in a layer bounded by heights h_1 and $h_2 > h_1$, with corresponding pressures q_1 and q_2, and to be homogeneous in concentration and ramdomly distributed in both the horizontal and vertical within the layer. The size distribution is taken to be of the Junge type, with number per unit volume dN in class-interval of radius $d(\log r)$ given by

$$dN = \text{const. } r^{-3}d(\log r) \tag{7}$$

and size limits of 0·04 μm and 10 μm. The density of the individual particles is 1·8 g cm^{-3} and the refractive index is real and equal to 1·5 at all wavelengths.

Since the size range encompasses much more than the visible spectrum, the scattering properties of this polydisperse aerosol must be computed from the general Mie theory. The properties of the aerosol were chosen so that the scattering extinction factor and the angular scattering coefficient could be taken from a set of published tables[5]. The wavelength dependence of the extinction factor, as taken from these tables and fitted by a simple power-law, is found to vary as $\lambda^{-1{\cdot}0088}$; no great loss in accuracy results from assuming the exponent to be exactly −1. If the total particulate loading per unit area in the layer be denoted by M (g ha^{-1}), then the extinction factor, or optical thickness, of the entire layer of aerosol is

$$s_2 = 0{\cdot}858 \times 10^{-4}M\lambda^{-1} \tag{8}$$

and, since the concentration is uniform within the layer, the extinction factor for a part of the layer, of thickness Δh, is simply $s_2\Delta h/(h_2-h_1)$.

The angular scattering function presents severe difficulties if one wishes to represent it in functional form with high accuracy. The wavelength dependence is as λ^{-1} except in the "aureole region" of $\beta < 2°$, where it tends toward $\lambda^{-1{\cdot}8}$ as β tends to zero. The "phase function", or polar directional pattern, however, is very strongly peaked in the forward direction, as shown in Fig. 1 for $\lambda = 0{\cdot}55$ μm. In contrast to the Rayleigh phase function $1+\cos^2\beta$, the aerosol phase function would involve terms up to at least $\cos^{12}\beta$, or, alternatively, Legendre polynomials of order 12, with wavelength-dependent coefficients. In view of the complexity of form of $\cos\beta$ when expressed in the spatial coordinates, it would be impossible to carry out the required integrations over these coordinates analytically. Since, as will be seen, two numerical integrations

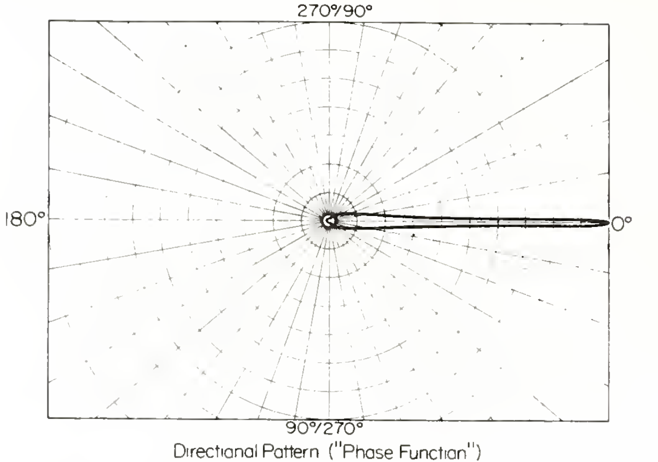

Fig. 1. Phase function of Mie scattering for the model aerosol used in the computations. Note strong major lobe in the forward direction and weak minor lobe toward the rear.

are unavoidable, steps must be taken to avoid the need for more (because the computation time increases roughly as some constant greater than unity raised to the power of the number of numerical integrations). Hence, a way must be found to represent the angular scattering function for the aerosol in a manner which is simple and yet reasonably realistic.

The fact that the aerosol scattering is so heavily concentrated in the forward direction suggests that it would be satisfactory to treat the fraction of the scattered energy which is scattered downward as if it were purely forward scattering, i.e. to consider it as an addition, with proper wavelength dependence, to the direct solar beam.

If one considers a layer of particles at some arbitrary distance h above the ground, and equates the true scattered energy incident normally on a unit area at the ground, after suffering extinction by passing through a medium with arbitrary but constant extinction coefficient, to an equal amount of parallel radiation coming vertically to the ground through the same medium, one finds that the aerosol scatter may be treated as though 65·14 per cent of the total scattered energy were contained in this equivalent parallel beam. The effective scattering function is therefore taken as $0{\cdot}6514 s_2/(h_2-h_1)$ m^{-1}, and the angle of arrival at the ground as the solar zenith angle Z. The aerosol scattering function f_A is then

$$f_A = 0{\cdot}55895 \times 10^{-4} M\lambda^{-1}/(h_2-h_1) \tag{9}$$

under this assumption. The assumption violates reality most severely as Z approaches 90°, but under that condition the true aerosol scatter which reaches the ground by the shortest path is that scattered at $\beta \doteq 90°$, which, as is evident from Fig. 1, is very weak. This weakness is simulated in the simplified model by the multiplication of the scattered power received at the ground by $x = \cos Z$ to convert to normal incidence. In this way, *all* space integrations except that with respect to height (or pressure) are avoided in calculation of the aerosol contribution to the irradiance at the ground, at the cost of a slight underestimate of this contribution at large zenith angles.

The spectral radiance at a point on the ground is composed of five contributions. The direct solar beam suffers extinction, by passage through both the air and the particles, in accordance with the Lambert–Bouguer law. The resulting spectral flux $I_1(\lambda, x)$ normally-incident on the ground is

$$I_1(\lambda, x) = I_0(\lambda)x \exp\{-x^{-1}[s_1(1, 0, \lambda) + s_2(M, \lambda)]\} \tag{10}$$

in which $s_1(1, 0, \lambda)$ is the optical thickness for the entire atmosphere for Rayleigh scattering, $9{\cdot}0613 \times 10^{-3}\,\lambda^{-4}$. The spectral radiance $I_2(\lambda, x)$ scattered to the ground by the aerosol is, under the foregoing simplifying assumptions,

$$I_2(\lambda, x) = I_0(\lambda)xs_2(M, \lambda) \exp\{-x^{-1}[s_1(1, 0, \lambda) + s_2(M, \lambda)]\} \tag{11}$$

after integration with respect to q from q_2 to q_1, to obtain the contribution from each slab of pressure-thickness dq within the aerosol layer.

The remaining contributions are the Rayleigh-scattered light from; (a) the atmosphere above the aerosol layer; (b) the air molecules within the aerosol layer; and (c) the atmosphere below the layer. Calculation of these three contributions requires integration over cylindrical coordinates r and θ as well as height h or pressure q, since radiance arrives at the ground from all directions. The scattering angle β at a point in the atmosphere in terms of cylindrical coordinates r, θ, h, and solar zenith angle Z is derived by use of the law of cosines as

$$\cos\beta = (r^2 + h^2)^{-1/2}[hx + r(1 - x^2)^{1/2}\cos\theta]. \tag{12}$$

Contribution (a) is then given by the integral

$$\begin{aligned} I_3(\lambda, x) = I_0(\lambda) \int_0^{q_2}\int_0^{\infty}\int_0^{2\pi} & f_R(q, \lambda)\,(1 + \cos^2\beta)h(r^2 + h^2)^{-1/2} \\ & \times \exp\{-x^{-1}s_1(q, 0, \lambda) + (r^2 + h^2)^{1/2}h^{-1}[s_1(1, q, \lambda) + s_2(M, \lambda)]\} \\ & \times \frac{dh}{dq}\,r\,d\theta\,dr\,dq. \end{aligned} \tag{13}$$

The first term in the exponential factor represents the extinction of the solar beam before arriving at the scattering point. The second term represents the extinction of the scattered radiance along the path from the scattering point to the ground point (origin of cylindrical coordinates); the factor $s_1(1, q, \lambda)$ gives the extinction due to Rayleigh scattering and the factor $s_2(M, \lambda)$ that due to the particles. In this and the following, it is understood that vertical distance h is to be expressed in terms of q by use of the hydrostatic equation before the final integration with respect to q. The factor $h(r^2 + h^2)^{-1/2}$ is the cosine of the zenith angle of scattered radiance reaching the ground.

Contribution (b) is somewhat more complex in form because part of the extinction by the particles occurs before scattering, and part occurs afterwards. The integral is

$$\begin{aligned} I_4(\lambda, x) = I_0(\lambda) \int_{q_2}^{q_1}\int_0^{\infty}\int_0^{2\pi} & f_R(q, \lambda)\,(1 + \cos^2\beta)h(r^2 + h^2)^{-1/2} \\ & \times \exp\{-x^{-1}[s_1(q, 0, \lambda) + (h_2 - h)\,(h_2 - h_1)^{-1}s_2(M, \lambda)] \end{aligned}$$

$$+ (r^2+h^2)^{1/2}h^{-1}[s_1(1, q, \lambda) + (h-h_1)(h_2-h_1)^{-1}s_2(M, \lambda)]\}$$

$$\times \frac{dh}{dq} r d\theta dr dq \tag{14}$$

in which, it is to be recalled, h_1 and h_2 are the heights of the bottom and top, respectively, of the aerosol layer, with corresponding nondimensional pressures q_1 and q_2.

Contribution (c) is of the same form as (a), except that the extinction by the particles occurs prior to scattering

$$I_5(\lambda, x) = I_0(\lambda) \int_{q_1}^{1} \int_0^{\infty} \int_0^{2\pi} f_R(q, \lambda)(1+\cos^2\beta)h(r^2+h^2)^{-1/2}$$

$$\times \exp\{-x^{-1}[s_1(q, 0, \lambda) + s_2(M, \lambda)] + (r^2+h^2)^{1/2}h^{-1}s_1(1, q, \lambda)\}$$

$$\times \frac{dh}{dq} r d\theta dr dq. \tag{15}$$

Evaluation of integrals in Eqs. (13) and (15) presents no particular difficulty. Integration with respect to r and θ is elementary. Integration with respect to q is accomplished by first changing the variable from q to the argument of the exponentials in Eqs. (13) and (15) and then performing some tedious but straightforward integrations by parts. The final results are exact in these two cases. A complication does arise in the integration of Eq. (14); this arises from the fact that the optical thickness of a layer of air molecules is proportional to the pressure difference $p_1 - p_2$ between the bottom and the top of the layer, while that of an aerosol layer is proportional to the geometric thickness $h_2 - h_1$ of the layer when the concentration of particles is independent of height. As a result, when the change of variable referred to above is carried out, it is found that the factor $(dh/dq)dq$ is nonlinear in the new variable and the integral cannot be evaluated in closed form. The procedure followed in this case is to linearize this factor under the assumption that the thickness $h_2 - h_1$ is small, transfer the resulting constant coefficient outside the integral, and then reverse the process to transform this coefficient to its nonlinear form; this leads to the factor C which will appear subsequently. This procedure introduces a small error which increases with the thickness of the aerosol layer.

After all integrations, x is replaced by B^{-1}, the reciprocal of Bemporad's function (4), wherever it has entered by way of an extinction factor, but is retained as is whenever it has entered by way of a conversion to normal incidence at the ground. The integrals, after evaluation, are conveniently expressed in terms of the following quantities:

$$P_1 = 3x^2 - 1$$
$$P_2 = (P_1B^{-2} - x^2 + 3)/2$$
$$P_3 = (B+2)B^{-2}P_1/4 + 4/3$$
$$P_4 = B - 1$$
$$a = s_1(1, 0, \lambda) = 9{\cdot}0613 \times 10^{-3}\lambda^{-4}$$
$$b = s_2a^{-1} = 9{\cdot}468 \times 10^{-3}M\lambda^3$$
$$w = a(1+b)$$
$$y = a(1+b-q_2)$$
$$v = a(1-q_1)$$
$$C = 8430b/[8430b + (h_2-h_1)(1-2{\cdot}2557 \times 10^{-5}h_1)^{4{\cdot}2603}].$$

In this last quantity C, the number 8430 is the scale height of the atmosphere at sea level; the numerical factor involving h_1 is the ratio of the air density at height h_1 to the air density at sea level. All heights are in meters. The quantities P_i ($i = 1$ to 3) arise from the integrations by parts mentioned earlier. In derivation of C it has been assumed that the aerosol layer lies in the troposphere; if it were in the stratosphere the numerical constants would be changed.

In terms of these quantities, the sum of Eqs. (13), (14) and (15), which is the total Rayleigh-scattered sky light received by the ground, is

$$\begin{aligned}I_3+I_4+I_5 &= 0{\cdot}3744 I_0 \times \mathrm{e}^{-Bw}([w/12(w-3x-1)P_1+P_3]\,\mathrm{e}^{P_4w}+[w^2/12(w-3x)P_1\\ &+(w-x)P_2]\,\mathrm{e}^{Bw}Ei(-w)+xP_2[Ei(P_4w)-\ln P_4]+C\{[v/12(v-3x-1)P_1+P_3]\,\mathrm{e}^{P_4v}\\ &+[v^2/12(v-3x)P_1+(v-x)P_2]\,\mathrm{e}^{Bv}Ei(-v)+xP_2Ei(P_4v)-[y/12(y-3x-1)P_1+P_3]\,\mathrm{e}^{P_4y}\\ &-[y^2/12(y-3x)P_1+(y-x)P_2]\,\mathrm{e}^{By}Ei(-y)-xP_2Ei(P_4y)\}).\end{aligned} \tag{16}$$

The function $Ei(u)$ is the standard exponential-integral function defined by

$$Ei(+u) = \int_{-\infty}^{u} v^{-1}\mathrm{e}^{v}\mathrm{d}v,\, Ei(-u) = -\int_{u}^{\infty} v^{-1}\mathrm{e}^{-v}\mathrm{d}v. \tag{17}$$

The spectral radiances contributed by the direct solar beam, the Rayleigh scattering by the air, and the Mie scattering by the aerosol are given by Eqs. (10), (16) and (11), respectively. To compute the daily totals of irradiance at the ground, it is necessary to integrate each of these expressions with respect to wavelength and zenith angle (as a function of time). Due to the complicated dependence on both λ and x, these integrations must be done numerically. A FORTRAN IV computer program has been prepared, in which expressions (10), (11) and (16) are computed for 56 wavelengths between 0·3 and 5 μm. An interval of 0·02 μm is used from 0·3 to 1 μm, and a coarser interval of 0·2 μm between 1 and 5 μm (since the contribution from the longer wavelengths is small). The radiance for a particular zenith angle is obtained by numerical integration over λ. This procedure is repeated for 51 values of x, distributed evenly with respect to time (hour angle), between sunrise and noon. Numerical integration with respect to time, and multiplication by two, then gives the total daily irradiance for a particular latitude, solar declination and particulate loading M.

The computations have been carried out for seven solar declinations (so as to give twelve values spaced equally throughout the year), for each five degrees of latitude from equator to pole, and for eight particulate loadings, distributed approximately logarithmically, between zero and 10^4 g ha^{-1}.

PRESENTATION AND DISCUSSION OF RESULTS

Computed absolute values of daily irradiance for the equinox, the solstices and the annual mean are shown in Fig. 2, as a function of latitude and particulate loading. Only the curves for the heavier loadings (and zero loading) are shown, to avoid too-close packing of curves. It is evident that the effect of increasing particulate loading during most of the year is to decrease the difference in heat input between low and high latitudes, thereby decreasing the baroclinicity of the atmosphere, and so reducing the mean intensity of the jet stream. It thus appears that a heavy world-wide particulate loading would lead to a "low-index" type of general circulation pattern as well as a general cooling. Near the time of summer solstice, however, the irradiance decreases more rapidly with particulate loading in high latitudes than in the tropics; in this season, increased particle concentration leads to an increase in baroclinicity (horizontal temperature gradient), a stronger belt of westerlies and a weaker trade-wind circulation. The summer circulation under conditions of heavy loading would thus tend to resemble the winter circulation pattern in the absence of aerosol.

Since these computations assume no clouds, the effect of the aerosol tends to be exaggerated. It is of interest to note that the curve for $M = 3000$ at the summer solstice agrees quite closely with the early calculations of the direct insolation in the presence of mean cloudiness by Milankovitch[6]. In the presence of mean cloudiness, the increase of baroclinicity in summer in middle latitudes with increase of particulate loading would be less noticeable, and the net effect over the year would be a weakening of the westerlies in the general circulation.

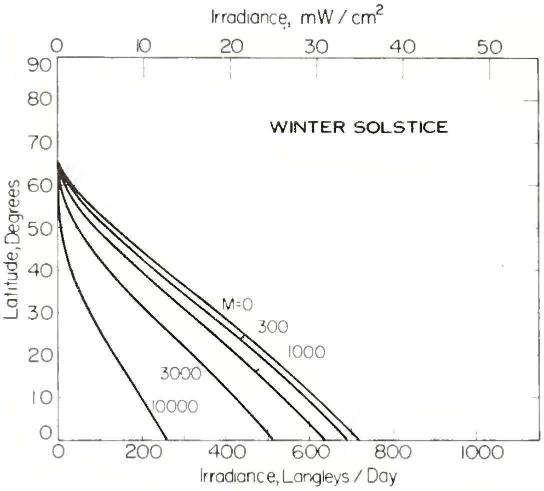

Fig. 2(a)

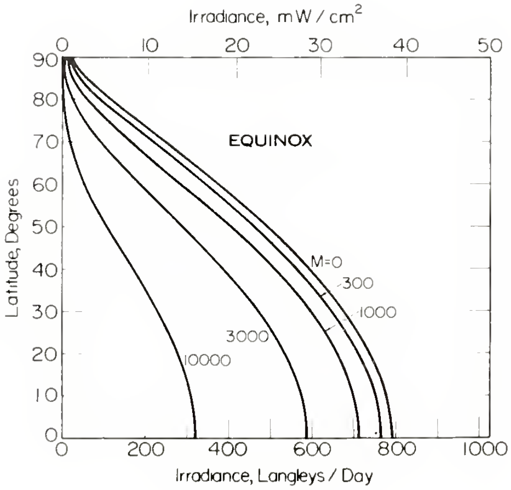

Fig. 2(b)

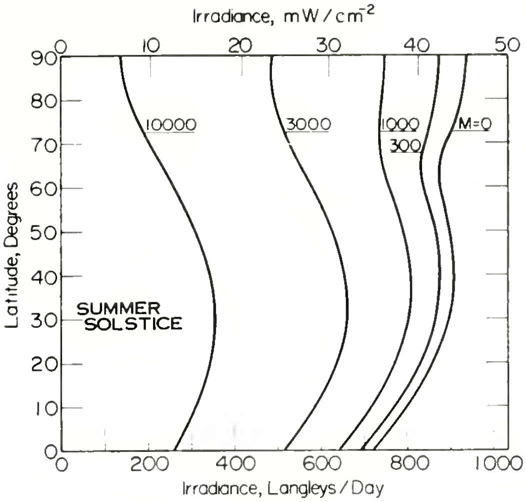

Fig. 2(c)

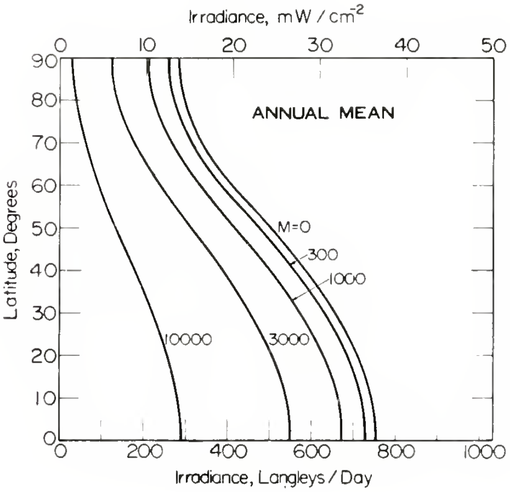

Fig. 2(d)

Fig. 2. Computed irradiances at the ground as a function of latitude, for the equinoxes, the solstices and the mean for the year, with particulate loading M in grams per hectare as parameter. $M = 0$ corresponds to a clean, dry atmosphere.

The percentage by which the irradiance reaching the ground through a clear, dry atmosphere is depleted by various particulate loadings is shown in Fig. 3. These figures do not depend on absolute values, and hence should be a more accurate depiction of the effect of aerosol. It is evident that the higher latitudes suffer more fractional loss at all times of the year. This fact should be considered when extensive industrial expansion in high latitudes is contemplated; more stringent pollution-control measures are required than in lower latitudes.

The numbers labelled T in the figure are the Linke turbidity indices[7] for atmospheres with particulate loadings M. For those who are more accustomed to particu-

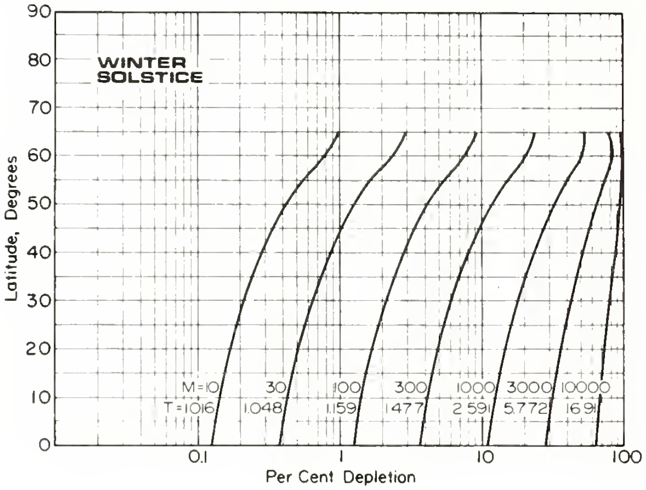

Fig. 3(a)

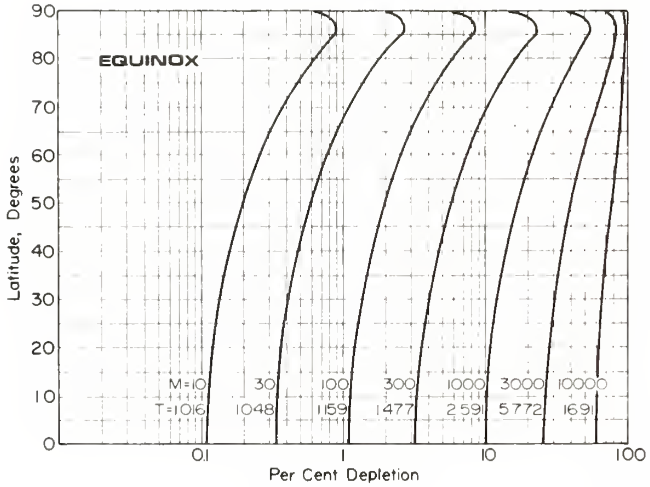

Fig 3(b)

late loadings expressed in English engineering units, 1 g ha^{-1} = 0·57 lb mi^{-2}. Also, for the model aerosol used in these calculations, 1 g ha^{-1} corresponds to $1{\cdot}25 \times 10^6$ particles cm^{-2}.

In Fig. 4, the global annual-mean values of absolute irradiance and percentage depletion (weighted by the areas of latitude zones) are shown. It can be seen that, for low particulate loading, the percentage depletion is a linear function of M. A particulate loading of 100 g ha^{-1} results in 1·5 per cent depletion; the loss is 13 per cent at 1000 g ha^{-1}. Particulate loadings measured by the lidar technique[8] at a rural location near Boulder, Colorado, during October 1968 yielded a mean value of 164 g ha^{-1}; the mean for August 1969 was 67 g ha^{-1}. The average of these two months, 116 g ha^{-1}, would appear to be reasonably representative of this location. The loss of insolation in the Boulder area on clear days would thus be of the order of 1·75 per cent.

On a global long-term basis, the Earth's surface must achieve radiative equilibrium

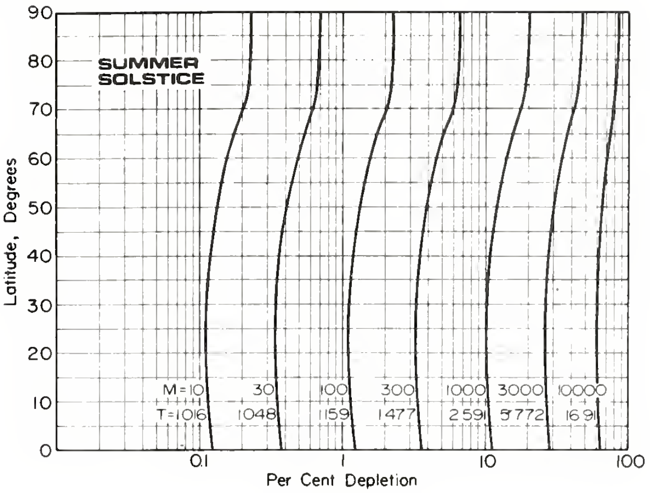

Fig. 3(c)

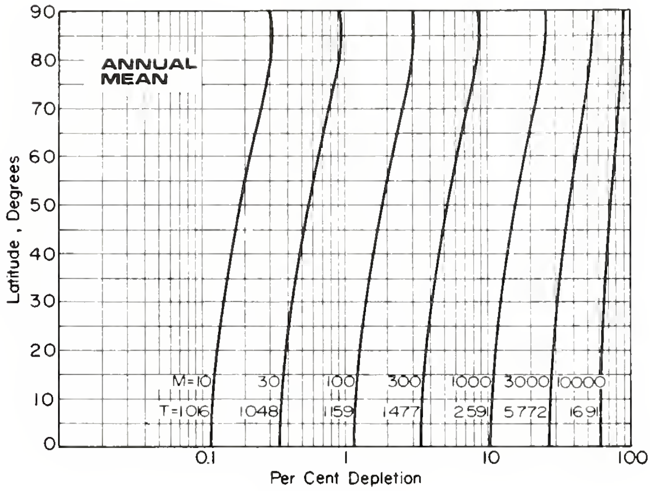

Fig. 3(d)

Fig. 3. Computed percentage depletion of irradiance, relative to a clean, dry, standard atmosphere, as a function of latitude, for the equinoxes, the solstices and the mean for the year, for various particulate loadings *M* in grams per hectare. The numbers labelled *T* are the Linke turbidity indices corresponding to the given particulate loadings.

with the received power from the Sun. If the surface characteristics remain fixed, the global annual-mean equilibrium temperature will decrease with increase in particulate loading. The magnitude of this effect is shown in Fig. 5. It is clear that heavy loadings, if maintained for long periods uniformly over the Earth, can in fact induce drastic climatic change. A loading of 1000 g ha^{-1}, for example, will ultimately reduce the mean sea-level temperature from the standard-atmosphere value of 15 to approximately 5°C; under these conditions, most of the globe would be ice-covered and little plant life would be found outside the tropics. The 116 g ha^{-1} observed at Boulder corresponds to a temperature of 13·8°C, or a drop of 1·2°C below that for a clean atmosphere.

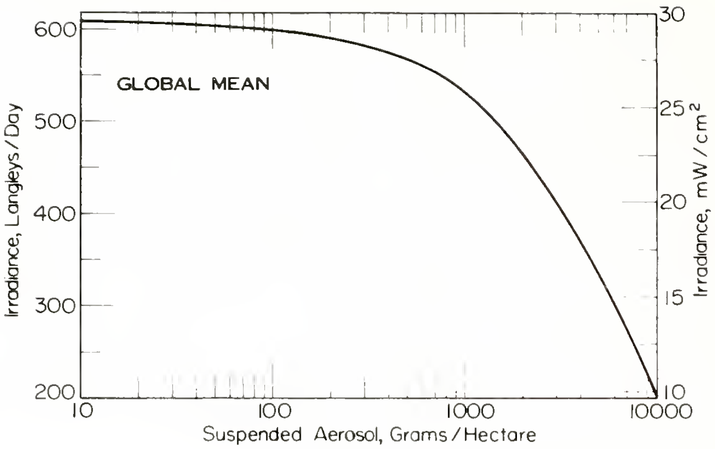

Fig. 4(a)

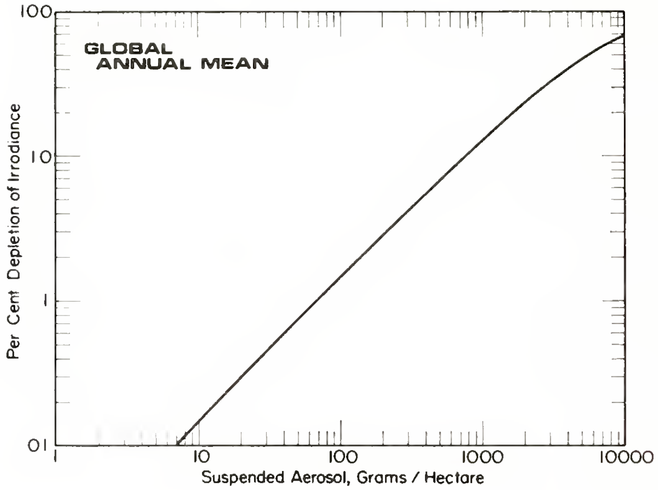

Fig. 4(b)

Fig. 4. Global annual-mean values of irradiance and percentage depletion of irradiance, as functions of particulate loading.

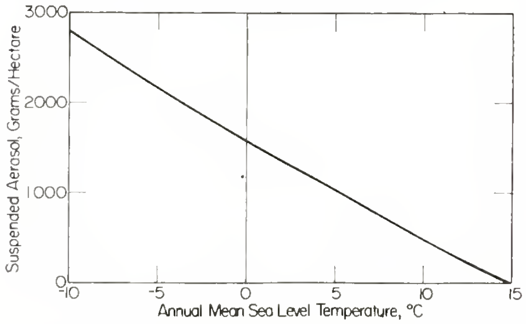

Fig. 5. Global annual-mean sea-level temperature as a function of particulate loading, under assumption of achievement of radiative equilibrium and no other change in the atmosphere or the Earth's surface.

A uniform loading of 1000 g ha^{-1}, when multiplied by the area of the Earth, yields a total aerosol burden of 51×10^6 metric tons. No accurate determination of the present level of this burden has been made; rough estimates by Mitchell[9] and others suggest a figure of 2–4 million tons. Of this amount, it has been estimated that about 20 per cent is man-made. To produce the drastic change of 10°C in mean surface temperature it would thus be necessary to increase the present rate of particle emissions by a factor of 60–100. It therefore appears that the initiation of a glacial epoch by man-made pollutants, while not imminent, is not entirely outside the realm of possibility.

It has often been suggested that past climatic recessions were brought about by an increase in interstellar particle concentrations. If a layer containing 1000 g ha^{-1} of the model aerosol used in the foregoing computations is imagined to extend from the Sun to the Earth, the resultant number density of particles is 84 m^{-3}. This writer has no basis for judging whether or not such a density is likely to be found in the galaxy. However, at this density, the number of particles per second which would be swept out by the Earth in its orbital motion (assuming the cloud to be essentially at rest with respect to the Sun),

$$(84\ \mathrm{m}^{-3})\ (2{\cdot}45 \times 10^{14}\ \mathrm{m}^2)\ (3 \times 10^4\ \mathrm{m\ sec}^{-1}) = 6{\cdot}17 \times 10^{20}\ \mathrm{sec}^{-1} \qquad (18)$$

is the number of micrometeorites entering the atmosphere per second. This number appears to be absurdly large; such a "shower" would produce a rather spectacular night sky! It thus appears, unless the computations in this paper are in error by orders of magnitude, that the interstellar-dust hypothesis of climatic change seems unlikely.

By way of conclusion, some possible sources of error in the computations will be considered. The error made by treating the aerosol scatter as an equivalent beam of parallel radiation has already been mentioned. It will be most severe at high solar zenith angles. Since, however, this modeling assumption does not alter the dominant contribution to the depletion, namely, the extinction of the direct solar beam, the percentage error is small except possibly at high latitudes. Variations of the parameters of the aerosol size distribution do affect the aerosol extinction and angular scattering coefficients; an earlier study[8] indicates that variations in s_2 of the order of ±50 per cent are possible as extremes; thus, 50 to 150 per cent of a given M value might be required to produce a particular depletion of irradiance.

The scattering model used in this work is incomplete in that it permits the once-scattered radiation to suffer extinction on its path to the ground, but ignores the fate of the scattered energy which accompanies this extinction. It can thus be called a "$1\frac{1}{2}$-order" scattering model. The sum of the directly-transmitted, downward-scattered and upward-scattered fluxes (if the latter were computed) will always be less than the incident radiation. This means that the computed depletion of irradiance is always too large. On the other hand, real particles will always exhibit some absorption, which will act to deplete the flux reaching the ground (although this energy will be returned to the earth-atmosphere system at long wavelengths). The model used in this paper can thus be considered to have a built-in absorption which, hopefully, is not too different from that occurring in nature.

It would be desirable to employ a model which includes all orders of scattering, so as to insure conservation of energy. Chandrasekhar[10] does, in fact, develop a formal solution to this problem for the Rayleigh-scattering case: in principle, this could be extended to a mixture of Rayleigh and Mie scattering. It appears, however, that this approach is not feasible on economic grounds. The computations reported in this paper required 138 min running time (using a compiled binary-deck program) on a CDC-3800 computer. If more "nested" numerical integrations were required, the cost would be prohibitively large.

Work is in progress, at the time of writing, on computation of the effect of aerosol layers on the diffuse longwave radiation in the atmosphere. In this case, essentially the same approach is used, except for the assumption of diffuse rather than parallel radiation incident on the layer from both sides. By multiplying the calculated forward- and backward-scattered spectral fluxes by an empirical function of the optical thickness s_2, it is possible to conserve energy to within a few tenths of one per cent over a five-order-of-magnitude range of s_2 (in the absence of absorption). This approach will be applied at a later date to the problem treated in this paper, to determine whether the refinement produces any significant change in the results.

Because of the high computation cost, only a few experiments were made to determine the effect of varying the vertical extent of the aerosol layer and the height of the base of the layer. It was found that the computation is quite insensitive to these parameters. The only effect is on the amount of Rayleigh-scattered light reaching the ground. When the particle layer is at a great height, the sunlight suffers extinction by the aerosol before appreciable Rayleigh scattering takes place, but the subsequent Rayleigh scattering is unaffected by the aerosol. On the other hand, when the layer is near the ground, nearly all the Rayleigh scattering occurs above the particle layer and is subjected to extinction by passage through the layer. Moving the layer base from 100 m to 9·9 km produced only a few per cent change in the Rayleigh-scatter contribution to the irradiance. In all computations reported above, the layer was taken to be 1 km thick and based at 100 m above the ground.

REFERENCES

[1] G. S. Callendar, The artificial production of carbon dioxide and its influence on temperature. *Q. J. Roy. Met Soc.* **64**, 223 (1938).

[2] S. Manabe and R. T. Wetherald, Thermal equilibrium of the atmosphere with a given distribution of relative humidity. *J. atmos Sci.* **24**, 241 (1967).

[3] J. H. Ludwig and R. A. McCormick, Climate modification by atmospheric aerosols. *Science* **156**, 1358 (1967).

[4] W. Marlatt, Unpublished contribution to the 1970 International Solar Energy Society Conference.

[5] E. de Bary, B. Braun and K. Bullrich, Tables related to light scattering in a turbid atmosphere. *Special Reports, No.* 33, *Air Force Cambridge Research Laboratories, Office of Aerospace Research, U.S. Air Force* (1965).

[6] M. Milankovitch, in Koeppen-Geiger, *Handbuch der Klimatologie*, Vol. 1, Gebrueder Borntraeger, Berlin (1930). Also reproduced in: G. J. Haltiner and F. L. Martin, *Dynamical and Physical Meteorology*, p. 96, McGraw-Hill, New York, Toronto and London (1957).

[7] F. Linke, Die Theorie der Zerstreuung, Extinktion, und Polarization des Lichtes in der Atmosphaere. *Handbuch der Geophysik* **8**, 120 (1942).

[8] E. W. Barrett and Oded Ben-Dov, Application of the lidar to air pollution measurements. *J. appl. Meteor.* **6**, 500 (1967).

[9] J. M. Mitchell, A preliminary evaluation of atmospheric pollution as a cause of the global temperature fluctuation of the past century. In *Global Effects of Environmental Pollution* (Edited by S. Fred Singer), p. 97 Reidel, Dordrecht, Holland, (1970).

[10] S. Chandrasekhar, *Radiative Transfer*, Dover Publications, New York (1960).

Reprinted with permission from Am. Meteorol. Soc. Meeting, San Diego, California, Mar. 1972.

BACKGROUND AND METHODOLOGY OF BENCHMARK STATIONS

Earl W. Barrett and Helmut K. Weickmann

Atmospheric Physics and Chemistry Laboratory
Environmental Research Laboratories
National Oceanic and Atmospheric Administration
Boulder, Colorado 80302

1. INTRODUCTION

In the language of geodesy, the term "benchmark" refers to a marker, affixed to a part of the Earth's crust which has the maximum tectonic stability, which is to be used as the origin of a spatial coordinate system (local or global). It carries the connotations of stability, reliability, and permanence; a standard of reference valid over a long period of time. The term may also be applied in a broader sense to quantities having dimensions other than length; we use it in this paper in connection with those properties of the Earth-atmosphere system which exert critical influences on the terrestrial ecology and which are subject to secular change.

In order to observe these secular changes, to investigate the correlations between them, and to develop prediction models, it is necessary to have a globally-distributed set of benchmark stations at which the relevant variables are measured in a consistent and standardized way over an extended time period. A well-operated climatological station located in an environment which has suffered no artificial alterations during the term of its records is a good example of a benchmark station in the atmospheric boundary layer.

The possibility that large-scale human activity is capable of producing significant secular changes in the physics and chemistry of the atmosphere has created the need for benchmark measurements of quantities other than the usual climatological variables, as well as for measurements outside the surface boundary layer. In particular, reliable data on existing levels and secular trends of trace substances, both natural and man-made, in the free atmosphere away from source regions of pollutants are required. Although there have been occasional efforts in the past to collect such data, these efforts have usually been regional in scope, sporadic in time, and confined mainly to the surface layer. Within the last few years, however, various agencies such as the National Oceanic and Atmospheric Administration and the World Meteorological Organization have been making plans for benchmark stations on a global scale.

2. CRITERIA FOR BENCHMARK MEASUREMENTS

In order to qualify as benchmark data, measurements must meet certain criteria of accuracy, precision, and representativeness: (a) they must be made at locations distributed over the planet; (b) they must have high and stable relative accuracy, in the sense that an interchange of instruments between stations should produce no detectable discontinuity in the records, and that drifts of calibration with time must be held to an absolute minimum and verified frequently by checks against reliable standards; (c) to insure this, the measuring techniques should be the same at all stations or, if this is impossible, frequent intercomparison tests must be made; (d) when a change in technique is introduced, the old and new must be run concurrently for a period long enough to insure compatibility of past and future data; (e) the precision of measurement, in terms of the reciprocal of least count or noise level, must be high enough to reveal all of the significant parameters of the time-series of data such as trends, cyclical fluctuations, etc., at a high level of confidence; (f) the measurements should represent all levels of the atmosphere and not be confined to the planetary boundary layer; and (g) they should be made in an environment which is altered only by natural changes and not by human activities in the immediate vicinity.

It is evident that it will rarely be possible to satisfy all of the above criteria for all types of measurements; the last two, in particular, can rarely be satisfied completely even for the simple climatological elements. When measurements of trace materials are considered, the state of technology is often not adequate to meet the requirements for accuracy. stability, and precision.

If only a single parameter is considered, absolute accuracy of measurement is less critical than relative accuracy. The net effect of secular changes in many variables on climate and ecology is. however, the result of many nonlinear interactions and feedbacks; for this reason one should demand the highest absolute accuracies obtainable for each measurement.

3. VARIABLES TO BE MEASURED

The most general statement one can make concerning variables to be measured at benchmark stations is that they should define completely the representative physical and chemical state of the terrestrial atmosphere and its energy exchange with the rest of tha Universe. Like most general or ideal objectives, this is impossible of attainment; we can not as yet close the set of parameters, such as chemical species, which are needed to give a convergent solution to the definition of the total state of the atmosphere. We can, however, establish a hierarchy of parameters in approximate order of importance.

3.1 Energy Input

The solar energy input to the Earth, and its spectral composition, are of prime importance as the forcing function for the total terrestrial ecosystem. It should be measured outside the atmosphere, from a satellite or lunar observatory, so as to separate secular trends in the source from those in the atmosphere.

3.2 Energy Transmission Through the Atmosphere

The availability of the solar input to the biosphere and atmosphere depends strongly on the spectral transmittance of the atmosphere. The total and spectral intensities of radiation arriving at the surface must therefore be measured and compared with that outside the atmosphere.

3.3 Energy Flux to Space

Since the thermal state of the atmosphere depends on the balance between incoming radiation, convective transport of heat, and outward radiative flux, the latter must be measured over all spectral regions where the intensity is appreciable. The spectral albedo of the Earth in the solar-input band should be measured accurately from satellites, together with the long-wave flux. Both the hemispheric totals and values at points over the globe are required. It is of great importance to separate albedo and long-wave flux variations due to cloudiness from those due to other factors; this is also true for the measurements of received solar energy. In this way, dependence on subjective cloudiness estimates or sunshine recorder data (which are not of benchmark quality) can be avoided. It is of great importance to be able to separate secular trends in atmospheric extinction due to variations in cloudiness from those due to other aerosols. In addition to satellite "top sounders", the long-wave flux from sky to ground should be measured in the free atmosphere and at the ground with "bottom sounders" and radiometersondes.

3.4 Standard Climatological Data

Since one purpose of baseline or benchmark measurements is to predict climatic change, it is obvious that the climate itself must be monitored. The fields of temperature, motion (wind), water vapor, precipitation, evaporative flux at the surface, ground temperature, sea-surface temperature, and surface albedo (i.e., snow cover) are more important in the present context than, say, hours of sunshine or frequency of damaging weather phenomena.

3.5 Atmospheric Gases

Since the terrestrial ecology is tightly linked with the relative abundances of the chemically-active gaseous constituents, changes in these must be carefully monitored. Recent measurements (Machta and Hughes, 1970) have yielded the comforting information that the oxygen concentration has remained steady for the last half-century or more, but do not constitute an assurance that no future changes will occur. The situation with regard to carbon dioxide is quite different; measurements too numerous to list here have shown a continuous increase during the past century. Since CO_2 is important to biology and in long-wave radiative exchange, variations in its concentration may perturb a large and complex set of feedback loops within the atmosphere-biosphere-hydrosphere system. Estimates of the direct physical effect of CO_2 variations have been made by, among others, Manabe and Wetherald (1967).

Ozone, although a minor constituent in terms of mixing ratio, is of great importance to the biosphere and to the climatology of the stratosphere by virtue of its absorptive power for short-wave radiation. A substantial reduction in the overburden of this gas would result in an increase in solar flux reaching the ground in the wavelength region around 300 nanometers; this increased flux could be harmful to many life forms (including man). An ozone decrease would also give rise to a colder stratosphere, which might in turn produce alteration of the atmospheric general circulation.

The equilibrium mixing ratio for O_3 is established by a complex set of chemical reactions. In a pure oxygen-nitrogen atmosphere, the partial pressures of these gases and the flux of solar radiation determine the ozone production and destruction rates. However, other trace gases, such as oxides of nitrogen (in all valence states), organic radicals, hydroxyl and peroxyl radicals (derived from photolysis of water vapor) can react with O_3 or its precursor, atomic oxygen, and thus shift the equilibrium ozone concentration. It is therefore necessary to monitor not only ozone but also oxides of nitrogen, water vapor, and,ideally, organic vapors in the lower stratosphere. Such measurements are particularly necessary in view of the fact that aircraft operations in the vicinity of the altitude of maximum ozone partial pressure will increase heavily in the coming decades; the oxides of nitrogen released by these aircraft might cause a significant change in ozone. Unfortunately, the kinetics of the interlocking set of chemical reactions are so poorly known that it is not possible to calculate with any accuracy the end effect of this pollution.

A recent analysis (Komhyr et al, 1971) of data from a number of ozone benchmark stations over the world has shown a significant increase in ozone loading, with the greatest rises over North America, during the past decade. It is not possible, because of lack of data on the other trace gases, to determine whether this rise is due to chemical changes or to a secular change in the stratospheric general-circulation pattern.

Gaseous sulfur compounds are introduced into the atmosphere from the biosphere, by volcanoes, and by combustion of fossil fuels. In addition to their toxic effects on higher life forms, they can play a role in climatic alteration as precursors of sulfate or sulfuric-acid aerosols. There is a dearth of data on the rates of conversion of H_2S, SO_2, and SO_3 to aerosols under atmospheric conditions. Data on the relative abundances of these gases in the free atmosphere and their secular variations are needed.

3.6 Atmospheric Aerosols

Small solid particles and liquid micro-drops (e.g. H_2SO_4) can affect climate in essentially two ways. They influence the patterns of cloudiness and precipitation by acting as cloud-droplet or ice-crystal nuclei and they modify the thermal climate by scattering and absorbing radiation. Most of the atmospheric aerosol burden is of natural origin, but a fraction (estimated variously at from 5 to 20 per cent) is man-made. Local effects on precipitation patterns downwind from strong sources of particulate pollution have already been noted. Global data on aerosol concentrations outside the boundary layer are very sparse and must be greatly augmented. Analyses of solar-radiation records at Mauna Loa, Hawaii, show no significant linear trend in atmospheric turbidity on cloudless days from 1958 to 1970 but do reveal a turbidity increase following the Agung eruption of 1963, with subsequent return to the pre-Agung level (Ellis and Pueschel, 1971).

Although such radiation measurements give indirect evidence of aerosol variations, it is not possible to separate the extinction variations due to aerosols from those due to clouds in a completely satisfactory way; unambiguous measurements of aerosol burden, size distribution, and chemical species are needed to complete the picture and to permit distinction between natural and man-made contributions.

The greater part of the atmospheric aerosol is inorganic in nature, but a fraction is contributed by the biosphere. Plants, especially coniferous trees, emit volatile organic materials which, after partial oxidation in the atmosphere, become solid or liquid aerosols. Very little information exists on the amounts and species of these organic constituents of atmospheric dust and their possible role in cloud microphysics.

4. TYPES OF BENCHMARK STATIONS

Although the word "station" implies permanence of geographical location, it is neither necessary nor desirable that benchmark measurements be confined to fixed ground stations. Suitably-equipped spacecraft, aircraft, and surface vessels, operated repetitively over global tracks, can give benchmark data with much greater geographic coverage. A complete benchmark network will make use of all of these facilities. The planned upgrading of satellite instrumentation will (hopefully) provide the needed data on outgoing radiative flux to the accuracy and precision required of benchmark information. The various scientific missions carried out in the upper troposphere and lower stratosphere by the Convair 990 aircraft of NASA's Ames Research Center have demonstrated the value of a large aircraft with long range, high speed, large payload, and walk-around environment as a mobile benchmark station. Ships, by virtue of their ability to provide e platform for measurements over the sea surface remote from local pollution, can provide meaningful data within the planetary boundary layer; as an example, measurements of electrical conductivity (using the same technique) from many oceanographic vessels during the past half-century have shown a downward trend in this parameter over the North Atlantic but no detectable trend over the South Pacific (Cobb and Wells, 1970). This indicates that aerosol loading over the North Atlantic has increased significantly since the start of this century.

Both fixed and mobile benchmark stations must be capable of both in-situ and remote measurements. In the case of ground stations, the latter type of measurements may involve either remote sensors or balloon-sounding instruments, as determined by the cost/effectiveness ratio. Aircraft and satellites must necessarily rely on remote sensors, either passive or active, for other than in-situ data.

5. PRESENT STATUS

The current status of benchmark measurements varies widely with respect to the parameters being measured. Globally-distributed solar observatories have provided long-term records of received energy flux, but lack of standardization of techniques and intercomparison checks renders the earlier data somewhat unsatisfactory. Many of the existing climatological stations are located in areas which have been altered over the years by local human activity, and therefore do not provide data of benchmark quality. The climatology of the free troposphere, as obtained from radiosondes, has improved in quality and quantity in the past quarter-century as the result of technological progress, but (as has been shown by intercomparison tests) some small but systematic differences between instruments used in different regions of the globe act to bias the data. This problem is most severe for water-vapor measurements (which are the poorest radiosonde information), but small differences in temperature sensors and their response to radiation also contribute to systematic pressure-altitude discrepancies. These last are most serious in the stratosphere.

Considering next the trace-gas constituents, one finds that long-term records of total ozone obtained with the Dobson spectrophotometer are available from several tens of stations over the Earth. Vertical distributions of ozone obtained by ozonesondes are as yet relatively few in number and no long series (ten years or more) exist. Carbon-dioxide measurements, using the infrared absorption technique developed at the Scripps Institute of Oceanography, and subjected to intercomparison checks and standardization by that laboratory, have been conducted at several sites; one of the longest continuous records has been obtained at Mauna Loa, Hawaii, from 1958 to date.

The state of affairs for other trace gases and for aerosols is rather poor; such measurements as have been made have been sporadic and scattered, and in most cases suitable techniques of benchmark quality have not been developed. In the area of long-wave radiation, ascents of Suomi-Kuhn radiometersondes have been made at a few stations, mainly in high latitudes, since the International Geophysical Year. Satellite measurements of long-wave emission have given increasingly large volumes of global data in the last few years, but most of this has been only semi-quantitative, apparently due to difficulties with on-board calibration and data processing. This seems also to be the case with radiation measurements in the solar-input band; the authors are rather surprised to find that, after more than a decade of satellite operations, no definitive figures for the average terrestrial albedo or the solar constant have been forthcoming.

The closest approach to a complete benchmark station in the United States is NOAA's Mauna Loa Observatory, located at approximately 3,200 m elevation in an otherwise uninhabited area. It is protected from local pollutants (most of the time) by the prevailing trade-wind inversion, and is therefore representative (except for occasional volcanic contaminants) of the middle troposphere. Electrical power from commercial mains is used throughout the station to preclude the possibility of local pollution by combustion, and vehicular traffic is kept to an absolute minimum. This station has provided high-quality 12-year records of CO_2 and total ozone, and an equally-long run of solar-radiation data of slightly lesser quality (due to some lapses in calibration). Aerosol concentration measurements (in the form of Aitken-nucleus counts) have been carried out more irregularly over the same time period, as have atmospheric electric field and small-ion conductivity measurements. Standard climatological data are also recorded, but at another site at a lower elevation on the mountain (2,530 m).

6. PROJECTIONS AND NEEDS

Establishment of a global network of fixed benchmark stations is a task which should receive high priority. The World Meteorological Organization has endorsed this viewpoint and is encouraging such development. NOAA is planning to upgrade the Mauna Loa Observatory to the highest state of technology, and to establish three or four more stations at other locations including northern Alaska and the South Pole. Next in order of priority is one or more aircraft benchmark stations. These mobile stations should be operated on global tracks which overfly the fixed stations; the latter would serve as check points to insure compatibility of the aircraft data.

The need for new or improved instrumentation for benchmark stations should provide considerable stimulation for instrument designers. Gas analyzers which can give rapid, precise readouts at mixing ratios of 10^{-10} or less of oxides of nitrogen, SO_2, SO_3, CO, CH_4, etc., without the need of hand manipulation or wet chemistry, are required. In the aerosol field, an analysis system is needed which gives number of particles per unit volume, size or mass per particle, and masses of a selected set of chemical elements (e.g., Na, K, Ca, Mg, Pb, Hg, Cl, S, C, Si) per particle, again without the need for tedious microscopic examination of filter samples. Some progress has been made in these directions. The technique of plasma chromatography has been used successfully to detect certain gases at mixing ratios of 10^{-11} or less, but it may not be applicable to all of the trace gases of interest. For aerosol particles, atomic-emission spectroscopy in a reducing atmosphere (Pueschel, 1969, Barrett et al, 1970) together with optical particle sizing instruments, appear to be capable of giving the physical, and at least a part of the chemical information. Neither problem can, however, be regarded as totally solved at this time.

The present state of technology for solar and infrared radiometry is, in general, adequate for fixed and aircraft stations. It is to be hoped that, in the near future, satellite radiometry can be brought to the same level; this should certainly be possible when manned satellites such as SKYLAB are operational.

A special problem of aircraft benchmark stations is the reduction of memory effects due to the vehicle itself on in-situ sampling. Since air samples are drawn from the aircraft boundary layer and passed through ductwork, any outgassing or shedding of particles from these surfaces render the data unrepresentative. This phenomenon currently sets a limit on the accuracy of stratospheric water-vapor measurements from aircraft. This suggests that emphasis should be placed on developing short-range remote-sensing techniques which interrogate a volume of air outside the aircraft boundary layer. In the case of water vapor, the Raman lidar (Cooney, 1970, 1971) may provide a solution.

Future developments should be directed toward fullest possible use of remote sensing, at both fixed and mobile stations, with emphasis on systems such as lidar which give information as a function of range. It is also essential, because of the large number of data bits generated by a station, that all instrument outputs be in computer-compatible digital format (with analog backup records where feasible).

Some of the material in this paper has already appeared in a previous publication (Barrett et al, 1970), which also gives a more complete list of references.

7. REFERENCES

Barrett, E. W., R. F. Pueschel, H. K. Weickmann, and P. M. Kuhn, 1970: Inadvertent modification of weather and climate by atmospheric pollutants. ESSA Technical Report ERL 185-APCL 15, U. S. Dept. Commerce, Environmental Res. Labs., Boulder, Colo.

Cobb, W. E., and H. J. Wells, 1970: The electrical conductivity of oceanic air and its correlation to global atmospheric pollution. J. Atmos. Sci., 27, 814-819.

Cooney, J., 1970: Remote measurements of atmospheric water-vapor profiles using the Raman component of laser backscatter. J. Appl. Meteor., 9, 182-184.

Cooney, J., 1971: Comparisons of water-vapor profiles obtained by radiosonde and laser backscatter. J. Appl. Meteor., 10, 301-308.

Ellis, H. T., and R. F. Pueschel, 1971: Solar radiation: Absence of air pollution trends at Mauna Loa. Science, 172, 845-846.

Komhyr, W., E. W. Barrett, G. Slocum, and H. K. Weickmann, 1971: Atmospheric total ozone increase during the 1960's. Nature, 232, 390-391.

Machta, L., and E. Hughes, 1970: Atmospheric oxygen in 1967 to 1970. Science, 168, 1582-1584.

Manabe, S., and R. T. Wetherald, 1967: Thermal equilibrium of the atmosphere with a given distribution of relative humidity. J. Atmos. Sci., 24, 241-259.

Pueschel, R. F., 1969: Thermal decomposition of sodium-containing particles in a flame. J. Colloid. Interface Sci., 30, 120-127.

U.S. DEPARTMENT OF COMMERCE
National Oceanic and Atmospheric Administration
Environmental Research Laboratories

NOAA Technical Memorandum ERL APCL-13

GEOPHYSICAL MONITORING AT MAUNA LOA OBSERVATORY

J. F. S. Chin
H. T. Ellis
B. G. Mendonca
R. F. Pueschel
H. J. Simpson

Atmospheric Physics and Chemistry Laboratory
Boulder, Colorado
July 1971

FOREWORD

The ever progressing deterioration of man's environment during the past decades resulted in originating and sometimes successfully applied abatement programs. Most efforts spent in air pollution technology dealt with small-scale events such as the photochemical reactions of trace concentrations of hydrocarbons, and the effect on vegetation of small amounts of SO_2. The rate of increase of CO_2, documented by the monitoring of this gas at MLO, called attention to the possible effects of pollutants on the earth's climate on a global scale. As a consequence, the monitoring program at MLO includes now besides CO_2, particulate matter and ozone as the atmospheric constituents which influences weather and climate with the greatest likelihood. Progress in the program was detrimentally affected by persistent funding problems and in 1965 the station was even in danger of being eliminated altogether. With the creation of a benchmark station program in the newly formed Atmospheric Physics and Chemistry Laboratory, the significance of that station was recognized and MLO was taken over by that Laboratory which supported and improved the station facilities at considerable sacrifice. This support and the perseverance of the resident staff at MLO have made it possible to firmly establish the station now as a global Geophysical Monitoring Observatory as well as expanding the monitoring program.

Helmut Weickmann

Helmut K. Weickmann
Atmospheric Physics and Chemistry Laboratory

TABLE OF CONTENTS

Page

FOREWORD ii

INTRODUCTION 1

Map 3

Rainfall Data 4

Minimum and Maximum Temperatures 5 - 7

Temperature Inversions 8

Tradewind Inversions 9

Wind Rose Data 10 - 13

Surface Moisture 14

Precipitable Water 15

Carbon Dioxide 16

Solar Radiation 17 - 18

Cloudiness 19 - 23

Surface Ozone 24 - 25

Spectrophotometric Ozone 26 - 27

Aerosol Chemical Data 28 - 34

LIST OF FIGURES 35

LIST OF TABLES 36

Reprinted from
21 May 1971, Volume 172, pp. 845-846

SCIENCE

Solar Radiation: Absence of Air Pollution Trends at Mauna Loa

Howard T. Ellis and Rudolf F. Pueschel

Copyright© 1971 by the American Association for the Advancement of Science

Solar Radiation: Absence of Air Pollution Trends at Mauna Loa

Abstract. *Measurements of solar radiation made at Mauna Loa, Hawaii, over a period of 13 years give no evidence that human activities affect atmospheric turbidity on a global scale. Short-term fluctuations in insolation appear to be associated with naturally produced tropospheric aerosols. The intrusion of volcanic dust into the stratosphere results in prolonged increases in atmospheric opacity due to the extended residence times of aerosols in the stratosphere.*

Concern over the earth's energy balance has been expressed in discussions about the diminution of solar radiation and the associated variations in world climate, consequent on the continuing and increased emission into the atmosphere of particulate matter by industrial processes. Observations of an increase in atmospheric turbidity, which is a measure of the extinction of solar radiation in excess of that to be expected from a clean atmosphere, in Washington, D.C., and Davos, Switzerland, led McCormick and Ludwig (*1*) to hypothesize the long-term effects of pollutant aerosols. Flowers *et al.* (*2*) have examined the data from a network of stations designed to measure turbidity and have established a pattern for the continental United States which clearly shows a correlation between high turbidity concentrations and geographic locations with heavy industrialization.

The occurrence of air pollution, however, to which these turbidity increases can be attributed, is a property of the lower troposphere and thus subject to temporal and spatial variations within short intervals. In each of the documented episodes of acute pollution in the past (for example, the Meuse Valley, 1930; Donora, Pennsylvania, 1948; London, 1952 and 1962; and the U.S. East Coast, 1970) a prolonged period (several weeks) of unusual weather conditions accompanied the air pollution incidence, which resulted in a failure of the usual natural processes to dilute and dissipate air pollutants.

In order to detect secular trends in turbidity on a global scale, it is necessary to subdue by experimental design the short-term existence of airborne particulate matter in the lowest portions of the atmosphere in the proximity of pollution sources. Fischer (*3*) carried out measurements of atmospheric turbidity in Antarctica in 1966–1967. A comparison of these data with earlier data on Antarctica led him to conclude that no pronounced change in Antarctic turbidity had occurred in the 16-year period prior to 1966. Mauna Loa Geophysical Observatory (19°32′N, 155°35′W) at an altitude of 3400 m qualifies as a bench-mark station for probing the trace constituents of the atmosphere in virtue of its great distance from continents, the absence of potential pollution sources on the island of Hawaii, and the protection of the measurement site from local emissions, including water vapor, afforded frequently by a persistent trade wind inversion. The monitoring of solar radiation at Mauna Loa is part of a bench-mark program initiated at the beginning of the International Geophysical Year (*4*). Eight pyrheliometers have been used in a continuing program to monitor the normal component of the solar beam. Peterson and Bryson (*5*) concluded, from the evaluation of radiation data taken at Mauna Loa Observatory, that a steady increase in turbidity has taken place between 1958 and 1963.

We have carefully evaluated the data presented in this report (collected over a 13-year period) in order to eliminate as much as possible all contributions to turbidity from random variations of the optical density of the atmosphere, including those caused by locally produced tropospheric aerosols such as sea spray and volcanic effluents. Control days, distinguished from the

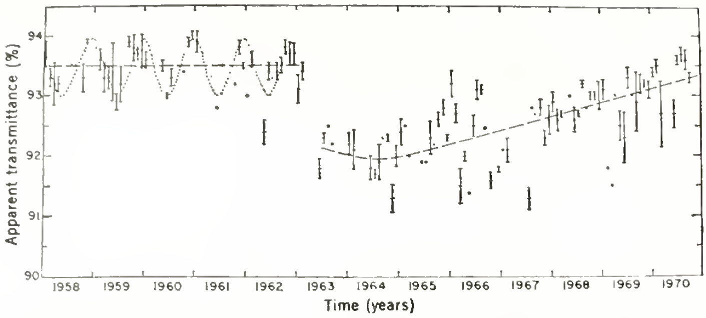

Fig. 1. Temporal variations of the monthly means of transmission factors of solar radiation, which transverses through air masses that differ by units of the secant of the zenith angle.

other days by atmospheric uniformity in addition to clearness, were determined by inspection of the strip-chart traces of the pyrheliometer output and the weather records. Only 410 out of 4473 days, or approximately 9 percent of the total, qualified as control days, an indication that local tropospheric disturbances remain quite frequent at Mauna Loa despite its favorable topographic and climatological features. Evaluation of data for these control days revealed that, for zenith angles (in units of the secant of the zenith angle z) between 2 and 5, the atmosphere exhibited the minimum amount of fluctuation in the optical density. In this discussion, in order to eliminate local influences as much as possible, we therefore present only data taken on control days for sun elevations corresponding to these zenith angles. Transmission factors, q, as identified by Bouguer's law,

$$I_n = I_0 q^n$$

(where I_0 is the solar constant), were computed from measurements of the wavelength-integrated intensity I_n by adaptation of the formula:

$$q = \frac{I_n}{I_{n-1}}$$

where the exponent of q is unity (n is the secant of the zenith angle corrected for refraction). For the broad spectrum, the transmission factor is influenced by the zenith angle; however, by averaging q for a representative interval ($2 \leqq n \leqq 5$) in the forenoon of each day, a relative representation of the optical transmittance of the atmosphere was obtained. This method of evaluating data recorded at the Mauna Loa Observatory on control days eliminates errors due to uncertainties in the calibration of the sensors, compensates for seasonal changes in the sun-earth distance, and excludes short-term fluctuations in turbidity due to aerosol clouds in the lower atmosphere.

Figure 1 shows the monthly mean values of the apparent optical transmittance q of the atmosphere (in percent) as a function of time for the 13-year period. The root-mean-square deviations from the means are indicated by vertical bars for all cases for which a sufficient number of data are available. Within a margin of about ± 1 percent fluctuation in data there is not discernible any systematic trend in solar insolation for the period 1958–1963, contrary to the conclusion drawn by others (*5*). The decrease in insolation in the summer of 1963 coincides with the eruption of Mount Agung, Bali. We conclude from the data that only after 7 years does the transmission recover to the pre-1963 level. This long residence time of the volcanic aerosols in the stratosphere, if compared to the average stratospheric residence time of tracers such as ^{90}Sr and ozone (of the order of 1 year), indicates that the volcanic dust has probably been emitted up to heights exceeding 60 km (*6*). The long recovery period cou'd also be caused by a delayed and continuing production of aerosols (for example, the formation of sulfuric acid by the oxidation of sulfur dioxide in volcanic gases) or by the input of additional particles by subsequent volcanic eruptions (for example, Mount Taal, Philippines, 1965; Saputan, Indonesia, 1966; Kutinoerabu, Japan, 1968), or both; these two mechanisms counteract the natural removal of the original volcanic particulate matter (*7*). A final answer on which of these processes plays the predominate role in determining the lifetime of stratospheric aerosols cannot be given on the basis of radiation measurements alone, but will require direct investigations of the physical and chemical properties of these particles and their variations in time.

On the basis of the data collected prior to 1963, it follows that solar radiation received by the earth apparently undergoes annual cycles such that atmospheric transmission is lower during the summer months, most likely the result of increased worldwide photochemical aerosol formation caused by the oxidation of volatile organic materials of plant origin in the atmosphere (*8*), or the result of the seasonal variations in general atmospheric circulation, or both. From the time scales of recovery it can be concluded that such an aerosol is confined, for the most part, to the troposphere, in contrast to the volcanic aerosol which must have penetrated the stratosphere to a large extent.

If an annual cycle in solar radiation is caused by variations in the production rate of aerosols, rather than by seasonally altered atmospheric residence times, such an annual cycle supports the interesting proposition that at geographic locations sufficiently remote from pollution sources the natural aerosol component predominates over the particulate air pollutants that affect solar radiation. Furthermore, a decrease in the amplitude of the annual variations would be indicative of an increased influence of anthropogenic contaminants on the earth's radiation budget.

The data presented here for Mauna Loa, in conjunction with findings reported by Fischer (*3*) for the Antartic, support the hypothesis that on a global scale natural sources contribute more than man to the turbidity of the atmosphere.

HOWARD T. ELLIS
RUDOLF F. PUESCHEL
National Oceanic and Atmospheric Administration, Mauna Loa Observatory, Hilo, Hawaii 96720

References

1. R A. McCormick and J. H. Ludwig, *Science* **156**, 1358 (1967).
2. E. C. Flowers, R. A McCormick, K R. Kurfis, *J. Appl. Meteorol.* **8**, 955 (1969).
3. W. H. Fischer, *ibid.* **6**, 958 (1967).
4. S. Price and J. C. Pales, *Mon. Weather Rev.* **91**, 665 (1963).
5. J. T. Peterson and R. A. Bryson, *Science* **162**, 120 (1968).
6. O. I. Leipunskii, J. E. Konstantinov, G. A. Federov, O. G. Scotnikova, *J. Geophys. Res.* **75**, 3569 (1970).
7. F. E. Volz, *ibid.*, p. 5185.
8. R. A. Rasmussen and F. W. Went, *Proc. Nat. Acad. Sci. U.S.* **53**, 215 (1965).

5 January 1971; revised 1 March 1971

Reprint from the Review
PURE AND APPLIED GEOPHYSICS (PAGEOPH)
Formerly 'Geofisica pura e applicata'

Vol. 100, 1972/VIII BIRKHÄUSER VERLAG BASEL Pages 70–80

Atmospheric Electric Measurements in the Arctic and Antarctic

By Heinz W. Kasemir[1])

Summary – During the International Geophysical Year, 1958, and extending into 1959, the atmospheric electric field, current, and conductivity were recorded at Thule, Greenland (78°N). During the International Year of the Quiet Sun, 1964, records of the atmospheric electric field were obtained at the Amundsen-Scott Station at the South Pole (90°S). The diurnal variation averaged over the year of the normalized current at Thule and the normalized field at the South Pole show a surprisingly good agreement. These two curves combined into one represent the world time variation of the air-earth current (or field) in the Polar regions. Compared with the oceanic diurnal field variation obtained at the Carnegie ship cruises, the Polar curve shows a very similar shape but a much reduced amplitude. The maximum and minimum in the Polar regions are 1.07 and 0.92. The corresponding values on the oceans are 1.20 and 0.85. The difference is greater than the measuring error or statistical scatter and has to be accepted as real. No conclusive explanation of the deviation of the two curves can be offered.

The diurnal variation of the Polar data averaged over a season displays very smooth and similar curves during Northern autumn and winter. The spring and summer curves show a much more detailed structure with several maxima and minima. It is somewhat unexpected that the summer curve with a variety of fine structure is the flattest curve of all seasons. The minimum never drops below 0.95, and the maximum does not exceed 1.06. If the data are broken down into hourly means averaged over one month and split into an Arctic and Antarctic part, the similarity between corresponding curves of the same month vanishes for the months of January to July. This may partly be due to the fact that the number of fair-weather days of the individual month is too small to obtain a representative statistical average. Usually averaging over seven or more days is necessary for the oceanic pattern to emerge. However, there is a strong possibility that another agent besides the worldwide thunderstorm activity modulates the global circuit. The seasonal differences, and especially the difference between Arctic and Antarctic pattern, point to such a conclusion.

Zusammenfassung – Während des internationalen geophysikalischen Jahres (IGY) 1958 und bis in das Jahr 1959 hinein wurden Registrierungen des luftelektrischen Feldes, des Vertikalstromes und der Leitfähigkeit durchgeführt in Thule, Grönland (78°N). Während des internationalen Jahres der Ruhigen Sonne (IQSY) 1964 wurde das luftelektrische Feld an der Amundsen-Scott Station am Südpol (90°S) registriert. Die normalisierte Tagesvariation des Stromes, gemittelt über das Jahr 1958, in Thule, und die normalisierte Tagesvariation des Feldes am Südpol, gemittelt über das Jahr 1964, zeigen eine überraschend gute Übereinstimmung. Diese zwei Tagesgänge sind zu einem gemittelten Tagesgang zusammengefasst, der den weltzeitlichen Tagesgang des Stromes oder des Feldes in den polaren Regionen repräsentiert. Im Vergleich zu dem Tagesgang des Feldes auf den Ozeanen, wie er während der Carnegie-Fahrten bestimmt wurde, zeigt der Tagesgang in polaren Gebieten einen sehr ähnlichen Verlauf, hat aber eine viel kleinere Amplitude. Die Werte für das Tagesmaximum und Minimum in polaren Gebieten sind 1.07 und 0.92. Die entsprechenden Werte auf dem Ozean sind 1.20 und 0.85. Der Unterschied ist so gross, dass er nicht durch Messungenauigkeit oder statistische

---

[1]) Dr. H. W. Kasemir, NOAA, APCL, R 31, Boulder, CO, 80302, USA.

Streuung hätte hervorgerufen werden können. Er muss deshalb als real akzeptiert werden. Eine Erklärung für diesen Unterschied konnte nicht gefunden werden.

Der Tagesgang in polaren Gebieten gemittelt über die verschiedenen Jahreszeiten zeigt für die nördlichen Herbst und Wintermonate sehr glatte und ähnliche Kurven. Die Frühlings- und Sommerkurven haben eine mehr detaillierte Struktur mit mehreren Maxima und Minima. Es ist etwas überraschend, dass die Sommerkurve mit einer grossen Variation in der Feinstruktur die flacheste Kurve von allen Jahreszeiten ist. Die Minima sind niemals kleiner als 0.95 und die Maxima überschreiten nicht den Wert 1.06. Wenn die Daten weiter unterteilt werden in Tagesgänge gemittelt über Monate, dann verschwindet die Ähnlickeit zwischen arktischen und antarktischen Gängen desselben Monates für die Monate Januar bis Juli. Das mag teilweise darauf zurückzuführen sein, dass die Anzahl der Schönwettertage für die einzelnen Monate zu klein ist, um statistisch repräsentativ zu sein. Eine Mittelung über mindestens 7 Tage ist notwendig, damit der weltweite Tagesgang zum Vorschein kommt. Es ist aber auch sehr gut möglich, dass andere Einflüsse als die weltweite Gewittertätigkeit den Tagesgang modulieren. Unterschiede im Tagesgang der Jahreszeiten und auch des vollen Jahres legen eine solche Erklärung nahe.

1. Introduction

It was one of the main achievements of the last half century in the field of atmospheric electricity that the worldwide thunderstorm activity was recognized as the driving generator of the global atmospheric electric current. (For the history of this development see ISRAËL [3, 4]). The proof of this theory was based mainly on the close correlation of the average diurnal variation of the world thunderstorm activity and the average diurnal variation of the atmospheric electric field on the oceans (WHIPPLE and SCRASE [11][2])). Measurements supporting this theory were carried out by several scientists of the Carnegie Institute during a number of cruises from 1915 to 1929 (MAUCHLEY, [8]; PARKINSON and TORRESON, 1931). Since this time, the pattern of the average diurnal variation of the field on the oceans has been the yardstick for atmospheric electric measurements, which claim to reflect the global atmospheric electrical current flow. Even field or current records of a single day or sporadic balloon or airplane soundings have been compared with the oceanic pattern and usually they agree with it. It may be well to remember that the oceanic field variation is a statistical average of about 130 days spread over several years. The chance to obtain this statistical curve on a single day or as the average of a few days is small. Under these circumstances, one would expect a number of reports that the oceanic field variation has not been found. The lack of such publications shows probably more a bias in selecting the material as a true state of affairs.

Furthermore, we should keep in mind that the world time variation of the field is obtained over the oceans. It does not follow that the same variation has to appear in the Polar areas or at other places which are considered to reflect the global pattern. We will see later in this report that the average field or current variation in the Arctic and Antarctic shows similarities as well as deviations from the oceanic picture.

In general, atmospheric field or current measurements on the continents do not follow the global pattern. This indicates an overriding local influence. The driving force of the local effect is the austausch (turbulence) in the lower layer of the atmosphere. The effect on the atmospheric electric circuit is twofold. Positive space charge is carried by the austausch to higher altitudes against the force of the existing electric field. This constitutes the generator effect of the austausch (KASEMIR [6]). Aitken nuclei are distributed throughout the austausch region which lower the conductivity and increase the columnar resistance in the affected area. The austausch generator will affect the atmospheric electric field and current locally, i.e., in the region where the austausch occurs. Its global component is probably negligible. The same is not true for the variation of the columnar resistance, if larger areas – for instance, continents – are affected.

---

[2]) Numbers in brackets refer to References, page 80.

The increase of the columnar resistance over continents facing the sun would deflect a part of the air-earth current to the night side of the globe or to regions where the columnar resistance is constant during the whole day, for instance, the oceans or the polar regions. The rotation of the earth combined with this resistance modulation would produce a similar variation of the field and current in areas with constant columnar resistance as the worldwide thunderstorm activity (KASEMIR [5]). This indicates the need to have the thunderstorm activity determined by an independent parameter, for instance, lightning count in the extremely low frequency range (ELF) and to work out a detailed analysis of the columnar resistance variation.

If we assume that the austausch phenomena is the controlling factor of the local influence on the atmospheric electric parameters, it is easy to specify the requirements of a location at which global variations may be recorded. The austausch itself should be absent or at least the acting agents, space charge and Aitken nuclei should be absent or very much reduced. These conditions are almost ideally fulfilled at the poles. For this reason, an atmospheric electric station was set up at Thule, Greenland, 78°N, during the International Geophysical Year (IGY), 1958, and a field recorder at the South Pole Amundsen-Scott Station during the International Year of the Quiet Sun (IQSY), 1964.

The instruments and the results of the measurements of these two stations will be discussed in this report.

2. *Atmospheric electric instruments used at Thule, Greenland, and Amundsen-Scott Station at the South Pole*

The instruments used at Thule, Greenland, have been described in detail by J. KRIEG [7]. The measuring system consists of an antenna array for field, current, positive and negative conductivity feeding into a four-channel input switch which is connected to a picoamperemeter. The picoamperemeter acts as an electrometer amplifier and its output is connected to a four-channel potentiometric recorder. Input switch and recorder channel are switched synchronously so that the four atmospheric electric parameters are recorded in cyclic rotation with about 4-sec time interval from one measurement to the next. To have the sensors of the four atmospheric electric parameters as similar and comparable as possible, horizontal wire antenna were used throughout. The field antenna was about 10 m long and 1.5 m above the ground with a radioactive probe attached to its midpoint. The load resistor was 10^{12} ohm. The current antenna was of about the same height and length as the field antenna. The time constant of the input impedance was 600 sec. For the conductivity measurement an antenna arrangement was used similar to that of SCHERING [10]. It is, in essence, a large Gerdien tube with natural ventilation. The inner electrode is again a horizontal wire of 10 m length, which is connected to the input switch of the picoamperemeter. The outer electrode with a driving voltage of ± 250 volt is not a solid tube as by the Gerdien apparatus, but consists of large numbers of wire antennas symmetrical surrounding the central wire in a cylindrical fashion.

The system operated very satisfactorily over the whole year with a minimum of maintenance. Snowstorms, even blowing snow, can be recognized from the records and separated from the fair weather records. However, there are two error sources which could easily go undetected. These are the change of the ground level by snow cover and the icing up of the antenna and antenna insulators. Especially during the long polar night, these events may be overlooked.

The best method to detect – even afterwards – a malfunction of the instrument or to determine the so-called fairweather condition is the fulfillment of Ohm's Law. For the last decades it has been an open question how to define in an atmospheric electric sense fair weather and disturbed weather. The main characteristic of disturbed weather is precipitation and the strong and varying fields accompanying it. From the electrical point of view, the essential fact would be the convection current represented by the charged precipitation. It may be worthwhile to consider to base the separation of the two main electric conditions of the atmosphere on the presence or absence of convection current. The first state would indicate that the station is inside a generator or – expressed in the more meteorological terminology – in disturbed weather. In this case, Ohm's Law would not be fulfilled. In the second case, the station would be outside a generator or in fair weather. Ohm's Law should be fulfilled.

This definition of fair weather conditions has been applied to the Thule data and all times have been eliminated during which Ohm's Law was not fulfilled inside an accuracy of ± 15 percent. The term, 'Ohm's Law,' is used here in a somewhat modified sense. The relation between the air-earth current density i, the atmospheric electric field E, and the positive and negative conductivity λ_+ and λ_- defined in the textbooks as Ohm's Law is the following:

$$i = E(\lambda_+ + \lambda_-). \tag{1}$$

However, after careful calibration of all atmospheric electric channels in Thule, the relation was obtained

$$i = E(\lambda_+ + \lambda_-)/2. \tag{2}$$

This is probably due to the fact that the slightest air movement prevents the establishment of an electrode effect on the wire antenna. As no negative ions can emerge from the surface of the wire, the electrode effect would be a necessity to enable the positive ions to carry the full current. Without electrode effect the antenna will receive only about half of the current which is then given by

$$i = E\,\lambda_+ \,. \tag{3}$$

If the positive and negative conductivity is almost equal as was the case in Thule, Greenland, equation (2) can be reduced to equation (3). It is quite possible that this reasoning will apply to all current sensors built from nonporous solid material, for instance, the Wilson plate. This would explain the difference between theory and current measurement sometimes noted in the literature.

The selection principle for fair weather based on the fulfillment of Ohm's Law resulted in a reliable and homogeneous material extracted from the Thule records. Another advantage is that the selection can be done by a computer. As soon as the percentage of the permitted deviation from Ohm's Law is given, the simple yes or no answer for automatic selection can be programmed. The application of this method to the evaluation of the material compiled during the atmospheric electric ten year program can be highly recommended.

As could be expected from theoretical considerations and the experience of others (HOLZER [2], REITER [9], COBB [1]), the air-earth current is not as much influenced by local conductivity changes as the field. For this reason, the current records are used in the following discussion. At the South Pole, only a field recorder was set up, but – as will be seen later – the close agreement between the average current variation at Thule and the average field variation at the South Pole may justify the comparison between these two different atmospheric electric parameters. Furthermore, it can be assumed that at the Pole the diurnal variation of the austausch has completely vanished. Therefore, the conductivity would be constant or at least would not show any diurnal variation. In such a case field and current records would be equivalent.

The field at the South Pole was measured with a quadrant electrometer recorder. Each of the quadrant pairs was connected to a horizontal wire antenna with a radioactive probe at its midpoint. The vertical distance between the two antennas was 1 m with the lower antenna about 1 m above ground. Measured is the voltage difference between the two wires. This set-up has several advantages as compared with the single horizontal wire. If the field is constant with altitude in the first 2 m above ground level, difficulties in obtaining a good ground would be avoided. The circuit would act like one with a balanced floating input. If there is an electrode effect in the lowest meter above ground, the measurement would not be affected by it. The instrument itself has no electronics and the chart drive is powered by a hand-wound spring. This makes the whole system independent of electric power and its voltage and frequency changes. On the other hand, the recorder is a delicate instrument, needs careful handling, and cannot compete in accuracy, linearity, and overall roughness with the more commonly used potentiometric recorder.

3. *Evaluated field and current records from the South Pole and Thule, Greenland*

The discussion in this report is limited to the diurnal variation averaged over a month, season, and year of fair weather days extracted from the field records at the South Pole and the current records at Thule, Greenland. To compare the two different atmospheric electric parameters, they are represented as the deviation from the mean value, i.e., the hourly absolute value has been divided by the mean value of the month, season, or year, respectively. Only full days were accepted for evaluation with very few exceptions. If, for instance, the zero check was recorded for almost one hour on an otherwise perfect day, the beginning and the end of the break in the record was connected by a straight line and the hourly mean estimated using the so completed record. Sometimes, even on a single day, the record was similar to the oceanic pattern, but more often the shape of the curve was dissimilar to it. Usually it requires 7 to 10 day averaging for the oceanic pattern to emerge. At the South Pole, fair weather records were obtained on 105 days during 1964 with the month of December completely missing. At Thule, Greenland, 190 days of fair weather records were obtained with the month of November missing, there the records started on May 1958 and ended April 1959.

Figure 1 shows the normalized diurnal variation averaged over the full year, with the solid line representing the air-earth current density at Thule and the dashed line the electric field at the South Pole. The time is GMT or world time. It is remarkable that from 1000 to 2400 the curves are practically the same. The difference never exceeds one percent. In the forenoon, the South Pole curve shows a more pronounced dip with a minimum of 0.88 at 0230 in the morning. It recovers then faster than the Thule curve and passes through the overall average value 1.00 at about 0715. The

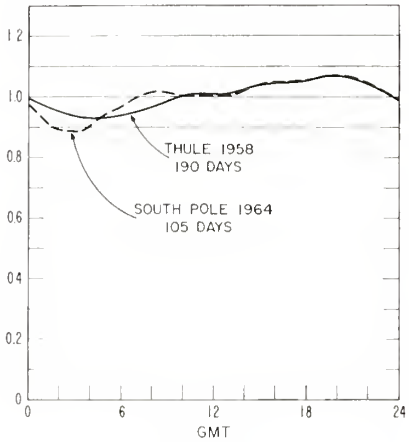

Figure 1

Normalized diurnal variation of the air-earth current density at Thule, Greenland, 1958 (solid line). Normalized diurnal variation of the atmospheric electric field at the South Pole, 1964 (dashed line)

Thule curve has a less pronounced dip with a minimum of 0.93 at about 0400 and a crossing of the 1.00 line at 0920. The maximum difference between the two curves does not exceed five percent. Several explanations can be offered for the deviation of the two curves in the forenoon. The two stations were located almost on antipode points on the globe. One set of data was obtained in 1958, the year with maximum sunspot activity, the other set, 1964, during the year of the quiet sun. There is also still the possibility that the deviation is a result of comparing two different atmospheric electric parameters or that the superior selection methods and the much larger number of the Thule data is the cause of the deviation. However, the difference of five percent is relatively small, and it may be justified to combine the Thule and South Pole data according to their weight in days to one single curve representing the world time variations in the Polar regions.

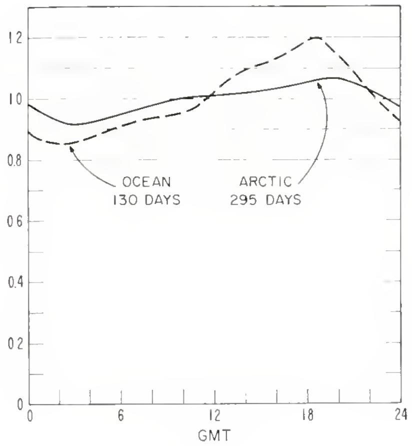

Figure 2
Normalized diurnal variation of the air-earth current density (field) in the Arctic and Antarctic, 1958 and 1964 (solid line). Normalized diurnal variation of the atmospheric electric field on the oceans (WHIPPLE and SCRASE [11]) (dashed line)

This curve is shown in Figure 2 as a solid line and compared to the normalized oceanic variation after Whipple and SCRASE [11], drawn as a dashed line. The similarity in shape is quite apparent. Both curves have their minimum at about 0330, crossing the 1.00 line at 0930 and 1130, respectively, and have their maxima at 1830 to 2030. The dissimilarity lies in the smooth appearance and the remarkably smaller swing of the Polar curve. The oceanic maximum and minimum is 1.20 and 0.85, whereas the Polar values are 1.07 and 0.92. The maximum difference between the two curves occurs at 1830, and it is 14 percent. This is a rather large deviation and its significance is emphasized by the fact that the two Polar curves differ less than one percent from each other in the afternoon, and only five percent in the forenoon. It is not too likely that the material being from different years will have caused the deviation. The two Polar curves, figure 1, are also from different years but agree much better with each other. An explanation based on the fact that one set of data was obtained on the ocean and the other set in the Polar regions would imply a damping effect there. However, such an effect is hard to visualize under the assumption that the earth is an equipotential surface.

Statistical results always show an inherent scatter. But here again the close agreement between the Polar curves does not point to a solution in that direction. Nevertheless, a more detailed statistical analysis is planned to determine the probability that the deviation is inside or outside a reasonable confidence level.

Again the question may be asked, could the difference be due to the fact that two different atmospheric electric parameters, field and current, are compared? The field at Thule has a larger swing than the current due to the fact that the conductivity is not exactly constant during the day. The normalized field curve of Thule is shown in Figure 3 as the solid line and in comparison the oceanic curve as a dashed line. The three peaks reflecting the maximum thunderstorm activity on the three main land masses are very pronounced in the Thule curve. For demonstrating the correlation between the thunderstorm generator and the global circuit, one cannot ask for a better example. Even so, the Thule curve is more modulated and overshoots the oceanic curve sometimes by 15 percent. The overall impression is that of a better fit then between the oceanic field and the Arctic field curve. Because of the larger standard deviation of the field as compared to the current, it is quite possible that the two field curves agree with each other inside a reasonable scatter band. The discussion of

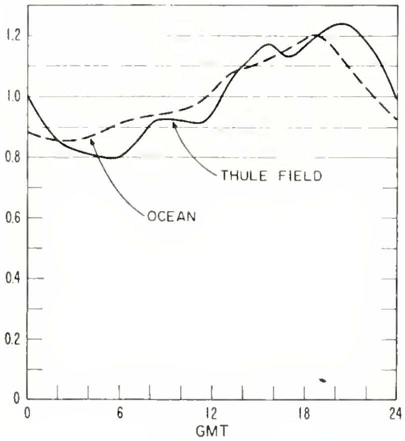

Figure 3
Normalized diurnal variation of the atmospheric electric field at Thule, Greenland (solid line). Normalized diurnal variation of the atmospheric electric field on the oceans (WHIPPLE and SCRASE [11]) (dashed line)

the somewhat controversial conclusion arising from such a result will be postponed until the statistical analysis is carried out.

Figure 4 shows the Polar variation for the four seasons. During the months August, September, October and during the months November, December, and January, the curves are very smooth and quite similar to each other. The three peaks which reflect the maximum thunderstorm activity on the three main continents are almost absent. The August-to-October curve is shaped very symmetrically. The minimum of 0.89 occurs at 0500 in the morning. The curve then increases with a constant slope, crosses the 1.00 line after eight hours at 1300, reaches its maximum at 2100 and drops then steadily to the minimum with a 1.00 crossing at 0100. In the November-to-January curve, there is a very slight secondary maximum at about 0800 which probably reflects the thunderstorm activity in Australia. In the February-to-July curves, this peak becomes more pronounced and shifts to 1000. This could be interpreted by the fact that the thunderstorm activity in the forenoon of GMT is now produced by the Asiatic continent, which is larger than Australia and has its maximum thunderstorm activity about two hours later. The February-to-July curves lose the smooth appearance of the August-to-October curve and contain a number of maxima, which could reflect the peak thunderstorm activities of the different continents. However, a detailed analysis does not lead to a clear-cut picture. One gets the impression that

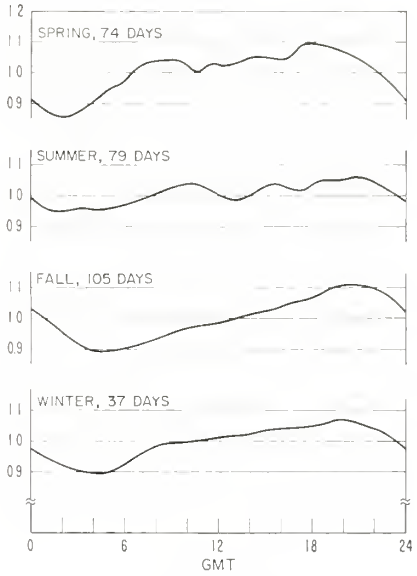

Figure 4

Normalized diurnal variation of the air-earth current density (field) in the Polar areas averaged over the four seasons. Spring: February to April; Summer: May to July; Fall: August to October; Winter: November to January besides the thunderstorm activity, another modulating influence exists. This influence is more pronounced in the February-to-July period than in that of August-to-January. The same conclusion can be drawn from Figure 5, which shows the diurnal variation averaged over each month on the left side of the current at Thule and on the right side of the field at the South Pole. From August to December, the curves of each station show a fair resemblance to the Polar pattern averaged over the year (Figure 2). From January to July, at least on one, more often on both stations, the similarity is either weak or lacking.

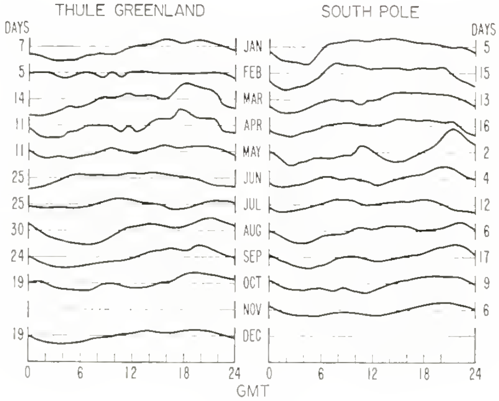

Figure 5
Normalized diurnal variation of the air-earth current density at Thule, Greenland, averaged over one month (left side) and of the atmospheric electric field at the South Pole averaged over one month (right side)

4. *Conclusions*

The similarity in the shape of the oceanic and the polar curves may be considered as a confirmation of the former. However, if we stop with this result the gain of new knowledge would be small because the validity of the oceanic field pattern is generally accepted. The more significant aspect, which is emphasized in this report, is the deviation between these two curves. The Polar curve is more flat with a much reduced maximum and minimum as compared with the oceanic curve. The close agreement between Arctic and Antarctic variation shows that the deviation from the oceanic pattern cannot be explained by the fact that the measurements were made in different years or that it is a mere statistical scatter. There seems to be a better fit of the oceanic field pattern with the Thule field pattern than there is with the current pattern. However, the conductivity in Thule was not constant during the day. Therefore, the atmospheric electric field there is not completely free from local influence. The ocean field pattern was obtained with constant conductivity; therefore, the better agreement between the two field curves is somewhat mysterious. A final solution to this problem can only be obtained by future measurement carried out simultaneously in the Polar areas and on the oceans. It would be necessary to measure all three basic atmospheric electric elements, field, current, and conductivity, and to apply an objective selection principle of the so-called fair-weather days. The fulfillment of Ohm's Law inside a certain error limit is suggested for the determination of fair-weather records. The worldwide thunderstorm activity should be obtained by separate means, for instance ELF or VLF recording, again preferable in the Polar regions. Most of these suggestions have also been proposed by other scientists. The international atmospheric electric Ten-Year Program would be an excellent opportunity to realize them.

5. *Acknowledgement*

The author wishes to express his sincere thanks to persons and institutions who made it possible to carry out the reported research. These are Dr. Lothar Ruhnke who helped to set up and kept operating the atmospheric electric station at Thule, Greenland, and the U.S. Army Radio Propagation Agency, which housed and maintained this equipment at their Ionospheric Station at Thule, Greenland. The field measurements at the South Pole were carried out by Mr. Schroeder at the Amundsen-Scott Station, which was maintained by the Overseas Operations Division of the National Oceanic and Atmospheric Administration and the National Science Foundation.

References

[1] W. E. Cobb, *The atmospheric electric climate at Mauna Loa, Hawaii.* Presented at AMS-AGU Meeting, Washington, D.C. (1967). (In print).

[2] R. E. Holzer, *Studies of the universal aspect of atmospheric electricity.* Contract No. AF 19(122) –254 (Final Report 1955).

[3] H. Israël, *Atmosphärische Elektrizität*, Teil I: *Grundlagen, Ionen, Leitfähigkeit* (1957); *Atmosphärische Elektrizität*, Teil II: *Felder, Ladungen, Ströme* (1961). Akademische Verlagsgesellschaft Geest U. Portig KG. Leipzig.

[4] H. Israël, *Atmospheric Electricity*, Volume I: *Fundamentals, Ions, Conductivity.* Israel Program for Scientific Translations, Jerusalem (1970).

[5] H. W. Kasemir, *Zur Strömungstheorie des luftelektrischen Feldes I.* Arch. Meteor., Geophys., Biokl (A) *3* (1950), 84–97.

[6] H. W. Kasemir, *Der Austauschgenerator.* Arch. Meteor., Geophys., Biokl. (A) *9* (1956), 357–370.

[7] J. J. Krieg, *Measurement of electric field, air-earth current, and conductivity.* USASRDL Tech. Report 2085 (1959).

[8] S. J. Mauchly, *Studies in atmospheric electricity based on observations made on the Carnegie, 1915–1921.* Res. Rep. Terr. Magn. Carnegie Institution V, 383–424 (1926).

[9] R. Reiter, *Felder, Ströme und Aerosole in der unteren Troposphäre.* (Steinkopff Verlag, Darmstadt, 1964).

[10] H. Schering, *Registrierungen des spezifischen Leitvermögens der atmosphärischen Luft.* Göttinger Nachrichten, 201–218 (1908).

[11] F. J. H. Whipple and F. J. Scrase, *Point discharge in the electric field of the earth.* Geophysical Memoirs *VII*, No. 68, (1936), 3–20.

U.S. DEPARTMENT OF COMMERCE
Maurice H. Stans, Secretary

NATIONAL OCEANIC AND ATMOSPHERIC ADMINISTRATION
Robert M. White, Administrator
ENVIRONMENTAL RESEARCH LABORATORIES
Wilmot N. Hess, Director

NOAA TECHNICAL REPORT ERL 200-APCL 18

Development of an ECC Ozonesonde

W. D. KOMHYR

T. B. HARRIS

BOULDER, COLO.
February 1971

TABLE OF CONTENTS

	Page
LIST OF FIGURES	iv
LIST OF TABLES	v
ABSTRACT	1
1. INTRODUCTION	1
2. GENERAL DESCRIPTION OF THE INSTRUMENT	2
3. THE ECC OZONE SENSOR	5
3.1 Principle of Operation	5
3.2 Construction of the Basic Cell	7
3.3 The Carbon-Iodine Ozone Sensor	10
3.4 Sensor Response Time Tests	10
3.4.1 Variation of Sensor Response Time With Load	11
3.4.2 Dependence of Sensor Response Time on Sampling Rate	14
3.4.3 Dependence of Sensor Response Time on Temperature	15
3.5 Efficiency of Ozone Collection	18
3.6 Accuracy of Ozone Measurement	19
4. TEFLON GAS SAMPLING PUMP	24
4.1 Pump Cooling During a Sounding	27
4.2 Pumping Efficiency at Reduced Pressures	30
4.3 General Features of Pump Performance	32
5. DATA TELEMETRY SYSTEM	35
5.1 Electronic Coupler	37
5.2 Data Sequencing Switch	41
6. OZONESONDE CONDITIONING AND TEST UNIT	45
7. SAMPLE DUAL-INSTRUMENT SOUNDING	49
8. ACKNOWLEDGEMENTS	52
9. REFERENCES	53

LIST OF FIGURES

		Page
Figure 1.	Model 1A ECC ozonesonde.	2
Figure 2.	Ozone-radiometersonde flight package.	4
Figure 3.	Details of sensor construction.	6
Figure 4.	Variation of ECC sensor response time with load resistance.	12
Figure 5.	Response of ECC sensor to step changes in ozone input.	13
Figure 6.	Variation of ECC sensor response time with ozone input rate.	14
Figure 7.	Variation of ECC sensor response time with temperature.	16
Figure 8.	Chemical heater for ozonesonde.	17
Figure 9.	Details of construction of gas sampling pump.	26
Figure 10.	Ozonesonde flight box and pump temperatures.	29
Figure 11.	Variation of pump air flow rate with ambient pressure.	32
Figure 12.	Ozone partial pressure correction curve.	33
Figure 13.	Model 1A ECC ozonesonde circuit diagram.	37
Figure 14.	Calibration curves for ECC ozonesondes.	40
Figure 15.	Sequencing switch stepping mechanism.	42
Figure 16.	Sequencing switch commutator decks.	44
Figure 17.	Ozonesonde conditioning and test unit.	46
Figure 18.	Schematic diagram of ozonesonde conditioning and test unit.	47
Figure 19.	Dual-instrument ozone sounding.	50

LIST OF TABLES

Page

Table 1. Preparation of Sensing Solution 19

Table 2. Corrections for Sensitivity of Sensor to Oxygen 22

Table 3. Data Sequencing Switch Contacts 43

DEVELOPMENT OF AN ECC OZONESONDE

W. D. Komhyr and T. B. Harris

An electrochemical concentration cell (ECC) ozonesonde has been developed for measuring the vertical distribution of atmospheric ozone up to about 35 km. The sondes are normally flown coupled to NOAA National Weather Service or Air Force military type balloon-borne meteorological radiosondes; although, provision has been made in certain models of the instrument for additional coupling to Mastenbrook frost point hygrometers or Suomi-Kuhn net radiometers. This report describes the ozonesondes and their performance characteristics. Specifications for fabricating the instruments, as well as dies and stamping tools used in manufacturing the sondes, have also been developed.

(*Reprinted from Nature, Vol.* 232, *No.* 5310, *pp.* 390–391, *August* 6, 1971)

Atmospheric Total Ozone Increase during the 1960s

NAMIAS[1] has postulated that sea–air interactions on a regional basis, and not necessarily air pollution, volcanic activity, or solar intensity variations, may have caused the cooling trend that was observed in numerous areas of the world during the past decade[2,3]. In particular, he attributed the United States temperature anomaly, that is, lower than normal winter temperatures in the eastern two-thirds of the country, and, higher than normal winter temperatures in the west, to intensification of the Rossby wave at the 700 mbar level. This intensification strengthens the ridge over western North America and deepens the trough to the east, thus increasing the frequency of deployment of Arctic air masses into the eastern United States. Namias attributed the change in the character of the Rossby wave to abnormal cyclonic activity that occurred in the winter atmospheric circulation over the North Pacific, the surface waters of which were unusually warm during the 1960's.

Because the effects of a deepened 700 mbar trough over the eastern United States might reasonably be expected to extend to higher altitudes, we considered the possibility that the increased southward flow of air in the troposphere and low stratosphere led to an average increase in total ozone amount over central and eastern North America during the 1960s. Ozone is transported poleward from the equatorial stratosphere source region in the winter hemisphere, before it descends to lower levels[4]. To determine whether an increase in total ozone occurred, we analysed data obtained during the decade 1961 to 1970 at Edmonton, Goose Bay, and Toronto, in Canada, and at Boulder, Bismarck, Green Bay, Caribou, Bedford, Nashville, and Tallahassee, in the United States. The periods of record ranged from 7 to 10 years for all stations except Tallahassee, where observations were made for only 5 yr. At eight of the ten stations, we found statistically significant increases in ozone that varied between 4.4% per decade at Goose Bay, to 8.8% per decade at Nashville, with an average increase for the eight stations of 5.6% per decade. At Green Bay and Toronto, although the calculated trends in ozone were not found to be statistically significant, they produced small positive values, 2.0% and 3.5% per decade, respectively.

To ascertain whether the trough deepening described by Namias extended into the low stratosphere, the geopotential heights of the 200, 100, and 50 mbar pressure surfaces at two stations—Caribou and Nashville—were investigated for the period January 1961 to August 1970. The results of the analysis suggest to us that trough intensification occurred at both stations, particularly during February and March and to a lesser extent in September, October, and November. During other months of the 10 year period, progressive weakening of the trough occurred.

Our total ozone data analyses also yielded statistically significant ozone increases during the 1960s at Dobson spectrophotometer stations distant from the North American continent. At Mauna Loa Observatory in Hawaii, the upward trend was 2.5% per decade, while at Huancayo, Peru, the trend was 6.0%. Subsequent analyses of data from several foreign stations (Fig. 1) confirmed that increases in ozone were not confined to the North American region, but were also characteristic of other areas of the world.

Fig. 1 shows mean monthly total ozone deviations from monthly normals, based on the periods of record indicated, for seven stations in the northern and southern hemispheres. The ozone monthly means were calculated, in most instances, from

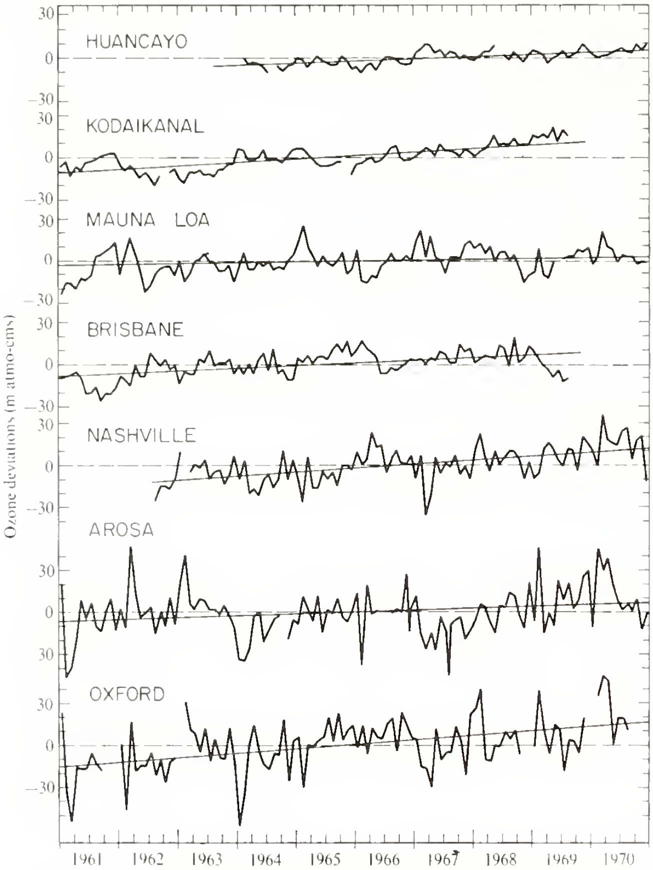

Fig. 1 Plots of mean monthly total ozone deviations from monthly normals for selected stations. Linear trend lines have been fitted to the data.

observations during 25 or more days per month; in isolated cases, however, the means were determined from as few as 10 days of observations. The ozone trend lines were fitted to the data by the least squares method. Table 1 summarizes the results.

Note that the calculated rates of ozone increase range from 2.4±0.6% per decade at Mauna Loa Observatory in Hawaii, to 10.0±0.4% per decade at Kodaikanal in India. Errors given with the trend figures are computed probable errors. In calculating the trends we have assumed that the calibration levels of the spectrophotometers, operated at the stations listed in Table 1, remained constant in time. Using the criterion that the sign of the ozone trend is significant, provided that it does not change within the range of ±3 probable errors, the data clearly indicate that statistically significant increases in total ozone amount were detected at the stations listed in Table 1.

Table 1 Summary of the Data Analyses presented in Fig. 1

Station	Lat., long.	Mean O_3 in m atmo-cms †	% O_3 increase per decade *
Huancayo, Peru	12° 03′ S, 75° 19′ W	262	6.0±0.4
Kodaikanal, India	10° 14′ N, 77° 28′ E	257	10.0±0.4
Mauna Loa, Hawaii	19° 32′ N, 155° 35′ W	276	2.4±0.6
Brisbane, Australia	27° 28′ S, 153° 02′ E	289	6.6±0.6
Nashville, USA	36° 15′ N, 86° 34′ W	332	8.8±0.7
Arosa, Switzerland	46° 46′ N, 09° 40′ E	333	4.1±1.0
Oxford, England	51° 45′ N, 01° 11′ W	354	8.9±1.0

* Extrapolated from the periods of record shown in Fig. 1.
† The unit "m atmo-cms" or "milli-atmo-cms" is used to denote the total amount of ozone in a vertical column of the atmosphere, expressed as the thickness of the ozone layer at STP, assuming that the ozone is separated from the rest of the air.

Although additional data analyses yielded increases in ozone at most stations investigated, the results were not always statistically significant. For example, a small but statistically insignificant increase in ozone of 1.1±0.9% per decade was calculated for Aspendale, Australia (38° 02′ S, 145° 06′ E). We also analysed data obtained at Tateno in Japan (36° 03′ N, 140° 08′ E), and Vladivostok in Siberia (45° 07′ N, 131° 54′ E). Both these stations lie near a region that, according to Namias, experienced a deepening of the 700 mbar trough during the past decade similar to the trough intensification that occurred over eastern North America. Although a positive trend in total ozone of 6.2±3.3% per decade was computed for Vladivostok, we cannot classify this as significant under the criterion that it did not change sign within the range of ±3 probable errors. For Tateno, on the other hand, a downward trend in ozone was calculated, also statistically insignificant, and of magnitude $-3.4 \pm 1.3\%$ per decade.

The tentative linear analyses of the North American total ozone data, as well as the analyses of the data from foreign stations shown in Fig. 1, suggest that an increase in total ozone occurred in many areas of the world during the past decade. This increase cannot be interpreted as an apparent ozone increase that has arisen because of errors in measurement associated with changing atmospheric turbidity. The fundamental method of measuring ozone with Dobson ozone spectrophotometers[5], using wavelength pairs *A*(3055 Å, 3254 Å) and *D*(3176 Å, 3398 Å), is highly insensitive to scattering of solar radiation by particulate matter because, through the subtraction of two nearly equal terms, the scattering term that appears in the equation from which total ozone amounts are calculated is rendered negligibly small. The possibility that the computed rates of ozone increase are due to long term drift in spectrophotometer calibrations should, however, not be discounted. We recently compared the calibration level of our Caribou spectrophotometer with that of a standard spectrophotometer maintained at Boulder, Colorado, and found a drift in the calibration of the Caribou instrument. The magnitude and direction of the drift are such as to account for about one-half of the 5.9% calculated rate of ozone increase per decade at Caribou. In June 1970, on the other hand, the Nashville spectrophotometer was brought to Boulder and compared with our standard instrument. The intercomparison tests showed that the calibration level of the Nashville spectrophotometer did not change by more than 2% during 8 years of operation. Thus, the deduced 8.8% per decade increase in ozone at Nashville cannot be attributed, in large measure, to drift in instrument calibration.

A more comprehensive analysis than that presented here is needed to determine whether a global increase in atmospheric total ozone occurred during the past decade, or whether ozone increases in certain areas of the world were compensated by decreases in other areas. Such an analysis should not only involve data from the worldwide network of total ozone observatories, but should also take into account the calibration histories of the instruments with which observations were made. We are currently recalibrating our Dobson ozone spectrophotometers in an effort to determine the influence of drift in instrument calibrations on the accuracy of the North American ozone measurements.

The Huancayo station is operated in cooperation with the Instituto Geofisico del Peru.

W. D. KOMHYR
E. W. BARRETT
G. SLOCUM
H. K. WEICKMANN
Atmospheric Physics and Chemistry Laboratory,
Boulder,
Colorado 80302

Received May 10, 1971.

[1] Namias, J., *Science*, **170**, 741 (1970).

[2] Mitchell, jun., J. M., in *Global Effects of Environmental Pollution* (edit. by Singer, S. F.) (Springer, New York, 1970).

[3] Wahl, E. W., and Lawson, T. L., *Mon. Weather Rev.*, **98**, 259 (1970).

[4] Dütsch, H. U., in *World Survey of Climatology*, **4** (edit. by Landsberg, H. E.) (Elsevier, Amsterdam, 1969).

[5] Dobson, G. M. B., and Normand, C. W. B., in *Annals of the International Geophysical Year*, **16**, 161 (Pergamon, Oxford, 1962).

Printed in Great Britain by Flarepath Printers Limited, Watling Street, Colney Street, St. Albans, Herts.

U.S. DEPARTMENT OF COMMERCE
Maurice H. Stans, Secretary

NATIONAL OCEANIC AND ATMOSPHERIC ADMINISTRATION
Robert M. White, Administrator
ENVIRONMENTAL RESEARCH LABORATORIES
Wilmot N. Hess, Director

NOAA TECHNICAL REPORT ERL 203-APCL 19

Radiative Transfer Observations and Calculations During BOMEX

P. M. KUHN

L. P. STEARNS

BOULDER, COLORADO
April 1971

TABLE OF CONTENTS

Page

ABSTRACT 1

1. INTRODUCTION 1

2. RADIATION MEASUREMENTS: THE RADIOMETERSONDE 2

3. RADIATION CALCULATIONS 8

4. DATA PRESENTATION 9

5. DISCUSSION OF MEASUREMENTS AND CALCULATIONS 10

6. REFERENCES 18

APPENDIX 19

RADIATIVE TRANSFER OBSERVATIONS AND CALCULATIONS DURING BOMEX

P. M. Kuhn and L. P. Stearns

ABSTRACT

During the Barbados Oceanographic and Meteorological Experiment in 1969, over 220 balloon borne radiometersonde ascents were made from the NOAA research vessels *Discoverer* and *Rainier*, the U. S. Coast Guard Vessel *Rockaway*, and the Seawell Airport on Barbados. The radiative power derived from these ascents provided a massive comparison between observed values and calculations using temperature and moisture profiles of the radiosonde. A summary and brief analysis of the observations and calculations by the radiative transfer equation is examined, along with comments on the radiative cooling.

Key Words: Balloon-borne radiometer, mixing ratio, net radiation, radiation, radiative cooling, radiometersonde, radiosonde, thermal radiation.

Reprinted from Journal of Applied Meteorology, Vol. 11, No. 1, February, 1972, pp. 130-135
American Meteorological Society
Printed in U. S. A.

Radiosonde Humidity Retrieval by Simultaneous Radiation Measurements[1]

P. M. Kuhn and L. P. Stearns

Atmospheric Physics and Chemistry Lab., ERL, NOAA, Boulder, Colo. 80302

(Manuscript received 21 January 1971)

ABSTRACT

A radiometric method for the retrieval of moisture data at altitudes above the radiosonde hygristor cutoff region or in situations where a malfunction of the hygristor occurs is described. The method was applied to BOMEX radiation soundings. Regardless of the exact moisture profile, the method is designed to radiometrically infer the average decrease of moisture through the entire atmospheric column through a solution of the radiative transfer equation. This enables recovery of the total mass of atmospheric water vapor.

In at least 25% of all BOMEX radiometersonde ascents, humidity retrieval did produce a more realistic moisture profile and total mass of precipitable water vapor. In these cases, the radiosonde hygristor humidity deficiencies averaged from -45% at 800 mb to -30% at 600 mb. For such pressure levels, the optical mass of water vapor retrieved for the soundings discussed averaged 1.68 gm cm^{-2}. This represents 56% of the hygristor-measured optical mass. Above 400 mb the optical mass recovered averaged 0.7 gm cm^{-2} for all BOMEX radiometer soundings. It is suggested that a simple radiometer could be used to improve moisture measurements for soundings requiring the best possible water vapor data.

1. Introduction

It is known that the standard U. S. radiosonde and the U. S. military AMT-4 and AMT-12 radiosondes employing the carbon sensor hygristor do not correctly indicate atmospheric moisture at levels above mid-troposphere (approximately 400 mb in the tropics and 450 mb in mid-latitudes). This is due, among other causes, to the low humidities and low temperatures at such levels. There is also evidence to be presented that on occasion the hygristor may not indicate correct humidities at levels well below 400 mb. For some meteorological applications this humidity discrepancy is not important. For others it is a critical but unavoidable shortcoming. Among the latter are infrared (IR) radiative transfer calculations. In fact, it was as a result of radiative transfer calculations and comparisons with BOMEX (Kuettner and Holland, 1969) radiometersonde radiation measurements that one estimate of the hygristor discrepancy at high altitudes and, on occasion, at low altitudes became evident. The purpose of this research is to develop a radiometric method for retrieval of moisture data above the hygristor cutoff region or in regions where the hygristor malfunctions. Regardless of the exact moisture profile, the method is designed to radiometrically infer the average decrease of moisture through the entire atmospheric column. This, in turn, will recover the total mass of atmospheric water vapor.

The magnitude of the humidity discrepancies between those measured by the hygristor and those radiometrically inferred by the technique to be described were found in some cases to be as large as 45% at 800 mb, 24% at 700 mb and 36% at 600 mb. The humidity differences for these lower tropospheric levels correspond, respectively, to 20.0, 7.0, and 17.0C dew point temperature differences. At mid-tropospheric levels the humidity differences for 300 and 200 mb were frequently 50–85% lower for the hygristor than the radiometrically inferred humidities. These differences correspond to 18.0 and 7.0C dew point temperature differences, respectively.

The radiation measurements that are proposed as a control for the humidity measurements have been made for several years with the balloonborne radiometersonde described by Suomi and Kuhn (1958) and Suomi *et al.* (1958). This instrument, attached to the standard radiosonde, was employed in some 300 BOMEX ascents. It is a simple but accurate hemispheric IR radiometer with upward and downward facing shielded and blackened sensing surfaces. It responds to incident power over the spectral range 0.40–50.0 μm, operating with the radiosonde through a self-contained multiplexer but in no way degrading the sonde data. Its basic design and critical dimensions have not changed since the earliest model.[2] This insures a long record of some 7000 comparative radiometric ascents. In principal, the radiometersonde provides separate measurements of upward and downward radiant power by furnishing a direct method of assessing the magnitude of the vertical flux of thermal power through its structure. Convective power transfer is totally suppressed by the unique layered construction.

---

[1] The research described in this paper was sponsored by the BOMAP Project, NOAA, Rockville, Md., and by the Atmospheric Physics and Chemistry Laboratory, ERL, NOAA, Boulder, Colo.

[2] Radiation Measuring Device, U. S. Patent Office No. 3098380.

The rms instrument error of the radiometersonde was evaluated by Bushnell and Suomi (1961). The error for a single measurement is 0.0035 cal cm^{-2} min^{-1}, approximately 2.5 W m^{-2}. This corresponds to an average water vapor mixing ratio error of 0.20 gm kg^{-1} at a level where the mixing ratio is 15.0 gm kg^{-1}, 0.15 gm kg^{-1} at 10.0 gm kg^{-1}, 0.10 gm kg^{-1} at 1.50 gm kg^{-1}, and 0.05 gm kg^{-1} at 0.30 gm kg^{-1}. Thus, even at low mixing ratio levels, the radiometersonde accuracy is adequate to retrieve a more realistic moisture profile in many instances than the hygristor.

2. Design of the moisture retrieval method

Basically the technique involves simultaneous radiometersonde measurements and iterative calculations of the downward IR radiant emittance. The calculations are moisture-adjusted to achieve agreement between measured and calculated radiation by insertion of a modified humidity profile into the radiative transfer equation (RTE). Downward radiative power calculations are preferred to upward because they are more sensitive to water vapor changes. This occurs because downward calculations are made against a zero radiation background transmission.

Upper level moisture, for tropical (this study) or mid-latitude regions (after Mastenbrook, 1968, and Kuhn and Cox, 1967) are entered for all calculations. However, between approximately 180 mb and the measured hygristor-moisture cutoff or discontinuity, as indicated by the profile of the first radiation calculation employing the hygristor-measured moisture, a humidity profile (after Smith, 1966) is inserted in the RTE. His power-law relationship between total precipitable water vapor and surface or reference-level mixing ratio is employed to provide the second iteration moisture profile. Subsequent iterative solutions of the downward power are made, after changing the mixing ratio, only to improve agreement between calculated and measured radiant power. A convergence criterion between measured and calculated radiant power was established for cloudy conditions ($\geqslant 8/10$ reported total sky cover), broken sky conditions (4/10 to 8/10 cover), scattered sky conditions (2/10 to 4/10), and cloudless ($\leqslant 2/10$). Both the power-law estimate of the moisture profile and the convergence criterion are further discussed in the succeeding sections.

The atmospheric saturation mixing ratio profile establishes the theoretical maximum of total precipitable water vapor which may exist. This control profile results from our prior knowledge of the temperature sounding. In each radiometric inference of the moisture profile, a calculation of the downward radiant power is made assuming saturated conditions. This calculated radiometric profile then establishes the *limiting value* of radiant power that can exist due to emission from water vapor, carbon dioxide and ozone. In fact, the "saturated" profile equaled or slightly exceeded the measured downward power in less than 25% of the soundings. This ever-present excess of measured over computed radiation is due primarily to clouds and atmospheric particulates. However, one cannot rule out the possibility that the absorption coefficients for water vapor, carbon dioxide and ozone that are employed in this and other RTE models may be in error to some degree.

It is interesting to note in the succeeding figures, which are typical of the bulk of the 300 soundings, that the particulate structure evidenced by the relatively sharp increase in the gradient with increasing pressure of the downwelling radiation, generally occurs from 850 mb downward. However, on days when Harmattan haze reaches the BOMEX area, the radiation soundings exhibit this gradient increase at a higher level, ~675 mb. The main criterion we have chosen for a properly inferred moisture profile is agreement between calculated and measured radiant power.

3. Radiation calculations

The downward radiant emittance (cal cm^{-2} min^{-1}) was evaluated by a particular numerical solution of the RTE. The mathematical representation of the calculated radiance (cal cm^{-2} min^{-1} sr^{-1}), viewed at zenith angle θ, is

$$I(\theta)=-\int_0^\infty \int_{\tau=1.0}^{\tau} B(\nu,T)d\tau(u_{H_2O})d\nu -\int_0^\infty \int_{\tau=1.0}^{\tau} B(\nu,T)d\tau(u_{CO_2})d\nu. \quad (1)$$

The radiant emittance follows from Eq. (1) and may be written as

$$N\downarrow = 2\pi \int_0^{\pi/2} I(\theta)\downarrow \sin\theta \cos\theta d\theta, \quad (2)$$

where τ is the transmissivity, B the Planck function, ν the wavenumber (cm^{-1}), T the absolute temperature, and u the pressure-corrected optical mass (gm cm^{-2}). Pressure-broadening effects on the optical mass of water vapor were determined from

$$u=U(p/p_0)^{\gamma(p)}, \quad (3)$$

where U is the measured or inferred optical mass, and γ is a function of the pressure p (Kuhn, 1963). For carbon dioxide and ozone, $\gamma(p)$ is replaced by 0.6.

The RTE model employed has a spectral density of 10 cm^{-1} and employs the water vapor absorption coefficients of Möller and Raschke (1964), continuum (atmospheric window) transmission coefficients of Saiedy

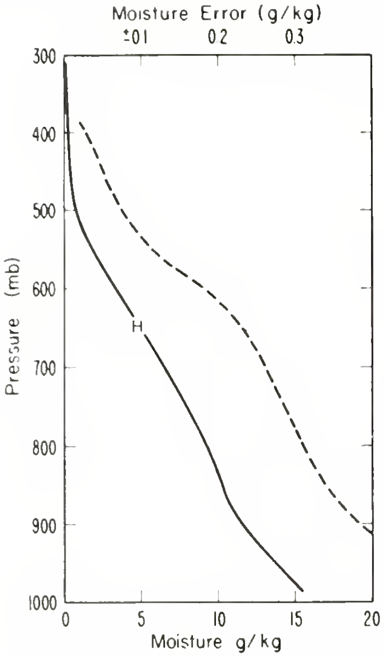

FIG. 1. Average mixing ratio profile for BOMEX radiometersonde ascents (solid curve) and mixing ratio error profile (dashed curves) due to the rms radiometersonde radiation error for the average curve.

and Hilleary (1967), and the carbon dioxide transmission data of Smith (1969). Computations can be made for any number of atmospheric levels and for any spectral interval (in this case, 0–2280 cm^{-1}).

The iterative solution method employing the RTE to infer the water vapor amount is possible since the emission due to CO_2 is a function of the atmospheric temperature and the total atmospheric centimeters (gm cm^{-2}) of CO_2 above any level in the atmosphere. Both quantities are known, leaving only the transmissivity of water vapor, $\tau(u_{H_2O})$, as a variable in Eq. (1). We have disregarded the small contribution of O_3 to the downward radiance, $I(\theta)$, in Eq. (1). It is thus possible to iterate through solutions of Eq. (2) until required convergence of measured minus calculated radiant power is achieved. This is done by employing and adjusting the moisture profile representation described by Smith (1969).

Smith has shown that regardless of the exact moisture profile, with the proper choice of the power λ for a given atmospheric situation, the average decrease of moisture through the entire atmospheric column may be described by a power law

$$w=w_0(p/p_0)^{\lambda}. \qquad (4)$$

Here, w is the mixing ratio at any pressure level p, w_0 the mixing ratio at the earth's surface or at a reference level, and p_0 the corresponding pressure. For the BOMEX area during summer, Smith gives a value of 3.0 for λ.

4. Application of the method to typical soundings

We have applied the humidity retrieval method described to approximately 40 BOMEX radiometersonde ascents. This did not exhaust the number of ascents that could possibly be moisture-adjusted. It did serve, however, to demonstrate that this procedure could improve the humidity profiles and total atmospheric optical mass of water vapor for many soundings.

From this group of 40 radiometersonde ascents we chose four typical soundings to illustrate the results. Cloud conditions for the four runs ranged from 0.3 to 0.8 cumulus, typical for the Barbados region. One of the four ascents required no humidity adjustment and appears as a standard.

In applying the radiometric humidity retrieval method to a sounding judged by inspection to be well below the average seasonal moisture profile for the Barbados (or any other) region, we adopted the following computational procedure:

1) Computer-calculate downward radiant emittance with the actual hygristor-measured humidity.

2) Compare these RTE-calculated results with the radiometersonde-measured downward radiant emittances either graphically (CRT output) or numerically.

3) If agreement does not meet the radiant emittance profile convergence criterion, apply Smith's moisture profile as a "first guess" for the first RTE iteration. Convergence of the RTE-calculated and measured-downward radiation profiles at levels generally above 850 mb is defined by that condition in which

$$\sum|(N_0\downarrow-N_c\downarrow)_i|/N_0\leqslant 0.0035 \text{ cal cm}^{-2}\text{ min}^{-1}+\epsilon, \qquad (5)$$

where ϵ is the cloud factor and i the pressure-level index.

The value 0.0035 ly min^{-1}, the rms error of an individual radiometersonde measurement, was the obvious choice for a convergence criterion. How much this error affects the mixing ratio is shown in Fig. 1. This is a plot of the average mixing ratio profile for the BOMEX radiometersonde ascents together with the mixing ratio error profile for a 0.0035 ly min^{-1} radiometersonde rms error. RTE-calculated radiant power throughout the sounding cannot reach the measured power since the RTE calculations do not take into account clouds, aerosols and haze. Fig. 2, illustrating a sounding not requiring humidity adjustment, typifies the mean discrepancy between RTE-calculated and measured radiant power. The discrepancy is due, primarily, to the 8/10 cumulus cloud cover and lower level particulates. The difference of 0.07 ly min^{-1} is average for cloudy BOMEX ascents. By examining the average radiation profiles for cloud covers $\geqslant 8/10$, 4/10 to 8/10, and

$<4/10$, the values for ϵ [Eq. (5)] were set at 0.06, 0.04 and 0.02 ly min^{-1}, respectively. Below 800–900 mb, the discrepancy between measured and calculated radiant power becomes considerably larger due to the inability of the RTE to handle particulates and haze as well as sea spray. Again, this is evident in Fig. 2 from an examination of the calculated downward radiant emittance (CDE) and the measured downward radiant emittance (MDE).

4) Using Smith's method successive moisture profile approximations are then entered in the RTE until convergence is reached.

5) The radiometrically inferred water vapor mixing ratio profile must not exceed saturation.

6) Moisture profile approximations are initiated from that pressure level where there is an evident moisture discontinuity or clear departure from a power-law lapse of moisture with height.

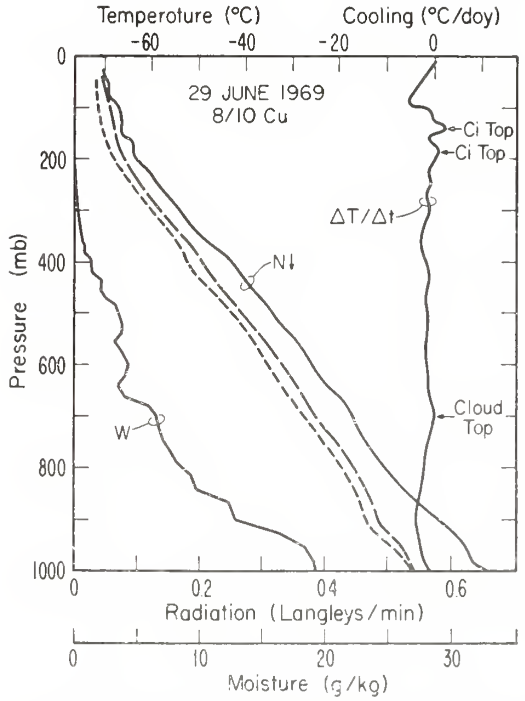

FIG. 2. A Barbados radiometersonde showing the mixing ratio profile (solid curve W), the RTE-calculated downward radiant emittance (CDE) based on hygristor moisture (short dashed curve), and the downward radiant emittance for saturation conditions (long dashed curve). The solid curve labelled $N\downarrow$ is measured downward radiant emittance (MDE). The solid curve labeled $\Delta T/\Delta t$ is the layer atmospheric cooling due to divergence of the net radiation. This is a sounding not requiring humidity adjustment.

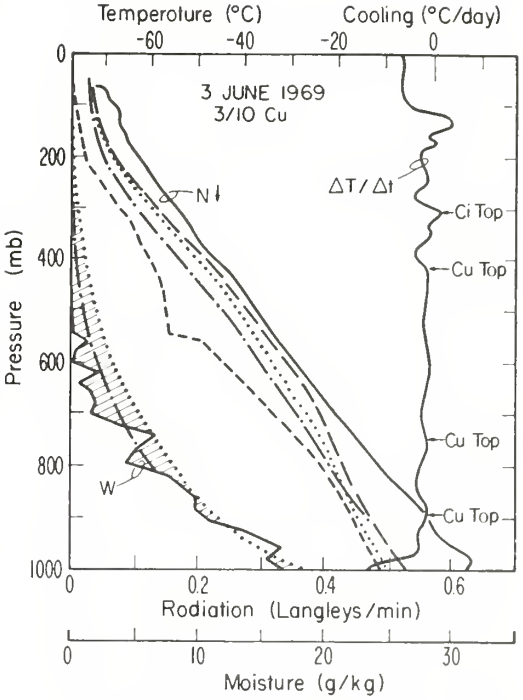

FIG. 3. A Barbados radiometersonde with labelled curves identified as in Fig. 2. The dot-dashed curve through the cross-hatched area is the Smith water-vapor profile for the first radiation iteration, while the dotted curve bounding the cross-hatched area is the Smith water-vapor profile for the second radiation iteration. The short dash curve is the CDE, the dot-dash curve the first radiation iteration and the dotted curve the final iteration. The long-dashed curve is the downward radiation for saturation. The figure illustrates the normal humidity adjustment procedure.

Fig. 2 illustrates a radiometersonde sounding under almost overcast cumulus conditions where the hygristor evidently functioned properly throughout the ascent. This was concluded from a RTE calculation of the CDE and a comparison of this profile with the MDE. Other than the overall average MDE-CDE discrepancy, no significant differences appear. The CDE curve for saturated conditions is illustrated for reference. The first tops of a rather deep cumulus system occur at ~700 mb from the increase in the radiational cooling rate. Another top is at 425 mb with cirrus-layer tops at 190 and 145 mb.

Fig. 3, illustrating a Barbados radiometersonde ascent, allows us to examine the results of the humidity retrieval procedure for typical BOMEX weather conditions. The CDE employing hygristor-measured moisture diverges widely from the MDE profile. The large MDE-CDE difference from 800 mb upward and the absences of any indicated moisture above approximately 550 mb shows the presence of water vapor not measured by the hygristor. Two radiation iterations employing the Smith power-law determination of the water vapor mixing ratio moved the CDE to within the convergence criterion from 700 mb upward.

Below 700 mb the presence of heavy Harmattan haze, reported by independent island observers, pro-

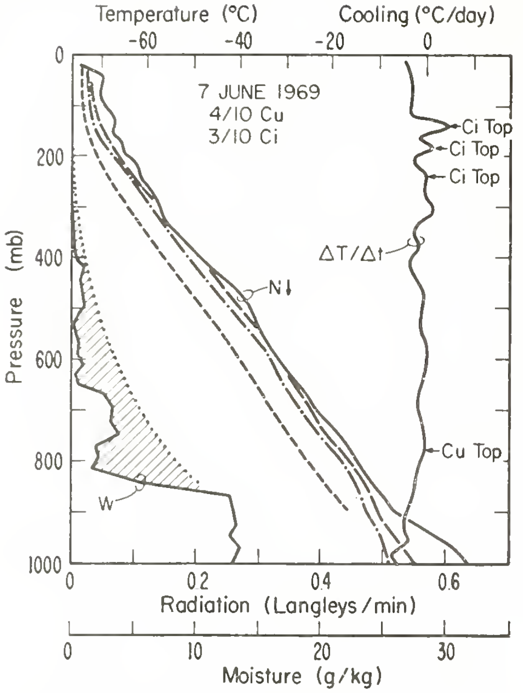

Fig. 4. A Barbados radiometer with labelled curves identified as in Fig. 2, with all other curves being identified in Fig. 3. The situation is one occurring in nearly 25% of all BOMEX soundings, where there was very low hygristor indicated above the 850–750 mb level and more above 550 mb.

duces sharp divergence between MDE and CDE profiles. The presence of haze up to 10,000 ft sweeping off Africa in easterly waves in the trades was verified in July 1969 from direct radiometric and visual observations from NASA's Convair-990.

Again, note that the final CDE does not reach the saturation CDE. The actual optical mass of water vapor retrieved by radiometric inference for this sounding was 1.57 gm cm^{-2}. In a sense, it is represented by the cross-hatched area of Fig. 3.

The water vapor profile retrieved by radiometric inference (Fig. 4) illustrates a situation that occurred in nearly 25% of all BOMEX radiometersonde (and, presumably, radiosonde) soundings. It is that of very low hygristor-indicated moisture above approximately 850–750 mb with virtually no water vapor indicated above 550 mb. To achieve agreement between MDE and CDE, it was only necessary to apply the Smith power-law water vapor profile to our CDE once. The moisture adjustment is quite large, represented by the cross-hatched area, and amounts to an increase of 1.52 gm cm^{-2}, total optical mass, over that indicated by the hygristor. Three rather distinct cirrus sheet tops at 250, 190 and 140 mb appear distinctly.

Fig. 5 displays another situation quite similar to that of Fig. 4 except that the retrieved optical mass of water vapor is 1.60 gm cm^{-2}, indicating a partial failure of the hygristor above 890 mb and the usual failure above approximately 550 mb. Two iterations employing the Smith water vapor profile first from the surface and then from 890 mb achieved convergence between MDE and CDE. The CDE employing the saturation water vapor mixing ratio profile as a control is quite close to the MDE. In both Figs. 4 and 5, the haze layer reaches only to about 900 mb; the level is indicated by the sharp divergence in the MDE and CDE profiles.

The computer solution of the radiometrically inferred moisture is extremely swift, requiring only some 3—4 sec (CDC-3800 computer type).

5. Conclusions

It appears evident that humidity retrieval by radiometric inference can, in at least 25% of all BOMEX radiometersonde ascents, produce a more realistic moisture profile and total mass water vapor above ~800 mb. Generally, above 550 mb, virtually all of

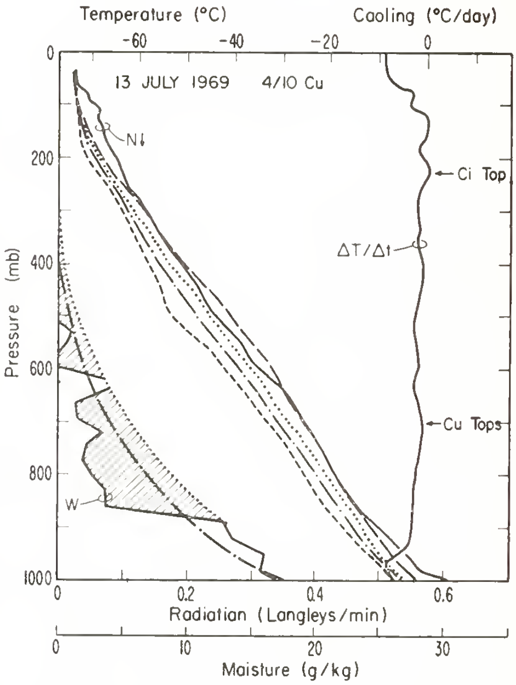

Fig. 5. A Discover radiometersonde with labelled curves identified as in Fig. 2 with all other curves being identified in Fig. 3. The situation is similar to that of Fig. 4 except for a retrieved optical mass of water vapor of 1.60 gm cm^{-2}, indicating a partial failure of the hygristor above 890 mb and the usual failure above ~550 mb.

the BOMEX radiometersonde ascents require humidity adjustment.

This apparent shortcoming in the radiosonde hygristor is well known at higher levels with low temperatures and low humidities, but perhaps is not as well recognized between 550 and approximately 800 mb and could affect BOMEX "core" experiments on the total energy and water vapor budgets. Presumably they should be considered and some adjustments made. Admittedly this is difficult post facto but can be considered for the future.

The comparison of calculated downward radiant emittance and the radiometersonde-measured downward radiant emittance and the recognition of discrepancies between the two profiles suggests a future alternative. The attaching of a simple, single thermistor, miniaturized Suomi-Kuhn radiometer to the radiosonde and keying it into the radiosonde-blocking oscillator and transmitter in place of the hygristor below a chosen pressure level could provide more accurate high-level moisture measurements.

Additional circuit modifications to the radiosonde could provide hygristor and radiation measurements resulting in comparative moisture observations (hygristor and radiometric inference) at higher pressures (lower levels). A simple version of this "humidity radiometer" was recently flown successfully as part of a standard radiosonde ascent. After several additional flights, the results will be reported.

REFERENCES

Bushnell, R. H., and V. E. Suomi, 1961: Experimental flight verification of the economical net radiometer. *J. Geophys. Res.*, **66**, 2843–2848.

Kuettner, J. P., and J. Holland, 1969: The BOMEX project. *Bull. Amer. Meteor. Soc.*, **50**, 394–402.

Kuhn, P. M., 1963: Radiometric observations of infrared flux emissivity of water vapor. *J. Appl. Meteor.*, **2**, 368–378.

——, and S. K. Cox, 1967: Radiometric inference of stratospheric water vapor. *J. Appl. Meteor.*, **6**, 142–149.

Mastenbrook, H. J., 1968: Water vapor distribution in the stratospheric and high troposphere. *J. Atmos. Sci.*, **25**, 299–311.

Möller, F., and E. Raschke, 1964: Evaluation of TIROS III radiation data. NASA Contractor Rept. CR-112, University of Munich, Germany, 84 pp.

Saiedy, F., and D. T. Hilleary, 1967: Remote sensing of surface and cloud temperatures using the 899 cm^{-1}. *Intern. Appl. Opt.*, **6**, 911–918.

Smith, W. L., 1966: Note on the relationship between total precipitable water and surface dew point. *J. Appl. Meteor.*, **5**, 726–727.

——, 1969: A polynomial representation of carbon dioxide and water vapor transmission. ESSA Tech. Rept., NESC 47, Washington, D. C., 19 pp.

Suomi, V. E., and P. M. Kuhn, 1958: An economical net radiometer. *Tellus*, **10**, 160–163.

——, D. O. Staley and P. M. Kuhn, 1958: A direct measurement of infrared radiation divergence to 160 mb. *Quart. J. Roy. Meteor. Soc.*, **84**, 134–141.

Reprinted from
24 December 1971, Volume 174, pp. 1319-1321

SCIENCE

Water Vapor: Stratospheric Injection by Thunderstorms

P. M. Kuhn, M. S. Lojko and E. V. Petersen

Copyright© 1971 by the American Association for the Advancement of Science

Water Vapor: Stratospheric Injection by Thunderstorms

Abstract. *Infrared radiometric inference measurements of the mass of water vapor injected into the lower stratosphere and upper troposphere by a number of plains thunderstorms show an average threefold increase over the fair weather background mass of water vapor. These airborne measurements, made from the National Aeronautics and Space Administration Convair 990 jet laboratory, extended over a sample size much larger than that possible by balloon and other techniques.*

High-altitude infrared measurements of the total mass of water vapor above flight level in the vicinity of thunderstorms, at and just below the base of the stratosphere, were made in July 1971 over the Central Plains. Observations revealed that the vertical drive of these huge storm cells resulted in the local injection of large amounts of water vapor into the atmosphere. The National Aeronautics and Space Administration (NASA) Ames Research Center's Convair 990 (CV-990) jet laboratory provided the long-range, high-speed, and high-altitude capability required in this study. The purpose of the flight measurements was to determine, in situ, the amount of water vapor transported vertically into the lower stratosphere by a thunderstorm cell or system. A summary of the instrumentation, the numerical treatment, and typical results of the experiments follows.

Infrared inference techniques were used to avoid the difficulty of obtaining satisfactory, uncontaminated samples of water vapor from aircraft with frost-point or wet chemical instrumentation. It was possible to modify the existing on-board (CV-990) radiometer to operate over the 17.5- to 26.32-μm portion of the rotational spectral band of water vapor as a bottom sounder. Bottom-sounding measurements, as opposed to satellite top-sounding measurements, require careful purging of the system with dry nitrogen (*1*). This procedure is necessary because the mass of water vapor above the aircraft is very small, approximately 10^{-4} of the mass above the earth's surface, and contamination from the aircraft cabin must be eliminated. The in-line chopper-bolometer radiometer used exhibited a noise equivalent change in radiance (ϵ) of 2.00×10^{-6} watt cm^{-2} steradian^{-1} in the spectral interval of measurement. At an altitude of approximately 13.0 km and for a typical July temperature sounding for Denver, this corresponds to a root-mean-square error in the columnar mass of water vapor above 13.0 km measured by infrared techniques of 1.0×10^{-4} g cm^{-2}. The standard error (the root-mean-square error divided by the square root of the number of observations of the same target) is approximately one-tenth of the root-mean-square error. A second infrared channel operating in the 10.0- to 12.0-μm band provided a constant check on the presence of any cloud particles in the path that would negate the values being recorded on the channel being used to measure the mass of water vapor. Self-emission from the KRS-5 (potassium thallium bromoiodide) window, the radiometer 10.0-cm Cassegrain optics, and the exterior mirror system were monitored by strategic location of gold-coated thermistors. The KRS-5 window has a very low emissivity (~0.02) and is atmospherically cold-soaked at high altitudes to approximately −40°C, thus ensuring a low emission.

An inverse solution of the radiative transfer equation is used to infer the mass of water vapor above a reference plane in the atmosphere. The rapidly converging solution is obtained by iteration (*2*). Briefly, the downward radiance $N_c\downarrow$ is expressed mathematically as

$$N_c\downarrow = - \int_{\nu_1}^{\nu} \int_{\tau = 1} B[\nu, T(p)] d\tau [p, u(\mathrm{H_2O})] d\nu \qquad (1)$$

where ν is the wave number, τ is the transmissivity, B is the Planck function, T is the temperature, p is the pressure, and $u(\mathrm{H_2O})$ is the mass of water vapor. Since we have a temperature profile directed upward, we can calculate the downward radiance, $N_c\downarrow$, assuming an initial water vapor mass profile. This assumption is one of a constant mixing ratio profile, $\bar{s}(p)$, in grams of water per gram of air. A unique mass of water vapor above the reference level is found by computer calculation of $N_c\downarrow$ such that the difference between the observed and calculated downward radiance, $|N_o\downarrow - N_c\downarrow|$, is minimized. This minimization is accomplished by a conventional iterative method (Newton's) to obtain repeated values of $(N_o\downarrow - N_c\downarrow|$ from successive approximations of $u(\mathrm{H_2O})$.

We summarize the iterative, radiometric inference of the mass of water vapor in the following functional notations:

$$N_o\downarrow = N_o\downarrow(u) \qquad (2)$$

$$N_c\downarrow = N_c\downarrow(\tau) \qquad (3)$$

$$\tau = \tau(u) \qquad (4)$$

$$u = u(\bar{s}) = 1/g)\bar{s}\Delta p \qquad (5)$$

$$\bar{s} = \bar{s} \ (|N_o\downarrow - N_c\downarrow \leq \epsilon) \qquad (6)$$

In Eq. 5 g is the acceleration due to gravity and $\bar{s}$ is the mixing ratio (water vapor to air in parts per million). The use of mean monthly temperature soundings gives "first look" real-time solutions on a small, on-board computer during flight operations.

In all, six isolated thunderstorm cells penetrating the tropopause and two squall-line cell systems were investigated. The difference between the mass of water vapor upstream and that downstream of the storm cell is a measure of the amount of water vapor transported vertically by the thunderstorm, since, on the average, the wind moves through and above the visible top of the storm cell, generally from west to east. It appears logical, then, to look for any addition of water vapor into the upper troposphere and lower stratosphere in a volume translated downstream from the top of the storm cell itself. Since the water vapor is presumably swept along in this wind field, this procedure will ensure measurement of any actual addition of water vapor to the stratosphere or upper troposphere persisting away from the cell.

A typical and interesting reconnaissance of a single cell system is that of

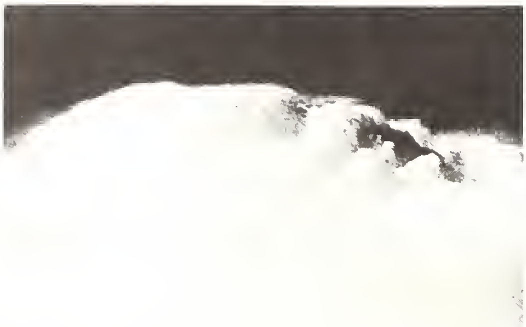

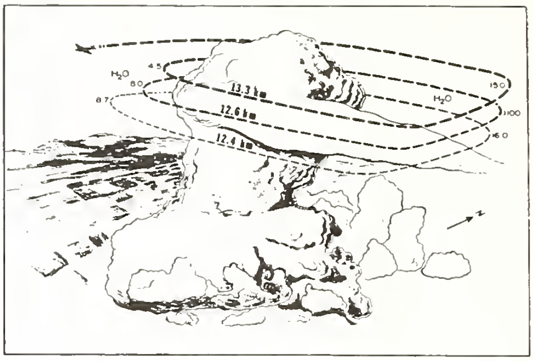

Fig. 1 (left). View of the Colorado thunderstorm cell from CV-990 (15 July 1971) looking to the north on an eastward traverse at an altitude of 12.6 km. The cell is 20.0 km from the aircraft. Fig. 2 (right). Flight paths around the Colorado thunderstorm cell. Section lines on the surface run south-north to the right on the illustration and east-west to the left. The water vapor mass is in units of 10^{-4} g cm^{-2}, and the altitudes are in kilometers.

15 July 1971 between 0000 and 0130 G.M.T. (Fig. 1). This experiment was conducted upstream, azimuth 280°, and downstream, azimuth 100°, of an isolated thunderstorm cell 150 km north-northeast of Denver, Colorado, at altitudes of 12.4, 12.6, and 13.3 km. The cell top is at 14.8 km. The tropopause averages approximately 13.3 km but is not clearly bounded. Mastenbrook (*3*) has emphasized that true stratospheric air in the summer over the west-central United States occurs principally above 16.0 km. The measurements we are discussing were made in the transitional or mixing zone at the base of the stratosphere.

In situ measurements of the temperature and the concentration of solid particles indicate that the CV-990 was just at the base of the stratosphere. Figure 2 illustrates the flight paths around this system from 0000 to 0130 G.M.T. The east-west tracks are approximately 80 km long, whereas the north-south tracks are on the order of 64 km long. The observations approximately spanned the life cycle of the cell system. In the three circumferential flight tracks, the mass of water vapor (in grams per square centimeter) above the flight level was considerably larger, as far as 20 km downstream of the cell, than upstream. Within the resolution accuracy of the radiometric inference system, at 45 km downstream the water vapor was again equivalent to the upstream mass at the end of the first traverse. The upstream values of water vapor mass (Fig. 1) are in general agreement with those reported by Mastenbrook (*4*).

The core of the cell moved approximately 15 km eastward during the total observation period of 90 minutes. For all three traverses the maximum downstream range at which excess water vapor mass above the aircraft could be detected approximated 45 km. One may assume that the residence time above flight level for the excess of thunderstorm water vapor above background water vapor within the limits of the radiometer sensitivity is 90 minutes. At this time only background concentrations of water vapor were detectable.

To further establish the validity of the radiometric inferences, we calculated saturation conditions and noted the presence or absence of cirrus clouds. If the entire mass of 16×10^{-4} g cm^{-2} of water vapor observed downstream and above the lower flight level of 12.4 km (Fig. 2) is contained in the column between 12.4 km and 14.8 km (the cell top), we calculate a mean water vapor mixing ratio of water vapor to air of 23 parts per million (ppm). Saturation conditions over ice for this column at a measured temperature of −73.0°C would require a mixing ratio of 43 ppm. In agreement with this calculation, no cirrus clouds were observed above the aircraft during the first pass.

During the second traverse of the cell at 12.6 km some 20 minutes later, the mixing ratio inferred from measurements of the mass of water vapor reached 110 ppm. This value is due to cirrus which remained above flight level during most of the traverse and resulted in a "false" water vapor mass. The 10.0- to 12.0-μm channel clearly indicated the presence of cirrus above. The last traverse around the cell was at 13.3 km. If the entire mass of water vapor measured above the aircraft, 15.0×10^{-4} g cm^{-2}, were concentrated in the column between 13.3 km, flight level, and 14.8 km, the cell top, saturation would just be reached. On this pass, cirrus occurrence approximately one-half of the time was consistent with the calculation. Restricting the layer to 14.8 km, the visible cell top, precludes any assumptions that the water vapor extends above the cloud top in the lower stratosphere and is an extreme case for saturation.

Before examining the mechanism for the vertical transport of water vapor by thunderstorms, we can summarize the mean water vapor mass upstream and downstream of the six cells studied. All of the cells penetrated the tropopause, and the water vapor masses were averaged at the highest flight levels (~13.3 km). The water vapor mass upstream of the cells averages 5.0×10^{-4} g cm^{-2}, whereas that downstream of the cells averages 16.0×10^{-4} g cm^{-2}, larger than the value upstream by a factor of 3. This increase was not measurable 45 km downstream of the cells.

Let us now consider a vertical transport mechanism in thunderstorms that increases the water vapor mass by 10×10^{-4} g cm^{-2} in a column above the downstream flight level of 12.4 km (Fig. 2). This total turbulent transport upward, Tr, assumed to continue for approximately 20 minutes, is given by

$$Tr = \rho W \bar{s} t = 10 \times 10^{-4} \text{ g cm}^{-2} \qquad (7)$$

where ρ is the density (1.8×10^{-4} g cm^{-3}), $\bar{s}$ is the mixing ratio of water vapor to air (23.0 ppm or 23.0 g g^{-1}), and t is the time (1.2×10^3 seconds). Solving for W in Eq. 7, we obtain 2.0

m sec^{-1} for the vertical velocity over the 20-minute period. This velocity is consistent with previous values from thunderstorm research (5) for an average cell. Range height indication radar indicated a top growth rate of approximately 1.6 km in 20 minutes.

Thus we can speculate on the vertical mass transport of water vapor over larger areas into the upper troposphere and stratosphere. Thunderstorms east of Colorado reach much higher altitudes than storms in the Western Plains such as the storm discussed in detail, pushing well into the lower stratosphere. In addition, the tropopause is lower to the East during the thunderstorm season than in the Western Plains, and, as a result, there is a much higher stratospheric penetration in the East. Recently Lee and McPherson (6) reported on an observational survey of the tops of Oklahoma thunderstorms, stating that the tops of 469 thunderstorms exceeded 12.2 km during April, May, and June, 1967 through 1969. Of that number 33 percent exceeded 15.2 km. They (6) found the average base of the stratosphere during this period to be 12.2 km. On the other hand, only 25 percent of all Colorado thunderstorms penetrate into the stratosphere during the May-September thunderstorm season.

The Oklahoma thunderstorm statistics are at least typical for the eastern continental United States. If each of these approximately eight cells per day averages 10 km^2 and has a stratospheric injection of water vapor per cell of 20×10^{-4} g cm^{-2}, twice that of the drier Colorado storms, thunderstorms can transport vertically 1.6×10^9 g of water vapor per day into the Oklahoma stratosphere. Since the annual variability in the number of thunderstorms ranges from ½ to 1½ times the average number, we should consider this information when speculating on the effects of man-made additions of water vapor to the stratosphere. What finally happens to this injected water vapor remains an object for further study, as it may be swept out during the storm's dissipating stage.

P. M. KUHN
M. S. LOJKO
Environmental Research Laboratories, National Oceanic and Atmospheric Administration, Boulder, Colorado
E. V. PETERSEN
Airborne Science Office, National Aeronautics and Space Administration, Moffett Field, California 94035

References and Notes

1. P. M. Kuhn, *J. Atmos. Sci.* **27**, 937 (1970).
2. W. L. Smith, *Appl. Opt.* 9, 1993 (1970).
3. H. J. Mastenbrook, personal communication.
4. ———, *J. Atmos. Sci.* **25**, 299 (1968).
5. H. R. Byers and R. R. Braham, Jr., *The Thunderstorm* (U.S. Weather Bureau, Washington, D.C., 1949).
6. J. T. Lee and A. McPherson, *Proceedings of the International Conference on Atmospheric Turbulence* (Royal Aeronautical Society, London, 1971), p. B1.

7. Work supported by the National Aeronautics and Space Administration, the Department of Transportation, and the National Oceanic and Atmospheric Administration.

17 August 1971

Reprinted with permission from Tellus *24*, No. 24, 1972.

Sources of atmospheric particulate matter on Hawaii

By R. F. PUESCHEL and B. G. MENDONCA, *National Oceanic and Atmospheric Administration, Mauna Loa Observatory, Hilo, Hawaii 96720*

(Manuscript received September 24, 1971)

ABSTRACT

Sources and advection of atmospheric particulate matter on the Island of Hawaii were assessed to properly evaluate the benchmark qualities of the air at the Mauna Loa Geophysical Observatory. A manually operated Gardner counter, a continually recording Aitken counter and a nephelometer were used to measure diurnal and long term trends of concentrations and light scattering coefficients of atmospheric particulate. Significant sources of aerosol particles result from combustion activities on the island, both man-made and volcanic. Volcanic effluent can penetrate the tradewind inversion when conditions are right and show up on long term Aitken counts at the Mauna Loa Observatory. The relative contribution of marine aerosols to the total particle population in the air masses over the island is small. The difference in concentration and the light scattering coefficient of particles in the air masses above and below the tradewind inversion are in the order of one magnitude or more.

1. Introduction

The island of Hawaii by virtue of its distance (>3 000 km) from continents, the persistence of a marine inversion separating higher air masses above 2 500 m from maritime air below, the presence of two major natural aerosol sources, viz., Pacific Ocean and Kilauea Volcano, and the absence of major sources of industrial pollution, has attracted many scientists in the past who have most extensively investigated the atmosphere in and around the island (e.g. Woodcock, 1953). Nevertheless, a study of the aerosol inventory of Hawaii has been necessary in conjunction with Mauna Loa Observatory's mission as a geophysical benchmark station. Information about the variability of the aerosol content of the atmosphere at Mauna Loa and its causes is essential for a meaningful interpretation of the geophysical data collected by the Observatory. For example, a recent evaluation of solar radiation data only for atmospheric conditions that apparently were unaffected by locally produced aerosols (Ellis & Pueschel, 1971) led to the conclusion that strong volcanic eruptions, but no human derived particulate loading, affect the turbidity of the higher atmosphere. This is in direct contradiction to the conclusion reached by Peterson & Bryson (1967) who evaluated radiation data from the same station irrespective of the contributions to atmospheric opacity by locally produced aerosols.

In order to assess properly the effect of particulate matter on the air quality in Hawaii, particularly at Mauna Loa, we investigated the Pacific Ocean, Kilauea Volcano, sugar cane harvesting activities, automobile traffic, and household activities as sources for atmospheric aerosols. The instruments employed in this study were a manually operated Gardner counter, a continuously recording Aitken counter and a nephelometer.

The findings indicate that: (1) long term trends (3 years) of Aitken nuclei monitored at Mauna Loa positively correlate with high fountaining of Kilauea Volcano; (2) combustion aerosols from Kilauea Volcano's larger vents and from sugar cane fires have been the most prolific sources of Aitken nuclei with a strong effect on atmospheric visibility; (3) automobile traffic and home heating produce the smallest size particles at a significant number concentration; (4) sea-salt aerosols, on the other hand, consist of relatively large particles at low concentrations; (5) the total mass concentration of sea-salt produced by the ocean is a function of both wind speed and humidity; (6) the presence of the tradewind inversion is necessary but not sufficient to

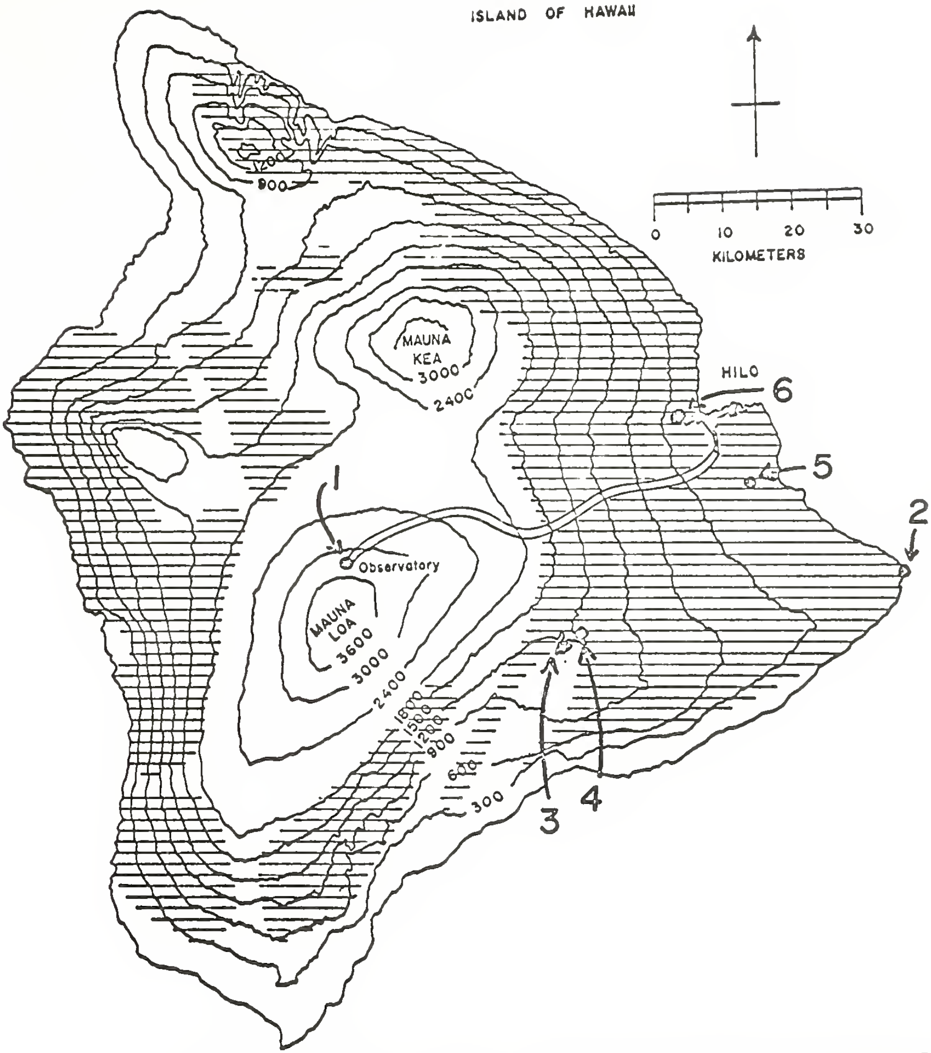

Fig. 1. Location of aerosol sampling sites on Hawaii: (1) Mauna Loa Observatory; (2) Cape Kumukahi; (3) Hawaii Volcanoes National Park residential area; (4) Halemaumau fire pit; (5) Puna sugar cane field; (6) Rural roadside.

inhibit the penetration of aerosols of low altitude terrestrial origin into the higher atmosphere.

2. Results and discussion

Fig. 1 shows the location of the sampling sites on Hawaii relative to each other. They are marked in the following sequence: (1) Mauna Loa Observatory, (2) Cape Kumukahi Station, (3) Kilauea Volcano, (4) Hawaii Volcanoes National Park residential area, (5) sugar cane field, and (6) a roadside in Kaumana west of Hilo. The data from all the sources are summarized in Table 1. The first two columns contain date, location and conditions under which sampling was performed. The third and fourth columns, contain the Aitken nuclei concentration and the light scattering coefficient, i.e. the two atmospheric parameters that were measured independently. The last three columns contain variables related to these two inde-

Table 1. *Parameters for aerosols on Hawaii*

Date and time	Location and condition	Aitken counts (cm^{-3})	Light scattering coefficient (m^{-1})	Visibility (m)	Mass concentration ($\mu g\ m^{-3}$)	Relative size (μm)
Aug. 14, 1971	Mauna Loa Observatory					
1630		2.5×10^3	0.9×10^{-4}	4.3×10^4	34	0.15
1730	Aerosols from volcanic fountaining reaching the Observatory site	7.5×10^3	2.2×10^{-4}	1.8×10^4	83.6	0.14
1830		7.5×10^3	2.6×10^{-4}	1.5×10^4	98.8	0.15
2000		1.5×10^4	2.5×10^{-4}	1.6×10^4	95.8	0.12
2030		7.8×10^3	1.4×10^{-4}	2.8×10^4	53.2	0.12
March 17, 1971	Mauna Loa Observatory					
0500	Before	$6. \times 10^2$	1.8×10^{-5}	2.2×10^5	1.0[a]	0.08
Afternoon	Upslope wind carrying haze	$5. \times 10^2$	2.1×10^{-4}	1.9×10^4	74	0.34
2100	After	$6. \times 10^2$	1.9×10^{-5}	2.1×10^5	1.5[a]	0.09
March 4, 1971	Mauna Loa Observatory					
1200	Upslope air movment	2×10^2	0.6×10^{-4}	6.6×10^4	17.0[a]	0.27
0000	Downslope air movement	$5. \times 10^2$	0.2×10^{-4}	2.0×10^5	1.90[a]	0.10
May 27, 1971	Cape Kumukahi					
1400	Onshore flow 90 % RH	$5. \times 10^2$	0.9×10^{-4}	4.4×10^4	34.2	0.25
May 26, 1971	Cape Kumukahi					
1400	60 % RH, Onshore	$4. \times 10^2$	0.7×10^{-4}	5.6×10^4	27.6	0.25
0600	Offshore flow	$5. \times 10^2$	0.4×10^{-5}	9.8×10^4	15.2	0.19
May 13, 1971	Kilauea Volcano					
1100	Upwind	$4. \times 10^3$	0.6×10^{-4}	6.5×10^4	22.8	0.11
1400	Downwind	$1. \times 10^4$	13.8×10^{-4}	2.8×10^3	524	0.23
May 12, 1971	Ranger residential area					
1830	Evening	$6. \times 10^4$	1.0×10^{-4}	3.9×10^4	38	0.05
0200	Night	$2. \times 10^2$	0.3×10^{-4}	1.3×10^5	11.4[a]	0.24
0630	Morning	$6. \times 10^4$	1.2×10^{-4}	3.2×10^4	46	0.06
May 18, 1971	Puna Sugar Field					
0830	Before burning offshore flow	$5. \times 10^3$	0.7×10^{-4}	5.6×10^4	26.6	0.11
0930	Before burning onshore flow	$3. \times 10^2$	0.7×10^{-4}	5.6×10^4	26.6	0.28
1100	During burning	$5. \times 10^5$	70.0×10^{-4}	5.6×10^2	2660	0.11
May 11/12, 1971	Roadside, downslope flow commencing at night					
	During traffic	$1. \times 10^5$	0.6×10^{-4}	6.5×10^4	17.0[a]	0.03
	Background	$2. \times 10^2$	0.4×10^{-4}	9.8×10^4	9.5[a]	0.23

[a] Light scattering value corrected for Rayleigh scattering.

pendent parameters. The visibility, given in the fifth column, is based on the Koschmieder (1924) relationship between visual range and the light scattering coefficient. Its basic assumption is that of atmospheric homogeneity throughout the entire path of sight. The aerosol mass concentration, given in the sixth column, is one of the usual quantities used in air pollution studies to describe the amount of aerosol present. Although independent and simultaneous measurements of this parameter can be performed and are contemplated for the future, the quantities in column six are derived from the light scattering measurements based on an empirical relationship found by Charlson et al. (1968) and Horvath & Noll (1969). It has been established for city pollution aerosols that this relationship, i.e., mass concentration in grams per cubic meter equals 0.38 times the light scattering coefficient in meters^{-1}, is of the factor-of-two characteristic for a confidence interval of 90 %. The seventh and last column

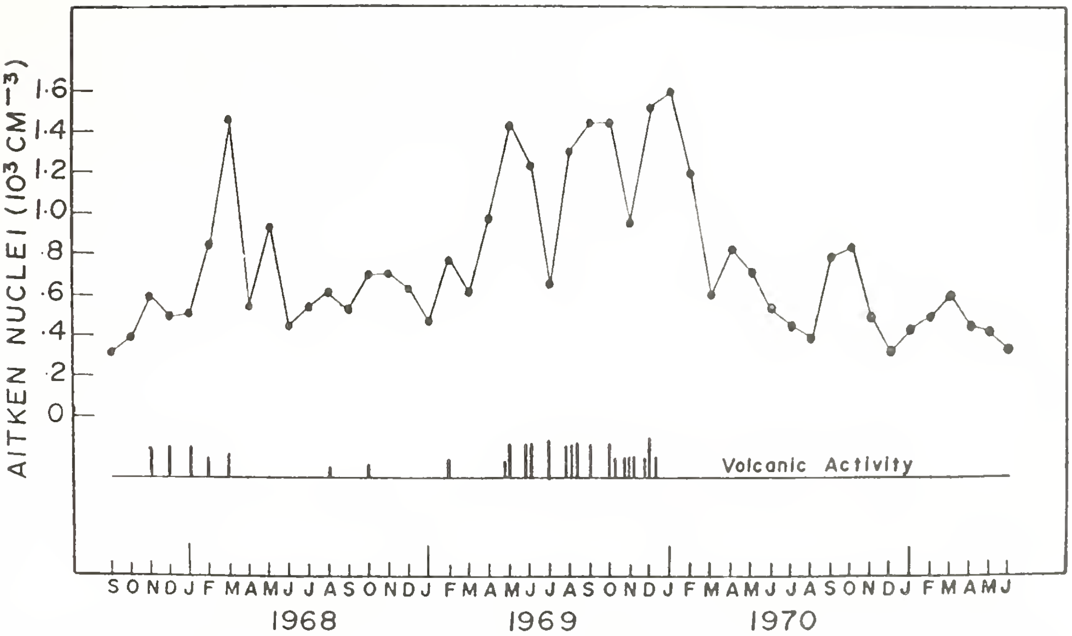

Fig. 2. Monthly means of the Aitken nuclei concentration at Mauna Loa (3 400 m) and its relation to local volcanic activity.

contains a relative size based on the mass and number concentration values. The same qualifications need to be considered as for the derivation of the aerosol mass concentration. Furthermore, a density of one is assumed regardless of the type of aerosol investigated. The error introduced by this assumption is, however, of the order of 50 %, i.e., less than we accept in the light scattering–mass concentration relationship.

2.1. *Mauna Loa data*

The first row in Table 1 represents data from Mauna Loa Observatory at 3 400 m elevation under "typical" conditions (4 March) and on "polluted" days (17 March and 14 August). On 14 August the haze was definitely of volcanic origin from active fountaining (200 feet) at Kilauea Volcano. The nighttime downslope flow conditions (southerly wind) are characterized by low atmospheric light scattering coefficients, i.e., excellent visibility, in any case. This is a characteristic property of the descending air in the nocturnal downslope flow. On 4 March the light scattering at night is essentially due to Rayleigh scattering by the air molecules. This is supported by the small number of Aitken nuclei (50 cm^{-3}) which approaches the limit of detectability of the instrument. Conditions are usually different during the day. Air from lower elevations penetrates the inversion layer at about noon, increases the Aitken nuclei counts (usually to several hundred per cubic centimeter) and reduces visibility. At other times, like on 14 August, Mauna Loa Observatory is directly downwind from Kilauea volcano whose effluents are carried to the monitoring site by southeast winds.

The size of the particles observed in the upslope flow are of a magnitude that is typical for disintegrated soil dust or aerosols from volcanic effluents. In particular, the latter gives the most significant contribution to the aerosol concentration on Mauna Loa (see Fig. 2) whenever volcanic fountaining coincides with a weak inversion layer.

Aitken nuclei at Mauna Loa Observatory have been monitored since 1967 with a manually operated Gardner counter. This instrument operates at high supersaturations to cause condensation of water vapor on any particle exceeding the minimum size of 10^{-6} cm radius. Monthly averages of the Aitken nuclei measured during daylight hours since the September of

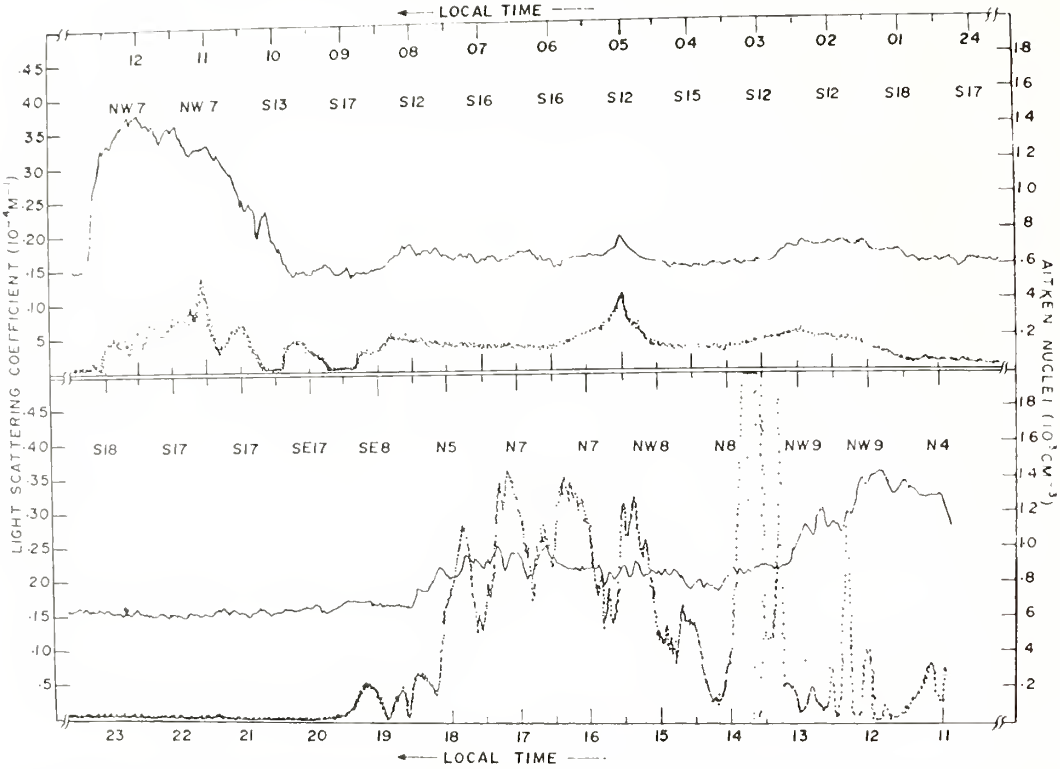

Fig. 3. Diurnal variations of light scattering coefficient (solid line) and Aitken nuclei concentration (dotted line) at Mauna Loa (3 400 m) on 3 and 4 March 1971. (Note that the time starts in the lower right corner and proceeds to the left.)

1967 are shown in Fig. 2. Indicated by vertical bars is the volcanic activity of Kilauea Volcano which is located on the south flank of Mauna Loa. Each bar represents an occurrence of significant fountaining (3.5×10^6 to 12×10^6 m^3 effluent) and heavy loading of particulate matter into the atmosphere.

The data compiled in Fig. 2 give evidence of a positive correlation between the Aitken nuclei concentration at Mauna Loa Observatory and local volcanic fountaining increasing the typical daytime background concentration of 400–500 cm^{-3} by a factor of up to four.

The Gardner counter has been supplemented recently by an Aitken nuclei monitor manufactured by the Environment/One Corporation. This unit performs automatically the measuring cycle which involves pulling in the sample at water vapor saturation, producing supersaturation by adiabatic expansion and flushing out the sample, at a frequency of one per second. An additional recording instrument that has been used to detect particulate matter is an integrating nephelometer (Charlson et al., 1967) which responds to the scattering coefficient due to aerosols. The device has sufficient sensitivity to distinguish particle-free gases on the basis of their Rayleigh scatter. Thus it is possible to utilize air, CO_2 and Freon 12 in the calibration of the instrument.

Fig. 3 shows a typical 24 hour strip chart record from both the Aitken nuclei monitor (dotted curve) and the integrating nephelometer (solid curve) at Mauna Loa Observatory with the following characteristic features: Starting at 1100 hours on 3 March in the lower graph, upslope winds generally from north–northwest during the day (Mendonca, 1969), carry enough particulate matter from terrestrial sources on the island to significantly affect both the Aitken count and the light scattering coefficient. At 1900 hours, after sunset, a downslope

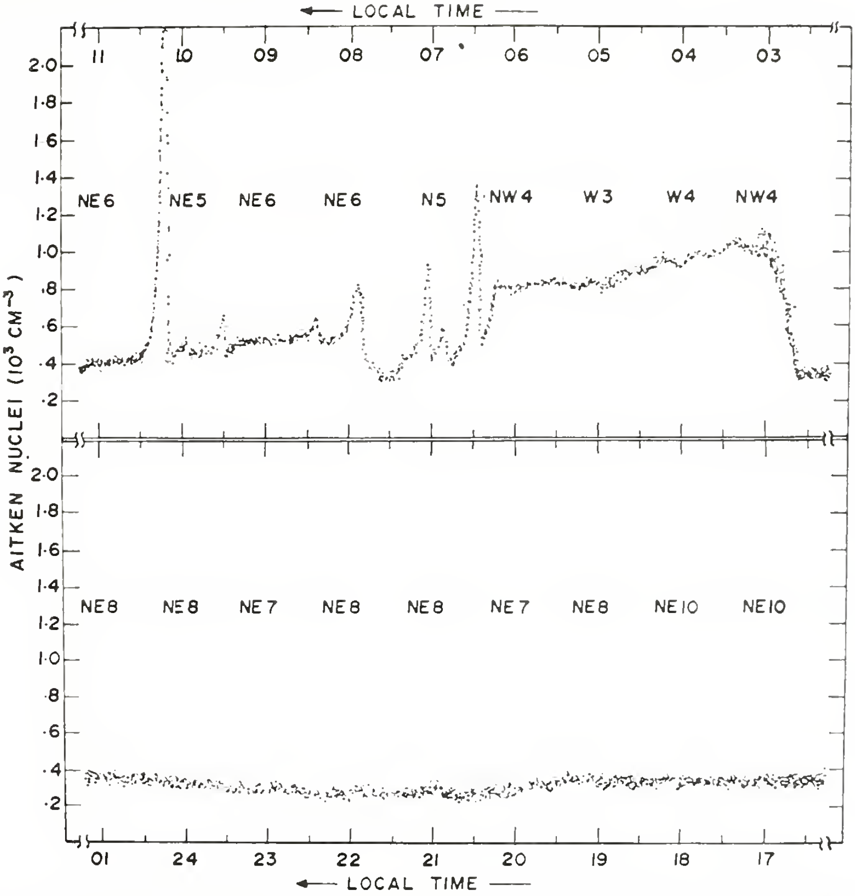

Fig. 4. Diurnal variation of Aitken nuclei concentration at Cape Kumukahi on 14 and 15 May. (Note that the time starts in the lower right corner and proceeds to the left.)

flow predominates, resulting from the cooling of the mountain. The purity of the air during these conditions is evident from both the low Aitken nuclei concentration (generally less than 100 cm^{-3}) and the atmospheric light scattering coefficient which occasionally approaches Rayleigh scattering of particle-free air. Contrary to the relationship prevailing during the day, the two parameters are positively correlated during downslope flow whenever they exceed their background values at a significant signal-to-noise ratio, for example, at 0500 hours on 4 March. This suggests a well-aged aerosol in a state of dynamic equilibrium in the night-time air, whereas the aerosol in the upslope air appears to be too young to have reached a stable size distribution (Junge, 1952*b*). After the reversal of air-mass movement at 1 000 hours on 4 March, an increase of the atmospheric aerosol loading is noted which is comparable to the amount that was observed during the day before. This diurnal pattern repeats itself daily with only a few exceptions.

2.2. *Cape Kumukahi data*

A typical diurnal pattern for atmospheric particulate matter also exists at Cape Kumukahi, the most eastern point of Hawaii. Fig. 4 shows a diurnal variation in the measurements of the Aitken nuclei concentration. (Note that the time scale goes from right to left.) During most of the day and early evening with northeasterly onshore flow and Aitken count is low (300 cm^{-3}) and steady, representing a background concentration that is typical for maritime air. With a wind shift from northeasterly

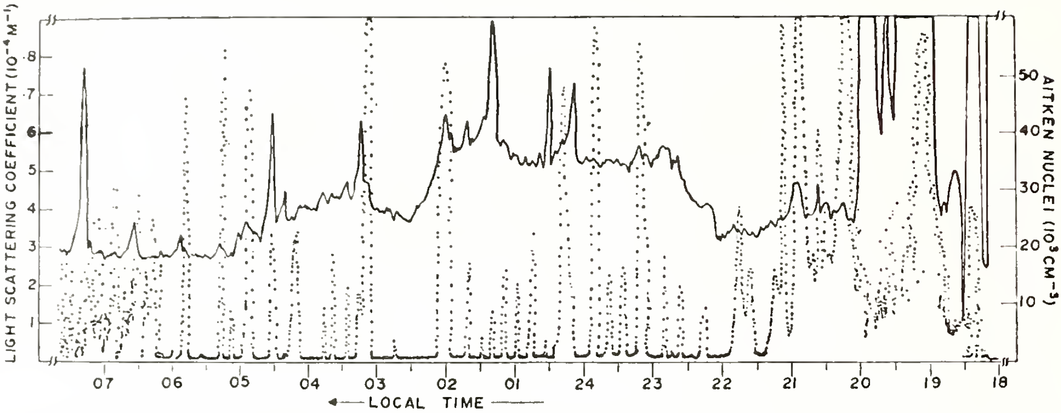

Fig. 5. Effect of human activities on Aitken nuclei concentration (dotted line) and light scattering coefficient (solid line) taken on 11 and 12 May 1971. (Note that time proceeds from right to left.)

to northwesterly the Aitken nuclei concentration increases by a factor of three due to the advection to the measurement site of particles from island related sources. This increased concentration persists for as long as there is a westerly component in the wind velocity. The onset of a northerly wind at 0615 hours causes the concentration to drop abruptly. Subsequent intermittent spikes are associated with westerly flows of short duration.

The sea-salt aerosol investigated at Cape Kumukahi is reported in the second row of Table 1 and shows the expected behavior: The background concentration of Aitken nuclei in the maritime air is 400–500 cm^{-3}. A visibility of between 40–60 km, depending slightly on the relative humidity, has been calculated from the nephelometer data. This humidity effect can result from the hygroscopic growth of individual particles. The data in Table 1 suggest also that an increase in their number concentration can result in visibility reduction which follows from the identical size of particles at two humidity levels in the last row. Apparently, the relative humidity above the ocean never reaches a value small enough to let the droplet overcome the hysteresis of phase change that would be necessary to completely dry out the sea-salt droplets produced by the bursting of bubbles to result in a significant change in size between 60 and 90 % relative humidity.

An increase in the sea-salt aerosol mass concentration by a factor of 2–3 was noted whenever the wind speed exceeded 14 knots. It is at this wind speed that white caps occur (Moore & Mason, 1954) an event which apparently has a noticeable effect on the maritime aerosol mass concentration.

2.3. *Data from terrestrial sources*

In order to compare the data from Mauna Loa Observatory's two permanent sampling stations with typical values in the proximity of aerosol origins, viz., human activities, volcanic vents and sugar cane burning, the same instrumentation was operated in the vicinity of these potential sources at different geographic locations on the island. A properly equipped bunk trailer served as a mobile laboratory for the duration of the test period.

Fig. 5 shows the temporal variations of light scattering and Aitken nuclei concentration at roadside in a rural community of Hilo. The effect of general human activity (traffic, cooking, etc.) in the evening and morning hours is clearly indicated. During the night there is a relatively small background concentration in Aitken counts except for short intervals at which diesel trucks hauling sugar cane pass by the sensors. The fact that the light scattering coefficient is influenced to a lesser degree is indicative of the small particles of which this combustion-produced aerosol consist, which also follows from the relative size in the last row of Table 1.

The effect of volcanic activity on the air quality at Mauna Loa, manifested by Fig. 2

and the first row of Table 1, necessitated measurements at Halemaumau (Kilauea's main vent which can be considered the largest source for Hawaiian air pollution). As can be seen from row 3 in Table 1, the source concentration has been found to be higher by a factor of 20 if compared with the concentration at Mauna Loa Observatory that was measured at times when volcanic fumes were advected to this measuring site on 17 March. The relative size of the particles at the source is slightly smaller than it was at this day at Mauna Loa. This suggests that coagulation takes place within this aerosol cloud during the time when it is transported to Mauna Loa Observatory. This, besides gravitational settling of the larger particles, is probably a significant sink for this type of aerosol. How efficient the coagulation process is remains to be established by performing measurements in the same aerosol cloud.

The aerosol investigated on 13 May at Kilauea has probably little in common with the one observed at Mauna Loa on 14 August. The latter resulted from active fountaining compared to the emission of fumes in the previous case. The slightly smaller relative size is indicative of the higher temperature (1 000°C) at which the aerosol formation took place in this latter case.

Our scattering-derived particle size is smaller in either case than that resulting from impactor samples by Cadle et al. (1967) at this same location. It must be borne in mind, however, that due to the hygroscopic nature of the volcanic particles their growth rate varies with the amount of water vapor available (a variable with time) while they are air-borne. The finding of sub-micron sizes of droplets is supported by the bluish appearance of the cloud during the times the samples were taken at Halemaumau and by the fact that the cloud is carried, at times, several hundred miles over the ocean.

Investigations of particulate loading from sugar cane fires, row 5, Table 1, permitted measurements at the same site in three different air masses: (1) air approaching the site from a rural area prior to burning, (2) maritime air being advected to the sampling site before the fire was started, and (3) air containing the effluents from the fire. It follows from the data that rural air contains several thousand particles of sizes less than one tenth of a micron, whereas maritime air contains only a few hundred particles of typical marine aerosol size. Visibility in these two air masses is approximately the same, i.e., the lower concentration of aerosol in the marine air is compensated by their larger size and greater light scattering capability. The fire increased the number and mass concentrations by a factor of 100 or more, if compared to the background concentration in rural air. Interestingly, the light scattering deduced size is still small, which is characteristic of a combustion-produced aerosol. The much lower visibility, then, is caused mainly by the increased number concentration and differences in the optical properties of the particles.

A comparison between human-derived particulate loading of the atmosphere and the natural background concentration is possible from the data in the fourth and sixth rows of Table 1 from measurements in the proximity of human activities. The background air in both cases was very similar and consisted of air descending down the mountain slopes from higher elevations as is typical during nights. A comparison of the background aerosol light scattering of $b = 1 \times 10^{-6}$ m^{-1} at Mauna Loa and $b = 1 \times 10^{-5}$ m^{-1} at sea level (both corrected for the contribution of molecular scattering) indicates that the difference in visual air quality above and below the marine inversion under otherwise similar conditions is of the order of a factor of ten. Both background levels of Aitken nuclei at the Hawaiian Volcanoes National Park residential area and at roadside in Kaumana, a rural community west of Hilo, are approximately the same during the night. Deviations from this background level are caused by two different kinds of human activities, viz., cooking and home heating at the National Park residential area versus automobile traffic at the roadside in Kaumana. Both of these activities produce about the same concentration of aerosols, with the size of the automobile exhaust aerosol being slightly smaller.

3. Significance

The island of Hawaii provides an ideal background for atmospheric aerosol research because of the possibilities of isolating particulate sources from each other. The geographic location of the island in the mid-Pacific and its topography give, in conjunction with thermally induced mountain flow, an opportunity to investigate simultaneously air masses above the inversion layer and maritime air below. The diurnal air flow patterns at various geographic points on the island permit the choice of sampling sites to ensure the least interference between particulate sources. Thus it is possible to utilize instrumentation responsive to bulk aerosol properties, such as the total particle concentration or the integrated light scattering coefficients, to deduce secondary characteristic aerosol parameters, such as relative size and mass concentration, for a particular type of aerosol. These properties need to be known for all aerosol clouds to which the particulate sensors are exposed at various times, in order to establish air quality criteria that make Mauna Loa Observatory's mission as geophysical benchmark station possible.

It has been demonstrated that aerosols of different origin are advecting to the monitoring site at various rates. The positive correlation between volcanic fountaining and Aitken nuclei concentration, and between Aitken counts and light scattering, leads to the conclusion that the volcano is a significant source of aerosol that conceivably affects the solar radiation and particulate matter monitoring programs at Mauna Loa. This interference must be taken into account if global atmospheric properties are to be deduced from the solar radiation data collected at Mauna Loa Observatory.

It has been established very recently (Langer et al., 1971) that there exists a prolific source for freezing nuclei on Hawaii in the activities of sugar cane harvesting. It is conceivable and has been verified in preliminary tests that a positive correlation exists on Mauna Loa under upslope conditions between atmospheric light scattering and freezing nuclei concentration. This is an additional interference to be reckoned with in the aerosol monitoring program of Mauna Loa Observatory for globally distributed particulate matter.

Of probably little significance at Mauna Loa is the ocean-produced aerosol that is characteristic for maritime air. The relative humidity that exists below and within the trade-inversion should be high enough to allow each of the hygroscopic sea-salt particles to grow to precipitation size.

It appears as though the aerosol at Mauna Loa during downslope conditions is in dynamic equilibrium with its environment. This indicates a well aged aerosol which has established a stable size distribution (Junge, 1952*a*) and conceivably can be used to estimate the life history of air masses that reach the monitoring site.

The effect of automotive exhaust on the Aitken nuclei concentration has been clearly demonstrated. As a consequence, automotive traffic in the vicinity of a monitoring site completely obscures the background concentration of aerosols and makes monitoring of this parameter meaningless. The distance at which traffic can be tolerated depends on a number of parameters, such as variation of wind velocity and of the height of the tradewind inversion (Mendonca, 1969), the concentration of contaminants in auto exhaust, their emission rate, etc.

4. Summary and conclusion

An attempt has been made to classify aerosols from different sources on the island of Hawaii in regard to their number concentration, determined with Aitken counters, and light scattering coefficients, measured with an integrating nephelometer. Secondary parameters which are frequently used in the air pollution literature, such as visibility and aerosol mass concentration, have been deduced from these measurements. These are based on the assumptions of optical homogeneity of the atmosphere and an empirical light scattering–aerosol mass relationship that has been found to hold true for city pollutant aerosols. Unless these relationships have been verified for the Hawaiian aerosols, a task that is contemplated for the future, these secondary parameters should be applied with caution. From Table 1 it follows nevertheless, that they appear physically meaningful: the combustion aerosol consists of relatively small particles as compared to those formed by condensation, from oceanic and volcanic effluents, and the smaller size of the longer lived aerosol reaching Mauna Loa Observatory under downslope conditions as compared to the younger island-produced aerosol measured during upslope conditions. Furthermore, our light scattering derived aerosol mass measured on a typical day on Mauna Loa agrees with the mass concentration determined from the weight of high-volume filter mats by NAPCA. Although this is part of a continuing study for the purpose of determining interfering factors for MLO's benchmark program for globally distributed trace constituents, the data collected to date can be summarized as follows:

(1) The most prolific sources for Aitken nuclei have been found in activities associated with combustion, viz., automobile operation, cane burning and household activities (home heating). These aerosols, however, are relatively small and consequently have little effect on visibility with the exception of the smoke emanating from cane fires.

(2) Particles of larger sizes are produced by the sea, the fumes from Kilauea Volcano, and cane fire burning. The effect of sea-salt aerosols on visibility at prevailing environmental humidities is negligible due to their small number concentration. Smoke emanating from the volcano and from cane fires, on the other hand, has detrimental effects on visibility due to the high concentrations of particles that are formed.

(3) The atmospheric aerosol at Mauna Loa is subject to temporal variations. An upslope airflow during afternoons is rather regular and results in reduction of visibilities by about a factor of two. Occasionally, these conditions deteriorate appreciably due to the influx of volcanic haze to the Observatory level.

We conclude from the study that it is important to consider volcanic fumes as interference in the monitoring program for aerosol parameters and visibility. With respect to the freezing capabilities of certain particles termed ice nuclei, a recent investigation (Langer et al., 1971) suggests that terrestrial sources (e.g. sugar cane fires) are more important than Kilauea Volcano for this particular type of aerosol. Preliminary tests indicating a correlation between freezing nuclei concentration and light scatter strongly suggest an advection of aerosol cluds from these sources to Mauna Loa Observatory. Hence, the existence of the marine inversion is a necessary but not always sufficient condition to protect a monitoring station above it from atmospheric contamination below. Therefore care must be enforced in the evaluation of data collected at geophysical monitoring stations for the purpose of information on climatic changes by human activities.

The information presented in this study will help to eliminate by data evaluation procedure and/or experiment design the interference with the geophysical monitoring program at Mauna Loa from local aerosol sources.

Acknowledgements

The authors wish to acknowledge the Hawaii Volcanoes National Park Service for their assistance and guidance with the observations taken in the park and at the volcano; both Mauna Kea and Puna Sugar Companies for their permission in allowing the monitoring of sugar cane fires in the field; and to Mrs Judy Pereira for secretarial help and data tabulation in the preparation of this paper.

REFERENCES

Cadle, R. D., Wartburg, E. R. & Frank, E. R. 1967. Particles in volcanic fume. *Nature 213*, 581–82.

Charlson, R. J., Horvath, H. & Pueschel, R. F. 1967. The direct measurement of light scattering coefficient for studies of visibility and air pollution. *Atm. Env. 1*, 469.

Charlson, R. J., Ahlquist, N. C. & Horvath, H. 1968. On the generality of correlation of atmospheric aerosol mass concentration and light scatter. *Atm. Env. 2*, 455–464.

Ellis, H. T. & Pueschel, R. F. 1971. Solar radiation: Absence of air pollution trends at Mauna Loa. *Science 172* (3985), 845–846.

Horvath, R. and Noll, K. E. 1969. The relationship between atmospheric light scattering coefficient and visibility. *Atm. Env. 3*, 543–552.

Junge, C. 1952*a*. Gesetzmässigkeiten in der Grössenverteilung atmosphärischer Aerosole über dem Kontinent Beri deut. *Wetterdienstes US — Zone 35*, 261–277.

Koschmieder, H. 1924. Theorie der horizontalen Sichtweite. *Beitr. Phys. Freie Atm. 12*, 33.

Langer, G., Garcia, C., Pueschel, R. F. & Mendonca, B. G. 1971. In preparation.

Mendonca, B. G. 1969. Local wind circulation on the slopes of Mauna Loa. *J. Appl. Meteor. 8*, 533–541.

Moore, D. J. & Mason, B. J. 1954. The concentration, size distribution and production rate of large salt nuclei over the oceans. *Quart. J. Roy. Met. Soc. 80*, 583–590.

Orr, C., Hurd, F. K. & Corbett, W. J. 1958. Aerosol size and relative humidity. *J. Coll. Sci. 13*, 472–482.

Peterson, J. T. & Bryson, R. A. 1968. Atmospheric aerosols: Increased concentrations during the last decade. *Science 162*, 120–121.

Woodcock, A. H. 1953. Hawaii as a cloud physics laboratory. *Pacific Science 7*, 522–524.

ИСТОЧНИК ТВЕРДЫХ ЧАСТИЦ В АТМОСФЕРЕ НА О. ГАВАЙИ

Для правильной оценки степени чистоты воздуха над Геофизической обсерваторией Мауна Лоа были рассмотрены источники и адвекция посторонних частиц в атмосфере на о. Гавайи. Для измерения суточного и более длительного хода концентрации частиц и коэффициентов рассеяния света использовались ручной счетчик Гарднера, счетчик Айткена с непрерывной регистрацией и нефелометр. Значительным источником аэрозольных частиц являются процессы сгорания, как вулканические, так и связанные с деятельностью человека. Частицы вулканического происхождения при подходящих условиях могут проникать сквозь пассатную инверсию и затем в течение долгого времени регистрироваться счетчиком Айткена на обсерватории Мауна Лоа. Относительный вклад аэрозолей морского происхождения в полное число частиц в воздушных массах над островом невелик. Разница в концентрациях частиц и в коэффициентах рассеяния света в воздушных массах над пассатной инверсией и под ней достигает порядка величины или больших значений.

U.S. DEPARTMENT OF COMMERCE
Maurice H. Stans, Secretary

NATIONAL OCEANIC AND ATMOSPHERIC ADMINISTRATION
Robert M. White, Administrator
ENVIRONMENTAL RESEARCH LABORATORIES
Wilmot N. Hess, Director

NOAA TECHNICAL REPORT ERL 209-APCL 22

Fog Droplet Sizes at the Panama Canal

L. H. RUHNKE

BOULDER, COLO.
May 1971

TABLE OF CONTENTS

Page

ABSTRACT 1

1. INTRODUCTION 1

2. MEASUREMENT METHODS FOR CONDENSATION NUCLEI 2

3. MEASUREMENT METHODS FOR FOG DROPLETS 3

4. RESULTS OF CONDENSATION NUCLEI MEASUREMENTS 4

5. RESULTS OF FOG DROPLET MEASUREMENTS 4

6. DISCUSSION OF RESULTS 7

7. ACKNOWLEDGEMENTS 11

8. REFERENCES 11

APPENDIX 13

FOG DROPLET SIZES AT THE PANAMA CANAL

Lothar H. Ruhnke

Data of fog droplet spectra and condensation nuclei concentrations were taken during December 1970 at the Panama Canal. Mass median diameter of fog droplets was 21 microns. Nuclei concentrations varied between 500 and 5000 particles per cm^3. A high frequency of persistent meteorological conditions for radiation fog, low wind, and a thin fog layer make this area a good testing ground for warm fog modification concepts.

VOL. 77, NO. 27 JOURNAL OF GEOPHYSICAL RESEARCH SEPTEMBER 20, 1972

Aerosol Cations at Mauna Loa Observatory[1]

H. J. Simpson

Lamont-Doherty Geological Observatory, Columbia University
Palisades, New York 10964

Aerosol and precipitation samples collected 3.4 km above sea level on the Island of Hawaii have only 1% of the concentrations of Na that samples collected at sea level have. This difference suggests a short residence time for marine aerosols moving up the slopes of Mauna Loa. The major increase in the bulk chemistry of K, Ca, and Mg relative to Na occurs during the rapid loss of the first 90% of the aerosol mass. The chemistry of the remaining 'fractionated' aerosols resembles that of Hawaiian rain. A second population of aerosols, with substantially lower Na concentrations than fractionated marine aerosols, is present above the trade wind inversion. The major cation chemistry of these aerosols resembles that of continental rain.

The sources, distribution, and removal paths of atmospheric particulate matter are difficult to unravel. In contrast to the uniform composition of the major dissolved components of sea water, the chemistry of tropospheric aerosols shows large variations in both space and time. This complexity encourages the study of atmospheric chemistry in areas where the number of variables is as small as possible. The subtropical marine atmosphere, especially near the Island of Hawaii, has been intensively studied (see *Tellus* [1957, 1967] for examples), with strong emphasis on the relation of marine aerosols to rain formation.

Two large, gently sloped mountains on the Island of Hawaii protrude well above the mean height of the trade wind inversion, which, to a large extent, defines the thickness of the moist air containing aerosols recently derived from the sea surface. A meteorological research station has been maintained at an elevation of 3.4 km a few kilometers north of the summit of Mauna Loa since the late 1950's [*Price and Pales*, 1963]. Monitoring programs at MLO (Mauna Loa observatory) of the CO_2 concentration of the atmosphere [*Pales and Keeling*, 1965] and of the amount of solar radiation received at the site [*Ellis and Pueschel*, 1971] for almost fifteen years have been extremely important in providing data on temporal changes in the global atmosphere.

The quantity- and size-distributions of aerosols in much of the upper troposphere, over both oceans and continents, appear to be remarkably similar [*Junge*, 1968]. Chemical data from aircraft sampling also indicate a convergence in aerosol chemistry over both oceanic and continental areas in the upper troposphere [*Gillette and Blifford*, 1971]. The composition of this 'background' aerosol must reflect some balance between the addition of aerosols (from the sea surface and the land surface) and the removal of aerosols (largely by precipitation). The site of MLO appears to offer the possibility of a surface location where the upper tropospheric background aerosols are a major fraction of the aerosol population.

The work described here is primarily the determination of the bulk chemistry of sodium, potassium, calcium, and magnesium in aerosols collected at MLO. These data are used to evaluate the premise that aerosols can be collected at MLO that are typical of the air above the trade wind inversion and probably of the tropospheric background aerosol. The possibility of differences in the amounts of the major cations in marine aerosols relative to sea water is also discussed.

Sample Collection and Analytical Procedures

The aerosol concentration at MLO is very low. As a result, the filtering of large volumes of air was necessary to obtain sufficient material

---

[1] Lamont-Doherty Geological Observatory contribution 1841.

Copyright © 1972 by the American Geophysical Union.

for the chemical procedures and to maintain high ratios of samples to blanks.

Aerosol samples integrated over approximately 1 week were collected by using high-volume pumps and polystyrene filters (20 × 25 cm). Although MLO is approximately 1 km above the mean trade wind inversion altitude, local circulation induced by heating of the island surface can bring moist sub-inversion air up to displace the dry air that is typical of the free atmosphere above the inversion. During periods of well developed diurnal circulation on the Island of Hawaii, moist air moves upslope past the inversion elevation, reaching MLO within a few hours of noon [*Price and Pales*, 1963; *Mendonca*, 1969]. Moist air remains at and above the elevation of MLO usually until early evening, when it is displaced by dry air moving downslope. Filter samples were collected during two complementary time periods, one of which had a high probability of filtering only the dry air present during downslope flow. One filter operated from 9 P.M. to 6 A.M. (night) local time and the other operated from 6 A.M. to 9 P.M. (day). The high-volume pumps were turned on and off with timers. Filters were changed approximately once a week; thus each sample represents a composite of a number of collection days, during a fixed time period each day. These filters were exposed approximately 5 meters above the lava surface in a remote corner of the observatory site.

A few filter samples were also collected from two sea level locations. At one of these locations, Cape Kumukahi (Figure 1), were collected samples that were dominated by marine aerosols, which probably still retained a large fraction of the giant nuclei produced at the sea surface. These samples were collected 5 meters above ground approximately 300 meters from the shore line, during periods of strong trade wind flow when continuous monitoring of

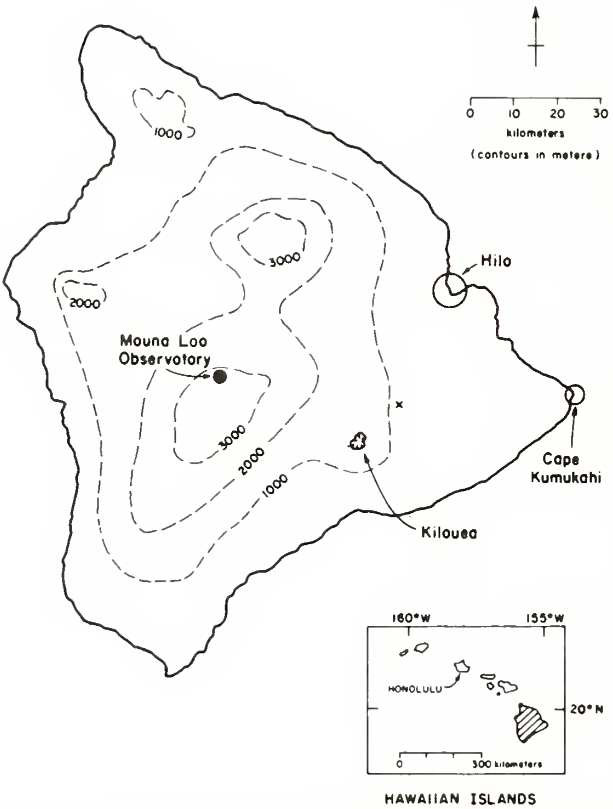

Fig. 1. Aerosol and precipitation sampling locations on the Island of Hawaii.

Aitken nuclei counts at the site showed no local island contamination. A few samples were also collected in Hilo, the largest town on the Island of Hawaii. These samples were continuous 24-hour samples; they represent periods of both upslope and downslope flow and also include significant local contamination, as well as marine aerosols.

Precipitation samples were collected by using polyethylene funnels and bottles located near the high-volume filter sites at MLO, Hilo, and Kumukahi and at a fourth location at 1-km elevation on the eastern slope of Mauna Loa (Figure 1).

The analytical procedures used for filter samples were similar to those described by *Hoffman* [1971]. Portions (usually ⅓ or ½) of each filter were ashed at 425°C for six hours to remove the polystyrene filter matrix. The residual particulate material was covered with ~7 ml of concentrated HCl and HNO_3 for a number of hours and then diluted to 25 ml and analyzed with atomic absorption spectrometry.

Another set of samples was also analyzed to complement the day and night composite samples collected at MLO. Surface air filter samples are collected at MLO for HASL (Health and Safety Laboratory of the Atomic Energy Commission) for determination of a number of radioactive aerosol components [*Volchok and Kleinman*, 1972]. They are collected with the same filter matrix employed for all samples in this study, using a high-volume pump operating continuously for approximately one week per sample. The filter intake is located about 0.5 meter above the ground surface about 100 meters from the site used for the day and night samples at MLO. The filter-changing schedule for the day and night samples was coordinated with that for the HASL filter, providing an internal check on the aerosol concentrations determined from two separate sets of samples at MLO. Approximately one fourth of each of the HASL samples from the period of this study was cut from the filter and analyzed.

BLANK DETERMINATIONS

A large amount of effort was expended to obtain a reliable estimate of blank values. Numerous filters were analyzed that had no air passed through them. Most blanks, however, were run on exposed filters that had the outer portion of the filter separated after sample collection. Aerosols penetrate only ~10% of the filter thickness, and so the back ½ to ¾ of each filter could be analyzed separately to obtain a more representative blank estimate which includes any contamination introduced during filter handling. About thirty blank samples were analyzed with the filter samples. The concentrations of Na, K, Ca, and Mg in the blank solutions are plotted as parts per million in 25 ml of solution in Figure 2, against the weight of filter used for each analysis. Linear regression lines were fitted to these points; the equations are given below (results are in grams).

$$\mathrm{Na} = 0.106 \pm 0.045X$$

$$\mathrm{K} = 0.023 \pm 0.006X$$

$$\mathrm{Ca} = 0.018 \pm 0.091X$$

$$\mathrm{Mg} = 0.016 \pm 0.017X$$

One can interpret the data as indicating two contamination components of varying impor-

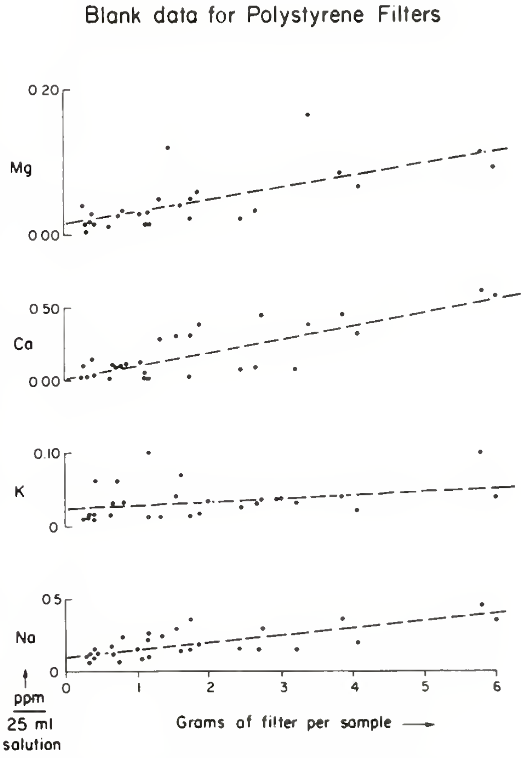

Fig. 2. Blank concentrations plotted as a function of the weight of filter used for analysis. The equations of the regression lines are given in text.

TABLE 1. Percentage of the Average Sample Subtracted as Blank

Sample	Na	K	Ca	Mg
MLO day	~4	~10	~25	~5
MLO night	~10	~15	~30	~15
MLO continuous	~5	~10	~10	~3
Hilo	~1	~2	~3	~1
Kumukahi	<1	<1	<1	<1

tance for the four elements. One component is proportional to the quantity of filter used, whereas the other (independent of filter weight used) probably results from the handling and processing of the sample. The scatter of the blank data around the fitted line gives some estimate of the uncertainty in the blank values subtracted from each exposed sample.

There was no systematic difference between blanks determined for unexposed filters and those determined for the back portions of exposed filters; nor was there any difference between the filters used for the HASL samples and those used for the day and night samples. Blanks without filter materials included (which indicated reagent blank or processing contamination such as contact with glassware) were lower than the values shown in Figure 2 by more than 1 order of magnitude.

Aerosol concentrations in exposed filters were corrected for blanks on the basis of the weight of filter analyzed, using the regression lines from Figure 2. Except for Ca, the blank corrections for an average sample were generally 10% or less. The average blank contribution subtracted for five different sample categories is shown in Table 1.

RESULTS

The concentrations of Na, K, Ca, and Mg in 11 pairs of day and night samples are listed in Table 2. The data are expressed as nanograms (10^{-9} g) per cubic meter of air, with the sampling periods and total air volumes included. The data for the continuous samples also collected at MLO (HASL samples) are shown in Table 3, and the data for sea-level samples collected in Hilo and at Cape Kumukahi are shown

TABLE 2. Day[1] and Night[2] Samples of MLO Aerosol Cations

Sample	Collection Period, 1970–1971	Volume Sampled, m³ × 10³	Na, ng/m³	K, ng/m³	Ca, ng/m³	Mg, ng/m³
P1 D	Nov. 2–9	13	36	2.2	0.8	6.9
P2 N	Nov. 2–9	9	9	3.4	6.7	7.3
P3 D	Nov. 9–16	23	40	1.1	1.0	5.5
P4 N	Nov. 9–16	14	3	0.3	−0.2	1.9
P7 D	Nov. 23–Dec. 2	21	16	0.2	0.8	3.3
P8 N	Nov. 23–Dec. 2	12	5	0.7	2.4	3.2
P9 D	Dec. 2–16	26	8	1.1	0.7	2.7
P10 N	Dec. 2–16	16	4	1.1	0.3	2.4
P11 D	Dec. 16–23	12	19	0.6	2.0	5.7
P12 N	Dec. 16–23	7	3	0.6	3.4	3.3
P13 D	Dec. 23–30	17	18	1.7	6.2	6.2
P14 N	Dec. 23–30	11	11	1.0	4.4	5.9
P103 D	March 15–22	12	75	6.7	11	22
P104 N	March 15–22	10	11	3.6	10	8.6
P105 D	March 22–31	16	46	2.1	2.0	9.5
P106 N	March 22–31	12	26	1.0	1.3	6.2
P107 D	March 31–April 7	12	12	1.5	1.8	3.3
P108 N	March 31–April 7	9	7	1.2	4.1	2.6
P109 D	April 7–14	12	43	3.6	5.6	13
P110 N	April 7–14	9	10	1.0	2.0	3.8
P111 D	April 14–21	14	24	5.1	5.6	14
P112 N	April 14–21	9	16	3.0	8.9	7.8
Even numbered samples (day)			31	2.4	3.4	8.4
Odd numbered samples (night)			10	1.5	3.9	4.8

[1] Collected from 6 A.M.–9 P.M. daily.

[2] Collected from 9 P.M.–6 A.M. daily.

TABLE 3. MLO Ground-Level Continuous Samples

Sample	Collection Period, 1970–1971	Volume Sampled, 1000 m³ STP	Na, ng/m³	K, ng/m³	Ca, ng/m³	Mg, ng/m³
H1	Aug. 21–31	10	40	4.5	4.2	13
H2	Sept. 9–16	7	88	9.3	7.9	24
H3	Sept. 16–21	5	53	5.0	8.7	19
H4	Sept. 21–30	9	75	9.8	10.0	23
H5	Sept. 30–Oct. 7	7	39	4.4	6.3	13
H6	Oct. 7–14	7	66	4.9	6.2	17
H7	Oct. 14–21	7	103	8.6	6.4	20
H8	Oct. 21–Nov. 2	12	25	3.4	9.9	11
H9	Nov. 2–9	7	42	3.7	5.3	10
H10	Nov. 9–16	7	36	2.5	4.7	11
H11	Nov. 16–23	7	34	1.5	2.6	8.3
H12	Nov. 23–Dec. 2	9	21	2.8	3.2	5.8
H13	Dec. 2–9	8	5	1.3	2.5	3.3
H14	Dec. 9–16	8	18	2.0	21.0	18
H15	Dec. 16–23	8	18	1.8	6.0	7.7
H16	Dec. 23–30	7	24	4.0	20.0	16
H101	Dec. 30–Jan. 8	7	49	9.2	32.0	22.0
H102	Jan. 8–15	5	24	5.3	7.2	6.2
H103	Jan. 15–27	9	23	6.3	5.5	8.6
H104	Jan. 27–Feb. 1	4	3	0.3	3.9	2.2
H105	Feb. 1–8	7	53	4.3	14.0	19
H106	Feb. 8–16	8	83	8.7	13.0	25
H107	Feb. 22–March 1	8	116	9.3	26.0	35
H108	March 1–8	7	71	6.4	6.6	18
H109	March 8–15	7	37	8.6	17.0	17
H110	March 15–22	7	96	16.1	29.0	36
H111	March 22–31	10	81	9.3	7.2	20
H112	March 31–April 7	7	17	3.4	8.6	8.4
H113	April 7–14	8	49	6.8	9.8	19
H114	April 14–21	7	30	5.2	6.8	13
Average			47	5.6	10	16

in Table 4. The concentrations of Na, K, Ca, and Mg in a number of precipitation samples are shown in Table 5. The average values for five different categories of samples are shown at the bottom of Tables 2, 3, and 4.

The Kumukahi samples collected during strong trade wind flow have concentrations very similar to those found by *Hoffman* [1971] for windward Oahu. Although it is possible that some surf-zone aerosols are incorporated in

TABLE 4. Sea-Level Aerosol Cations from the Island of Hawaii

Sample	Collection Period, 1970–1971	Volume Sample, $m^3 \times 10^3$	Na, ng/m³	K, ng/m³	Ca, ng/m³	Mg, ng/m³
C1	Nov. 19–20	6.3	450	73	19	79
C2	Nov. 24–25	5.5	125	20	4	21
C101	Jan. 21–22	3.7	200	19	18	41
C102	Jan. 27	0.8	160	27	35	78
K1	Jan. 25–28	4.7	260	7	103	41
K2	Feb. 9–11	3.5	4500	172	169	386
K3	Feb. 11–16	6.9	3000	109	112	210
Average Hilo samples			234	35	19	55
Average Kumukani samples[1]			3700	140	140	300

[1] K1 is excluded. This sample was collected during a period of heavy volcanic haze at Cape Kumukahi and extremely weak, southerly winds and is thus not typical of the normal trade wind flow.

TABLE 5. Precipitation Samples from the Island of Hawaii

Location, Fig. 1	Collection Data, 1970–1971	Na, ppm	K, ppm	Ca, ppm	Mg, ppm
Kumukahi	Feb. 16	15.0	1.15	1.84	2.7
Kumukahi	April 1	15.0	0.55	0.57	1.8
Kumukahi	April 13	16.0	0.63	0.63	1.7
Hilo	Nov. 24	0.78	0.18	0.10	0.12
Glenwood	Sept. 11	1.42	0.22	0.16	0.17
Glenwood	Nov. 20	0.48	0.08	0.04	0.03
MLO	Nov. 20	0.01	~0.01	~0.01	0.001
MLO	Nov. 25	0.01	~0.01	~0.01	0.001
MLO	Dec. 16	0.19	0.11	0.37	0.050
MLO	Dec. 2	0.03	0.03	0.02	0.004
MLO	Jan. 15	0.02	~0.01	~0.01	0.006
MLO	Jan. 1	0.01	~0.01	~0.01	0.003
MLO	March 31	0.06	0.004	0.040	0.022
MLO	April 7	0.05	0.003	0.028	0.025
MLO	April 14	0.07	0.005	0.020	0.021
MLO	April 21	0.07	0.005	0.008	0.015
MLO	April 27	0.02	0.005	0.008	0.010

these samples, the average value of 3–4 $\mu g/m^3$ of Na does not indicate a significant mass fraction of additional surf-zone aerosols. *Duce and Woodcock* [1971] collected impactor samples at the top and the base of a 20-meter tower located 4 meters above sea level on a sea cliff a few kilometers up the coast from Cape Kumukahi. They found Na concentrations of 3–10 $\mu g/m^3$ at the top of the tower, compared with amounts greater by 20–50 times at the base. The values found here are near the lower limit of the data of *Duce and Woodcock* [1971] for samples free from surf particles and should be reasonably typical of fresh marine aerosols produced in the open sea.

The samples collected in Hilo and one collected at Cape Kumukahi during very light southerly winds have Na concentrations approximately 10% of the Kumukahi samples. Collected continuously over 24-hour periods, the Hilo samples represent air that has moved of the order of 10 km from open-sea conditions during onshore flow (~1/2 of sampling period) plus air collected during offshore flow (~1/2 of sampling period) which has been away from the sea many hours and subjected to substantial condensation of water vapor. If we assume that ~90% of the aerosol mass of marine air is in the giant-nuclei size range, it is plausible that this fraction of the 'fresh' marine aerosol is not present in the Hilo samples, leaving only the remaining 10% of the aerosol mass primarily in the category of sizes smaller than 1 μ.

The samples collected at MLO have Na concentrations lower than the Hilo values by an order of magnitude. Thus the average amount of Na at MLO is only 1% of that at Kumukahi and only 10% of the fraction remaining after loss of the giant nuclei. Samples collected during the hours normally dominated by dry air at MLO (night samples) show K and Ca concentrations similar to those of samples collected during the remainder of the day (day samples). Na and Mg values in the night samples average ⅓ and ½, respectively, of the day sample concentrations.

In Table 6, data for the day and night samples are compared with those for the HASL samples. The HASL samples have values approximately twice those of the time-weighted day and night samples, except for iron, which is nearly 100 times as much. The HASL filter samples contain substantial dust (3–5 $\mu g/m^3$ of air sampled) because of the fact that the filter was located less than one meter above the ground surface near areas with substantial personnel activity at the observatory site. This dust is not present on the filters collected 5 meters above ground in a more remote corner of the observatory site. The contribution of dust to the bulk chemistry data reported here is evaluated by using two plausible alternative

TABLE 6. Comparison of MLO Sample Averages

Sample Type	No. Samples	Na, ng/m³	K, ng/m³	Ca, ng/m³	Mg, ng/m³	Fe, ng/m³
Day	11	31	2.4	3.4	8.4	~9
Night	11	10	1.5	3.9	4.8	~7
Continuous	30	47	5.6	10	16	~650
Day and night[1]	11	23	2.1	3.6	7.1	~8
Continuous[2]	12	36	4.9	10	14	~650

[1] Computed from the first two lines, weighted by the relative sampling times.

[2] Include only those run simultaneously with the day and night samples.

assumptions and is shown to be insignificant for the day and night samples. If we assume that the dust on the HASL filters has a composition similar to that of an average of basalt near the observatory and Pahala ash, (a widespread fine grained formation covering much of the windward side of Hawaii [*Macdonald*, 1949]), the processing of samples by leaching with concentrated HCl and concentrated HNO_3 could have released only very small fractions of Na, K, Ca, and Mg from the dust (if we assume that all the Fe was released and that the day-night sample average is correct). For Na, only 7% of the total Na in the dust was leached, whereas for Ca, only 1% of the total Ca was leached. Alternatively, if we assume a minor systematic correction in the air volumes sampled (~25%, discussed below) and no leaching from the dust component on the HASL filters, the aerosol concentrations of Na, K, Ca, and Mg in both sets of samples agree within less than a factor of 2, and there are no systematic differences in the relative amounts of these elements.

Since the day and night samples had only 1% of the Fe concentration of the HASL samples, the amounts of Na, K, Ca, and Mg present in the day and night samples that might have been leached from any dust present are insignificant compared with the contribution of more soluble salts.

The presence of ground-level dust in small quantities on the HASL filters has no effect on the surface-air radioactivity measurements, for which the samples are primarily collected.

Different aerosol sample categories in this investigation can be compared with relatively little data manipulation, since all samples involved the same pumps, filter materials, and chemical procedures (except the HASL filters, for which the high-volume pumps were different). More attention must be devoted to absolute calibration for comparison of aerosol and precipitation data and for comparison with other investigations.

One of the largest uncertainties results from estimation of air volumes sampled. The pumps used for the day and night samples were rotated continuously to remove any systematic bias from flow-meter errors. The flow rates used here were taken directly from the high-volume pumps. The ambient pressure at MLO is somewhat less than 700 mb. Thus a systematic increase of approximately 40% in the aerosol concentrations at MLO could be made. However, the flow meter is partially 'self-correcting,' since the flow rates indicated by the flow meters are lower at 3.4 km than at sea level for the same pumps. A more realistic correction of the MLO data to standard cubic meters, based on tests made in reduced-pressure chambers (W. H. Zoller, personal communication, 1972), would be to increase the day and night sample concentrations by 25%. The absolute calibration of the HASL filtering system is somewhat uncertain, owing to the long period since the pump has been calibrated. The chemical data for the HASL filters cannot be used unequivocally to correct the sample volumes, owing to the uncertainty introduced by the presence of dust in the HASL samples.

Several adjustments due to refinement in the chemical calibrations should also be made. Method-of-additions experiments and comparison tests of dry ashing versus dissolution of the filter with organic solvent suggest several corrections. The Na and Mg data should be increased by 10%, primarily because of viscosity differences between samples and standards. The K data should be increased by 50%, primarily owing to losses during the dry ashing procedure. The Ca data should be increased by 50%, primarily owing to chemical interference in the atomic absorption analysis. These last two corrections are based on experiments on a number of filters from both day and night categories, by using duplicate portions of the filters for two processing techniques, and by analyzing by a method of standard additions. No lanthanum was added, because of the contamination problems associated with adding large amounts of any reagent, since a number of different elements were being analyzed in each sample.

On the basis of these systematic corrections, the best estimate of the absolute concentrations in the two categories of samples collected at MLO are shown in Table 7. Since both day and night samples represent aerosols collected from both dry and moist air, the tabulated data represent the minimum differences existing between the aerosols typical of the dry air above the inversion and those typical of the moist air below the inversion level, after removal of 99% of the marine aerosol mass.

The systematic corrections have not been applied to the data reported in any tables except Table 7. The same techniques were used for all the samples reported here, and so any systematic corrections do not affect comparisons between sample categories. Duplicate samples run at different times agreed to within 10%. The uncertainty of the average values reported here for comparison between categories is estimated to be substantially better than ±25%.

TABLE 7. Absolute Concentrations for Two Categories of MLO Aerosols

	Day, ng/m³	Night, ng/m³
Na	42	14
K	4	3
Ca	6	7
Mg	11	7
(K + Ca + Mg)/Na	0.50	1.21

DISCUSSION OF RESULTS

The sampling schedule for the day and night samples was designed to utilize the 'normal' diurnal flow pattern to obtain one sample of each pair which would be collected entirely in dry air. However, no pair of samples was collected during the entire set of data shown in Table 2 that resulted in a night sample free of any period of moist air. Figure 3 shows the hygrothermograph record of the sample pair with the best separation of air mass types achieved. Although the contrast in average con-

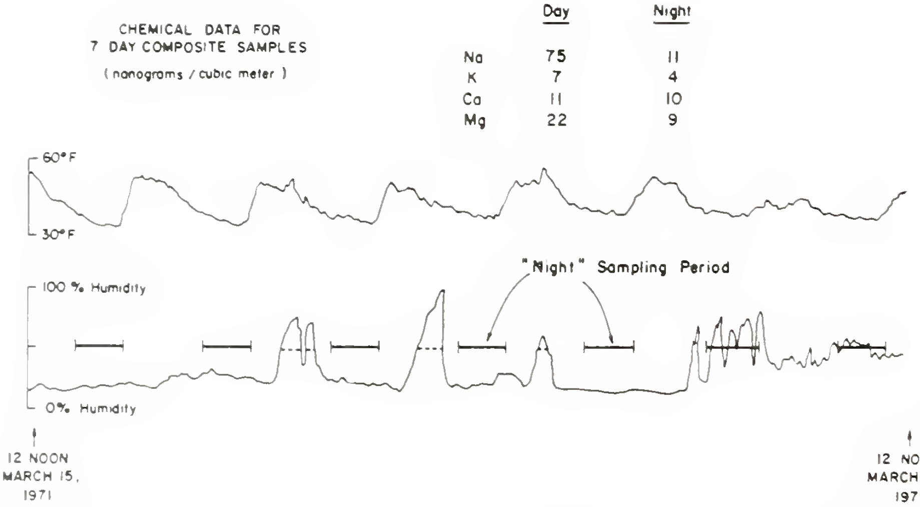

Fig. 3. Humidity and temperature record for sampling period with maximum diurnal circulation development.

centrations of Na and Mg in the day and night samples is substantial, there was still significant 'contamination' of the night sample with periods of moist air (if we assume that ≥50% humidity indicates sub-inversion air transported upward to the observatory site). A more nearly typical record of the periods for most of the sample pairs would show much less diurnal pattern and a large fraction of moist air during the night sampling period. Thus the degree of separation indicated by the chemical data (which was achieved by sampling in time segments) is surprisingly good, considering the lack of diurnal pattern in the humidity during this period of late fall and spring.

For continuous samples (Table 3), the highest Na values occurred during periods of most prominent diurnal circulation. The amount of Na reaching the observatory was enhanced by shorter periods of rapid upslope movement. Midwinter periods having high humidity for almost the entire week sampling interval showed relatively low Na concentrations. The fact that a plot of Na concentration versus per cent of sampling period with humidity ≥50% shows hardly any correlation indicates that moist air that remains continuously (for a number of days) at the observatory site may have very little marine aerosol (high Na) remaining. Thus more Na reaches MLO during summer and early fall (i.e., during 'diurnal-circulation' periods) than during late fall and winter, in spite of the fact that moisture is present at higher elevations more often during the winter.

The deviation of the major element chemistry of marine aerosol from the relative amounts found in sea water (usually denoted as 'fractionation') has been the focus of a number of papers [*Komabayasi*, 1962] and of a symposium sponsored in 1972 by the American Meteorological Society and the National Science Foundation. The trend in major cation chemistry (Na, K, Ca, Mg) that has been most frequently observed in a lower quantity of Na (relative to one or all of the other three cations) in marine aerosols than in sea water. Since agreement on the magnitude of this effect is not universal the data of this study are examined in terms of their possible implications relative to marine-aerosol fractionation.

The variations of K, Ca, and Mg as a function of Na concentration have been examined for all the MLO aerosol samples. There is a reasonably strong correlation between Na and Mg variations, for both the day-night and the HASL samples. There is very tenuous correlation between Na and K and hardly any correlation between Na and Ca in both sets of data. The fact that Na and Mg are covariant and that Na and K and Na and Ca are not suggests two populations of aerosols, one aerosol a 'marine' population dominated by Na with smaller concentrations of Mg and much less K and Ca and the other aerosol containing major fractions of K and Ca. If the K and Ca are supplied primarily by a second population of aerosols (low Na), no correlation of the amounts of these elements with the amount of Na would be expected.

The possibility of changes in the major cation ratios in marine aerosols relative to sea water can be examined in a variety of ways from the data presented here. One simple way to compare the data is by considering the amount of (K + Ca + Mg) relative to Na. For sea water this number is about 0.18 (Na : K : Ca : Mg = 28 : 1 : 1 : 3). The aerosol and precipitation samples collected at Cape Kumukahi had (K + Ca + Mg)/Na values of about 0.16. All other samples had higher values. The aerosol samples collected in Hilo averaged 0.47 (6 : 1 : 1 : 1). Although the absolute quantities in the MLO day samples were lower by an order of magnitude, the average (K + Ca + Mg)/Na value was also 0.50. It is interesting to note that precipitation data reported here that have Na greater than 0.5 ppm, as well as those reported by *Eriksson* [1957] for samples collected in Hawaii during Project Shower, nearly all lie within ±0.15 of 0.48.

The data here support a model of marine aerosols having a mass fraction of 90% with (K + Ca + Mg)/Na= 0.20 (giant nuclei) and a mass fraction of 10% with (K + Ca + Mg)/Na = 0.50. This latter fraction dominates after the giant nuclei are rapidly removed, and these aerosols probably account for the major cation chemistry of Hawaiian precipitation falling more than a few kilometers inland from the shoreline. *Woodcock et al.* [1971] recently suggested a similar explanation for the halogen composition of Hawaiian rain, indicating the importance of large nuclei rather than giant nuclei in rain formation. Only 10–20% of the marine aerosol remaining after loss of the giant nuclei reaches the elevation of MLO, but there is no substantial change in the cation ratios once the giant nuclei are lost. Since only 1% of the aerosol mass produced at the sea surface reaches 3.4 km at MLO, it appears that the marine aerosol found there represents a reasonable estimate for the maximum fractionation of marine aerosol cations from sea water ratios, at least for the marine aerosols penetrating the inversion elevation in Hawaii.

The night samples have an average (K + Ca + Mg)/Na value of 1.21, whereas the HASL samples have an average value of about 0.80. The relationship of the five different types of aerosol samples collected here is shown in Figure 4. The line connecting the Kumukahi, Hilo, and day samples indicates the trend of fractionation of the bulk composition of a sample of marine aerosol, nearly all of which occurs during the loss of the first 90% of aerosol mass.

The HASL samples fall between the day and night averages, on a mixing line, as would be expected. The night samples cannot be explained by further fractionation of marine aerosols along the line connecting the Hilo and day samples. They can be explained as a mixture of fractionated marine aerosols (day samples) plus background aerosols with a much higher (K + Ca + Mg)/Na ratio.

Although straight lines are drawn on Figure 4 to show both fractionation trends and mixing of components, neither line should be precisely straight on the semilogarithmic plot used. A mixing curve of night and day samples would bow slightly in the direction of the HASL samples. A trend line connecting the Kumukahi and Hilo samples, based on the model outlined above of 10% large aerosols and 90% giant aerosols, with (K + Ca + Mg)/Na ratios of 0.5 and 0.2, respectively, would be slightly concave upward. Straight lines are used for simplicity to illustrate that the continuation of the trend of change in chemistry shown by marine aerosols (as the total mass is reduced by 99%) cannot produce the chemistry of the night aerosol samples if the aerosol mass is reduced by another factor of 3.

Throughout this discussion, it has been assumed that the marine areosols reaching MLO have moved upslope from near sea level, losing approximately 99% of their total mass in

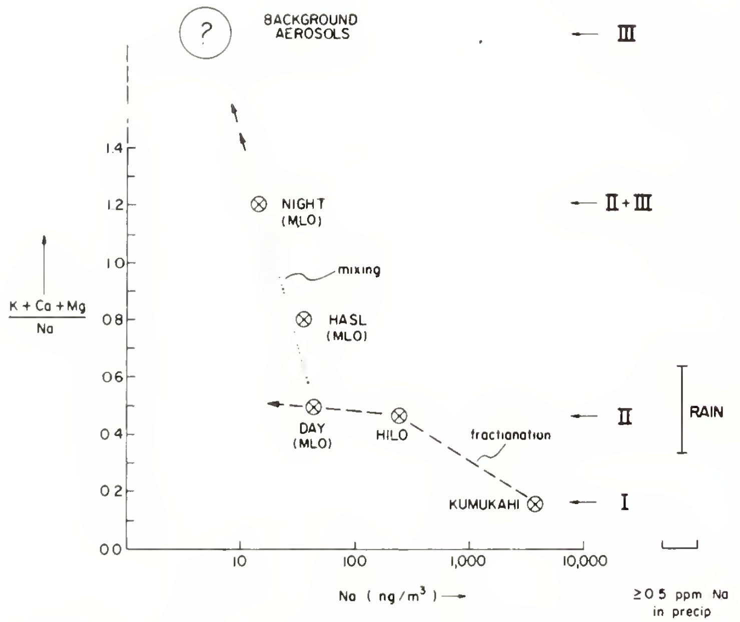

Fig. 4. Summary of aerosol types in Hawaii. I is fresh marine aerosols ((K + Ca + Mg)/Na ≈ 0.20). II is fractionated marine aerosols ((K + Ca + Mg)/Na ≈ 0.50). III is background aerosols ((K + Ca + Mg)/Na ≈ 2–3 ?).

transit. It could be argued that the low-aerosol mass found at Mauna Loa is the result of mixing of air from far above the lowest few hundred meters of marine air, since it has been well established that there is a large vertical gradient in mass of sea-salt particles in the trade wind atmosphere. *Woodcock* [1953] found sea-salt particle masses collected at altitudes between 1300 and 2300 meters ranging from 1 to 20% of the masses found at 500 meters, the lowest relative values being over the Island of Hawaii. For considerations of the extent of fractionation of marine aerosols indicated by the MLO day samples, the precise path of movement of the aerosols is not important. The relationship between the ratios of the major cations and the total amount of Na (Figure 4) indicate that the aerosols present in the dry air above the inversion cannot be simply residual marine aerosols produced by continuous removal of the largest particles. There is additional evidence, however, that the actual path of the sub-inversion air that reaches the observatory has had substantial contact with the layer of air just above the island surface. The moist air containing marine aerosols that reaches the observatory site almost invariably has high Aitken nuclei counts, which are typical of the ground layer air below the inversion (B. G. Mendonca, personal communication, 1972).

The ultimate origin of the major cation composition inferred for background aerosols is beyond this discussion. The evidence presented here indicates that a simple process of differential removal of marine aerosols that have a range of bulk chemistry cannot produce the aerosol chemistry suggested for the aerosols above inversion. An important fact, however, is that the major cations of the background aerosols are soluble in the strong acid solutions used here, whereas those same ions were not extracted in large amounts from the silicate lattice of the volcanic dust present in the HASL filters. This makes it more difficult to explain the major cation composition of the background aerosol as resulting from a dust component.

A more complete discussion of the analytical procedures and data on the heavy metal composition of aerosols collected at MLO will appear elsewhere (H. J. Simpson, unpublished report, 1972).

SUMMARY

The quantity of aerosol present at MLO, as measured by the concentration of Na, K, Ca and Mg is approximately 1% of sea level values for marine air. Thus sea-salt aerosols appear to have a very short residence time in air moving up the slopes of Mauna Loa to 3.4 km. Samples collected at MLO can be interpreted as including two separate aerosol populations, one a fractionated marine aerosol containing about 67% Na (sea water = 85% Na) and the other aerosol containing <45% Na. The contribution of Na, K, Ca, and Mg from local dust in these samples is extremely small and is probably less than experimental error.

The low Na aerosol population, possibly having Na concentrations of only ~25% of the total cations, is probably typical of the air above the trade wind inversion. *Junge* [1957] suggested from measurements of two impactor samples that the NH_4/Cl ratio in aerosols above the inversion was large, probably greater than 5, indicating a non-marine origin. The evidence obtained here suggests that the aerosols above the inversion have substantial major cation differences from the 'fractionated' local marine aerosols. This evidence supports the premise that aerosols typical of the 'background' aerosol of the upper troposphere can be collected from a surface location at MLO. Sampling during well developed diurnal circulation, with pumps regulated to operate only during periods of low humidity, should enable 'pure' background aerosols to be obtained.

MLO thus appears to offer a unique location for investigation of the chemistry of upper tropospheric 'aged' aerosols, with the convenience of sampling from the ground. The origins of Na, K, Ca, and Mg in the background aerosol population samples collected at MLO are not clearly defined from this study. They do not appear to originate from local fractionated marine aerosol. The fact that the relative concentrations resemble mid-continent precipitation [*Junge*, 1963] supports the theory of a continental origin.

Acknowledgments. This study was initiated under an Environmental Science Services Administration postdoctoral research program sponsored by the National Research Council. The Scientific Adviser, Dr. Helmut K. Weickmann of the National Oceanographic and Atmospheric Administration in Boulder, provided generous support and guidance. R. Pueschel, J. Pereira, B. Mendonca, H. Ellis, and J. Chin of Mauna Loa Observatory helped throughout sample collection. J. Bowen, J. Naughton, and V. Lewis of the University of Hawaii provided analytical equipment. R. Duce and G. Hoffman of the University of Rhode Island and A. Lazrus and B. Gandrud of the National Center for Atmospheric Research provided advice on analytical techniques. H. Volchok of the Health and Safety Laboratories of the Atomic Energy Commission supplied the filter materials and extensive logistic support. M. Bender and W. Broecker provided discussion and criticism of the manuscript.

REFERENCES

Duce, R. A., and A. H. Woodcock, Difference in chemical composition of atmospheric sea salt particles produced in the surf zone and on the open sea in Hawaii, *Tellus, 23,* 427-435, 1971.

Ellis, H. T., and R. F. Pueschel, Solar radiation: Absence of air pollution trends at Mauna Loa, *Science, 172,* 845-846, 1971.

Eriksson, E., The chemical composition of Hawaiian rainfall, *Tellus, 9,* 509-520, 1957.

Gillette, D. A., and I. H. Blifford, Jr., Composition of tropospheric aerosols as a function of altitude, *J. Atmos. Sci., 28,* 1199-1210, 1971.

Hoffman, G. L., Particulate trace metals in the Hawaiian marine atmosphere, Ph.D. thesis, 286 pp., Univ. of Hawaii, Honolulu, Hawaii, 1971.

Junge, C. E., Chemical analysis of aerosol particles and of gas traces on the Island of Hawaii, *Tellus, 9,* 528-537, 1957.

Junge, C. E., *Air Chemistry and Radioactivity,* 382 pp., Academic, New York, 1963.

Junge, C. E., Airborne dust at Barbados and its relation to global tropospheric aerosols, *Geochim. Cosmochim. Acta., 32,* 1219-1222, 1968.

Komabayasi, M., Enrichment of inorganic ions with increasing atomic weight in aerosol, rainwater and snow in comparison with sea water, *J. Meteorol. Soc. Jap., 40,* 25-38, 1962.

Macdonald, G., Petrography of the Island of Hawaii, *U.S. Geol. Surv. Prof. Pap. 214D,* 51-96, 1949.

Mendonca, B. G., Local wind circulation on the slopes of Mauna Loa, *J. Appl. Meteorol., 8,* 533-541, 1969.

Pales, J. C., and C. D. Keeling, The concentration of atmospheric carbon dioxide in Hawaii, *J. Geophys. Res., 70,* 6053-6076, 1965.

Price, S., and J. C. Pales, Mauna Loa Observatory: The first five years, *Mon. Weather Rev., 91,* 665-680, 1963.

Tellus, Project shower, *Tellus, 9,* 471-590, 1957.

Tellus, Warm rain project, *Tellus, 19,* 347-461, 1967.

Volchok, H. L., and M. T. Kleinman, Radionuclides and lead in surface air, *Rep. HASL-246,* U.S. Atomic Energy Commission, Appendix, C-1 through C-102, January 1972.

Woodcock, A. H., Salt nuclei in marine air as a function of altitude and wind force, *J. Meteorol., 10,* 362-371, 1953.

Woodcock, A. H., R. A. Duce, and J. L. Moyers, Salt particles and raindrops in Hawaii, *J. Atmos. Sci., 28,* 1252-1257, 1971.

(Received March 20, 1972;
revised May 30, 1972.)

U.S. DEPARTMENT OF COMMERCE
Maurice H. Stans, Secretary

NATIONAL OCEANIC AND ATMOSPHERIC ADMINISTRATION
Robert M. White, Administrator
ENVIRONMENTAL RESEARCH LABORATORIES
Wilmot N. Hess, Director

NOAA TECHNICAL REPORT ERL 208-APCL 21

Effects on the Stratosphere of SST Operation

CHARLES C. VAN VALIN

BOULDER, COLO.
May 1971

FOREWORD

The problem of SST operations has many ramifications in areas of technology, economy, and environment. The following study deals with the effects of SST engine emissions on the environment in which the SST will cruise. Included are the possible chemical reactions and reaction products in the stratosphere and the subsequent increase in the concentration of trace gases and particulates in the stratosphere due to SST operations.

The general impression coming out of this review is one of guarded optimism regarding the effects of SST operations on the environment and weather. We must say, however, that the knowledge of the composition and the very complex chemistry of the atmospheric layers concerned is very incomplete. Therefore, the true message of the study is an urgent call for support of research into the physical, chemical, and photochemical processes of the lower stratosphere.

Helmut Weickmann

Helmut K. Weickmann
Director, Atmospheric Physics & Chemistry Laboratory

TABLE OF CONTENTS

Page

ABSTRACT 1

1. INTRODUCTION 1

2. ENVIRONMENT OF THE SST 4

3. REACTIONS AND CONSEQUENCES OF SST EMITTANTS 9

3.1 Carbon Dioxide 9
3.2 Water 10
3.3 Carbon Monoxide 21
3.4 Oxides of Nitrogen 23
3.5 Sulfur Dioxide and Sulfate 26
3.6 Hydrocarbons 29
3.7 Ozone 31
3.8 Soot 32

4. CONCLUSIONS 32

5. ACKNOWLEDGEMENTS 36

6. REFERENCES 37

EFFECTS ON THE STRATOSPHERE OF SST OPERATION

Charles C. Van Valin

Some consequences of SST engine emissions in the lower stratosphere are considered. Projected emission quantities of H_2O, CO, CO_2, NO_x, SO_2, soot, and unburned hydrocarbons are compared with naturally occurring quantities of these substances. There is some present evidence that emissions from the SST will not produce measurable changes in the stratosphere. However, the very restricted knowledge of some stratospheric and operational parameters demands full exploration of the lower stratosphere before commercial use of the SST aircraft is achieved.

Reprinted from Journal of Atmospheric Sciences, Vol. 28, No. 6, September 1971, pp. 1076–1078
American Meteorological Society
Printed in U. S. A.

Water Cloud Stabilization with Chlorinated Silanes

Charles C. Van Valin and Paul A. Allee

Atmospheric Physics and Chemistry Laboratory, NOAA, Environmental Research Laboratories, Boulder, Colo.

9 September 1970

1. Introduction

The alkylchlorosilanes and tetrachlorosilanes react vigorously with water to yield a dimer or polymer which is insoluble in water. The film of such an insoluble polymer formed on the surface of water droplets comprising a cloud would retard the rate of transfer of water from small to large droplets, or retard evaporation of the cloud droplets when their environment is mixed with drier air, thus stabilizing the cloud.

Bradley (1955) has placed the theoretical value of Fuchs' evaporation coefficient (Fuchs, 1964) in the order of 10^4 smaller for water droplets coated with an insoluble monolayer when compared to pure water droplets. Archer and LaMer (1955) and Eisner *et al.* (1960) have shown a rather good agreement, experimentally, with this number using long-chain fatty acids or alcohols. Snead and Zung (1968) studied the evaporation of water droplets coated with *n*-decanol and suspended in an electric field. Derjaguin *et al.* (1960) postulated an increase in the evaporation coefficient in certain circumstances where water droplets are coated with a surface active substance, but this postulate has been effectively contradicted by the observed reduction in reported instances (Archer and LaMer, 1955; Eisner *et al.*, 1958, 1960; Snead and Zung, 1968; Langmuir and Schaefer, 1943).

2. Experimental methods and results

To test the stabilizing effect of various organosilicon compounds on cloud droplets, we evaporated small quantities of the test substance in the lower part of a small (0.15 m^3) freezer, at a temperature of −16 to −18C. The substances tested are shown in Table 1. The

Table 1. Chemicals tested for cloud stabilizing action.

Name	Formula	Boiling point (°C)	Amount tested (minimum)	Cloud life† (min)
Dimethylsilane	$(CH_3)_2SiH_2$	−20	5 sec burst from pressurized can	4/4
Tetramethylsilane	$(CH_3)_4Si$	26.6	100 μl	4/4
Dimethylchlorosilane	$(CH_3)_2SiHCl$	36	10 μl	12/4
Trimethylchlorosilane	$(CH_3)_3SiCl$	59	1 μl	7/5
Dimethyldichlorosilane	$(CH_3)_2SiCl_2$	69.4	1 μl	13/5
Methyltrichlorosilane	CH_3SiCl_3	64.6	1 μl	25/5
Ethyltrichlorosilane	$CH_3CH_2SiCl_3$	100.5	1 μl	25/5
Allyltrichlorosilane	$CH_2{=}CHCH_2SiCl_3$	117.5	1 μl	25/5
n-Butyltrichlorosilane	$CH_3CH_2CH_2CH_2SiCl_3$	142	1 μl	25/5
Tetrachlorosilane	$SiCl_4$	57.6	2 μl	20/4
Chloromethyldimethylsilanol	$ClCH_2(CH_3)_2SiOH$		100 μl	7/5
Diphenylsilanediol	$(C_6H_5)_2Si(OH)_2$	140*	100 mg	45/5**
Hexamethyldisiloxane	$(CH_3)_3SiOSi(CH_3)_3$	100	100 μl	7/5
Hexamethyldisilazane	$(CH_3)_3SiNHSi(CH_3)_3$	126	100 μl	10/5
Hydrochloric Acid (36.5%)	HCl		100 μl	6/4

† Values shown are for treated, first, and untreated, second.
* Melting point (decomposes).
** This result is considered unreliable because of the formation of decomposition products.

trichlorosilanes are most effective, dichlorosilanes somewhat less so, the monochlorosilanes less effective yet, and the unchlorinated silicon compounds have very little effect or none at all. For most of the tests we built a cloud in the freezer after having introduced the silane, but for some we evaporated the silane as the cloud was being built. We then measured the time elapsed before the cloud evaporated. An ultrasonic nebulizer was used to build a 1 gm cloud with a droplet diameter of 6–8 μm and a total surface area of $\sim$0.8 m^2.

A pure water cloud without an added substance endured from $3\frac{1}{2}$–$6\frac{1}{2}$ min before evaporating. With 20 μl of the more effective substances a moderate cloud remained 30 min, and a Tyndall beam was visible even after 4 hr. Part of the gradual thinning was due to fallout. At a terminal velocity of 0.1 cm sec^{-1}, fallout of droplets of 6 μm diameter would be complete in 10 min. Fallout of droplets 3 μm in diameter would be complete in about 33 min.

When there is an adequate moisture supply, a cloud can be generated within 4–5 min by evaporating 20 μl or more of one of the most active chlorosilanes in the freezer. Such a cloud behaves the same way as clouds prepared with the nebulizer.

The presence of an electrolyte dissolved in the cloud droplets, such as the HCl generated by the reaction of the chlorosilanes with water, lowers the water vapor pressure over the droplets. To evaluate such an effect, we evaporated 100 μl of concentrated HCl in the freezer and then built a cloud. This cloud lasted about 30% longer than an untreated cloud, but this extension is of little significance when compared with the stabilization effect from the reaction of chlorosilanes with the water droplet surface.

The lowering of the vapor pressure over the droplet surface is inferred from the retardation of evaporation. To determine such an effect we installed a dewpoint hygrometer consisting of a polished metal container, which was held in the lower part of the freezer. By controlling the flow rate of antifreeze solution through the container, we were able to lower the temperature of the polished surface gradually to about −20C. The results are summarized in Table 2. The addition of 50 μl of the silane to a cloud in the freezer resulted in an apparent dewpoint depression of about 5C in the range from approximately −20 to 0C.

TABLE 2. Dewpoint depression in silane-treated clouds.

Cloud treatment	Observed dewpoint (°C)	Freezer temperatures (°C)	Difference (°C)
None	4	7	3
None	−3	−1	2
50 μl Me_3SiCl	−12	−7	5
50 μl Me_2SiCl_2	−7	1	8
50 μl Me_2SiCl_2	−14	−6	8
50 μl Me_2SiCl_2	−16	−8	8
50 μl Me_2SiCl_2	−23	−16	7
50 μl $MeSiCl_3$	−9	1	10
50 μl *n*-$BuSiCl_3$	−14	−8	6

In another test of dewpoint lowering, about 1 ml of methyltrichlorosilane was added to the water in a half-full 1-gal bottle. Measurements with a dewpoint measuring apparatus showed a dewpoint of 18.5C over the silane and water mixture when the dewpoint over pure water was 24C. In another trial the dewpoint over the silane-water mixture was 7.5C, and over pure water 13C. Thus, in both instances the dewpoint lowering was about 5C.

The effect of dimethyldichlorosilane upon condensation nuclei was investigated with the test chamber at −18C. The chamber was open to room air and contained approximately 4000 nuclei ml^{-1} active in a thermal diffusion chamber at 1% water supersaturation. When 50 μl of dimethyldichlorosilane was added to the chamber, the number of condensation nuclei active at 1% water supersaturation increased by about 10,000 nuclei ml^{-1}. The silane apparently reacted with the water vapor in the chamber, forming condensation nuclei in addition to those already present. After a few minutes, the droplets became visible within the chamber, and a stable cloud was generated. Since the vapor pressure over these nuclei surfaces was lower than that for the chamber walls, droplets would grow within these condensation nuclei until their size was such that the cloud stabilized. These condensation nuclei would effect a transfer of vapor from cloud droplets that had no silane surface, or a surface imperfectly coated with silane, until equilibrium had been established.

The silanes that are active in cloud stabilization are also effective in modifying or preventing ice crystal growth within a supercooled cloud.

Homogeneous ice nucleation can be produced in a supercooled cloud by any means which will cool the cloud to below the critical temperature of −38.9C, including adiabatic expansion or the use of dry ice. Silane treatment of a supercooled cloud apparently does not interfere with the homogeneous ice nucleation process, but it does interfere with the growth of the embryonic ice nuclei, because of the reduction of the dewpoint temperature, or ambient water vapor pressure, within a silane-treated cloud.

As noted above, the effect on ambient water vapor pressure above a water surface treated with an alkylchlorosilane amounted to a reduction in the pressure equivalent to cooling the water by about 5C. This same effect of dewpoint depression was found when a supercooled cloud was treated with dimethyldichlorosilane. With the treated cloud, neither adiabatic expansion nor dry ice seeding resulted in ice crystals until the cloud temperature was lowered at least to −30C. A very few ice crystals were observed when dry ice was used at −30C; a silane-treated cloud at −35C formed large numbers of crystals when homogeneously nucleated, although comparative visual observations indicate that the growth process is slower in the treated than in an untreated cloud.

Fig. 1, derived from the *Smithsonian Meteorological Tables* (List, 1958), illustrates the effect of a 3C depression of the saturation vapor pressure over water. The solid lines represent saturation vapor pressures over water and over ice in the temperature range shown. The dashed line represents the saturation vapor pressure over silane-treated water, assuming a 3C depression of the dewpoint. In this case, instead of having a higher vapor pressure over water than over ice, the reverse is true at temperatures above −29C, and sublimation of vapor to the ice nuclei would not occur. The lines cross at about −29C, and presumably ice crystals could grow very slowly at −30C, and somewhat faster at −35C.

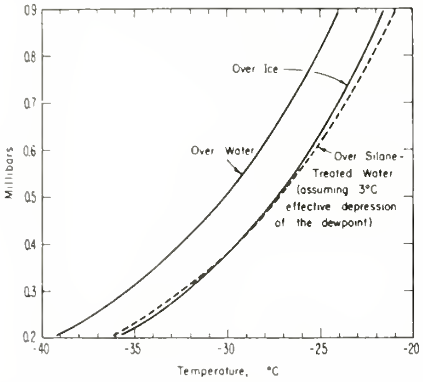

FIG. 1. Saturation vapor pressures over water, over ice, and over silane-treated water, assuming a 3C effective depression of the dewpoint.

We determined that the threshold level was about 10 μl of dimethyldichlorosilane for essentially complete inhibition of ice nucleation at a temperature of about −20C.

3. Summary

The tests which we conducted indicate that the use of silanes for cloud stabilization could be practical in specific situations. The lowest rate of application tested, 1.0 μl for the usual sample cloud at −16C, extended the life of the cloud by a factor of 4 or 5, but during this time there was considerably more thinning than experienced with the higher rates of application. At this rate of application, a cloud containing 1 gm of liquid water per cubic meter and occupying 0.1 km^3 would require 100 liters of silane. At higher temperatures the efficiency would be lower because of the greater quantity of water vapor present. However, in a natural cloud the wall effect of the test chamber would not be present, and because of this the efficiency could be much greater.

Subsequent to this laboratory study, Sartor (1969) and his co-workers at the National Center for Atmospheric Research have observed the stabilization of a cloud in a natural situation. They released a mixture of methyltrichlorosilane and toluene into the upwind side of a mountain wave cloud, and about 20 sec later observed an oblong cloud emerging from the downwind side of the wave cloud. They noted that the small cloud traveled several kilometers downwind before finally dissipating. Two hundred milliliters of a 1:1 mixture was released from an aircraft; the resulting stabilized cloud was on the order of 100 m in width and thickness, and 1 km in length.

REFERENCES

Archer, R. J., and V. K. LaMer, 1955: The rate of evaporation of water through fatty acid monolayers. *J. Phys. Chem.*, **59**, 200–208.

Bradley, R. S., 1955: The rate of evaporation of micro drops in the presence of insoluble monolayers. *J. Colloid. Sci.*, **10**, 571–575.

Derjaguin, B. V., S. P. Bakanov and I. S. Kurghin, 1960: The influence of a foreign film on evaporation of liquid drops. *Disc. Faraday Soc.*, **30**, 96–99.

Eisner, H. S., F. R. Brookes and B. W. Quince, 1958: Stabilization of water mists. *Nature*, **182**, 1724.

——, B. W. Quince and C. Slack, 1960: The stabilization of water mists by insoluble monolayers. *Disc. Faraday Soc.*, **30**, 86–95.

Fuchs, N. A., 1964: *The Mechanics of Aerosols*. New York, Macmillan, 408 pp.

Langmuir, I., and V. J. Schaefer, 1943: Rates of evaporation of water through compressed monolayers on water. *Surface Chemistry*, Washington, D. C., Amer. Assoc. Adv. Sci., No. 21, 17–39.

List, R. J., 1958: *Smithsonian Meteorological Tables*. Washington, D.C., The Smithsonian Institution, 351–364.

Sartor, J. D., 1969: Mountain wave clouds as steady-state cloud and aerosol physics laboratories. *Proc. 7th Intern. Conf. Condensation and Ice Nuclei*, Prague and Vienna, 304–308.

Snead, C. C., and J. T. Zung, 1968: The effects of insoluble films upon the evaporation kinetics of liquid droplets. *J. Colloid. Interface Sci.*, **27**, 25–31.

Reprinted with permission from 14th Interagency Conference on Weather Modification, Skyland, Virginia, Oct 1972.

INADVERTENT WEATHER MODIFICATION

Helmut K. Weickmann

Atmospheric Physics and Chemistry Laboratory
Environmental Research Laboratories
National Oceanic and Atmospheric Administration
Boulder, Colorado 80302

Numerous instances, mostly unnoticed, of local inadvertent weather modification occurs nowadays due to anthropogenic nuclei sources. We had frequently the opportunity to observe such effects in connection with our research work in the Great Lakes Basin. Smoke stacks from metal foundaries are prolific sources of freezing and condensation nuclei. We have penetrated the plume downwind of the stacks and have measured freezing nuclei concentrations up to 2000 per liter and strong glaciation in supercooled stratus downwind of the plume. During proper cloud conditions snow showers developed downwind of cities and industrial centers. How is the present situation concerning world wide pollution from such sources?

Let us first assess the relative significance of natural and artificial aerosol production. Table 1 conveys the results of a recent survey by Robinson and Robbins (1971). It is a summary of the global particulate emissions from pollutant and natural sources. It is to be noted that the natural aerosol sources are nowadays still considerably more abundant than the artificial sources, the natural producing 2312 x 10^6 tons or 88.5% of the total while the artificial sources amount to 296 x 10^6 tons or 11.5% of the total. For the natural sources we like to point out that the oceanic production roughly equals land production whereby soil dust constitutes quite a large portion. The artificial production of course is limited to the world's industrial centers and if we consider the land areas of Eastern USA, Europe, Japan and part of Australia as the main centers we find that the 296 x 10^6 tons are produced over only about 2.5% of the surface of the globe. The natural production over the same area amounts to 58 x 10^6 tons or only about 20% of the artificial production. If we further consider that in the last decade the energy consumption has almost tripled (Fig. 1) (Cook 1971) then there can be no doubt that inadvertent weather modification on a large scale may soon become a real possibility. What is the status now? Can we aside from the above mentioned local effects observe or measure regional or global effects? It appears practical to subdivide for this estimate the atmosphere into three layers: the lower boundary layer which reaches from the surface to the top of the Ekman layer (about 1200 m) over the continent or to the top of the trade wind inversion (about 2000 m) over the oceans, the troposphere between the top of the boundary layer and the tropopause, and finally the stratosphere. The residence times for particles in these layers amount to days for the boundary layer, weeks for the troposphere and months to years for the stratosphere.

So far, the only layer in which with certainty large scale modifications of the aerosol concentration have been observed is the lower boundary layer (Cobb and Wells, 1970). Figure 2 shows that the conductivity over the Atlantic Ocean as measured on board of the research vessel "Oceanographer" and compared with other measurements during the last 60 years has steadily decreased. Decrease of conductivity is proportional to increase of aerosol content. Note from Fig. 2 that a similar trend has not prevailed over the South Pacific Ocean. The American traveler in Europe is struck by the permanently poor visibility in all European countries which seldom is better than ten km and it is known that Sweden is much concerned about pollution of its fresh water lakes from contaminants which originate in Europe's main industrial areas and are washed out by the rain. It is however known that above the boundary layer during non-convective climatic conditions visibilities of over 100 km occur.

This laboratory has made an interesting series of measurements above the boundary layer, the trade wind inversion, over the Pacific Ocean: in 1960 and again in 1968 members of APCL (Mr. B. Phillips and Mr. W. Cobb) have made throughout several months very carefully conducted measurements of atmospheric electric parameters such as the potential gradient, the air conductivity and the small ion density. Table 2 shows average values of these measurements and neither the small ion density nor the conductivity which are related show any differences, indicating that at least from 1960 to 1968 the tropospheric turbidity has not increased above the trade wind inversion of the Pacific Ocean. This conclusion is also confirmed by recent analyses of the aerosol concentration in ice cores taken from the Greenland ice cap for the period 1880 to 1968 (Federer,1971). Finally, Fig. 3 taken from Ellis and Pueschel (1971), confirms that in the 1960's the turbidity in the stratosphere was only temporarily increased as a consequence of volcanic eruptions, notably that of Mt. Agung in March 1963, but that now the turbidity is back to its pre-Agung value.

Gaseous constituents in the stratosphere have however increased as shown on Figs. 4, 5, and 6. Analyses of the Dobson network which was operated by APCL until 1971 indicates a slow increase of total ozone during the last decade (Fig. 4); a similar trend has been observed for various world stations with carefully conducted records (Fig. 5). Likewise Fig. 6 indicated that the water vapor content as measured by radiosonde (Mastenbrook 1971) has increased also.

We define an atmospheric retainment factor for aerosols as being the ratio between the yearly production and that which is retained by the atmosphere. Figure 7 gives data which have been compiled by J. Simpson (1972) showing the aerosol mass in air in micrograms per m^3. The value over the cleanest site, Central Greenland, should reflect the worldwide concentration in the troposphere. The air flowing continuously downhill east and westward from the ridge of the Greenland ice cap (3000m) to the coastline is being replaced by air descending through the troposphere consequently the value measured in Central Greenland should be typical of the general conditions in the troposphere. If we assume that the aerosol is equally distributed throughout the volume of the homogeneous atmosphere the Greenland value suggests a total amount retained of 3.69×10^5 tons, or retainment factor R

$$R = \frac{3.69 \times 10^5}{2.608 \times 10^9} = 1.41 \times 10^{-4}$$

A similar value can be computed for the cleanest continental site but this time under the assumption that this value represents what is left over from the natural and artificial contamination which was released over 2.5% of the earth's surface and remained essentially within the boundary layer of 1.5 km thickness. We obtain a retainment factor of $R = 5.7 \times 10^{-4}$. Finally from Fig. 8 a similar value can be derived for lead. Lead is a particularly interesting and important contaminant as it is purely man-made (aside from a small amount which is released as a radon product). The yearly release of lead into the atmosphere is 600,000 tons of which 230,000 come from metal smelters and 370,000 from automobiles. Taking the Siberia value as typical of the entire atmosphere we find that 500 tons are being retained which amounts to a retainment factor for lead of 8.3×10^{-4}.

The relatively close agreement of all three values, but particularly of the boundary layer value with the two others for the entire atmosphere permits the important conclusion that it is the residence time typical of boundary layer conditions which determines the retainment factor. This conclusion is valid for particles which originate at the surface, volcanic aerosol which is directly blown into the stratosphere is retained of course in agreement with stratospheric residence times.

Conclusion:

It would seem from the sparse data available that at this time global pollution above the lower boundary layer from autoprogenic sources is virtually non-existent. The normal natural background value of particle concentration (Aitken nuclei) over the Atlantic Ocean below the trade wind inversion near Barbados (13^{O}N, 59^{O}W) is between 200 and 350 per cc (BOMEX DATA, unpublished). In unpolluted air over Arizona below 10,000 ft. msl. the concentrations were between 300 and 800 per cc. The outlook for a global increase of these values can be derived from Fig. 1. Figure 1 shows the increase of total power requirements, the incremental increase during 1969 was more than 10% (Cook, 1971). If we assume a levelling off at 10% per year and assume further that the present power consumption is compatible with the present aerosol production then simple arithmetic would indicate that in about 23 years the aerosol production reaches the amount of the natural production, and the aerosol content may then have doubled. While this need not be alarming, it may nevertheless signal the beginning of global inadvertent weather modification. Since we are only just now beginning to combat air pollution we are convinced that the problem can be solved within 23 years, as the problem of the London smog has been solved within a few years through the application of a thorough change of the home heating technology. It however calls for a survey and monitoring of the freezing nuclei population which APCL is planning to conduct.

There are two major reasons for establishing a network to measure the ice crystal nuclei (ICN) concentration. First, to establish the current average ICN concentration throughout the seventeen Western United States, and second, to detect variations from that average concentration. It is anticipated that there will be seasonal, air mass source, and "ice nucleus storm" variations of the ICN concentration. One study by Grant and Mielke (1967) of the ICN concentration in Colorado has shown that there is usually a deficiency of nuclei (ice crystals) observed in cloud areas when the cloud top temperatures are warmer than -20°C, and that the inadvertent increase of ice nuclei concentration under these conditions can lead to enhanced precipitation. At cloud top temperatures below -24°C abundant natural seeding occurs and the precipitation rate may remain unaffected. Table 3 shows a summary of previous airborne ICN concentration measurements made by APCL. It is apparent that urban activity does increase the concentration of ICN, and their effect upon supercooled clouds in the vicinity has been mentioned above. The network for measuring ICN concentration will furnish data to determine the current background ICN concentration, and the effect of urban produced and natural variations of ICN concentration upon precipitation patterns within the Western United States.

The research reported here has been carried out by personnel of the Atmospheric Physics and Chemistry Laboratory. Some of the project responsibility has since been transferred to the Air Resources Laboratories.

Table Legend:

Table 1. Summary of global particulate emissions per year from pollutant and natural resources.

Table 2. Average atmospheric electric data for Mauna Loa Observatory for the years 1960 and 1968. Measurements by B. Phillips and W. Cobb, NOAA, for fair days without low and middle level clouds.

Table 3. Ice nuclei concentrations over the Atlantic Ocean near Barbados and over the U. S. continent.

Figure Legend:

Figure 1. Increase of energy consumption for electricity generation, transportation and other applications.

Figure 2. Secular change in electrical conductivity of the atmospheric boundary layer from 1907 to 1967 in two oceanic regions. In the South Pacific the conductivity has remained fairly constant, in the North Atlantic a decrease of at least 20% has occurred during the time period considered.

Figure 3. Relative atmospheric transmissivity measured on Mauna Loa Observatory.

Figure 4. Increase of total ozone as measured with a Dobson spectrometer for 10 U.S. stations.

Figure 5. Increase of total ozone as measured with a Dobson spectrometer for 7 stations.

Figure 6. Increase of stratospheric water content as measured by Mastenbrook (unpublished data).

Figure 7. Aerosol mass comparison in µg/m^3. Data compiled and measured by J. Simpson, 1971.

Figure 8. Concentration of trace constituents in Air (ng/m^3) Compiled and measured by J. Simpson, 1971.

References:

Cobb, W., and H. J. Wells (1970), The electrical conductivity of oceanic air and its correlation to global atmospheric pollution, JAS, 27, No. 5, pp. 814-819.

Cook, E., (1971), The flow of energy in an industrial society, Scient. American, 225, pp. 135-144.

Ellis, A. T., and R. F. Pueschel (1971), Solar radiation: Absence of air pollution trends at Mauna Loa, Science 172, pp. 845-846.

Federer, B. (1971), Investigation of the aerosol content of Greenland snow between 1880 and 1968, Suppl. Vol. Proc. 7th Internat. Conf. on Condensation and Ice Nuclei, Prague and Vienna, Sept. 18-24, 1969. Academia Prague, pp. 280-287.

Grant, Lewis O., and Paul W. Mielke, Jr., (1967), A randomized cloud seeding experiment at Climax, Colorado, 1960-65, Proc. 5th Berkeley Symposium on Mathematical Statistics and Probability, Vol. 5, pp. 115-131.

Mastenbrook, John (1971), Personal communication.

E. Robinson and R. C. Robbins (1971), Emissions, Concentrations, and fate of particulate atmospheric pollutants. Final Report, SRI Project SCC 8507.

Simpson, J. H., Jr., (1972), Aerosol and precipitation chemistry at Mauna Loa Observatory, NOAA-ERL-APCL Tech. Report to be published.

Table 1

SUMMARY OF GLOBAL PARTICULATE EMISSIONS FROM POLLUTANT AND NATURAL SOURCES

	Source	Production Tons/Year	
Pollution	Pollutant Particulate Materials	92×10^6	296×10^6 11.5 %
	Particles Formed from Gaseous Pollutants		
	Sulfate from SO_2	147×10^6	
	Nitrate from NO_x	30×10^6	
	Photochemical from hydrocarbons	27×10^6	
Natural	Soil Dust	200×10^6	2312×10^6 88.5 %
	Particles from Natural Gaseous Emissions		
	Sulfate from H_2S	204×10^6	
	Nitrate from NO_x	432×10^6	
	Ammonium from NH_3	269×10^6	
	Photochemical from terpenes	200×10^6	
	Volcanic (small particles)	4×10^6	
	Forest Fires	3×10^6	
	Sea Salt	1000×10^6	
		2608×10^6	100%

Table 2

ATMOSPHERIC ELECTRIC ELEMENTS AT MAUNA LOA

Parameter	1960	1968
Potential Gradient	120 Vm^{-1}	130 Vm^{-1}
Total Conductivity	7.2×10^{-14}	7.2×10^{-14}
Small ion density	960 ions cm^{-3}	960 ions cm^{-3}

Table 3

Location	ICN l^{-1}, $-20^{\circ}C$ Background	ICN l^{-1}, $-20^{\circ}C$ Urban
Barbados, 1969	1 to 2	
Colorado	0.5	20
Great Lakes	5	180
Great Lakes (above inversion)	<0.5	<0.5

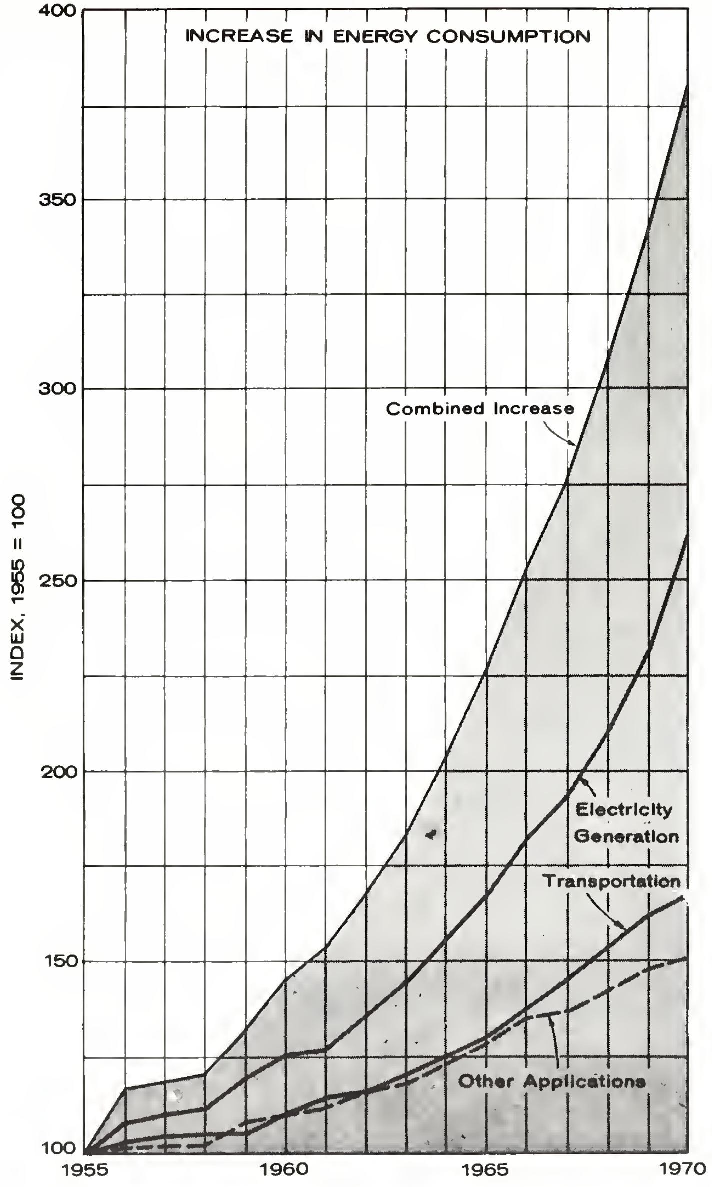

Figure 1.

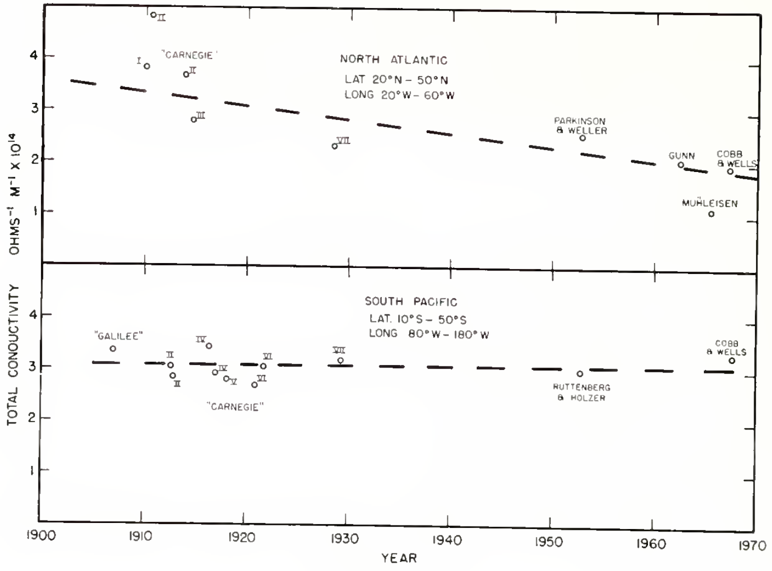

Figure 2.

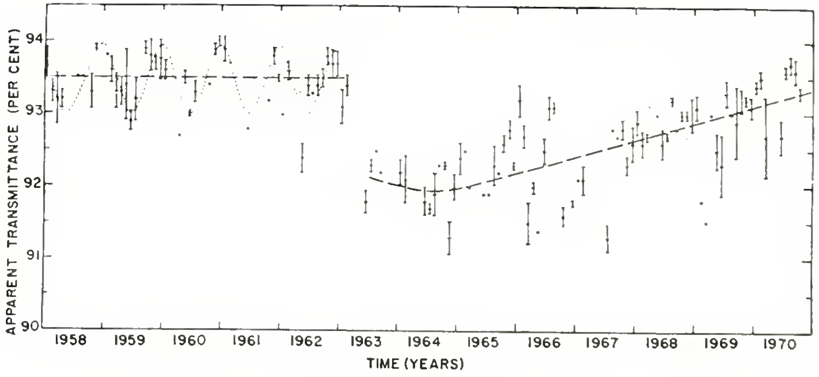

Figure 3.

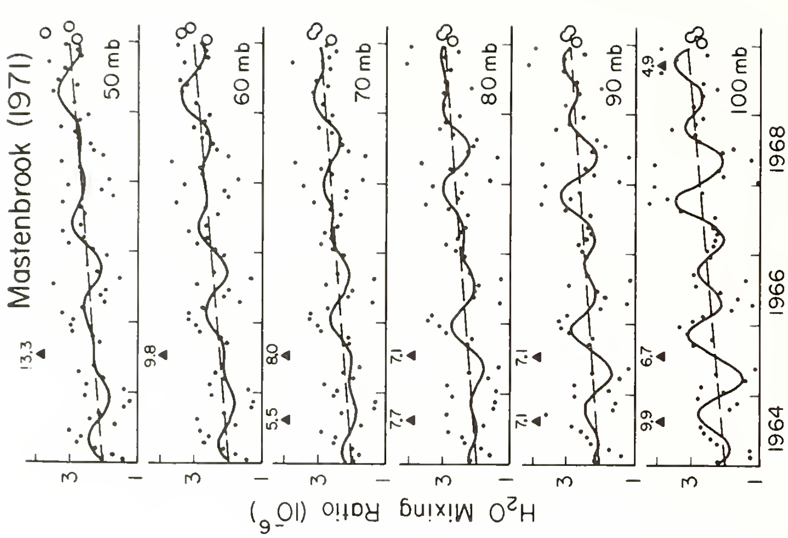

Figure 6.

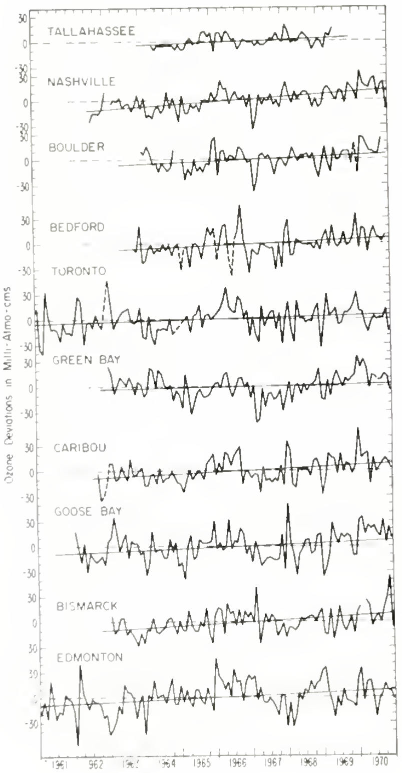

Figure 4.

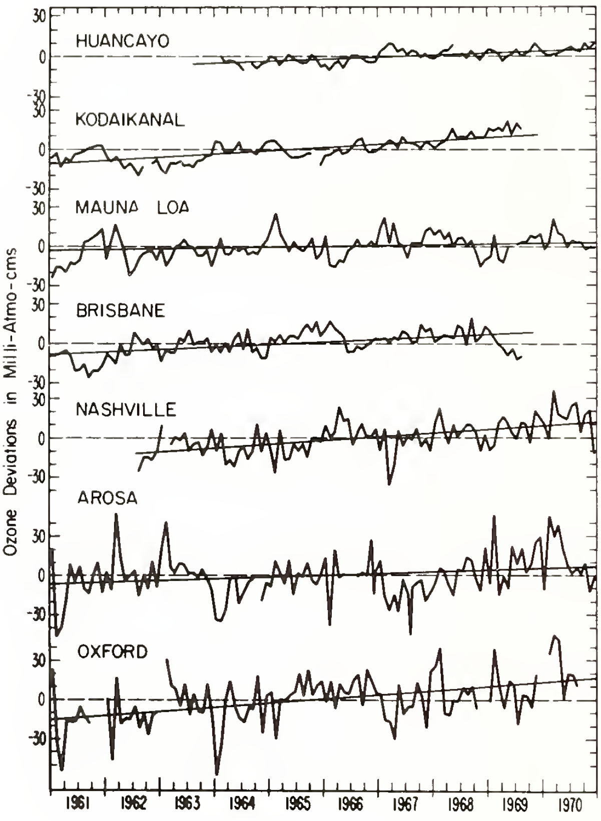

Figure 5.

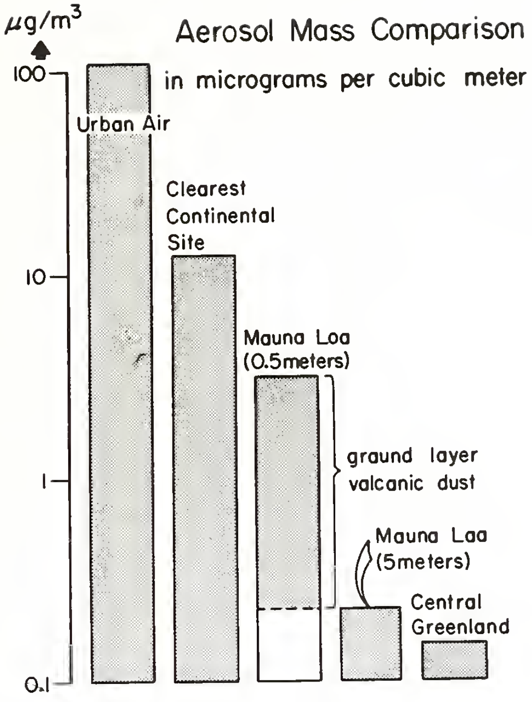

Figure 7.

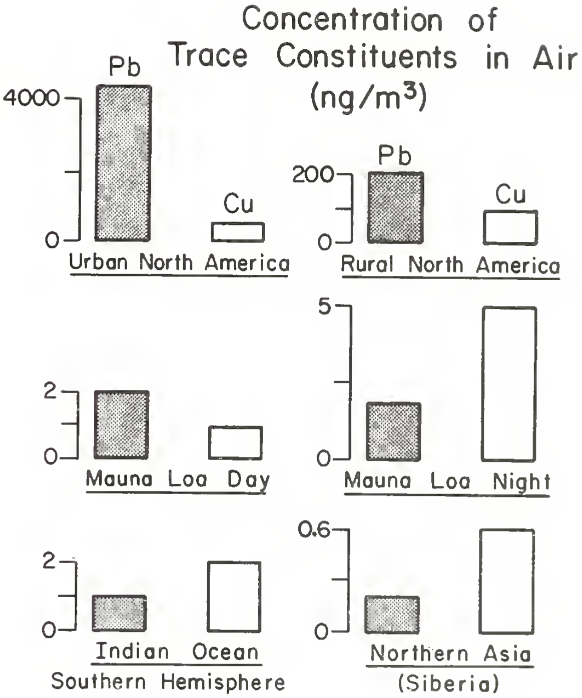

Figure 8.

Reprinted from Preprint Volume of the International Conference on Aerospace and Aeronautical Meteorology, May 22-26, 1972, Washington, D.C., published by AMS, Boston, Mass

THE SOURCES AND SINKS OF WATER VAPOR IN THE UPPER ATMOSPHERE

Helmut K. Weickmann and Charles C. Van Valin

Atmospheric Physics and Chemistry Laborstory
Environmental Research Laboratories
National Oceanic and Atmospheric Administration
Boulder, Colorado 80302

1. INTRODUCTION

1.1 Present state of H_2O concentration in stratosphere.

A number of studies have indicated a minimum mixing ratio of about 2 ppm for the lower stratosphere. McKinnon and Morewood (1970) deduced water vapor concentrations from solar spectra recorded from a high flying jet aircraft. During the 1967-68 Northern Hemisphere winter they found a maximum concentration of 1.75 ppm above the flight track of 17.7 km at 65N, and a progressive decline to a minimum of 1.25 ppm near 30S. Mastenbrook (1971) reporting a series of stratospheric water vapor concentration measurements at Washington, D. C., for the period 1963-69, has found a trend of increasing mixing ratio from 2 to 3 ppm (variability 1 - 5 ppm) although more recent measurements seem not to fit the rising trend (decrease during the past two years, Mastenbrook, private communication). Sissenwine et sl. (1968) found mixing ratios in the lower stratosphere at Chico, Calif. to be typically about 2 ppm at the minimum and increasing with altitude up to about 25 km. The mixing ratio reached a maximum of from 10 to 40 ppm within a few km of 25 km. Sporsdic measurement (Barclay et al. 1960), as well as the occurrence of mother-of-pearl clouds suggest the occurrence of even higher values.

If we assume a constant mixing ratio throughout the stratosphere (beginning at an average of 120 mb) of 3 ppm the total water content turns out to be 1.8×10^{15}g H_2O.

1.2 Residence time

Residence times of atomic bomb debris in the lower stratosphere are found to be between 12 and 18 mo half-life. There is a strong anisotropic diffusion in the stratosphere; horizontal diffusion coefficients have been found to be 10^9-10^{10}cm^2 sec^{-1}, while vertical diffusion coefficients are about 10^3cm^{2}sec^{-1} for the tropical stratosphere and 4×10^4cm^{2}sec^{-1} for middle latitudes (Dyer, 1970; Newell, 1962). This makes the definition of an average residence time for the entire stratosphere somewhst academic as it will depend on the level of injection.

2. SOURCES OF STRATOSPHERIC MOISTURE

The general opinion regarding moisture influx into the stratosphere is that the primary entry is through the equatorial tropopause filter. Convective upwelling to the tropopause level causes an adiabatic temperature of near -80C; this temperature is the approximate dewpoint in the stratosphere (Brewer, 1949; Junge, 1963). We feel that this argument is insufficient and that other mechanisms exist which transport H_2O into the stratosphere. High reaching convective storms, jet stream and mountain wave related interchange, seepage through the quasi-horizontal tropopause structure, and methane oxidation are examples of alternate mechanisms. We have attempted to attach transport values to some of these processes which we will discuss subsequently.

2.1 Hadley cell circulation.

The powerful circulation process of the Northern and Southern hemispheric Hadley cells is related to the Intertropical Convergence Zone and its meridional movements during the seasons. Its circulation mechanism reaches above the tropopause at least to the 10 mb level (Vincent, 1968). In computing the water vapor flux we follow the argument of Newell et al. (1969). According to Newell et al., a rising motion of about 0.02 cm sec^{-1} through the tropical tropopause is necessary to balance the heating rate of about 0.25C day^{-1} from the 15 micron CO_2 band minus the horizontal heat flux divergence of about 0.05C day^{-1}. In a later article, Newell (1970) assumed this mean rising motion to extend over a 15° latitude strip around the globe with a resulting upward movement of 2.4×10^{12}g of air per second.

Assuming a mixing ratio of 2 ppm to apply to the moisture carried into the stratosphere in a 15° latitude strip, Newell (1970) estimated the flux of moisture into the stratosphere at about 5×10^6g sec^{-1} (1.5×10^{14}g yr^{-1}) at the tropicsl tropopause. On the basis of Mastenbrook's findings, a mixing ratio of 3 ppm seems to be more realistic. Thus, the moisture flux would be 7.5×10^6g sec^{-1}, or 2.2×10^{14}g yr^{-1}. It is envisioned here that the Hadley cell flux passes slowly through the tropopause without affecting its location as this is determined by radiative parameters rather than by the dynamic conditions. For convective currents however the tropopause still is a barrier.

2.2 Convective storm contribution to stratospheric moisture.

Examples of tops of convective clouds at altitudes well above the tropopause are extensively documented. For example, Lee and McPherson (1971), in reporting their observations of thunderstorms over Oklahoma and Malaysia, noted that mean heights of tops in both areas during the study were 14.6 km (48,000 ft). Of 469 storms in Oklahoma with tops above 12.2 km (40,000 ft), 29 (6.2 percent) had tops in excess of 16.5 km (54,000 ft), with 4 of these exceeding 18.3 km (60,000 ft). Of 62 Malaysian storms, 5 (8 percent) had tops above 16.5 km, but none exceeded 17.7 km (58,000 ft).

A tropopause height of 12.2 km over Oklahoma is common, whereas, in tropical regions such as Malaysia, the tropopause is usually at about 15.2 km (50,000 ft). Therefore, one can assume that every Oklahoma storm which creates cloud tops above 12.2 km has at least entered the transition zone, and most have penetrated into the stratosphere. According to Lee and McPherson about 20 percent of tropical thunderstorms rise into the stratosphere.

That a cloud mass has entered the lower stratosphere does not mean, however, that the water contained therein is available for distribution within the stratosphere. It is entirely possible that most of the water merely sinks back into the troposphere when the storm decays. The mechanism by which the storms penetrate the tropopause is not entirely clear; we hesitate to subscribe entirely the parcel buoyancy theory and believe that in changing the stratospheric temperature structure strong radiation cooling effects of the spreading anvil play an important role in paving the way to reach the next higher level for subsequently rising storm turrets. The storm might be said to create its own tropopause when the thrust of the rising turrets pushes past the existing tropopause. Adiabatic expansion will create a region of very cold air which will subside to its equilibrium level when the storm updraft is removed. As an example, a typical plains states tropopause is about 12.2 km, with a temperature of about 213K. An air parcel carried to 15.2 km along the moist adiabat without mixing and radiant energy exchange would achieve a temperature of about 186K. This agrees with an analysis by Roach (1967).

In such a situation as just described, the uplifted cloud parcel could even act as a sink for stratospheric moisture. The density of water vapor at saturation over ice at 186K is about 1.9 x 10^{-10}g cm^{-3},whereas the water vapor density at 15.2 km, assuming a 3 ppm mixing ratio, would be about 6.1 x 10^{-10}g cm^{-3}. This, obviously, is an extreme case in which there is no mixing. In reality, a wind shear almost always exists and cloud parcels will mix with the ambient atmosphere, which is much warmer.

In the following discussion we estimate the vapor input into the stratosphere from the large thunderstorm of May 12, 1970, in norhteast Kansas, which was analyzed by Fujita (1972). This storm developed during a period of about 2 hr. At 1845 local time the anvil covered an area of about 60,000 km^2. Up to this time several tornadoes had formed, three of which touched ground, at least briefly. The tropopause was indicated at 11.9 km and a temperature of 212K. The greatest areal extent of the anvil occurred at 12.5 km, which was 0.6 km above the tropopause. More than half the area of the cloud top was above 13.1 km and several turrets rose from the anvil to altitudes as great as 15.8 km.

At the average altitude of the cloud top, ambient temperature was 213K and pressure was 160 mb. If the cloud had risen above the tropopause along its moist adiabat, its temperature would have been 199K. One can assume that mixing between cloud and ambient air produced a temperature at the interface of about 206K and that this interface was about 100 m thick. The environmental air which experienced such turbulent mixing within the interface assumed ice saturation,therefore acquired about 2.2 x 10^{10} g H_2O during its passage through the stratospheric anvil. This number is based upon an upstream humidity of 3 ppm, an anvil area of 60,000 km^2 and a mixing depth of 0.1 km. The stratospheric wind vector on this day required 5 hr for complete passage through the anvil. The downstream humidity increase is a factor of 5 which is in excellent agreement with the measured value of Kuhn et al. (1971) on another storm.

The assumptions upon which this result is based are rather conservative, and it seems entirely probable that this quantity of evaporated water would be mixed with stratospheric air, and would remain in the stratosphere after the bulk of the anvil subsided back to the troposphere following decay of the storm. In cases of higher wind shear between troposphere and stratosphere, a much deeper layer of the anvil would be turbulently mixed with stratospheric air, and proportionately more moisture would be contributed to the stratosphere.

There exists a great difficulty in estimating the influx of water vapor into the stratosphere from thunderstorm activity due to the lack of climatological statistics of thunderstorm frequency. If we accept - faute de mieux - Brooks' 1925 statistics of 44,000 thunderstorms occurring each day around the globe, we feel to be very conservative in the assumption of a daily number of 100 thunderstorms of the type described above, then the stratospheric input from this source would be 8 x 10^{14} g yr^{-1}. Sissenwine et al. (1972), using an entirely different approach, have obtained a similar though somewhat smaller magnitude for the vapor input by storms.

2.3 Stratospheric-tropospheric interchange through the mid-latitude tropopause gaps.

Vincent (1968) studied mean-meridional circulations in the lower stratosphere (100 to 10 mb) for for the years 1964 and 1965 between 22.5N and 82.5N. In winter, he found upward motion over high latitudes and downward motion over middle latitudes. There was a progression of the overall flow toward the pole with the approach of the summer season and toward the equator with approaching winter. North of 50N, the flow is predominantly downward and equatorward in May, and downward and poleward in September.

In winter months, the motions are much more intense than in summer. Lower stratospheric motions over mid-latitudes seem to be an extension of the tropospheric Ferrel cell (Vincent, 1968).

Reiter et al. (1967) have shown the jet stream region to be one of the major areas of stratospheric-tropospheric interchange. They studied the period 18-21 April 1963 involving a jet stream of average intensity and average cyclogenetic activity. Their study indicated that outflow of air from the stratosphere by the jet stream system under consideration exceeded the inflow of air through the same system almost by a factor of 2. In the 210 mb layer, which was considered to be a representative total thickness of the three isentropic levels studied, 310, 320, and 330K, the net outflow of air from the stratosphere was estimated to be 6.0×10^{16} g hr^{-1}.

The gross inflow of air is inferred, therefore, to be of similar magnitude. For average conditions we assume the following humidities for inflow and outflow: outflow - lower stratospheric value of 25 ppm; inflow - upper tropospheric value of 50 ppm. The latter value amounts to 25 percent relative humidity at a temperature of -50C. These values are conservative as on the anticyclonic inflow sides permanent vapor trails behind jet aircraft have an "excess frequency" (Endlich and McLean, 1957). This indicates that ice saturation frequently occurs which, at the temperature given, occurs at a water vapor density 65 percent of that over water.

With such humidities as mentioned above the mass of water transferred between the upper troposphere and the lower stratosphere would be in approximate balance. Such a balance is seen as reasonable in view of Mastenbrook's (1971) stratospheric humidity data at Washington, D. C., showing maximum mixing ratios in late summer. An appreciable net-infusion of moisture into the stratosphere in connection with the jet stream would likely produce a higher mixing ratio in late winter, following the period of maximum jet stream activity. We accept Danielsen's (1968) concept; he considers the lower stratosphere as a deep transition layer where mean flow is across the tropopause from the troposphere to the stratosphere. The inflow increases the mass of the stratosphere, which increase is offset by a mass outflow accompanying tropopause folding. Fall and winter are times of net mass inflow to the stratosphere, with removal occurring during spring and summer. Danielsen calculates that 75 percent ± 25 percent of the stratospheric mass is exchanged annually.

From these considerations we conclude that jet stream systems do not produce a net gain of water vapor into the stratosphere. However, we must add a caveat to this conclusion. The computation of the balance between inflow and outflow involves the difference between two large numbers. Any assymmetry in the inflow-outflow could mean either a large net gain or large net loss of stratospheric water. If, instead of the 25 ppm water vapor mixing ratio, suggested for the lower stratosphere, the true ratio was 15 ppm, the net result would be transfer of 1.2×10^{12} g of water per hour to the stratosphere. Assuming such a system operates over the northern hemisphere through a No. 4 Rossby wave for half of each year, the infusion of water to the northern hemisphere stratosphere could be on the order of 2×10^{16} g annually.

R. M. Smith (1968) derived an even larger infusion of water vapor in his study of the transport of tritium and water vapor upward through the tropopause during July 1962 through the combined influences of the jet stream region, the baroclinic zones, and tropopause gaps.

As mentioned above, balance between water vapor inflow and outflow is seen as reasonable in light of Mastenbrook's data. However, occasional large injections are not ruled out, and could, in fact, be indicated by the appreciable number of Mastenbrook's determinations which are in excess of 6 ppm.

2.4 Methane oxidation contribution to stratospheric moisture.

Methane is present in the troposphere at about 1.5 ppm (Bainbridge and Heidt, 1966; Kyle et al., 1969; Ehhalt, 1967; Robinson and Robbins, 1968). The mixing ratio above the tropopause has been found to decrease with altitude, going approximately to zero at or below the stratopause (Scholz et al. 1970). Bainbridge and Heidt (1966) deduced vertical transport of methane by eddy diffusion across the mid-latitude tropopause to be about 4.4×10^{-6} g $cm^{-2} yr^{-1}$, or about 2.2×10^{13} g yr^{-1} worldwide. From $^{14}C/^{12}C$ ratios they deduced that 75 percent of atmospheric methane is produced by contemporary biological reactions, with the remainder coming from fossil sources, such as oil fields and volcanoes.

Koyama (1963) estimated methane production at 2.7×10^{14} g yr^{-1}. However, Robinson and Robbins (1968) considered this too low because of neglect of methane production from swamps and from humid tropical areas. Robinson and Robbins estimated annual production of methane from all sources to be about 1.5×10^{15} g yr^{-1}, or roughly five times the production estimated by Koyama.

If one uses the estimate of Newell (1970) for rising motion of air at the tropical tropopause, the flux of methane into the stratosphere through Hadley cell circulation would be approximately 3.5×10^{6} g sec^{-1}, or 1.1×10^{14} g yr^{-1}. Methane is presumably oxidized completely to water and carbon dioxide through the reaction with atomic oxygen, wherein two molecules of water are derived from each methane molecule. Therefore, the flux into the stratosphere of 1.1×10^{14} g of methane per year would be a potential source of 2.5×10^{14} g of water. Undoubtedly, however, an appreciable portion of this methane is recycled back to the troposphere with descending Hadley or eddy circulation before reaction and formation of water can take place. Singer (1971) computed a rate of disappearance of methane in the stratosphere of 3×10^{-13}g cm^{-2} sec^{-1}, or 1.53×10^{6} g sec^{-1}worldwide. This is 42 percent of the calculated flux into the stratosphere according to Newell's Hadley cell flux estimates. Intuitively, it seems reasonable that more than half of the injected methane returns to the troposphere. It is well, of course, to keep in mind that there is some disagreement on the strength of the Hadley cell rising motions (Newell, 1969, 1970; Manabe and Hunt, 1968; Reed and Vlcek, 1969; Kidson et al., 1969), with most authors using a value of about 0.04 cm sec^{-1}, and on the latitudinal extent of the rising motions. Assuming Singer's estimate of methane oxidation to be correct, we get the formation of 3.4×10^6 g sec^{-1} (1.1×10^{14} g yr^{-1}) H_2O.

2.5 Volcanic activity as a source of water vapor.

It has been long recognized that water is a major constituent of volcanic gases, and the force required to produce an explosive eruption is thought to derive from a release of pressure sufficient to permit vaporization of the water in the magma (Bullard, 1962, pp. 37-43). Day and Shepard (Bullard, loc. cit.) in 1912 determined that steam averaged 68.2 percent by volume in the gases of Kilauea Crater, which at that time had a permanent lake of molten lava. More recently, Heald et al. (1963) used more modern techniques to analyze the gases from Kilauea during and following the eruptions of 1959 and 1960. They found water and carbon dioxide to be the dominant gases, with most samples containing water at more than 90 mole percent.

The volcanic cycle beginning in 1963 and ending in 1970 has seen seven eruptions in which the eruption cloud entered the stratosphere. In March, 1963, Agung volcano on the island of Bali erupted in the single most significant explosive event since Bezymianny in 1956. A month later Trident in Alaska erupted, spewing gas and ash clouds to 15 km altitude, and in November, 1963, Surtsey began to form in the sea off Iceland. Surtsey exploded with the greatest violence when the crater was open to the sea, but the eruption cloud rose to the greatest altitude after the crater rim blocked entry of the water. Surtsey's eruption cloud apparently rose to about 50,000 ft (Cronin, 1971). Other eruptions which ejected gas and ash into the stratosphere were Taal valcano in the Phillipines in September, 1965, Redoubt in Alaska in January and February, 1966, Fernandina, in the Galapagos Islands in May, 1968, and Hekla in Iceland in May 1970.

Although all volcanoes emit considerable amounts of water, three of these seven eruptions, Surtsey, Taal, and Fernandina, were phreatic or submarine explosions, and may have injected significant quantities of water vapor into the atmosphere. Surtsey, during its first 3 months when sea water had access to the tephra walls, may very well have been a source of stratospheric water for the northern stratosphere. It is interesting that Mastenbrook's (1971) data show no special H_2O increase in 1964 except for a high value during mid-1964 several months after the Surtsey eruption. Of course, this high value is considered by the author to be a measuring error.

Wilson and Nichparenko (1966) estimated the volume of gas ejected during the climactic eruption of Redoubt to be 9 km^3. If, to conjecture an extreme situation, one assumes that Surtsey, Taal, or Fernandina had ejected 10 km^3 of water vapor, beginning at a density of about 1 kg m^{-3}, to stratospheric altitudes, the resulting mass of water in the stratosphere, about 10^{13} g, would probably have been notable before dispersion. However, following dispersion, but assuming no loss, the water density from the volcanic injection would be only one percent of the normal stratospheric water vapor. From this it seems very unlikely that volcanic eruptions during the recent period of activity have in any way affected stratospheric water vapor concentrations.

3. REMOVAL OF STRATOSPHERIC MOISTURE

Above ca 70 km water vapor is destroyed through photochemical presses, largely through photodissociation by solar ultraviolet of wavelength <2340Å. The water vapor density in the vicinity of the mesopause at photochemical equilibrium would be approximately two orders of magnitude lower than the actual density based on the assumption that noctilucent clouds are water clouds. Thus, at least for the summer mesopause, mechanisms for upward transport of water vapor are necessary. Christie (1969) postulates a mesospheric water vapor mixing ratio of 3 ppm, and a mean upward motion of 1 cm sec^{-1} and an eddy diffusion coefficient of 10^7 cm^2 sec^{-1} to account for observed noctilucent clouds between 82 and 85 km with temperatures of 138K to 140K. Hesstvedt (1968) assumes a water vapor mixing ratio of 5 ppm up to 65 km, with upward eddy diffusion coefficients ranging from 4×10^5 cm^2 sec^{-1} at 65 km to 7×10^6 cm^2 sec^{-1} at 100 km. Since these diffusion coefficients are valid for both upward and downward motions, we may draw the guarded conclusion that the noctilucent cloud levels do not constitute a major sink for stratospheric water.

Because water is not consumed within the stratosphere the only significant mechanism for removal from the stratosphere must, of necessity, lie in the large scale atmospheric circulation, primarily the Hadley and Ferrel cells, and general seepage through the tropopause.

4. CONCLUSION

Present evidence supports the acceptance of an average stratospheric water vapor mixing ratio of 3 ppm. If the average tropopause level is assumed to lie at 120 mb, the stratosphere then contains about 1.8×10^{15} g of water vapor. We have herein presented evidence supporting sources of stratospheric moisture as follows:

Hadley cell tropical updraft:	2.2×10^{14} g yr^{-1}
Severe local storms	8×10^{14} g yr^{-1}
Methane oxidation:	1.1×10^{14} g yr^{-1}

Thus, the total infusion from these sources is on the order of 1.1×10^{15} g yr^{-1}. This figure has a very reasonable relationship to the estimated total quantity of water vapor in the stratosphere, considering the estimates of residence time of radioactive debris in the stratosphere of 12 to 18 months.

It is well to appreciate the limitations in the derivation of these numbers, however. First and foremost, of course, is the incomplete state of knowledge regarding thunderstorm frequency and intensity, and the mechanism whereby these storms push above the tropopause. As presented here, the thunderstorm mechanism is the largest single source of stratospheric moisture, and uncertainty about the frequency of occurrence of even 50 percent would cause a large change in the estimate of residence time.

Also, present evidence indicates that mid-latitude thunderstorms contribute in a much more significant way to stratospheric water than do tropical thunderstorms. Injections in mid-latitudes, however, are much more likely to occur in areas of general subsidence of stratospheric air than are tropical injections. In addition, mid-latitude injections are in much closer proximity to regions of northward and downward flow, which have been shown to be regions of primary removal of nuclear bomb blast debris. For these reasons, material injected at mid- or high latitudes will have somewhat shorter residence times than material injected in the low latitudes.

We have accepted the arguments of Newell and his co-workers regarding the velocity and areal extent of the mean rising motions in the Hadley cell circulation. The uncertainty regarding these parameters has been mentioned earlier. One of the reasons for uncertainty in this very difficult computation is the fact that the Hadley cells do not operate continuously around the globe, but operate in a few, or several, areas simultaneously, and not in others. The spacing of active Hadley cells could possibly be related to a Rossby wave.

Reports of research quoted in this paper repeatedly mention the possibility of quasi-biennial cycles and the consequences for stratospheric circulation. J. W. Smith (1971) has presented some interesting thoughts on the origin of the quasi-biennial oscillations and the resulting stratospheric circulation patterns. For example, he argues that rapid transport of tropical stratosphere air parcels, and occasional rapid overturning of the stratosphere are consequences of the imposition of the approximate 11 yr sunspot cycle on a biennial atmospheric cycle.

Finally, SST engine water emissions in the stratosphere, expected to be about 0.8 x 10^{14} g yr^{-1} during the years of projected full utilization, is seen in the context of the water vapor sources as presented to be relatively minor.

5. REFERENCES

Bainbridge, A. E., and L. E. Heidt, 1966: Measurements of methane in the troposphere and lower stratosphere. Tellus, 18, 221-224.

Barclay, F. R., M. J. W. Elliott, P. Goldsmith, and J. V. Jelley, 1960: A direct measurement of the humidity in the stratosphere using a cooled-vapour trap. Quart. J. Roy. Meteor. Soc., 86, 259-264.

Brewer, A. W., 1949: Evidence for a world circulation provided by the measurements of Helium and water vapour distribution in the stratosphere. Quart. J. Roy. Meteor. Soc., 75, 351-363.

Brooks, C. E. P., 1925: The distribution of thunderstorms over the globe. Geophys. Mem., 3, 145-164.

Bullard, F. M., 1962: Volcanoes in history, in theory, in eruption. Austin, Univ. of Texas Press.

Christie, A. D., 1969: The genesis and distribution of noctilucent cloud. J. Atmos. Sci., 26, 168-176.

Cronin, J. F., 1971: Recent volcanism and the stratosphere. Science,172, 847-849.

Danielsen, E. F., 1968: Stratospheric-tropospheric exchange based on radioactivity, ozone and potential vorticity. J. Atmos. Sci., 25, 502-518.

Dyer, A. J., 1970: Anisotropic diffusion coefficients and the global spread of volcanic dust. J. Geophys. Res., 75, 3007-3012.

Endlich, R. M., and G. S. McLean, 1957: The structure of the jet stream core. J. Met., 14, 543-552.

Enhalt, D. E., 1967: Methane in the atmosphere, J. Air Pollut. Contr. Assoc., 17, 518-519.

Fujita, T. T., 1972: Tornado occurrences related to overshooting cloud-top heights as determined from high-resolution ATS pictures showing anvil clouds near Salina, Kansas. SMRP Research Paper No. 97, University of Chicago.

Heald, E. F., J. J. Naughton, and I. L. Barnes, Jr., 1963: The chemistry of volcanic gases. J. Geophys. Res., 68, 545-557.

Hesstvedt, E., 1968: On the effect of vertical eddy transport on atmospheric composition in the mesosphere and lower thermosphere. Geofys. Publikasjoner, 27, No. 4, 35 pp.

Junge, C. E., 1963: Air chemistry and radioactivity. New York Academic Press.

Kidson, J. W., D. G. Vincent, and R. E. Newell, 1969: Observational studies of the general circulation of the tropics: long term mean values. Quart. J. Roy. Meteor. Soc. 95, 258-287.

Koyama, T., 1963: Gaseous metabolism in lake sediments and paddy soils and the production of atmospheric methane and hydrogen. J. Geophys. Res., 68, 3971-3973.

Kuhn, P. M., M. S. Lojko, and E. V. Petersen, 1971: Water vapor: stratopsheric injection by thunderstorms. Science, 174, 1319-1321.

Kyle, T. G., D. G. Murcray, F. H. Murcray, and W. J. Williams, 1969: Abundance of methane in the atmosphere above 20 kilometers. J. Geophys. Res., 74, 3421-3425.

Lee, J. T., and A. McPherson, 1971: Comparison of thunderstorms over Oklahoma and Malaysia based on aircraft measurements. Proc. Intern. Conf. Atmospheric Turbulence (Royal Aeronautical Society, London), p. B1.

Manabe, S., and B. G. Hunt, 1968: Experiments with a stratospheric general circulation model, 1. Radiative and dynamic aspects. Mon. Wea. Rev., 96, 477-502.

Mastenbrook. H. J., 1971: The variability of water vapor in the stratosphere. J. Atmos. Sci., 28, 1495-1501.

McKinnon, D., and H. W. Morewood, 1970: Water vapor distribution in the lower stratosphere over North and South America. J. Atmos. Sci., 27, 483-493.

Newell, R. E., 1962: The general circulation of the atmosphere and its effects on the movement of trace substances. Studies of the Stratospheric General Circulation, Final Report, Planetary Circulations Project, V. P. Starr, Dir., Dept. of Meteorology, Massachusetts Institute of Technology, 304-347.

Newell, R. E., J. W. Kidson, and D. G. Vincent, 1969: Annual and biennial modulations in the tropical Hadley cell circulation. Nature, 25, 76-78.

Newell, R. E., 1970: Water vapour pollution in the stratosphere by the supersonic transporter? Nature, 226, 70-71.

Reed, R. J., and C. L. Vlcek, 1969: The annual temperature variation in the lower tropical stratosphere. J. Atmos. Sci., 26, 163-167.

Reiter, E. R., M. E. Glasser, and J. D. Mahlman, 1967: The role of the tropopause in stratospheric-tropospheric exchange processes. Atmospheric Science Paper No. 107, Colorado Station University, 32 pp.

Roach, W. T., 1967: On the nature of the summit areas of severe storms in Oklahoma. Quart. J. Roy. Meteor. Soc., 93, 318-336.

Robinson, E., and R. C. Robbins, 1968: Sources, abundance, and fate of gaseous atmospheric pollutants. Final Report, SRI Project PR-6755, Stanford Research Institute, 123 pp.

Scholz, T. G., D. H. Ehhalt, L. E. Heidt, and E. A. Martell, 1970: Water vapor, molecular hydrogen, methane, and tritium concentrations near the stratopause. J. Geophys. Res., 75, 3049-3054

Singer, S.F., 1971: Stratospheric water vapour increase due to human activities. Nature, 233, 543-545.

Sissenwine, N., D. D. Grantham, and H. A. Salmela, 1968: Humidity up to the mesopause. Air Force Surveys in Geophysics, No. 206, AFCRL, Cambridge, Mass.

Sissenwine, N., A. J. Kantor, and D. D. Grantham, 1972: How dry is the sky? - A decade later and the SST. Unpublished manuscript, 40 pp.

Smith, J. W., 1971: The genesis of sudden stratospheric warnings and the quasi-biennial cycles. NASA Technical Note, NASA TN D-6522, Marshall Space Flight Center, 23 pp.

Smith, R. M., 1968: A preview on the determination of mass return flow of air and water vapour into the stratosphere using tritium as a tracer. Tellus, 20, 76-81.

Vincent, D. G., 1968: Mean meridional circulations in the Northern Hemisphere stratosphere during 1964 and 1965. Quart. J. Roy. Meteor. Soc., 94, 333-349.

Wilson, C. R., S. Nichparenko, and R. B. Forbes, 1966: Evidence of two sound channels in the polar atmosphere from infrasonic observations of the eruption of an Alaskan volcano. Nature, 211, 163-165.

☆ U.S. GOVERNMENT PRINTING OFFICE: 1973 — 784-572 / 1233 REGION NO. 8

PENN STATE UNIVERSITY LIBRARIES
A000072832844